

AD-A273 664



**12<sup>th</sup>  
International  
Corrosion  
Congress**

**PRECEEDINGS**

**S DTIC  
ELECTE  
DEC 09 1983  
A**

**September 19-24, 1983  
Volume 3B  
Houston, Texas USA**

**93-29557**

This document has been approved  
for public release and sale; its  
distribution is unlimited.

**CORROSION:  
SPECIFIC ISSUES**

**NACE**  
International

**93 12 2 098**

**Best  
Available  
Copy**

# ***CORROSION CONTROL FOR LOW-COST RELIABILITY***



**12<sup>th</sup>  
International  
Corrosion  
Congress**

**PRECEEDINGS**

**VOLUME 3B**

***CORROSION: SPECIFIC ISSUES***

*The manuscripts in this volume have been printed from camera-ready copy and have been accepted without editing by NACE International.*

*Neither NACE International, its officers, directors, members thereof, nor instructors accept any responsibility for the use of the methods and materials discussed herein.*

*Any goods, products, and/or services mentioned are mentioned as items of information only. Such mention does not constitute an endorsement by NACE International.*

*The information is advisory only, and use of the materials and methods is solely at the risk of the user.*

Printed in the USA. All rights reserved. This book, or parts thereof, may not be reproduced in any form without permission of the copyright owners.

Copyright, NACE International, 1993

ISBN: 1-877914-65-7

Published by

NACE International  
P.O. Box 218340  
Houston, TX 77218-8340

Accession For	
NTIS	CRASH <input checked="" type="checkbox"/>
DTIC	148 <input type="checkbox"/>
Unannounced	<input type="checkbox"/>
Justification	
By	Vol 3B-142
Distribution	STC 400
Availability Codes	
Dist	Availability for Special
A-1	21

DTIC QUALITY INSPECTED 3

**NACE**  
International



## Corrosion in Heavy-Duty Diesel Engine Cooling Systems

Benjamín Valdez Salas  
Universidad Autónoma de Guadalajara  
ICET-Química  
Av. Patria 1201 C.P. 44100  
Guadalajara, Jalisco, México

### Abstract

Pitting and cavitation corrosion in ferrous components of heavy-duty diesel engine cooling systems are actually a serious problem in the Mexican transport industry. To avoid this, a corrosion inhibitor formulation for an antifreeze-coolant was developed, chemical analysis, metallographic assays, gravimetric and electrochemical polarization corrosion studies, were carried out for the evaluation of corrosion inhibition. The causes of the problem were found and the new developed formulation had a good performance according with the corrosion parameters established in operation specifications of the heavy-duty diesel engine truck manufacturers. Problem solutions and recommendations are given for a more long life of the diesel engines.

### Introduction

The corrosion problem in automotive cooling systems have been studied (1,2). Damages by corrosion in heavy-duty diesel engine cooling systems occurs in less than a year (3,4). Coolants for such systems are composed by water, monoethylenglycol (or another glycol), corrosion inhibitors, anti-foaming and scale inhibitors, the last three are named supplemental coolant additives (SCAs). Most of antifreeze coolant is formulated to meet the less demanding needs of passenger cars, thus the blend of chemicals results inadequate to prevent heavy-duty diesel engine damage. When these formulations are used in heavy-duty service, liner pitting and deposits on heat transfer surfaces (heads, radiator, etc) occurs, such problems will be controlled. To do this SCAs employ water-soluble polymers and detergents, not found in automotive type antifreeze.

The more frequently corrosion problems that occur are pitting of wet sleeve liners and cavitation corrosion on water pump impellers, wet sleeve liners are subject to intense vibration during normal operation, thus, wet sleeve liners will be perforated in less than 160,000 km of service. If the chemistry of coolant is not properly maintained. When this occurs, coolant can leak into the crankcase, destroying the bearings and crankshaft and requiring an expensive engine rebuild. Grade of corrosion is affected for various factors like, aeration, presence of salts, temperature, pressure, galvanic pairs, and principally maintenance (3). So, methods have been described by ASTM (5,6) for evaluation of corrosive effects in automotive cooling systems, with them a formulation developed in our laboratory will be evaluated in their corrosion inhibition properties and chemical stability.

The main metallic component in heavy-duty diesel cooling systems is cast iron, although, copper, aluminium, tin, tinbrass and steel are metals to be considered, because they are presents in cooling system treated in this study.

## Experimental

### Chemical analysis

Qualitative chemical analysis were performed on samples of water obtained or radiator purge in different trucks. In this way, presence of sulphate, chromate, Chloride and nitrite anions was confirmed. A similar analysis was carried out on aqueous solutions of the cake contained in cartridges of new and old conditioner water filters, 10.0g of this cake were dissolved in 1 l. of tap water to simulate a more real characteristics of cooling fluid in operation. Metallic samples of wet sleeve liners and water pump impellers were donated by heavy transport lines, the most of them has a pitting corrosion and cavitation. A small portion was cut, immersed in polyester resin and polished with alumine-0.1 m, after that, a metallographic analysis to 400 X was carried out without previous chemical etch, for this purpose a Versamat metallographic microscope was necessary.

### Foaming test

Foaming test was executed on solutions with 33% (w/w) of antifreeze, following the standar ASTM D-1881-73 a portion of 150 ml was placed in a 500 ml graduated to be and heated to  $88 \pm 1$  C with a controlled temperature bath, then air was bubbled by five minutes through a porous stone diffusor to give a 100 ml/min flow rate. Initial and final volume of foam in the tube were registered and the levels difference reported like foam height, the airflow is turned-off and time at which liquid-surface begin to appear is recorded.

### Antifreeze development

The antifreeze-coolant formulation was developed using 95% (w/w) of monoethylenglycol, 0.01% w/w antifoaming (Dow. Co.), corrosion inhibitors like sodium molybdate, sodium benzoate, sodium nitrite, phosphates, mercapto benzothiazol, sodium hidroxide and sodium silicate in a percent weight by weight no more than 3.4% were added, the rest was water to give 100%.

### Gravimetric corrosion tests

Gravimetric corrosion tests were performed according to ASTM D-1384. Metallic samples of tin, brass, tin brass, copper, cast iron, steel and aluminium were cut at dimensions of 5 cm x 10 cm, polished to 600 SiC paper, washed with detergent and water and dried with hot air and benzene they were weighed and ensambled like (5). Plates were immersed in an aqueous solution of 1% (w/w) of cake cartridge of conditioner water filter, heating was provided by hot plate under aeration conditions for two weeks at this time samples were removed and cleaned to eliminate corrosion products, dried and weighed to get the gravimetric factor.

### Electrochemical measurements

A three electrode cell was used for electrochemical measurements, working electrodes were made with the metals mentioned previously to give a surface of  $2 \text{ cm}^2$ . Counter electrode was a graphite rod of 0.2 cm of diameter and 15 cm of length. Reference electrode was a saturated calomel electrode (SCE) with a luggin capillary-like junction. A solution of developed antifreeze at 33% (w/w) in corrosive water (5) was used like solution test. Previously to each experiment. Solution was circulated, through a conditioner filter and chemical stability was checked by presence of absence of precipitates and colour changes. Solutions with shown good chemical

cal stability were placed in a electrochemical cell and an air flow rate was placed necessary to saturate solution, cell was heating to  $88 \pm 1$  C. Electrodes were immersed into solution and polarization measurements were carried-out of - 250 mV to + 250 mV - over rest potential  $E_e$ , with a potentiostat galvanostat PG5-150 (IN TERTECH SYS). Results were fed to a microcomputer and plots of potential (E) vs current logarithm (log I) were obtained. A similar experiment was run for a blank.

## Results and discussions

Qualitative analysis of water is positive to sulphates and chlorides principally, while chemical analysis practiced over cakes of cartridge filters give higher concentration of chromate ions for about 7-8% (w/w). This a hoped result, because it is the main corrosion inhibitor used by Mexican manufacturers of filters. Moreover, also was detected, small quantities of several anions like nitrites, nitrates, silicates, phosphates, and a great quantity of cationic interchange resin. Analysis in old cakes with more than 5000 km of use, give presence of chloride ions for 3178 mg/l.

Table I, show results of gravimetric test when the corrosive solution was the developed formulation, and the solution of cake cartridge of conditioner filter against specifications of general motors Co.

A visual examination of the plates after experimentation in aqueous solution of cake, show light darkness film over copper and brass surfaces, while tin brass plates undergoes dissolution of tin, cast iron and steel present pitting corrosion, aluminium was covered for a black film and no show depletion.

Figure 1, show, metallographic analysis performed on cast iron surface without previous chemical etch, morphology is characteristic of an alloy with approximately 3.5% w/w of carbon content and high content of phosphorus stabilized with silicon, this can be observed like a continuous phase structure of cementite and ferrite -- this result is in agreement with specifications<sup>8</sup> for irons used in wet sleeve-liners manufacturer.

Table II, show current density ( $i_{corr}$ ) data for each metal, which were calculated from experimental results of electrochemical polarization tests. Also, plots of potential vs log. I can be observed in figures 2a of 2f. Polarization curves for copper and their alloys show, how brass materials have a tendency to passivation, however, shifting to low  $i_{corr}$  values are minimums, copper have a tendency to remain a minimum  $i_{corr}$  without passivation over a 150 mV range, approximately (-364 to -214 mV). Anodic curve for cast iron having a minimum tendency to arise  $i_{corr}$  in a 200 mV range, while steel is slowly passivated in a range of 300 mV. Aluminium is quickly oxidized and protected after 50 mV in anodic zone.

In this sense I can say that a decrease in corrosion rate is obtained by the formation of protective films and no pure passivation. This is a good new, because a passive film can be depleted by presence of chloride or sulphate ions.

## Conclusions

1. Serious problems of corrosion in heavy-duty engine cooling. Systems occurs by a bad maintenance program of the trucks and low quality of antifreezes and SCAs in conditioner filters. SCAs deplete at very different rates, therefore, one must be careful as to which conditioner filters are chosen as a measure of the coolant fluid condition.

2. Metals used in wet sleeve liners construction are in agreement with specification of alloy composition.

3. The new developed formulation have satisfactory effects in the corrosion inhibition, because, it's a mixed inhibitor and not a passivating agent also show high-chemical stability.

In this way chloride and sulphate concentrations will have a minimum effect on corrosion rate.

## References

- 1.- D. Hungens; N. Bulgeski, Truck engineering, SAE, Nov. (1990), pp. 40-46.
- 2.- B. Valdez, A. Medrano, E. Zavala, M. Arevalo. Memoria XXVI Congreso Nacional de Química Pura y Aplicada, Monterrey N.L., 1990. No. 47.
- 3.- B. Valdez, G. Guerra, J. Sampedro, N. Rosas. CORROSION, Vol. 2, No. 3, 1991, pp. 11-15.
- 4.- B. Valdez, G. Guerra, A. González, R. Doniz. CORROSION, Vol. 3, No. 4, 1992, pp. 33-37.
- 5.- American Society for Testing Materials, Annual Book of ASTM, Standards, ASTM, - Philadelphia, 1976, D-1881.
- 6.- American Society for Testing Materials, Annual Book of ASTM Standards, ASTM, - Philadelphia, 1976. D-1384.
- 7.- General Motors Company, General Motors Engineering Standards. G.M. Company, Materials and Processes, 1977. pp. J-41-103.
- 8.- Taylor Lyman, Metals Handbook, ASM, Metals Park, Novelty, Ohio, 1960.

TABLE I

Gravimetric corrosion tests. Weight loss data

Metal	Weight Loss (mg)		
	A	B	C
Copper	7.90	3.50	10.00
Brass	13.40	4.60	10.00
Tin brass	8.70	4.80	20.00
Steel	16.40	4.00	10.00
Cast Iron	25.50	6.20	10.00
Aluminium	53.90	10.80	20.00

A: Comercial Antifreeze

B: Developed Antifreeze

C: Estandar GM 1899-M, especifications.

TABLE II

Results of electrochemical corrosion tests. Corrosion currents using the developed antifreeze.

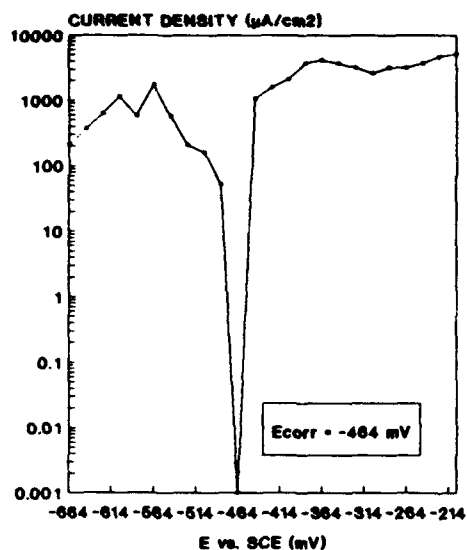
Metal	Corrosion Current	
	A	B
Copper	19.6	413.0
Brass	7.1	7850.0
Tin brass	16.0	3943.0
Steel	16.2	5163.0
Cast Iron	124.0	4540.0
Aluminium	439.0	6680.0

A: Antifreeze within inhibitor  
B: Antifreeze without inhibitor



Figure 1. Photomicrography of a sample of cast iron used in construction of wet sleeve (400X).

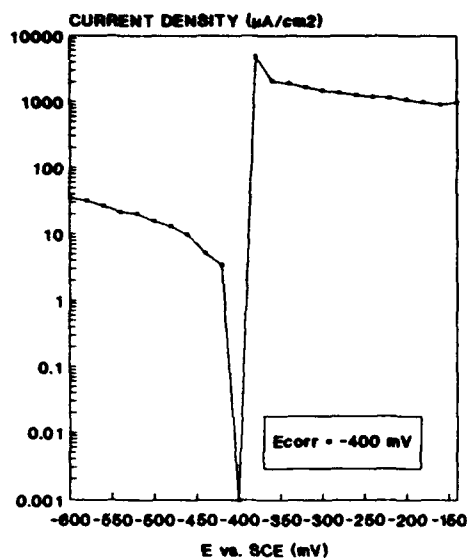
### POLARIZATION CURVE COPPER



DEVELOPED ANTIFREEZE

FIGURE 2.a

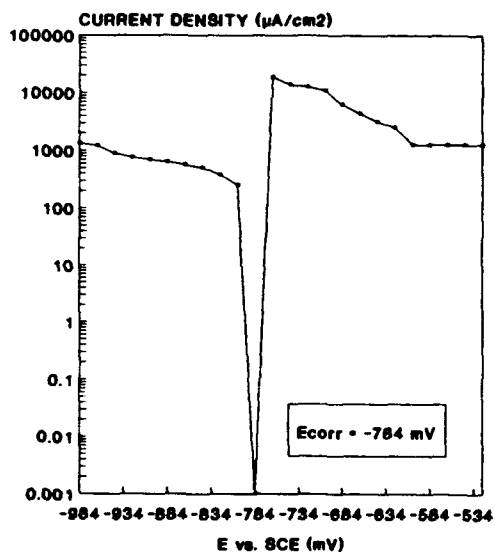
### POLARIZATION CURVE BRASS



DEVELOPED ANTIFREEZE

FIGURE 2.b

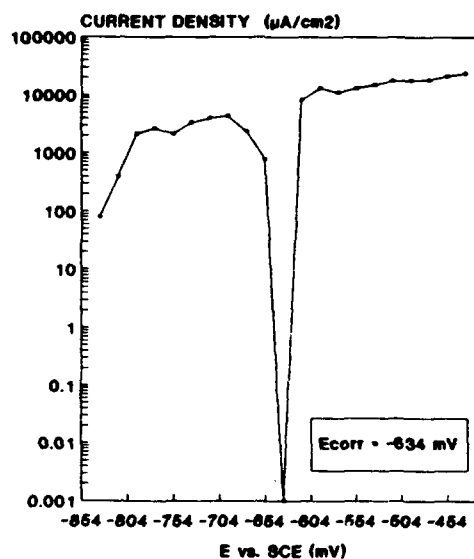
### POLARIZATION CURVE TIN BRASS



DEVELOPED ANTIFREEZE

FIGURE 2.c

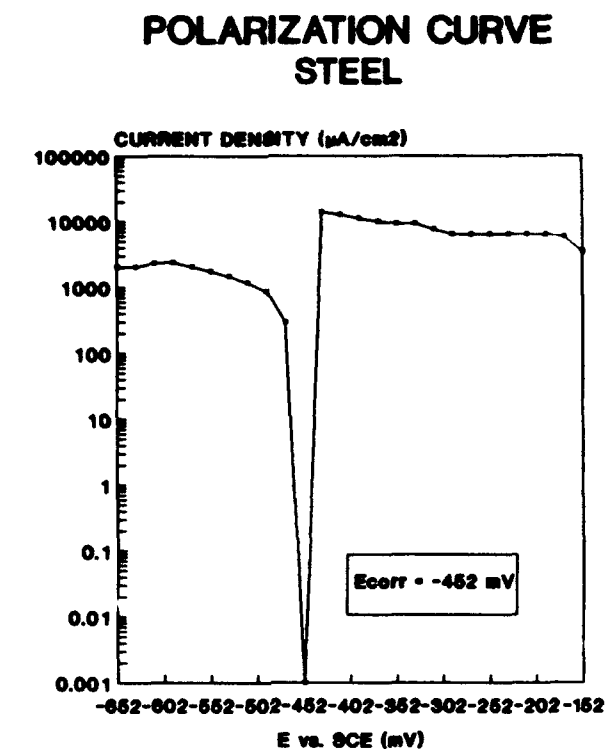
### POLARIZATION CURVE CAST IRON



DEVELOPED ANTIFREEZE

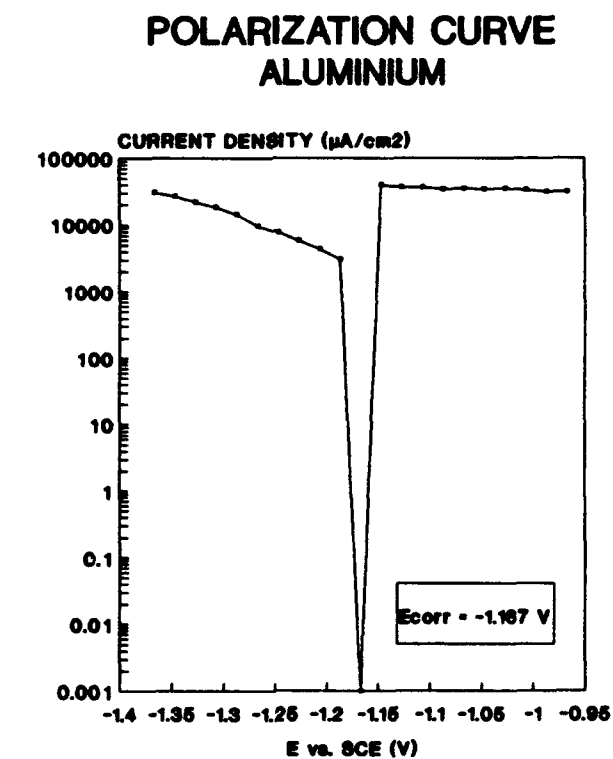
FIGURE 2.d

FIGURE 2.e



DEVELOPED ANTIFREEZE

FIGURE 2.f



DEVELOPED ANTIFREEZE

## SYNTHESIS AND STUDY OF DIFFERENT THIOAMIDES AS CORROSION INHIBITORS

Khawaja M. Ahmed  
Petroleum Research Centre  
P.O. Box 79142  
Shuhada Abu Jalil  
Tripoli-Libya.

Salem R. Abu Oun  
Petroleum Research Centre  
P.O. Box 6431  
Tripoli-Libya.

Mahmood A. Shariff  
Petroleum Research Centre  
P.O. Box 6431, Tripoli-Libya.

### ABSTRACT

Many organic compounds having electron rich atoms in their structure, such as nitrogen, and sulphur, are widely in use as lubricating additives, in the Oil Industry to minimise corrosion. The presence of electron rich atoms in the molecules of compounds under discussion, increases the ability of these substances to form co-ordinate covalent bonds with the metal atoms, involved in the corrosion environment.

Compounds based on fatty amine, aromatic amine, imidazoline, di-imidazoline and fatty amide are now a days, in use, as corrosion inhibitors. Less attention has been given to study thiocarboxylic acid amides as corrosion inhibitors, in the oil field.

In this work some phenylacetothioamide and benzylacetothioamide are synthesised. The chemical and physical data of the prepared compounds are compiled. The solubility, cold stability, heat stability and corrosion inhibition characteristics, of the synthesised compounds have been measured in the artificial environment (10 % crude in artificial brine at the pH in between 4.5 to 4.8). Anticorrosive properties of few of the amine based commercially available oilfield corrosion inhibitors and few of the above mentioned synthesized compounds are measured, in the test environment, in order to compare their activity. Prepared thioamides differs in their molecular weights, due to presence of different organic substituents, on the thioamide group. Synthesis of the above mentioned compounds are based on the Willgerodt-Kindler reaction.

The synthesised compounds are confirmed by IR, UV/Vis, DTA and other traditional analytical techniques. The experimental values of the elemental composition of these compounds were compared with the calculated values and found agreeing. UV/Vis. and IR spectras also shows the absorption peaks, which confirms the presence of thioamide group in the prepared compounds. The possible



reaction mechanism regarding the synthesis of the above mentioned compounds is discussed. Mechanism of corrosion inhibition of these compounds in the corrosive environment is explained.

## INTRODUCTION

Chemical antidegradants means the chemical species which inhibit corrosion of metals and stabilise or adjust the environment in which it has been applied. Corrosion inhibitors form a protective barrier on the surface of a substrate by physical absorption, chemical sorption or reaction with the substrate. Corrosion problems in the operation of petroleum drilling installation are to be solved by the aid of corrosion inhibitors in the injection water. The crude comes out with plenty of minerals containing water and the pH of this aqueous and oily mixture varies but lies on the acidic side. This acidic pH, mineral contents and dissolved gases are responsible for metallic corrosion.

Variety of organic compounds having electron rich atoms in their molecules such as nitrogen and sulphur, are widely used as corrosion inhibitor, because of their anticorrosive and antioxidation properties 1-2. A large number of these compounds have been synthesised in the Petroleum Research Centre. They showed different percentage composition of nitrogen and sulphur and varying in unsaturations. It has been proved experimentally that higher the molecular weight of the above mentioned types of compounds, higher is the anticorrosive and antioxidation properties. It may be due to more surface area of the molecules. It is also established that the sulphur containing substances are more effective anticorrosive and antioxidative compared to nitrogen containing compounds, provided the molecular weight and molecular unsaturations are the same.

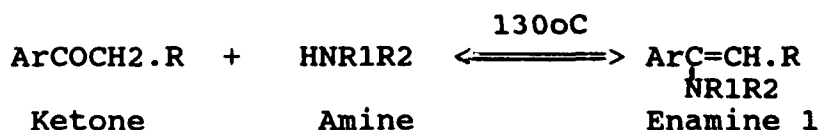
Corrosion and oxidation inhibitors are routinely used in oil fields and in the refineries, in order to minimise the corrosion of the oil transporting pipelines, pumps, valves and other involved equipments and also the refinery installations.

Commercial corrosion inhibitors are unique mixture that may contain surfactants, film enhancers, demulsifiers, or an oxygen scavenger in addition to inhibitor moiety.

The purpose of this work was to synthesise some sulphur containing organic compounds which are higher in boiling point, rich in electron density and higher in molecular weight (such as compounds of thioamide series). Synthesised thioamides were supposed to be evaluated regarding their anticorrosive properties in the artificial corrosive environment, similar to the formation water, in order to locate the suitable compounds which can compete with the preparations, already available in the market for such purpose.

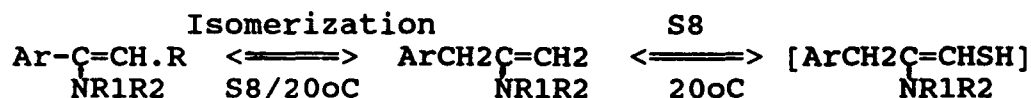
## PREPARATION

The synthesis of thioamides are based on the Willgerodt Reaction(3-6). The reaction is carried out by adding suitable amine in the mixture of sulphur and suitable ketone, in equimolar proportion. Thioamides results in the reaction of enamine with sulphur at 20oC. Enamine generates at elevated temperature by the reaction of ketone and amine. The following is the general reaction model:

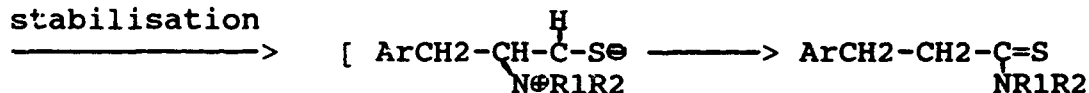


Where R = H or organic group  
 R1 = H or organic group  
 R2 = H or organic group

Then reaction of elemental sulphur with enamine results the isomerisation and thiolysis. This reaction is very fast and take place favourably even at 20 oC, as shown below:



Irreversible  
 stabilisation



## ANALYTICAL CHARACTERISATION OF THIOAMIDES

### A. Study of I.R. Spectra:

I.R. absorption bands of thioamides fall in the "Finger print" region of the spectra and is difficult to trace out normally 7 . Secondly the vibrations of the -CSN= group are not clearly seen due to strong coupling with other vibrations of the molecules. Strong absorption bands were found in the I.R. Spectra of the synthesized compounds. The were in the region of 700-850  $\text{cm}^{-1}$ , 700-800  $\text{cm}^{-1}$ , and in the region of 850-1000  $\text{cm}^{-1}$ , for the primary, secondary and tertiary thioamides

respectively. These bands indicate the presence of  $=N-C=S$  (double bond) group in the compound under analysis. The above mentioned regions are the absorption regions of  $N=C-S$  (single bond) group also.

Strong absorption bands in the region of  $1300-1400\text{ cm}^{-1}$  in case of primary, secondary and tertiary thioamide, in I.R. spectra of the synthesised compounds are due to presence of C-C and C-N (single bond), which is also the absorption region of C=N (double bond).

The above mentioned observation supports the concept of resonance stabilised planar S-C-N skeleton of the thioamide molecules.



The absorption bands in the I.R. spectra of synthesised compounds, in the region  $1200-1300\text{ cm}^{-1}$  in case of primary thioamide, in the region  $950-1150\text{ cm}^{-1}$  in case of secondary thioamide and in the region  $1000-1200\text{ cm}^{-1}$  in case of tertiary thioamides, indicates the presence of N-C-S group.

Strong absorption bands in the I.R. spectra of the synthesised compounds, in the region  $1415-1480\text{ cm}^{-1}$  in case of primary thioamide, in the region  $1525-1565\text{ cm}^{-1}$  in case of secondary thioamide and in the region  $1490$  to  $1530\text{ cm}^{-1}$  in case of tertiary thioamide are due to the presence of C-N and  $NR_2$  groups.

The above observations confirm the presence of thioamide group in the synthesised compounds under investigation. I.R. spectra were obtained in KBr pellets by using PU-9512 IR spectrophotometer.

## B. Ultraviolet Spectroscopic Evidence.

C=S group of thioamide has chromophoric properties. These compounds are bright yellow and yellowish brown in colour. The majority of their parent substances (ketones and amines) are colourless and few are white crystalline in nature. This interesting fact led to the identification of thioamide by UV/Vis Spectrophotometry. The UV/Vis spectra of the synthesised compounds were obtained by using Milton Roy-1201 UV Spectrometer, in benzene. The results indicate that the synthesised compounds have characteristic long wavelength, low intensity (R) band and the more intense (K) bands at shorter wavelength, in accordance to the behaviour of thioamides in these regions, as mentioned in the literature. According to the Kasha's terminology (R) and (K) bands are due to the  $n \rightarrow n^*$  and  $\pi \rightarrow \pi^*$  transition respectively<sup>8</sup>. This classification is based on the MO calculations, polarised u.v. absorption spectra, solvent shifts, intensities and behaviour on protonation.

## EVALUATION OF ANTICORROSIVE PROPERTIES OF THE SYN- THESISED COMPOUNDS

Anticorrosive properties are measured by applying the procedure mentioned in the ID 182, using persistent film technique, in order to separate the compounds having more than 50 % metal protection properties(9-10). The oil Brine water ratio was chosen 10:90 (oil-to-Brine water) and chemical concentration based on the total volume of mixture of oil and brine was chosen 1%. Prepolished carbon steel coupons were used through out the experiment as test metal. The used coupons have available surface area equal to  $13.2098 \times 10^{-4} \text{ m}^2$  each. The procedure mentioned in the ASTM Designation G1-88 for preparing, cleaning, and evaluating corrosion test specimens was adopted in this work(11). The anticorrosive test was carried out at ambient temperature for 72 hours and wheel speed was kept 6 r.p.m. Table no. 1 shows the experimental results in percentage protection and weight loss of the test coupons. Anticorrosive properties of few of the mentioned compounds and compounds commercially available as crude oil corrosion inhibitor in the concentration ranges from 10 to 100 ppm are measured in Brine water as well as in Sea water by using standard NACE Wheel Test method. The test conditions for all the above experiments are given in Table 2. Schematic diagram of the gas purging system and gas blanket assembly, used in the test experiments is illustrated in Fig.1.

## RESULTS AND DISCUSSION

Anodic process of corrosion is the passage of metal ions from the oxide free metal surface into the solution. Cathodic process of corrosion is the discharge of hydrogen ion to produce hydrogen gas. In air saturated acid solutions, cathodic reduction of dissolved oxygen also take place but for iron the rate does not become significant compared to the rate of hydrogen ion discharge until pH exceeds about 3. An inhibitor may decrease the rate of the anodic process, the cathodic process or both(12).

The adsorbed inhibitor may form a surface film which acts as a physical barrier to restrict the diffusion of ions or molecules to or from metal surface and so retard the corrosion reaction. This effect occurs particularly when the inhibitors species are large molecules e.g. compounds containing long hydrocarbon chains and the elements of group (V) and (VI) of the periodic table, such as N, P, As, O, S and Se and organic compounds containing the multiple bonds. The surface film of these type inhibitors give rise resistance polarisation and the concentration polarisation. This increase, affects the anodic and cathodic reactions.

Similar effects also occur when the inhibition undergo reactions to form a multimolecular film e.g. acetylenic compounds and sulphoxides(13). It is likely that absorbed inhibitors with the surface metal atoms may prevent these metal atoms from precipitating in either the anodic or cathodic reactions of corrosion.

The effect of hydrogen sulphide is thought to be responsible for acceleration of corrosion of iron observed with some inhibitive sulphur compounds e.g. thiourea in low concentrations, since hydrogen sulphide has been identified as a reduction product. However the effects of hydrogen sulphide are complex, since in the presence of inhibitors such as amines, quaternary ammonium cations, thiourea, synergistic enhancement of inhibition is observed due to interaction of adsorbed HS<sup>-</sup> ion with the adsorbed inhibitor.

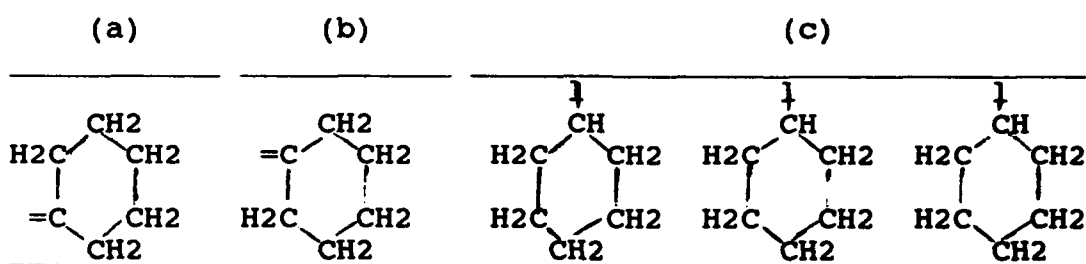
Inhibitors may also retard the rate of hydrogen evolution on metals by affecting the mechanism of reaction as indicated by increases in the Tafel slopes of cathodic polarisation curve. This effect has been observed for iron in the presence of inhibitors such as phenyl thiourea, acetylenic hydrocarbons, aniline derivatives, benzaldehyde derivatives and pyrilium salts. The addition of the above mentioned groups of compounds to corrosive environment containing HCl, tends to retard the discharge of hydrogen ions to form adsorbed hydrogen atoms on iron, therefore controlling the rate of the overall hydrogen evolution reaction.

The inhibitors of corrosion in acid solution can interact with metals and affect the corrosion reaction in a number of ways. Some of which may occur simultaneously. The mechanism of action of inhibitors, may vary due to variety of factors, such as its concentration; the pH of the acid; the nature of the anion of acid; the presence of other species in the solution; the extent of reaction to form secondary inhibitors and the nature of the metal. The mechanism of action of inhibitors with the same functional group may additionally vary with factors such as the effect of the molecular structure, electron density of the functional group and the size of the hydrocarbon portion of the molecule, unsaturations of the molecule and presence of electron rich elements.

Corroding metal surfaces in acid solution are oxide free, whereas in neutral solutions, the metal surfaces is covered with films of oxides, hydroxides or salts owing to reduced solubility of these species. Inhibition in neutral solution is due to compounds which can form or stabilise protective surface film. The organic compounds containing sulphur inhibits the corrosion of metals in acid solution perhaps by donation of electrons from adsorbed molecules to the metal atoms or ions. Sulphur containing compounds are superior in inhibition compared to nitrogen and oxygen containing compounds as ionisation energy of sulphur is less than oxygen and nitrogen. These compounds attach themselves at the points which suffer anodic attack preferentially and they form a protective film on the metal by making co-

ordinate covalent type of linkage with the metal atoms and by london forces. At anodic points it increases the electron atmosphere and render more difficult the detachment of positive metallic ions.

The inhibition of sulphur compounds made more affective by introducing cyclic or aromatic group into the compounds. This not only increase the surface area of the molecule, but make the sulphur more nucleophilic. The other groups which increase the nucleophilicity of the molecule of these compounds, when introduce into its molecules, increases the effectiveness of the compounds, regarding its anticorrosive activity. Shielding effect of organic inhibitors depends on the position of side chain. This effect can be explained by the following structures (9):



Structure (a) produce better shielding than one with the side chain as in structure (b). The (c) structure suggests that a larger number of molecules could be placed in close array; more material per unit area would be demanded for inhibition, but if this is provided, inhibition should be more complete.

The corrosion of metals in aqueous acid solutions can be inhibited by a very wide range of substances, such as chloride, bromide, iodide ions and carbon monoxide and by many other substances of organic in nature, particularly those containing the elements of group (V) and (VI) of the periodic table, such as nitrogen, phosphorous, arsenic, oxygen, sulphur and selenium. Organic compounds containing multiple bonds and are higher in molecular weight are found to be corrosion and oxidation inhibitors.

The effect of synthesised thioamides on the corrosion properties of steel coupons is given in the Table 1. The test conditions for all the corrosion evaluation experiments are given in Table 2. List of synthesised compounds and their percentage composition of sulphur and nitrogen is mentioned in the Table 3. The list of the compounds having percentage protection greater than 50% are given in the Table 4. The solubility data of the synthesised thioamides in benzene, xylene, kerosene, methanol and brine are mentioned in the Table 5. Heat stability data of these compounds are also given in the Table 5. Schematic diagramme of the gas purging system and gas blanketing assembly, used in the test experiments, is illustrated in Fig. 1. Fig. 2-5 shows the

corrosion protection properties versus concentration of inhibitor, of few of the synthesised compounds and some of the commercially available crude oil corrosion inhibitors, in the concentration range 10 to 100 ppm, using NACE Wheel Test method. Comparative studies shows that synthesised compounds are good anticorrosive preparations.

All the evaluation experiments are performed on laboratory scale. The results need revaluation regarding their behaviour under high pressure and high temperature and in the presence of CO<sub>2</sub> and H<sub>2</sub>S. Beside the above mentioned parameters it is also necessary to find out the emulsion tendencies and solubility percentage in the aqueous and oily medium, in order to locate, in case of success, the suitable oil field application, for the synthesised formulation/s.

### CONCLUSION

In this work series of thioamides which differ from each other, in molecular weight, molecular structure and molecular saturation, have been synthesised successfully. Their chemical characterisation and evaluation of anticorrosive properties are made in the artificial environment, similar to the formation water. Out of the synthesised compounds seventeen compounds were found to have percentage protection above than fifty percent in the above mentioned environment. Comparative corrosion protection properties of, few of the evaluated synthesised and commercial available corrosion inhibitors shows that the synthesised compounds are also good anticorrosive in nature.

### ACKNOWLEDGEMENT

The author would like to thank PRC Administration for providing facilities and necessary approval for executing this study and for their permission to publish the work. Thanks are also extended to supervisor of chemistry department for his assistance in providing the required chemical material and other necessities in time, which were needed by the author during this study. The author is thankful to Mrs. Ebtisam Al-Tabany for her contribution in this work by reevaluating few of the mentioned compounds, as part of his B.Sc. Project.

## REFERENCES

1. M. W. Ranney, Corrosion Inhibitors (Manufacture and technology). Chemical Technology Review No. 60, (ndc), (1976): page 1.
2. J. Zabicky (Editor), The Chemistry of Functional Groups (The Willgerodt Reaction). Interscience Publishers, New York, (1970): page 145-147.
3. M. J. Janssen, Organo Sulphur Chemistry (The Willgerodt and Kindler Reaction). Interscience Publishers, New York, (1967): page 229-232.
4. R. C. Denney, Named Organic Reactions. Published by Butterworth, London, (1969): page 234-237.
5. Marrison and Boyd, Organic Chemistry (Alkylation of Carbonyl Compounds via enamine). Published by Allyn and Bacon, Inc., (1987): page 1071-1072.
6. J. March, Advanced Organic Chemistry (Reaction Mechanisms, and structure " Willgerodt Reaction). Published by Mc Graw-Hill Book Company, (1968): page 9:63 to 9:65.
7. Standard Practice for Preparing, Cleaning, and Evaluating Corrosion Test Specimens, Annual Book of ASTM Standards, vol. G01.05, (1988): page 61-67.
8. L. L. Shreir, Corrosion Inhibition (Principles and Practice). Published by Newnes Butterworth. Vol. 2, (1977): page 18:28 to 18:29.
9. L. L. Shreir, Corrosion Inhibition (The Mechanism of Corrosion Prevention by Inhibitors). Published by Newnes Butterworth. Vol. 2, (1977): page 18:34 to 18:35.
10. L. Meites, Hand book of Analytical Chemistry. (Analysis of thioamides). Published by Mc. Graw Hill, Inc. (1963): Page 12 to 168.
11. J. Zabicky (Editor), The chemistry of functional groups (The ultraviolet spectroscopic evidence of thioamides), (1970): page 400-406. Interscience publishers, New York.
12. M. A. Sheriff, A. Hassan and A. Abusnena, Evaluation of Oil Field Corrosion Inhibitors by NACE Static Test Method and Wheel Test Method. Petroleum Research Journal, vol. 2, (1990): page 67-70.
13. Wheel Test Method used for Evaluation of Film Persistent Inhibition for Oil Field Applications, NACE Publication no. ID 182, (1982): page 45-47.



#### FIGURE CAPTION

1. Schematic diagramme of the gas purging system and gas blanketing assembly used in the test experiments.
2. Comparison of corrosion rate of different synthesized thioamides in brine water, at pH in between 4.5 to 4.8, in concentration ranges from 10 to 100 ppm, by using NACE standard wheel test method.
3. Comparison of corrosion rate of different synthesized thioamides in sea water, at pH in between 4.5 to 4.8, in concentration ranges from 10 to 100 ppm, by using NACE standard wheel test method.
4. Percentage inhibition of different commercially available amine base crude oil corrosion inhibitors in brine water, at pH 4.5 to 4.8, in the concentration ranges from 10 to 100 ppm, by using NACE standard wheel test method.
5. Percentage inhibition of different commercially available amine base crude oil corrosion inhibitors in sea water, at pH 4.5 to 4.8, in the concentration ranges from 10 to 100 ppm, by using NACE standard wheel test method.

TABLE-1

EFFECT OF SYNTHESISED COMPOUNDS ON THE CORROSION PROPERTIES OF THE CARBON STEEL COUPONS

Code of compound	Percentage protec.	Loss of wt. in g/m <sup>2</sup>
BLANK	00.00	24.522 g/m <sup>2</sup>
TH-xiv	86.12	2.342 g/m <sup>2</sup>
TH-xii	18.78	13.708 g/m <sup>2</sup>
TH-xxii	88.78	2.751 g/m <sup>2</sup>
TH-xiii	13.88	14.535 g/m <sup>2</sup>
TH-i	58.15	10.264 g/m <sup>2</sup>
TH-xxxi	21.07	19.360 g/m <sup>2</sup>
TH-ii	63.20	9.024 g/m <sup>2</sup>
TH-x	64.90	5.924 g/m <sup>2</sup>
TH-xx	86.73	3.254 g/m <sup>2</sup>
TH-xxviii	21.63	19.220 g/m <sup>2</sup>
TH-v	80.34	4.822 g/m <sup>2</sup>
TH-xxxv	87.57	3.048 g/m <sup>2</sup>
TH-iii	64.04	8.817 g/m <sup>2</sup>
TH-xxix	48.88	12.540 g/m <sup>2</sup>
TH-viii	35.92	10.815 g/m <sup>2</sup>
TH-iv	48.31	12.675 g/m <sup>2</sup>
TH-xi	19.59	13.570 g/m <sup>2</sup>
TH-xxvi	15.45	20.730 g/m <sup>2</sup>
TH-xviii	83.88	3.953 g/m <sup>2</sup>
TH-xv	81.43	4.554 g/m <sup>2</sup>
TH-xxxvii	89.59	2.553 g/m <sup>2</sup>
TH-xxxii	87.14	3.154 g/m <sup>2</sup>
TH-vii	26.69	14.879 g/m <sup>2</sup>
TH-xxvii	89.18	2.653 g/m <sup>2</sup>
TH-vi	84.69	3.754 g/m <sup>2</sup>
TH-ix	14.69	19.357 g/m <sup>2</sup>
TH-xxx	13.76	21.150 g/m <sup>2</sup>
TH-xxv	86.33	3.352 g/m <sup>2</sup>
TH-xxiv	87.14	3.154 g/m <sup>2</sup>

TABLE-2

TEST CONDITIONS FOR ALL THE EXPERIMENTS

Test method	Temp. oC	Time (hrs)	CO <sub>2</sub> solubi- lity at R.Temp.	O <sub>2</sub> solubi- lity at R.Temp.	Crude oil (v/v) %	Brine water (v/v) %	Sea water (v/v) %
Wheel test method	25 oC	72	1.5g/l	.001g/l	10	90	---
Wheel test method	25 oC	72	1.5g/l	.001g/l	10	---	90

TABLE-3

## LIST OF THE SYNTHESISED COMPOUNDS AND THEIR ELEMENTAL COMPOSITION

Comp.code number	Formula	Percentage composition of S & N w/w			
		Calculated		Found	
		N	S	N	S
xiv	CaHbNS	2.8	6.4	2.6	6.2
xii	CaHbNS	4.3	9.7	4.1	9.6
xxii	CaHbNS	4.3	19.6	4.1	19.4
xiii	CaHbNS	4.4	10.1	4.6	10.3
i	CaHbNS	4.4	10.2	4.3	10.1
xxxvi	CaHbNS	4.8	11.0	4.7	10.9
ii	CaHbNS	5.0	11.5	4.9	11.4
x	CaHbNcS	10.4	11.8	10.5	11.9
xx	CaHbNS	5.3	12.2	5.2	12.1
xxviii	CaHbNS	5.3	12.2	5.2	12.1
v	CaHbNcS	6.2	10.9	6.1	10.8
xxxv	CaHbNS	5.5	12.6	5.6	12.7
iii	CaHbNcSO	7.9	11.1	8.0	11.3
xxix	CaHbNcS	16.7	12.7	16.6	12.6
viii	CaHbNcS	11.2	12.8	11.1	12.6
iv	CaHbNcSO	11.8	13.4	11.9	13.5
xi	CaHbNcS	17.7	13.5	17.5	13.4
xxvi	CaHbNcS	11.9	13.6	11.7	13.4
xviii	CaHbNS	5.9	13.6	5.7	13.4
xv	CaHbNS	6.0	13.7	5.8	13.5
xxxvii	CaHbNS	6.2	14.1	6.1	14.0
xxxii	CaHbNSO	6.3	14.5	6.3	14.4
vii	CaHbNS	6.3	14.5	6.2	14.4
xxvii	CaHbNS	6.4	14.6	6.2	14.4
vi	CaHbNS	6.8	15.4	6.7	15.3
ix	CaHbNS	6.8	15.4	6.6	15.2
xxx	CaHbNS	6.8	15.6	6.7	15.5
xxv	CaHbNS	7.6	16.9	7.4	16.8
xxiv	CaHbNS	7.3	16.8	7.2	16.7

## Note:

In the above compounds the x, y and z are in the following range:

a	=	11 to 33
b	=	13 to 60
c	=	2 to 3

TABLE-4

## LIST OF THE SYNTHESISED COMPOUNDS HAVING PERCENTAGE PROTECTION MORE THAN 50%

Compound code no.	Percentage protection	Weight loss
Blank	00.00	24.522 g/m2
TH-xiv	86.12	2.342 g/m2
TH-xxii	88.78	2.751 g/m2
TH-i	58.15	10.264 g/m2
TH-ii	63.20	9.024 g/m2
TH-x	64.90	5.924 g/m2
TH-xx	86.73	3.254 g/m2
TH-v	80.34	4.822 g/m2
TH-xxxv	87.57	3.048 g/m2
TH-iii	64.04	8.817 g/m2
TH-xxix	48.88	12.540 g/m2
TH-iv	48.31	12.675 g/m2
TH-xviii	83.88	3.953 g/m2
TH-xv	81.43	4.554 g/m2
TH-xxxvii	89.59	2.553 g/m2
TH-xxxii	87.14	3.154 g/m2
TH-xxvii	89.18	2.653 g/m2
TH-vi	84.69	3.754 g/m2
TH-xxv	86.33	3.352 g/m2
TH-xxiv	87.14	3.154 g/m2

TABLE-5

## PHYSICAL CONSTANTS OF THE SYNTHESISED COMPOUNDS

Comp. code	Solubility in					Stability in		
	Benz.	Methanol	Xyllene	Keros.	Brine	Cold 20oC	Hot 100oC	Brine
TH-xiv	+++	+++	+++	+++	---	St.	St.	St.
TH-xii	+++	+++	+++	++	---	Unst.	Unst.	St.
TH-xxii	+++	+++	+++	+++	---	St.	St.	St.
TH-xiii	+++	+++	+++	+++	---	Unst.	Unst.	St.
TH-i	+++	---	+++	++	---	St.	Unst.	St.
TH-xxxv	+++	++	+++	+++	---	St.	St.	St.
TH-ii	+++	+++	+++	+++	---	Unst.	Unst.	St.
TH-x	+++	++	++	++	---	St.	St.	St.
TH-xx	+++	+++	+++	+++	---	St.	St.	St.
TH-xxviii	+++	+++	+++	+++	---	St.	St.	WPPT
TH-v	++	+++	++	++	---	Unst.	Unst.	St.
TH-xxxv	+++	+++	+++	+++	---	St.	St.	St.
TH-iii	+++	++	++	---	---	St.	St.	St.
TH-xxix	++	+++	++	++	---	St.	Unst.	PPT
TH-viii	+++	++	++	+++	---	St.	Unst.	PPT
TH-iv	++	++	++	++	---	Unst.	Unst.	PPT
TH-xi	+++	+++	++	++	---	St.	St.	St.
TH-xxvi	+++	+++	+++	++	---	St.	Unst.	St.
TH-xviii	+++	+++	+++	+++	---	St.	St.	St.
TH-xv	+++	+++	+	---	---	St.	St.	St.
TH-xxxvii	+++	+++	+++	+++	---	St.	St.	St.
TH-xxxii	+++	+++	+++	+++	---	St.	St.	St.
TH-vii	+++	+++	+	++	---	St.	St.	PPT
TH-xxvii	+++	+++	+++	---	---	St.	St.	St.
TH-vi	++	+++	++	---	---	St.	St.	St.
TH-ix	+++	+++	+++	+++	---	Unst.	Unst.	St.
TH-xxx	+++	+++	+++	+++	---	St.	St.	St.
TH-xxv	+++	+++	+++	---	---	St.	St.	St.
TH-xxiv	+++	+++	+++	+++	---	St.	St.	St.

## Note:

- +++ = Completely soluble  
 ++ = Soluble with difficulty, not completely.  
 + = Partially soluble and partly forming susp.  
 - = Very little soluble.  
 St. = Stable  
 Unst. = Unstable  
 PPT = Decomposition of the compound  
 (Precipitation of sulphur)  
 WPPT = Decomposition of the compound  
 (White precipitate appeared)

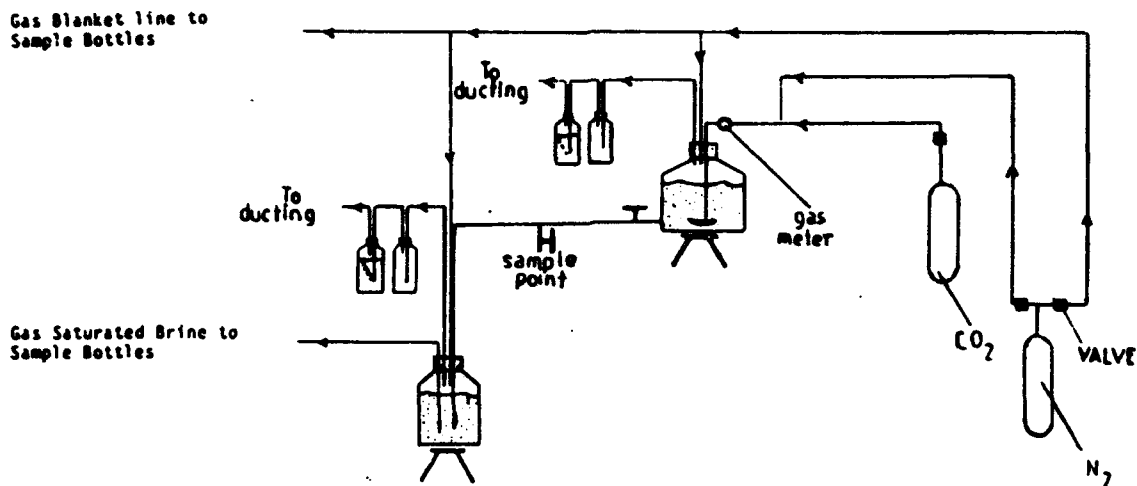


Fig. 1.

COMPARISON OF CORROSION RATE OF DIFFERENT THIOAMIDES IN BRINE WATER AT pH IN BETWEEN 4.5 TO 4.8 AT VARYING CONCENTRATION RANGES.

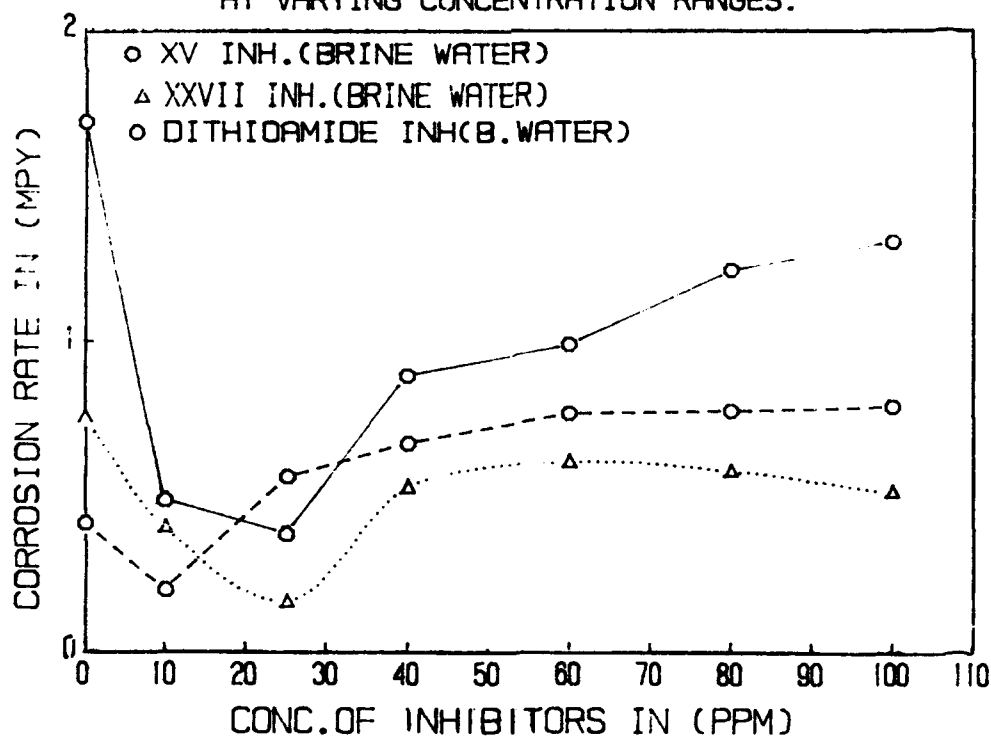
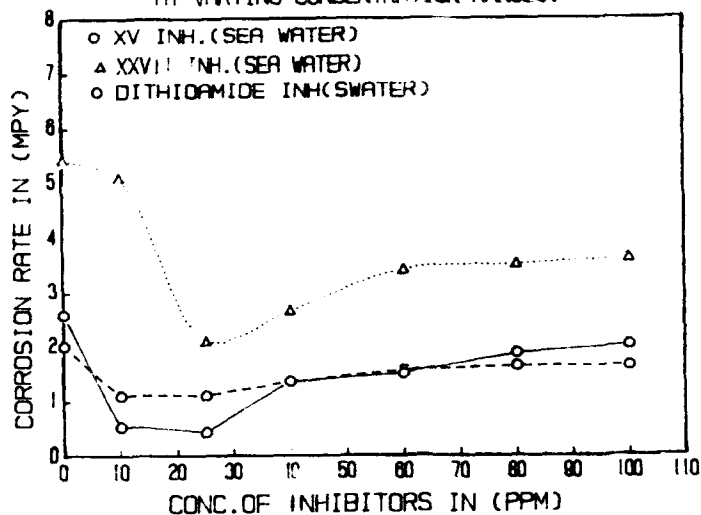


Fig. 2.

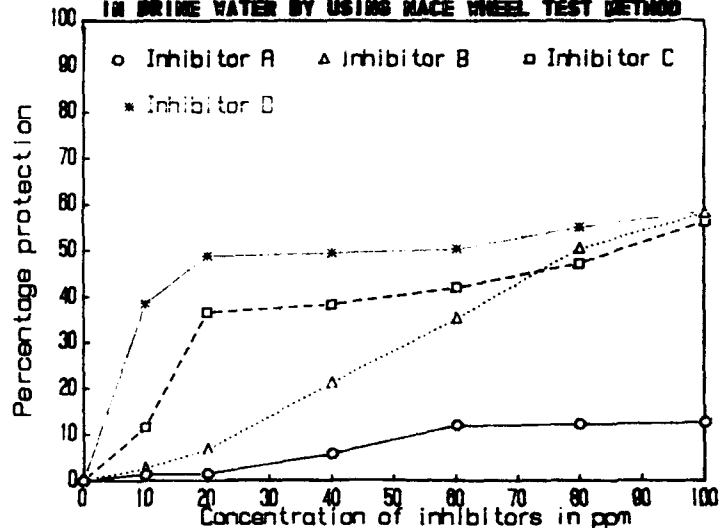
COMPARISON OF CORROSION RATE OF DIFFERENT THIOPAMIDES IN  
SEA WATER AT pH IN BETWEEN 4.5 TO 4.8  
AT VARYING CONCENTRATION RANGES.

Figure 3



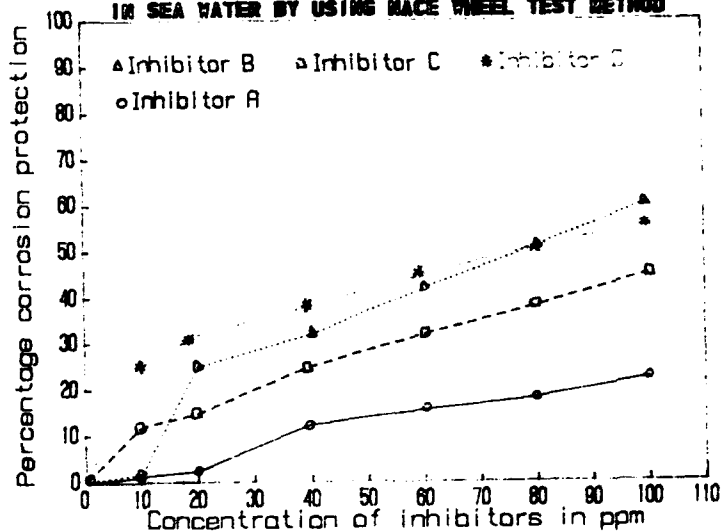
PERCENTAGE OF CORROSION INHIBITION OF SOME OF THE ARINE  
BASE COMMERCIALY AVAILABLE CRUDE OIL CORROSION INHIBITORS  
IN BRINE WATER BY USING RACE WHEEL TEST METHOD

Figure 4



PERCENTAGE OF CORROSION INHIBITION OF SOME OF THE ARINE  
BASE COMMERCIALY AVAILABLE CRUDE OIL CORROSION INHIBITORS  
IN SEA WATER BY USING RACE WHEEL TEST METHOD

Figure 5



# **Corrosion Resistance of Copper and Copper Alloys Surface Treated with a Benzotriazole Derivative in Sodium Chloride Solutions**

**F. Zucchi**  
Corrosion Study Center of the University  
Via L. Borsari, 46  
44100 Ferrara Italy

**G. Brunoro**  
Corrosion Study Center of the University  
Via L. Borsari, 46  
44100 Ferrara Italy

**C. Monticelli**  
Corrosion Study Center of the University  
Via L. Borsari, 46  
44100 Ferrara Italy

**G. Trabanelli**  
Corrosion Study Center of the University  
Via L. Borsari, 46  
44100 Ferrara Italy

## **Abstract**

It was previously shown that copper specimens prefilmed with 5-n-hexyl-1,2,3-benzotriazole ( $C_6BTA$ ) could be maintained corrosion free in high purity water containing some ppm of oxygen and carbon dioxide, and also in 0.1 M sodium chloride (pH 6 or 3) at 40°C, at the end of 720 hours of testing. The prefilming treatments of the metallic specimens were carried out in  $1 \cdot 10^{-3}$  M aqueous solutions of  $C_6BTA$  for 14 hours at 80°C or in  $5 \cdot 10^{-4}$  M aqueous alcoholic solutions of  $C_6BTA$  for 1 hour at 40°C.

In the present paper we investigated the influence exerted on the corrosion resistance of copper and copper base alloys by some parameters of the prefilming treatment with  $C_6BTA$ , such as the additive concentration, temperature and immersion time.

The prefilming conditions of the electrodes were the following:

- aqueous solutions containing  $1 \cdot 10^{-4}$  M or  $2 \cdot 10^{-4}$  M of  $C_6BTA$ ;
- immersion time: 5, 15 and 60 minutes;
- temperature: 60, 70 and 80°C.

The protective efficiency of the surface films was evaluated by electrochemical techniques (polarization curves recording and polarization resistance measurements) in 0.1 M and 0.6 M NaCl, at 40°C.

The film persistence was evaluated by polarization resistance determinations on electrodes immersed for 1000 hours in stagnant 0.1 M NaCl, at 40°C.

Some series of measurements were also carried out on copper cylinder electrodes, rotating for almost 48 hours in NaCl solutions.

From the overall results the protective characteristics of the surface films were deduced.

**Key terms:** inhibition, 5-n-hexyl-1,2,3-benzotriazole, copper corrosion, sodium chloride solutions.

## Introduction

The inhibitors against copper and copper alloys corrosion are mainly constituted by various classes of heterocyclic organic compounds (1-3). Some of these substances are used as inhibitors from about forty years.

The best known chemicals are benzotriazole and its alkyl derivatives, imidazole derivatives and benzimidazole, benzoxazole and benzothiazole thio-substituted.

The quoted substances can be generally applied dissolved in the aggressive aqueous solutions, but they have also found application as prefilming agents of copper and copper alloy surfaces. The last technique may constitute a method of temporary protection of the metallic materials during their storage and transport, waiting time before assembling of industrial apparatus and/or the starting periods of industrial plants.

1,2,3-Benzotriazole (BTA) and some of its alkyl derivatives have been studied in our laboratory (4,5) as prefilming agents for the protection of copper surfaces in contact with flowing (2 m/s) high purity water containing 5 ppm of oxygen and 0.5 ppm of carbon dioxide, at 40°C. Among the tested derivatives, 5-n-hexyl-1,2,3-benzotriazole ( $C_6$ BTA) was found to be very efficient, during 720 hours of testing.

The protectivity of surface films obtained by prefilming copper in aqueous alcoholic solutions of  $C_6$ BTA was confirmed in 1000 hours immersion tests in 0.1 M NaCl solutions at 40°C.

Purpose of the present paper is to investigate the influence exerted on the corrosion resistance of copper and copper alloys by some parameters of the prefilming treatment with  $C_6$ BTA, such as additive concentration, temperature and immersion time.

The characteristics of the surface films, such as their persistence and protectivity, have been evaluated, by using various electrochemical techniques, in sodium chloride solutions, both in stagnant or flowing conditions.

## Experimental

The metallic electrodes were constituted by cylinders of oxygen free high conductivity copper C10200, aluminum brass C68700, 90Cu-10Ni C70600, 70Cu-30Ni C71500, exposing to the aggressive environment lateral surface areas of different sizes (20 cm<sup>2</sup> for stagnant tests and about 3 cm<sup>2</sup> for rotating cylinder electrode measurements), depending on the type of test to be conducted.

In all cases, the electrode surfaces were prepared by treatments with emery papers till n. 600, followed by thorough degreasing with acetone and accurate rinsing with distilled water, before the test.

The prefilming conditions of the electrodes were the following:

- aqueous solutions containing  $1 \cdot 10^{-4}$  M or  $2 \cdot 10^{-4}$  M of  $C_6$ BTA;
- temperatures: 60, 70 and 80°C;
- immersion times: 5, 15 and 60 minutes.

The prefilmed electrodes, after accurate rinsing with distilled water, were immersed in pure and not deaerated 0.1 M or 0.6 M NaCl solutions, at 40°C.

The protectivity of the film, after 1h immersion of the electrodes in stagnant solutions, has been evaluated by recording the cathodic and anodic polarization curves, starting from the free corrosion potential, at a scanning rate of 0.1 mV/s, by using an EG & G PARC 350A corrosion measurement console, in the potentiodynamic configuration.

The cathodic polarization curves have been recorded, at a scanning rate of 0.5 mV/s, on cylinder electrodes rotating in the range from 100 to 1600 rpm.

By measuring the polarization resistance ( $R_p$ ) values on prefilmed electrodes, the film persistence



has been followed during:

- 1000 hours in 0.1 M NaCl solutions, at 40°C, in stagnant conditions;
- 48 hours in 0.1 M or 0.6 M NaCl solutions, at 40°C, by using rotating cylinder electrodes.

## Results

### A. Evaluation of the film protectivity

By working on copper electrodes prefilmed with  $2 \cdot 10^{-4}$  M  $C_6BTA$  for different times and at different temperatures, the cathodic and anodic polarization curves have been recorded, after immersion of the electrodes for 1 hour in 0.1 M NaCl solutions, at 40°C. Figure 1 represents an example of the trend of the recorded polarization curves.

The evaluation of the effects of the various prefilming conditions on the electrochemical behaviour of the electrodes has been obtained by comparing the cathodic ( $\eta_c$ ) and anodic ( $\eta_a$ ) overvoltages, necessary to reach current density of  $1 \mu A/cm^2$ , calculated from the polarization curves (Table 1).

The influence of the prefilming time is clearly evident on both the corrosion partial processes, and particularly on the cathodic one. On the contrary, it can be shown that the effect connected to the increasing of temperature on the cathodic behaviour of the electrodes is not particularly evident.

Figure 2 reports the polarization curves recorded on copper electrodes prefilmed in  $1 \cdot 10^{-4}$  M  $C_6BTA$  at 80°C, for 5, 15 and 60 minutes. By comparing these curves with those collected in Figure 1, the effect of the additive concentration, mainly in correspondence of the short prefilming times, is evident.

The protectivity of the surface layers formed by prefilming treatments has been also verified in flowing conditions, in a series of tests with rotating cylinder electrodes. To this purpose, copper electrodes have been prefilmed for different times (15' and 60') at 60°C in solution of  $2 \cdot 10^{-4}$  M  $C_6BTA$ . By using not prefilmed electrodes as a blank, the cathodic polarization curves have been recorded after 1 h of permanence in 0.1 M NaCl solutions, at 40°C, at rotation speeds of up to 1600 rpm. As it was expected, the current density values were clearly higher than in stagnant conditions. In the blank test a linear relation was found between the limiting current density values and the square root of the rotation speed. On the contrary, in the case of the prefilmed electrodes, the cathodic process resulted strongly blocked in the overvoltage interval of about 600 mV, and a limiting current density appeared only at more negative potentials. These results confirmed the protectivity of the treatments, also in flowing conditions.

Another parameter for the evaluation of the film protectivity was considered to be represented by the aggressivity of the environment. For this reason, a series of polarization curves on prefilmed or not prefilmed copper electrodes has been recorded, after 1 h of immersion in 0.6 M NaCl solutions at 40°C. As an example, Figure 3 collects the curves recorded on electrodes not prefilmed or prefilmed for 60 minutes at 60°C or 80°C. The blank showed an anodic curve with a linear trend, whereas in the cathodic branch, before reaching the limiting diffusion current, a current peak was found, due to the reduction of corrosion products formed during the waiting time before the starting of polarization. On prefilmed electrodes, both the anodic and the cathodic processes were sharply inhibited, confirming also in 0.6 M NaCl aggressive solutions the positive effect of the surface treatment.

The protective effect of prefilming treatments, evidenced on copper, has been investigated also on some copper base alloys, by working on Al-brass, 90Cu-10Ni and 70Cu-30Ni electrodes. As an example, Figure 4 reports the cathodic and anodic polarization curves recorded in 0.1 M NaCl solutions, at 40°C, on electrodes of the quoted alloys not prefilmed or prefilmed by immersion in  $2 \cdot 10^{-4}$  M  $C_6BTA$ , for 60 minutes at 80°C. The positive effects of the surface treatments are clearly evident. Independently of the alloys composition, the cathodic process

was strongly inhibited, more than in the case of pure copper, not showing evidence of limiting diffusion current. Also the anodic dissolution processes of the alloys resulted inhibited. In the case of Cu-Ni alloys, the treatment with  $C_6BTA$  was accompanied by a shift of the corrosion potential towards noble direction.

#### B. Evaluation of the film persistence

This characteristic of the surface film has been evaluated by measuring the variations of the polarization resistance ( $R_p$ ) values in long time tests.

Figure 5 collects the trends of the polarization conductance values ( $1/R_p$ ), directly proportional to the corrosion rates, measured on not prefilmed or prefilmed copper electrodes, during 1000 hours of testing at 40°C, in 0.1 M NaCl stagnant solutions. The corrosion rate of not prefilmed copper electrodes decreased rapidly during the first 24 hours of tests, then slowly till 200 hours. Successively, the polarization conductance data remained quite constant, around  $10 \cdot 10^{-6} \Omega^{-1} \cdot cm^2$ , till the end of the test. The prefilmed electrodes, on the contrary, showed constant and very low (about  $0.4 \cdot 10^{-6} \Omega^{-1} \cdot cm^2$ ) polarization conductance data, during all the testing period. The difference of more than one order of magnitude in the  $1/R_p$  values seems to support a satisfactory persistence of the surface layer during long time immersion in aggressive chloride solutions.

The film persistence has been also evaluated during 48 hours of testing in flowing conditions. Copper cylinder electrodes, not prefilmed or prefilmed with  $C_6BTA$ , were rotated at 1600 rpm in 0.1 M or 0.6 M NaCl solutions, at 40°C, measuring polarization conductance values as a function of time. These data are collected in Figure 6. On not prefilmed copper electrodes, the corrosion rate in 0.6 M NaCl is high (around  $150 \cdot 10^{-5} \Omega^{-1} \cdot cm^2$ ) and quite constant during all the test. In the same chloride solution, on the prefilmed electrodes, the initially very low corrosion rate values show a tendency to increase after 24 hours of test. A final value of  $7 \cdot 10^{-5} \Omega^{-1} \cdot cm^2$  is measured. The very high difference with the corresponding value of the blank tests testifies the persistence of the surface layer in aggressive and flowing chloride solution.

During the blank test conducted in less aggressive solution (0.1 M NaCl), a tendency of the corrosion rate to decrease with time is evident, probably connected to the formation of a partially protective corrosion product. At the end of the test a  $1/R_p$  value of  $10 \cdot 10^{-5} \Omega^{-1} \cdot cm^2$  is found.

On  $C_6BTA$  prefilmed copper electrodes the polarization conductance values are maintained very low during all the test. In correspondence of the 48 hours, a  $1/R_p$  value of  $0.8 \cdot 10^{-5} \Omega^{-1} \cdot cm^2$  was measured. As it was to be expected, by lowering the aggressivity of the environment, a corresponding increase in the film persistence arose.

#### Discussion

The results of the present paper confirm those previously obtained (6) by prefilming treatments of copper surfaces with aqueous alcoholic solutions of  $C_6BTA$ . In that preliminary phase, 10% of n-propanol was used to increase the solubility of the organic additive.

The prefilming treatment of copper with aqueous solutions of  $C_6BTA$  promotes the formation of highly protective surface layers, which remain stable for almost 1000 hours in 0.1 M NaCl stagnant solutions, at 40°C.

In flowing conditions (1.2 m/s) the surface film remained stable for almost 48 hours, in 0.1 M NaCl at 40°C. After 24 hours of copper electrode rotation in the more aggressive 0.6 M NaCl, the surface film slowly lost its protective properties. Nevertheless, at the end of 48 hour test, a 95% inhibiting efficiency value was calculated by polarization conductance values.

From the recording of the polarization curves on prefilmed copper and copper alloy electrodes, it was deduced that the action of the organic additive is mainly to be attributed to the formation of a physical barrier against the cathodic process of oxygen reduction on the electrode.

From the overall results it can be concluded that the prefiling treatments of copper and copper alloy surfaces with  $C_6$ BTA bring to the formation of thick and hydrophobic layers, highly protective also in very aggressive chloride solutions.

The formation of a polymolecular thick layer, as a consequence of prefiling treatments with  $C_6$ BTA, has been confirmed by determining the weight increase of copper sheets, after immersion in aqueous solutions of  $C_6$ BTA at 80°C, for different times. In Figure 7 it is shown that, by increasing the immersion time of copper sheets from 30 minutes to 16 hours in  $C_6$ BTA aqueous solutions, the amount of organic additive present on the metal surface is continually increased without reaching a steady state value. After a prefiling time of 16 hours, an inhibitor concentration of  $9 \cdot 10^{-8} \text{ moles} \cdot \text{cm}^{-2}$  of apparent surface area was calculated.

These data are in agreement with the results of preceding XPS measurements performed on copper specimens prefilmed with  $C_6$ BTA (7). In that case, an indication of the layer thickness was obtained from the cross over values of copper and carbon lines in function of the sputtering time.

A tentative was carried out to differentiate the effect of the physically adsorbed surface layer from that of an eventual underlying film chemisorbed on the metal surface. To this purpose, some series of cathodic polarization curves have been recorded on copper electrodes, initially prefilmed for different times (5' and 60') at 80°C with  $2 \cdot 10^{-4} \text{ M } C_6$ BTA, and then treated with organic solvent. In fact, it has been previously shown that most part of the organic compound could be removed from the surface by immersion of the copper sheets for 10' in acetone, in presence of ultrasonic radiations.

Figure 8 collects the cathodic polarization curves recorded in the various experimental conditions. The polarization curves recorded on copper electrodes initially prefilmed and then immersed in acetone, showed current density values lower than in the blank tests, but higher than on electrodes prefilmed and not treated with solvent. The shape of the curves recorded on electrodes prefilmed and then immersed in acetone is similar to those measured on electrodes prefilmed for 5', not showing limiting diffusion currents almost for overvoltages of 600 mV.

These data seem to indicate that the protection afforded to copper by prefiling treatments with  $C_6$ BTA may be attributed to both physically and specifically adsorbed layers present on the surface. We can assume that the organic additive should be fixed on the copper surface through a chemical bonding with copper, or better with cuprous ions present at the metal surface as first oxidation products. The formation of bonding can be favoured by inductive effect of the n-hexyl-chain present on the aromatic ring. According to Hollander (8), the alkyl derivatives show higher basicity than BTA, contributing in this way to the formation of a stronger ligand-metal bond. In our opinion, the presence of alkyl chains with high number of carbon atoms contributes to the formation of polymolecular layers, through interactions of the van der Waals type. These layers present great hydrophobicity and impermeability to the electrolyte penetration. These characteristics can explain both the protectivity and the persistence of the surface layer formed on copper and copper base alloys by prefiling treatments with  $C_6$ BTA.

### Conclusions

The results of the present research showed that:

- a) the influence of the immersion time in the prefiling solutions is more important than the prefiling temperature, for what concerns the protective efficiency of the surface film;

- b) the prefilming treatment with C<sub>6</sub>BTA provides a very protective surface film, which remains stable for more than 1000 hours in stagnant 0.1 M NaCl, at 40°C;
- c) in chloride solution the surface film appears to be stable even under flowing conditions;
- d) the surface film is constituted by multilayers, an outer layer soluble in acetone and an inner layer more strongly bonded to the metal. Both these layers contribute to the protective characteristics of the film.

### Acknowledgements

This work was financially supported by 60% MURST (Rome).  
The assistance of Mr. V. Grassi in performing the experiments is gratefully acknowledged.

### References

- 1) G. Trabanelli - Corrosion Inhibitors, in Corrosion Mechanisms (F.Mansfeld ed.), Chemical Industries, Vol.28, Marcel Dekker, Inc., New York 1987, p. 119.
- 2) J.B. Cotton, R.B. Scholes - Br.Corros.J., **2** (1967), 1.
- 3) G. Trabanelli, F. Zucchi, G. Brunoro, V. Carassiti - Werkst. und Korros., **24** (1973), 602.
- 4) G. Brunoro, F. Parmigiani, G. Perboni, G. Rocchini, G. Trabanelli - Br.Corros.J., **27** (1992), 75.
- 5) G. Trabanelli, G. Brunoro, F. Zucchi, G. Perboni - Proc. EUROCORR '92, Vol.II, Dipoli, Espoo, Finland (P.J.Tunturi ed.), 523.
- 6) F. Zucchi, G. Brunoro, G. Trabanelli, M. Fogagnolo - Proc. Scientific Congress La Sapienza University, Rome, April 1992, Vol. I, p. 41.
- 7) G. Trabanelli, G. Brunoro, A. Frignani, C. Monticelli, F. Zucchi, G. Perboni, G. Rocchini - Accepted for publication by "La Revue de Métallurgie".
- 8) G. Hollander, G. Dronne, J. Briquet, S. Dunn, M. Fealy - Proc. 7th SEIC, Ann. Univ. Ferrara, N.S., Sez. V, Suppl. N.9, 1990, p.517.

Table 1 - Cathodic ( $\eta_c$ ) and anodic ( $\eta_a$ ) overvoltages measured at  $1 \mu A \cdot cm^{-2}$  on C<sub>6</sub>BTA prefilmed copper electrodes immersed in 0.1 M NaCl at 40°C. The values of  $\eta_c$  and  $\eta_a$  obtained on non prefilmed electrodes were respectively 15mV and 19 mV.

Prefilming temperature	60°C			70°C			80°C		
Prefilming time (min)	5	15	60	5	15	60	5	15	60
$\eta_c$ (mV)	110	260	390	150	300	400	210	350	380
$\eta_a$ (mV)	65	73	140	117	127	187	70	125	200

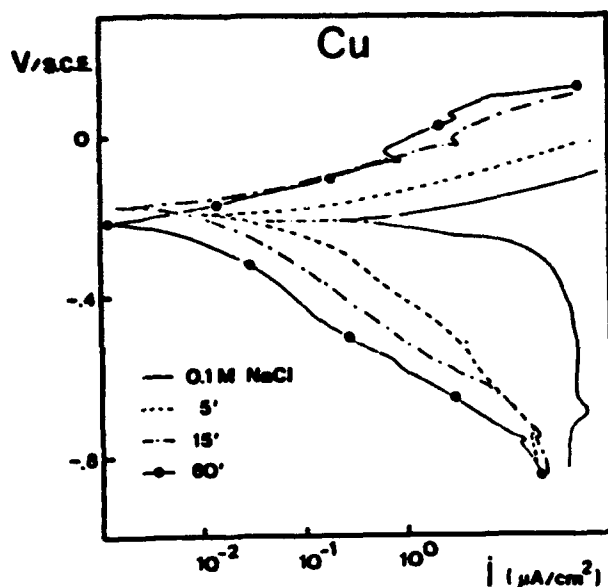


Figure 1. Polarization curves on copper electrodes prefilmmed or not prefilmmed in  $2 \cdot 10^{-4}$  M  $C_6BTA$  solution at  $80^\circ C$ .

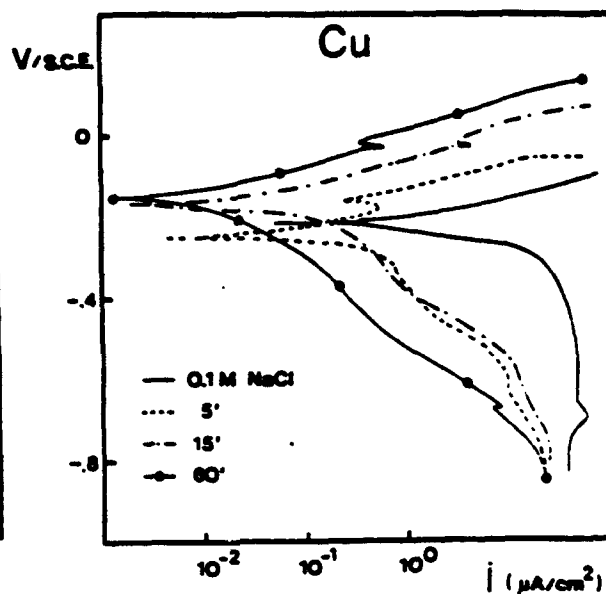


Figure 2. Polarization curves on copper electrodes prefilmmed or not prefilmmed in  $1 \cdot 10^{-4}$  M  $C_6BTA$  solution at  $80^\circ C$ .

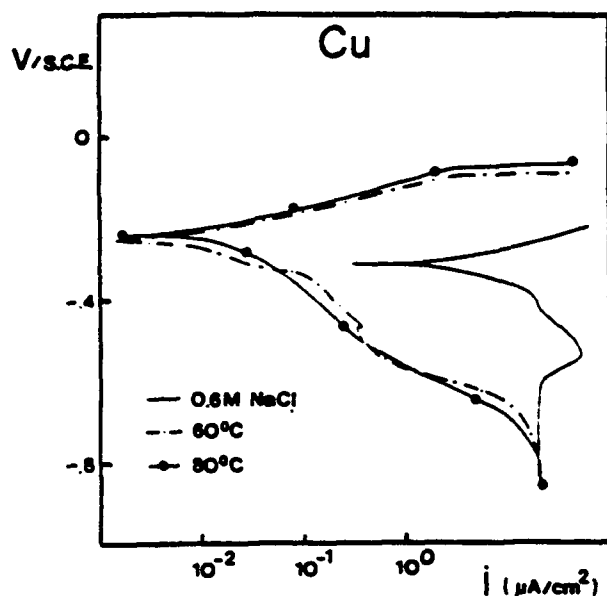


Figure 3. Polarization curves on rotating copper cylinder electrodes prefilmmed or not prefilmmed in  $2 \cdot 10^{-4}$  M  $C_6BTA$  solution.

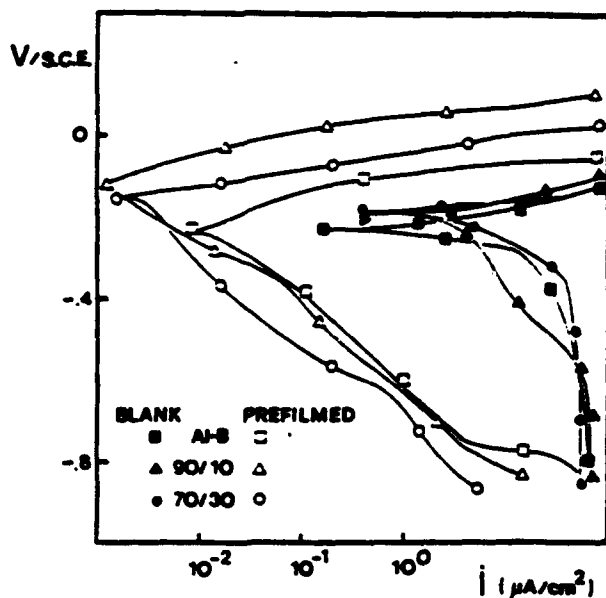


Figure 4. Polarization curves on different copper alloys electrodes prefilmmed or not prefilmmed in  $2 \cdot 10^{-4}$  M  $C_6BTA$  solution at  $80^\circ C$ .

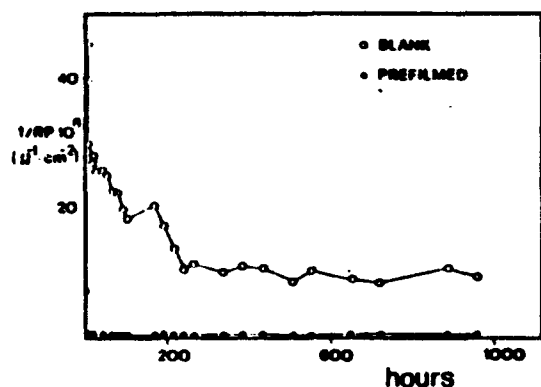


Figure 5. Polarization conductances on copper electrodes prefilmed or not prefilmed in  $C_6BTA$  solution at  $80^\circ C$ . Test solution is  $0.1 M NaCl$  at  $40^\circ C$ .

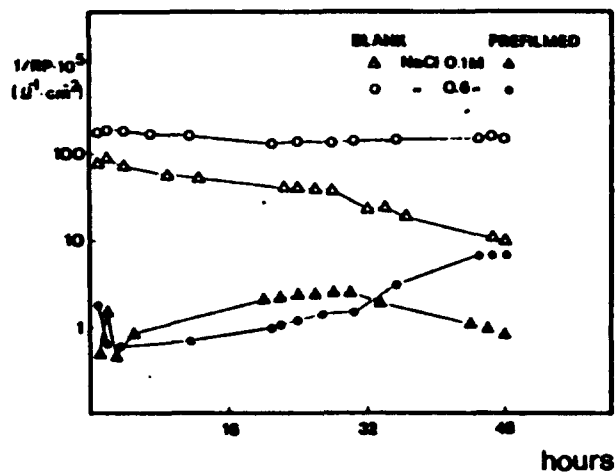


Figure 6. Polarization conductances on rotating copper cylinder electrodes prefilmed or not prefilmed in  $C_6BTA$  solution at  $80^\circ C$ .

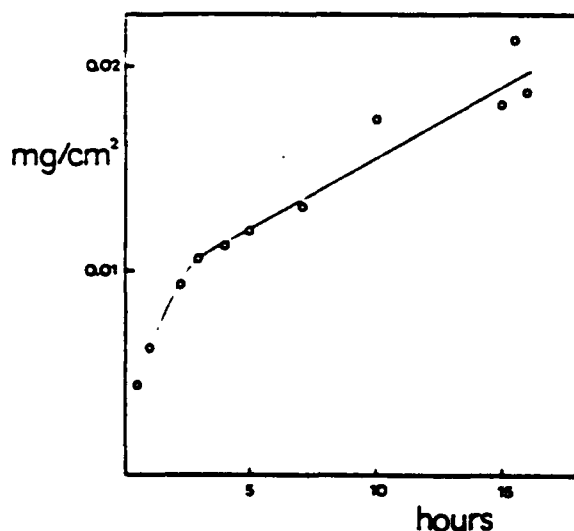


Figure 7. Amount of organic additive on the metal surface as a function of time.

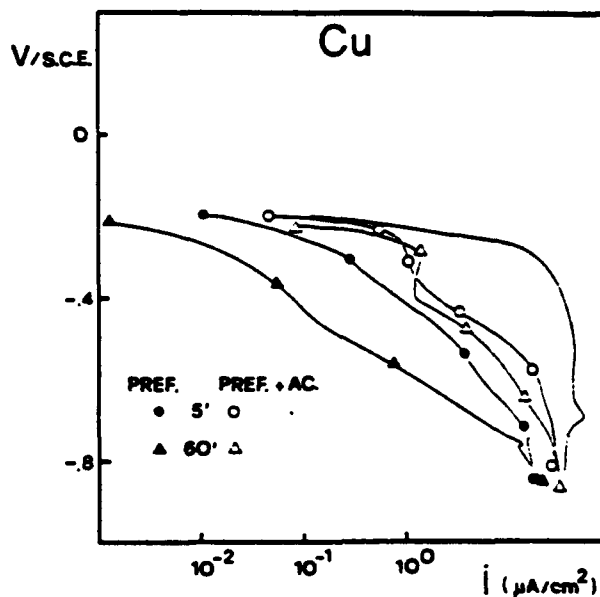


Figure 8. Cathodic polarization curves on prefilmed copper electrodes washed or not washed with acetone.

# Study of the Effect of Inhibitors on the Removal of Scale From Mild Steel Surface During Pickling

G. Banerjee and S.N. Malhotra

Corrosion Sc. & Engg.,  
Dept. of Metallurgical Engg.,  
Indian Institute of Technology,  
Powai, Bombay - 400 076, India.

## Abstract

Several organic compounds are widely used as corrosion inhibitors for pickling of mild steel in acid solutions. While the mechanism of their action on bare steel surface has been investigated thoroughly, their effect on the oxide scale during pickling and the mechanism of the removal of scale from steel surface during pickling have not yet been reported. The present paper discusses the mechanism of scale removal from steel surface during pickling and the effect of inhibitor on the removal of oxide scale.

**Keywords** — Pickling, inhibitor.

## Introduction

The term *pickling* normally means the removal of scale, formed on steels during shaping operations and heat treatment, in acid solution. Two different types of scale are normally found to form on the plain-carbon and low-alloy steels[1] :

- i) High temperature scale which forms above 570°C has a layered structure and consists of a layer of wustite( $\text{FeO}$ ) adjacent to the metal, a layer of magnetite ( $\text{Fe}_3\text{O}_4$ ) and an outer layer of hematite( $\text{Fe}_2\text{O}_3$ ) The thickness of the scale and the relative amounts of the different phases present depend on the temperature, gas composition, alloying elements and time of scale formation.
- ii) Low temperature scale which forms below 570°C is a two layer scale and consists of an internal layer of magnetite and an

external layer of hematite. The phases often have pronounced boundaries. They may interpenetrate and contain inclusions of unoxidized metal, slags, cracks and other defects.

Pickling scale from steels in acid solutions is a complicated process. The rate of this process is determined by the thickness, composition and continuity of the scale, the composition of the pickling solution and pickling conditions. The pickling solution always contains corrosion inhibitors. These inhibitors are generally organic compounds. The mechanism of action of these compounds as acid corrosion inhibitors has so far been discussed in published literatures, considering their effect on bare steel surface[2-3]. But no information is as yet available about the effect of inhibitor on the mild steel surface, covered with oxide scale, during pickling. This information is considered to be very important, since, it is the oxide scale and not the bare steel surface which matters in the initial stages of pickling. In this paper, the mechanism of scale removal from steel surface during pickling and the effect of inhibitor on the removal of scale have been discussed.

### Experimental

Several mild steel panels (of size 5 cm x 5 cm x 0.1 cm) were polished up to 400 grit and kept at 700°C for two hours. They were then air cooled to get the blue black mill-scale on the surface. The composition of the steel was as follows :

*C 0.148%, S 0.034%, Mn 0.656%, Si & P undetected, balance Fe.*

The XRD spectrum of mild steel surface with mill scale was recorded before pickling. The variations of the open circuit potential (OCP) of steel with mill scale in freshly prepared pickling solution with and without inhibitor formulation were observed from the time of dipping to the end of pickling. The pickling experiments were done at two different temperatures, viz. 30°C and 40°C. During each experiment, the temperature of the system was kept constant with the help of a constant temperature bath (Julabo model F 20 VC). The pickling solution was prepared



by adding a mixture of diphenyl amine and para anisidine (which acted as corrosion inhibitor) to a bath of 5% hydrochloric acid solution. The inhibitor mixture has earlier been found to have very good efficiency[4]. When the pickling was over, the undissolved scale, settled at the bottom of the bath, was collected over benzene (to avoid air-oxidation) and its XRD spectrum was recorded.

To find out the nature of the cation being dissolved in the acid, a small amount of potassium ferricyanide was added to the bath containing inhibitor and also to the bath without inhibitor, when the pickling was in progress. Both the baths were kept under ultra pure  $N_2$  atmosphere. The color change in both the baths were observed.

The above experiments were repeated with the addition of a small amount of potassium thiocyanate instead of ferricyanide, at the end of pickling. Again the color of the solutions were observed.

### Results and Discussions

The typical variation in open circuit potential(OCP) of various specimens with time is shown in fig. 1. The OCP of steel with mill scale in freshly prepared pickling solution kept at 30°C and without inhibitor was observed as +10 mV at the time of dipping. It soon changed to negative value and reached a value of -460 mV within 2 minutes accompanied with hydrogen evolution. Flaking of the scale was found to start a few seconds after dipping the steel panel in the acid. When the specimen with mill scale was exposed to acid containing inhibitor formulation, at the same temperature, the OCP was found to be +280 mV just after dipping and it slowly decreased for about 2 minutes. At this point, it was observed that flaking of the scale began. Thereafter the OCP changed to negative values and reached a constant potential -510 mV in next 2 minutes. When the temperature of the pickling bath was raised to 40°C, the same OCP value, i.e., -510 mV was reached within 3 minutes from the time of dipping. The evolution of hydrogen was much slower compared to that observed in the case of pickling without inhibitor at both the temperatures.

Fig. 1 shows three distinct stages in the pickling process :

- i) the first stage, identified with the positive OCP at the beginning of the pickling;
- ii) the second stage, during which the OCP slowly moves towards zero; and,
- iii) the third stage, marked by a much sharper change in the nature of OCP from positive to negative to attain a steady potential.

In the first stage, i.e., at the beginning of the pickling, a high positive OCP is observed in presence of inhibitors. This can be attributed to the adsorption of inhibitors on the oxides which impede their dissolution[5]. It is supported by the observation that the color of the solution, which was kept under ultra pure  $N_2$  atmosphere, remained unchanged initially in the presence of potassium ferricyanide. The XRD spectrum of a steel panel with mill scale at the surface (fig. 2) shows the presence of wustite( $FeO$ ) peak along with that of hematite( $\gamma-Fe_2O_3$ ) and magnetite( $Fe_3O_4$  or  $Fe_2O_3 + FeO$ ). Since the rate of dissolution of wustite in acid is faster than hematite[6], if there were any dissolution of  $FeO$ , the presence of  $Fe^{2+}$  ions would have changed the color of the solution to prussian blue. This means that wustite does not immediately come in physical contact with the when inhibitor is present in the acid.

In absence of inhibitor, however, wustite comes in direct physical contact with the pickling acid. The rate of dissolution of wustite is quite fast in this case which is manifested by the rapid change of OCP from the initial positive value towards zero. The instant change of color of the pickling bath to prussian blue was also observed when pickling was done in absence of inhibitor.

Inhibitor retarded the dissolution of wustite( $FeO$ ) and kept the potential of the system positive for a relatively longer period by being adsorbed on the active sites of the steel surface (defects in the scale where  $FeO$  was exposed). During the second stage, however, slow dissolution of wustite took place. This was indicated by the slow change in color of the solution to prussian

blue, when potassium ferricyanide was present in the solution. When, instead of potassium ferricyanide, potassium thiocyanate was added to the pickling bath, no visible change in color of the solution could be observed. This strongly suggests that there was hardly any dissolution of  $\text{Fe}_2\text{O}_3$  or hematite phase.

As the second stage approaches the end, at a certain moment of time, the scale loses contact with the metal and starts flaking out exposing the bare metal surface. This time represents the complete dissolution of wustite. From this time the OCP shows a sharp change from positive to negative values and attains a steady-state potential along with hydrogen evolution. This is the third stage which represents the end of pickling.

The undissolved scale which settled at the bottom of the bath after flaking out from steel was collected over benzene (to avoid air-oxidation) and was analyzed by X-ray diffraction method. The analysis shows that this scale is hematite or  $\gamma\text{-Fe}_2\text{O}_3$  (fig.3). This analysis thus corroborates the previous observation that there was no change in color or no red coloration of the solution at the end of pickling when potassium thiocyanate was added to the pickling bath.

### Conclusions

- \* The XRD spectrum of mild steel with mill-scale showed the presence of wustite( $\text{FeO}$ ) peak along with that of hematite( $\text{Fe}_2\text{O}_3$ ) and magnetite( $\text{Fe}_3\text{O}_4$ ).
- \* The instant blue coloration of the pickling solution without inhibitor, on addition of potassium ferricyanide, while the pickling was in progress, proved that the  $\text{FeO}$  got dissolved first.
- \* The inhibitor retarded the rate of dissolution of wustite.
- \* The hematite was not dissolved in the pickling process.

### References

1. J.M. Benar, *Oxidation of Metals*, Metallurgya, Moscow, 1, (1968), p. 174.
2. G. TrabANELLI and V. Carassiti, in *Advances in Corrosion Sc. & Tech.*, Ed. M.G. Fontana and R.W. Staehle, Plenum Press, NY, 1, (1970), p. 147.
3. G. TrabANELLI, in *Corrosion Mechanisms*, Ed. F. Mansfeld, Marcel Dekker Inc., NY, (1986), p. 119.
4. G. Banerjee, *Ph.D. Dissertation*, I.I.T.-Bombay, India, 1992.
5. N.I. Podobaev, in *Hydrogen in Metals*, Ed. I.M. Bernstein and A.W. Thompson, 1st Edn., ASM, Metals Park, OH, 1, (1974), p. 595.
6. M.N. Maksimenko and N.I. Podobaev, *Inhibitors of Metal Corrosion*, MGPI, Moscow, (1969), p. 144.

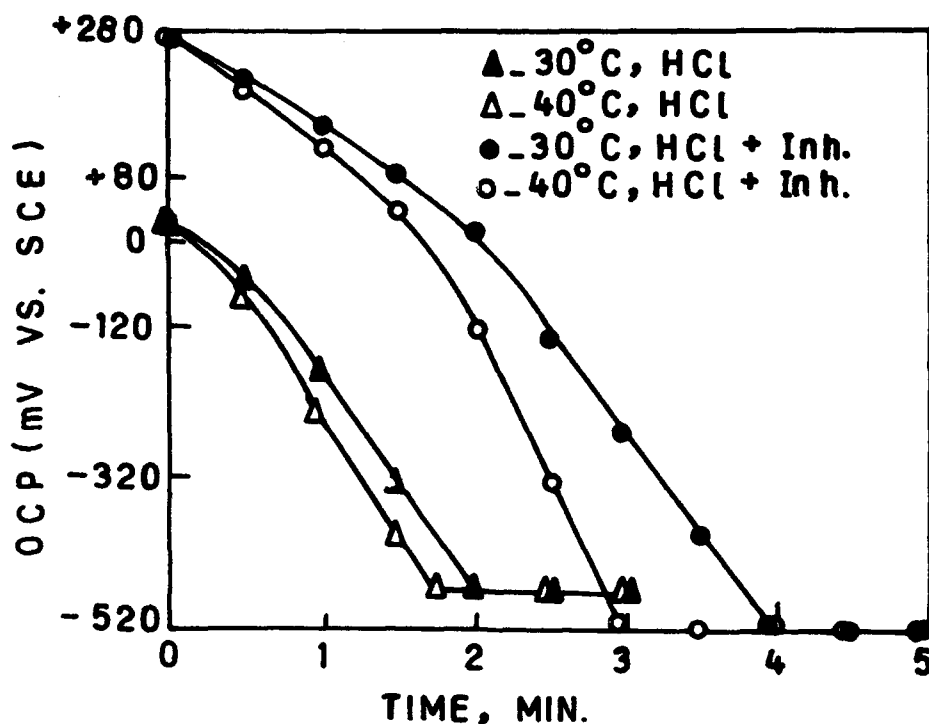


FIG. 1 - VARIATION OF OCP WITH TIME

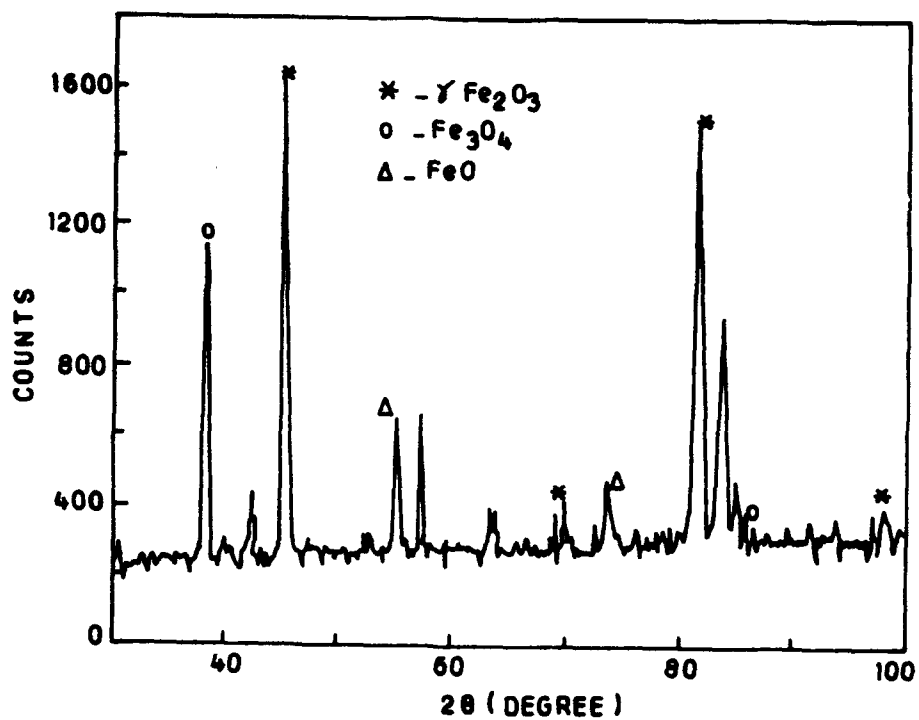


FIG.2 - XRD SPECTRUM OF MILD STEEL SURFACE WITH MILL SCALE

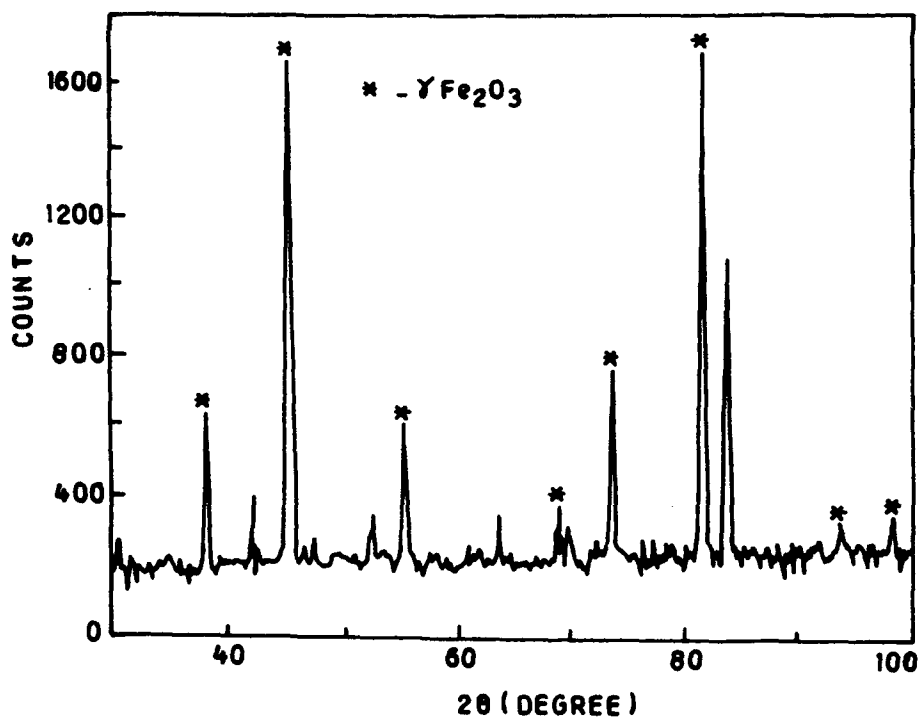


FIG.3 - XRD SPECTRUM OF UNDISSOLVED MILL SCALE

**Theoretical Calculation and Experimental Verification of Critical Passivation  
Concentration of Oxidizing Inhibitors in Acid Solutions**

Mingqi Zhao  
Nanjing Power Institute  
Nanjing 210042  
P. R. China

**Abstract**

If oxidizing inhibitor is used in corrosive media, the critical passivation concentration is the most important parameter evaluating the properties of oxidizing inhibitors. The theoretical calculation formula of critical passivation concentration and the reduction characteristics of oxidizing inhibitors  $K_2CrO_4$ ,  $NaVO_3$ ,  $Na_2MoO_4$  are investigated in this paper. By polarographic technique and copper amalgam rotating disk electrode (RDE) method, the range of limiting diffusion of reduction, the electron number of reduction and the diffusion coefficient of  $CrO_4^{2-}$ ,  $VO_3^-$  or  $MoO_4^{2-}$  are obtained. Then the passivation potential  $\varphi_p$ , which is found to fall in to the range of limiting diffusion of  $K_2CrO_4$ ,  $NaVO_3$  or  $Na_2MoO_4$  reduction and the passivation current density  $i_p$  of stainless steel (SS) or titanium alloy ( $TiCl_3$ ) which is proved to be equal to the limiting diffusion density  $i_d$  of  $K_2CrO_4$ ,  $NaVO_3$  or  $Na_2MoO_4$  are determined by measuring the anodic polarization curves of SS or  $TiCl_3$  RDE. Then, the theoretical calculation formula of critical passivation concentration of  $K_2CrO_4$ ,  $NaVO_3$  or  $Na_2MoO_4$  for metal RDE in  $H_2SO_4$  solution is deduced:

$$C_{crit} = \frac{i_p}{0.62nFD^{2/3}\nu^{-1/6}\omega^{-1/2}}$$

Potentiometric titration method is employed to measure the practical critical passivation concentration to verify the theoretical  $C_{crit}$  at any rotating rate. Results show that the theoretical  $C_{crit}$  and practical  $C_{crit}$  are approximately equal to each other at the same rotating rate.

**Key terms:** oxidizing inhibitor, passivation, rotating disk electrode,  
critical passivation concentration

## Introduction

Oxidizing inhibitor may be a dangerous one<sup>(1)</sup>; meager dosage can accelerate the corrosion of metal and excessive dosage can increase the operational cost. So determination of critical passivation concentration ( $C_{crit}$ ) of oxidizing inhibitor is the most important in passivation process of metal<sup>(2)</sup>.

Though passivation concentration of oxidizing inhibitor such as  $K_2CrO_4$ ,  $NaVO_3$ ,  $Na_2MoO_4$ ,  $FeCl_3$ ,  $NaNO_2$  is so far got in some corrosive media by using weight loss method, resistor method and static potentiometric titration method<sup>(1,3,4)</sup> the results are rough or half-quantitative. Studies about how to get or how to deduce theoretically the critical passivation concentration are much lesser. Besides, many scholars are mainly interested in the effect of oxidizing inhibitor on the anodic polarization behavior of metal while overlooking its cathodic reduction process, and the later is very important to probe the passivation mechanism of oxidizing inhibitor to metal.

In this paper the cathodic reduction process, the diffusion coefficient and the theoretical calculation and verification of critical passivation concentration of oxidizing inhibitors are studied in the passivation step by selecting  $K_2CrO_4$ ,  $NaVO_3$ ,  $Na_2MoO_4$  as oxidizing inhibitors, 0.55 mol/L and 3.0 mol/L  $H_2SO_4$  as corrosive media, stainless steel (SS) and titanium alloy ( $TiC_4$ ) as active-passive metals.

## Experimental

### 1. Apparatus

The polarographic curves of  $K_2CrO_4$ ,  $NaVO_3$ ,  $Na_2MoO_4$  are determined with Polarecord E<sub>506</sub>. The cathodic polarization curves of copper amalgam rotating disk electrode (RDE) and the anodic polarization curves of SS RDE and  $TiC_4$  RDE are determined with ATA-1A RDE device, RDE-4 potentiostat and LZ 3-104 X-Y recoder. Platinum sheet and saturated calomel electrode are used as the auxiliary and reference electrodes, respectively. The chemical composition of SS is C: 0.006; Cr: 16.78; Ti: 0.17; N: 0.011% and its area is 0.1278 cm<sup>2</sup>. The chemical composition of  $TiC_4$  is AL: 5.5~6.8; V: 3.5~4.5; Fe ≤ 0.30; Si ≤ 0.50; C ≤ 0.10; Ni ≤ 0.05; H ≤ 0.015; O ≤ 0.20%. and its area is 0.1859 cm<sup>2</sup>.

The Kinematic viscosity (viscosity/density) is determined with viscosimeter and pycnometer.

### 2. Reagents and corrosive systems

A. R grade chemical reagents are used in this work, except C. P grade  $NaVO_3$ ,  $H_2SO_4$  solutions are prepared from A. R grade  $H_2SO_4$  and distilled water. Experiments are performed in the following deaerated system:

A: 0.55 mol/L  $H_2SO_4$ , 30°C

B: 3.0 mol/L  $H_2SO_4$ , 50°C

## Results and Discussions

1. The polarographic behaviors of  $K_2CrO_4$ ,  $NaVO_3$  or  $Na_2MoO_4$  in  $H_2SO_4$  solutions.

The polarographic curves of  $K_2CrO_4$ ,  $NaVO_3$  or  $Na_2MoO_4$  are studied with mercurimetric electrode in order to understand their characteristics of cathodic reduction and find their electron numbers of reduction and diffusion coefficients.

A. the exchanged electron number of oxidizer in electrode reaction

In order to avoid the oxidization of mercury to produce  $Hg^{2+}$  by  $K_2CrO_4$ ,  $NaVO_3$  in acid solutions, a cathodic potential as large as  $-0.20$  V (v. s. Ag/AgCl) is applied to the mercurimetric electrode before experiment. The polarographic curves of  $K_2CrO_4$ ,  $NaVO_3$ ,  $Na_2MoO_4$  beginning with  $-0.20$  V are shown in Figure 1 and 2. It can be seen that the polarographic curves of  $K_2CrO_4$  or  $NaVO_3$  are similar in  $0.55$  mol/L  $H_2SO_4$ ,  $30^\circ C$  and  $3.0$  mol/L  $H_2SO_4$ ,  $50^\circ C$ . The reduction of  $K_2CrO_4$  or  $NaVO_3$  goes into limiting diffusion region as soon as the electrode is polarized. The passivation potential  $\varphi_p$  of SS RDE or  $TiC_4$  RDE discussed lately falls into the range of limiting diffusion of  $K_2CrO_4$  or  $NaVO_3$ . Because the  $Na_2MoO_4$  is a weaker oxidizer compared with the  $K_2CrO_4$  or  $NaVO_3$ , its cathodic reduction is not controlled by limiting diffusion step until less than  $-0.50$  V (v. s. Ag/AgCl).

In figure 1 and 2, the polarographic curves of  $Cd^{2+}$  which redox reaction is reversible are given for comparison. It is known that the electron number of  $Cd^{2+}$  gained in following reaction is 2:



According to Ilković formula

$$I_d = 607nD^{1/2}m^{2/3}t^{1/6}C^0 \quad (2)$$

where

- $\bar{I}_d$  — the average limiting diffusion current,  $\mu A$
- $n$  — electron number transferred in electrode reaction
- $D$  — the diffusion coefficient of reactant  $cm^2/sec$
- $m$  — velocity of mercury drop,  $mg/sec$
- $t$  — dropping time of mercury drop,  $sec$
- $C^0$  — the bulk concentration of reactant,  $mol/cm^3$

If the bulk concentration  $C^0$  of two oxidizers is the same and their diffusion coefficients  $D$  are approximately equal to each other (generally  $10^{-5} cm^2/sec$ ), then  $\bar{I}_d$  is in proportion to electron number  $n$ , that is,  $\bar{I}_d \propto n$



n. From Figure 1 and 2, the magnitude of the limiting diffusion current of  $K_2CrO_4$ ,  $NaVO_3$  or  $Na_2MoO_4$  is 1.5 times, 0.5 times of or similar to that of  $CdSO_4$  while their bulk concentration remains same. So it could be obtained that the electron number of  $K_2CrO_4$ ,  $NaVO_3$  or  $Na_2MoO_4$  gained in reduction process is 3 (—0.20 V — —1.0V), 1 (—0.20V — —0.90V) or 2 (—0.20V — —1.0 V)

From Figure 1 and 2, it is also discovered that the second reduction step of  $NaVO_3$  begins at —0.90V in 0.55 mol/L  $H_2SO_4$ . According to the height of cathodic reduction wave we could conclude that the electron number of  $NaVO_3$  gained in this step is 2. Because of the reduction of  $H^+$  in advance in 3.0 mol/L  $H_2SO_4$ , the obvious appearance of the second wave of  $NaVO_3$  reduction cannot be observed.

B. diffusion coefficients of  $CrO_4^{2-}$ ,  $VO_3^-$ ,  $MoO_4^{2-}$ :

According to Equations 2, the diffusion coefficient is:

$$D = \left( \frac{I_d}{607 \pi m^{2/3} t^{1/6} C^0} \right)^2 \quad (3)$$

the calculations of diffusion coefficients of  $CrO_4^{2-}$ ,  $VO_3^-$ ,  $MoO_4^{2-}$ ,  $Cd^{2+}$  are shown in Table 1. The D for every ion is near to  $10^{-5} \text{ cm}^2/\text{sec}$ .

2. The cathodic polarization curves of copper amalgam RDE in  $K_2CrO_4$  or  $NaVO_3$  containing  $H_2SO_4$  solutions

The cathodic polarization curves of copper amalgam RDE in 0.55 mol/L  $H_2SO_4$  containing 10 mmol/L  $K_2CrO_4$  or 10 mmol/L  $NaVO_3$  are shown in Figure 3, 4 in order to demonstrate the cathodic reduction behaviors of  $K_2CrO_4$ ,  $NaVO_3$  on rotating disk electrode. It is found that the passivation potential of SS is also in the range of limiting diffusion of  $K_2CrO_4$  or  $NaVO_3$  reduction and the limiting diffusion current density  $i_d$  of  $K_2CrO_4$  or  $NaVO_3$  increases with increasing the rotating rate  $\omega$  of copper amalgam RDE. The relationship between the  $i_d$  and  $\omega^{1/2}$  is a straight line that passes through the origin of coordinate shown in Figure 5. The gradients for  $K_2CrO_4$  and  $NaVO_3$  are  $1.778 \times 10^{-3} \text{ A} \cdot \text{s}^{1/2}/\text{cm}^2$  and  $0.48 \times 10^{-3} \text{ A} \cdot \text{s}^{1/2}/\text{cm}^2$  respectively. The formula of limiting diffusion current density on RDE is:

$$i_d = 0.62 \pi F D^{2/3} \omega^{1/2} \nu^{-1/6} C^0 \quad (4)$$

where:  $i_d$ ——the limiting diffusion density of oxidizing inhibitor on RDE,  $\text{A} \cdot \text{cm}^{-2}$

n——the electron number of reactant ion gained in cathodic reduction process

F——Faraday constant (96500 A.s)

D——the diffusion coefficient of reactant ion  $\text{cm}^2 \cdot \text{s}^{-1}$

$\omega$ ——the rotating rate of RDE,  $\text{rad} \cdot \text{s}^{-1}$

$\nu$ ——kinematic viscosity of  $H_2SO_4$  solutions,  $\text{cm}^2 \cdot \text{s}^{-1}$

$C^*$ —the bulk concentration of reactant ion, mol/cm<sup>3</sup>

We can have

$$D = \left[ \frac{1}{0.62nF\nu^{-1/6}C^*} \left( \frac{\partial i_a}{\partial \omega^{1/2}} \right) \right]^{3/2} \quad (5)$$

The density  $d$  and the viscosity  $\eta$  of 0.55 mol/L  $H_2SO_4$  are measured from experiments;  $d = 1.0271 \text{ g} \cdot \text{cm}^{-3}$ ,  $\eta = 1.0783 \times 10^{-2} \text{ P}$  thus the kinematic viscosity

$$\nu = 1.0498 \times 10^{-2} \text{ cm}^2 \cdot \text{s}^{-1} \quad (6)$$

The bulk concentration  $C^*$  of  $K_2CrO_4$  or  $NaVO_3$  is 10 mmol/L, then substituting Equation (6), the value of  $C^*$  and the gradient of plot of  $i_a$  to  $\omega^{1/2}$  into Equation (4) gives

$$D_{CrO_4^{2-}} = 0.998 \times 10^{-5} \text{ cm}^2/\text{sec}, D_{VO_3^-} = 0.727 \times 10^{-5} \text{ cm}^2/\text{sec} \quad (7)$$

Above results are also listed in Table 1. It can be seen that the diffusion coefficients of  $CrO_4^{2-}$ ,  $VO_3^-$  got by polarographic technique and RDE method are approximately equal to each other, that is, the reduction process of  $CrO_4^{2-}$ ,  $VO_3^-$  is similar on mercurimetric electrode and on rotating disk electrode.

### 3. The anodic polarization curves of SS RDE and $TiCl_3$ RDE in $H_2SO_4$ solutions.

The anodic polarization curves of SS in 0.55 mol/L  $H_2SO_4$  and  $TiCl_3$  in 3.0 mol/L  $H_2SO_4$  are shown in Figure 6, 7. It is shown that in  $H_2SO_4$  solutions, the anodic polarization curves of rotating SS and  $TiCl_3$  disks can be divided into four parts: active, transitive, passive and over—passive region (for  $TiCl_3$  in 3.0 mol/L  $H_2SO_4$ , the over—passive region is not given in Figure 7). The shape of SS or  $TiCl_3$  anodic polarization curves and the critical passivation current density  $i_p$  are independent of the rotating rates. The critical passivation current density of SS or  $TiCl_3$  is 18.25 or 1.44 mA/cm<sup>2</sup>. The passivation potential  $\varphi_p$  of SS or  $TiCl_3$  is -400 mV or -515 mV(SCE).

### 4. Theoretical formula of critical passivation concentration

The passivation potential of SS RDE or  $TiCl_3$  RDE is in the range of the limiting diffusion of reduction of  $K_2CrO_4$ ,  $NaVO_3$  or near the range of limiting diffusion of reduction of  $Na_2MoO_4$  according to Figure 1—4. Suppose that  $K_2CrO_4$ ,  $NaVO_3$  or  $Na_2MoO_4$  reduction is diffusion controlled and reaches its limiting diffusion at passivation potential  $\varphi_p$  of metal, the relationship between the limiting diffusion current density and the critical passivation concentration of  $K_2CrO_4$ ,  $NaVO_3$  or  $Na_2MoO_4$  can be obtained by Equation (4)

$$i_a = 0.62nFD^{2/3}\nu^{-1/6}\omega^{1/2}C_{crit} \quad (8)$$

If the limiting diffusion current density  $i_L$  of  $K_2CrO_4$ ,  $NaVO_3$  or  $Na_2MoO_4$  is equal to the critical passivation current density  $i_{pp}$  of SS or  $TiCl_4$ , the existence of  $K_2CrO_4$ ,  $NaVO_3$  or  $Na_2MoO_4$  at its critical passivation concentration can make the active — passive metal passivate. In other words, if the addition of oxidizing inhibitor at certain concentration can make metal passivate, there must be:

$$i_{pp} = i_L = 0.62nFD^{2/3}v^{-1/6}\omega^{1/2}C_{crit} \quad (9)$$

then:

$$C_{crit} = \frac{i_{pp}}{0.62nFD^{2/3}v^{-1/6}\omega^{1/2}} = m\omega^{-1/2} \quad (10)$$

where:

$$m = \frac{i_{pp}}{0.62nFD^{2/3}v^{-1/6}} \quad (11)$$

If  $i_{pp}$  is a constant having nothing to do with the rotating rates, the  $m$  should be a constant. Thus, the relationship between  $C_{crit}$  and  $\omega^{-1/2}$  should be:

- (1) a straight line that passes through the origin of coordinates,
- (2) the slope of the line:  $m = \frac{i_{pp}}{0.62nFD^{2/3}v^{-1/6}}$

Besides, by means of the data of  $i_{pp}$ ,  $D$ ,  $V$  obtained from above experiment results we can obtain the theoretical value of  $m$  and  $C_{crit}$  at different rates. The calculations are shown in Table 2.

## 5. Experimental verification of theoretical $m$ and $C_{crit}$

The potentiometric titration method is used to verify the theoretical critical passivation concentration. The potentiometric titration curves in deaerated 0.55 mol/L  $H_2SO_4$  by using 0.55 mol/L  $H_2SO_4$  containing  $K_2CrO_4$ ,  $NaVO_3$  or  $Na_2MoO_4$  as titrant and SS RDE as indicating electrode are shown in Figure 8, 9, 10. The experimental results are given in Table 2. The critical passivation concentration of  $K_2CrO_4$  or  $NaVO_3$  for  $TiCl_4$  RDE in 3.0 mol/L  $H_2SO_4$  are also listed in Table 2. The relationship between theoretical or experimental  $C_{crit}$  and  $\omega^{-1/2}$  is shown in Figure 12, 11. It is shown that:

(1)  $K_2CrO_4$ ,  $NaVO_3$  and  $Na_2MoO_4$  are typical oxidizing inhibitors. Below the critical passivation concentration, the potential of SS or  $TiCl_4$  remains in the active region in spite of the redox potential of these oxidizing inhibitors staying in the passive region indicated by the potential of the platinum electrode. Once the concentration of  $K_2CrO_4$ ,  $NaVO_3$  or  $Na_2MoO_4$  reaches its critical passivation concentration, the potential of SS or  $TiCl_4$  will jump from active region into passive region.

(2) the critical passivation concentration of  $K_2CrO_4$ ,  $NaVO_3$  or  $Na_2MoO_4$  decreases with increasing rotating rates. The experimental result of critical passivation concentration is approximately equal to the theoretical one at certain rotating rates.

(3) the plots between  $C_{crit}$  and  $\omega^{-1/2}$  correspond to the deduction of Equation (10). The experimental result of  $m$  is near to the theoretical one. It is revealed that the reduction of  $K_2CrO_4$ ,  $NaVO_3$  or  $Na_2MoO_4$  is wholly diffusion controlled at metal passivation potential.

Above results indicate that in acid solutions by Equation (10) the critical passivation concentration (or dosage) of strong oxidizing inhibitors like  $K_2CrO_4$ ,  $NaVO_3$  or  $Na_2MoO_4$  can be calculated theoretically for active-passive metal.

### Conclusions

In  $H_2SO_4$  solutions

- (1) stainless steel or titanium alloy is a active-passive metal.
- (2)  $K_2CrO_4$ ,  $NaVO_3$ ,  $Na_2MoO_4$  are typical oxidizing inhibitors. The passivation of metal is due to the reduction of  $K_2CrO_4$ ,  $NaVO_3$  or  $Na_2MoO_4$ .
- (3) If the passivation potential  $\varphi_{pp}$  falls into or nears to the limiting diffusion range of certain oxidizing inhibitor, formula

$$C_{crit} = \frac{i_p}{0.62nFD^{2/3}v^{-1/6}}\omega^{-1/2}$$

can be used to calculate theoretically the critical passivation concentration of oxidizing inhibitor in certain corrosive media by measuring the anodic polarization curves of a active-passive metal.

### References

1. M. Stern, J. Electrochem. Soc., 11, 638 (1958)
2. Zhou Benshen and Yang Jinxin, Proceedings of the 6th European Symposium on Corrosion Inhibitors, 397, Ann. Univ. Ferrara (1985)
3. M. J. Pryor and M. Cohen, J. Electrochem. Soc., 100, 203 (1953)
4. S. Matsuda and H. H. Vhlig, *ibid*, 111, 156 (1964)

Table 1 Parameters of polarographic curves and copper amalgam RDE in  $H_2SO_4$  solutions containing  $Cd^{2+}$ ,  $CrO_4^{2-}$ ,  $VO_3^-$ ,  $MoO_4^{2-}$

solution	ions	m	t	C°	I <sub>d</sub>	n	D × 10 <sup>5</sup> , cm <sup>2</sup> /sec	
		mg/sec	sec	mM	μA		polarograph	RDE
0.55mol/L $H_2SO_4$ 30°C	$Cd^{2+}$	0.640	1	5	14.36	2	1.015	/
	$CrO_4^{2-}$	0.640	1	5	21.60	3	1.020	0.998
	$VO_3^-$	0.640	1	5	6.47	1	0.850	0.727
	$MoO_4^{2-}$	0.640	1	5	15.80	2	1.080	/
3.0mol/L $H_2SO_4$ 50°C	$Cd^{2+}$	0.647	1	5	12.91	2	0.808	/
	$CrO_4^{2-}$	0.647	1	5	21.09	3	0.959	/
	$VO_3^-$	0.647	1	5	6.65	1	0.860	/

Table 2 The theoretical and experimental value of  $m$  and  $C_{\text{ext}}$ 

rotating rates	rpm		200	600	1000	2000	3000	4000
SS/0.5M H <sub>2</sub> SO <sub>4</sub> 30°C	K <sub>2</sub> CrO <sub>4</sub>	$m, M \cdot s^{-1/2}$	theo.		0.102			
			expe.		0.110			
		$C_{\text{ext}}, \text{mM}$	theo.	22.27	12.86	9.97	7.05	5.76
			expe.	22.77	13.87	10.84	8.29	6.44
	NaVO <sub>3</sub>	$m, M \cdot s^{-1/2}$	theo.		0.342			
			expe.		0.318			
		$C_{\text{ext}}, \text{mM}$	/	43.13	33.43	23.64	19.30	16.71
			/	39.70	29.30	21.43	17.49	16.09
	Na <sub>2</sub> MoO <sub>4</sub>	$m, M \cdot s^{-1/2}$	theo.		0.146			
			expe.		0.150			
		$C_{\text{ext}}, \text{mM}$	theo.	/	18.38	14.27	10.05	8.15
			expe.	/	19.35	13.79	10.31	8.68
TiCl <sub>4</sub> /3.0M H <sub>2</sub> SO <sub>4</sub> 50°C	K <sub>2</sub> CrO <sub>4</sub>	$m, M \cdot s^{-1/2}$	theo.		$8.50 \times 10^{-3}$			
			expe.		$9.08 \times 10^{-3}$			
		$C_{\text{ext}}, \text{mM}$	theo.	/	/	0.83	0.59	0.48
			expe.	/	/	0.89	0.62	0.51
	NaVO <sub>3</sub>	$m, M \cdot s^{-1/2}$	theo.		$2.74 \times 10^{-2}$			
			expe.		$2.97 \times 10^{-2}$			
		$C_{\text{ext}}, \text{mM}$	theo.	/	/	2.68	1.89	1.55
			expe.	/	/	2.89	2.12	1.69

note:  $M = \text{mol/L}$ D used in theoretical calculation of  $C_{\text{ext}}$  is from polarographic method.

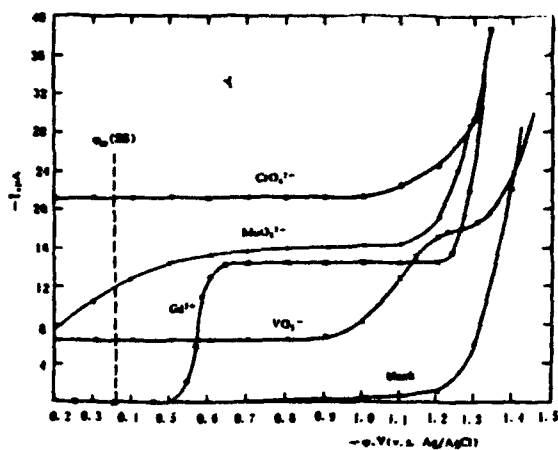


Figure 1 Polarographic curves of 5 mmol/L  $K_2CrO_4$ ,  $NaVO_3$ ,  $Na_2MoO_4$  and  $CdSO_4$  in 0.55 mol/L  $H_2SO_4$ , 30°C, deaerated, mercury column  $h = 54$  cm,  $m =$

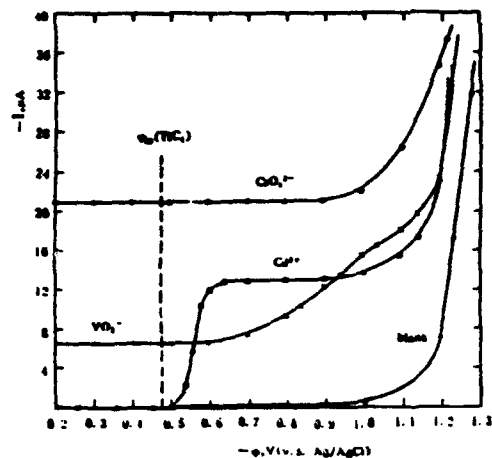


Figure 2 Polarographic curves of 5 mmol/L  $K_2CrO_4$ ,  $NaVO_3$ ,  $CdSO_4$  in 3.0 mol/L  $H_2SO_4$ , 50°C, deaerated mercury column  $h = 54$  cm,  $m = 0.647$  mg/s,  $t = 1$  s

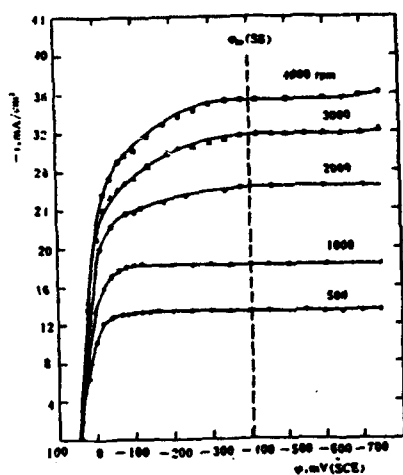


Figure 3 The cathodic polarization curves of copper amalgam RDE in 0.55 mol/L  $H_2SO_4$  containing 10 mmol/L  $K_2CrO_4$  at various rotation rates (30°C, deaerated)

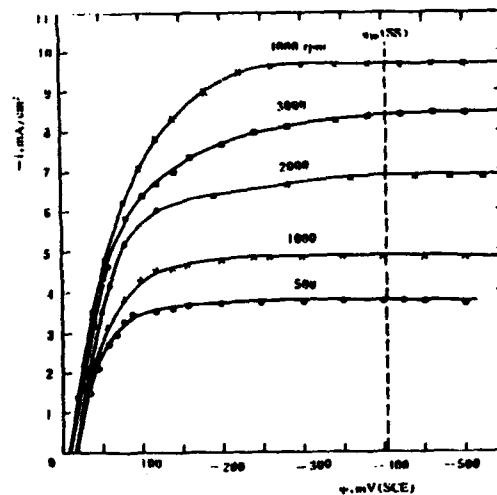


Figure 4 The cathodic polarization curves of copper amalgam RDE in 0.55 mol/L  $H_2SO_4$  containing 10 mmol/L  $NaVO_3$  at various rotating rates (30°C, deaerated)

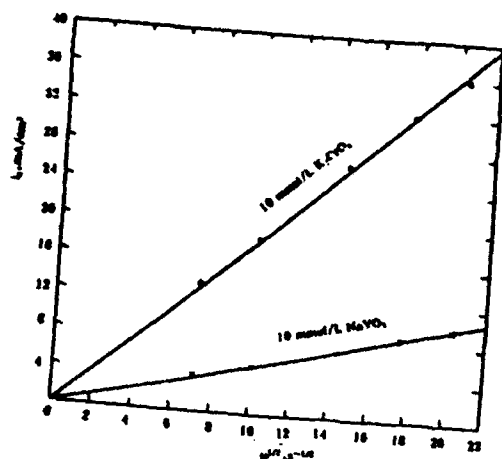


Figure 5 The dependence of  $i_a$  of  $K_2CrO_4$ ,  $NaVO_3$  reduction on  $\omega^{1/2}$  of copper amalgam RDE in 0.55 mol/L  $H_2SO_4$ , 30°C, deaerated.

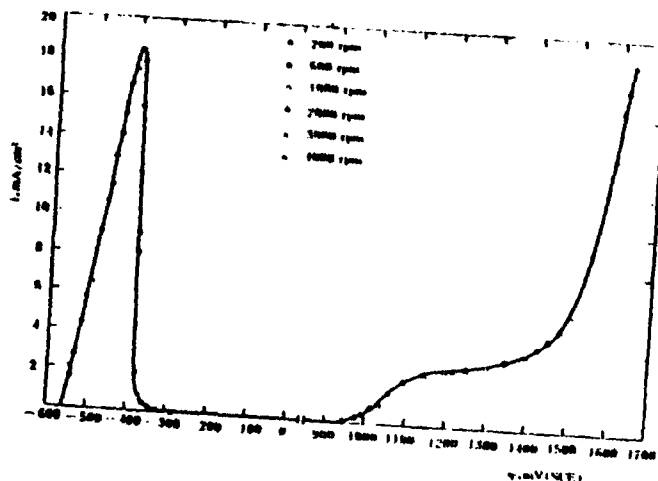


Figure 6 Anodic polarization curves of SS RDE in 0.55 mol/L  $H_2SO_4$  at various rotating rates (30°C, deaerated).

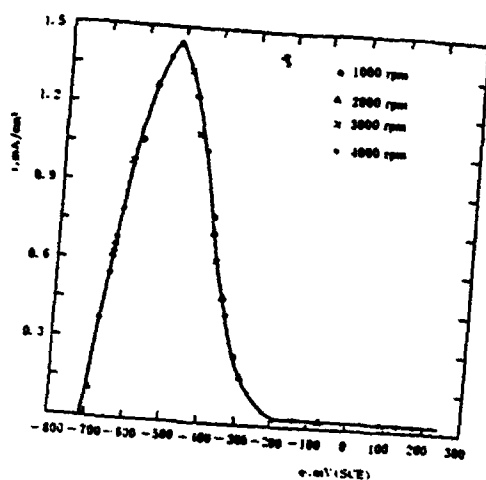


Figure 7 Anodic polarization curves of  $TiC_4$  RDE in 3.0 mol/L  $H_2SO_4$  at various rotating rates (50°C, deaerated).

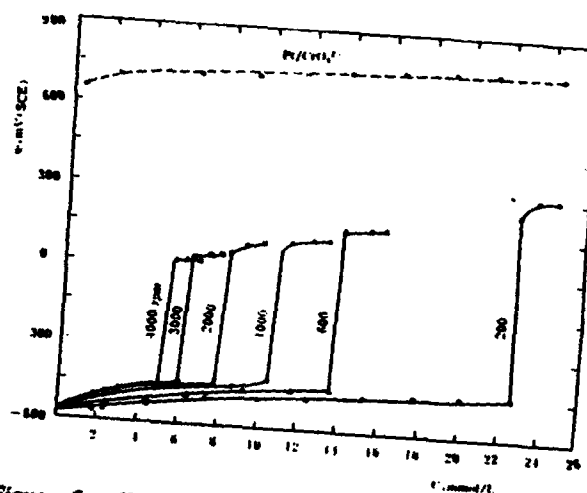


Figure 8 The potentiometric titration curves of SS RDE by  $K_2CrO_4$  in deaerated 0.55 mol/L  $H_2SO_4$  at various rotating rates, 30°C  
--- redox potential of  $K_2CrO_4$

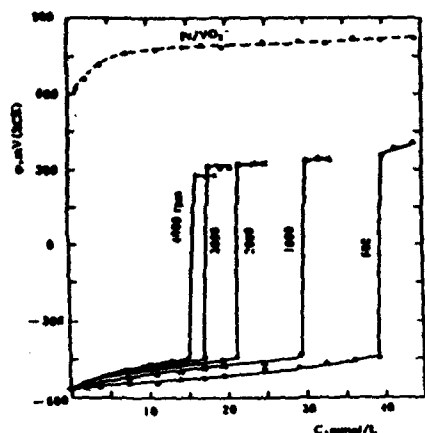


Figure 9 The potentiometric titration curves of SS RDE by  $\text{NaVO}_3$  in deaerated 0.55 mol/L  $\text{H}_2\text{SO}_4$  at various rotating rates, 30°C  
 --- redox potential of  $\text{NaVO}_3$

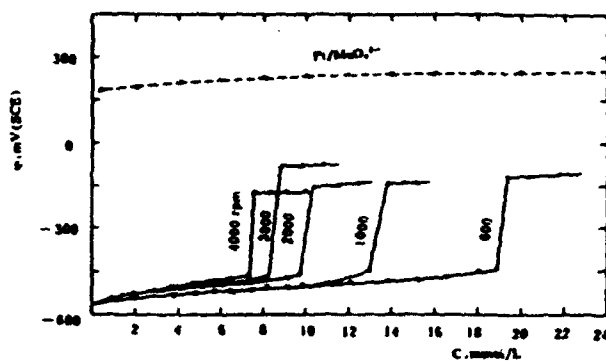


Figure 10 The potentiometric titration curves of SS RDE by  $\text{Na}_2\text{MoO}_4$  in deaerated 0.55 mol/L  $\text{H}_2\text{SO}_4$  at various rotating rates, 30°C  
 --- redox potential of  $\text{Na}_2\text{MoO}_4$

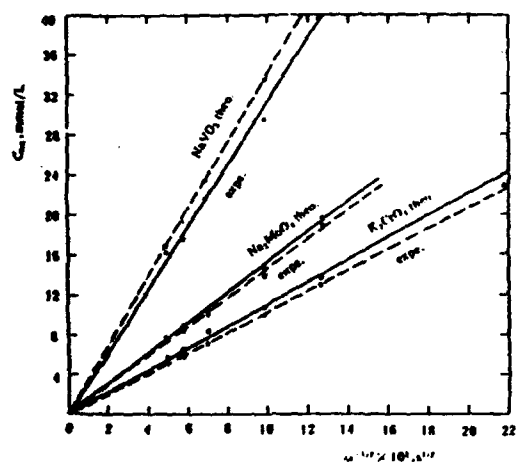


Figure 11 The dependence of  $C_{\text{crit}}$  of  $\text{K}_2\text{CrO}_4$ ,  $\text{NaVO}_3$ ,  $\text{Na}_2\text{MoO}_4$  on  $\omega^{-1/2}$  of SS RDE, in 0.5 mol/L  $\text{H}_2\text{SO}_4$ , 30°C, deaerated

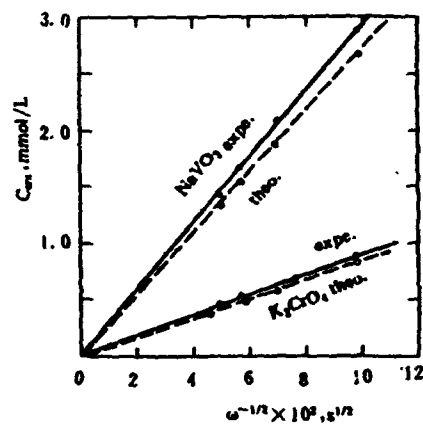


Figure 12 The dependence of  $C_{\text{crit}}$  of  $\text{K}_2\text{CrO}_4$ ,  $\text{NaVO}_3$  on  $\omega^{-1/2}$  of  $\text{TiC}_4$  RDE in 3.0 mol/L  $\text{H}_2\text{SO}_4$ , 50°C, deaerated



**Chemical Composition and Structure of Surface Layer  
Forming in Solutions of Chromate-ions and Corrosion  
Behaviour of Carbon Steel**

**E.Kh.Enikeev**

**Institute of Physical Chemistry,  
Russian Academy of Sciences  
Leninsky prospect 31  
117915 Moscow, Russia**

**M.K.Panov**

**Institute of Physical Chemistry,  
Russian Academy of Sciences  
Leninsky prospect 31  
117915 Moscow, Russia**

**I.M.Krashenninnikova**

**Institute of Physical Chemistry,  
Russian Academy of Sciences  
Leninsky prospect 31  
117915 Moscow, Russia**

**A.K.Feoktistov**

**Institute of Physical Chemistry,  
Russian Academy of Sciences  
Leninsky prospect 31  
117915 Moscow, Russia**

**Abstract**

By using the XPS and SIMS followed by the layer-by-layer etching, the chemical composition and structure of surface layers formed onto the carbon steel in aqueous solutions of chromate-ions were determined. The kinetics of formation and thickness growth of the passivating layers was defined by measuring the shifts of the  $E(t)$  open circuit electrode potential via time. It was discovered that the higher the chromate-ion concentration  $C_{CrO_4^{2-}}$  the lower the  $E_{CO_2}(t)$  curve is positioned. The outer layer was found to represent the  $Cr^{3+}$ hydroxylated compound. The inner layer corresponds to the compounds of variable composition where the  $Fe^{3+}$  component increases monotonically and the  $Cr^{3+}$  component falls mirror-like on approaching the inner blurred layer-metal interface. With rising  $C_{CrO_4^{2-}}$  the relative  $Fe^{3+}$  on concentration increases and that of  $Cr^{3+}$  ions falls, the  $Fe^{3+}/Cr^{3+}$  ratio  $\rightarrow 1$  in the bulk layer. The evidence for the considerable importance of acid-base functions of the chromate-ions in formations of compositions and structure of the passivating layers and corrosion behaviours of steel are presented.

## Introduction

At present, sufficient number of data have been published obtained using in-situ and ex-situ methods in order to draw a conclusion that electro-chemical corrosion of metals and alloys proceeds in all practically important media in the presence of phase layers forming from the reaction products of metal and medium. The determination of dependence of chemical composition and structure of these layers consisting of corrosion products on the composition and pH of aggressive media, alloy composition, and electrode potential becomes rapidly an important part of corrosion process studies. Accumulation of such the data can refine our understanding of the nature of elementary stages and driving forces determining the kinetics of anodic and cathodic processes and the rate of corrosion as a whole, including the corrosion occurring in the presence of inhibitors.

A variety of articles reports the data on the chemical composition and structure of passivating layers formed in aqueous media onto iron and steel surfaces in the presence of chromate-ions [1-3]. In particular, it was established by the method of X-ray photoelectron spectroscopy (XPS) [1] that the chromate-ions when reduced form a thin layer consisting of the mixture of  $\text{Fe}^{3+}$  and  $\text{Cr}^{3+}$  oxides on the iron (steel) surface. As this takes place, the majority of  $\text{Cr}^{3+}$  ions is concentrated on the outer surface of the passivating layer and is hydroxylated in contrast to the passivating layer on the stainless steel where the concentration of  $\text{Cr}^{3+}$ -containing component peaks near the inner boundary [4]. The  $\text{Fe}^{3+}$  ions in this case are concentrated in the vicinity of the inner boundary with formation of the  $\text{Fe}_2\text{O}_3$ -type oxides.

In [3] it is assumed that the outer layer boundary is enriched with compound containing the  $\text{Cr}^{3+}$  ions and is hydroxylated, however, in a bulk layer the permanent variation of the Cr/Fe ratio takes place rather than the definite stoichiometry. The chromium in so doing is in other state than on the outer surface of the passivating layer. In this connection the analysis of chemical composition of the layers and concentration profiles of the main components on variation of the chromate-ion concentration in solution along with the simultaneous monitoring the open-circuit potential are assumed to be able to shed additional light on both the chemical composition/structure of the passivating layers and the mechanisms of growth and dissolution of protective layers in the inhibitor solutions.

## Experimental

The average chemical composition of the passivating layers and the depth distribution of main components formed onto the carbon steel in aqueous solutions of chromate-ions of the concentration ranging from  $10^{-4}$  to  $10^{-1}$  mol/l were determined with the help of XPS and secondary ion mass-spectrometry (SIMS). The kinetics of formation and growth of the passivating layer thickness and the time required for a quasi-steady state of the surface to be achieved were

determined by measuring the shift of the open circuit electrode potential  $E_{CO_2}$  through time.

After mechanical polishing the steel samples were normally held in open solutions of the chromate-ions for 10 days, then they were successively removed from solution, rinsed with distilled water, dried in argon flow, and were placed immediately into a lock chamber of an ESCALAB MKII spectrometer in which analyzer chamber an operating vacuum at a level of  $10^{-9}$  mbar was maintained. The energetical scale of the spectrometer was calibrated taking the Cu  $2P_{3/2}$  and Au  $4f_{7/2}$  maximum positions to be equal to 932.7 and 83.8 eV respectively.

The SIMS spectra were taken using an MM-12-12S quadrupole only after the photoelectron spectrum was finally recorded. The energy of  $Ar^+$ -ion primary beam was equal to 5 keV, the current density not exceeded 75 nA/cm, and the spot area where the surface etching was performed amounted to 4 mm<sup>2</sup>. The relatively low current densities increased the run duration, however, this fact allowed the variations in secondary ion mass-spectra observed in the act of etching of thin passivating layers to be studied in more detail. Under these operating conditions we obtained the positive ion mass-spectra in the range from 1 to 125 of mass and from 100 to 225 of mass. The high-resolution review SIMS spectra were taken at the primary beam current density of 300-750 nA/cm<sup>2</sup> using a 10 mm<sup>2</sup> square of the sample surface.

## Results

The data representing the variations in open circuit potential  $E_{CO_2}(t)$  versus the time of dipping the carbon steel in chromate-ion solutions of protective concentration are depicted in Fig. 1.

These results show the fairly rapid rise in potential during the first 20 minutes accompanied by the  $E_{CO_2}(t)$  followed by the slower monotonic increasing. What deserves our attention is the tendency of the  $E_{CO_2}(t)$  curve position. The higher the chromate-ion (oxidizing-type inhibitors) the lower is the  $E_{CO_2}(t)$  curve position. At the highest chromate-ion concentration ( $C_{Cr} = 5 \cdot 10^{-1}$  mol/l) the processes responsible for decreasing  $E_{CO_2}(t)$  make so much considerable contribution to  $E_{CO_2}(t)$  that overlapping at the first 20-30 minutes with the  $E_{CO_2}(t)$  growth kinetics stemming from the oxidizing attacks by chromate-ion, they distort it, and the  $E_{CO_2}(t)$  curve passes through the minimum.

At rather low but protective chromate-ion concentrations in solution the contribution of the processes decreasing  $E_{CO_2}(t)$  is not so much appreciable and the rise in the  $E_{CO_2}(t)$  potential is approximated by the cubic relationship

$$E(t) = A + B(t + t_0)^{1/3}$$

The chemical composition of surface layers onto the steel samples reached to the saturation state in the chromate-ion solutions of various concentrations was

determined by comparing the binding energy of the Fe  $2p_{3/2}$ , Cr  $2p_{3/2}$  and O  $1s$  bands with the findings obtained previously using XPS method for the bulk Fe- and Cr-oxides and hydroxides [5,6]. The layer averaged content of the cationic components was calculated in terms of empirical coefficients of sensitivity. The shape and the binding energy ( 577 eV) of the Cr  $2p_{3/2}$  band not dependent upon the chromate-ion concentration in solution and testified that the chromium into the layer is reduced to Cr and exists essentially in the form of hydroxide. On the spectra of Fe  $2p_{3/2}$  band the emission band intensity from metal surface with 707 eV binding energy is slightly detected against the background of intensive signal with 711 eV binding energy, responsible for the Fe oxyhydroxide. Based upon this result we can draw the conclusion that the passivating layer thickness is equal to 50-60 Å.

The findings on calculations are listed in Table 1 where one can clearly see the tendency to decrease in portion of the chromium cations and to increase in that of the iron cations in the passivating layer with rising the chromate-ion concentration in solution. Nevertheless, over the entire interval of inhibitor concentrations in solution the portion of the  $X_{Cr}$  chromium cations in the layer evaluated from the expression  $X_{Cr} / (X_{Cr} + X_{Fe})$  falls within the range between 0.6 and 0.8. This is in agreement both with the data obtained for ion passivated in the chromate-ion solutions and the results on Fe-Cr alloys [1] where the increase in Cr-ion content of the layer was observed at the onset a steel passive state that contained 13% of chromium.

The fall in portion of the chromium ions in a layer on the passive metal surface detected with increasing the chromate-ion concentration in solution was also pointed out in [1] where it was reasoned that it takes place as a result of rise in pH of solution at the process of chromate-ion reduction to  $Cr(OH)_3$  or  $Cr_2O_3$ . In this connection the layer-averaged of chemical composition appears to be supplemented by the data on variations in concentration profile of the layer components that may result from the variation in the chromate-ion concentration in solution. We assume this goal may be achieved most likely by a combination of the layer-by-layer etching technique with permanent secondary ion mass-spectroscopy analysis (including the analysis of complex clusters) where the depth resolution reaches to 1-2 monolayers. The last circumstance is of particular importance when analysing the thin layers of thickness up to 50-60 Å [4].

The review positive ion mass-spectrum is shown in Fig.2. The concentration profile of certain of them was recorded as  $Ar^+$ -ion beam sputtering of the passivating layer. The presence of 168 mass in the spectrum implies that during the process of sputtering the inner layer - metal interface is achieved and the  $Fe^+$  secondary ion emission from metal phase becomes available [7].

Fig.3 demonstrates the variations in relative  $Cr^+$  and  $Fe^+$  secondary ion yield in the course of passivating layer sputtering formed in the chromate-ion solutions of different concentrations. In this case as the relative ion yield we

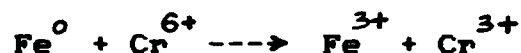
present the ratio of signal intensity for the secondary ions given to the total ion current of the most intensively emitted ions. These findings testify that the composition of the passivating layer onto steel, represented here by the relative yield of the  $\text{Cr}^+$ ,  $\text{Fe}^+$  ions and their combinations, varies rapidly with layer depth approaching the inner layer-metal interface.

From the data of Fig.3 it follows specifically that independent of the chromate-ion concentration in solution the maximum proportion of the chromium containing component occurs on the outer boundary of the passivating layer contacting with solution. The major part of the component above mentioned decays over the distance 10-15 Å not exceeding 15-20 % from average layer thickness. The concentration of the Cr-containing component decays rather slowly on the remained layer portion as far as the boundary which is considerably blurred. The opposite feature takes place for the concentration profile of the Fe-containing component whose concentrations on the outer layer boundary is minimum and increases readily, tending to saturation on approaching the inner boundary.

Comparing the concentration profiles of the Cr - and Fe - containing components of passivating layers formed in solutions of  $10^{-3}$ ,  $10^{-2}$  and  $10^{-1}$  mol/l concentrations (intermediate concentrations were also followed the relationships given below), one can see that the higher the chromate - ion concentration in solution, the lower is the concentration of Cr - containing component on the surface and in the depth of a layer. By contrast, with the rising chromate-ion concentration in solution of Fe - containing component on the surface and in the bulk layer increases.

In such manner the results obtained by the layer-by-layer sputtering technique with mass-spectroscopy analysis of the layer composition are consistent with the averaged data listed in Table 1.

At the 10 g/l chromate-ion concentration in solution the concentration depth profiles are rapidly brought into proximity and the ratio of the Fe- and Cr- containing components approaches unity, closely approximating the stoichiometric one that fits the process of currentless oxidation.



The decrease in ratio of the  $\text{Fe}^{3+}/\text{Cr}^{3+}$  concentrations in layer relative to the stoichiometric one on approaching the outer layer boundary accounts for the process of this layer dissolution in solution at virtually constant  $\text{Cr}^{3+}$ -ion concentration in the 10-15 Å -thick outer layer. The chemical composition of this thin outer layer is taken to be distinct from that of the remained portion of the passivating layer as evidenced by the data presented in Fig 4. Actually, the rapid drop in the yield of  $\text{Cr}_2^+$ - clusters within the limits of this layer and continuous low yield over the rest of the layer area with simbate increasing yield of the  $\text{FeCr}^+$  and  $\text{FeCrO}^+$  clusters referred to compounds of  $(\text{Cr}_{1-x}\text{Fe}_x)^{3+}\text{O}_y$  variable composition

suggest that a double-layered dielectric film is formed onto steel surface in chromate-ion solution. Note, that the outer, solution-contacting layer, represents a hydroxylated  $\text{Cr}^{3+}$  compound of 10-15 Å thickness, involving a bare handful of the Fe-component depending on the chromate-ion concentration in solution. The inner layer adjacent to metal relates to the partially hydroxylated compounds of variable  $(\text{Cr}_{1-x}\text{Fe}_x)^{3+}\text{O}_y$  composition, where the Fe component rises monotonically, and the  $\text{Cr}^{3+}$ -component decreases mirror like on approaching the inner metal-film interface, which is not sharp at atomic scale. This fact is evidenced by the the slow increase in the yield of  $\text{Fe}_3^+$  clusters and the sharp rise in that of  $\text{Fe}_2^+$  clusters since the  $\text{Fe}_3^+$  cluster inception on retention of rather intensive yield of the  $\text{Cr}^+$  and chromium-containing  $\text{FeCrO}^+$  and  $\text{FeCr}^+$  clusters.

The relatively low concentration of the  $\text{Fe}^{3+}$ -containing component on the outer layer boundary observed after the exposure to dilute solutions of chromate-ions result from its passing into solution in the double-layer electrical field. We discovered that the high concentration of  $\text{Cr}^{3+}$  hydroxide in the layer on the layer-electrolyte interface (for the fixed chromate-ion concentration in solution) has a steep decline of the  $\text{Cr}^{3+}$  component in the inner layer (taking into account the boundary effects whose presence is essentially inevitable on ion etching and concentration profile recording, this gradient should be still further). This result along with the formation of relatively high gradients of the  $\text{Fe}^{3+}$  component concentration in layer testify that the redox-process of  $\text{Cr}^{6+}$  ion reduction proceeding through a number of steps (electron transport within the dielectric layer and generation of  $\text{OH}^-$ -particles in the double layer) follows rather simply and the steady-state is virtually achieved in 20-30 minutes.

The generation of the  $\text{OH}^-$ -particles and increasing pH over the double-layer region shift the potential of this spatial area to the negative side. At the same time the charge transfer from the metal phase to the adsorbed oxidant, and appearance of the  $\text{Cr}^{3+}$  ions which are still not compensated by occurrence of the  $\text{Fe}^{3+}$  ions, reflects the surface charge density in metal phase and the electrical field into a dielectric layer, thus shifting the potential in this layer into the positive side.

Under these circumstances the variation in  $E_{\text{Co}_2}(t)$  representing the sum of changes in potential jumps into the dielectric and double layers is bound to be dependent on ratio of these contributions. At short exposure times and still rather small dielectric layer thicknesses a contribution in the double layer is dominated, and with increasing the chromate-ion concentration the  $E_{\text{Co}_2}(t)$  curves shift toward the negative potential region. In the case of longer times, when the  $\text{Fe}^{3+}$  ion transports to the outer layer boundary where the processes of formation and dissolution of the layer take place, occurs less rapidly, the slow cubic-like shift of  $E_{\text{Co}_2}(t)$  potential (more exactly, of the  $E_{\text{Co}_2}$  component localized into the dielectric layer) toward the positive side is observed until the equalization of growth and dissolution rates into the layer.

The explanation of the regularities discovered during the layer-by-layer analysis of the passivating layers by the SIMS method and the tendencies of time-dependent variation in  $E_{Co_2}(t)$  open circuit potential at the changing chromate-ion concentration in solution may be found in more detailed analysis of the chemical composition of surface layer using the XPS technique. The shift of the Fe  $2p_{3/2}$  band maximum to the low binding energy side and increase in the 530 eV band intensity relative to the 531.5 eV band in the O 1s spectrum (Fig.5), shows that with the rising chromate-ion concentration in solution. The relative concentration of Fe-O bonds on the surface increases, while that of Fe-OH falls. The feature is most pronounced at the  $5 \cdot 10^{-1}$  mol/l concentration where the concentration of the former is already equal to or exceeds that of the latter, bearing witness to an appreciable increase in pH within the near-surface area during the process of  $CrO_4^{2-}$  ion reduction. As a result, the acid-base equilibrium in double layer shifts to the side of the base FeO-type center formation, and drop in the layer solubility in the form of  $Fe^{3+}$ -ions on the one hand, along with decrease in the potential jump into the double layer and the  $E_{Co_2}(t)$  potential as a whole with rising chromate-ion concentration in solution on the other hand, take place.

Thus, both the effects are related to each other and explain respective increase in the  $Fe^{3+}$  ion concentration in the layer and fall in  $E_{Co_2}(t)$  curves with the rising chromate-ion concentration in solution, pronounced at the highest concentrations of the latter.

The analysis on results was carried out reasoning from the fact that the layer dissolution proceeds essentially in the form of  $Fe^{3+}$ -ions at relatively high stability of the  $Cr^{3+}$ -containing components. The data shown in the review SIMS spectra (Fig.2) are the circumstantial evidence of this effect. If the intensity of monoatomic  $Cr^+$  ions yield is higher than that of the same  $Fe^+$  ions (that is concerned to the ratio of their concentrations on the layer surface), then the yield of polyatomic  $CrO^+$  and  $FeO^+$  clusters (where the emission proceeds with breaking of the Me-O or Me-OH bonds) is already equalized but in the case of double-atomic  $Cr_2^+$  and  $Fe_2^+$  clusters where the greater number of the Me-O (or Me-OH) bond breaking takes place, the  $Fe_2^+$  emission is dominated. With increasing the oxygen content of the cluster ( $Cr_2O_2^+$ ,  $Fe_2O_2^+$ ) the ratio of yields varies in favour of the chromium-containing ions.

### Conclusions

Thus, both redox and acid-base functions of chromate-ions were taken into account to explain the complex run of the  $E_{Co_2}(t)$  curves and the variation in composition and structure of the passivating layers formed in solutions.

### References

1. E. McCafferty, M.K. Burnett, J.S. Murday, Corrosion

- Sci., 28 (1988): p. 559-576.
2. W. Meisel, E. Mohs, H.-J. Guttman, P. Gutlich, Corrosion Sci., 23 (1983): p. 465-471.
  3. J. Calvo, C.D. Pallotta, S. Hild, E. Garsia, J. Electrochem. Soc., 135 (1988): p. 314-320.
  4. S.-C. Tjong, R.W. Hoffman, E.B. Yeager, J. Electrochem. Soc., 129 (1982): p. 1662-1668.
  5. K. Asami, K. Hashimoto, Corrosion Sci., 17 (1977): p.559.
  6. N.S. McIntyre, D.G. Zetaruk, Anal. Chem., 49 (1975): p. 1521.
  7. J.A. Bardwell, Corrosion Sci., 30 (1990): p. 1009-1017.

Table I

$\text{Fe}^{3+}$ - and  $\text{Cr}^{3+}$ - cations contentions in passivating layers in accord with XPS data

$\text{CrO}_4^{2-}$ concentration in solution ( $\text{Mol} \cdot \text{l}^{-1}$ )	$\text{Fe}^{3+}(\% \text{ at.})$	$\text{Cr}^{3+}(\% \text{ at.})$
$5 \cdot 10^{-4}$	20	80
$10^{-3}$	22	78
$2.5 \cdot 10^{-3}$	19	81
$5 \cdot 10^{-3}$	19	81
$10^{-2}$	28	72
$10^{-1}$	33	67
$10^{-1}$ (grazing angle)	23	77
$5 \cdot 10^{-1}$	33	67



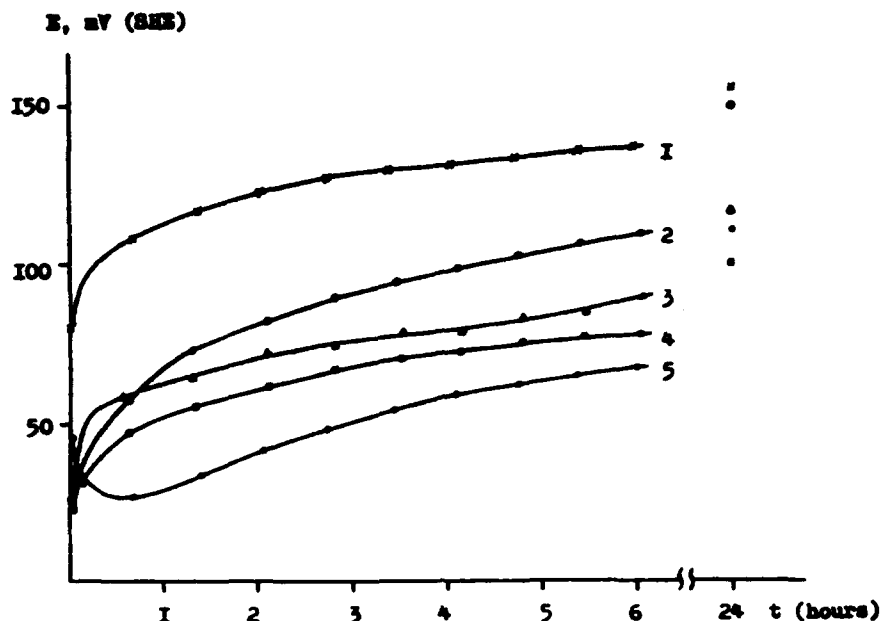


Figure 1. Open-circuit potential time dependence in aqueous aerated solutions at various chromate-ion concentrations :  
 1 -  $10^{-3}$  Mol. $\cdot$ l $^{-1}$ , 2 -  $10^{-1}$  Mol. $\cdot$ l $^{-1}$ , 3 -  $5 \cdot 10^{-3}$  Mol. $\cdot$ l $^{-1}$ ,  
 4 -  $10^{-2}$  Mol. $\cdot$ l $^{-1}$ , 5 -  $5 \cdot 10^{-1}$  Mol. $\cdot$ l $^{-1}$

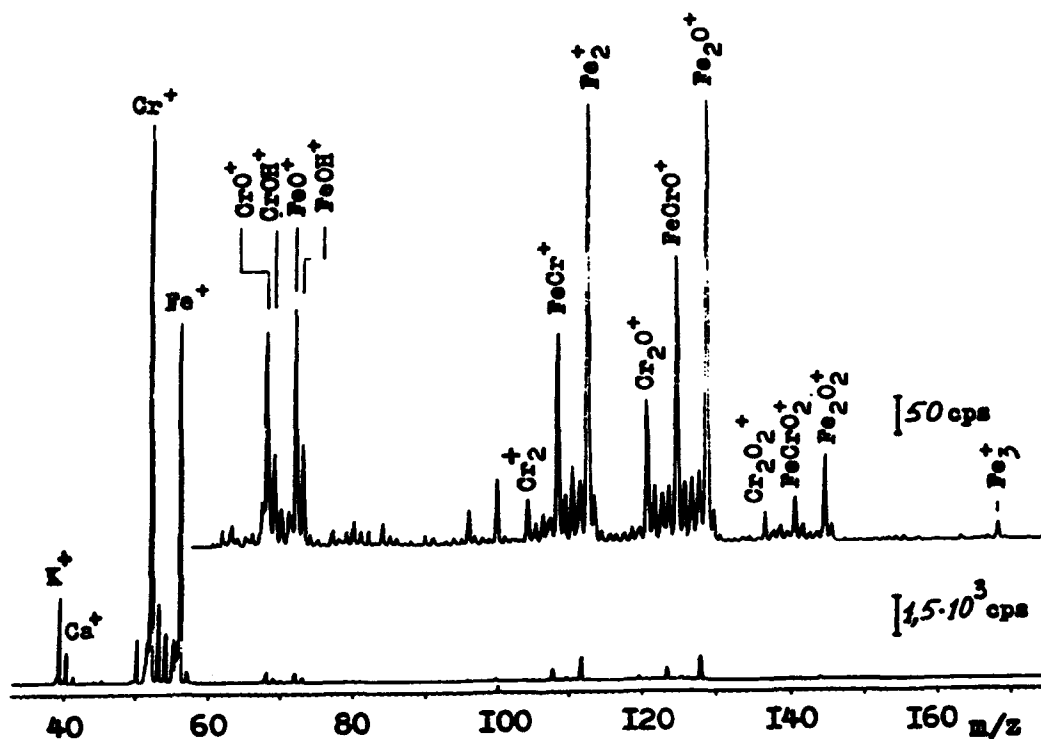


Figure 2. Positive ion SIMS spectrum from steel surface exposed to  $0,005$  Mol  $l^{-1}$   $[CrO_4^{2-}]$  solution ( $300$  nA  $cm^{-2}$  of  $5$  KeV  $Ar^+$ )

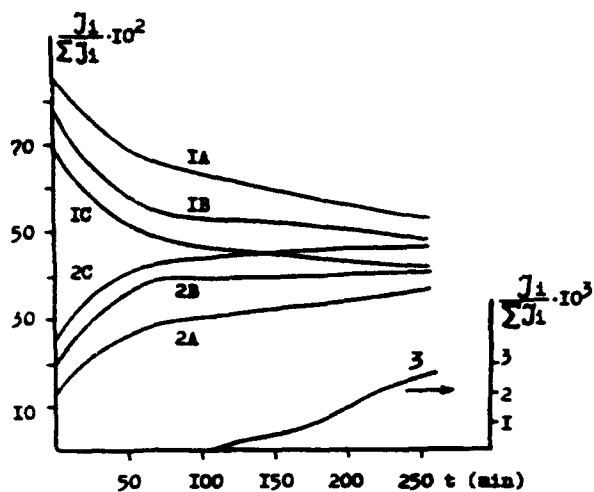


Figure 3. Variation of  $\text{Cr}^+(1)$ ,  $\text{Fe}^+(2)$ ,  $\text{Fe}_3^+(3)$  secondary ion yields versus time of sputtering ( $40 \text{ nA cm}^{-2}$  of  $5 \text{ KeV Ar}^+$ ) upon exposures to different  $[\text{CrO}_4^{2-}]$  concentrations (A -  $0,001 \text{ Mol} \cdot \text{l}^{-1}$ , B -  $0,01 \text{ Mol} \cdot \text{l}^{-1}$ , C -  $0,1 \text{ Mol} \cdot \text{l}^{-1}$ )

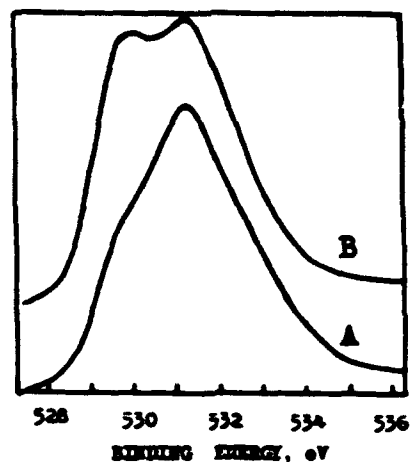


Figure 5.  $\text{O1s}$  spectra measured on steel samples exposed to  $0,005 \text{ Mol l}^{-1}$  (A) and  $0,5 \text{ Mol l}^{-1}$  (B)  $[\text{CrO}_4^{2-}]$  solutions

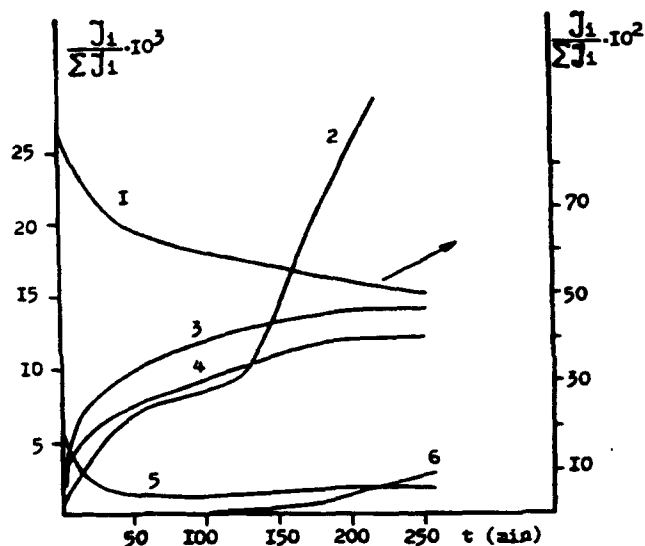


Figure 4 Variation of secondary ion yields from steel surface exposed to  $0,005 \text{ Mol l}^{-1} [\text{CrO}_4^{2-}]$  solution versus time of sputtering ( $40 \text{ nA cm}^{-2}$  of  $5 \text{ KeV Ar}^+$ ); 1 -  $\text{Cr}^+$ , 2 -  $\text{Fe}_2^+$ , 3 -  $\text{FeCrO}^+$ , 4 -  $\text{FeCr}^+$ , 5 -  $\text{Cr}_2^+$ , 6 -  $\text{Fe}_3^+$

## **A Quantum Chemical Study of Inhibition Effect of Isoquinoline Derivatives**

L. A. Yao, M. D. Lou, P. Kong, F. G. Kung  
Department of Environmental Science,  
Wuhan University, Wuhan, P. R. China 430072

C. L. Yao  
Department of Chemistry, University of Houston  
Houston, Texas, USA 77204

### **Abstract**

HMO and CNDO methods were used to calculate the molecular structural properties of seven isoquinoline derivatives and correlate with their corrosion inhibition efficiency on iron in the 1.0 M HCl solution. The calculation results show that the isoquinoline corrosion inhibition efficiency increases with an increase in the negative electron density on the pyridine ring, while the efficiency decreases with an increase in the net nitrogen-electron density ( $N_e$ ) and  $\pi$  electron density ( $N\pi$ ). The interaction between  $\pi$  electron on the pyridine-ring and Fe empty d-orbital results an increased  $\pi$  electron density on the pyridine ring, hence its nucleophilic characteristics. These resulted a stronger absorption stability of the molecules on the metal surface and better inhibition efficiency. The absorption models for isoquinoline and its derivatives can be described as that the molecule is attached to the metal surface in a flat face-down fashion with a pyridine-ring  $\pi$ -electron centered absorption, not a vertically nitrogen-centered absorption.

The corrosion inhibition properties of these isoquinoline derivatives were investigated by electrochemical methods and experimental results confirmed the prediction obtained from the molecular orbital calculation.

**Key terms:** isoquinoline, inhibition,

## Introduction

The inhibiting effect of the organic inhibitors on metal corrosion is through the formation of an absorption layer at the metal surface. Iron atom has unfilled outside d orbitals. These unfilled d-orbitals enable them to accept the donor electron to form the donor-bond. If the organic inhibitors contain the lone pair electrons or their molecular structure consists of double bonds, triple bonds, or aromatic rings, these electron rich molecules can provide electrons to the empty metal d-orbital to form the coordination bonds. Hence, the inhibition characteristics of the organic inhibitors is strongly related to their molecular structures. The stronger the electron donor ability of these compounds are, the better the inhibition effect.

Vosta and Aleybeeva studied the relationship between the quantum chemistry parameters and the inhibition effect using the HMO method [1-2]. It is believed that the higher the HOMO orbital of the inhibitor molecules, the easier these electron will be lost. Also, the lower the LUMO, the easier it is for these molecules to accept the donor electrons. As a result, the inhibition effect increases with the increase in the electron density on the organic function groups. Utilizing the semi-empirical MINO/3 SCF method, Costa, et al, explained the inhibition effect of the fatty alcohol and the effect of phenol, nitrobenzene, and aniline on zinc and carbon steel corrosion [3-5]. Abdu-Ahad found that good correlation existed between the calculated electronic parameters of para-substituted anilines using the DO/2 method and the experimental results [6].

Macek used the expended EHO method to calculate the aromatic compounds containing N and S atoms and explained the differences in the absorption capabilities among the organic inhibitors [7]. Other authors used the HMO method to calculate the N-compound and found that the inhibition effect increased with the electron density on the functional groups [8]. The energy calculation and experimental results agreed well. The calculation using CNDO/2 method on electron density of other organic N-compounds and frontier orbital energy revealed that the inhibition effect and the HOMO and LUMO orbital had linear correlation [9].

Currently, there is an increasing interest on the relationship between quantum chemical parameters and the molecular structures of organic inhibitors. The correlation between the quantum chemical calculation and the experimental results on the tested inhibitors can be used not only to explain the inhibition mechanism, but also to provide the theoretical background for future search and design of the high efficiency inhibitors.

This study reports the investigation of the inhibition effect of several isoquinoline derivatives. The electron density of these derivatives were calculated using the HMO and CNDO/2 methods. The correlations between the inhibition effect of the inhibitors and the electron density on the organic

functional groups were established based on the experimental data and molecular orbital calculation. The data were further used to establish the absorption model and provide the information on the design of new inhibitors.

## Experimental

Pure iron was used as the working electrode. The electrode was polished with #5-7 emery papers to a mirror finishing, washed with distilled water, and digressed with ethanol. The cleaned electrode was then submerged in the nitrogen purged study solution for one hour. The counter electrode was platinum and the reference electrode was a saturated calomel electrode (SCE). An EG&G Model M322 or M368 electrochemical measurement system was used for electrochemical study. The linear polarization range used was  $E_{\text{corr}} \pm 10$  mV. The potential scan rate was 0.2 mV/s. The Tafel range was  $E_{\text{corr}} \pm 150$  mV with a scan rate of 0.5 mV/s.

Six isoquinoline derivatives were used for the study. Their corrosion inhibition effects on the Fe electrode were investigated in a 1.0 M HCl solution at 30 °C. All isoquinoline derivatives were purchased from Aldrich Chemical CO (USA) and used without further purification. Their nomenclature and molecular structures are shown in Figure 1.

## Results

### 1. Electrochemical Measurement.

Results obtained from the electrochemical measurement are summarized in Table 1. The data in Table 1 can be grouped into two series based on the substituted functional groups on the isoquinoline derivatives. One series is the OH functional group. The inhibition effect on iron corrosion follows the order  $\text{IQC} > \text{IQ} > \text{IQA} > \text{IQB}$ . The second series is the -COOH (carboxylate acid) functional group. Their inhibition efficiency is ranked as  $\text{IQE} > \text{IQD} \approx \text{IQF} > \text{IQ}$ .

### 2. Quantum Chemistry Calculation.

The frontier orbital electron density parameters of isoquinolines were calculated using HMO and CNDO/2 methods [10]. The results are shown in Tables 2 and 3 and the bond lengths and angles used for calculation were obtained from the literature [11].

## Discussion

### 1. Relationship Between the Corrosion Inhibition Efficiency and Isoquinoline N-atom Electron Density.

It can be seen from Tables 2 and 3 that the corrosion inhibition efficiency of isoquinoline derivatives can be related to the  $N_p$  and  $N_q$  calculated from the CNDO/2 method and to  $N_q$  obtained from the HMO method. The plots in Figures 2-4 using the data in Tables 2 and 3 further reveal the correlation. The corrosion inhibition efficiency decreases with an increase in the N-atom net charge (CNDO/2 method) and  $\pi$ -electron density (both CNDO/2 and HMO methods).

## 2. Relationship Between the Corrosion Inhibition Efficiency and Isoquinoline Pyridine-ring Net Charge.

As shown in Table 2 and Figure 5, the smaller the pyridine-ring net charges on the isoquinoline and its OH and COOH derivatives (from the CNDO/2 calculation) are, the better the inhibition efficiency. This relationship is not observed for the net charge on the benzene or isoquinoline ring.

The net charge calculation on the pyridine ring includes the consideration of the net charge on the OH functional group. This is because the relatively large electronegativity of the oxygen atom can also co-absorb with the pyridine ring on the Fe electrode surface. The data also indicate that, except for IQB, the inhibition efficiency increases with an increase in the net negative  $\pi$  electron density on the pyridine ring for IQA, IQ and IQC. This relationship does not exist for the benzene ring.

The calculation of the COOH substituted isoquinolines using the HMO method shows some irregularity. For example, the net charge for the COOH functional group in IQF is -0.0514, while it is -0.0481 for IQE. However, the former has a net charge of 0.0129 on the pyridine ring and the latter is 0.0188. This is in contrast to the prediction that the electron withdrawing COOH group should generate larger positive charge on the pyridine ring. It also disagrees with the results from the CNDO/2 method, which shows that the larger the positive net charge on the pyridine ring, the poorer the corrosion inhibition efficiency.

## 3. Relationship Between the Inhibition Efficiency and Free Valence State.

Free valence state can be used as an indicator on the molecular reactivity. As shown in Figures 6 and 7 that, in both types of substituted isoquinoline derivatives, the following relationships exist: a) an increase in the N-atom free valence state of the isoquinoline molecule will result in a decrease in inhibition efficiency, and b) an increase in the sum of valence state of all six C-atoms on the pyridine ring generates a higher inhibition efficiency. When the sum of free valence states for the pyridine ring increases, the molecular reactivity increases correspondingly. This results in a stronger absorption at the Fe surface, hence increases the corrosion inhibition efficiency.

The above discussion indicates that, the inhibition behavior of isoquinoline derivatives is not merely the effect of the individual N-atoms. In fact, it should be the integral effect of entire the pyridine ring. Also, atomic coordinates of the isoquinoline at the Z-axis direction, calculated by the MNDO method, show that the carbon atoms on the pyridine frame basically lie on a horizontal plane (see Figure 8), while benzene frame is bend upward at an angle. Thus, we can postulate that the isoquinoline absorption on the metal surface is in a flat face-down direction.

#### 4. Relationship Between the Inhibition Efficiency and the Nucleophilic Frontier-orbital Electron Density.

The analytical date indicate that the corrosion inhibition efficiency increases as the electron density in the nucleophilic frontier orbital increases. The linear least square regression shows the following relationship:

$$\eta = -73.407 + 106.729 F_p^n \quad (r=0.995) \quad (1)$$

where  $\eta$  is the inhibition efficiency and  $F_p^n$  is the electron density. The linear plot is shown in Figure 9.

#### 5. Predication of the Corrosion Inhibition Efficiency of Isoquinoline Derivatives.

Using the quantum chemical calculation as a tool, we not only can have a better understanding of the inhibition mechanism and absorption model of the organic inhibitors, but also predict the effectiveness of the new inhibitors with similar molecular structures. This should aid in searching and synthesizing of new types of organic inhibitors.

Using the ENDO/2 method, the net charge on several isoquinoline derivatives can be calculated (see Figure 10). The previous results already predicates an increase in the inhibition efficiency corresponding to a decrease in the N-atom electron density ( $N_e$ ). Since IQG has the lowest  $N_e$  and  $N_e$  electron density (-0.02369 and -0.1114, respectively) as compared with that of IQA, IQB, and IQC, we can expect that IQG may exhibit a better inhibition efficiency.

It should be pointed out that, the current inhibition efficiency is investigated under the same temperature, HCl concentration and inhibitor concentration, the effect of other ionic species in the solution is regarded as approximately the same.

## Conclusion

1. This work investigated the inhibition efficiency of isoquinoline and its OH and COOH derivatives in the HCl solution. The electron density distributions of these isoquinolines were calculated using the HMO and CNDO methods. The calculation and experimental results show that the inhibition efficiency increases with a decrease in the net electron density on the N-atom and an increase in the negative charge on the pyridine ring.

2. The inhibition efficiency decreases with an increase in the N-atom free valence and increases with an increase in the sum of free valence state in the pyridine ring.

3. In the HCl solution, these type of organic inhibitors follows a flat face-down absorption model on the metal surface.

## Reference

1. Vosta, J., Corr. Sic., Vol 11, 223 (1971).
2. Alcybeeva, A. I., Proc. 3th Eupo. Symp. Corr., No 7, 501 (1970).
3. Costa, J. M., Corr. Sci. Vol 24, 929 (1984).
4. Savos, R., Corr. Sci., Vol 26, 827 (1986).
5. Grocock, F. B., Corrosion, Vol 45, 1007 (1989).
6. Abdu-Ahad, P. G., Corrosion, Vol 45, 78 (1989).
7. Zhao, J. G., Chinese Corrosion and Protection. Vol 6, 217 (1986).
8. Ning, S. G., Chinese Corrosion and Protection, Vol 10, 383 (1990).
9. Wu, J. A., "Quantum Chemistry Programs", Shanghai, China, 1984.
10. Pople, J. A. and Beveridge, D. L., "Principle and Theory of Molecular Orbital Approximation Methods" Science Publication, Beijing, 1978.

Table 1. Inhibition Efficiency Measurement of Isoquinoline Derivatives.

Compd	Ecorr	Rr	ba	bc	Icorr	Efficiency
Blank	-541	54	57	85	0.278	
IQ	-538	85	51	84	0.175	37
IQA	-528	116	102	94	0.183	34
IQB	-535	67	56	86	0.218	21
IQC	-537	148	94	86	0.132	52
IQD	-530	109	77	89	0.164	40.4
IQE	-532	124	75	79	0.135	51
IQF	-535	102	69	89	0.165	40.1



Table 2. Frontier Orbital Energy Levels and Net Charge Calculated  
By the CNDO/2 Method.

	E(a,u)	E(a,u)	Nu*	Ne**	Pyridine	Benzene	Isoquino
IQ	-0.4121	0.0630	-0.0577	-0.1381	0.0357	0.0547	0.0366
IQA	-0.3762	0.0725	-0.1482	-0.1986	0.0894	0.1077	0.1967
IQB	-0.3916	0.0701	-0.1659	-0.2073	0.1154	0.0353	0.1232
IQC	-0.3897	0.0677	-0.0394	-0.1277	0.0168	0.1329	0.0490
IQD	-0.4150	0.0486	-0.0485	-0.1382	0.0294	0.0748	0.0404
IQE	-0.4191	0.0249	-0.0293	-0.1344	0.0110	0.0615	0.0008
IQF	-0.4184	0.0460	-0.0506	-0.1384	0.0362	0.0780	0.0490

Note:\* Nu is the N-atom net pi electron density;  
\*\* Ne is the total N-atom net electron density.

Table 3. Frontier Orbital Energy Levels and Net Charge Calculated  
By the HMO Method.

	energy	energy	Nq*	Pyd	BZ	N-atom	Pyd	F**
IQ	0.6414	-0.5856	-0.1599	-0.0233	0.0395	0.1040	1.6362	1.0429
IQA	0.4749	-0.7035	-0.2288	-0.0110	0.0024	0.1462	1.4678	1.0009
IQB	0.5616	-0.6518	-0.2308	-0.0580	0.0023	0.1469	1.4527	0.8800
IQC	0.5342	-0.6322	-0.1576	-0.0472	-0.0677	0.1028	1.6492	1.1672
IQD	0.5766	-0.4783	-0.1445	0.0230	0.0581	0.1237	-	-
IQE	0.6582	-0.4817	-0.1254	0.0159	0.0709	0.1235	1.4388	1.1022
IQF	0.6537	-0.5638	-0.1470	0.0238	0.0608	0.1353	1.4337	1.0164

Note:\* Ng is the N-atom net pi charge on isoquinoline;  
\*\* F is the nucleophilic frontier orbital electron density.

Table 4. Z-coordinates of the Isoquinoline Frame.

Atom No	1	2	3	4	5	6	7	8	9	10
Z-coord (x1000)	0.00	0.00	0.00	0.08	0.20	0.28	0.49	0.67	0.67	0.50

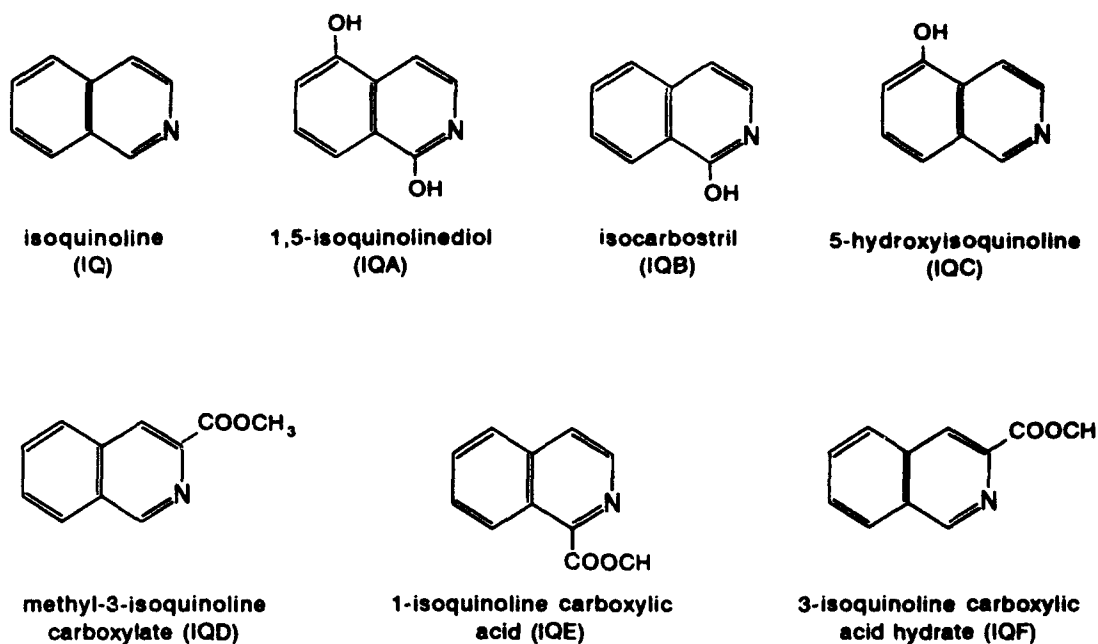


Figure 1. Molecular structure and nomenclature of isoquinolines.

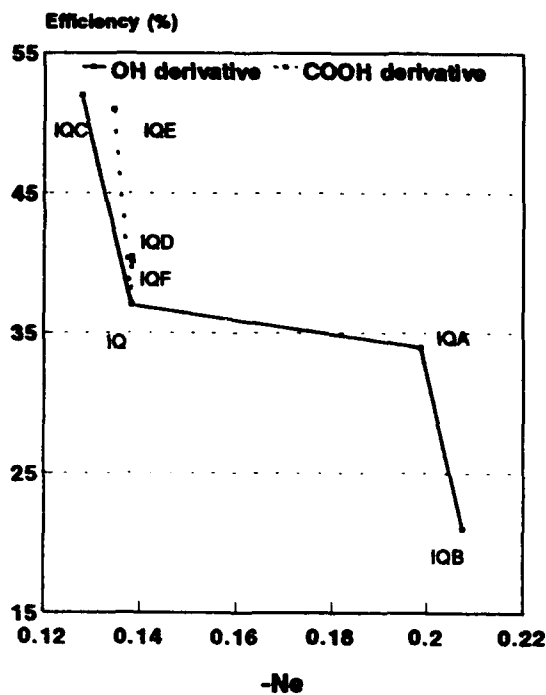
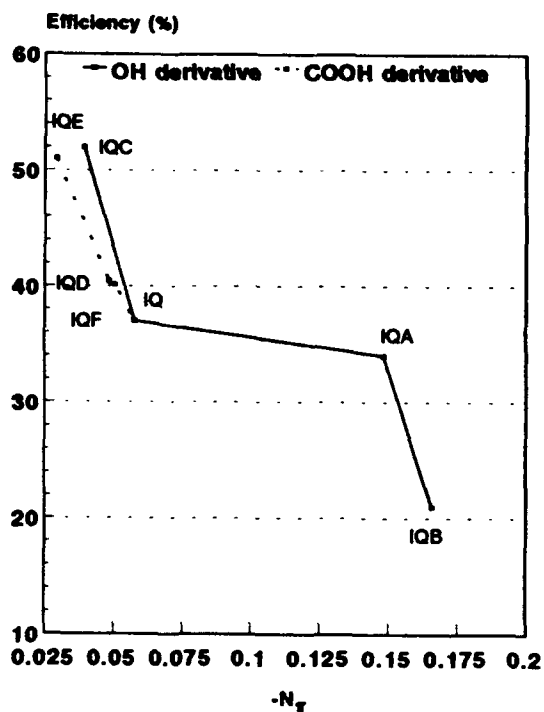


Fig 2. Inhibition efficiency vs N-atom electron density. Fig 3. Relationship between inhibition efficiency and N-atom electron density (CNDO method).

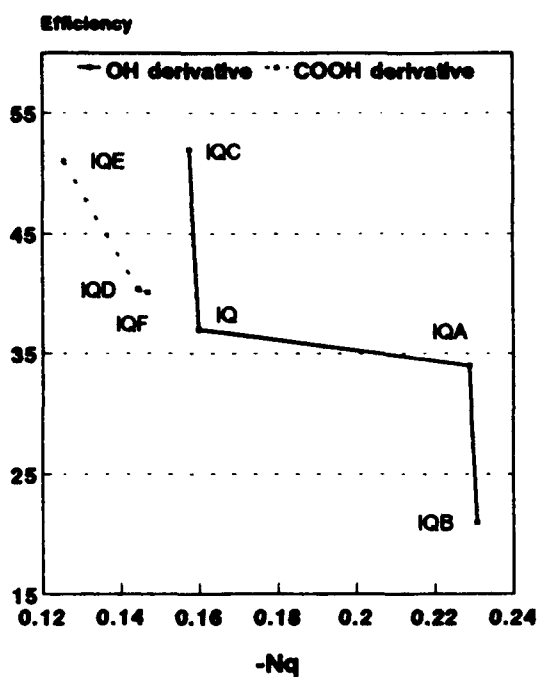


Fig 4. Relationship between Efficiency and  $Nq$  electron density (HMO method).

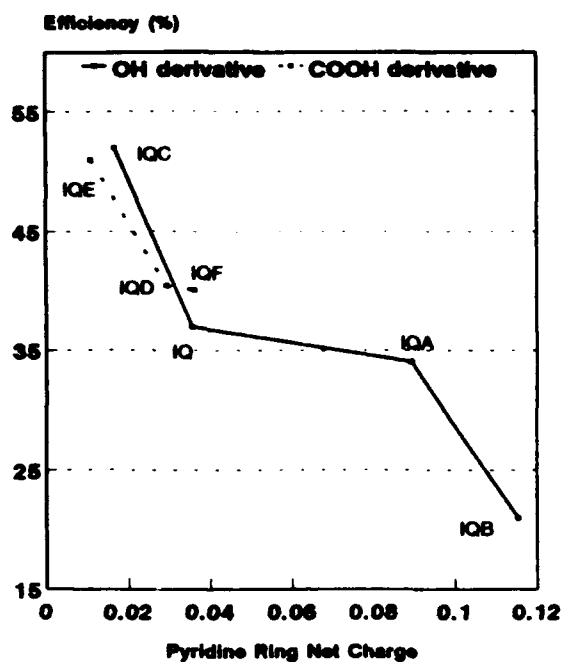


Fig 5. Relationship between pyridine ring and inhibition efficiency.

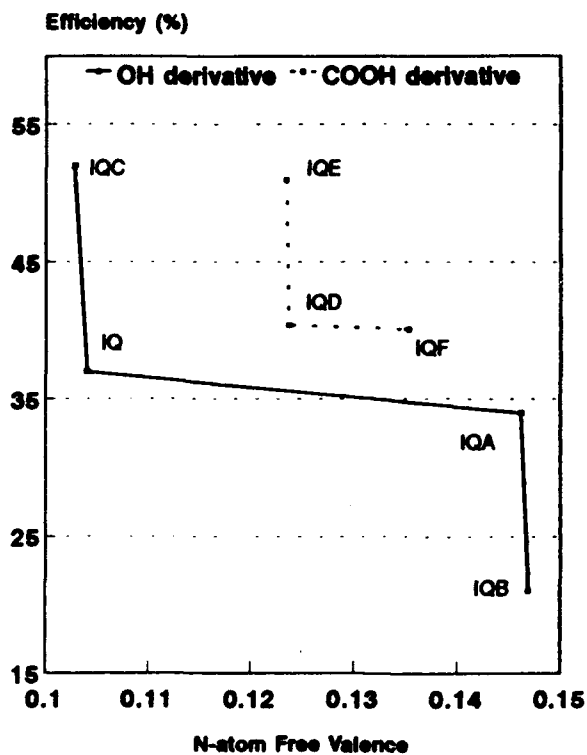


Fig 6. Relationship between efficiency and N-atom free valence.

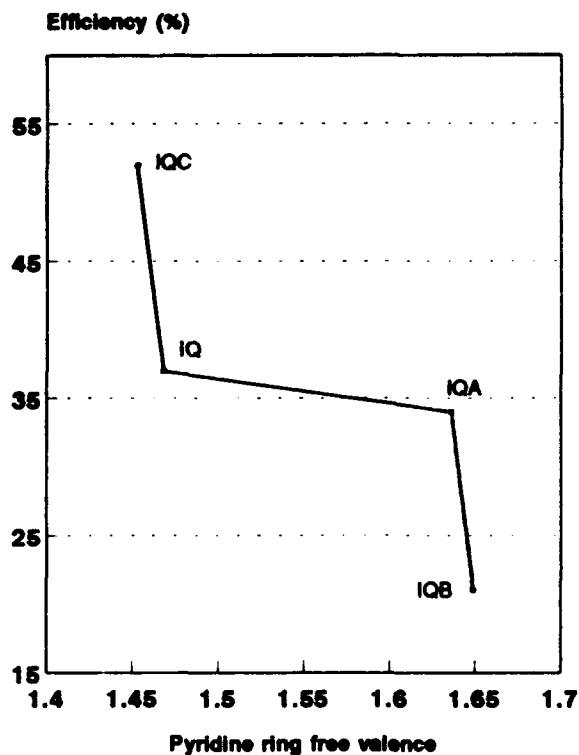


Fig 7. Relationship between the inhibition efficiency and pyridine ring free valence.

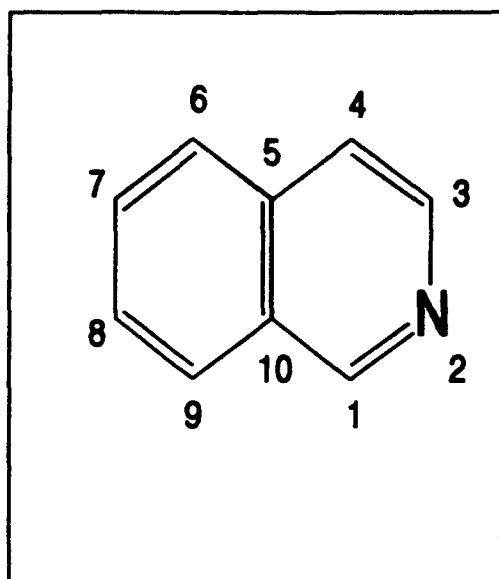


Fig 8. Atomic coordinates of isoquinoline frame.

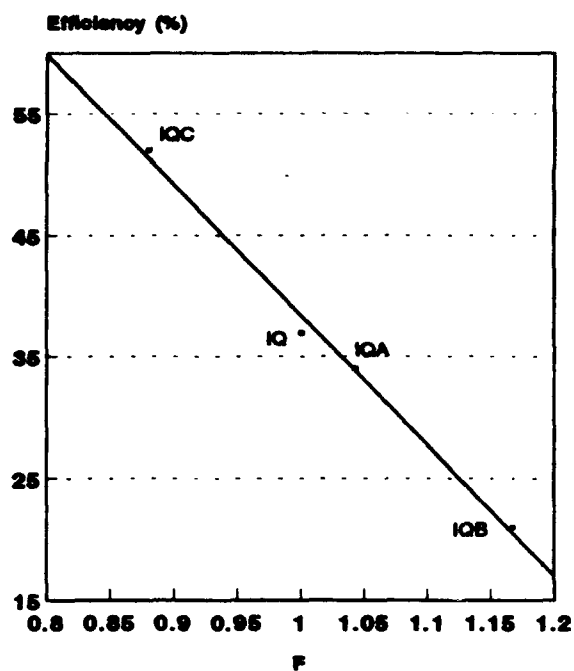


Fig 9. Linear plot of efficiency vs the frontier orbital nucleophilic index (F).

	<b>IQG</b>	<b>IQH</b>	<b>IQI</b>	<b>IQJ</b>	<b>IQK</b>
$N_r$	-0.02369	-0.1348	-0.0934	-0.0581	-0.0760
$N_l$	-0.1114	-0.2170	-0.1767	-0.1580	-0.1421

Figure 10. The calculated net charge on the designed isoquinoline derivatives.

**A Spectroscopic Investigation on Inhibition Mechanism  
of Dibenzyl Sulfoxide for Iron Corrosion  
in a Hydrochloric Acid Solution**

**Kunitsugu Aramaki  
Keio University  
Hiyoshi, Yokohama, Japan**

**Noriyuki Ohno  
Keio University  
Hiyoshi, Yokohama, Japan**

**Hiroshi Nishihara  
Keio University  
Hiyoshi, Yokohama, Japan**

**Abstract**

Inhibition mechanism of dibenzyl sulfoxide for iron corrosion in acid solutions was investigated by polarization measurement and surface-enhanced Raman scattering (SERS) and x-ray photoelectron spectroscopy. Dibenzyl sulfoxide was an effective inhibitor suppressing cathodic and anodic processes of iron corrosion in 0.5M HCl at  $1 \times 10^{-4}$ M. Dibenzyl sulfide was not effective for iron corrosion in a 0.5M HCl solution saturated with the compound. SERS spectra of these compounds adsorbed on silver and on iron-covered silver in 0.5M HCl were measured in the same manner as previously described. It was concluded from results of SERS experiments that dibenzyl sulfide formed through the cathodic reduction of the sulfoxide is strongly chemisorbed on the iron surface by the formation of a coordinate bond between sulfur and iron atoms. X-ray photoelectron spectra of a layer prepared at the iron surface in 0.5M HCl with dibenzyl sulfoxide revealed the presence of a multimolecular layer comprising the sulfide and ferrous chloride and oxide. Because this layer seems less protective against iron corrosion, the high inhibition efficiency of dibenzyl sulfoxide is mainly attributed to the strong chemisorption of the sulfide resulting from the cathodic reduction of the sulfoxide at the surface.

**Key terms:** inhibition mechanism, iron corrosion, dibenzyl sulfoxide, dibenzyl sulfide, surface-enhanced Raman scattering spectroscopy, x-ray photoelectron spectroscopy

## I. Introduction

Surface-enhanced Raman scattering (SERS) spectroscopy is a useful tool for providing an in situ molecular-level information of species adsorbed on metals like copper, silver, and gold in an aqueous solution.<sup>1</sup> The authors have measured SERS spectra of species adsorbed on a SERS-active silver electrode covered with an electrodeposited iron layer of minimum thickness.<sup>2,3</sup> Adsorption and inhibition mechanism of nitrogen, sulfur and antimony compounds on the iron surface in acid solutions have been investigated by SERS spectroscopy.<sup>4-7</sup>

It is well-known that dibenzyl sulfoxide  $(C_6H_5CH_2)_2SO$  is an effective inhibitor for corrosion of iron and iron alloys in acid solutions.<sup>8-15</sup> The inhibition mechanism of this compound for iron corrosion in acid solutions has been studied by a number of investigators. Protonated dibenzyl sulfoxide which forms in an acid solution,



is electrochemically reduced at the electrode forming dibenzyl sulfide as



Since the solubility of dibenzyl sulfide is extremely low in the solution, a protective multimolecular layer forms on the iron surface by accumulation of the sulfide, resulting in the high inhibition efficiency.<sup>8-10,13,14,16</sup> Schwabe<sup>8</sup> and TrabANELLI<sup>16</sup> have observed using a radiotracer technique with <sup>35</sup>S-labeled dibenzyl sulfoxide that a multimolecular layer of dibenzyl sulfide forms on the iron surface in acid solutions, but the latter author has claimed that only the first layer contributes to the corrosion inhibition.

UV spectra of the product desorbed from the stainless steel surface inhibited with dibenzyl sulfoxide have neither be distinguished from spectra of pure sulfoxide nor sulfide.<sup>17</sup> Pirnät et al.<sup>18</sup> have described that the rate of iron corrosion in 0.5M H<sub>2</sub>SO<sub>4</sub> containing 5X10<sup>-5</sup>M dibenzyl sulfide is one order larger than in the solution with dibenzyl sulfoxide at the same concentration. They have thus suggested that a dibenzyl sulfoxide molecule is adsorbed on the iron surface and the adsorbed molecule blocks the anodic and cathodic processes of corrosion reaction, though the fomation of an intermediate by the sulfoxide reduction has not been excluded. On the other hand, recent impedance studies have revealed that dibenzyl sulfide is a more effective inhibitor for iron corrosion in a 25 % ethanol solution of 0.5M H<sub>2</sub>SO<sub>4</sub> at 1X10<sup>-4</sup>M than dibenzyl sulfoxide.<sup>16,19</sup>

These results do not seem definitive for elucidating the inhibition mechanism of dibenzyl sulfoxide because in situ or ex situ spectral investigations of species adsorbed or accumulated on the iron surface are still lacking in data of the corrosion inhibition experiments. In this work, adsorption and accumulation of species on iron in 0.5M HCl with

dibenzyl sulfoxide were investigated by surface-enhanced Raman scattering and x-ray photoelectron spectroscopy (XPS). Inhibition mechanism of dibenzyl sulfoxide for iron corrosion in acid solutions was discussed based on results of the surface analyses.

## II. Experimental

### A. Materials

Dibenzyl sulfoxide ( $C_6H_5CH_2$ )<sub>2</sub>SO and dibenzyl sulfide ( $C_6H_5CH_2$ )<sub>2</sub>S were obtained as high-grade reagents and purified by recrystallization. A 0.5M HCl solution and other electrolyte solutions used in this experiment were prepared by diluting analytical reagents with redistilled water and deaerated by passing nitrogen gas through them.

Rods of 99.999% silver and 99.99% iron (Johnson Matthey Chemicals) were embedded in Teflon holders and used as electrodes. After abrasion of the surfaces with emery papers and 0.3  $\mu$ m alumina powder, the electrodes were ultrasonically cleaned in water and in acetone.

### B. Polarization measurement

Polarization measurements of the iron electrode in 0.5M HCl without and with the inhibitor were potentiostatically carried out at 25°C under a nitrogen atmosphere after immersion for 1 h.

### C. SERS measurement

A schematic diagram of apparatus for measuring the SERS spectra is shown in Figure 1. A spectroelectrochemical cell was used for the measurement, equipped with the silver electrode, a platinum counter electrode, a saturated calomel electrode (SCE), gas inlet and outlet tubes, and a tube connected to a syringe for injecting and draining solutions. The system was maintained under a pure nitrogen atmosphere throughout the SERS experiment. The 514.5 nm radiation from an Ar<sup>+</sup> laser was used to make the measurement.

The silver electrode was first activated with three oxidation-reduction cycles between 0.15 and -0.40 V vs. SCE in a 0.1M KCl solution at pH 3.5. Iron was then electrodeposited on the activated silver surface in a solution of 0.05M FeSO<sub>4</sub>(NH<sub>4</sub>)<sub>2</sub>SO<sub>4</sub> plus 0.1M KCl at -1.0 V vs. SCE with the cathodic charge of 80 mCcm<sup>-2</sup> for dibenzyl sulfoxide or of 100 mCcm<sup>-2</sup> for dibenzyl sulfide. SERS spectra of the compounds were measured using the silver electrode uncoated and coated with iron in a 0.5M HCl solution containing  $1 \times 10^{-4}$ M of the sulfoxide or saturated with the sulfide at the potential of -0.5 V vs. SCE, near the corrosion potential of the iron electrode in these solutions. The measurement was carried out with a spectrometer consisting of a double monochromator, a photon-counting system and a computer. After the measurement, the electrode potential of the silver electrode covered with deposited iron was maintained at the potential near the corrosion potential of the iron electrode.

A normal Raman spectrum of the compound was also recorded on the spectrometer with an optical cell.

#### D. XPS measurement

A disk of 99.99% iron (Japan Lamp Industries, 10 mm $\phi$ ) was fixed at the end of a Teflon holder with a thermoshrinkable Teflon tube. The disk surface was abraded with emery papers and 0.3  $\mu$ m alumina powder and ultrasonically cleaned in water and in acetone. The disk was immersed in a 0.5M HCl solution containing  $1 \times 10^{-4}$ M of dibenzyl sulfoxide at 30°C under a nitrogen atmosphere for 1 h. After being rinsed with deaerated water, the disk was dried in vacuo overnight.

X-ray photoelectron spectra of the disk surface inhibited with the sulfoxide were recorded on a JEOL JPS-90SX spectrometer. Mg K $\alpha$  radiation was used as an x-ray source. All manipulations prior to the XPS measurement were performed under an argon or nitrogen atmosphere in a dry box or a dry bag. Components of interest on the disk surface were Fe (2p), O (1s), C (1s), Cl (2p), and S (2p). Binding energies were referred to the C (1s $_{1/2}$ ) binding energy at 284.6 eV. Ion bombardment of the surface was carried out with an Ar $^{+}$  gun for observing depth profiles of the components in a surface layer.

### III. Results and Discussion

#### A. Polarization curves

Figure 2 shows polarization curves of the iron electrode in 0.5M HCl with and without the inhibitors. Dibenzyl sulfoxide at  $1 \times 10^{-4}$ M suppressed both cathodic and anodic processes of iron corrosion, whereas dibenzyl sulfide inhibited the anodic process to some extents in its saturated solution.

The corrosion current density was obtained by extrapolating cathodic and anodic Tafel lines and the inhibition efficiency  $I$  was calculated by

$$I / \% = 100(1 - i_{cor}/i_{cor}^0) \quad (3)$$

where  $i_{cor}^0$  and  $i_{cor}$  represent the corrosion current densities in the absence and presence of the inhibitor, respectively. The efficiencies of the sulfoxide at  $1 \times 10^{-4}$ M and the sulfide at the saturation concentration were 89 and 25 %, respectively. The former inhibitor was effective but the latter one was not for iron corrosion in 0.5M HCl.

#### B. SERS spectra

Figure 3 demonstrates a Raman spectrum of dibenzyl sulfoxide (a) and SERS spectra of the compound adsorbed on silver (b) and on iron-deposited silver in 0.5M HCl at -0.5 V vs. SCE (c). Strong signals could not be observed in the SERS spectrum of the sulfoxide adsorbed on the iron-coated silver electrode even though the SERS-active silver electrode was covered with the deposited iron layer of minimum thickness. Since SERS spectra of dibenzyl sulfoxide adsorbed on both uncoated and coated electrodes with the deposited



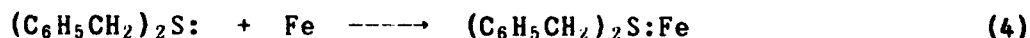
iron differed from the Raman spectrum of the compound, species in a different structure from that of the sulfoxide must be adsorbed on the electrode surfaces.

No evident signals assigned to the S-O stretching mode, which should appear in the region of the wave number between 1070 and 1020  $\text{cm}^{-1}$ ,<sup>20</sup> were detected in the Raman and SERS spectra. The relative intensity of a band at 1031  $\text{cm}^{-1}$  due to the in-plane C-H deformation mode in the Raman spectrum seemed to be higher than the intensities of bands at about 1030  $\text{cm}^{-1}$  in Raman and SERS spectra of other benzylthio compounds like dibenzyl sulfide and disulfide. The ratio of the intensity of the band at 1031  $\text{cm}^{-1}$  to that of the band at 1004  $\text{cm}^{-1}$  for the sulfoxide was 0.268, while the values for the other compounds were in the range between 0.139 and 0.207. It was thus concluded that the S-O stretching band of the sulfoxide overlaps the in-plane C-H deformation band at 1031  $\text{cm}^{-1}$  in its Raman spectrum. Because the ratios in the SERS spectra of the sulfoxide, 0.181 and 0.202 were evidently lower than 0.268, it was suggested that the S-O bond of the sulfoxide was cleaved when the compound was adsorbed on the metal surface. The S-O bond cleavage of the sulfoxide supported its electrochemical reduction to form dibenzyl sulfide as expressed by Equations (1) and (2).

Signals assigned to the C-S stretching mode appeared at 680  $\text{cm}^{-1}$  in the Raman spectrum (a) and at 644  $\text{cm}^{-1}$  in the SERS spectra on both metals (b) and (c). Since a decrease in energy of the C-S stretching vibrations for a molecule adsorbed on the surface is associated with electron withdrawal from the C-S bond by a S-metal bond, a downward shift in the wave number of the C-S stretching band implies the formation of a chemisorption bond between sulfur and metal atoms.<sup>6, 21</sup>

Figure 4 shows a Raman spectrum of dibenzyl sulfide (a) and SERS spectra of the compound adsorbed on silver (b) and on iron-coated silver in 0.5M HCl at -0.5 V vs. SCE (c). The in-plane ring deformation bands at 1205 and 1254  $\text{cm}^{-1}$  in the Raman spectrum emerged at 1206 and 1226  $\text{cm}^{-1}$  in the SERS spectrum on silver and at 1207 and 1220  $\text{cm}^{-1}$  on iron-deposited silver. The C-S stretching signal at 677  $\text{cm}^{-1}$  in the Raman spectrum appeared at 656 and 649  $\text{cm}^{-1}$  in the SERS spectra on the respective metals. These differences in the wave number of peaks between the Raman and SERS spectra are attributed to adsorption behavior of the sulfide on metals. Because the wave numbers of these bands in the SERS spectrum on iron-coated silver differed from those in the SERS spectrum on silver, it was suggestive that the SERS spectra shown in Figure 4(c) arises from a species adsorbed on the iron surface.

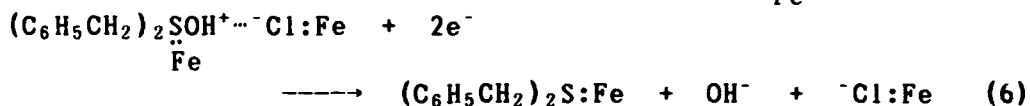
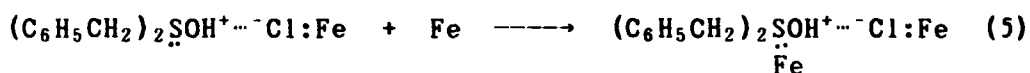
The wave number of the C-S stretching band on the Raman spectrum of the sulfide shifted to lower numbers in the SERS spectra on silver and iron-coated silver, indicating the formation of chemisorption bonds between sulfur and metal atoms. This compound chemisorbs on the iron surface by the formation of a coordinate bond as



Relatively large shifts in wave numbers of the C-S stretching bands indicated the formation of fairly strong chemisorption bonds between sulfur and metal atoms. The low inhibition efficiency of dibenzyl sulfide shown in Figure 1 is thus attributable to its extremely low solubility.

As shown in Figures 3 and 4, wave numbers of main bands in the SERS spectra of dibenzyl sulfoxide adsorbed on silver and iron-deposited silver almost agreed with those of dibenzyl sulfide on respective metals with a few exceptions. It was thus concluded that the sulfide formed by the electroreduction of the protonated sulfoxide was adsorbed on the iron surface. Bands due to the C-S stretching mode appeared at  $644\text{ cm}^{-1}$  in the SERS spectra of the sulfoxide [Figure 3(b) and (c)] while those emerged at  $656$  and  $649\text{ cm}^{-1}$  in the SERS spectra of the sulfide [Figure 4(b) and (c)], respectively. Since the larger downward shift of the C-S stretching band is ascribed to the stronger chemisorption of a sulfur compound on the metal surface, the sulfide derived from the sulfoxide through the cathodic reduction is more strongly chemisorbed on the metal surface than the sulfide adsorbed from the solution directly. This difference of bond strengths may be associated with mechanism of the chemisorption process for the sulfide derived from the sulfoxide on the surface.

Dibenzyl sulfide is chemisorbed on the iron surface by the formation of a simple coordinate bond between sulfur and iron atoms, as expressed by Equation (4). Protonated dibenzyl sulfoxide, which is jointly adsorbed with chloride ion on the iron surface via electrostatic interaction, is cathodically reduced with electrons passing through a chemisorption bond between sulfur and iron atoms and the sulfide molecule is strongly chemisorbed on the surface following the cleavage of a hydroxide ion, as



Dissociative adsorption of the protonated sulfoxide provides the improved chemisorption bond between sulfur and iron atoms. A similar improvement of a chemisorption bond by dissociative adsorption has been observed in the SERS spectra of dibenzyl disulfide.<sup>22</sup> It was concluded that dibenzyl sulfoxide is cathodically reduced at the iron surface in acid solutions to form dibenzyl sulfide strongly adsorbed on the surface, resulting in the high inhibition effect for iron corrosion in 0.5M HCl.

If dibenzyl sulfide molecules formed by the electroreduction accumulated on the monolayer of the adsorbed sulfide, the C-S stretching band of the sulfide may appear at  $677\text{ cm}^{-1}$  in the SERS spectra. No evidence of the sulfide accumulation on the metal surface was, however, observed in the SERS spectra of the sulfoxide because SERS spectra provide informations of species in the range of only a monolayer or a few layers at the interface.

### C. X-ray photoelectron spectra

In order to elucidate a structure of the layer accumulated on the surface, x-ray photoelectron spectra of Fe (2p), O (1s), C (1s), Cl (2p), and S (2p) for the surface layer on iron inhibited with dibenzyl sulfoxide in 0.5M HCl were measured. Depth profiles of the spectra are illustrated with the sputtering time  $t$ , in Figure 5. The spectra of Fe (2p<sub>3/2</sub>) showed peaks at about 711 and 707.5 eV of the binding energy, indicating the presence of Fe<sup>2+</sup> in the surface layer. Peaks of oxide and chloride ions appeared at 530.5 and 198.5 eV in the spectra of O (1s<sub>1/2</sub>) and Cl (2p<sub>3/2</sub>), respectively. A peak of carbon atom emerged at 284.6 eV in the spectra of C (1s<sub>1/2</sub>) and a weak peak appeared at about 162 eV in the spectra of S (2p<sub>3/2</sub>), indicating the presence of a sulfur compound in the surface layer. Since most of peaks were detected in the range of  $t$ , between 0 and 20 s, the layer formed at the iron surface is composed of Fe<sup>2+</sup>, O<sup>2-</sup>, Cl<sup>-</sup>, C, and S. The presence of carbon and sulfur atoms implied the accumulation of dibenzyl sulfide formed by the cathodic reduction of the sulfoxide on the iron surface. Because peaks of C (1s<sub>1/2</sub>) and S (2p<sub>3/2</sub>) for a monolayer of alkanethiol adsorbed on copper have been diminished at  $t$ , < 10 s by Ar<sup>+</sup> bombardment of the surface in the same manner as adopted in the present work,<sup>20</sup> it is concluded that a thick multimolecular layer of the sulfide is formed on the iron surface.

Relative concentrations of atoms and ions are plotted against  $t$ , in Figure 6. Large amounts of Fe<sup>2+</sup>, Cl<sup>-</sup>, and O<sup>2-</sup> were included in the sulfide layer on the surface. The presence of Fe<sup>2+</sup> in the film is not ascribed to oxidation with oxygen gas during the XPS experiment since the surface of iron disk was never allowed to expose to air. Because the anodic, iron dissolution reaction occurs along with the cathodic reduction of the sulfoxide at the surface, it seems reasonable that the sulfide layer is composed of Fe<sup>2+</sup> and counter anions Cl<sup>-</sup> and O<sup>2-</sup>. The layer comprising a mixture of the organic sulfide and inorganic ferrous chloride and oxide cannot be expected to be protective against iron corrosion in the acid solution. Especially, the presence of water-soluble ferrous chloride suggests a porous film containing the chloride solution at the electrode-solution interface. Hence, the formation of the sulfide layer on the iron surface is of minor importance to the inhibition of iron corrosion in acid solutions by dibenzyl sulfoxide.

#### IV. Conclusions

Inhibition mechanism of dibenzyl sulfoxide for corrosion of iron in a 0.5M HCl solution was studied by polarization measurement and surface-enhanced Raman scattering (SERS) and x-ray photoelectron spectroscopy. Because the SERS spectra of dibenzyl sulfoxide adsorbed on the metal surface were similar to those of dibenzyl sulfide, the latter compound formed by the cathodic reduction of the former was chemisorbed on the surface. From results of the SERS experiment, it is concluded that the sulfide molecule formed by the cathodic reduction of the sulfoxide is strongly chemisorbed on the iron surface.

An XPS study of the layer prepared on the iron surface inhibited with the sulfoxide in 0.5M HCl revealed the formation of multimolecular layer which comprises the sulfide formed by the cathodic reduction and ferrous oxide and

chloride afforded by the anodic dissolution of iron. Since this surface layer does not seem to be protective against acid corrosion of iron, the high inhibition effect of dibenzyl sulfoxide is mainly attributed to the strong chemisorption of dibenzyl sulfide on the iron surface.

#### References

1. M. Fleischmann, I. R. Hill, Surface Enhanced Raman Scattering, R. K. Chang, T. E. Furtak ed. (New York: Plenum Press, 1982), p. 275; B. Pettinger, H. Wetzel, *ibid.*, p. 293.
2. K. Aramaki, J. Uehara, J. Electrochem. Soc. 136 (1989): p. 1299.
3. K. Aramaki, J. Uehara, J. Electrochem. Soc. 137 (1990): p. 185.
4. K. Aramaki, J. Uehara, H. Nishihara, Proceedings 11th International Corrosion Congress, 3 (Milano: Associazione Italiana di Metallurgia, 1990), p. 31.
5. J. Uehara, H. Nishihara, K. Aramaki, J. Electrochem. Soc. 137 (1990): p. 2677.
6. J. Uehara, K. Aramaki, J. Electrochem. Soc. 138 (1991): p. 3245.
7. N. Saito, H. Nishihara, K. Aramaki, Corros. Sci. 33 (1992): p. 1253.
8. K. Schwabe, Z. Phys. Chem., Leipzig, 226 (1964): p. 1.
9. H. Ertel, L. Horner, Comptes Rendus du 2ème Symposium Européen sur les Inhibiteurs de Corrosion, (Ferrara, Italy: Università Degli Studi di Ferrara), p. 71.
10. J. W. Lorenz, H. Fischer, Comptes Rendus du 2ème Symposium Européen sur les Inhibiteurs de Corrosion, (Ferrara: Università Degli Studi di Ferrara), p. 81.
11. L. Felloni, A. Cozzi, Corros. Sci. 7 (1967): p. 481.
12. L. Horner, H. Hinrichs, H. Ertel, Werkst. Korros. 22 (1971): p. 930.
13. H. Vosta, J. Pelikán, M. Smrz, Werkst. Korros. 25 (1974): p. 750.
14. H. H. Przewlozcka, H. Bala, Zashch. Metal. 19 (1983): p. 722.
15. G. Trabanelli, A. Frignani, G. Brunoro, C. Monticelli, F. Zucchi, Materials Performance 24, 6 (1985): p. 33.
16. G. Trabanelli, Corrosion 47 (1991): p. 410.
17. L. Baldi, V. Carassiti, G. Trabanelli, F. Zucchi, G. L. Zucchini, Proceedings 3rd International Congress on Metallic Corrosion, 2 (Amsterdam: Swets-Zeitlinger, 1969), p. 127.
18. A. Pirnât, L. Mészáros, B. Lengyel, Proceedings 7th European Symposium on Corrosion Inhibitors, 2 (Ferrara: Università Degli Studi di Ferrara), p. 885.
19. A. Frignani, M. Tassinari, Proceedings 7th European Symposium on Corrosion Inhibitors, 2 (Ferrara: Università Degli Studi di Ferrara), p. 895.
20. J. G. Grasselli, M. K. Snavely, B. J. Bulkin, Chemical Applications of Raman Spectroscopy (New York: John Wiley & Sons, 1981), p. 37.
21. Y. Yamamoto, H. Nishihara, K. Aramaki, J. Electrochem. Soc. 140 (1993): p. 443.
22. N. Ohno, H. Nishihara, K. Aramaki, Submitted to J. Electrochem. Soc.

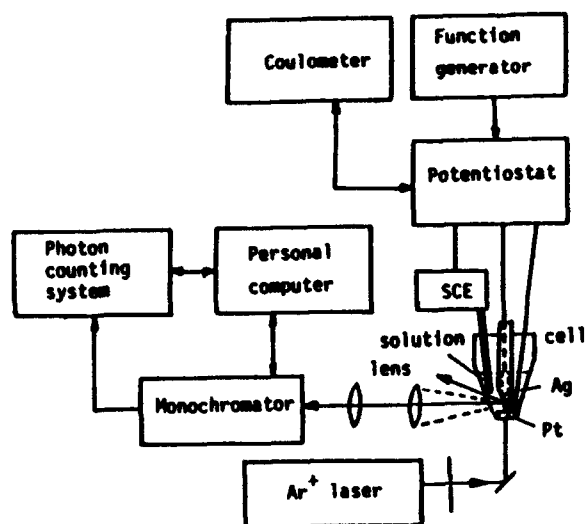


FIGURE 1. Apparatus for measuring SERS spectra.

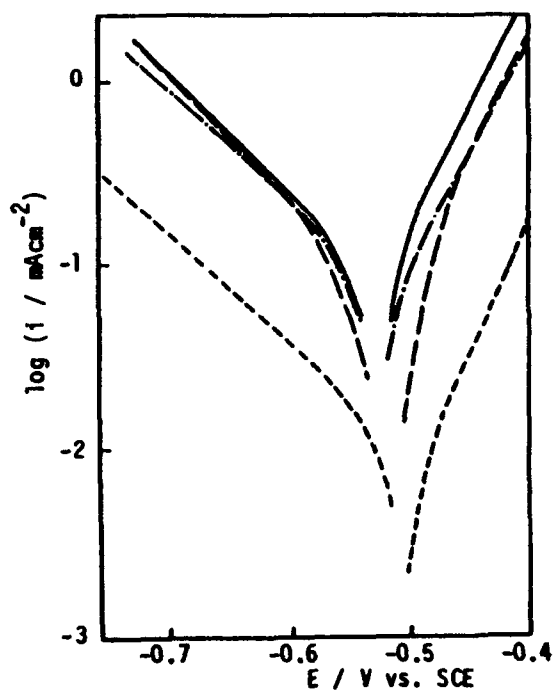


FIGURE 2. Polarization curves (potential  $E$  and current density  $i$ ) of iron electrode in 0.5M HCl uninhibited (—) and inhibited with dibenzyl sulfoxide at  $1 \times 10^{-6}$  M (---) and  $1 \times 10^{-4}$  M (-.-.-) and with dibenzyl sulfide (saturated, . . .).

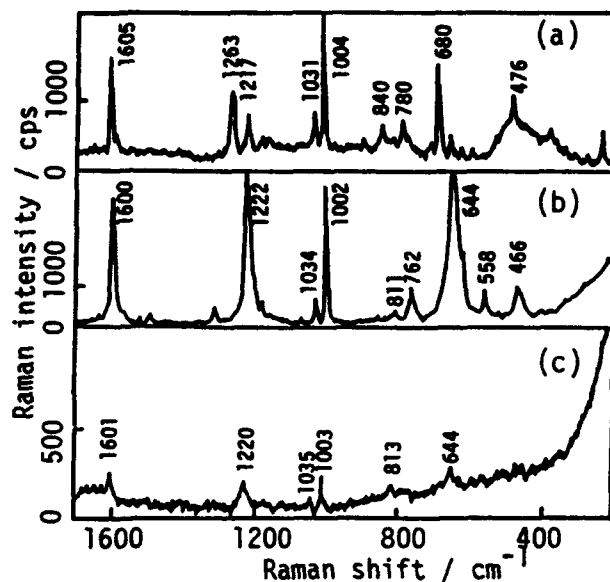


FIGURE 3. Raman spectrum of dibenzyl sulfoxide (a) and SERS spectra of the compound adsorbed on silver (b) and iron-deposited silver (c) in 0.5M HCl at -0.5 V vs. SCE.

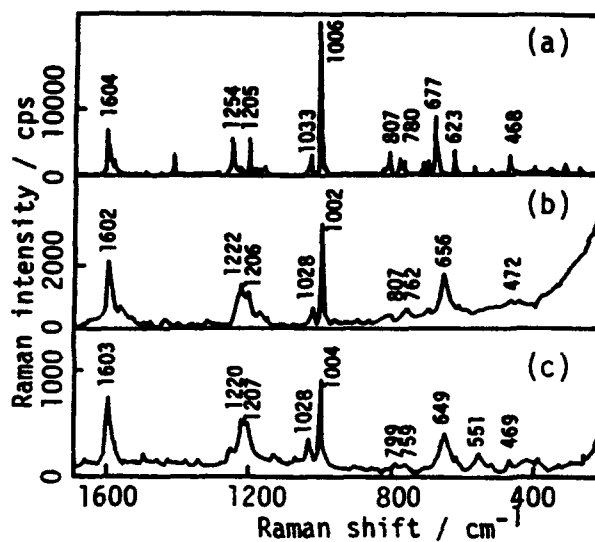


FIGURE 4. Raman spectrum of dibenzyl sulfide (a) and SERS spectra of the compound adsorbed on silver (b) and iron-deposited silver (c) in 0.5M HCl at -0.5 V vs. SCE.

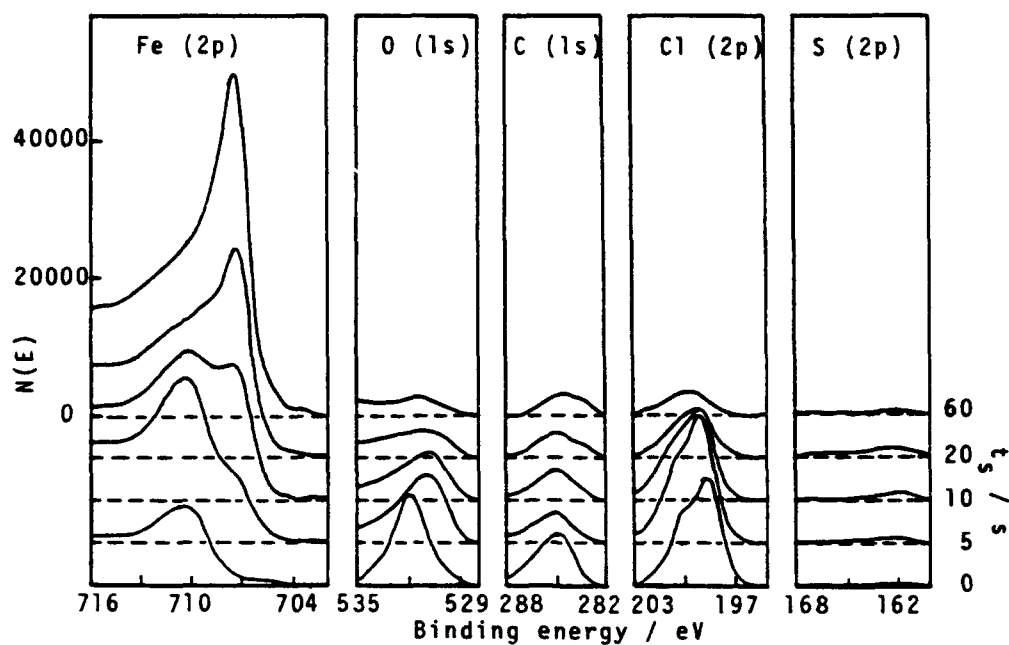


FIGURE 5. Depth profiles at various sputtering times  $t_s$  in x-ray photoelectron spectra of Fe (2p), O (1s), C (1s), Cl (2p), and S (2p) for the surface layer prepared on the iron surface in 0.5M HCl containing  $1 \times 10^{-4}$ M of dibenzyl sulfoxide.

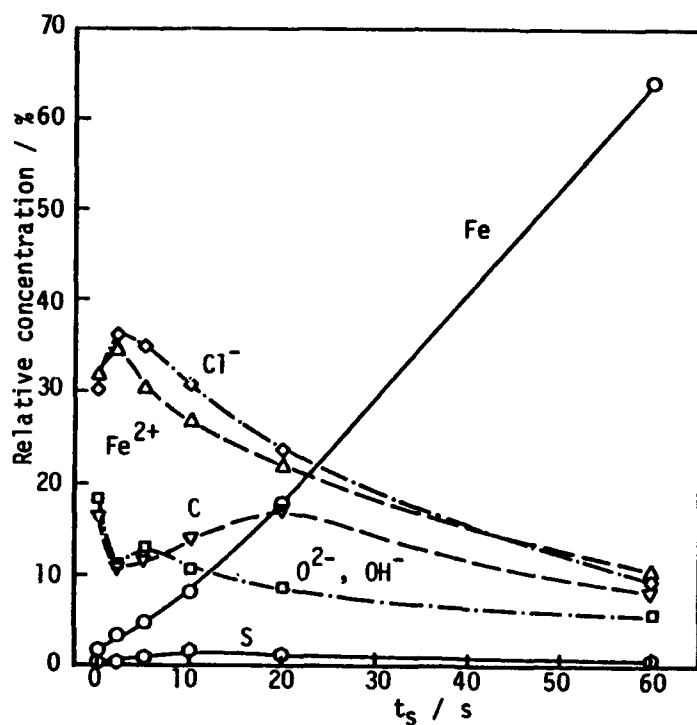


FIGURE 6. Relative concentrations of atoms and ions versus the sputtering time  $t_s$ .

## **The Role of Synergism and Molecular Structure in the Mechanism of Inhibition**

**Erika Kálmán**

**Central Research Institute for Chemistry  
Hungarian Academy of Sciences  
H-1525 Budapest, Pf.17.**

**István Lukovits**

**Central Research Institute for Chemistry  
Hungarian Academy of Sciences  
H-1525 Budapest, Pf.17.**

**Gábor Pálinkás**

**Central Research Institute for Chemistry  
Hungarian Academy of Sciences  
H-1525 Budapest, Pf.17.**

### **Abstract**

The role of synergistic effects and molecular structure of inhibitors in the mechanism of inhibition have been studied by means of multiple regression calculations.

The study of correlation between structure and inhibitor efficiency will lead to the concept of computer design of corrosion inhibitors, i.e., developing inhibitors on the drawing-board.

**Key terms:** corrosion inhibition, synergism, computer modelling

### **Introduction**

Aqueous solutions are by far the most common corrosive systems in which corrosion inhibitors are applied. Although the detailed mechanism of inhibition in aqueous media in many cases, is not yet clear, the importance of the adsorption phenomena, the synergistic effects and the molecular structure of the inhibitor molecules on the mechanism of inhibition is well recognized already in the early stages of the inhibitor research.

The role of adsorption in the formation of protective layers on the metal surface has been extensively studied. Only over narrow limits of concentration do aqueous inhibitors adsorb in a monolayer and obey Langmuir's isotherm. This isotherm which treats surface as a uniform layer on which adsorption can occur randomly at a rate proportional to the area left uncovered and assumes that a monolayer forms before any double or multiple layers of adsorbed molecules starts to form. In practice adsorption of inhibitor compounds on metal surface in aqueous solutions might be expected to conform to the Freundlich or Frumkin

isotherms. These isotherms treat a metal surface as heterogeneous one and assume that adsorption occurs preferentially on certain sites, which requires more energy to form until all the surface is covered. The driving force, in the formation of adsorbed protective layers on the metal surface which obey Freundlich or Frumkin isotherms, is the interaction either between inhibitor molecules and the metal or between the adsorbed molecules themselves.

During the corrosion process in aqueous solution the corrosion product layers constitute a new distinct phase between metal and bulk corrodent; the inhibitor will necessarily interact with this interphase (Fig.1). The rate-controlling phenomenon in interphase inhibition is the diffusion controlled charge transfer inhibition.

It has recently been shown<sup>1</sup> by computer simulation based on stochastic model developed (Fig.2.) for statistical description of corrosion process of metals and inhibition by adsorption mechanism, that a very simple model for interaction between the adsorbed species is able to distinguish between Langmuir and Frumkin type adsorption mechanisms (Fig.3).

The composition of 3D-layers may be weakly soluble compounds consisting of oxidic corrosion products, intermediates and inhibitors. The efficiency of corrosion inhibitors depends on the mechanical, structural and chemical properties of the layer formed.

Two important factors influencing the mechanism of inhibition, the synergism and the correlation between molecular structure of inhibitor molecules and their inhibiting efficiency seem to have received less attention so far. The aim of this paper is to show the usefulness of methods of mathematical statistics for studies of these factors.

### The Synergistic Effect

Certain compounds when they are applied together increase inhibitor efficiency. This phenomenon termed as the synergistic effect due either to interaction between the components of inhibitor composition or to interaction between the inhibitor and one of the ions present in the aqueous media. This is a non-linear effect resulting in non-additive efficiencies of the separate components.

During the past two decades a number of phosphonates have been used in different inhibitor composition<sup>3</sup>. Typical example of these is 1-hydroxy-ethane 1,1-diphosphonic acid (HEDP). It is known that the presence of some divalent cations such as  $Zn^{2+}$  in aqueous media synergistically increase the inhibitor efficiency of HEDP inhibitor compound. Fig.4. shows the synergistic effects of different phosphonic acids ( mono- (MP), di- (DP), poly-phosphonic acids (PP)) with  $Zn^{2+}$ .

An appropriate mathematical model which describes the corrosion rates including the possibility of interactions is

$$v = v_0 + \sum_{i=1}^n v_i c_i + \sum_{i,j=1}^n v_{ij} c_i c_j \quad (1)$$

where  $v$  and  $v_0$  are corrosion rates with and without inhibitor,  $c_i$  is the concentration of the  $i$ -th component and  $v_i$ ,  $v_{ij}$  are parameters to be determined.



The form of this equation contains terms for the main effects,  $v_i$  and interactions  $v_{ij}$ . Equations of this type are termed as multiple regression equations. By utilizing the coded variables in developing the regression equation by means of computer calculation, we can give physical interpretations of the coefficients.

The linear coefficients  $v_i$  represent the predicted change in the corrosion rate when the independent variable  $c_i$  is changed by one unit. The interaction term  $v_{ij}$  reflects the dependency of one factor on the level of another factor. The interaction term,  $v_{ij}$ , unless negligible, can be either negative or positive, which indicates synergistic or antagonistic effects between the two factors.

Synergism is due to interactions between variables and reflects non-linearity of the individual effect.

The results of regression analysis of inhibitor efficiency for the compositions of phosphonic acid and zinc salt at different pH values in a model cooling water are presented in Fig.5. The regression coefficient  $v_{ij}$  corresponding to interaction between HEDP and  $Zn^{2+}$  ions is found to be negative, reflecting the appearance of synergism between these two components. The values of corrosion rates were found to be different at each pH, as shown by the contour plot of iso-corrosion lines as a function of concentrations. According to the plots optimal concentration ratio is almost the same at different pH values, although the minima appear at different values of the concentrations. The numbers in Fig.3. denote the corrosion rates at the first corrosion line. The increment between the contours is 0,05 mm/y. The best inhibitor effect is reached under nearly neutral conditions.

Investigation of the mechanism of HEDP adsorption by radiotracer method by  $^{14}C$  labelled HEDP,  $^{65}Zn$  and  $^{45}Ca$  isotopes has shown that HEDP by itself forms a loosely bound adsorption layer on iron oxide surface, and that the presence of zinc or calcium ions in solution leads to an increased adsorption of HEDP molecules (s.Fig.6,7). The maximum value in the efficiency of HEDP-Zn mixtures is achieved at about molar ratio of  $Zn/HEDP = 2$  in the solution. In the case of higher values, this ratio in the protective film remains about the same. HEDP adsorption is monotonously enhanced with increasing amounts of  $Ca^{2+}$  in the solution, i.e., the ratio of  $Ca/HEDP$  on the metal surface is 1:1. These results indicate presence of complexes on the metal surface and a precipitation mechanism for the inhibition in both cases. Different poorly soluble complex compounds of HEDP with zinc or calcium ions, which precipitate on the metal surface, provide a protective layer.

The use of phosphonates in addition to polyphosphates, zinc and polymers in corrosion inhibitor blends allows further reduction of total inhibitor concentration necessary for effective protection, compared to earlier inorganic formulations. The higher inhibitor efficiency of mixtures containing phosphonates is due to the synergistic effect of the components. Synergism is one of the most important effects in inhibition processes and serves as a basis for all modern corrosion inhibitor formulations for neutral aqueous solutions.

The synergistic effect between components of inhibitor blend containing HEDP,  $ZnSO_4$ , (Zn) hexametaphosphate (HM), sodiummetavanadate ( $VO_3$ ) and a low molecular weight acrylate polymer (PL) has been investigated at two different pH values by using multiple regression analysis with more than 200 experimental data.

The model solution was a cooling water model at 40°C (temperature with hardness) and the corrosion rates of mild steel coupons were measured by weight loss method. All compounds were used in 20 ppm concentration.

The independent variables used in the multiple regression analysis of the data indicated the presence ( $c_i = 1$ ) or absence ( $c_i = 0$ ) of the component. For modelling synergism binary variables were used ( $c_{ij} = d_{ij}$ ). If both component  $i$  and  $j$  were present, the value of binary variable was  $c_{ij} = 1$  in all other cases,  $c_{ij} = 0$ .

Although the standard deviation of the experimental data was about 10 %, the results indicates significant reduction of corrosion rates for HEDP,  $ZnSO_4$ ,  $NaVO_3$  and HM. The polymer component had no significant effect at  $pH = 7$ . Synergism was detected between components HEDP-Zn, HEDP-Zn-HM, HEDP- $VO_3$ , HEDP- $VO_3$ -HM and HM- $VO_3$ . A part of the results is shown in Fig.8. The upper and lower sections of Fig.8. represent data for  $pH = 7$  and  $pH = 8$ , respectively. The histograms represent the results obtained with (in front) and without (in the rear)  $NaVO_3$  component in the blends.

In the x axis the presence (1) or absence (0) of HM the is indicated. There are 4x4 bars in both histograms. Each of the 4 blocks represents date for different compositions with the other three components (HEDP, Zn, PL). The order of blocks in the Fig.8. from left to right is (000), (100), (110) and (111), respectively.

Recently synergism of substituted amino acids with  $Ca^{++}$  and  $Mo^{VI}$  additives has been investigated in our laboratory by varying five parameters. The compounds studied are given in Table 1. The corrosion rates of mild steel coupons in 0.5 mol/l  $NaClO_4$  solutions were measured by weight loss method as a function of the number of phosphono groups (1,2,3) attached to the skeleton structure. The other parameters were the follows:

- temperature            25-60°C
- pH                        6-9
- concentration of  $Ca^{II}$  ion (0-1,5.10<sup>-4</sup> mol/l)
- concentration of  $Mo^{VI}$  ion (0,75-12.10<sup>-4</sup> mol/l)

Because of the great number of all possible combinations a random number generator has been used to select 140 experiments.

The experimental data were analysed by multiple regression calculation.

In Fig.9. some of the results are shown. The corrosion rates of carbon steel is shown for a blank solution and solutions without molybdenum containing 30 ppm different carboxylic, phosphonic acids ( $pH = 7$ ,  $T = 77^\circ F \cong 25^\circ C$ ).

The two sets of histograms illustrate cases with and without 1.10<sup>-4</sup> mol/l  $Ca^{2+}$ .

First, as is evident from the Fig.9. the efficiency of all inhibitor compounds increases in the presence of  $Ca^{2+}$ . Secondly the greatest effect is observable for carboxylic-phosphonic acid with one carboxylic and two phosphono groups (DPMG)

Both temperature and molybdenum ions have some slight effect on the corrosion rate of carbon steel in the whole range of parameters.

The parameters values given in the Table 1 are calculated from the multiple regression function with parameters fitted to the experimental data. The usefulness of the regression function and coefficients is that it allows the prediction of corrosion rates for all three

inhibitor compounds at any value of the other 4 variables in the range studied.

In Table 1 the values of linear coefficients and non-negligible cross terms are given together with t values indicating the reliability of the regression coefficients.

There are 10 possible interaction terms composed of 5 variables (12 13 14 15) (23 24 25) (34 35) (45) almost all cross terms  $x_i x_j$  were negligible except for compound-Ca interaction.

These values are shown at the bottom of the table. Multiple correlation resulted in 0.85, which is not a bad correlation related to the 10 % standard deviation for the experimental data.

#### Correlation between structure and inhibiting efficiency of amino phosphonic acids

Introducing different substituents into a skeleton molecule corrosion and scale inhibitors with systematically changed structure can be developed<sup>4</sup>. Amino phosphonic acids are used as corrosion inhibitors, however, the effect of the different side chains attached to atom N has been investigated. A newly introduced  $\text{CH}_2\text{COOH}$  or  $\text{CH}_2\text{PO}_3\text{H}_2$  group (especially the latter) also increased the effectivity of a molecule. The higher the  $\text{PO}_3\text{H}_2$  ratio in a molecule is, the higher is the efficiency that can be attained, although the length of the carbon skeleton must also be taken into account. On the basis of experimental data it may be stated that another negatively charged group will increase the corrosion inhibition effect.  $\text{CH}_2\text{OH}$  substitution hardly decreases the anti-corrosion effect of a basic molecule, whereas activity against different microorganisms increases.

Introduction of the Free-Wilson method, opened up new vistas of research<sup>5</sup> heading to the determination of quantitative correlations between the structure of compounds and their inhibiting efficiency in neutral aqueous solutions.

Although, this model is well known in pharmacology, it was practically not used for corrosion studies.

The aim of our work was to derive quantitative correlations between the structure of amine derivatives and their inhibiting potencies in neutral solutions.

The Free-Wilson method is based on multiple linear regression analysis, and is used to derive quantitative correlations between the chemical structure of molecules and their properties. It is assumed that for a series of closely related structures a common "parent structure" exists, and that the contributions of the various substituents (the "group contributions") are additive. The inhibiting efficiency of the molecules may be described as the difference between the corrosion rates in the inhibited ( $v_i$ ) and in the uninhibited ( $v_o$ ) systems:

$$\Delta v_i = v_o - v_i \quad (2)$$

The Free-Wilson model assumes that the dependent variable

( $\Delta v_k$ ) is the sum of the contributions of the substituents of a common parent structure:

Here  $\Delta v_k$  denotes the efficiency of compound k,  $x_{kj} = 1$  if molecule k contains substituent j, and  $x_{kj} = 0$ , and  $a_j$  denotes the "group contribution" of substituent j. The same substituent appearing in non-equivalent substitution sites must be considered separately; c denotes the

$$\Delta v_k = \sum_1^n x_k a_j + c \quad (3)$$

intercept. The group contributions  $a_j$  may be obtained by multiple regression analysis. For the actual calculation the Fujita-Ban version of the Free-Wilson method was used.

The quality of the correlation will not be affected if instead of  $\Delta v_k$  the corrosion rate  $v_k$  is considered as the dependent variable in the multiple regression equation. The more negative the regression coefficients (group contributions), the better the effect of the actual substituent.

Table 2. lists the compounds and their experimental and calculated inhibiting efficiencies. Note that  $R_1$  and  $R_2$  and also  $R_3$  and  $R_4$  denote equivalent substituents, respectively. Of course in molecule 18 all three substituents of N should be equivalent, whereas they are not in the present model. This discrepancy could be removed by defining equivalent substituents on atom N, but the multiple correlation coefficient would be much lower in that case, because of the reduced number of parameters. In this series of derivatives the calculated multiple correlation coefficient was  $R = 0.89$ , the standard error of estimate was  $s = 0.067$ , and the result of Fischer's F-test was equal to 5.45, indicating that the equation (i.e. the statistics) was significant at the  $p < 0.05$  level. The intercept  $c$  was found to be 0.47. The calculated group contributions are as follows:

Site  $R_1$  and  $R_2$ :  $\text{CH}_2\text{PO}_3\text{H}_2 = -0.12$ ,  $\text{CH}_2\text{OH} = 0.05$ ,  $\text{CH}_2\text{COOH} = 0.02$ .

Site  $R_3$  and  $R_4$ :  $\text{COOH} = -0.09$ ,  $\text{CH}_2\text{COOH} = -0.06$ ,  $\text{PO}_3\text{H}_2 = 0.02$ .

$\text{CH}_2\text{CH}_2\text{COOH} = 0.05$

Further computations with more elaborated models are in progress.

#### Acknowledgments

This work was supported by the National Scientific Foundation, OTKA /N. 1808 and No. T 4278/. The experimental work of Mrs. E. Kéthely-Bella, Dr. F.H. Kármán and Dr. J. Telegdi are gratefully acknowledge.

#### References

1. E. Kálmán, G. Pálinkás: Corros. Sci. (1993) in press
2. H.D. Held, G. Bohnsack: Kühlwasser, Vulkan Verlag, Essen (1984)
3. F.H. Kármán, E. Kálmán, L. Várallyai, J. Kónya: Z. Naturforsch. 46a (1991) p. 183.
4. J. Telegdi, E. Kálmán, F.H. Kármán: Corros. Sci. 33 (1992) p. 1099.
5. E. Kálmán, I. Lukovits, F.H. Kármán, J. Telegdi: Proc. Eurocorr 91. (1991) p. 7.

TABLE 1.  
Regression analysis of corrosion rate data

No.	variables $x_i$	linear regression coefficients $v_i$	t values
1.	k	-78.70	-8.5
2.	pH	- 1.83	0.6
3.	t	- 0.47	0.2
4.	$c_{Me}$	- 2.43	-1.6
5.	$c_{Ca}$	-19.10	-3.4

non negligible cross coefficients

k		$v_{15}$	T
1.	PIDDA	-4.24	-2.4
2.	DPGly	-7.20	2.2
3.	ATMP	-4.10	-1.1

intercept  $v_0 = 322 \mu/\text{year}$

k stands for codes of compounds

unit of corrosion rate is  $\mu/\text{year}$

t values measured the uncertainty in the average values

TABLE 2.

The structure and the efficiency (expressed as corrosion rate mm/y) of some amino acids

Generalized formula :  $R_1\text{-CHR}_2\text{-NR}_1\text{R}_2$

No.	$R_1$	$R_2$	$R_3$	$R_4$	$v_{exp.}$ (mm/y)	$v_{calc.}$ (mm/y)
1.	H	H	H	COOH	0.37	0.39
2.	H	CH <sub>2</sub> OH	H	COOH	0.36	0.44
3.	CH <sub>2</sub> OH	CH <sub>2</sub> OH	H	COOH	0.52	0.49
4.	H	CH <sub>2</sub> PO <sub>3</sub> H <sub>2</sub>	H	COOH	0.24	0.26
5.	CH <sub>2</sub> COOH	CH <sub>2</sub> COOH	H	COOH	0.26	0.27
6.	H	H	CH <sub>2</sub> COOH	COOH	0.32	0.32
7.	H	CH <sub>2</sub> OH	CH <sub>2</sub> COOH	COOH	0.39	0.37
8.	H	CH <sub>2</sub> COOH	CH <sub>2</sub> COOH	COOH	0.25	0.34
9.	H	CH <sub>2</sub> PO <sub>3</sub> H <sub>2</sub>	CH <sub>2</sub> COOH	COOH	0.27	0.20
10.	H	H	CH <sub>2</sub> CH <sub>2</sub> COOH	COOH	0.47	0.45
11.	H	CH <sub>2</sub> OH	CH <sub>2</sub> CH <sub>2</sub> COOH	COOH	0.47	0.48
12.	H		CH <sub>2</sub> CH <sub>2</sub> COOH	COOH	0.39	0.45
13.	H	CH <sub>2</sub> PO <sub>3</sub> H <sub>2</sub>	CH <sub>2</sub> CH <sub>2</sub> COO H	COOH	0.35	0.31
14.	H	H	H	CH <sub>2</sub> COOH	0.40	0.41
15.	H	CH <sub>2</sub> OH	H	CH <sub>2</sub> COOH	0.47	0.46
16.	H	CH <sub>2</sub> COOH	H	COOH	0.49	0.40
17.	CH <sub>2</sub> PO <sub>3</sub> H <sub>2</sub>	CH <sub>2</sub> COOH	H	COOH	0.34	0.28
18.	CH <sub>2</sub> PO <sub>3</sub> H <sub>2</sub>	CH <sub>2</sub> PO <sub>3</sub> H <sub>2</sub>	H	PO <sub>3</sub> H <sub>2</sub>	0.25	0.25

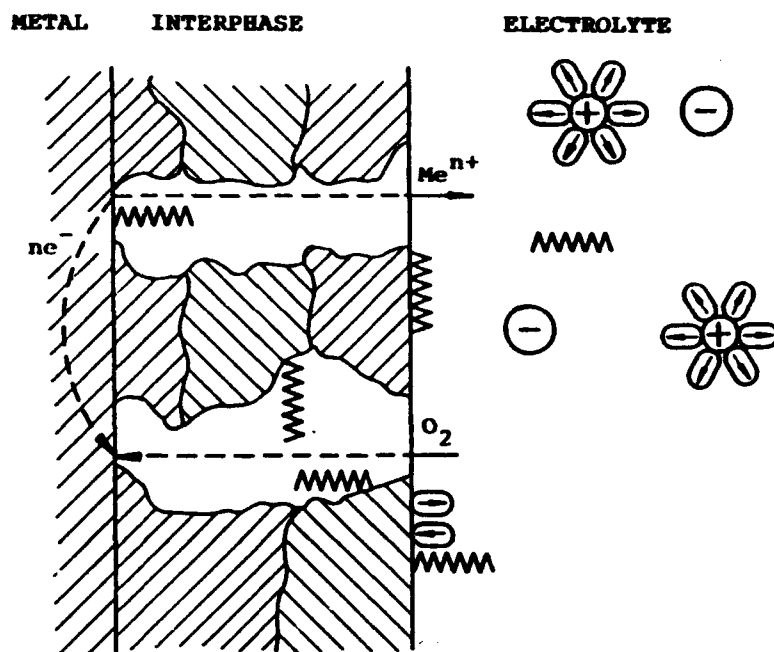


Fig. 1. Schematic corrosion inhibition model on a metal surface covered with porous oxide layer

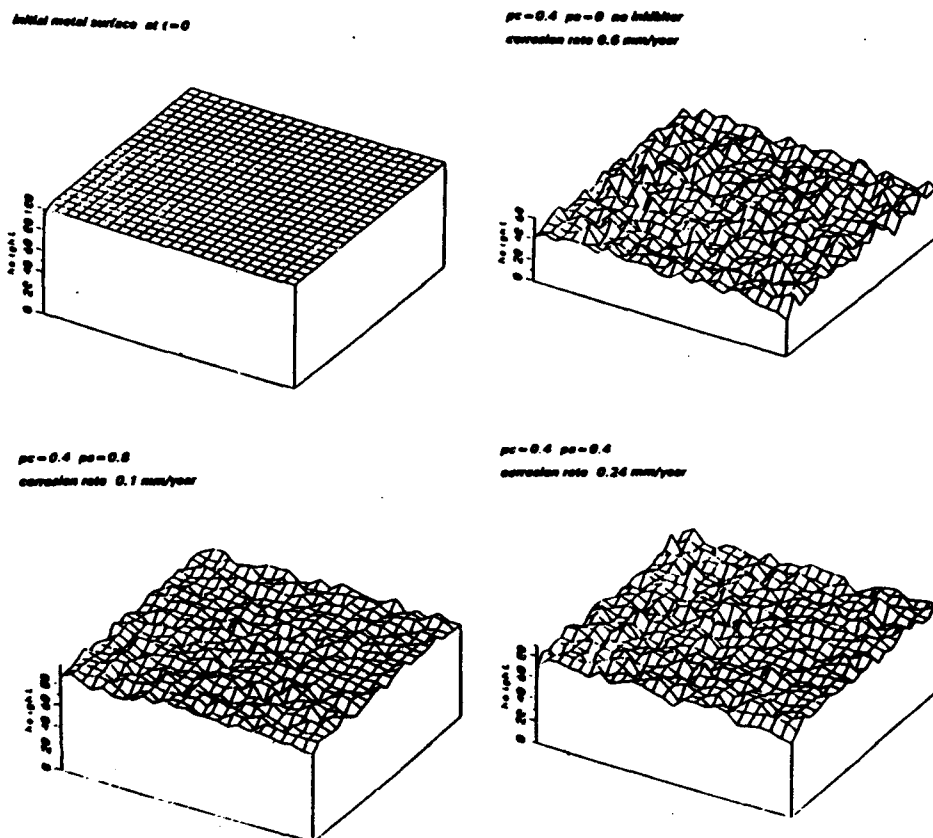


Fig. 2. Plot of the metal surfaces at the beginning and at the end of simulation with a probability for metal dissolution of  $p_d = 0.4$  and different probabilities  $p_a$  for adsorption process

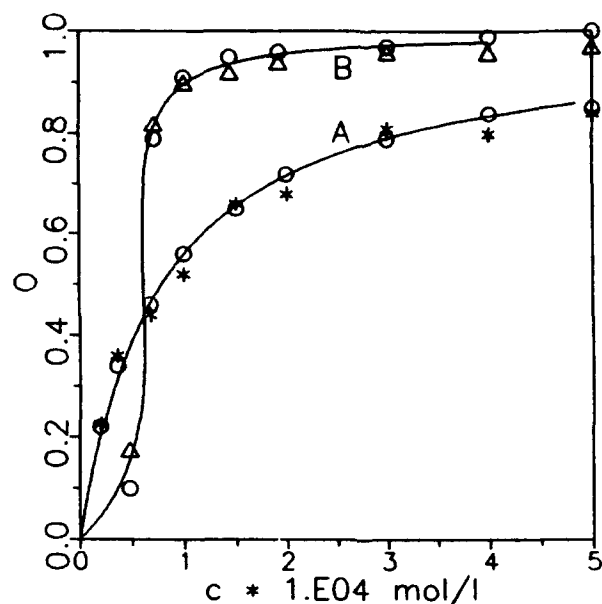


Fig.3. Fractional coverage of carbon steel in  $\text{NaClO}_4$  solutions as a function of HEDP inhibitor concentration in the absence (A) and in the presence (B) of Ca ions. Stars and triangles stand for experimental data (A and B, respectively), full lines represent Langmuir and Frumkin isotherms fitted to experimental data (A) and (B), respectively. Open circles are the results of computer simulations.

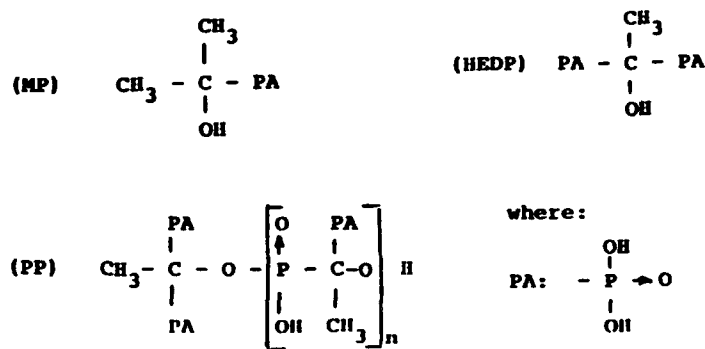
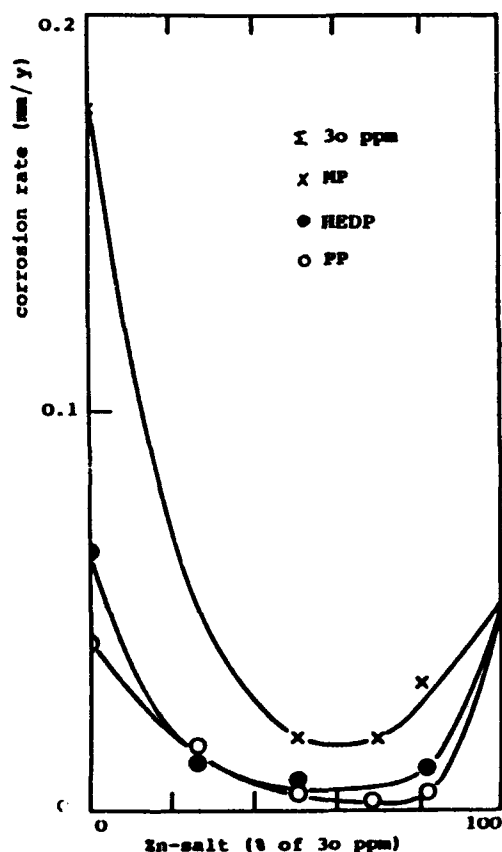
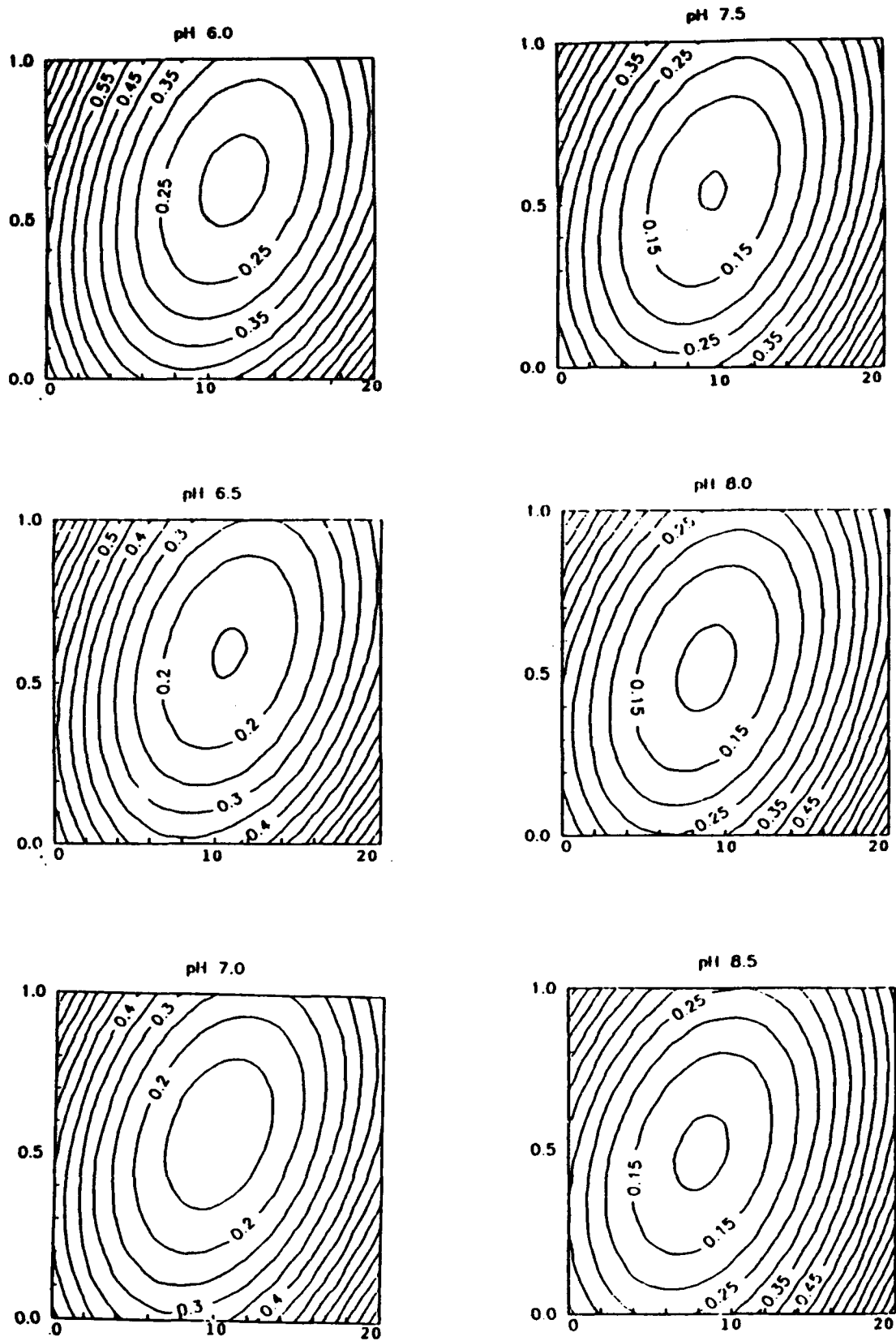


Fig.4. Synergism of different phosphonic acids with zinc salt



**Fig.5. Countur plots of isocorrosion lines (mm/year) as function of HEDP and Zn concentrations at different pH values**



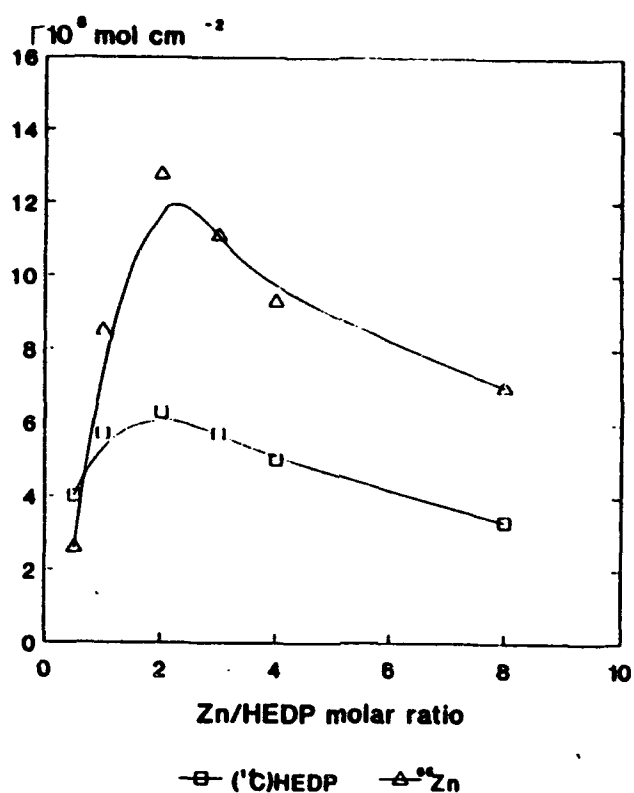


Fig.6. Adsorption of labelled HEDP ( $^{14}\text{C}$ ) and  $^{65}\text{Zn}$  versus the Zn/HEDP molar ratio in aqueous  $0.5 \text{ mol.dm}^{-3} \text{ NaClO}_4$

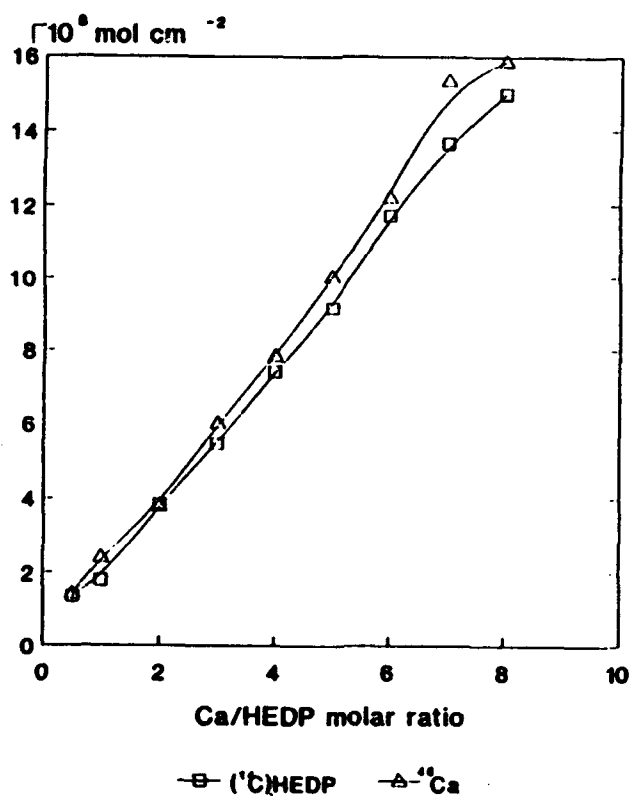


Fig.7. Adsorption of labelled HEDP ( $^{14}\text{C}$ ) and  $^{45}\text{Ca}$  versus the Ca/HEDP molar ratio in aqueous  $0.5 \text{ mol.dm}^{-3} \text{ NaClO}_4$

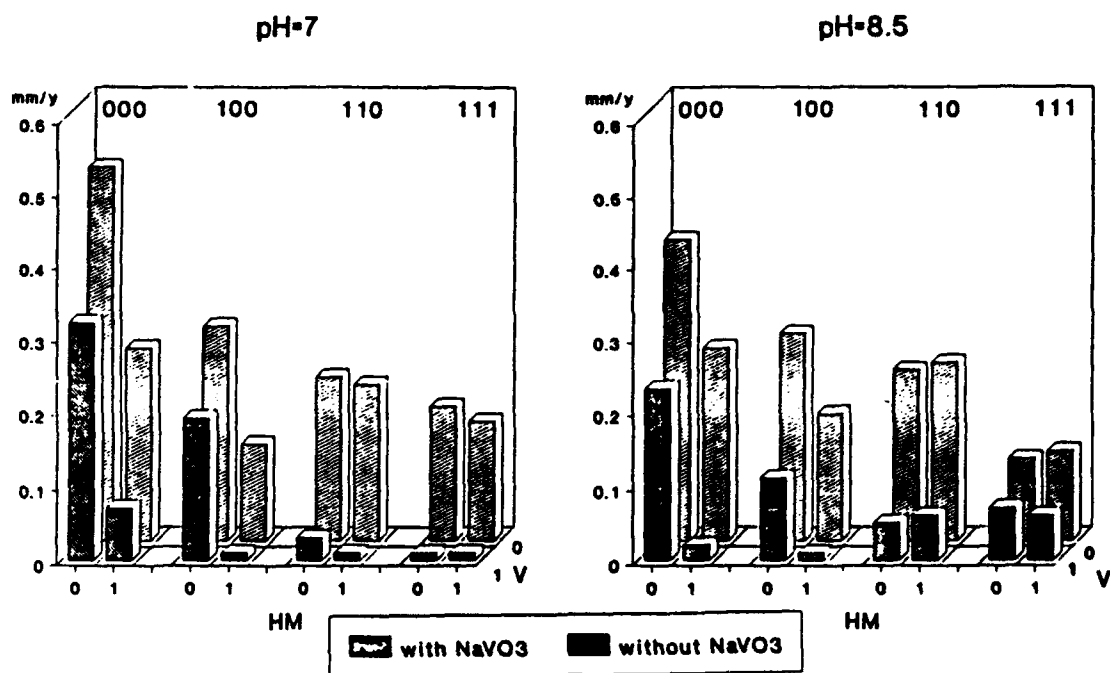


Fig.9. Synergistic effects between Ca ions and different phosphonates

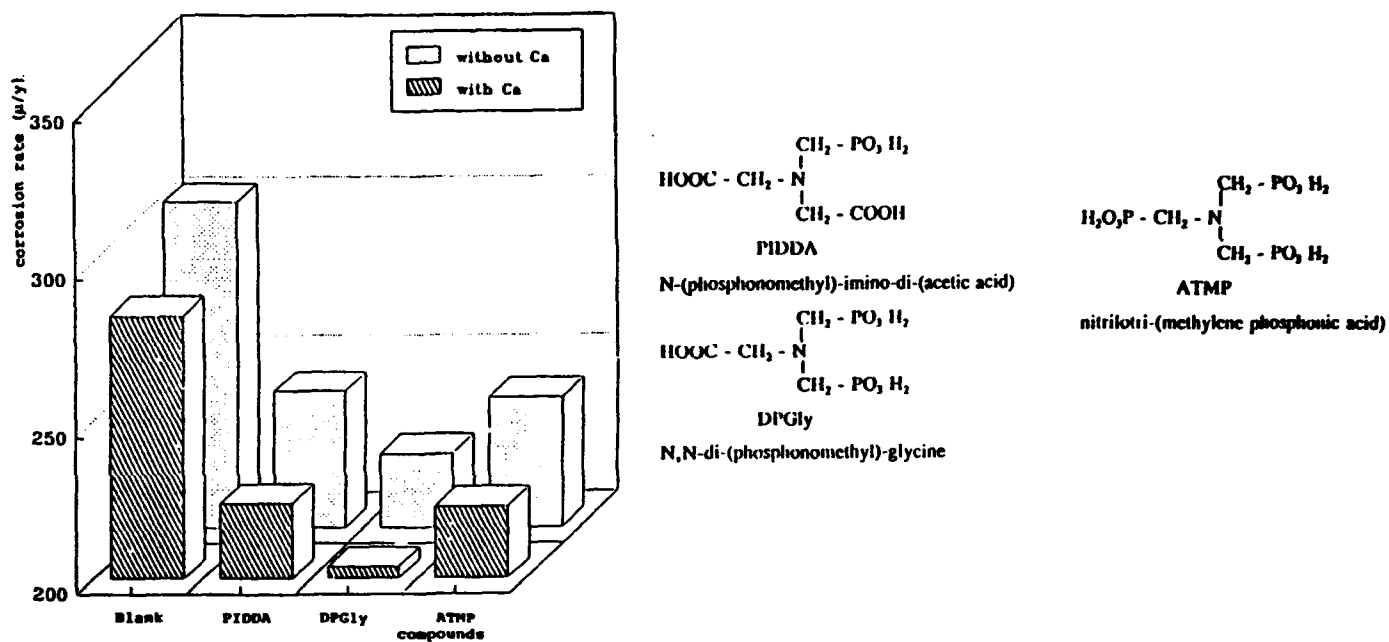


Fig.8. Synergistic effects between components of inhibitor mixtures at two pH values in a cooling water model

# EFFECT OF SOME ORGANIC INHIBITORS ON CORROSION OF STAINLESS STEEL IN HYDROCHLORIC ACID

A.A. Ismail and S.H. Sanad

Electrochemistry Department, National Research Centre,  
Dokki, Cairo, Egypt.

## A B S T R A C T

The inhibition effect of hexamine, quinoline and thiourea on different types of stainless steel in 1 M hydrochloric acid solution has been examined by means of electrochemical measurements.

Polarisation curves indicate that these compounds act as mixed type inhibitor. It can be concluded that the charge transfer reaction, i.e.,  $\text{Fe} \rightarrow \text{Fe}^{2+} + 2\text{e}$  and  $\text{H}^+ + \text{e} \rightarrow \text{H}$  are inhibited simultaneously and individually by organic absorption film at the metal/solution interface and consequently the corrosion-rate of the stainless steel is reduced effectively in hydrochloric acid solution.

The results obtained for the different types of stainless steel show that hexamine and quinoline are more effective for stainless type 430 and 440. The inhibitor concentration at which efficiency was over 80% was  $10^{-2}$  and 0.15 M hexamine for the two types 430 and 440 respectively.

In presence of quinoline the maximum efficiency was about 90% at concentration  $10^{-1}$  M for the two types of stainless steel. Thiourea was found to be an excellent inhibitors for stainless steel type 316 as the maximum efficiency about 86% at concentration  $10^{-4}$  M.

## INTRODUCTION

Acid solutions are widely used in industry, the most important fields of application being acid pickling, industrial cleaning, acid descaling and oil well acidizing. Because of the general aggressiveness of the acid solutions the practice of inhibition is commonly used to reduce the corrosive attack on metallic materials(1).

So far, the literature has been reported the great problems involved in inhibiting corrosion in steels by means of inhibitor(2-11,12-14).

The aim of this work was to elucidate the mechanism of the inhibition of the acid corrosion of stainless steels by some organic compounds in hydrochloric acid.

## EXPERIMENTAL TECHNIQUES

Four types of stainless steel were used in this experiments. Chemical composition of stainless steels are given in Table (1).

Table (1) Chemical composition of stainless steels (wt.%).

Type of specimen	Cr	Ni	Mo	C
304	18.2	8.12	-	0.08
316	16.18	10.14	2.00	0.08
430	14.18	-	-	0.12
440	16.18	-	0.75	0.60

The electrodes, which were in the form of sheets, were inserted into a cylindrical teflon plug, leaving an area of  $1\text{ cm}^2$ . Before use, the exposed surface of the electrode was abraded with emery paper 320, 400 and 600. A test solution 250 ml of 1 M HCl was used with or without different concentration of inhibitors hexamine, quinoline and thiourea.

The corrosion rates of stainless steel were determined by two types of measurements.

1. Galvanostatic polarisation was measured by using a Metrohm type E-353 potentiometer. A saturated calomel electrode (SCE) was used as the reference electrode, and a platinum wire was used as a counter electrode.
2. Potentiodynamic measurements.

The electrodes used were the same as those employed in galvanostatic measurement. A working potentiostat was used in these measurements.

## RESULTS AND DISCUSSION

Anodic and cathodic polarisation measurements were conducted separately for different types of stainless steel. Figs. (1 to 4) show a representative polarisation curves in 1 M HCl in absence and presence of different concentrations of hexamine. Tafel regions extending over about a decade of the current axis. The corrosion current and the corrosion potential were given by the intersection

of extrapolated anodic and cathodic Tafel lines. Electrochemical parameters determined for all the samples studied in 1 M HCl are summarized in Table (2).

Table (2) Electrochemical parameters for different types of stainless steel in 1 M HCl.

Type of stainless steel	Rest potential $E_{rest}$ mV	Corr. potential $E_{corr}$ mV	Corr. current $I_{corr}$ $\mu A/cm^2$	$b_a$ mV/log i	$b_c$ mV/log i
304	-150	-200	33.11	84	-133
316	- 81	-136	28.84	90	-100
430	-242	-256	144.54	80	-124
440	-278	-233	100.00	43	-107

Table (2) shows that the cathodic Tafel slope  $b_c$  for all specimens investigated lie within the range 100 to 130 mV/log i which was agreement with the theoretical value 120 mV for  $H^+ + e \rightarrow H$  and the value of  $b_a$  for the anodic reaction ranges between 40 to 90 mV/log i which was not so far from the theoretical value 60 mV/log i.

Stainless steel types 304 and 316 (higher Ni or Mo content) exhibit lower corrosion current than those far stainless steel types 430 and 440. The corrosion potential  $E_{corr}$  shifts towards more noble value in the order  $430 < 440 < 304 < 316$ .

Tables (3-13) show the electrochemical parameters in absence

Table (3) Electrochemical parameters of stainless steel type 304 in 1M Hcl in absence and presence of hexamine.

Hexamine conc.	rest potential E <sub>rest</sub>	corrosion potential E <sub>corr.</sub>	corrosion current I <sub>corr.</sub>	Efficiency %	ba	-bc
<sup>-1</sup> M.L	mV	mV	<sup>2</sup> μA/cm		mV/Logi	mV/Logi
0	-150	-200	33.11		84	133
0.2	-101	-146	17.37	47.5	44	244
0.1	- 92	-186	19.05	42.4	130	160
0.05	-105	-143	16.59	48.8	40	104
<sup>-2</sup> 10	-134	-183	31.62	4.5	96	157
<sup>-3</sup> 10	-138	-156	23.98	27.5	68	170
<sup>-4</sup> 10	-139	-180	36.3	- 9.6	65	146

Table (4) Electrochemical parameters of stainless steel type 316 in 1M Hcl in absence and presence of hexamine.

Hexamine conc.	rest potential E <sub>rest</sub>	corrosion potential E <sub>corr.</sub>	corrosion current I <sub>corr.</sub>	Efficiency %	ba	-bc
<sup>-1</sup> M.L	mV	mV	<sup>2</sup> μA/cm		mV/Logi	mV/Logi
0	-81	-136	28.84		90	100
0.2	-78	- 93	5.75	80.06	130	153
0.1	-47	-123	12.58	56.4	190	157
0.05	-70	- 90	14.45	49.89	36	177
<sup>-2</sup> 10	-83	-110	19.95	30.83	73	173
<sup>-3</sup> 10	-89	-113	13.8	52.15	57	143
<sup>-4</sup> 10	-90	-126	23.98	16.82	77	123

Table (5) Electrochemical parameters of stainless steel type 430 in 1M Hcl in absence and presence of hexamine.

Hexamine conc.	rest potential E rest	corrosion potential E corr.	corrosion current I corr.	Efficiency %	ba	-bc
<sup>-1</sup> M.L	mV	mV	<sup>2</sup> $\mu\text{A}/\text{cm}$		mV/Logi	mV/Logi
0	-242	-256	144.54		80	124
0.2	-235	-253	38	73.7	43	134
0.1	-220	-236	45.7	68.4	70	163
0.05	-225	-240	39.8	72.5	47	87
<sup>-2</sup> 10	-239	-243	27.54	80.9	40	53
<sup>-3</sup> 10	-250	-246	52.48	63.7	40	94
<sup>-4</sup> 10	-248	-260	60.25	58.3	66	90

Table (6) Electrochemical parameters of stainless steel type 440 in 1M Hcl in absence and presence of hexamine.

Hexamine conc.	rest potential E rest	corrosion potential E corr.	corrosion current I corr.	Efficiency %	ba	-bc
<sup>-1</sup> M.L	mV	mV	<sup>2</sup> $\mu\text{A}/\text{cm}$		mV/Logi	mV/Logi
0	-278	-223	100		43	107
0.2	-283	-213	50.	50	37	53
0.1	-253	-223	38	62	43	43
0.05	-253	-220	43.65	56.3	43	53
<sup>-2</sup> 10	-283	-216	43.65	56.3	47	54
<sup>-3</sup> 10	-288	-226	57.5	42.5	40	77
<sup>-4</sup> 10	-298	-233	91.2	8.8	57	90



Table (7) Electrochemical parameters of stainless steel type 304 in 1M Hcl in absence and presence of quinoline.

Quinoline conc.	rest potential E rest	corrosion potential E rest	corrosion current I corr.	Efficiency %	ba	-bc
<sup>-1</sup> M.L	mV	mV	<sup>2</sup> μA/cm		mV/Logi	mV/Logi
0	-150	-200	33.11		84	133
0.1	-104	-136	10	69.79	47	180
<sup>-2</sup> 10	-128	-156	20.89	36.9	54	163
<sup>-3</sup> 5x10	-135	-206	20.89	36.9	87	134
<sup>-3</sup> 3x10	-141	-180	27.54	16.8	67	106
<sup>-3</sup> 10	-151	-206	43.65	~31.8	110	167

Table (8) Electrochemical parameters of stainless steel type 316 in 1M Hcl in absence and presence of quinoline.

Quinoline conc.	rest potential E rest	corrosion potential E corr.	corrosion current I corr.	Efficiency %	ba	-bc
<sup>-1</sup> M.L	mV	mV	<sup>2</sup> μA/cm		mV/Logi	mV/Logi
0	-81	-136	28.84		90	100
0.1	-69	-146	14.45	49.89	77	194
<sup>-2</sup> 10	-88	-110	18.19	36.9	53	200
<sup>-3</sup> 5x10	-88	-103	23.98	16.85	46	190
<sup>-3</sup> 3x10	-89	-156	23.98	16.85	100	180
<sup>-3</sup> 10	-87	-163	25.15	12.96	93	193

Table (9) Electrochemical parameters of stainless steel type 430 in 1M HCl  
absence and presence of quinoline.

Quinoline conc.	rest potential E <sub>rest</sub>	corrosion potential E <sub>corr.</sub>	corrosion current I <sub>corr.</sub>	Efficiency %	ba	-bc
<sup>-1</sup> M.L	mV	mV	<sup>2</sup> μA/cm		mV/Logi	mV/Logi
0	-242	-256	144.54		80	124
0.1	-220	-220	22.9	84.29	40	127
<sup>-2</sup> 10	-223	-233	31.6	78.1	33	106
<sup>-3</sup> 5x10	-226	-250	38	73.7	50	107
<sup>-3</sup> 3x10	-231	-253	50.1	65.3	53	126
<sup>-3</sup> 10	-243	-303	100	30.8	63	177

Table (10) Electrochemical parameters of stainless steel type 440 in 1M HCl  
absence and presence of quinoline.

Quinoline conc.	rest potential E <sub>rest</sub>	corrosion potential E <sub>corr.</sub>	corrosion current I <sub>corr.</sub>	Efficiency %	ba	-bc
<sup>-1</sup> M.L	mV	mV	<sup>2</sup> μA/cm		mV/Logi	mV/Logi
0	-278	-223	100		43	107
0.1	-208	-196	22.9	77.1	40	110
<sup>-2</sup> 10	-213	-213	36.3	63.7	36	47
<sup>-3</sup> 5x10	-228	-223	45.7	54.3	40	53
<sup>-3</sup> 3x10	-198	-223	66.06	33.94	43	77
<sup>-3</sup> 10	-213	-230	72.4	27.5	53	90

Table (11) Electrochemical parameters of stainless steel type 304 in 1M Hcl in  
absence and presence of thiourea .

thiourea conc.	rest potential E rest	corrosion potential E corr.	corrosion current I corr.	Efficiency %	ba	-bc
<sup>-1</sup> M.L	mV	mV	<sup>2</sup> $\mu A/cm$		mV/Logi	mV/Logi
0	-150	-200	33.11		84	133
0.1	-140	-193	13.8	58.3	100	110
<sup>-2</sup> 10	-137	-210	19.05	42.5	110	113
<sup>-3</sup> 5x10	-131	-223	19.95	39.7	46	120
<sup>-3</sup> 10	-141	-143	10.47	68.4	37	180
<sup>-4</sup> 10	-168	-190	19.95	39.7	46	106

Table (12) Electrochemical parameters of stainless steel type 316 in 1M Hcl in  
absence and presence of thiourea .

thiourea conc.	rest potential E rest	corrosion potential E corr.	corrosion current I corr.	Efficiency %	ba	-bc
<sup>-1</sup> M.L	mV	mV	<sup>2</sup> $\mu A/cm$		mV/Logi	mV/Logi
0	-81	-136	28.84		90	100
0.1	-89	-136	3.63	87.4	84	130
<sup>-2</sup> 10	-89	-123	4.78	83.4	77	150
<sup>-3</sup> 5x10	-78	-106	4.16	85.6	56	160
<sup>-3</sup> 10	-62	-140	3.8	86.8	50	126
<sup>-4</sup> 10	-70	- 96	3.8	86.8	17	143

Table (13) Electrochemical parameters of stainless steel type 430 in 1M Hcl in absence and presence of thiourea .

thiourea conc.	rest potential $E_{rest}$	corrosion potential $E_{corr.}$	corrosion current $I_{corr.}$	Efficiency $\%$	ba	-bc
<sup>-1</sup> M.L	mV	mV	<sup>2</sup> $\mu A/cm$		mV/Logi	mV/Logi
0	-242	-256	144.54		80	124
0.1	-270	-293	79.4	54.06	87	144
<sup>-2</sup> 10	-270	-303	36.3	74.8	94	120
<sup>-3</sup> 5x10	-268	-290	31.6	78.1	57	110
<sup>-3</sup> 10	-271	-260	38	73.7	40	134
<sup>-4</sup> 10	-287	-286	109.6	24.17	80	123

and presence of different concentrations of hexamine, quinaline and thiourea. For a direct comparison, the corrosion current  $I_{\text{corr}}$  decreases with increase of different inhibitors concentration and the corrosion potential  $E_{\text{corr}}$  shifts toward noble direction.

The effect of increase in inhibitors concentrations increase the cathodic Tafel slope values  $B_c$  for stainless steel types 304 and 316 than the corresponding values obtained in free acid solutions. For the two types 430 and 440 the value of  $B_c$  decreases or nearly the same as in free acid solutions, except the type of 430 in presence of thiourea show an increase in the value of  $B_c$ . These increase in cathodic Tafel slopes may suggest a slow discharge step (volmer mechanism)(15).

The anodic Tafel slopes  $B_a$  for all different types of stainless steel in presence of different inhibitors ranging 40-100 mV/long i. It can be noticed that as the quinoline concentrations increased a shorter linear regions and smaller Tafel slopes were measured. These indicate a possible acceleration of the metal dissolution by complex formation of iron with  $\text{Cl}^-$  and/or organic molecules(16).

Steady state open-circuit corrosion potentials ( $E_{\text{rest}}$ ) recorded after 3 hours exposure in the test solution are given in Tables (3 to 13). Corrosion potential  $E_{\text{corr}}$  in presence of hexamine and quinoline seems to be anodically controlled, as evidence by the shift of potential toward positive value at higher concentrations. The negative shift in the steady state potential at concentration less than  $10^{-2}$  M

of inhibition especially for stainless steel types 430 and 440 give an indications that these inhibitors influence also the cathodic process to the extent which depend on the concentration of inhibitors and the type of stainless steel.

The explanation of potential shifts towards positive or negative values in presence of hexamine or quinoline may suggest that these inhibitors are adsorbed on the whole surfaces of stainless steels and hence affect both anodic and cathodic area (mixed control)(7,17).

In presence of thiourea the steady state corrosion potentials are slightly shifted towards the positive direction for the three types of stainless steel 304, 316 and 440, while the reverse was observed for the type 430.

The inhibitor efficiencies (Tables 3 to 13) calculated from the polarisation method using the equation:

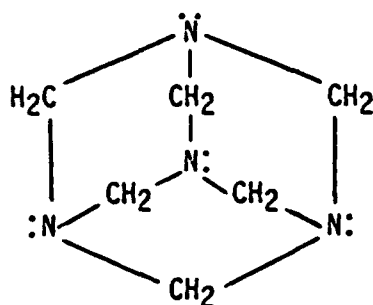
$$I = \frac{i_{\text{corr}} - i_{\text{inh}}}{i_{\text{corr}}} \times 100 \%$$

where  $i_{\text{inh}}$  and  $i_{\text{corr}}$  are the corrosion current density with and without inhibitor respectively.

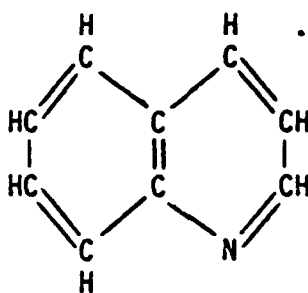
Analysis of these tables show that hexamine and thiourea have got the maximum efficiency depends on the inhibitor and the type of stainless steel. In presence of quinoline inhibitive efficiency was progressively increased with increase in the concentration of quinoline. From the above results it may be generally stated that hexamine and quinoline were more effective for the stainless steel

types 430 and 440 then on the two types 304 and 316. Thiourea was a good inhibitor for stainless steel types 316 and 430 and moderate for 304 while it accelerate the corrosion rate for type 440.

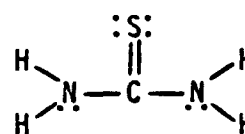
The chemical formulas of inhibitors used are as follows:



Hexamine



Quinoline



Thiourea

The polarisation characteristics observed in these experiments show that hexamine effect both the anodic and cathodic polarisation reaction (mixed control)(2,5).

Hexamine has functional groups with N atom having lone electron pair and hydrophobic groups in its molecule as shown by chemical formula. The electrochemical data indicates that this organic inhibitor is able to control the charge transfer reaction, i.e.  $\text{Fe} \rightarrow \text{Fe}^{2+} + 2e$ , and  $\text{H}^+ + e \rightarrow \text{H}$  by adsorbing its functional groups onto the anodic cathodic area on the corroding metal and by retarding the diffusion of water to the metal surface with its hydrophobic group, and consequently the corrosion of stainless steel in HCl solution is inhibited(6).

The presence of quinoline inhibited not only the anodic reaction but also the cathodic reaction. These results are in agreement with Hockerman(18) and Hoar(7). The anodic inhibition was explained on the basis of migration of electrons from the metal to the positively charged inhibitor rather than towards the cathodic areas within the metal(7). It should be pointed out however that organic compounds were generally regarded as producing cathodic inhibition, with probable minor additional anodic inhibition.

Unlike many other inhibitors, thiourea shows a maximum efficiency (Tables 11-13). Beyond this maximum, thiourea progressively loses its efficiency and eventually becomes a corrosion promotor(13,14), whereas some workers(19) have attributed this loss of efficiency to reduction of thiourea to yield corrosion promoting species, e.g.  $\text{HS}^-$  ion, other(20) attributed it to protonation on the assumption that the protonated species catalyzes the hydrogen evolution reaction and hence the corrosion reaction. Ammar(21) and Makrides(19) attributed the decrease in the inhibiting efficiency to the presence of  $\text{H}_2\text{S}$  which is one of the by-products of reduction of thiourea.

### Potentiodynamic Measurements

A typical potentiodynamic polarisation curves obtained for the different types of stainless steel in 1 M HCl alone and in presence of different concentrations of hexamine are shown in Figs. (5 to 8) respectively. E-I curves for quinoline show a similarity in behaviour to that observed in presence of hexamine (curves are not shown).



Examination of E-I curves of stainless steel types 304 and 316 show the appearance of one peak at a potential ranges -20 to 20 mV in acid alone and in presence of hexamine or quinoline. In this potential region active dissolution may take place according to the reaction:



with the rise in potential pitting begins to take place, not showing a distinct passive region. This may be due to the lower value of chromium content(22).

Stainless steel type 430 shows the appearance of two peaks at potential ranges (-40 to 0 mV and  $\approx 160$  mV) respectively in acid alone and in presence of lower concentration (less than  $10^{-2}$  M) of hexamine and quinoline, while at higher concentrations only one peak appears at potential  $\approx 0$  mV. In case of stainless steel type 440, the curves posses no anodic current maximum before reaching the pitting potential.

The corrosion parameters for all types of stainless steel are shown in Tables (14-25).

Following the results in both the polarization and the potentiodynamic measurements, quinoline is considered to be strongly adsorbed on the surface. However, with higher concentration of hexamine and quinoline, increase adsorption occurs and the existing film may thicken and/or unprotected area may be covered(17).

The potentiodynamic E/I curves for stainless steel types 304

Table (14) The corrosion parameters for stainless steel type 304 in 1M HCL in absence and presence of hexamine.

Conc. of hexamine <sup>-1</sup>	Corrosion Potential	Corrosion Current	Pitting Potential	Efficiency
M.L	E corr.	I corr. <sup>-2</sup>	E pp	
	mV	mA.cm	mV	%
-	20	6.1	-	-
0.2	-20	1.9	200	68.8
0.1	0	2.1	250	65.6
-2				
10	0	3.0	280	50.8
-3				
10	-20	3.4	240	44.3
-4				
10	+20	6.6	-	-8.2

Table (15) The corrosion parameters for stainless steel type 316 in 1M HCL in absence and presence of hexamine.

Conc. of hexamine <sup>-1</sup>	Corrosion Potential	Corrosion Current	Pitting Potential	Efficiency
M.L	E corr.	I corr. <sup>-2</sup>	E pp	
	mV	mA.cm	mV	%
-	0	1.1	300	-
0.2	20	0.16	400	85.5
0.1	20	0.16	240	85.5
-2				
10	0	0.5	450	54.5
-3				
10	20	0.76	300	30.9
-4				
10	20	1.1	280	0

Table (16) The corrosion parameters for the stainless steel type 430 in 1M HCL in absence and presence of hexamine.

Concentration of hexamine -1 M.L	Corrosion potential E corr. mV		Corrosion Potential I corr. mA.cm -2		Pitting Potential E PP mV	Efficiency %
	First	Sec.	First	Sec.		
-	-40	160	23	46	260	-
0.2	0		13		240	43.5
0.1	0		15		240	34.8
-2 10	-40	130	25	27	280	- 8.7
-3 10	-40	160	32	62	240	-39.1
-4 10	-40	160	32	76	240	-39.1

Table (17) The corrosion parameters for the stainless steel type 440 in 1M HCL in absence and presence of hexamine.

Concentration of hexamine -1 M.L	Pitting potential E PP mV
-	- 80
0.2	-100
0.1	-100
-2 10	-100
-3 10	-100
-4 10	-100

Table (18) The corrosion parameters for the stainless steel . type 304 in 1M HCL in absence and presence of quinoline.

Concentration of quinoline -1 M.L	Corrosion potential E corr. mV	Corrosion current I corr. -2 mA.cm	Pitting Potential E pp mV	Efficiency %
--	20	6.1	240	--
0.1 -2	0	4.2	280	31.1
10 -3	0	4.4	280	27.8
5 x 10 -3	0	4.4	300	27.8
3 x 10 -3	0	5.4	280	11.5
10 -3	0	5.6	280	8.2

Table (19) The corrosion parameters for the stainless steel type 316 in 1M HCL in absence and presence of quinoline.

Concentration of quinoline -1 M.L	Corrosion potential E corr. mV	Corrosion current I corr. -2 mA.cm	Pitting Potential E pp mV	Efficiency %
-	0	1.1	300	-
0.1	20	0.68	330	38.2
-2 10	20	0.92	320	16.4
-3 5 x 10	20	0.92	300	16.4
-3 3 x 10	0	0.98	320	10.9
-3 10	0	1.3	350	-18.2

Table (20) The corrosion parameters for the stainless steel type 430 in 1M HCL in absence and presence of quinoline.

Concentration of quinoline -1 M.L	Corrosion potential E corr. mV		Corrosion current I corr. -2 mA.cm		Pitting Potential E pp mV	Efficiency %
	First	Sec	First	Sec		
-	-40	160	23	46	260	-
0.1	-40	-	14	-	230	39.1
-2 10	-40	-	18	-	220	21.7
-3 5 x 10	40	-	19	-	240	17.4
-3 3 x 10	-40	-	19	-	240	17.4
-3 10	-40	160	27	46	-	-17.4

Table (21)      The corrosion parameters for the stainless steel type 440 in 1M HCL in absence and presence of quinoline.

Concentration of quinoline	Pitting potential E
-1 M.L	PP mV.
-	- 150
0.1	- 110
-2 10	- 120
-3 5 x 10	- 120
-3 3 x 10	- 170
-3 10	- 150

Table (22) The corrosion parameters for the stainless steel type 304 in 1M HCL in absence and presence of thiourea.

Concentration of thiourea -1 M.L	Corrosion potential E corr. mV	Corrosion current I corr. -2 mA.cm	Pitting Potential E PP mV
-	20	6.1	240
0.1	280	160	360
-2 10	200	115	240
-3 5 x 10	162	100	300
-3 10	122	64	240
-4 10	42	25	360

Table (23) The corrosion parameters for the stainless steel type 316 in 1M HCL in absence and presence of thiourea.

Concentration of thiourea -1 M.L	Corrosion potential E corr. mV	Corrosion current I corr. -2 mA.cm	Pitting Potential E PP mV
-	0	1.1	300
0.1	240	60	350
-2 10	202	68	320
-3 5 x 10	162	46	310
-3 10	140	34	330
-4 10	42	6.4	400

Table (24) The corrosion parameters for the stainless steel type 430 in 1M HCL in absence and presence of thiourea.

Concentration of thiourea	Corrosion potential		Corrosion current		Pitting Potential
-1 M.L	E corr.		I corr.		E PP
	mV		mA.cm <sup>-2</sup>		mV
	First	Sec	First	Sec	
-	-40	160	23	46	280
0.1	-	-	-	-	-160
-2 10	-	120	-	165	200
-2 5 x 10	-	120	-	155	200
-3 10	-	80	-	120	240
-4 10	0	120	68	36	240

Table (25) The corrosion parameters for the stainless steel type 440 in 1M HCL in absence and presence of thiourea.

Concentration of thiourea	Pitting potential
-1 M.L	E PP
	mV
-	- 150
0.1	- 100
-2 10	- 130
-2 5 x 10	- 140
-3 10	- 160
-4 10	- 180



and 316 in absence and presence of thiourea Tables (22 & 23) show one peak at a potential range from (0-20 mV) in free acid and this potential is shifted to the noble direction with increase of inhibitor concentration (40 to 280 mV). The maximum current obtained for stainless steel types 304 and 316 increases from 6.1 and 1.1 mA/m<sup>2</sup> in free acid to 160 and 68 mA/cm<sup>2</sup> respectively with increasing of the inhibitor concentration. This may be attributed to the direct oxidation of the iron to iron oxide in presence of thiourea which act as oxidising agent(23). Stainless steel type 430 represent two peaks in free acid alone and at lower concentration of inhibitor (10<sup>-4</sup> M) at a potential values (-40 and 160 mV) and (0 and 120 mV) respectively. With increasing the concentrations of thiourea only one peak is observed and potential shifts towards the noble value except at 0.1 M thiourea.

Stainless steel type 440 posses the same behaviour as that shown in presence of hexamine and quinoline. Comparison of the results obtained for the different types of stainless steel by the two methods indicate that hexamine and quinoline are more effective for stainless steel types 430 and 440. Thiourea was found to be an excellent inhibitors for stainless steel type 316.

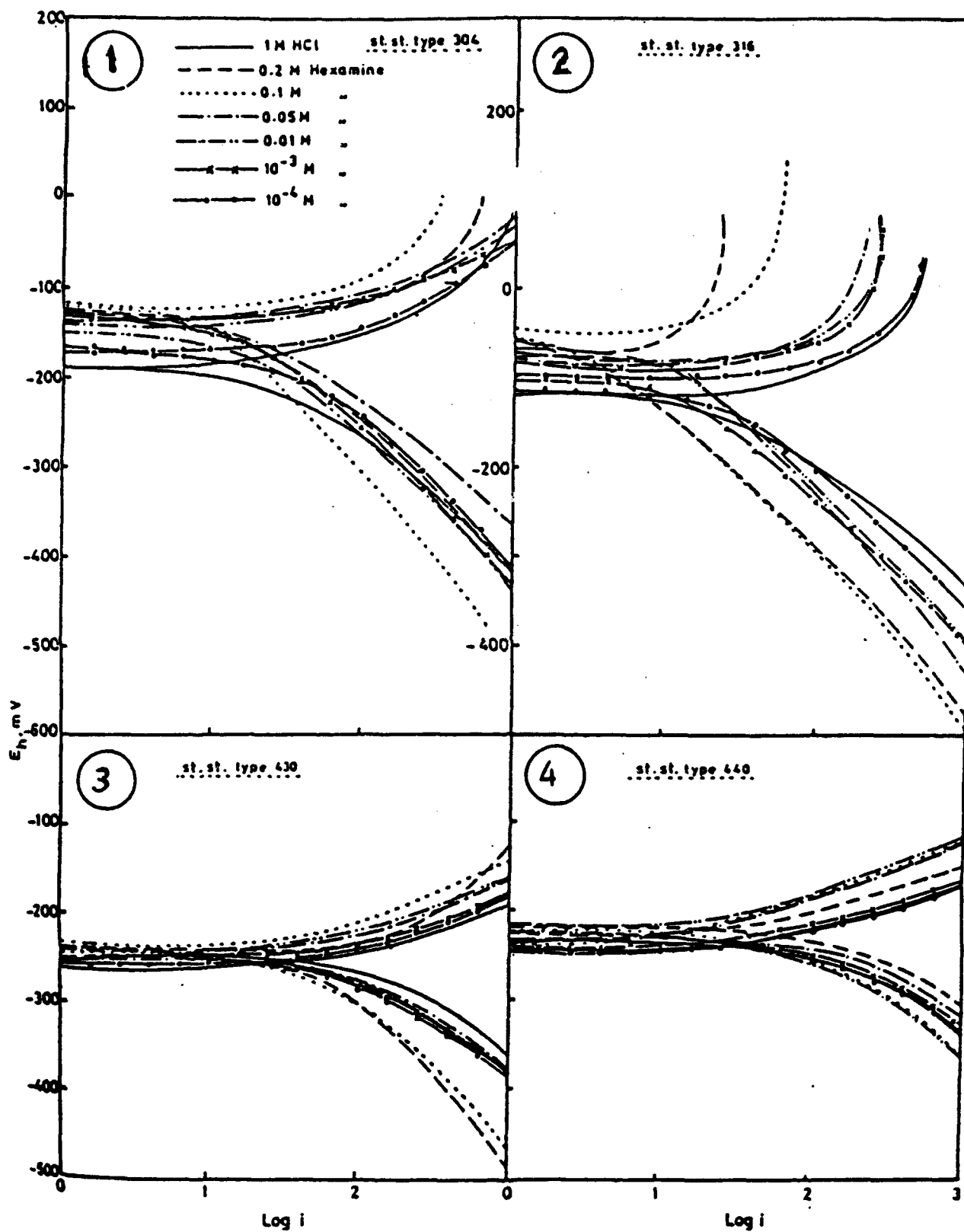
## REFERENCES

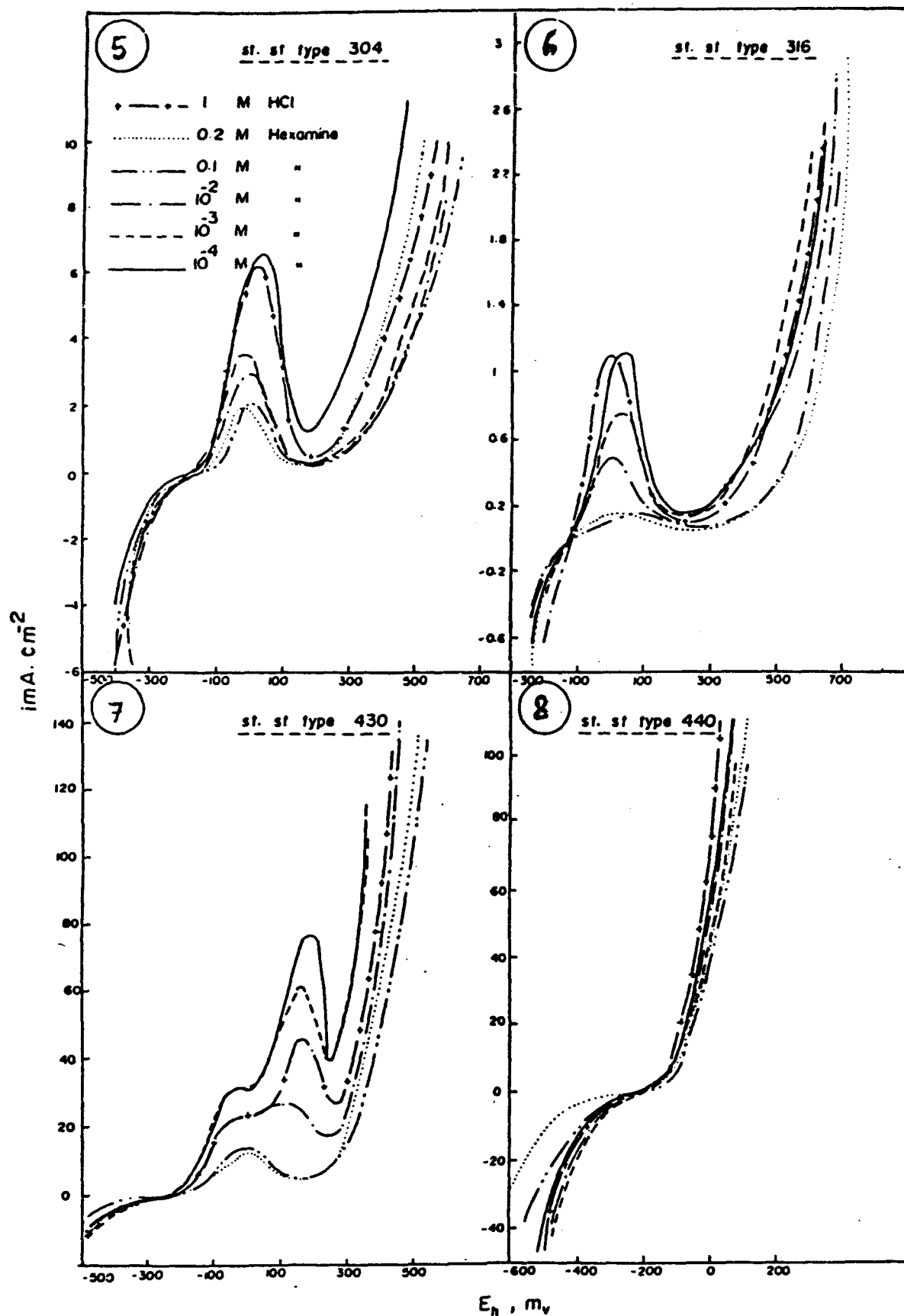
1. G. Schmitt, Br. Corros. J., 19, 165 (1984).
2. Hirendra, G.N. Pandey and B. Sanyal, Corrosion Prevention and Control, 27(3), 13 (1980).
3. Viorel Branzoi, Ahmed Kabir and Mihai Ciopec. Revue Roumaine de Chimie, 31(6), 571 (1986).
4. E. Mcaferty and N. Hackerman, J. Electrochem. Soc., 119, 146 (1972).
5. Gentaro Kano and Tutuk Subowo, Memoirs of the Faculty of Engineering, Fukui University, Vol. 34, No. 1, 9 (1986).
6. Gentaro Kano, Kigoshi Horita and Hartati Soeroso, Memoirs of the Faculty of Engineering, Fukui University, Vol. 35, No. 2, 213 (1987).
7. T.P. Hoar and R.D. Holliday, J. Appl. Chem., 3, 502, November (1953).
8. G. Okamoto, M. Nagayama, J. Kato and T. Baba, Corros. Sci., Vol. 2, 21 (1962).
9. G.G. Eldrege and R.B. Mears, Industr. Eng. Chem., 37, 738 (1945).
10. N. Hackerman, Industr. Engng. Chem., 46, 523 (1954).
11. Olen, L. Riggs, JR. and Ray M. Hurd, Corrosion, NACE, 23, 252, August (1967).
12. B. Donnelly, T.C. Downie and R. Grzeskowiak, Corros. Sci., Vol. 14, 597 (1974).
13. B.G. Ateya, B.E. El-Anadouli and F.M. El-Nizamy, Corros. Sci., Vol. 24, No. 6, p. 497 (1984).

14. B.G. Ateya, B E. El-Anadouli and F.M. El-Hizamy, Corros. Sci., Vol. 24, No. 6, p. 509 (1984).
15. K.J. Vetter, Electrochemische Kinetik. Springer-Verlag, Heidelberg (1961).
16. Ervin Laengle and N. Hackerman, J. Electrochem. Soc., 118, 1273 (1971).
17. Shashi Gupta, Dharendra, B. Sanyal and G.N. Pandey, Corrosion Prevention and Control, p. 21, Oct. (1981).
18. N. Hackerman and J.D. Sudbury, J. Electrochem. Soc., 97, 109 (1950).
19. A.C. Makrides and N. Hackerman, Ind., Eng. Chem., 47(9), 1773 (1955).
20. K.C. Pillaiand and R. Narayan, J. Electrochem. Soc., 125, 1393 (1978).
21. I.A. Ammer and S. Darwish, Corros. Sci., 7, 579 (1967).
22. I.N. Putilova, S.A. Balezin and V.P. Barannik, "Metallic Corrosion Inhibitors". p. 29, New York, Pergamon Press (1966).
23. H.H. Uhlig, "Corrosion and Corrosion Control", John Wiley and Sons, Chapter 16 (1963), New York.

## LEGENDS

- Fig. (1)** Polarisation curves for stainless steel type 304 in different concentrations of hexamine.
- Fig. (2)** Polarisation curves for stainless steel type 316 in different concentrations of hexamine.
- Fig. (3)** Polarisation curves for stainless steel type 430 in different concentrations of hexamine.
- Fig. (4)** Polarisation curves for stainless steel type 440 in different concentrations of hexamine.
- Fig. (5)** Potentiodynamic curves for stainless steel type 304 in 1 M HCl in absence and presence of different concentration of hexamine.
- Fig. (6)** Potentiodynamic curves for stainless steel type 316 in 1 M HCl in absence and presence of different concentration of hexamine.
- Fig. (7)** Potentiodynamic curves for stainless steel type 430 in 1 M HCl in absence and presence of different concentration of hexamine.
- Fig. (8)** Potentiodynamic curves for stainless steel type 440 in 1 M HCl in absence and presence of different concentration of hexamine.





# **CORROSION INHIBITION STUDY OF DIFFERENT AZOLES ON COPPER USING CARBON-PASTE ELECTRODES**

**V. Lakshminarayanan,**  
Raman Research Institute,  
Bangalore-560 080, India.

**R. Kannan**  
Materials Science Division,  
National Aeronautical Laboratory,  
Bangalore-560 017, India.

**S.R. Rajagopalan,**  
Materials Science Division,  
National Aeronautical Laboratory,  
Bangalore-560 017, India.

## **ABSTRACT**

In this investigation, the inhibitor efficiency of four different azoles for copper has been evaluated using azole modified carbon paste electrodes. Cyclic voltammetric behaviour of the modified electrodes has been studied. The studies reveal that the voltammetric peak heights can be related to the complexing abilities of the azoles with Cu(I) and Cu(II) and this in turn decides to their inhibiting properties. This has been verified from the measured corrosion rates of copper in neutral sodium chloride in the presence of azoles.

Key terms: carbon paste electrode, corrosion inhibitor, azole modified electrodes.

## **I. INTRODUCTION**

The approach of chemically modified electrodes (or CMEs), first demonstrated systematically in the early 1970s, has assumed a dominant position in modern electrochemistry. The CMEs can be targeted for a specific application or investigation and rationally designed to provide an optimum environment for that task. They find increasing applications in electrocatalysis, electrosynthesis, energy conversion and electroanalysis [1]. In this paper, we describe a novel application for chemically modified carbon-paste electrodes, namely evaluation of the relative corrosion-inhibiting efficiency of certain azoles on copper.

Benzotriazole (BTA), mercaptobenzothiazole (MBT), benzimidazole (BIMH), and imidazole (IMH) were chosen for this investigation. These are all well known corrosion inhibitors for copper. All these azoles have nitrogen atoms, and with the lone pair of electrons on the nitrogen atom they coordinate with either Cu (0) or Cu (I) to form certain complexes. These complexes are generally believed to be polymeric in nature and

form an adherent protective film on the copper surface which form a barrier to aggressive ions such as chloride [2,3]. The inhibitor action of these compounds may also be due to their chemisorption on the copper surface.

Several electrochemical studies have been employed to study the mechanism by which these azoles inhibit the anodic dissolution of copper. Several surface analytical techniques such as infra-red reflection absorption, X-ray photoelectron spectroscopy and Surface enhanced Raman spectroscopy have also been employed to investigate the process of reaction of these azoles on a copper electrode [4,5,6]. However, the electrochemical behaviour of electrodes covered with these films are still not very clear and there is no agreement on their mode of action and in particular on their relative efficiency.

We felt that useful information could be obtained on the nature of these copper-azole complexes, and on the relative efficiency of these azoles in inhibiting the anodic dissolution of copper, by cyclic voltammetric studies using pure carbon-paste electrodes (PCPE) and chemically modified carbon-paste electrodes (CMCPE). The use of C-paste electrodes offer certain specific advantages in this investigation. Controlled amounts of Cu(0), Cu(I), and Cu(II) can be incorporated in the C-paste matrix so that their interaction with the azoles can be studied in a manner not attempted earlier. The azoles themselves can be made to take part in the electrochemical reaction by incorporating them in the C-paste matrix. As will be shown later, the current voltage characteristics of these azoles, when present in solution, and when incorporated in the electrode matrix are markedly different. In this communication, by such a study, we demonstrate the utility of chemically modified C-paste electrodes in evaluating the relative corrosion-inhibiting efficiency of these azoles. It will be shown that the corrosion rates obtained correlate well with the cyclic voltammetric behaviour of different azoles using C-paste electrodes.

## **II EXPERIMENTAL**

### **A . Instrumentation**

Corrosion rate measurements were carried out using exponential relaxation technique and the instrumentation set up has been described earlier [7]. Corrosion rate was measured from the extrapolated portion of the anodic polarisation curve. Pure carbon-paste was prepared by a procedure reported earlier [8]. Chemically modified carbon-pastes were prepared by thorough mixing of the required amount of the modifying agent with the pure carbon paste in a mortar. The three electrode system used was a C-paste working electrode, a platinum foil auxiliary electrode, and an SCE.



## B. Procedures

Broadly three different types of experiments were performed in this investigation:

(1) Cyclic voltammetric studies of azole-modified C-paste electrodes in cuprous solution. PCPE and the 6% azole-modified CMCPs were prepared, dipped in a solution of 20.5 ppm of Cu(I) in the supporting electrolyte (0.5 M sodium acetate, pH 6.4), electrolysed at -0.5 V for 30 seconds in the well stirred solution, and then CVs recorded by scanning between -0.5 V and +0.67 V.

(2) Behaviour of PCPE in azole containing supporting electrolytes. The PCPE was immersed in the supporting electrolyte (0.5 M sodium acetate, pH 6.4) containing 20.5 ppm of Cu(I) and 30 mg of each azole, electrolysed for 30 seconds at -0.5 V and then CVs recorded by scanning between -0.5 V and +0.67 V.

(3) Behaviour of cuprous-modified CMEs and cupric-modified CMEs after dipping them in each azole solution. A 0.29% cuprous-modified C-paste electrodes and 0.3% cupric modified C-paste electrodes were prepared, dipped non electrochemically for 1 minute in a well stirred 0.1%, pH 9.2 solution of each azole, removed and washed well. Cyclic voltammograms were recorded by using these electrodes in the supporting electrolyte (0.5 M sodium acetate, pH 6.4), after electrolysing at -0.5 V for 30 seconds and by scanning between -0.5 V and +0.67 V. The scan rate employed was 2 V/15 sec.

## III RESULTS AND DISCUSSION

### A. Investigations using benzotriazole

1. Cyclic voltammetric studies of benzotriazole-modified C-paste electrode in sodium acetate solution containing cuprous ions. Fig.1.a'. shows the CV of pure C-paste electrode in 0.5 M sodium acetate solution. This is the reference voltammogram on which the entire discussion to follow on the relative inhibitor efficiencies of different azoles is based. Here, PCPE gives a straight line parallel to the X-axis. The CV of Fig.1.a. was obtained with the PCPE dipped in 20.5 ppm of Cu(I), and electrolysed for 30 sec at -0.5 V. At this potential Cu(I) gets deposited on the electrode surface as copper and during the anodic scan of the cycle i.e., between -0.5V to +0.67 V, a large peak at 0 V, with a peak height of 17.2 uA, appears and this corresponds to the dissolution of copper into the solution as  $\text{Cu}^+$ . In the reverse cycle (i.e., in the cathodic scan between +0.67V to -0.5V), cuprous ion in the solution gets reduced to copper at the PCPE surface giving a broad peak at -0.22 V with a peak height of ca. 5.6 uA.

Fig.1.b'. shows the CV for 6% benzotriazole-modified C-paste electrode in 0.5M sodium acetate solution. It is seen that in the anodic scan a steady background current, sloping downward and a

big hump in the reverse cycle were obtained. Otherwise the CV is featureless. The CV of BTA-modified CME, in the presence of 20.5 ppm of copper(I), reveals an important information (Fig.1.b.). In the anodic scan no peak corresponding to the dissolution of  $\text{Cu} \rightarrow \text{Cu}^+$  could be seen. Repeated CV scans using the same electrode (diagram not shown), after 30 sec electrolysis at  $-0.5\text{V}$  each time, failed to give any anodic dissolution peak for  $\text{Cu} \rightarrow \text{Cu}^+$ .

## 2. Behaviour of PCPE in benzotriazole containing solutions:

Fig.2.a.& a'. show the behaviour of PCPE when 30 mg of benzotriazole was added to the supporting electrolyte. The CV was a straight line indicating that the presence of benzotriazole in the solution does not alter the shape of the voltammogram (Cf. Fig.1.a'.& 2.a'). When  $\text{Cu}^+$  was added to the solution, and CV recorded after 30 sec electrolysis at  $-0.5\text{V}$ , no peak could be seen for the anodic dissolution of copper. (Fig.1.a.) The cathodic scan is marked by the absence of any peak or hump. From these results it is obvious that the presence of BTA in the solution prevents in some way the redox reaction of copper at the pure carbon-paste electrode surface. It is of course possible that no anodic peak will be obtained for copper oxidation, if in the presence of BTA copper is not deposited on the PCPE surface by electrolysis at  $-0.5\text{V}$ . Hence another experiment was conducted using cuprous-modified CME.

3. Behaviour of cuprous-modified CME after a BTA dip. A 0.29% cuprous ion modified C-paste electrode was prepared, electrolysed for 1 minute at  $-0.5\text{V}$  in 0.5 M sodium acetate solution, and then a CV recorded. (Fig.3.a.). By the electrolysis at  $-0.5\text{V}$ ,  $\text{Cu}^+$  is reduced to  $\text{Cu}$  at the electrode surface, and during the anodic scan, a large peak with a peak height of ca.  $14.4 \mu\text{A}$  was obtained at  $+0.1 \text{V}$  for the anodic dissolution of  $\text{Cu}$  to  $\text{Cu}^+$ . The rising portion of the current in the cathodic scan is due to the reduction of  $\text{Cu}^+$  which is present on the electrode surface to copper.

A fresh surface of the above cuprous-CME was dipped in a well stirred 0.1% solution of BTA, pH 9.2, for 1 minute, transferred to the voltammetric cell containing the supporting electrolyte alone, electrolysed for 1 minute at  $-0.5\text{V}$  and then a CV recorded. It is seen (Fig.3.b) that no peak was obtained for the anodic dissolution of copper.

From these voltammograms, it is obvious that the presence of BTA prevents the oxidation of copper even at relatively large positive potential ranges. The mechanism of this process may be due to complex formation with  $\text{Cu}^+$  on the electrode surface which may form a surface layer on the electrode that acts as a barrier for copper oxidation. It is this remarkable ability that makes BTA unique as the most effective inhibitor for copper corrosion.

## B. Investigations using mercaptobenzothiazole (MBT)

### 1. Cyclic voltammetric studies of MBT-modified C-paste electrodes in sodium acetate solution containing cuprous ions.

Fig. 1.C' shows the CV of 6% MBT-modified CME in the supporting electrolyte. A hump is seen indicating the oxidation of MBT in the medium. By repeated scans (not shown in the diagram) the magnitude of this peak decreased. In the cathodic scan, however, no corresponding peak is obtained indicating that under the conditions employed, MBT does not get reduced at the electrode surface. In the presence of cuprous ions (Fig.1.c.), in the anodic scan, two humps were obtained, one at -0.04V and the other at +0.49V. The small peak at -0.04V can be attributed to the oxidation of  $\text{Cu} \rightarrow \text{Cu}^+$  and the hump at +0.49 V due to the oxidation of  $\text{Cu(I)-MBT}$  complex to dibenzo thiazolyl-disulphide (DBDS). (The experiments described in the next section explain why the hump at +0.49V can be assigned to the oxidation of  $\text{Cu-MBT}$  complex). In the cathodic cycle, no reduction peak could be seen. This very clearly suggests that probably a film of  $\text{Cu(I)-MBT}$  is formed on the electrode surface, and prevents the  $\text{Cu}^+$  in the solution from reducing to Cu at the CME surface.

Further, the MBT-modified CME was subjected to repeated CV scans, each after maintaining the electrode at -0.5 V for a fixed period, namely 30 sec, 30 sec, 60 sec, and 120 sec. While the hump at +0.49 V remains practically unaltered, the peak height for anodic dissolution of copper goes on increasing with each scan. This clearly suggests film break down and a consequent increase in the dissolution rate.

2. Behaviour of PCPE in MBT containing solutions. The cyclic voltammogram of PCPE in MBT containing sodium acetate solution (Fig.2.b') reveals a hump at ca. +0.19 V and shows that MBT is electrooxidizable at PCPE surface. When  $\text{Cu}^+$  was added to the solution, and the PCPE electrolysed for 30 sec at -0.5V, and the CV recorded, it is seen that the magnitude of the hump is shifted to more positive values and is decreased in size (Fig.2.b.). The electrode was subjected to further CV scans, after 1 min, and 2 min electrolysis at -0.5 V (diagram not shown), and the most important observation here was that, in the presence of MBT in solution along with  $\text{Cu}^+$ , the oxidation peak for  $\text{Cu} \rightarrow \text{Cu}^+$ , or the reduction peak for  $\text{Cu}^+ \rightarrow \text{Cu}$  were conspicuously absent. This clearly suggests the formation of a  $\text{Cu(I)-MBT}$  film on the electrode surface or a stable  $\text{Cu}^+\text{-MBT}$  complex in the solution as a result of which copper was neither deposited nor dissolved from PCPE.

3. Behaviour of cuprous-modified CME after a dip in MBT solution. As reported earlier for BTA, the cuprous modified CME was dipped in a 0.1% solution of MBT (pH 9.2), and then subjected to CV scans and the CV is shown in Fig. 3.c. The anodic scan is marked by a small peak at 0 V, with a peak height of 0.8 uA, due to the oxidation of  $\text{Cu} \rightarrow \text{Cu}^+$ , and a hump at +0.45 V due to the oxidation of  $\text{Cu(I)-MBT}$  complex. When compared with Fig 3.a, wherein 14.4 uA were obtained for fresh cuprous-CME, the corrosion inhibiting action of MBT is clearly seen by the appearance of just 0.8 uA at 0 V for the anodic dissolution of copper.

### C. Investigations using benzimidazole and imidazole

1. Cyclic voltammetric studies using BIMH and IMH modified C-paste electrodes. Fig.1.d'.& 1.d. show the CV of BIMH-modified CME in the supporting electrolyte with and without copper. While the CV in the supporting electrolyte (Fig.1.d'.) is featureless, the CV in the presence of  $\text{Cu}^+$  (Fig.1.d) showed a hump at ca. 0 V due to the anodic dissolution of copper. The magnitude of this hump was 2.4  $\mu\text{A}$ , a value much higher than that obtained for MBT (viz. 1.2  $\mu\text{A}$ , Ref Fig.1.c). Nevertheless the magnitude of this dissolution current was much lower than that obtained for pure C-paste electrode (viz., 17.6  $\mu\text{A}$ ; Ref Fig.1.a.) which is indicative of its ability as a corrosion inhibitor for copper. The CV of this CME in the presence of cuprous ions offered an anodic dissolution current of 12.8  $\mu\text{A}$  (Fig.1.e.). This clearly suggests that imidazole is the least effective in inhibiting the anodic dissolution of copper.

2. Behaviour of PCPE in benzimidazole and imidazole containing solutions. When 30 mg of BIMH was added to the supporting electrolyte, and the CV of PCPE was recorded under conditions similar to what has been reported earlier for BTA and MBT, it did not show any distinctive feature (Fig.2.c'.). In the presence of 20.5 ppm of  $\text{Cu(I)}$  in solution, the cyclic voltammogram of the PCPE (Fig.2.c.) is marked by the presence of a reversible anodic dissolution wave, with  $E_{1/2} +0.8\text{V}$  and a wave height of 2.9  $\mu\text{A}$ . In the cathodic scan, the corresponding  $\text{Cu}^+ \rightarrow \text{Cu}$  wave is seen.

Under similar conditions, PCPE in imidazole containing supporting electrolyte gave a straight line CV (Fig.2.d'); indicating that imidazole in solution does not take part in the electrochemical reaction. However, in the presence of 20.5 ppm of copper, an anodic dissolution wave with  $E_{1/2} -0.04\text{V}$  and waveheight of 3.2  $\mu\text{A}$  was obtained. In comparison with the BIMH behaviour, it is seen that imidazole in solution, is less effective than BIMH in preventing the anodic dissolution of copper.

3. Behaviour of cuprous modified CME after a dip in BIMH & IMH solutions. The 0.29% cuprous-modified CME was dipped for exactly 1.0 minute in a well stirred 0.1% solution of BIMH (pH 9.2), removed, washed, transferred to the voltammetric cell, kept at -0.5V for 1 minute, and then the cyclic voltammogram recorded. It is seen (Fig.3.d.) that the anodic dissolution current for  $\text{Cu} \rightarrow \text{Cu}^+$  is brought down to just 1.2  $\mu\text{A}$ . This experiment clearly reveals that when the  $\text{Cu}^+$ -CME was dipped in the BIMH solution, BIMH was chemisorbed on the electrode and formed a film which effectively prevented the anodic dissolution of copper.

Fig.3.e. shows the CV of the cuprous modified CME, after a dip in 0.1% imidazole solution of pH 9.2. The CV is marked by an anodic dissolution peak of magnitude 6  $\mu\text{A}$ . This experiment proves

that imidazole was also chemisorbed on the CME surface and prevented the anodic dissolution of copper to certain extent. This experiment also reveals that imidazole is the least effective in inhibiting the corrosion of copper since BTA, MBT and BIMH, all gave much lower anodic dissolution currents than IMH under similar conditions.

#### D. Experiments using cupric-modified electrodes:

The above experiment was repeated for everyone of the azoles using the cupric-modified C-paste electrodes. The results are shown in Fig.4. It is seen that the anodic dissolution current of copper was not inhibited to any significant step for all these azoles. From this it can be concluded that it is the Cu(I)-azole complex that is inhibiting the anodic dissolution of copper and not the Cu(II)-Azole complexes.

### IV. SUMMARY AND CONCLUSIONS

In this investigation the utility of pure carbon-paste and chemically modified carbon-paste electrodes were demonstrated for evaluating the relative efficiency of four different azoles as corrosion inhibitors for copper. Basically three different types of experiments were conducted.

Cyclic voltammetric studies of the azole modified C-paste electrodes in cuprous ion solutions were used to determine the anodic dissolution current of copper and from these results the relative corrosion inhibiting efficiency of these azoles are seen to lie in the order BTA>MBT>BIMH>IMH.

The second experiment was to estimate the anodic dissolution current of pure C-paste electrode when 30 mg of each azole was added to the voltammetric cell. These experiments revealed that in the presence of these azoles in solution, the anodic dissolution of copper from a pure C-paste electrode was inhibited, and the relative efficiency lie in the order BTA > MBT > BIMH > IMH.

The third experiment conducted was to prepare a cuprous modified electrode, dip it in a 0.1% pH 9.2 solution of each of these azoles and then subject it to CV studies in pure supporting electrolyte solution. The anodic dissolution currents for copper were compared with the current obtained when no such dip was made. This experiment also clearly suggested the relative efficiency for corrosion inhibition to lie in the order BTA > MBT > BIMH > IMH. Similar experiments conducted using cupric-modified C-paste electrodes revealed that the inhibition of the anodic dissolution current of copper is only due to Cu(I)-azole interaction and not the Cu(II)-azole interaction.

The corrosion rates obtained for copper in 1 M NaCl (N<sub>2</sub> saturated) with different azoles as inhibitors is shown in Table 1. From the table it can be seen that the corrosion inhibitor efficiencies of the different azoles lie in the order BTA > MBT >

BIMH > IMH. These results are in good agreement with the CV investigations using azoles and C-paste electrodes. This agreement suggests that of the three reasons responsible for corrosion-inhibition, namely, anodic inhibition, cathodic inhibition and passivation, the first-mentioned one -anodic inhibition- may be largely responsible for inhibiting the corrosion rate in this particular case.

\*\*\*\*\*

### REFERENCES

1. R. W. Murray, in Electroanalytical Chemistry, Vol 13, A.J. Bard (ed).p.191, Marcel Dekker, New York, 1984.
2. Aruchamy, A.Fujishima, A. Ibrahim and B.H. Loo, J. Electroanal. Chem., 281, (1990), 299
3. C.M. McCrory and J.M. Rosamilia, J. Electroanal Chem., 136 (1982) 105
4. K.T. Carren, G. Xue and M.L. Lewis, Langmuir, 7 (1991) 2
5. Gi. Xue, Q.Dai, S. Jiang, J. Am. Chem. Soc., 110, (1988) 2313
6. G.W. Poling, Corros. Sci, 10 (1970) 359
7. V. Lakshminarayanan and S.R. Rajagopalan, Proc. Indian Acad. Sci. (Chem. Sci.) 97 (1986) 465
8. R. Kannan, V. Lakshminarayanan and S.R. Rajagopalan, Project Document, PD MT 9114, June 1991, National Aeronautical Laboratory, Bangalore-560 017.

Table 1

Corrosion rates of copper in 1 M NaCl (N<sub>2</sub> saturated) with different azoles as inhibitors

Inhibitor 10 ppm	$i_{corr}$ ( $\mu A/cm^2$ )	Inhibitor efficiency
None	6.3	----
BTA	3.5	44%
MBT	4.8	23.8%
BIMH	4.6	26.9%
IMH	6.0	04.8%

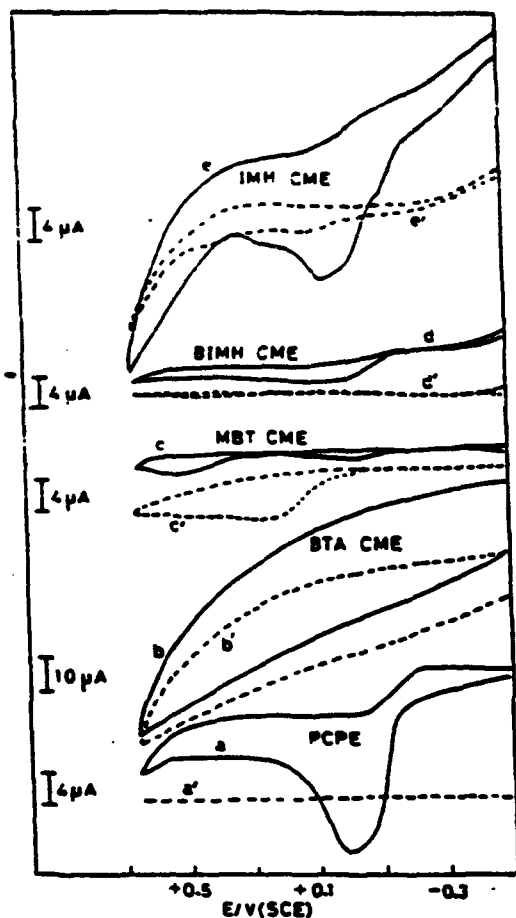


Fig. 1

Fig. 1. Cyclic voltammograms of the azole-modified CMEs in ---- pure supporting electrolyte; — in 20.5 ppm of  $\text{Cu}^+$  in the supporting electrolyte; a, a' for PCPE; b, b' for BTA CME; c, c' for MBT CME; d, d' for BIMH CME; e, e' for IMH CME.

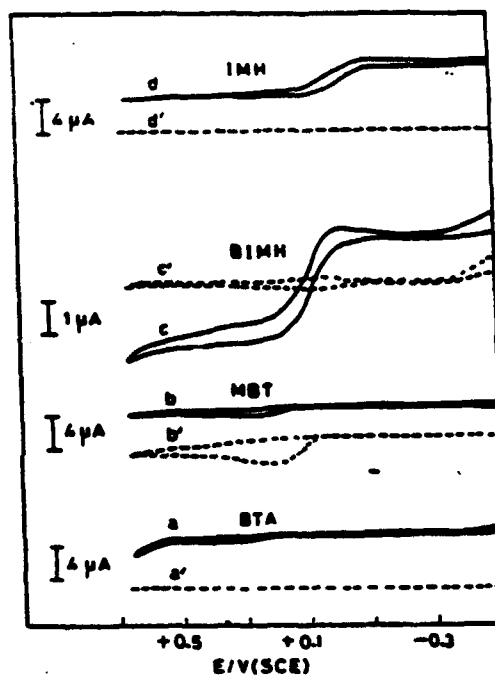


Fig. 2

Fig. 2. Cyclic voltammograms of pure carbon-paste electrode in the presence of, ---- 30 mg of particular azole in the solution; — 30 mg of particular azole + 20.5 ppm of  $\text{Cu}^+$  in the supporting electrolyte;

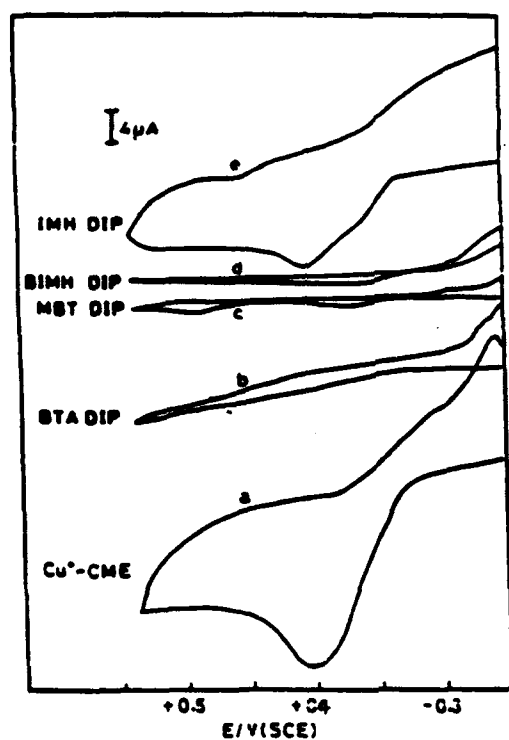


Fig.3

Fig.3. Cyclic voltammograms of cuprous ion modified CME in 0.5 M sodium acetate supporting electrolyte after a dip in differentazole solutions; a: no dip; b: BTA dip; c: MBT dip; d: BIMH dip; e: IMH dip;

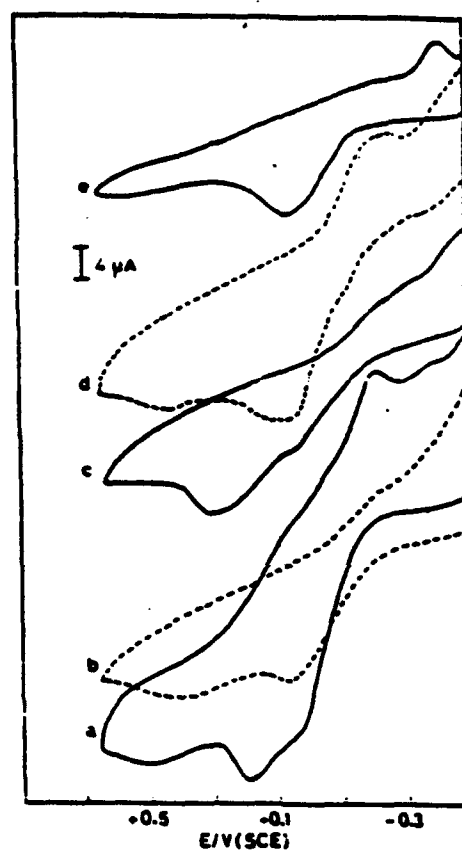


Fig.4

Fig.4. Cyclic voltammograms of cupric ion modified CME in 0.5 M sodium acetate supporting electrolyte after a dip in differentazole solutions; a: no dip; b: BTA dip; c: MBT dip; d: BIMH dip; e: IMH dip;



## **Inhibition of the Corrosion of Carbon Steel in Hydrochloric Acid by Phosphonium Species**

**B D Barker, I B Beech and F C Walsh**

**Applied Electrochemistry Group, Chemistry Department,  
University of Portsmouth,  
St Michael's Building,  
White Swan Road,  
Portsmouth PO1 2DT, UK.**

### **Abstract**

Hydrochloric acid is routinely used to remove rust, millscale and hardness salts from iron and steel surfaces. In order to minimise attack on the substrate, it is common to use organic adsorption inhibitors dissolved in the cleaning acid in applications such as pretreatment before metal finishing, scale removal from boilers and heat exchangers, the cleaning of tanks and pipelines and millscale removal from rolled steel sheet.

The inhibition of corrosion of carbon steel in hydrochloric acid using triphenyl phosphine and phosphonium derivatives is studied by weight loss, solution analysis, linear polarisation and Tafel extrapolation methods. The variables investigated include acid concentration (1 M, 5.7 M or 11.4 M), inhibitor concentration (typically  $10^{-5}$  M -  $10^{-3}$  M) and temperature (22°C - 80°C).

Polarisation studies using a rotating disc electrode show that this family of compounds act as mixed inhibitors and extrapolation of the cathodic Tafel slope may be used for the determination of corrosion rates. Triphenylphosphine follows a Langmuir type of adsorption isotherm. The most effective inhibitor studied was methyltriphenylphosphonium iodide which shows a percentage inhibition of approximately 99% in 1 M hydrochloric acid at 22°C.

Comparisons are made between the performance of phosphonium species and competitive compounds based upon hexamethylenetetramine. Possible mechanisms of adsorption and inhibition are discussed from the viewpoint of the structure of the inhibitors.

**Key terms:** triphenylphosphine, phosphonium compounds, corrosion of carbon steel, hydrochloric acid, inhibition.

## Introduction

It is generally accepted that the organic compounds used as inhibitors act via adsorption at the metal/solution interface. Although extreme cases of purely cathodic or purely anodic inhibitors are known, the majority of species function as mixed inhibitors, i.e. they retard the kinetics of both half-cell reactions<sup>1</sup>. One or more of the functional sites in the inhibitor molecule (or one of its reaction products) is capable of forming chemical bonds with the metal surface. The resultant reaction layer then acts as an energetic or diffusional barrier to electron transfer at, or charge transport to/from, the electrode surface. The mode of action of these inhibitors has been related to classical adsorption isotherms such as the Langmuir one.

A number of phosphonium compounds are known to be effective inhibitors for the corrosion of iron in acid solution under specific conditions<sup>2-11</sup>. This paper outlines studies on triphenylphosphine itself and a number of related phosphonium compounds in hydrochloric acid under a range of experimental conditions.

## Experimental

Samples were cut from a steel sheet of composition according to specification 040A10 BS 970 Part 1, 1983 (0.2% C, 0.17% Si and 0.48% Mn). Coupons of size 2 x 10 x 0.1 cm were used for weight loss and solution analysis measurements whilst electrochemical studies used 1 cm<sup>2</sup> area working electrodes flush-mounted in a close fitting, cylindrical PTFE shroud. Prior to use, the samples were wet abraded using 600 grade silicon carbide paper followed by solvent degreasing (ethanol swabbing), acid pickling (1 M, 5.7 M or 11.4 M HCl as appropriate) and rinsing in deionised water. Gravimetric samples were washed by water, dried and stored in a desiccator before weighing ( $\pm 0.0001$  g). Working electrodes for electrochemical measurements were transferred directly to the cell.

The inhibitors were used in the 'as-received' condition from BDH or Aldrich, or they were synthesised in-house. The typical purity was >99.0%. The majority of the inhibitors studied were relatively insoluble in dilute acid; electrolytes were therefore prepared by dissolution of a known amount of inhibitor in concentrated hydrochloric acid followed by dilution of the mixture to give the correct concentrations of acid and organic. All electrolytes were deaerated by a fast stream of nitrogen before use in order to minimise dissolved oxygen levels.

Electrochemical studies used a three-electrode, three-compartment cell. The working electrode was a rotating disc electrode (RDE) of surface area 0.75 cm<sup>2</sup> which was rotated at a constant speed of 700 rev min<sup>-1</sup>. The counter electrode (CE) was a high surface area platinum mesh and a saturated calomel electrode (SCE) communicated to a point approximately 1.5 mm away from the WE surface via a luggin capillary and salt bridge in order to minimise any uncompensated IR drop. The WE compartment was isolated from the CE one by a cation exchange membrane

(DuPont's Nafion 415). Current-potential curves were obtained potentiodynamically at a potential sweep rate of  $1 \text{ mV s}^{-1}$ , which gave pseudo-steady state behaviour. The RDE provided a controlled hydrodynamic environment and facilitated removal of hydrogen gas from the WE surface; it also provided an extended range for charge transfer controlled kinetics of iron dissolution, i.e. a longer anodic Tafel region.

Weight loss experiments and solution analysis (via atomic absorption spectroscopy using an air-acetylene flame) typically utilised five replicate experiments in order to determine a significant mean value of corrosion rate. The electrode area to electrolyte volume ratio was as high as 1:10 in order to minimise interference from: the buildup of  $\text{Fe}^{2+}$ , pH changes or a decrease in the bulk concentration of inhibitor during the experiments.

### Results and Discussion

In the case of weight loss and solution analysis, the results are reported as mean corrosion rates over the electrode surface and the immersion time. Electrochemical measurements were performed under pseudo-steady state conditions.

In all cases, the degree of effectiveness of the inhibitor is expressed via the percentage inhibition:

$$\%I = 100 \left( 1 - \frac{v}{v_0} \right) \quad (1)$$

where  $v_0$  and  $v$  are the corrosion rates in the absence and the presence of the inhibitor, respectively.

#### Triphenylphosphine in HCl

Figure 1 shows the variation in corrosion rate and the percentage inhibition as a function of triphenylphosphine concentration in 5.7 M HCl at  $22^\circ\text{C}$ . A weight loss value of  $8.0 \text{ mg cm}^{-2} \text{ h}^{-1}$  could be reduced to a value of  $0.1 \text{ mg cm}^{-2} \text{ h}^{-1}$  at the  $1 \times 10^{-3} \text{ M}$  inhibitor level. This corresponds to an inhibition of approximately 98.8%. Increases in inhibitor concentration above the  $1 \times 10^{-3} \text{ M}$  level does not significantly decrease the corrosion rate and the solubility limit is reached at a concentration of approximately  $4.5 \times 10^{-3} \text{ M}$ . Figure 1 shows the characteristic behaviour of an adsorption isotherm.

Table 1 indicates that solution analysis measurements showed comparable rates of corrosion to weight loss ones, although the former tended to give higher values, particularly at low inhibitor levels. The potential of the steel was typically  $-470 \text{ mV}$  in the uninhibited acid while a value of

-465 mV was obtained in solutions containing  $1 \times 10^{-3}$  M triphenylphosphine. The corrosion potential did not vary by more than 20 mV throughout the inhibitor concentration range studied, indicating that triphenylphosphine behaves as a mixed inhibitor.

Typical current versus potential curves for the uninhibited 5.7 M acid and the acid in the presence of  $1 \times 10^{-3}$  M inhibitor at 22°C are shown in figure 2. These measurements show that the inhibitor has a marked affect on both the anodic process:



and the cathodic one:



Due to the high rates of corrosion in uninhibited 5.7 M HCl, well-defined Tafel regions are not observed and Tafel extrapolation cannot be used as a route to the corrosion current density (and hence the corrosion rate) without the application of correction techniques for uncompensated IR drop between the tip of the luggin capillary and the surface of the WE. Under inhibited conditions, well-defined cathodic and anodic Tafel regions are observed as linear zones in figure 2. These linear portions may be extrapolated to the corrosion potential in order to estimate a value for the corrosion rate. In the case of  $1 \times 10^{-3}$  M triphenylphosphine in 5.7 M HCl, the cathodic and anodic Tafel regions were found to have values of 60 mV and 112 mV per decade of logarithmic current, respectively. It is also interesting to note that the corrosion potential showed relatively little change, in accordance with the ability of the triphenylphosphine to act as a mixed inhibitor.

The adsorption of triphenylphosphine or its reaction products may be considered as a dynamic process in which molecules of the adsorbate are continuously placed in contact with the metal surface and a certain fraction adhere to form a monolayer; at the same time, a number of molecules will be removed from the surface into the electrolyte. The adsorption process may be approximately described by the expression<sup>12</sup>:

$$\frac{v_0}{v} - 1 = Kc \quad (4)$$

where  $v_0$  and  $v$  are the corrosion rates in the absence and presence of the inhibitor,  $c$  is the concentration of inhibitor in the electrolyte and  $K$  is a constant.

If a wide range of inhibitor concentrations is studied, a plot of  $(v_0/v - 1)$  versus  $c$  should be

linear according to this simplified adsorption model. Such a plot is attempted in figure 3 and reasonable linearity is shown. The S-shaped adsorption isotherm in figure 1 also suggests that adsorption is more facile at higher inhibitor concentrations. Curves of this shape are usually observed when three conditions are fulfilled, namely the adsorbate: (i) is monofunctional, (ii) experiences moderate forces of intermolecular attraction, resulting in a tendency to vertical packing in a regular array and (iii) meets strong competition for adsorption at active sites from solvent based species (such as  $\text{H}_2\text{O}$ ,  $\text{H}^+$  or  $\text{Cl}^-$ ). These conditions are readily met in the present case as may be seen from a discussion of the structure of the inhibitor and its modes of interaction with the metal surface.

Triphenylphosphine dissolves in strong acids via protonation to form the phosphonium species:



Monofunctionality may be primarily due to electrostatic attraction between the triphenylphosphonium cation and negatively charged sites on the metal surface (which may arise via a negatively charged electrical double layer and be enhanced by adsorption of  $\text{Cl}^-$ ). Another possibility is overlap between the lone pair of 3d electrons on the P atom and those of comparable energy in the 3d level in Fe.

In practice, the situation is likely to be complicated by the following, additional, interactions between the inhibitor and the metal surface.

- (i) Coordination via overlap of the  $\pi$ -electrons in the phenyl rings with vacant d orbitals in the metal, assuming that the phenyl rings can lie in a plane which is reasonably parallel and close to the metal surface.
- (ii) The triphenylphosphine molecule is pyramidal in shape and has a dipole moment of 1.39 Debye, the P atom being positive. Electrostatic attraction may therefore take place to negative sites on the steel surface.
- (iii) The bulky phenyl rings may restrict diffusion of  $\text{H}^+$  and  $\text{Fe}^{2+}$  ions to and away from the surface, respectively, via steric hindrance effects.

The effect of temperature was studied for  $1 \times 10^{-3}$  M solutions of triphenylphosphine in 5.7 M HCl using weight loss methods. The behaviour of carbon steel in HCl is expected to follow an Arrhenius type of relationship according to an equation of the form:

$$v = k_2 \exp - \frac{E_{act}}{RT} \quad (6)$$

where  $v$  is the corrosion rate,  $E_{act}$  is the apparent energy of activation and  $k_2$  is a constant. Taking logarithms gives:

$$\log v = \log k_2 - \frac{E_{act}}{R} \cdot \frac{1}{T} \quad (7)$$

Hence  $E_{act}$  may be determined from a plot of the logarithm of corrosion rate versus the reciprocal temperature. Such a plot is shown in figure 4 for the uninhibited acid, the acid inhibited with  $1 \times 10^{-3}$  M triphenylphosphine and the acid inhibited with  $1 \times 10^{-3}$  M hexamethylenetetramine over a temperature range of 25°C to 60°C. The triphenylphosphine shows a higher degree of inhibition throughout the temperature range studied and the apparent energy of activation of approximately 80 kJ mol<sup>-1</sup> may be compared to values of approximately 60 kJ mol<sup>-1</sup> for both the uninhibited acid and the case of the hexamine. The higher value for the phosphine indicates that its effectiveness is reduced at higher temperatures.

#### Derivatives of Triphenylphosphine

A wide number of phosphonium compounds have been investigated<sup>1-11</sup> as inhibitors for the dissolution of iron (and also zinc). The present work was focussed upon derivatives of triphenylphosphine in order to examine relationships between the inhibitor structure and its efficiency. The phosphonium species studied are listed in table 2 together with their percentage inhibition at the  $1 \times 10^{-3}$  M level.

In order to register accurate differences between the compounds, the temperature of the 5.7 M HCl was raised to 80°C and the immersion time was increased to 16 hours. Both weight loss and solution analysis determinations were made and the corrosion rates found from these two methods were generally within 2% of the weight loss values. The values quoted in table 2 are the mean values of averaged data from each of the two techniques.

Triphenylarsine has a similar structure to triphenylphosphine; the arsenic atom has a lone pair of electrons and the electronegativities are similar. This suggests that triphenylarsine might have similar inhibiting properties. It is obvious from table 2 that the arsonium compound is not nearly as effective as the phosphonium one. A contributory reason for this is the presence of unfilled 3d levels in the phosphonium compound compared to the filled ones in the arsonium species. The empty 3d level in iron is comparable in energy with the vacant 3d in phosphorous and this appears to be an important structural feature in the design of an efficient inhibitor.

Once a phosphonium species is adsorbed on the metal surface via interaction with the lone pair of electrons on the P atom, subsequent (or simultaneous) bonding may occur to the surface via the  $\pi$ -orbitals of the phenyl rings. Methyl groups should increase the electron density in the p-system of the rings and it can be seen from table 2 that methyltriphenylphosphonium together with meta- and para-tritolylphosphonium species are all superior inhibitors to triphenylphosphine. It is desirable to maintain three aryl groups around the P atom in order to provide high values of electron density, as seen from the relatively low percentage inhibition value for methyldiphenylphosphine compared to the triarylphosphines. The importance of phenyl rings containing delocalised electrons is also evidenced by the low percentage inhibition values for tributyl phosphine and tricyclohexylphosphonium chloride; the former species has no ring structure whereas the latter contains an unsaturated carbon ring.

The halide ion has a relatively small effect on the effectiveness of the inhibitor, such that the triphenylphosphonium iodide and bromide produce almost identical degrees of inhibition.

Phosphonium compound of the type  $\text{Ph}_3\text{P}^+\text{R}^-\text{X}^-$  (where R is an alkyl or aryl group and  $\text{X}^-$  is usually a halide ion) were examined as inhibitors for iron in acid media as early as 1966<sup>2,3</sup>. Further mechanistic work has been performed by several groups<sup>4-11</sup> and a consensus of opinion<sup>12</sup> is that the reaction sequence involves the following steps.

- (i) The phosphonium compound may be reduced to the corresponding phosphine at active sites on the metal surface:



where  $\text{R}'$  is used to indicate an aryl radical.

- (ii) Formation of hydrocarbons via protonation of an aryl radical is also possible:



- (iii) In the presence of dissolved oxygen, phosphine oxides may also form:



Under the experimental conditions, the most efficient inhibitor was found to be methyltriphenylphosphonium iodide which showed a percentage inhibition exceeding 99%. In the highly acidic solutions involved, the most probable inhibitor species in solution is the methyltriphenylphosphonium cation. This species is likely to adsorb via electrostatic attraction

to negatively charged surface sites, while interactions between the surface and close-lying phenyl rings are also possible, as discussed above.

The effect of acid concentration on the degree of inhibition was studied for methyltriphenylphosphonium iodide at a temperature of 22°C. As shown in figure 5, the inhibitor remains effective at all hydrochloric acid levels studied (1 M, 5.7 M and 11.4 M). However, the percentage inhibition drops significantly at the higher acid levels. For example, at the  $1 \times 10^{-3}$  inhibitor level, the percentage inhibition values were approximately 99%, 96% and 80% at 1 M, 5.7 M and 11.4 M HCl concentrations.

### Conclusions

- 1) Triphenylphosphine and its compounds were effective inhibitors of the corrosion of a low carbon steel in aqueous hydrochloric acid at levels of approximately  $1 \times 10^{-3}$  M. For example, the % inhibition for triphenylphosphine reached a value of 98.8% in 5.7 M HCl at 22°C. At higher concentrations, this parent compound is poorly soluble (although related phosphonium compounds are soluble up to levels approaching  $1 \times 10^2$  M in some cases - particularly if alcohol is used as a cosolvent).
- 2) Triphenylphosphine (and many of its derivatives) follow a Langmuir adsorption isotherm type of behaviour; their tendency to adsorb is more marked at higher inhibitor levels.
- 3) An Arrhenius type of behaviour is shown with temperature, giving an apparent activation energy of approximately  $80 \text{ kJ mol}^{-1}$  over the temperature range 22°C - 80°C compared to a value of approx.  $60 \text{ kJ mol}^{-1}$  for the uninhibited acid.
- 4) Of the compounds studied, methyltriphenylphosphonium iodide proved to be the most effective inhibitor, values of 99.1% being recorded in 5.7 M HCl at 80°C.
- 5) Methyltriphenylphosphonium iodide was effective at the  $1 \times 10^{-3}$  M level over a wide range of HCl concentrations (1 M, 5.7 M and 11.4 M). However, the percentage inhibition fell significantly at the higher acid concentrations; approximate values of 99%, 96% and 80% were observed in 1 M, 5.7 M and 11.4 M HCl at 22°C.
- 6) The current-electrode potential characteristics showed that all of the phosphonium species studied were mixed inhibitors, i.e. they hindered the kinetics of both the hydrogen evolution reaction and the dissolution of iron to ferrous ions. The use of a rotating disc electrode allowed long and well-defined Tafel regions to be observed for the inhibited solutions.



### Acknowledgements

The authors are grateful to Mr G Clarke for technical assistance and to Mr M Hill for construction of the rotating disc electrode. Contributions to early experimental work were made by messrs D. Allan, G. M. Cox P. Evans and J. Magid. Part of this paper was presented at the UK Corrosion '92 Conference at Manchester, UK, on the 14th October 1992.

### References

1. U. R. Evans, The Corrosion and Oxidation of Metals, 2nd Supplementary Volume, Arnold, (1975): p. 94.
2. H. Ertel and L. Horner, Proc 2nd European Symp on Corr Inhibit, 1965, Ferrara, (1966): p. 81.
3. J. W. Lorenz and H. Fischer, Proc 3rd Cong Met Corr, Moscow, 2, (1966): p.99
4. J. M. Saveant and S. K. Binh, J Org Chem, 42, (1977): p. 1242.
5. C. Fiaud, I. Desaulnois, M. Tzinmann and I. Vastra, Proc 6th European Symp on Corr Inhibit, Ferrara, Suppl No 8, (1985): p. 495.
6. A. N. Doronin, T. K. Atanasyan and E. S. Ivanov, Elektrokhim, 16, (1980): p. 1016.
7. E. S. Ivanov, T. K. Atanasyan and A. V. Sakharov, Zh Priklad Khim, 53, (1980): p. 843.
8. B. Sanyal and K. Srivastara, Brit Corr J, 2, (1974): p. 103.
9. M. Troquet and J. Paghetti, Zashita Metallov, 19, (1983): p. 717.
10. M. Troquet and J. Paghetti, Werkstoff u Korr, 34, (1983): p. 557.
11. L. Horner and H. Hinrichs, Werkstoff u Korr, 22, (1971): p. 864.
12. B. D. Barker, T. Harvey and F. C. Walsh, British Corrosion Journal, in preparation.

Table 1 Comparison of weight loss and solution analysis techniques as a route to corrosion rate measurements. Triphenylphosphine in 5.7 M HCl at 22°C.

Inhibitor concentration $c$ /mol dm <sup>-3</sup>	corrosion rate (weight loss) $v_w$ /mg cm <sup>-2</sup> h <sup>-1</sup>	corrosion rate (soln. analys) $v_s$ /mg cm <sup>-2</sup> h <sup>-1</sup>	% inhibition (weight loss) %I	% inhibition (soln. analys) %I	% difference in corros. rate $100 \left( \frac{v_s - v_w}{v_s} \right)$
0	8.0	9.1	0	0	-
0.00001	8.0	8.6	0	5.7	12.0
0.00005	7.9	8.3	1.3	6.8	7.0
0.0001	7.3	7.6	6.3	16.6	3.9
0.00025	5.5	6.2	31.3	31.5	11.2
0.0005	2.6	2.7	67.5	70.4	3.7
0.00075	1.0	1.1	87.5	88.5	9.3
0.001	0.1	0.1	98.8	98.9	0
0.0025	0.1	0.1	98.8	98.9	0

Table 2 Percentage inhibition of a range of phosphine and phosphonium compounds at the  $1 \times 10^{-3}$  M level in 5.7 M HCl at 80°C.

Compound	Formula	% inhibition at the $1 \times 10^{-3}$ M level
methyltriphenylphosphonium iodide	$\text{CH}_3(\text{C}_6\text{H}_5)_3\text{P}^+ \text{I}^-$	99.1
methyltriphenylphosphonium bromide	$\text{CH}_3(\text{C}_6\text{H}_5)_3\text{P}^+ \text{Br}^-$	98.9
trimetatolylphosphine	$(\text{CH}_3\text{C}_6\text{H}_4)_3\text{P}$	98.6
methyltrimetatolylphosphonium bromide	$\text{CH}_3(\text{CH}_3\text{C}_6\text{H}_4)_3\text{P}^+ \text{Br}^-$	98.3
triparatolylphosphine*	$(\text{CH}_3\text{C}_6\text{H}_4)_3\text{P}$	98.2
triphenylphosphine	$(\text{C}_6\text{H}_5)_3\text{P}$	96.9
triphenylphosphine oxide	$(\text{C}_6\text{H}_5)_3\text{P} \rightarrow \text{O}$	96.4
trimesitylphosphine**	$(\text{CH}_3\text{CH}_2\text{CH}_2\text{C}_6\text{H}_3)_3\text{P}$	94.7
methyldiphenylphosphine	$\text{CH}_3(\text{C}_6\text{H}_5)_2\text{P}$	69.3
tributylphosphine	$(\text{C}_4\text{H}_9)_3\text{P}$	36.2
tricyclohexylphosphonium chloride	$(\text{C}_6\text{H}_{11})_3\text{P}^+ \text{Cl}^-$	19.3
triphenylarsine	$(\text{C}_6\text{H}_5)_3\text{As}$	24.8

\* a slight precipitate was noticed after 16 h.

\*\* a significant precipitate was present indicating solubility problems at this inhibitor level

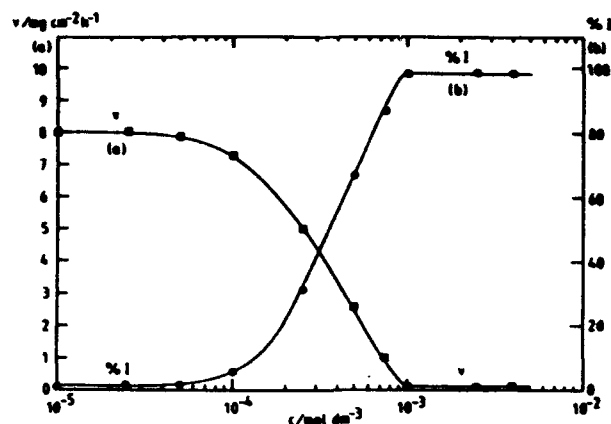


Figure 1 (a) Corrosion rate and (b) percentage inhibition as a function of inhibitor concentration. Triphenylphosphine in 5.7 M HCl at 22°C. Based upon weight loss measurements.

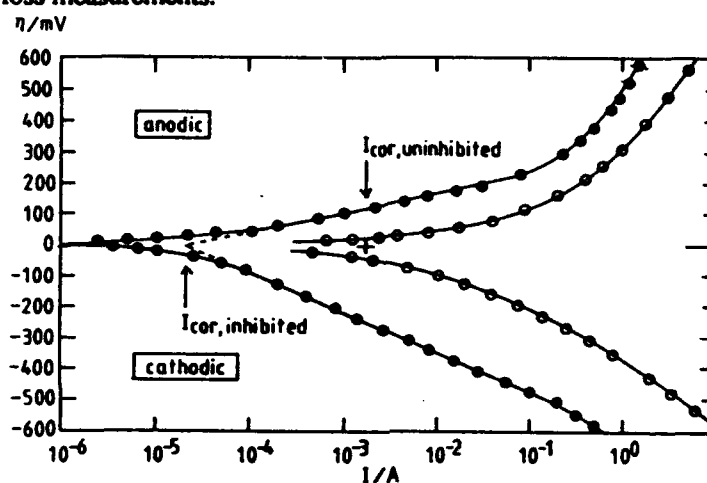


Figure 2 Polarisation versus current curves for a carbon steel RDE in 5.7 M HCl at 22°C, showing the inhibiting effect of  $1 \times 10^{-3}$  M triphenylphosphine.

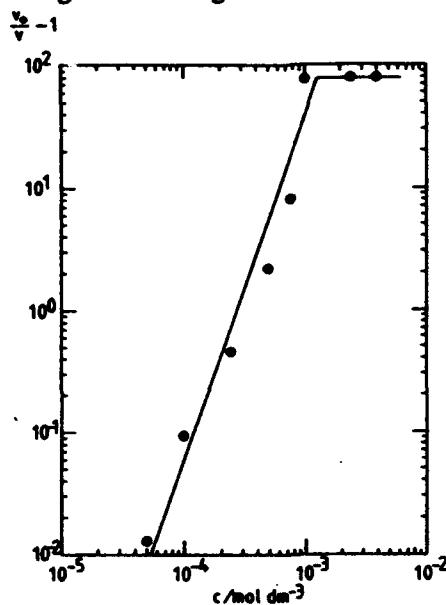


Figure 3 Log-log adsorption isotherm plot for triphenylphosphine in 5.7 M HCl at 22°C, according to the Langmuir type behaviour indicated by equation (4). ( $v_0$  and  $v$  are the uninhibited and inhibited corrosion rates;  $c$  is the inhibitor concentration).

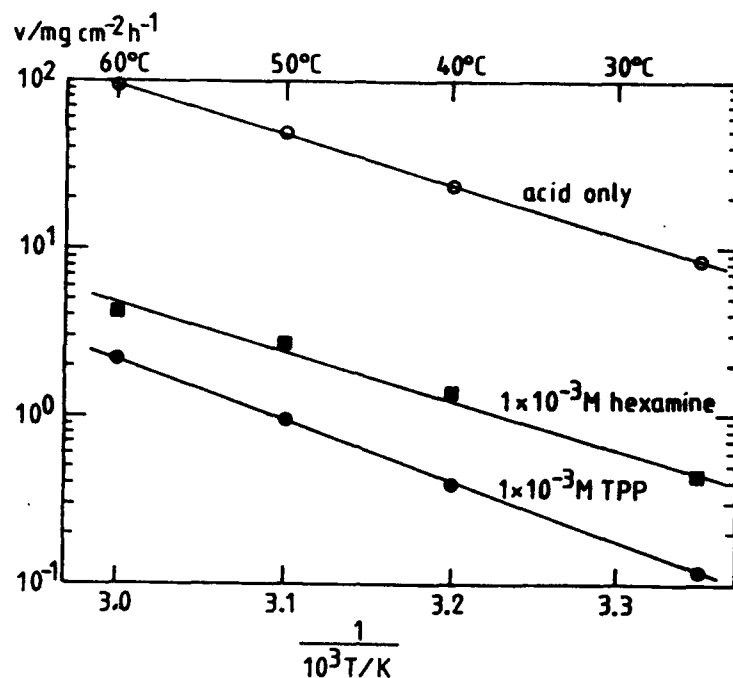


Figure 4 Arrhenius plot (logarithm of the corrosion rate versus reciprocal temperature) for uninhibited 5.7 M HCl and the acid inhibited by  $1 \times 10^{-3}$  M triphenylphosphine or  $1 \times 10^{-3}$  M hexamine.

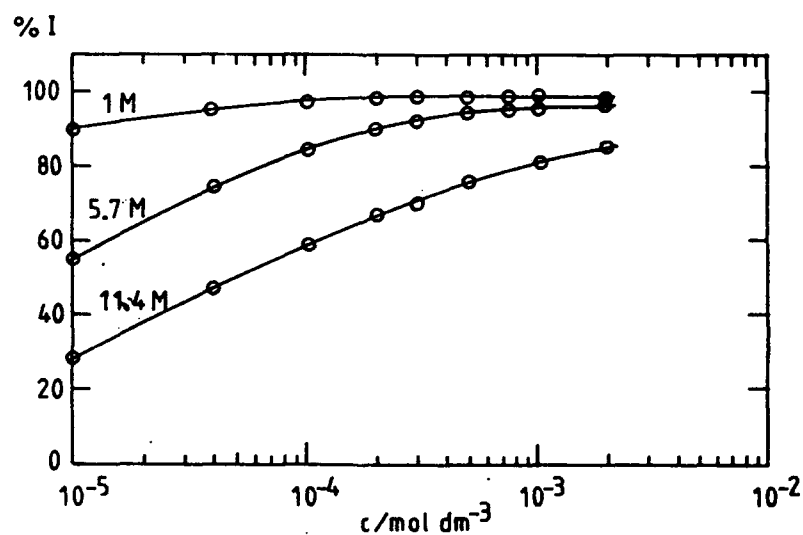


Figure 5 Percentage inhibition as a function of inhibitor concentration for methyltriphenylphosphonium iodide at 22°C, showing the performance of the inhibitor at various HCl concentrations.

**Prediction of Crevice Corrosion Resistance of  
Stainless Steels in Aqueous Environments  
- A Corrosion Engineering Guide**

**John W Oldfield  
Cortest Laboratories Ltd  
23 Shepherd Street  
Sheffield  
S3 7BA, UK**

**Robert M Kain  
LaQue Center for Corrosion Technology (LCCT)  
Wrightsville Beach  
NC 28480  
USA**

**Abstract**

Which stainless steel to use to resist crevice corrosion in a defined aqueous environment is frequently a difficult choice to make if the most economic solution is sought. Not only does detailed composition and chemistry play an important role in the corrosivity of the environment but also the temperature has a key role to play. To help alleviate this situation the Nickel Development Institute has sponsored an extensive research programme over the past 5 years to develop a Corrosion Engineering Guide (CEG) to aid the designer and engineer in material selection. The programme has involved the development of a mathematical model of crevice corrosion of stainless steels which is now in the form of a user-friendly computer software package. The model development has been aided by extensive natural exposure testing, these results being used to verify predictions, and by detailed electrochemical studies to provide technical inputs to the model. Specifically, the CEG can be used to help select the appropriate grade of austenitic stainless steel for an aqueous environment of given chloride and sulphate levels, together with water chemistry i.e. scaling or non scaling, pH and temperature. It can select for critical applications where no corrosion at all is permitted or for less severe applications where a limited amount of corrosion is acceptable. This paper will describes the development and use of the CEG in detail.

**Key terms :** crevice corrosion, stainless steels, seawater, waters, chlorides, mathematical modelling, computers.

**Introduction**

The Corrosion Engineering Guide (CEG) has been jointly developed by Cortest Laboratories in Sheffield, UK and LCCT in Wrightsville Beach, N.C., USA and has been fully sponsored by The Nickel Development Institute (NiDI). It is a predictive tool, aimed at designers or engineers to help them select the appropriate stainless steel for use in a given water. As such it is applicable to many industries, including desalination, power and water, pulp and paper and so on.

In aqueous, near neutral, environments at temperatures below around 60°C the form of corrosion to which stainless steels are most prone is a localised form of attack termed 'crevice corrosion'. The CEG is basically a mathematical model which predicts whether or not this form of corrosion will occur under the specific set of conditions given to it (1, 2). The computer program is written in an extremely 'user friendly' form allowing the non specialist to reach a material selection decision without detailed knowledge of the corrosion processes involved. The output from the CEG, while containing much information is clear and easily interpreted. The accuracy of the predictions is good; a significant number have been compared directly with exposure test results carried out by LCCT as part of the overall Project to develop the Guide.

This paper describes the development of the CEG and highlights the extent of its potential use in industry.

### **Background**

Austenitic stainless steels are extremely versatile materials offering a wide range of corrosion resistance for many applications. Under particular conditions they can suffer either general or localised corrosion; the principal form of corrosion on stainless steels is localised, when the protective oxide film breaks down locally. In aqueous, near neutral environments containing chloride ions, pitting and crevice corrosion can occur, while at temperatures above around 60°C in oxygenated waters chloride stress corrosion cracking (SCC) can occur. The CEG is concerned with guiding the selection of stainless steels for resistance to crevice corrosion.

The mechanism of crevice corrosion, which has been accepted by many, is one whereby initiation occurs by deaeration followed by acidification within the crevice to the point where breakdown of the passive film occurs, this is followed by propagation of attack (3). An alternative mechanism based on the dissolution of inclusions has also been proposed for the generally less resistant stainless steels (4). The CEG is based on the acidification mechanism being appropriate and is concerned with selecting materials to avoid the initiation of attack; it does not concern itself with the propagation stage of the corrosion process.

The CEG is essentially a mathematical model of crevice corrosion which requires various inputs and in turn gives predictions in various forms. The mathematical model described in references 3, 5 and 6 forms the basis of the model used in the CEG; partial developments of the CEG are described in references 1 and 2. During the development of the model, natural exposure test data has been obtained to help verify the theory; also extensive laboratory studies have been carried out to generate input data required by the model.

In its present form the CEG can be used to select the appropriate stainless steel for seawater and other aqueous environment as a function of water composition water chemistry and temperature. Whether or not the application is considered critical and/or severe from the designers point of view can also be taken into account.

## Mathematical Model of Crevice Corrosion

As noted above the original mathematical model, on which the CEG is based, is described in earlier work (3) which predicted the performance of stainless steels in simple chloride containing waters at ambient temperature. The model is based on the mechanism of crevice corrosion of deaeration within the crevice followed by the build-up of an aggressive solution eventually leading to breakdown of the passive film. The build-up of the aggressive solution is caused by the passive current flowing within the crevice as the anodic reaction, oxygen reduction outside the crevice supplying the cathodic reaction. Chromium ions generated by the passive current hydrolyse within the crevice thereby reducing the pH; mass transport between anode and cathode results in anions being carried into the crevice, in this case chloride ions. Thus the pH falls and the chloride ion concentration increases. Eventually the solution becomes severe enough to break down the passive film. The conditions at which this occurs are not predicted by the model but are determined electrochemically and are given as an input to the model.

The model thus takes account of alloy composition, as it effects the development of an aggressive solution, chromium being the significant element, crevice geometry by the way of gap and depth, and mass transport by way of migration and diffusion of species in and out of the crevice. Major inputs to the model are the passive current and critical crevice solution (CCS), namely that solution which will cause breakdown of the passive film.

In this work the model has been extended to handle mixed chloride and sulphate waters; the pH and water chemistry (i.e. scaling or non scaling) are taken into account and the influence of temperature up to 75°C has been considered. In carrying out this extension to the earlier model a number of simplifying assumptions have been made, namely:-

1. The equivalent conductivity ( $\text{ohm}^{-1} \text{cm}^2 \text{val}^{-1}$ ) and diffusion coefficient ( $\text{cm}^2 \text{sec}^{-1}$ ) of chloride and sulphate ions, when considered in terms of anion normality are equal. At 25°C actual values of equivalent conductivities are 76.35 and 80.02 for chloride and sulphate respectively (7). The assumption is thus accurate to within 5%. The temperature variation of this parameter for chloride ions has been taken from reference 7 and it is assumed to be the same for the sulphate ion. The relationship is linear such that the equivalent conductivity can be calculated from

$$\lambda(\text{Cl}^-) = \lambda(\text{SO}_4^{2-}) = 39 + 1.6T$$

where  $\lambda$  is the equivalent conductivity and  $T$  is the temperature in degrees centigrade similar equation has been derived for the sodium ion and a similar one has been assumed for the metal ions

$$\lambda(\text{Na}^+) = 23 + 1.16T$$

$$\lambda(\text{M}^{2+}) = 20 + 1.6T$$

2. The diffusion coefficient,  $D$ , can be calculated from the equivalent conductivity using the following relationship

$$D = \frac{\lambda}{|z|} \frac{R(T+273)}{F^2} \text{ cm}^2 \text{ sec}^{-1}$$

Where  $R$  is the gas constant  
 $F$  is the Faraday  
 $T$  is the temperature in degrees centigrade  
 $|z|$  is equivalents per mole

3. The relationship between mixed chloride sulphate solutions and pH is too complicated to be predicted accurately and therefore it is considered legitimate to determine this empirically and include it as a database within the model (2). The influence of temperature is taken account of indirectly. The model predicts a fall in pH with time in the crevice and identifies the onset of corrosion when the CCS is reached. CCS determinations at temperatures above and below 25°C are obtained using pH values measured at 25°C; in this way no temperature modification to the pH within the model needs to be made.
4. The passive current is assumed to be one of the key parameters in determining the corrosion resistance of a given stainless steel in a given environment. Within the model is a database giving the passive current for a given environment and temperature. As in previous versions of the model the passive current value is, in general, assumed the same, in a given water at a given temperature for all the stainless steels considered.
5. The CCS value for a given alloy must be determined for a given chloride-sulphate solution over the range of temperature being considered. Assumption 1 above has the consequence that this value will be a constant for a given chloride-sulphate ratio at a given temperature. The value need therefore only be determined for each ratio of chloride to sulphate rather than for all solution combinations. A data base containing measured CCS values in selected environments and at particular temperatures is contained within the model. Actual values for a particular environment and temperature are obtained by interpolation.

The original model has been modified taking account of the above assumptions. The data base relating to the passive current values and the CCS values is discussed below, together with results from the exposure tests. Finally the operation of the CEG is described and some actual predictions of the revised model, indicating its use, are given.

### Exposure Test Data

The experimental procedure relating to the exposure test programme carried out at the LCCT is detailed elsewhere (8). Only a summary of these procedures will be given here.



The results on 5 materials are used in the present exercise, UNS S30400, S31600, S31703, N08904, S31254. The chemical composition of these materials is given in Table 1. Note that two heats of S31600 and N08904 are listed. Heat 1 was used for environments 1-15 and heat 2 for environments 16-23. In environments 17 and 18 both heats were used for comparative purposes (see Table 2).

Test specimens were 100 x 150mm with a 13mm hole drilled in the centre for the attachment of a polymethyl methacrylate crevice assembly (8); a 50mm diameter area from the centre of the hole was ground to a 120 grit finish. The crevice assemblies had a 30mm OD and a 5mm annular plateau. The surface finish on the assembly was such as to give an order of magnitude difference from that of the ground test panels. The specimens were assembled wet and a torque of 8.5Nm applied. The test duration was 30 days and duplicate samples were exposed. Twenty three test environments have been studied; the nominal and actual compositions are given in Table 2. All solutions were made up with reagent grade material added to deionised tap water.

The purpose of this exposure testing was to check the predictions of the CEG; the results of interest are therefore whether or not corrosion occurred. The majority of results relate to 25°C although a limited number of tests were carried out at 5, 50 and 75°C. The pH of the bulk solution has a strong influence on the results and attempts to quantify these have been made by comparing data in low and high pH solutions e.g. environments 12 and 17, 14 and 18. In addition the effect of a scaling water as opposed to a non-scaling water was studied e.g. environments 14 and 19.

It is not appropriate to detail all the results obtained in this paper, however an indication of their consistency and usefulness will be given. Of the 5 alloys tested the 6% Mo alloy, S31254, did not corrode in any test. Of the remainder the resistance to initiation of attack increased through the series, S30400, S31600, S31703, N08904. Figures 1 and 2 show results for S30400 and S31600 in waters with pH in the 6-7 range. Results in waters with pH around 8 show much improved resistance. For example in environment 17 all alloys except S31254 corroded while in environment 12 no alloy corroded. Similarly in environment 18 S30400, S31600 and S31703 corroded while in environment 14 no alloy corroded. Whether or not the environment is scaling or not appears to be of secondary importance to the pH values. The effect of temperature shows the resistance to corrosion initiation decreasing going from 5°C to 25°C to 50°C. On going to 75°C there is no further reduction in resistance, maybe even a slight improvement. It is proposed to fully publish the results of these exposure tests elsewhere.

### **Critical Crevice Solution Values**

Critical crevice solution (CCS) values have been determined for all 5 alloys tested in a chloride-only solution and in solutions with chloride to sulphate normality ratios of 1:1, 1:10 and 10:1 (A 1:1 normality ratio corresponds to a 0.74 weight ratio). Values are given in Table 3; in determining these a potentiodynamic sweep rate of 30mV/min was used and a criteria of 30 $\mu$ A/cm<sup>2</sup> for the anodic peak height was used to define the CCS values. The influence of temperature on the CCS values has

been studied to a limited degree in chloride only solutions and in 1:1 chloride to sulphate ratios. These data are summarised in Tables 4 and 5 respectively. These CCS values in Tables 3, 4 and 5 form a database in the model and actual values are calculated by interpolation between the various chloride-sulphate ratios and between the various temperatures.

### **Passive Current Determinations**

Although it is extremely difficult to measure exact values of the passive current, attempts were made to establish the basic trends of this parameter as a function of environment, temperature and alloy. Samples were exposed in an environment and the potential held at 0mV vs SCE. The current was monitored and its value after 1 hour was taken as the passive current. Table 6 shows some of the values obtained.

There are a number of exceptionally high values observed in various environments on various alloys; these are probably caused by pitting corrosion occurring. Under conditions which are definitely passive such as 5°C in 300ppm Cl<sup>-</sup>, 3000 ppm SO<sub>4</sub><sup>2-</sup> solutions the value of the passive current is more or less the same for all alloys. This helps justify the assumption made above that the value is typically the same for all stainless steels in a given environment at a given temperature. The actual values of the passive current used in the model have been selected by using the results in Table 6 as a guide, running the model, comparing predictions with exposure test results and refining the values to optimise agreement. When this is done, values fall typically within the range 1 to 0.01  $\mu\text{A}/\text{cm}^2$ ; the influence of sulphate ions is to cause a reduction in the passive current. Some evidence can be seen for this theory in Table 6 e.g. S30400 and S31600 in 3000ppm chloride solution with 300ppm and 3000ppm sulphate additions. While this is clearly by no means conclusive, it does help support a general theory that the inhibiting effect of sulphate is via a reduction of the passive current as well as by modification of the CCS value.

### **Operating the Corrosion Engineering Guide**

The mathematical model of crevice corrosion described above has been converted into a user friendly computer program using the language PASCAL. In operating the CEG the user is asked to select and/or input the following information.

#### **Which Stainless Steel?**

In its present form the user can select one of 5 austenitic stainless steels which can be classed as S30400 type, S31600 type, S31700 type, N08904 type and the "6% Mo" stainless steels.

#### **What Applications?**

The user is asked whether the design is severe or not from a crevice corrosion point of view. To help make this yes/no decision he is guided by general information on the influence of crevice geometry on corrosion susceptibility. The user is also asked whether the application is critical or not. He is again guided in making this yes/no decision, critical being taken as meaning that no corrosion at all is allowed while non-critical meaning some corrosion can be tolerated.

### **What Environment?**

The user first selects the composition of the water. This is either seawater or a specified chloride and sulphate level. If the pH of the water and/or the hardness, alkalinity and TDS are known these are input. The Langelier index will be calculated if the information is available and the scaling properties of the water determined. This, with the pH value and temperature, is used by the model to select the appropriate passive current.

### **What is the Form and Condition of the Stainless Steel?**

The user is asked the form (wrought or cast) and surface finished (as received, ground, pickled, etc) of the stainless steel and whether or not it is welded. This information is not used directly by the program in its calculations. However, when the CEG output is given comments are made if appropriate on the influence of these factors on corrosion resistance.

Once the CEG has all the necessary input data the user can select one of three operating modes, depending on his particular requirements:-

#### **Mode 1**

In this mode, the CEG simply predicts whether or not corrosion will occur taking account of the input data given.

#### **Mode 2**

In this mode the CEG takes the stainless steel and environment that have been selected and predicts for the user the influence of application on the corrosion resistance. In other words it overrides the input data given on design severity and application criticality. This mode is extremely helpful in allowing the designer or engineer to assess the risk involved in selecting a particular material.

#### **Mode 3**

In this mode the CEG takes the stainless steel and the application that have been selected, together with the pH of the water and predicts the influence of water composition i.e. chloride and sulphate levels, on corrosion resistance. This mode is particularly useful if the composition of the water is not well defined; again it is helpful in allowing the designer or engineer to assess the risk involved in selecting a particular material.

### **Predictions of the Corrosion Engineering Guide**

Two examples have been selected to illustrate the type of prediction produced by the CEG; both relate to S30400, the grade of stainless steel used more than any other.

In the first example let us assume this material is to be used in a water with pH in the 6-7 range containing 300ppm chloride and 300ppm sulphate at around 25°C. Assume we wish to see the influence of application on whether or not corrosion will occur and therefore the CEG is run in Mode 2. Figure 3 shows the CEG predictive output for this situation. We see that for a critical application corrosion is likely to occur whether or not the design is severe; thus one would not select the S30400 for

such a critical application. For a non-critical application if the design is not severe the material is acceptable, if the design is severe it is not acceptable.

In the second example let us take the same input data as for the first example but assume that the application is in fact critical, with a severe design, and we wish to know what chloride sulphate levels are acceptable; in this case the CEG is run in Mode 3. Figure 4 shows the output, indicating again that at 300ppm chloride and 300ppm sulphate corrosion will occur but that if the sulphate level is increased to 1000ppm corrosion would not occur. Note that the data in Figure 4 agrees exactly with the exposure test results presented in Figure 1, highlighting the accuracy of the predictions.

These two simple examples help to show the range of predictions possible using the CEG. The key use of the CEG is to help designers/engineers and others to quickly establish what options are available to them, from a corrosion point of view. This applies both to when they know the environment and want to select the correct grade of material for a particular application and when they know the material and want to know the range of environments and applications for which it can be used.

### **Summary**

The development of a Corrosion Engineering Guide (CEG) for selecting stainless steels to resist crevice corrosion in waters has been described. The basic assumption made in developing the mathematical model within the CEG are detailed, together with a description of the methods used to derive the empirical data used within the model. A description of the operation of the CEG is given together with examples of its use.

### **Acknowledgements**

The authors wish to thank the Nickel Development Institute for sponsorship of this work and for their permission to publish it. They also wish to thank P J Howden who wrote the PASCAL computer program and contributed valuable suggestions to the development of the CEG.

### **References**

1. J W Oldfield, R M Kain, Proc. of 12th Int'l Sump on Desalination and Water Reuse, 15-18 April 1991, Malta, Vol 4, p22.
2. J W Oldfield, R M Kain, Proc. of 11th ICC, 2-6 April 1990, Vol 2, p527.
3. J W Oldfield, W H Sutton Brit. Corros. J. 13, (1978): p13.
4. R C Alkire, S E Lott, J Electrochem. Soc. 136, (1989): p3256.
5. J W Oldfield, W H Sutton, Brit. Corros. J. 13, (1978): p104.
6. J W Oldfield, W H Sutton, Brit. Corros. J. 15, (1980): p31.
7. J Koryta, et al, Electrochemistry, Methuen, London (1970): p83-138.
8. R M Kain, J W Oldfield, CORROSION/90, paper no. 384. (Las Vegas: National Association of Corrosion Engineers, 1990).

**Table 1. Chemical Analysis Of The Five Stainless Alloys  
Used In This Study**

UNS Number	C	Cr	Ni	Mo	Cu	Si	Mn	S	P	N
S30400	0.06	18.25	8.07	0.35	0.44	0.57	1.83	0.007	0.029	0.07
S31600										
(1)	0.05	16.44	10.16	2.09	-	0.43	1.55	0.002	0.026	0.04
(2)	0.04	16.28	10.08	2.08	0.40	0.42	1.54	0.0008	0.03	0.036
S31703	0.026	18.2	13.94	3.16	0.28	0.6	1.74	0.008	0.032	0.049
N08904										
(1)	0.014	20.00	24.90	4.29	1.43	0.26	1.41	0.001	0.023	0.06
(2)	0.02	19.66	27.1	4.59	1.32	0.36	1.49	0.001	0.022	n/a
S31254	0.016	20.0	17.9	6.06	0.74	0.36	0.43	0.001	0.023	0.19

**Table 2. Nominal and Actual Composition of Exposure  
Test Environments**

No	Nominal Cl <sup>-</sup>	mg/l SO <sub>4</sub> <sup>=</sup>	actual Cl <sup>-</sup>	mg/l SO <sub>4</sub> <sup>=</sup>	pH (start)	Temperature (±1)°C
1	100	-	119	-	6.3	25
2	300	-	312	-	6.8	25
3	1000	-	1104	-	6.5	25
4	3000	-	3360	-	6.7	25
5	20000	-	21650	-	7.8	25
6	300	300	346	339	7.1	25
7	300	1000	323	1089	6.2	25
8	300	3000	407	2974	8.2	25
9	1000	300	1144	327	-	25
10	1000	1000	1111	1164	7.3	25
11	1000	3000	1032	3142	5.8	25
12	3000	300	3120	305	8.2	25
13	3000	1000	3351	1100	6.5	25
14	3000	3000	2896	2944	8.1	25
15	-	1000	6	1164	7.8	25
16	3000	-	2667	-	7.9(S)	25
17	3000	300	2953	292	6.4	25
18	3000	3000	2953	3041	6.5	25
19	3000	3000	2750	3090	8.8(S)	25
20	3000	300	2913	284	6.7	50
21	3000	3000	2948	2950	7.9	50
22	3000	3000	2880	2930	7.7	75
23	3000	-	2900	-	6.6	5

Note S = Scaling Water

**Table 3. Critical Crevice Solution Data at 25°C**

**CSS pH Value**

<b>Alloy</b>	<b>All Cl<sup>-</sup></b>	<b>10:1 Cr:SO<sub>4</sub><sup>2-</sup></b>	<b>1:1 Cr:SO<sub>4</sub><sup>2-</sup></b>	<b>1:10 Cr:SO<sub>4</sub><sup>2-</sup></b>
S30400	2.05	2.15	1.67	1.75
S31600	1.68	1.85	1.38	1.45
S31703	1.48	1.60	1.24	1.28
N08904	1.10	1.30	1.00	0.95
S31254	0.95	0.85	0.75	0.75

**Table 4. Critical Crevice Solution Data in Chloride  
Only Solutions As A Function  
Of Temperature**

**CCS pH value**

<b>Alloy</b>	<b>5°C</b>	<b>25°C</b>	<b>50°C</b>	<b>85°C</b>
S30400	1.55	2.05	2.15	2.20
S31600	1.10	1.68	1.90	1.98
N08904	0.70	1.10	1.35	1.45
S31254	0.52	0.95	1.15	1.30

**Table 5. Critical Crevice Solution Data in 1:1  
Chloride To Sulphate Solutions as a  
Function of Temperature**

**CCS pH value**

<b>Alloy</b>	<b>5°C</b>	<b>25°C</b>	<b>50°C</b>	<b>85°C</b>
S30400	1.50	1.67	2.20	2.30
S31600	1.22	1.38	1.62	1.95
N08904	0.98	1.00	1.42	1.65
S31254	n/a	0.75	1.18	1.35

**Table 6. Passive Current Values ( $\mu\text{A}/\text{cm}^2$ )  
After 1 Hour Exposure At 0mV v SCE**

<b>Environment</b>	<b>Alloy</b>	<b>5° C</b>	<b>25° C</b>	<b>50° C</b>	<b>80° C</b>
1000ppm Cl <sup>-</sup>	S30400	-	0.50	-	-
	S31600	0.05	0.08	0.12	0.38
	S31703	-	0.03	-	-
	N08904	0.03	0.03	0.06	13.00
3000ppm Cl <sup>-</sup>	S30400	0.17	1.20	4.50	31.00
300ppm SO <sub>4</sub> <sup>2-</sup>	S31600	0.39	0.94	1.20	20.00
	S31703	0.05	0.07	0.10	0.10
	N08904	0.20	0.22	0.06	7.80
3000ppm Cl <sup>-</sup>	S30400	0.06	0.05	0.08	0.50
3000ppmSO <sub>4</sub> <sup>2-</sup>	S31600	0.08	0.07	0.48	5.50
	S31703	0.05	0.06	0.07	0.18
	N08904	0.18	0.25	0.13	15.00
300ppm Cl <sup>-</sup>	S30400	0.03	0.06	1.00	0.20
3000ppmSO <sub>4</sub> <sup>2-</sup>	S31600	0.06	0.56	0.32	5.90
	S31703	0.03	0.05	0.05	0.13
	N08904	0.03	0.09	0.05	9.50

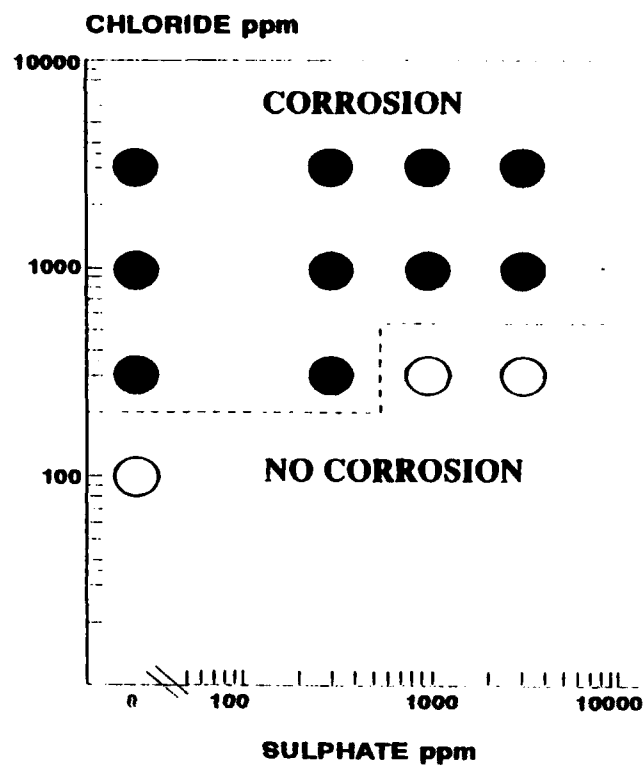


Figure 1. Exposure test results on S30400, 25°C, pH 6-7

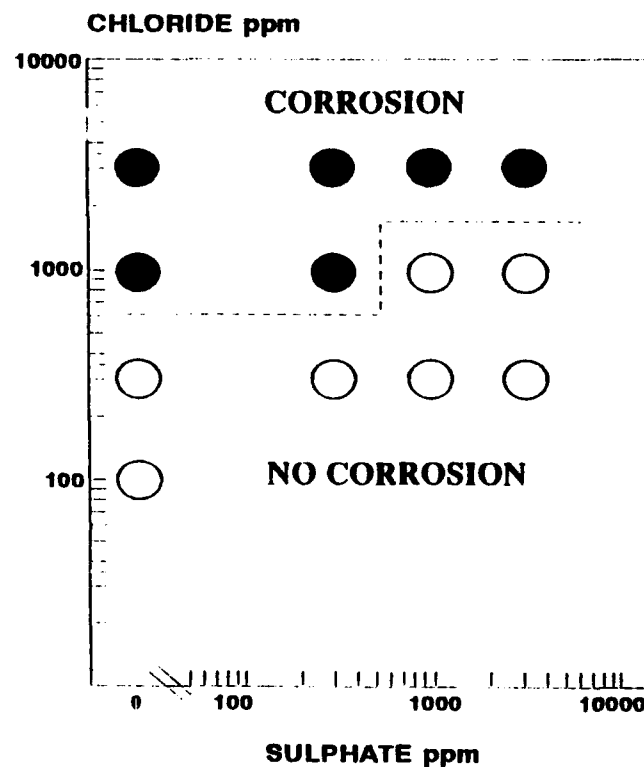


Figure 2. Exposure test results on S31600, 25°C, pH 6-7



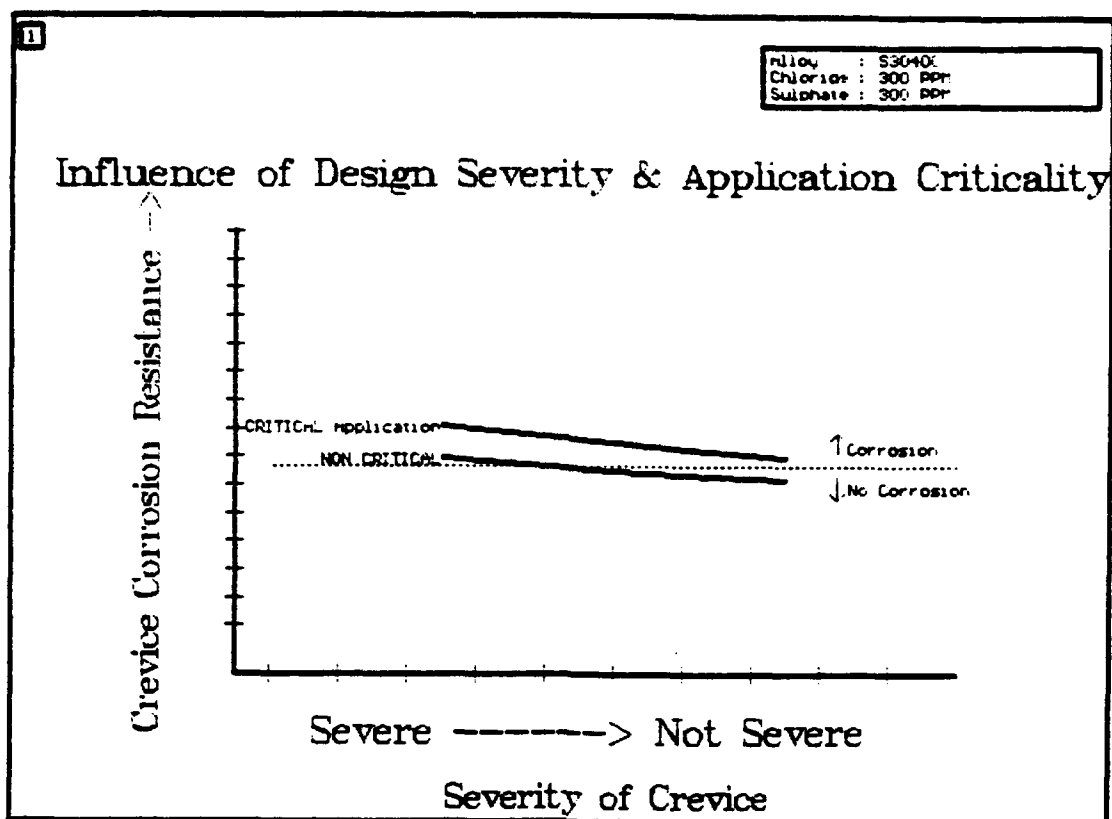


Figure 3. CEG Predictive Printout for S30400, 300ppm Cl<sup>-</sup>, 300ppm SO<sub>4</sub><sup>2-</sup>

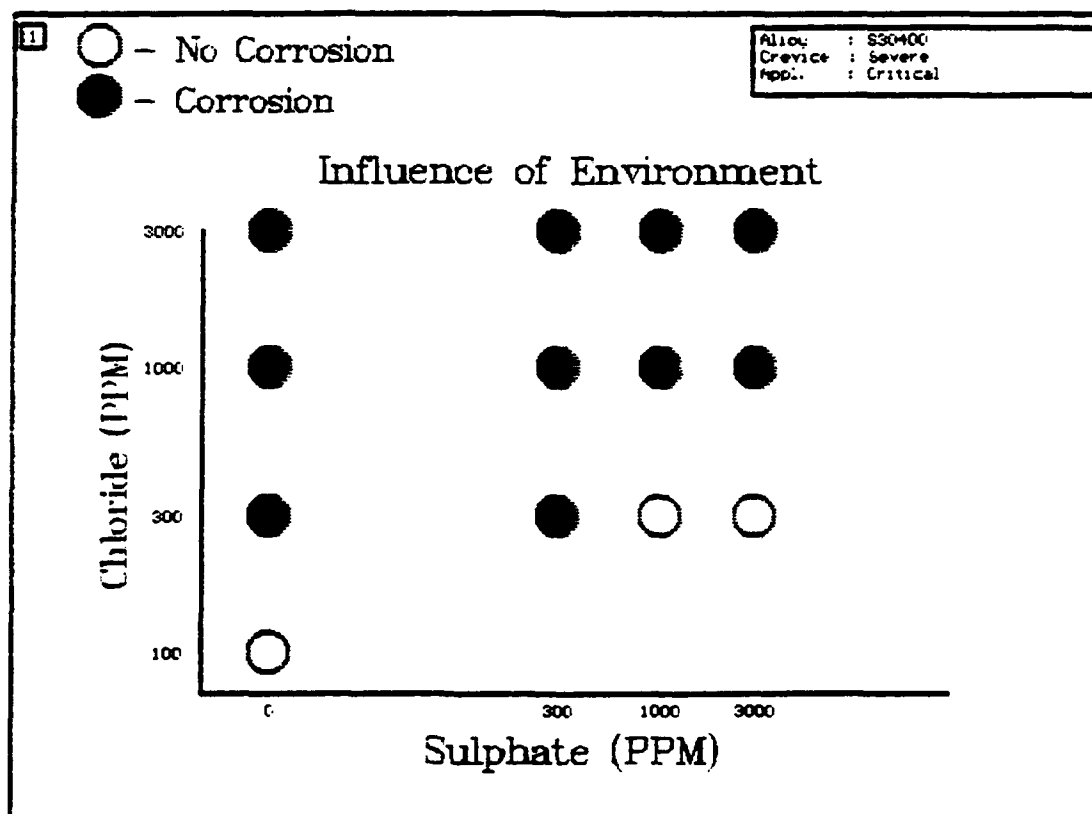


Figure 4. CEG Predictive Printout for S30400, Severe Crevice, Critical Application

## **Seawater Testing to Assess the Crevice Corrosion Resistance of Stainless Steels and Related Alloys**

**Robert M. Kain**  
LaQue Center for Corrosion Technology, Inc.  
Post Office Box 656  
Wrightsville Beach, North Carolina 28480 USA

### **Abstract**

Testing in natural seawater, under identical environmental conditions, has identified differences in the crevice corrosion behavior of several materials as a function of crevice-former-finish and metal-surface-finish, vis'-a-vis" mill vs. ground. Crevice corrosion resistance comparisons among alloys must consider these variables along with the specific differences in bulk alloy composition. Results from the present study have shown that the benefits derived from increased levels of Cr, Mo, N, and the effects of biofilm ennoblement of corrosion potentials can be overshadowed by crevice-former/metal-surface-finish conditions. In addition, there is some evidence that the copper content of the alloy affects crevice corrosion behavior within a given class of material.

**Key terms:** test method, crevice corrosion, seawater, austenitic stainless steel, duplex stainless steel, nickel-base alloys, crevice geometry, surface finish, compositional effects

### **Introduction**

From a corrosion standpoint, alloy selection for seawater service is frequently based on some combination of practical experience and supporting test data, preferably from exposure in natural seawater. In the absence of practical experience, the introduction of new materials, such as stainless steel type alloys, often relies heavily on comparative performance in natural seawater tests and those conducted in other chloride-containing media --- for example, synthetic seawater or ferric chloride solutions. In addition, attempts are often made to empirically correlate and rank alloys in terms of corrosion behavior versus alloy composition. In this regard, pitting and/or crevice corrosion "resistance numbers" have customarily been expressed on the basis of computations such as:  $\%Cr + 3.3 \times \%Mo + 16 \times \%N$ . Previous tests in seawater have elucidated differences in stainless type alloy behavior associated with variations in crevice geometry, vis'-a-vis", crevice gap and crevice depth, as well as material surface-finish.<sup>1-5</sup> Because different alloys may respond differently to such variables, it is unlikely that a single set of test conditions or a certain "resistance number" can be used to predict performance elsewhere, even when the bulk environment is nominally the same.

Recently, a multi-alloy crevice corrosion test program was conducted by the LaQue Center with the participation and support of five major alloy producers. In all, 176 specimens

representing 11 alloys were tested in natural seawater for sixty days. Eight combinations of crevice-geometry and surface-finish were investigated to identify those conditions where crevice corrosion resistance could be expected. All nine proprietary alloys submitted for testing clearly out-performed S31600 stainless steel, as did the N10276 control. For those alloys which exhibited some degree of susceptibility, one or more combinations of crevice-former and alloy surface-condition were found to be critical for crevice corrosion to occur.

While alloy rankings can be established from the results presented herein, the primary goal of this paper is to demonstrate that stainless type alloys with diverse compositions can exhibit crevice corrosion resistance over a range of metallurgical and crevice-geometry conditions.

## **Experimental**

### **Materials and Specimens**

Table 1 identifies each of the alloys tested by chemical composition (nominal or actual supplied by the alloy producer) and UNS number (if so designated). No independent verification of the test material composition was made. Subsequent references to the alloys in the text are by alloy code I to XI or control alloy UNS number.

A total of 16 specimens of each alloy were prepared by end-milling to remove rough sheared edges and to provide the same nominal panel size measuring 100 mm x 150 mm. Each specimen was stencil-coded and a center-hole drilled to facilitate attachment of the crevice formers. Specimens were degreased with acetone. Four panels of each alloy were ground to a 120-grit finish covering a 50 mm diameter area (concentric with the center hole) on both sides of each panel. This was achieved by first stone-grinding the required areas on a lathe and then circular wet grinding with 120-grit SiC papers. All the test specimens were cleaned with a detergent brush and given a final degreasing with fresh acetone. Two ground specimens of each material were then chemically treated by immersion for 10 minutes in a 15%  $\text{HNO}_3$  + 6% HF pickling bath at 40°C. This was followed by a 1-hour rinse in flowing tap water and an acetone dip. Surface grinding and cleaning operations were performed about one to two weeks before testing. Subsequent pickling treatments were all performed on the same day, about 48 hours prior to assembly and exposure. All other specimens were tested with their respective as-produced sheet or plate mill surface intact.

### **Crevice Assemblies**

Perspex crevice assemblies (PCAs) machined as annular acrylic plastic washers, details of which have been reported elsewhere,<sup>2,4,5</sup> were prepared. Table 2 identifies the various surface conditions of the PCAs, which were polished, ground or lathe turned to varying degrees of surface "roughness". A crevice enhancing, deformable tape was applied to the PCAs in one series (test B). Duplicate test panels for each combination of PCA and alloy surface condition were assembled.

All crevice formers were assembled dry, using an insulated (polyethylene sleeved) titanium

fastener, and tightened to an initial torque of 8.5 Nm (75 in-lbs). The torque was verified immediately prior to exposure. Each specimen was tested to confirm electrical isolation between the titanium fastener and test panel.

Four inter-connected polyethylene tanks (each 375 liter capacity) were used for simultaneous exposure of the 176 test panels. A non-metallic pump was used to recirculate filtered ( $5\ \mu\text{m}$ ), natural seawater constantly refreshed at a rate of 1 to 2 l/min. Temperature control was provided by an auxiliary loop connected to a refrigeration/heating bath. During testing, the mean controlled seawater temperature in the test tanks was  $25.2^\circ\text{C}$ . While filtration removed significant levels of fouling organisms, microbiological species smaller than  $5\ \mu\text{m}$  remained in the seawater. Table 3 provides a summary of the seawater hydrology data for the 60-day test period.

## **Results and Discussion**

### **Crevice Corrosion Initiation Resistance**

Table 4 provides an overall summary of stainless alloy and nickel alloy resistance to crevice corrosion in this series of tests. While some degree of crevice corrosion was incurred by the S31600 control under all eight test conditions, attack of the various proprietary grades was limited to only three test conditions. Initiation data from tests B, G and H, along with baseline data from test A are summarized in Table 5. Included in Table 5 are the approximate times to initiation --- based on in-situ inspections for discoloration or corrosion product buildup at the crevice sites --- and the total number of the four available sites attacked. Also provided in Table 5 are the approximate "corrosion resistance numbers", based on the  $\%Cr + 3.3 \times \%Mo + 16 \times \%N$  equivalents of the alloys.

Effect of Crevice Former Surface Roughness. Regardless of alloy composition, all nine proprietary alloys and the nickel alloy control, N10276, were fully resistant when non-deformable PCA washers (test conditions A, C, D, E and F) were applied to the respective mill surface finishes. In contrast, the S31600 controls exhibited some degree of crevice corrosion susceptibility under all test conditions. The behavior of S31600 in the present 60-day tests is generally consistent with that observed in other similar studies (Table 6). The most significant difference for S31600 is noted in the present tests, where extensive attack was incurred at one site formed by a lathe-turned PCA washer (test F). Because in-situ inspections identified crevice corrosion initiation at this particular site within seven days, the occurrence was not simply a function of the longer exposure duration compared to the proto-test program<sup>4,5</sup> indicated in Table 6. Except for the possibility of some unexplainable overtightening of the crevice washer and/or a "rogue" site, no other factor is readily identifiable. Also indicated in Table 6 are the results of test F repeated by three different participants in a subsequent Round-Robin program. There was no evidence of crevice corrosion of S31600 in the 30-day tests.

Effect of Deformable Crevice Former. As indicated in Table 5, introduction of a deformable tape insert, as in test B, between the otherwise rigid PCA (e.g., condition A), resulted in crevice corrosion of two of the 6% molybdenum-containing austenitics. However, in contrast to S31600 (alloy I) which exhibited attack at three of the four

available sites, susceptibility of alloy IX and alloy VI, in their respective mill-finish conditions, was limited to one or two sites. In addition, these alloys appeared to require somewhat longer times to initiate crevice corrosion than S31600.

**Effect of Surface Grinding (with and without HNO<sub>3</sub> + HF pickling).** Removal of the mill surfaces by grinding the crevice areas to a 120-grit (SiC) finish affected the corrosion resistance of some alloys, but not others. As indicated in Table 5, application of the polished PCA's (same as test A), to ground (test G) and ground plus HNO<sub>3</sub> + HF pickled (test H) specimens did not promote crevice attack of alloys III, V, IX and X within the 60-day test period.

On the other hand, alloys II, VI and VII were found to be susceptible in both surface conditions (tests G and H). The overall incidence of attack for these alloys, with widely varying compositions, was consistently less than the 100 percent incurred by the S31600 controls. Two of the 6% molybdenum-containing austenitics exhibited attack at either 50 percent of the sites on ground (alloy IV) or ground + pickled (alloy VII) specimens. One partially affected site was identified on a surface-ground N10276 control (alloy XI).

#### **Crevice Corrosion Propagation Resistance**

Table 7 provides crevice corrosion propagation data for each of the S31600 control specimens exposed in tests A through H. A summary of propagation resistance for all 11 alloys, again in tests A, B, G and H, is summarized in Table 8. In both Tables 7 and 8, data are provided on the percent affected areas of the susceptible sites and the maximum depths of attack for the indicated test conditions (i.e., alloy/crevice-former surface finish).

As shown in Table 7, S31600 exhibited considerable site-to-site differences in maximum depths of attack. Site-to-site and area-to-area differences of one to two orders of magnitude are not uncommon in crevice corrosion tests conducted in natural seawater. Sites which were only partially affected ( $\leq 15\%$  of area) exhibited the shallowest penetration ( $\leq 0.01$  mm). Penetrations in excess of 0.60 mm were found at all sites in which 100 percent of the nominal crevice area was affected. In two cases (both in test H), penetrations exceeded 2 mm in 60 days.

In the case of the susceptible proprietary alloys, maximum depths of penetration, shown in Table 8, were generally within the overall range measured for the various S31600 controls. In only one case did the maximum depth of penetration for a proprietary alloy exceed that of the corresponding S31600 control; this occurred for alloy VI in test B.

Penetration at the one partially affected site (where initiation was detected between 21 and 28 days) on the ground N10276 control was limited to 0.02 mm. The extent of the attack is consistent with that reported for this alloy, for example, by Kroughman and Ijsseling, in other seawater tests utilizing different crevice formers.

## Discussion

It is apparent from the tests described above that alloy resistance to crevice corrosion can be influenced by a number of factors. As such, results from tests involving only a single set of metallurgical and crevice geometry conditions, for example, cannot be used as absolute indicators of performance under other conditions. Moreover, the foregoing results demonstrate that even alloys with relatively high "pitting/crevice corrosion resistance numbers" (i.e.,  $\% \text{Cr} + 3.3 \times \% \text{Mo} + 16 \times \% \text{N}$ ) can, in a matter of days, incur significant crevice corrosion in natural seawater at ambient temperature when severe crevice geometries are present.

Some inconsistencies in behavior were exhibited by alloys within the same general class. In the case of the "20Cr-6Mo" molybdenum-containing austenitics, for example, all the test specimens were fully resistant in some of the same test conditions, while some alloys incurred attack in others (B, G and H). Only one alloy (III) in this class was resistant to all eight test conditions. Among those alloys exhibiting susceptibility under similar test conditions, e.g., tests G and H, the greatest differences appear to be related more to propagation than initiation behavior.

One factor which may influence this behavior, and which is not covered by the previously mentioned corrosion resistance number, is alloy copper content. Streicher<sup>7</sup>, in his analysis of earlier U.S. Navy<sup>8</sup> and Ocean Thermal Energy Conversion (OTEC)<sup>9</sup> program data, suggested that increased copper content (in stainless-type alloys) increases resistance to breakdown of mill-produced surface oxides, but has an opposite effect when the oxide is removed by surface grinding.

Present results are in agreement with those of Streicher on the negative effect of copper (in the alloy composition) on ground surfaces, but not the positive effect associated with mill-produced surfaces (as indicated by Streicher). For example, while alloy III which reportedly has a nominal copper of 0.2% remained resistant after surface grinding, three other alloys containing about 0.7 to 1.0% copper were susceptible in either or both tests G and H. In addition, a negative effect of increased copper content on crevice corrosion propagation resistance of "20Cr-6Mo" alloys is shown by the increase in maximum depth of attack (Figure 1).

Regarding crevice corrosion initiation resistance of mill processed materials, however, the results indicate that copper was not beneficial. In test B, for example, only alloy VI, which contained the highest (1.01%) copper content of the "20Cr-6Mo" alloys was found to be susceptible to crevice corrosion. Likewise, another high copper-containing (1.20%) alloy (IX), but with higher chromium and nickel than the more typical molybdenum-containing austenitics, also incurred attack in test B. The minimal extent of attack incurred in test B and the total absence of attack for alloy IX in tests G and H suggests that any detrimental effect of copper may be offset to some degree by increasing the other major alloying constituents. It is recognized that stainless alloy corrosion resistance to other environments may benefit from the addition of copper.

**Effect of Biofilm.** Corrosion potential ennoblement of stainless type alloys has been related to crevice corrosion by others<sup>10</sup>. In the present tests, corrosion potentials for resistant specimens, regardless of alloy composition, ranged from +0.247 to +0.331 volts (vs Ag-AgCl/seawater) after 1000 hours in (5 $\mu$ m filtered) seawater. Despite this ennoblement, two specimens of S31600 exhibiting potentials of about 0.310V, and 90 percent of the other alloy specimens, remained fully resistant. As noted previously (Table 7), these resistant S31600 specimens were fitted with the least severe crevice formers (E and F). Related discussion on alloy surface finishes and potential ennoblement in natural and synthetic seawater are found elsewhere.<sup>4,5</sup>

### Summary and Conclusions

A multi-alloy seawater test program has investigated alloy performance over a range of crevice conditions which may be described in as "most severe" (B, G, and H), "moderately severe" (A, C and D) and "least severe" (E and F). Of the nine proprietary alloys tested, only three (III, V and X) were found to be fully resistant to all eight test conditions. For the remaining six proprietary alloys, crevice corrosion was limited to one or more of the three most severe sets of conditions. For these and the S31600 controls, resistance to crevice corrosion was influenced by surface finish and crevice-former geometry. The most severe conditions were created when the crevice former was able to conform to the "contours" of the as-produced mill surface of the alloy (by deformation) and when smooth crevice formers were applied to relatively smooth ground metal. Under certain test conditions, described as "least severe" (E and F), the crevice corrosion resistance of S31600 was comparable with that of higher alloyed materials. Overall, however, all of the proprietary alloys tested offered greater crevice corrosion resistance to more test conditions than the S31600 controls.

In addition to the above, it was found that the test procedure, when followed at different times and/or by different individuals, gives similar results.

Alloy rankings associated with commonly accepted "indices" can change with relatively minor, yet critical, changes in test conditions. Differences in alloy crevice corrosion behavior, within a given class of materials, may also be dependent on copper content, along with the more recognized influences of, for example, Cr, Mo and N.

The test results on the effects of chemical treatment after grinding (case H) are consistent with earlier findings<sup>4</sup> which indicate that HNO<sub>3</sub> + HF pickling does not restore crevice corrosion resistance to the level normally associated with the original mill-produced surface under otherwise identical test conditions. This disparity may be related to surface chemistry and/or surface roughness differences between production and post-production surface treatments.

It is expected that increasing the surface roughness of the crevice-formers applied to ground metal surfaces will enable some or all of the alloys which exhibited susceptibility in this study to "pass" similar seawater tests.

The test results indicate that biofilm ennoblement of stainless alloys alone does not promote crevice corrosion. None of the materials, including the S31600 controls, exhibited any evidence of pitting on boldly exposed surfaces.

LaQue had suggested that some critical degree of tightness equivalent to that of crevices likely to be encountered in particular service should be established" — in contrast to the extreme "tightness" designed to promote, and hence study, crevice corrosion. Since other factors besides tightness influence crevice corrosion, no single geometry can be expected to achieve LaQue's idealistic challenge. Nevertheless, severe test conditions can be used to provide "worst case" benchmarks for alloy-behavior comparisons. The real challenge is to quantify the geometries of crevices which consistently create problems for whole classes of stainless alloys; or conversely, those associated with complete freedom from crevice corrosion so that, where appropriate, they can be "specified" for practical applications. The use of a multi-variable approach to crevice corrosion testing, such as that described here and elsewhere<sup>1-5</sup>, can help bridge the gap between laboratory testing in natural seawater and real-world experience.

### **Acknowledgement**

In addition to the LaQue Center for Corrosion Technology, Inc., the following alloy producers are acknowledged for their participation and support of the test program and publication of the results: Allegheny Ludlum, Avesta-Sheffield, Jessop Steel Company, KRUPP-VDM, and Sumitomo Metal Industries Ltd. The author thanks his colleagues at the LaQue Center who assisted in the conduct of the test program and in the preparation of this paper.

### **References**

1. R.M. Kain, Corrosion, 40 (1984), p. 313.
2. J.W. Oldfield, R.M. Kain, T.S. Lee, Proceedings of Stainless Steel '84 Symposium, Gotenberg, Sweden (1984), p. 205.
3. T.S. Lee & R.M. Kain, "Factors Influencing the Crevice Corrosion Behavior of Stainless Steels in Seawater", CORROSION/83, paper no. 69 (Houston, TX: National Association of Corrosion Engineers, 1983).
4. R.M. Kain, "Effects of Surface Finish on the Crevice Corrosion Resistance of Stainless Steels in Seawater and Related Environments", CORROSION/91, paper no. 508 (Houston, TX: National Association of Corrosion Engineers, 1991).
5. R.M. Kain, "Surface Treatments Affecting the Crevice Corrosion Resistance of Stainless Steels", Proceedings of International Conference on Stainless Steels, The Iron & Steel Institute of Japan, Chiba, Japan, 1991, p. 38.



6. J.M. Krougman, F.P. Ijsseling, Proceedings 5th International Congress on Marine Corrosion & Fouling, 1980, p. 214.
7. M.A. Streicher, Materials Performance, 22 5 (1983), p. 48.
8. H.P. Hack, Materials Performance, 22 6 (1983), p. 24.
9. R.M. Kain, "Crevice Corrosion and Metal-Ion Concentration Cell Corrosion Resistance of Candidate Materials for OTEC Heat Exchangers, Part I and II", Argonne National Laboratory/U.S. Dept. of Energy, ANL/OTEC-BCM-022 (1981).
10. A. Mollica et. al., Corrosion, 45 (1989), p.48.
11. F.L. LaQue, Materials Performance, 21 4 (1982), p. 18.

**Table 1**

**Identification of Materials Tested**

Alloy Code	UNS Designation	Weight Percent (actual unless indicated nominal)									
		Cr	Ni	Mo	N	Cu	Si	Mn	C	S	other
I	S31600	16.28	10.08	2.08	0.038	0.40	0.42	1.24	0.04	<0.001	
II	S31600	25.72	8.14	3.28	NR	1.88	0.42	0.88	0.022	0.008	0.20 Nb+Ti
III	N08987 (nom.)	21	24.5	8.5	0.18	0.2	1 max.	2 max.	0.35 max.	0.04 max.	
IV	S31204	20.00	18.24	8.04	0.188	0.72	0.38	0.42	0.018	0.001	
V	S32804 (nom.)	24	22	7.3	0.20	0.45	0.80 max.	3.00	0.02 max.	0.01 max.	
VI	none	20.13	24.85	8.21	0.14	1.01	0.48	0.85	0.014	0.001	
VII	N08988	20.80	24.85	8.48	0.187	0.83	0.45	0.84	0.018	0.002	
VIII	none	24.20	17.70	4.34	0.480	0.53	0.03	8.14	0.012	0.004	0.17 Nb
IX	N08991	28.75	21.85	8.50	0.182	1.80	0.04	1.58	0.008	0.003	
X	N08028	22.58	81.05	15.40	NR	NR	0.03	0.13	0.002	0.003	0.14 V
XI	N10278	15.85	58.85	18.10	NR	NR	0.05	0.20	0.003	0.005	0.20 V, 3.82 W, 8.25 Fe

NR = not reported  
Other = balance is Fe unless indicated

**Table 2**

**Identification of Alloy-Crevice Former Conditions**

Test Code	Alloy Condition	PCA Washer Finish
A	AR-mill*	0.05μ Alumia polished
B	AR-mill	above + tape insert
C	AR-mill	600 grit SiC
D	AR-mill	120 grit SiC
E	AR-mill	60 grit SiC
F	AR-mill	Lathe turned (~200 micro-inch)
G	Ground 120 SiC	0.05μ Alumia polished
H	Ground + Pickled**	0.05μ Alumia polished

\* AR-mill: As-Received Mill-Finish

\*\* 10 minutes in 15% $\text{HNO}_3$  + 6% $\text{HF}$  at 40°C

Table 3

## Raw Seawater Supply Hydrology

<u>Temperature</u> <u>°C</u>	<u>Salinity</u> <u>(g/L)</u>	<u>Chloride</u> <u>(g/L)</u>	<u>Sulfate</u> <u>(g/L)</u>	<u>pH</u>
20.0-28.5	32.9-36.7	18.2-20.3	2.6-2.9	7.8-8.0

Table 4

## Identification of Metallurgical/Geometrical Test Conditions Which Promoted Crevice Corrosion of Various Alloys in 60-Day Natural Seawater Tests

<u>Alloy*</u> <u>Code</u>	<u>Alloy Resistance (R) or Alloy Susceptibility (S)</u> <u>for Indicated Test Condition**</u>							
	<u>A</u>	<u>B</u>	<u>C</u>	<u>D</u>	<u>E</u>	<u>F</u>	<u>G</u>	<u>H</u>
I	S	S	S	S	S	S	S	S
II	R	R	R	R	R	R	S	S
III	R	R	R	R	R	R	R	R
IV	R	R	R	R	R	R	S	R
V	R	R	R	R	R	R	R	R
VI	R	S	R	R	R	R	S	S
VII	R	R	R	R	R	R	R	S
VIII	R	R	R	R	R	R	S	S
IX	R	S	R	R	R	R	R	R
X	R	R	R	R	R	R	R	R
XI	R	R	R	R	R	R	S	R

\* see Table 1 for alloy identification

\*\* see Table 2 for alloy/crevice-former surface finish

**Table 5**  
**Summary of Alloys Resistance to Crevice Corrosion**  
**Initiation Under the Indicated Test Conditions**

Alloy Code*	CRN <sup>1</sup>	Earliest Visual <sup>2</sup> Detection (days)				Number of Sites <sup>3</sup> Attacked After 60 Days			
		A**	B	G	H	A	B	G	H
I	24	7-10	<3	<3	3-5	3/4	3/4	4/4	4/4
II	37	OK	OK	ND <sup>3</sup>	ND <sup>3</sup>	0	0	1/4	3/4
III	45	OK	OK	OK	OK	0	0	0	0
IV	43	OK	OK	ND <sup>3</sup>	OK	0	0	2/4	0
V	56	OK	OK	OK	OK	0	0	0	0
VI	43	OK	5-7	3-5	3-5	0	2/4	2/4	2/4
VII	45	OK	OK	OK	3-5	0	0	0	2/4
VIII	46	OK	OK	5-7	7-10	0	0	2/4	4/4
IX	51	OK	7-10	OK	OK	0	1/4	0	0
X	73	OK	OK	OK	OK	0	0	0	0
XI	69	OK	OK	21-28	OK	0	0	1/4	0

1 - CRN - Corrosion Resistance Number ( $\%Cr + 3.3 \times \%Mo + 16 \times \%Ni$ )

2 - based on periodic in-situ inspections

3 - 4 maximum

\* - see Table 1 for alloy identification

\*\* - see Table 2 for alloy/crevice-former surface finish

**Table 6**  
**Comparison of Results from Three Different Programs**  
**Conducted for S31600 (2B mill) in Natural Seawater**

PCA Surface	Percent of Sites Attacked					
	30-day Tests				60-Day	
	Round Robin Test Results				Test	
	Ref. 4,5	No. 1	No. 2	No. 3	No. 4	Joint Program
Polished (A)	50	50	50	75	50	75 (50)*
600-grit SiC (C)	50	--	50	75	50	100 (50)*
120-grit SiC (D)	50	--	--	--	--	100 (25)*
60-grit SiC (E)	0	--	--	--	--	25 (0)*
Lathe-turned (F)	0	--	0	0	0	25

\* (%) exclusive of sites with  $\leq 15$  percent affected area and  $< 0.01$  mm penetration

**Table 7**

**Summary of Crevice Corrosion Propagation Results for S31600**

<u>Test Code</u>	<u>Crevice Site</u>	<u>Propagation at Indicated Crevice Site</u>	
		<u>Affected Area (%)</u>	<u>Maximum Depth of Attack (mm)</u>
A	1/2	100/0	1.67/0.00
	3/4	100/15	1.3/<0.01
B	5/6	100/100	0.16/1.21
	7/8	0/100	0.00/1.47
C	9/10	100/10	1.65/<0.01
	11/12	<10/100	<0.01/<0.01
D	13/14	100/<5	1.10/<0.01
	15/16	<5/<5	<0.01/<0.01
E	17/18	0/0	0.00/0.00
	19/20	<5/0	<0.01/0.00
F	21/22	0/0	0.00/0.00
	23/24	0/100	0.00/1.17
G	25/26	100/100	1.03/0.82
	27/28	10/100	<0.01/1.55
H	29/30	<5/100	<0.01/2.17
	31/32	<5/100	<0.01/2.14

Table 8

**Summary of Alloys Resistance to Crevice Corrosion  
Propagation Under the Indicated Test Conditions**

Alloy Code*	Percent Affected Crevice Area (Range for Attacked Sites)				Maximum Depth of Penetration (mm)			
	A**	B	G	H	A	B	G	H
I	15-100	100	10-100	<5-100	1.67	1.47	1.55	2.17
II	0	0	95	30-75	0.00	0.00	0.88	0.27
III	0	0	0	0	0.00	0.00	0.00	0.00
IV	0	0	40-70	0	0.00	0.00	0.27	0.00
V	0	0	0	0	0.00	0.00	0.00	0.00
VI	0	100	100	90-100	0.00	2.01	1.01	1.68
VII	0	0	0	65-100	0.00	0.00	0.00	0.72
VIII	0	0	50-85	40-70	0.00	0.00	0.19	0.09
IX	0	100	0	0	0.00	0.15	0.00	0.00
X	0	0	0	0	0.00	0.00	0.00	0.00
XI	0	0	30	0	0.00	0.00	0.02	0.00

\* refer to Table 1 for alloy identification

\*\* refer to Table 2 for alloy/crevice-former surface finish

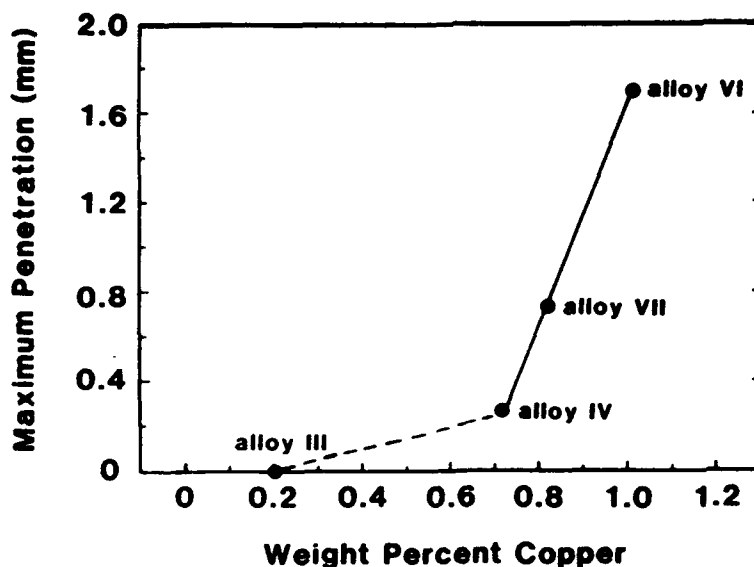


Figure 1. Effect of copper content on crevice corrosion propagation resistance of "20Cr-6Mo" alloys after removal of the original mill surface finish, with or without HNO<sub>3</sub> + HF pickling treatment.

# Modelling Crevice Corrosion of Fe-Cr-Ni-Mo Alloys in Chloride Solutions

Per Olav Gartland<sup>1</sup>  
SINTEF Corrosion Center  
N-7034 Trondheim, NTH

## Abstract

A mathematical model of crevice corrosion for Fe-Ni-Cr-Mo alloys in chloride solutions has been created. The model differs from previously published model in several ways of which the three most important ones are the inclusion of the potential variation, effects of temperature variations and the fact that it is a model of the initiation as well as the propagation stage.

The model is basically a one-dimensional model of galvanic corrosion, where the material in the internal crevice region has different electrochemical properties from that of the outside region. Relevant polarization curves for the inside as well as the outside of the crevice is based on experimental data in simulated crevice solutions. The model is run in a time stepping loop where calculation of the potential, the current density, the mass transport and the chemical equilibria for some 16 species is done repeatedly at short time intervals.

Model results compared to experiments with high alloyed stainless steels show very good agreement with respect to initiation, propagation and repassivation behaviour.

## Introduction

Crevice corrosion is known to be one of the most detrimental corrosion forms for stainless steels and nickel alloys in seawater. This has lead to a large variety of test methods all aiming at a proper characterization of the actual material in terms of crevice corrosion resistance. Whatever the method there seems to be a common experience that most methods suffer from a large scatter. This has frequently been related to the key role played by the geometry of the crevice, in particularly by the crevice width. However, there are also many other factors which may be important.

During the last 15 years there has been a few studies aiming at a better understanding of the crevice corrosion susceptibility using mathematical modelling. Initiation as a function of time has been studied by Oldfield and Sutton<sup>1,2</sup>, by Bernhardsson et al<sup>3,4</sup> and by Watson and Postlethwaite<sup>5</sup>, while criteria for steady state corrosion in occluded areas where studied by Galvele<sup>6</sup> and by Edwards<sup>7</sup>.

The work with the present model started in 1987, motivated by the previous studies and with the aim of creating a model that could simulate the behaviour of a crevice specimen from the initiation phase to the propagation phase, and where the potential variation along the crevice was included. The first presentation of the model was given in 1988<sup>8</sup>, and later on with some results of initiation studies with various stainless steels<sup>9,10</sup> and nickel alloys<sup>11</sup>. Temperature effects were included in the model and presented at Eurocorr '91<sup>12</sup>. In the present paper the purpose is to present the model with most of its details, assumptions, input requirements and possibilities for simulation. Some examples of experimental verification are given, but rather shortly. A more complete documentation on the model verification will be the topic of a forthcoming paper.

---

<sup>1</sup>Present address: CorrOcean as, Teglgården, N-7005 Trondheim, Norway

### Basic outline of the model

The model is based on a five step scheme of crevice corrosion:

- I. Oxygen depletion in the crevice
- II. Decrease of pH and increase of the chloride concentration
- III. Permanent breakdown of the oxide film when the pH reaches a critical value
- IV. Crevice corrosion propagation
- V. Repassivation

The crevice is one-dimensional, but the gap profile can be arbitrary. Like most model developments the present model relies on the assumption that the transport in the electrolyte can be described in terms of the dilute solution theory. Another common assumption also made here, is that all chemical reactions occur instantaneously with respect to the time scale of the steps in the transport calculations which are typically of the order a few seconds.

The model is not an *a priori* model, but more an engineering type model where all the various processes inside the crevice are calculated to the best possible quantitative level using experimental data. Conceptually, the model may be regarded as a model of galvanic corrosion, where the material in the internal crevice region has different corrosion properties from that of the outside region. When the oxygen is depleted in the crevice region, a net galvanic current will flow from the crevice region to the outer area. Unlike most galvanic corrosion modelling, however, the crevice problem is far more complicated due to the changes in the crevice electrolyte, caused by mass transport and chemical reactions as illustrated in Fig. 1.

Using the galvanic corrosion approach on the crevice corrosion problem means that we have a problem where most of the parameters depend on the time  $t$  as well as on the position  $x$  along the crevice. This is handled in a time stepping approach, where the galvanic corrosion problem is solved at fixed time points using boundary conditions and electrolyte conductivities relevant for that point of time. Between each solution of the galvanic corrosion problem, separate calculations are carried out to take account of the changes in the electrolyte concentrations. Thus, the entire calculation scheme consists of various computational steps which must be carried out repeatedly in a given order, as shown in the flow diagram of Fig. 2.

The first step in the calculation loop is to calculate the potential and current density distribution at a fixed time  $t = t_0$  (first time  $t = 0$ ), based on the input anodic and cathodic overvoltage curves. The production rates  $R_i$  of the various species can also be calculated at  $t = t_0$  when the current density is known. The mass transport calculation requires input from the potential variation and species production rates and provide as output a slightly modified concentration profile for all species considered going from time  $t_0$  to time  $t_0 + \Delta t$ . The next calculation step is to modify the species concentrations at  $t_0 + \Delta t$  with respect to hydrolysis and other chemical equilibria. The equilibrium concentrations are the basis for calculating the ionic strength  $I$ , which is defined as:

$$I = \frac{1}{2} \sum z_i^2 c_i \quad (1)$$

where  $z_i$  and  $c_i$  are the charge and the concentration of species "i". As will be shown below the ionic strength is the key parameter for calculating appropriate values of the mobility  $u_i$  and the resistivity  $\rho$  and also for calculating the pH for a given  $H^+$  concentration, i.e.  $pH(I, [H^+])$ .

As long as  $t < t_{\max}$ , where  $t_{\max}$  is the total simulation time, the calculations will go on in this time stepping approach. For each new calculation of the potential and current density distribution the overvoltage curves at any position inside the crevice are adjusted according the pH-profile calculated in the preceding cycle.

As shown in Fig. 2 the model input is the alloy composition, the bulk pH and  $\text{Cl}^-$  concentration, the crevice length and width, the area ratio, and the initial conditions, as well as overvoltage curves  $E(i, \text{pH})$ . The output is the resistivity  $\rho$ , the ionic strength  $I$ , the concentration of each species  $C_i$ , the pH, the potential  $E$ , the anodic current density  $i_a$  and the galvanic current density  $i_g$ . All these quantities are given at various crevice depths  $x$  at the end of the calculation when  $t = t_{\max}$ .

### Some model details

#### Calculation of potential variations

Following Fu and Chang<sup>13</sup> it can be shown that it is possible to separate the transport of charge and mass, with the result that we have a potential variation in the crevice following Ohms law:

$$i_g = -F^2 \sum z_i^2 u_i c_i \Delta E = -\sigma \Delta E \quad (2)$$

where  $F$  is Faradays constant and  $\sigma$  the conductivity. When this equation is combined with proper boundary conditions a solution of  $E(x)$  and  $i(x)$  can be found based on the finite difference method, where, as shown in Fig. 3, the continuous electrolyte in the crevice is divided into a number of finite cells. Within each cell the properties are assumed to be constant. This allows the calculation of the resistivity of the electrolyte within each cell and in turn the resistance  $R_{ij}$  between the midpoints of two neighbouring cells  $i$  and  $j$ . The nonlinear boundary conditions create a system of nonlinear equations which is solved by linearization and iteration.

The boundary conditions for the inside of the crevice are based on experimental polarization curves for the actual material, obtained in solutions of various strength. Fig. 4 shows the overvoltage curves used for modelling UNS S31254. These curves have been constructed on the basis of measured polarization curves at various concentrations, represented by the pH-values of 0.5, -0.34, -1.0 and -1.3 respectively. In this process the curves have been smoothened to a piecewise linear representation on the semi-log scale, a mathematical representation which is easily entered into the model computer program. Details of the experiments are given elsewhere<sup>10</sup>. The outside of the crevice, the cathodic area, can be represented by a proper cathodic polarization curve, or it can be kept at a constant potential, thereby simulating a crevice sample connected to a potentiostat.

#### Mass transport

With the potential variation found separately, the concentration variation of any species  $c_i$  can be calculated from the equation below:

$$c_i(t + \Delta t) = c_i(t) + \Delta t \left[ z_i F \left( \frac{du_i}{dx} c_i \frac{dE}{dx} + u_i \frac{dc_i}{dx} \frac{dE}{dx} + u_i c_i \frac{d^2 E}{dx^2} \right) + \frac{dD_i}{dx} \frac{dc_i}{dx} + D_i \frac{d^2 c_i}{dx^2} + R_i \right] \quad (3)$$

This equation is the one dimensional representation of the general mass transport equation allowing the



calculation of the spatial variation of any species at time  $t + dt$ , based on the knowledge of the spatial variation at time  $t$ . Again, the finite difference approach is used to find values for the single and double derivatives of the variables. The production rate  $R_j$  for a given species is a result of anodic dissolution of alloy constituents, chemical reactions in the electrolyte or a combination of both. For an alloy constituent  $j$  it can be shown that the production rate is

$$R_j = \frac{i_j y_j}{wF \sum z_j y_j} \quad (4)$$

Because of chemical reactions like hydrolysis an alloy constituent may occur as a part of several species, like chromium in the species  $\text{Cr}^{3+}$ ,  $\text{Cr}(\text{OH})^{2+}$ ,  $\text{CrCl}^{2+}$  etc. The production rate for these species is obtained by multiplying  $R_j$  by a distribution factor  $f_i$ , where  $f_i$  is obtained from equilibrium calculations.

### Chemical equilibria

In the crevice electrolyte a large number of different electrochemical reactions take place. These are reactions between metal ions and water (hydrolysis) and between metal ions and chloride ions (incomplete dissociation). Bernhardson et al<sup>4</sup> investigated the chemical stability of some 50 soluble species and 15 solid products in a 3 M concentrated solution representing the crevice electrolyte of Fe-Ni-Cr-Mo alloys. From their result and the tables of compiled equilibrium constants it was evident that many of the reactions could be neglected.

In the present model the reactions given in Table 1 are included. All together these reactions imply that we have to handle 16 different species. The equilibrium values of these species are calculated from the eight equations for the equilibria plus eight equations for the mass conservation of Cr, Fe, Ni, Na, Cl, Mo, H and O. The total of 16 non-linear equations are solved by linearization and iteration.

### pH corrections in strong salt solutions

The pH of a solution is defined as  $\text{pH} = -\log a_{\text{H}} = -\log([\text{H}^+] \gamma_{\text{H}})$  where  $a_{\text{H}}$  is the  $\text{H}^+$  ion activity,  $[\text{H}^+]$  the  $\text{H}^+$  ion concentration in moles per kg solvent (here water) and  $\gamma_{\text{H}}$  the  $\text{H}^+$  ion activity coefficient. The activity concept has been introduced to account for the non-ideal behaviour of strong solutions, in which  $\gamma_{\text{H}}$  increases strongly due to ion solvent interactions.

Data on  $\gamma_{\text{H}}$  for the complex salt solution in the crevice are not available. However, measurements of the pH lowering in various single salt solutions, as shown in Fig. 5, indicate that the effect depends on the ionic strength of the solution but not very much of the type of salt. The solid line in Fig. 5 is therefore assumed to be valid for the complex salt solution in the crevice. The ionic strength  $I$  in figure 5 is the apparent ionic strength, i.e. the ionic strength calculated assuming completely dissociated solutions. In the model this correction curve is used to calculate the pH in the solution with  $[\text{H}^+]$  and  $I$  as input.

### Mobility and diffusion constants at various solution strengths

In dilute solutions the diffusion constant  $D$  and the mobility  $u$  for a given species are related through the Nernst - Einstein relation:

$$D = RTu \quad (5)$$

In the model this equation is used to calculate the mobilities in dilute solutions based on the corresponding diffusion constants given by Bernhardson et al<sup>4</sup>. In strong solutions the relation is no longer valid. The ion mobility is strongly reduced in strong solutions. This is reflected in Fig. 6 where the relative equivalent conductivity of a number of single salt solutions is given as a function of the (apparent) ionic strength. Again, we find that the changes are related mainly to the ionic strength of the solution and not so much to the type of salt. Assuming the transport numbers for the negative and the positive ions involved to be negligibly affected by the solution strength the decay curve of Fig. 6 becomes a decay curve for the single ion mobilities as well, as is assumed in the present model.

The diffusion constants are less sensitive to concentration changes than the mobility of the same species. Data in Robinson and Stokes<sup>14</sup> book indicate that in salt solution with  $\text{CaCl}_2$  or  $\text{NaCl}$  there is a negligible reduction of the diffusion coefficient. These data are limited to 4 M solutions. In the model we use the diffusion coefficients for dilute solutions at all concentrations.

### Temperature effects

The strongest effect of a temperature change is on the internal polarization curves. Based on measurements in the temperature range 10 - 45 °C one observed that the loss of passivity both at high and low potentials occurred at a higher pH value when the temperature increased. In the modelling with UNS S31254 it was found to be a reasonable temperature correction to use the same set of curves as shown in Fig. 4 for a wide range of temperatures, but change the critical pH values in dependence of the temperature according to the following simple linear relation:

$$pH(T_c) = pH(35) - 0.0375[pH(T_c) - pH(35)] \quad (6)$$

The mobility and diffusion coefficients increase with increasing temperature. In the model a simple linear increase is assumed, with the absolute values increasing by a factor of two from 10 °C to 60 °C. Temperature corrections have not been included in the model for the equilibrium constants nor the pH corrections in strong salt solutions, simply because relevant data have not been found.

### Salt layer formation in the crevice

When the model is run past the initiation stage and into the propagation stage the current density increases rapidly, and hence also the ion concentration inside. The metal chloride solutions have, however, limited solubility and salts will precipitate at the metal surface. The salt film can be rather thin, of the order a hundred Angstrom or less, but it has a very high ohmic resistance by which it effectively reduces the current density at the surface<sup>15</sup>. In fact, the salt film may act as the mechanism that regulates the current density to a value where ion production rates are in balance with the transport rates out of the crevice. In the model this mechanism is assumed and implemented in the way that a damping factor is multiplied with the current density of the curves in Fig. 4. The regulating mechanism is made such that the damping factor decays exponentially with the excess concentration above 9.5 N. This is mathematically a very efficient

regulation mechanism that is believed to represent the most important effect of a salt film. The saturation concentration of 9.5 N is based on measurements with dissolved stainless steels by Hakkarainen<sup>16</sup>. In the model the salt layer damping mechanism becomes very important at high potentials, from about 200 mV SCE and upwards. At lower potentials saturation may not always occur due to the limited driving voltage, and the regulating mechanism will be the ohmic drop.

### Model verification

Any model of this kind has to be verified, which normally means that one compares the results from the model with experimental data. For the present model some studies have been done to verify different aspects of the model, of which some have already been published<sup>10-12</sup>. Without going into experimental details we shall here give a few examples of the model predictions in comparison to experimental data.

#### Crevice electrolyte composition

We have ourselves not made any attempt to measure the electrolyte composition, as this is very difficult without disturbing the crevice corrosion process. We have instead found some data published by Suzuki et al<sup>17</sup>, who measured the composition of the anolyte in artificial pits on stainless steels with different Mo content. The present model was run with AISI 316 until the pH at the crevice bottom was similar to the measured value. The measured and the calculated ion concentrations are compared in Table 2. The agreement is fairly good for most species, the largest deviation is observed for the chromium ion. In Fig. 7 the pH is shown as a function of the total  $\text{Cl}^-$  concentration for the stainless steels AISI 304, AISI 316 and 18Cr16Ni5Mo. Again there is a good agreement between model and measurements, with a maximum deviation of 0.25 pH units for the steel with the largest Mo-content. The figure also shows that we would not get this good agreement without correcting the pH for the effects of the salt concentration.

#### Initiation/repassivation temperatures.

It has become quite common to characterize the crevice corrosion resistance of stainless steels and nickel alloys in terms of the critical crevice temperature (CCT). Various techniques are applied to measure CCT values, the most common one being the ASTM G-48B  $\text{FeCl}_3$ -test and modifications thereof. At SINTEF a somewhat different method has been used, based on a potentiostatic control of the potential and using a 3 % NaCl-solution. The CCT values obtained with this technique are typically some 20 °C higher than with the  $\text{FeCl}_3$  method, but the materials show a similar ranking. The SINTEF method has the advantage that the crevice corrosion initiation is easily observed as a strong increase of the anodic current when the specimen switches from the passive to the active state.

Fig. 8 shows the results of an experiment with UNS S31254 in which the temperature is first increased stepwise until initiation at 60–64 °C, then reduced until repassivation. The observed hysteresis is a relatively recently observed phenomenon<sup>12</sup>. The repassivation temperature is also very dependent on the external potential level, as shown in Fig. 9. The model results simulating the initiation/repassivation is shown in Figs 10–12. The agreement is indeed remarkable, also when the effect of the potential is considered. Both the model and the experiments show that the repassivation temperature is lowered when the external potential is lowered. This is related to the shape of the anodic polarization curves, and how they change with the temperature and potential. At an outside potential of 600 mV SCE, the potential at the crevice bottom is typically in the range –100 to 300 mV SCE. At the highest potential in this range the anodic polarization curves show that passivation is the normal state when the temperature is below about 35 °C in saturated solution. When the outside potential is lowered to e.g. 0 mV, the potential at the crevice bottom will be in the range –300 to –200 mV SCE. Here, the active peak on the anodic polarization curve exists for temperatures as low as 10 °C. In the initiation/repassivation simulations above

the crevice gap was initially 0.2  $\mu\text{m}$ . Variation of the crevice gap up to 1  $\mu\text{m}$  is found to have a moderate effect on the initiation and repassivation temperatures, but the hysteresis and the effect of the potential still remain.

### Attack profiles

In the propagation stage the initial crevice profile changes with the time in proportion to the local current density along the crevice. The attacks are located relatively close to the crevice mouth, with a short passive "channel" between the crevice mouth and the onset of active corrosion. The length of this "channel" varies with the temperature and also with the time. Fig. 13 shows calculated and measured attack profiles on the material UNS S31254 at different temperatures after about 100 hours of propagation. The experimental data are from the Ph.D. thesis of Stein Valen<sup>21</sup>. Good agreement is observed, in particular for the 40 °C curves. It is a clear tendency for both experimental and calculated peaks to move closer to the crevice mouth with increasing temperatures.

### Conclusions

An advanced model for simulating crevice corrosion initiation, propagation and repassivation with stainless steels or nickel alloys in chloride solutions have been presented. The model is unique in three ways. It is the first model that covers both the initiation phase and the propagation phase. It is the first model that includes the potential as an important parameter from the very beginning. And it is the first model that includes the effect of temperature in such a way that it is possible to simulate initiation, propagation and repassivation as a function of the temperature.

The model is shown to compare reasonably well with experimental data on the crevice electrolyte composition, the crevice corrosion initiation and repassivation temperatures and the attack profiles created in the propagation stage.

### Acknowledgement

Financial support during the development of the model from SINTEF, the Norwegian Council for Scientific and Industrial Research (NTNF) and Avesta AB is gratefully acknowledged.

### References

- 1 J.W. Oldfield and M.H. Sutton: "Crevice Corrosion of Stainless Steels. I. A Mathematical Model". Br. Corros. J., Vol. 13, no. 1, 1978, p 13.
- 2 J.W. Oldfield and W.H. Sutton: "Crevice Corrosion of Stainless Steels. II. Experimental Studies". Br. Corros. J., Vol 13, no. 3, 1978, p 104.
- 3 S. Bernhardsson, L. Eriksson, J. Oppelstrup, I. Puigdomenech and T. Wallin: "Crevice Corrosion of Stainless Steels, Calculations of Concentration and pH Changes". Proc. 8th Int. Congress on Met. Corros., Mainz, 1981, 193.
- 4 S. Bernhardsson, L. Eriksson, J. Oppelstrup, I. Puigdomenech and T. Wallin: "A Model for the Initiation of Crevice Corrosion of Stainless Steels in Chloride Environment". Proc. 9th Scandinavian Corrosion Congress, Copenhagen, 1983.
- 5 M. Watson and I. Postlethwaite: "Numerical Simulation of Crevice Corrosion of Stainless Steels and Nickel Alloys in Chloride Solutions", Corrosion Vol. 46, No. 7, 1990.

- 6 J.R. Galvele: "Transport Processes and the Mechanism of Pitting of Metals". J. Electrochem. Soc., Vol. 123, No. 4, 1976, p. 464.
- 7 R.A.H. Edwards: "A Simple Mass-transport Analysis of Localized Corrosion". Paper at "The International Conference on Localized Corrosion", Orlando, Florida, June, 1987.
- 8 P.O.Gartland: "A Mathematical Model of Crevice Corrosion for Fe-Ni-Cr-Mo Alloys in Chloride Solutions", Research Symposium Paper at NACE CORROSION-88, St. Louis, 1988.
- 9 P.O.Gartland, R.Holthe and E.Bardal: "Evaluating Crevice Corrosion Susceptibility from Testing in Simulated Crevice Electrolytes and Mathematical Modelling", 11th Scandinavian Corrosion Congress, Stavanger, 1989.
- 10 P.O.Gartland and S.Valen: "Crevice Corrosion of High-Alloyed Stainless Steels in Chlorinated Seawater. Part II, Aspects of the Mechanism", Paper no. 511, NACE CORROSION-91, Chincinnati, 1991.
- 11 B.A.Shaw, P.J.Moran and P.O.Gartland: "The Role of Ohmic Drop in the Initiation of Crevice Corrosion on Alloy 625 in Seawater", Corrosion Science, Vol. 32, No. 7, 1991, p 707.
- 12 S.Valen and P.O.Gartland: "Critical Temperatures for Crevice Corrosion of High-Alloyed Stainless Steels in Seawater", EUROCORR '91, Budapest, 1991.
- 13 J.W. Fu and S. Chan: "A Finite Element Method for Modeling Localized Corrosion Cells". Corrosion 40, 1984, p 540.
- 14 R.A. Robinson and R.H. Stokes: "Electrolytic Solutions". 2nd ed., Butterworths, London, 1959.
- 15 H.S. Isaacs: "The Behaviour of Resistive Layers in the Localized Corrosion of Stainless Steel", J. Electrochem. Soc, Vol.120, No.11, Nov. 1973, p 1456.
- 16 T. Hakkarainen.: "Electrochemical Conditions inside Growing Corrosion Pits in Stainless Steel". Paper at "The International Conference on Localized Corrosion", Orlando, Florida, June, 1987.
- 17 T. Suzuki., M. Yamabe and Y. Kitamuras: "Composition of Anolyte within Pit Anode of Austenitic Stainless Steels in Chloride Solution". Corrosion, Vol. 29, No. 1, 1973, p 18.
- 18 Y. Hisumatsu: "Pitting Corrosion of Stainless Steels in Chloride Solutions", in Passivity and Its Breakdown on Iron and Iron Base Alloys, USA-Japan Seminar, NACE publication, 1976, p. 99.
- 19 J. Mankowski and Z. Szklarska-Smialowska: "Studies on Accumulation of Chloride Ions in Pits Growing during Anodic Polarization". Corrosion Sci., Vol. 15, 1975, p 493.
- 20 Landholt & Bernstein: Zahlenwerte und Funktionen, II. Band, 7. Teil, Springer Verlag, 1960.
- 21 S. Valen: "Initiation, Propagation and Repassivation of Crevice Corrosion of High-Alloyed Stainless Steels in Seawater", thesis at Department of Materials and Processes, Norwegian Institute of Technology, 1991.

# Nomenclature

$R_i$	production rate of species $i$	$u_i$	mobility of species $i$
$t$	elapsed time	$D_i$	diffusion constant of species $i$
$I$	ionic strength	$y_i$	molar fraction of element $i$ in the alloy
$z_i$	charge of species $i$	$w$	crevice gap profile
$c_i$	concentration of species $i$	$x$	distance from crevice mouth
$E$	potential	$f_i$	distribution factor of an element $i$ among various species
$\rho = 1/\sigma$	resistivity of electrolyte	$a_H$	$H^+$ ion activity
$i_a$	anodic current density	$\gamma_H$	$H^+$ ion activity coefficient
$i_g$	galvanic current density	$T$	absolute temperature
$F$	Faradays constant	$T_C$	temperature on the Celcius scale
$R_{ij}$	resistance between two neighbouring crevice elements $i$ and $j$	$R$	gas constant

Table 1. Chemical Equilibria

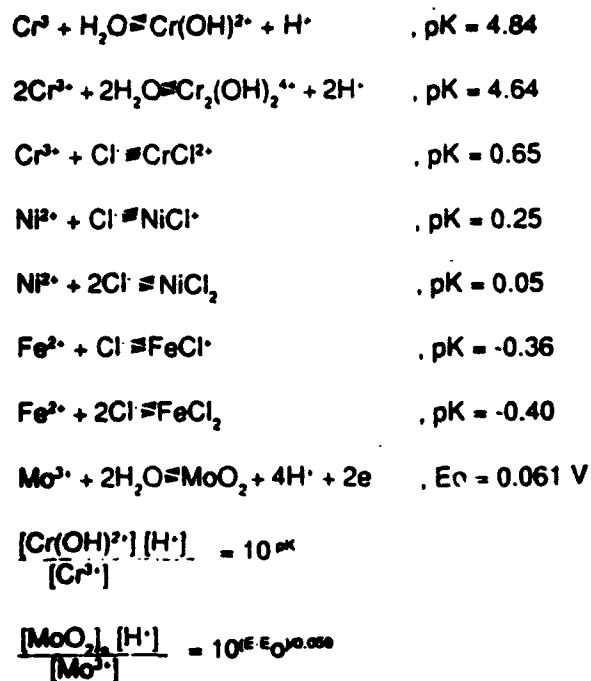


Table 2. Ion concentrations in an occluded cell of 316 ss when the pH has dropped to 0.1.

	Ion concentration (N)	
	Measured (Ref. 17)	Calculated
$\text{Cl}^-$	6.47	5.40
$\text{Fe}^{2+}$	4.30	4.14
$\text{Cr}^{3+}$	1.50	0.78
$\text{Ni}^{2+}$	0.68	0.42
$\text{Mo}^{3+}$	0.14	0.18
$\text{Na}^+$	0.08	0.007

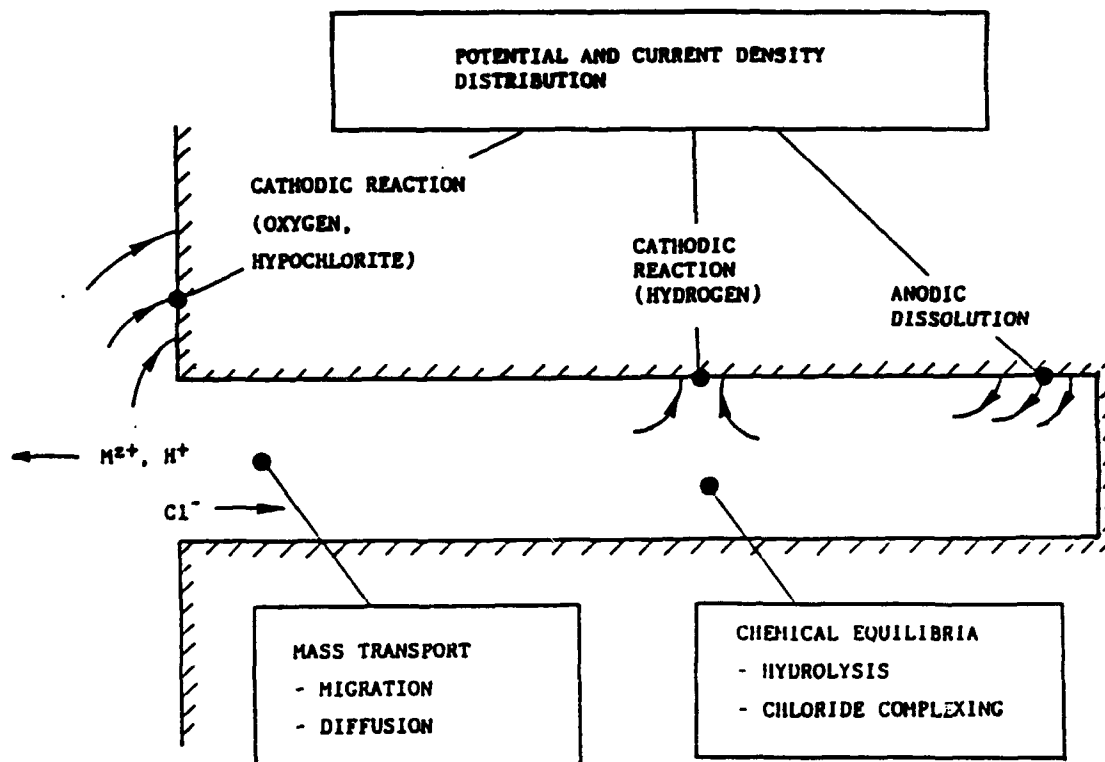


Figure 1. Illustration of the crevice as a galvanic problem, with mass transport and chemical reactions as complicating factors.

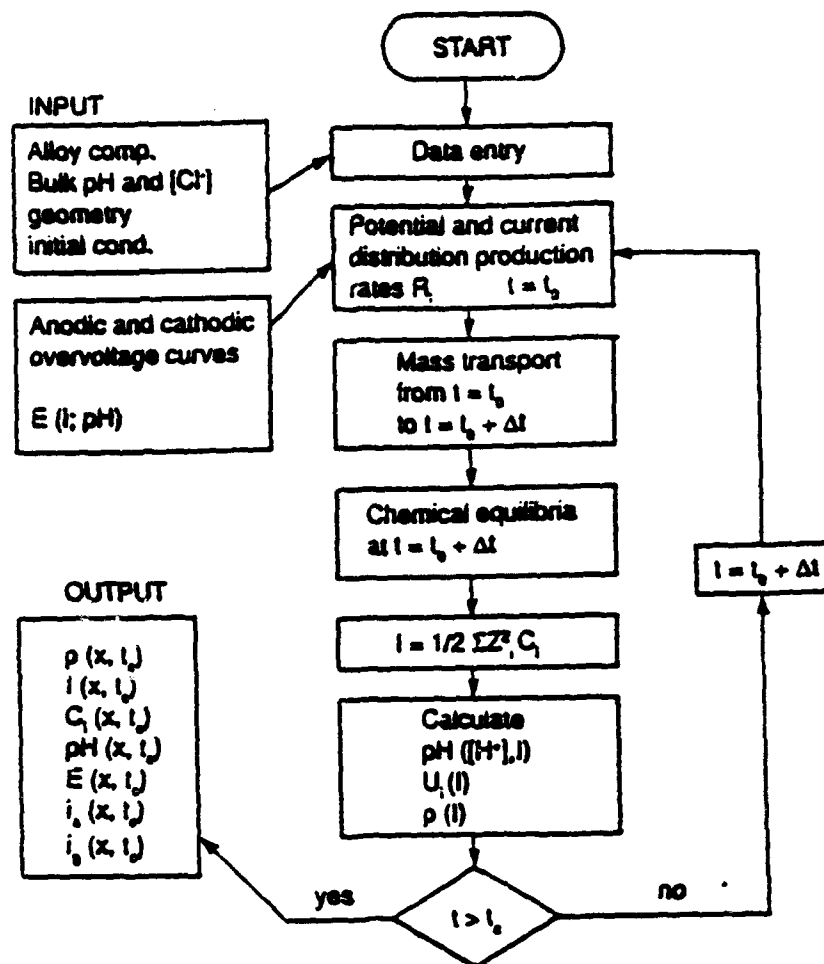


Figure 2. Flow chart of the mathematical model.

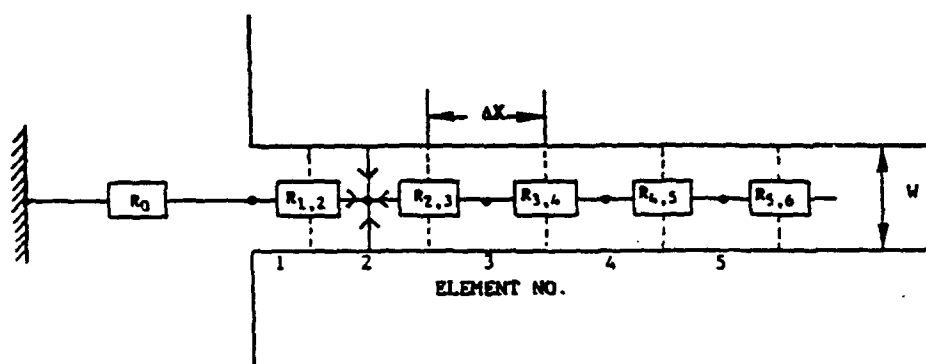


Figure 3. Illustration of the crevice as a chain of finite resistors in the finite difference approximation.



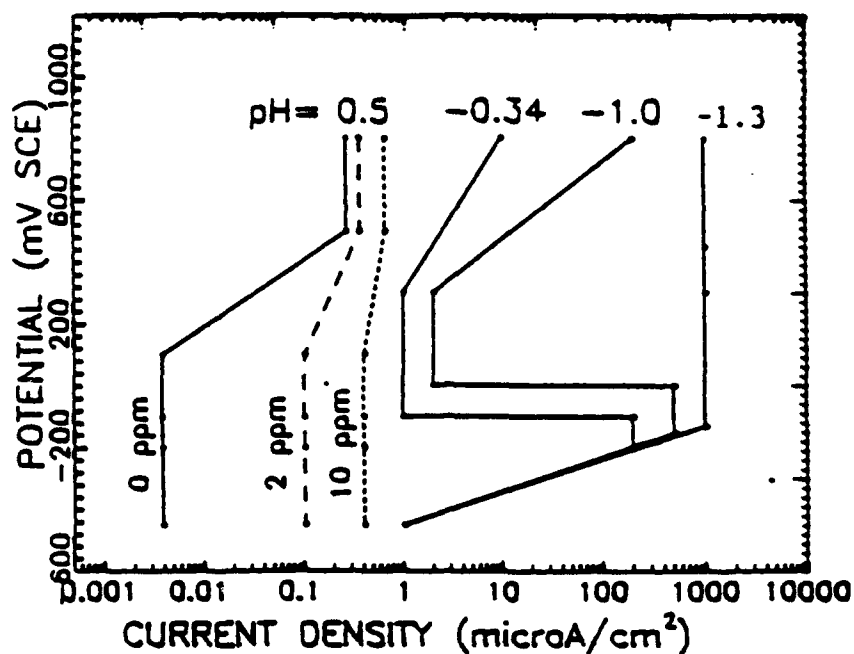


Figure 4. Schematic overvoltage curves for the stainless steel UNS S 31254 at 35°C. For pH values equal to 0.5 or larger the curves changes with the chlorine concentration (not applied in this study).

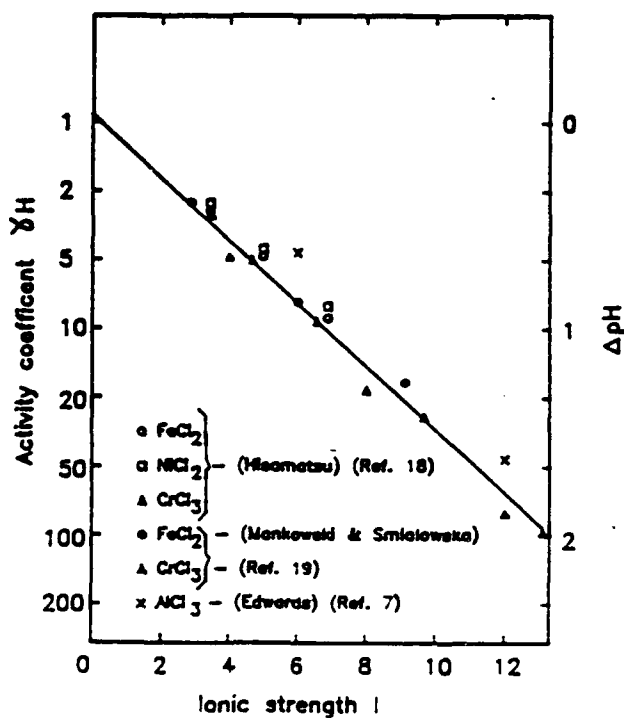


Figure 5. Hydrogen ion activity coefficient or the pH change in dependence of the ionic strength of the solution. Summary of experimental results.

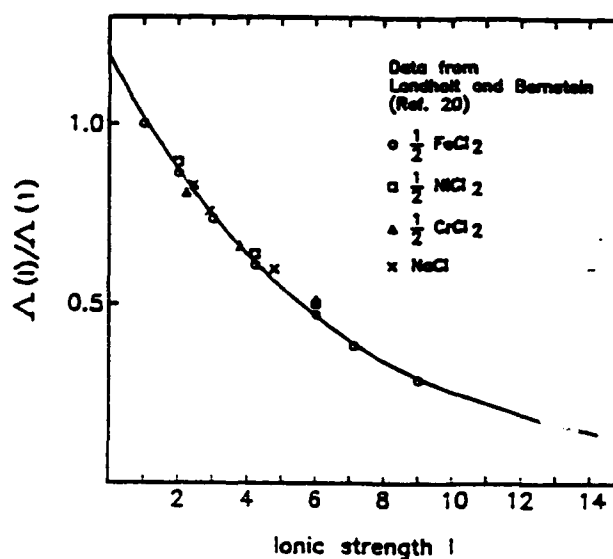


Figure 6. Relative variation of the equivalent conductivity  $\Lambda$  as a function of the ionic strength of the solution.

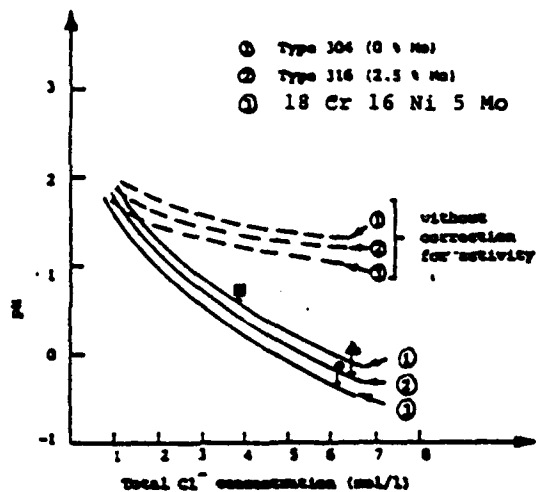


Figure 7. pH versus total chloride concentration as calculated at the bottom of a crevice (solid and dashed lines), and as measured in a pit cavity by Suzuki et al. (Ref. 17). (□ Type 304, △ Type 316, ○ 18Cr16Ni5Mo).

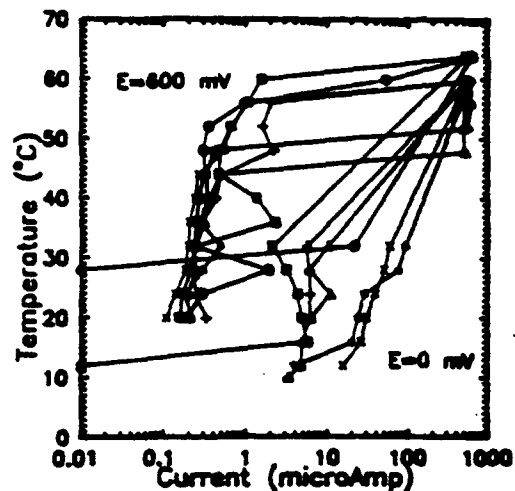


Figure 8. Initiation/repassivation experiments with UNS S 31254.

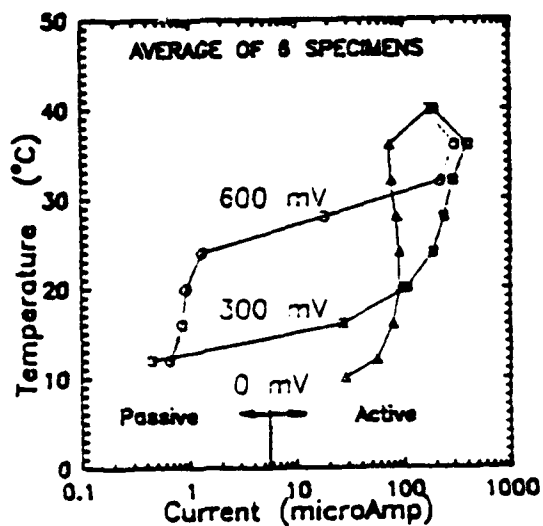


Figure 9. Repassivation experiment with UNS S 31254 at various outside potentials.

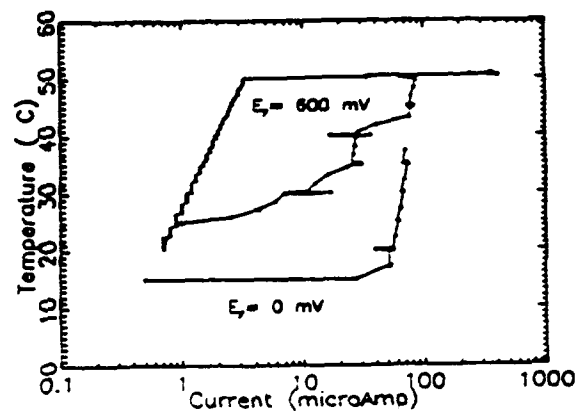


Figure 10. Current-temperature hysteresis obtained in the model calculations with two different potential levels during the temperature reduction phase.

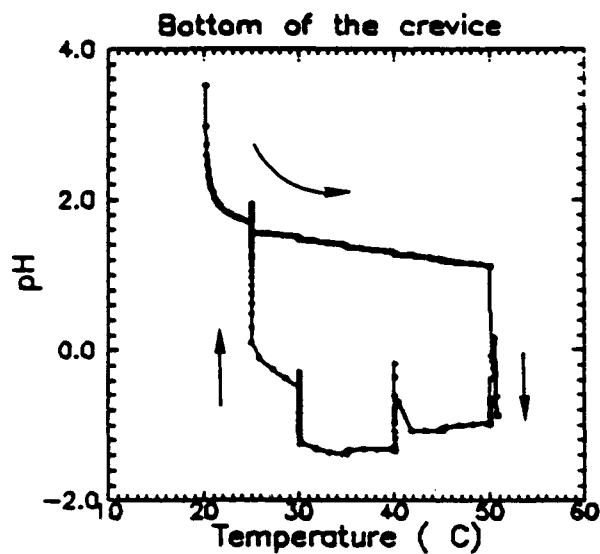


Figure 11. pH-temperature hysteresis obtained in the model calculations.

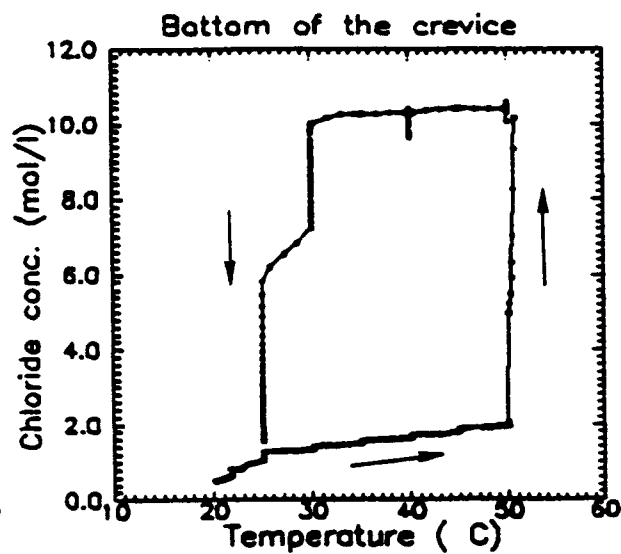


Figure 12. Chloride-temperature hysteresis obtained in the model calculations.

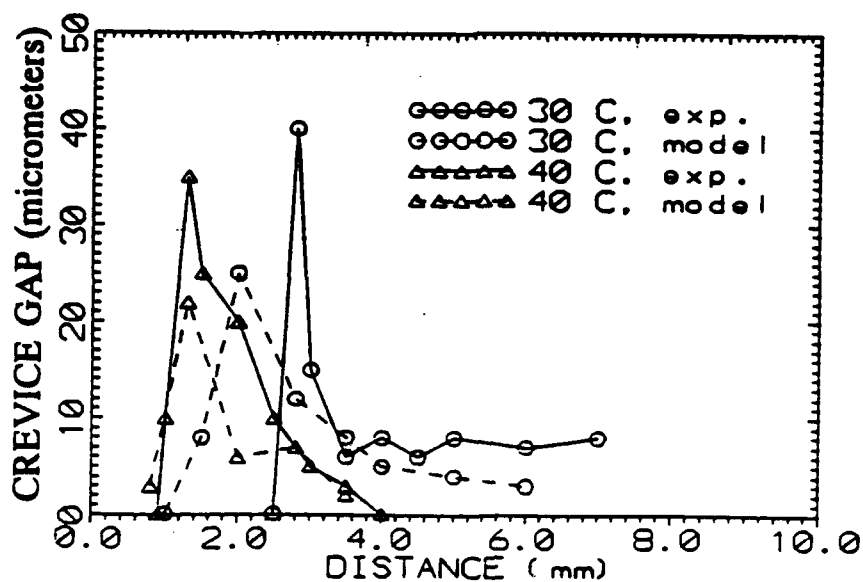


Figure 13. Experimental and calculated crevice attack profiles with UNS S 31254 at 30°C and 40°C after about 100 hours corrosion. Crevice depth 7 mm.

## **Crevice Corrosion of a Nickel-Based Superalloy in Natural and Chlorinated Seawater**

**B. A. Shaw**  
Department of Engineering Science and Mechanics  
Penn State University  
University Park, PA 16802

**P. J. Moran**  
Department of Mechanical Engineering  
U.S. Naval Academy  
Annapolis, MD

**P. Gartland**  
CorrOcean  
N-7005, Trondheim, Norway

### **Abstract**

Alloy 625 is a high strength, corrosion resistant Ni-Cr-Mo-Fe alloy that is being used increasingly by the chemical, offshore and power industries in environments where stainless steels suffer severe localized corrosion. Alloy 625 exhibits excellent resistance to pitting, but has been found to be susceptible to crevice corrosion in seawater and in oxidizing environments such as chlorinated seawater. In order to investigate the mechanism of crevice corrosion for alloy 625 and to assess the role that chlorination plays in crevice corrosion propagation a three fold approach was taken: 1) simulated environments corresponding to those present during the initiation and propagation stages of crevice corrosion were chosen based on mathematical model predictions, information in the literature and actual measurements; 2) steady state polarization behavior for alloy 625 in environments corresponding to those found inside and outside an active crevice was ascertained and anodic polarization curves were generated in these simulated crevice environments and cathodic polarization curves were generated in natural seawater and chlorinated seawater; and 3) mixed potential theory, including the effects of IR drop down a crevice, was applied to the polarization data to identify the crevice corrosion mechanism in natural seawater and to determine the role that chlorination plays in crevice corrosion propagation.

A mixed potential analysis utilizing an anodic polarization curve for alloy 625 generated in an environment simulating that found inside a crevice at initiation and cathodic polarization curve generated in natural seawater reveals that crevice corrosion initiates by an IR induced mechanism. During the propagation stage, mixed potential analysis reveals that the diffusion controlled portion of the oxygen reduction reaction drives crevice corrosion. In low level chlorinated seawater (1 mg/l total residual oxidant) it is the reduction of HOBr and OBr<sup>-</sup> and not O<sub>2</sub> that drive crevice corrosion propagation. The limiting current density for the reduction of HOBr/OBr<sup>-</sup> in the chlorinated environment is two orders of magnitude lower than the limiting current density for oxygen reduction in natural seawater and is responsible for the lower crevice corrosion rates observed in low level chlorinated seawater.

## Introduction

Crevice corrosion is considered by many to be the most deleterious form of corrosion because it occurs on shielded areas of a metal surface where visual examination of the underlying metal is difficult, if not impossible, and unpredicted catastrophic failures can result. Crevice corrosion has been observed on a variety of passive film forming metals<sup>1-14</sup> exposed in a number of different environments ranging from high purity water<sup>2</sup> to the human body<sup>15</sup>. This type of corrosion is inherent in metals and alloys that are easily passivated (e.g. stainless steels, aluminum and aluminum alloys, titanium and titanium alloys, and nickel base alloys), but also occurs on iron and mild steel exposed to highly oxidizing or passivating environments. Metal surfaces shielded by gaskets, washers, bolt heads, o-rings, barnacles or other surface deposits are typical sites for this type of corrosion.

In the early literature the concepts of differential aeration<sup>16, 17</sup>, metal ion concentration<sup>15</sup>, inhibitor concentration<sup>18, 19</sup> and hydrogen ion concentration cells<sup>20</sup> were proposed to explain crevice corrosion. Each of these mechanisms advanced the understanding of the phenomena, but none were sufficient explanations by themselves. In the mid sixties Fontana and Greene combined two of these ideas into a unified mechanism<sup>21</sup> in order to explain the crevice corrosion of stainless steels in neutral pH environments containing chloride ions. This unified mechanism consists of 4 stages: 1) depletion of oxygen within the crevice, 2) increase in chloride ion content and acidity of the crevice solution, 3) permanent loss of passivity for the metal in the crevice, and, finally, 4) propagation of attack within the crevice. The first three steps constitute the initiation phase of crevice corrosion and the fourth step is propagation. Initially, the anodic reaction of slow alloy dissolution and the cathodic oxygen reduction reaction occur both inside and outside the crevice. In time, the oxygen within the crevice is depleted faster than it can be replenished by diffusion and the cathodic reaction moves outside the crevice where it can be supported by the higher dissolved oxygen content of the bulk solution. Slowly metal ions concentrate in the crevice and Cl<sup>-</sup> ions migrate into the crevice to maintain charge neutrality. Hydrolysis of metal chloride complexes in the crevice leads to the formation of H<sup>+</sup> ions; dropping the pH of the crevice solution. A point is eventually reached when the metal in the crevice becomes active and propagation of attack within the crevice ensues. At this stage, rapid dissolution of the metal inside the crevice is driven by the reduction reactions outside the crevice and, if thermodynamically possible, some hydrogen evolution inside the crevice.

Mathematical model results<sup>22</sup> reveal that step 1, depletion of oxygen within the crevice, occurs quickly requiring only a few minutes or less for crevice gaps on the order of several microns. Step 2 of the mechanism, increase in chloride ion content and acidity of the crevice solution, has also been well documented. For neutral pH bulk solutions, low pH values and high chloride ion concentrations within crevices have been reported by a number of investigators<sup>23-26</sup>. Chloride ion concentrations as high as 6.2N and pH values as low as -0.13 have been documented for solutions removed from artificial pits (actually crevices) on 18Cr-16Ni-5Mo stainless steel<sup>24</sup>. Oldfield and Sutton determined that the critical crevice solution which forms inside alloy 625 crevices at initiation has a chloride ion content of approximately 6M and a pH of 0<sup>27</sup> or less<sup>28</sup>. Using a mathematical model developed by Gartland<sup>29</sup> it has been determined that even higher chloride ion concentrations and lower pH values are possible during the propagation stage of crevice corrosion. Much less has been reported concerning the third step in the mechanism, permanent loss of passivity within the crevice. Chloride ion induced breakdown and acidification are most often cited as the depassivation mechanisms responsible for the initiation of crevice corrosion. In this paper an alternative depassivation mechanism, involving the IR drop down a crevice, is presented. The mechanism is applicable to a variety of metals in a number of environments, but this research will specifically address crevice corrosion of alloy 625 in natural and chlorinated seawater.

## Experimental Procedure

The nominal composition for alloy 625 is: 61% Ni, 21.5% Cr, 2.5% Fe, 9% Mo, 3.65% Cb + Ta, 0.25% Mn, 0.25% Si, 0.2% Ti, 0.2% Al, 0.05% C and 0.008% S<sup>30</sup>. Anodic polarization curves were generated in environments simulating that found inside a crevice and cathodic polarization experiments were generated in environments simulating those found outside the crevice, i.e. natural and low level chlorinated seawater. Crevice free, continuous flag shaped specimens (exposed area = 14.28 cm<sup>2</sup>) were used in conjunction with a nitrogen purged cell for the anodic polarization experiments and the cathodic experiments in chlorinated seawater. Uncreviced disk shaped specimens were used for the cathodic polarization experiments in natural seawater. Prior to testing, all of the specimens were prepared by wet polishing to an 800 grit finish, degreasing in methanol, rinsing in deionized water and air drying for at least 2 hours. All experiments were conducted at a temperature of 25°C ± 3°C with no electrolyte agitation other than that created by the deaeration. All references to potential are versus a saturated calomel reference.

The anodic polarization curves were generated on crevice free specimens exposed to solutions simulating the crevice environment at the initiation and the propagation stages of crevice corrosion. The simulated crevice environment for the initiation experiments consisted of artificial seawater saturated with NaCl, acidified to a pH of -0.25 and deaerated with nitrogen. For the propagation studies the simulated crevice environment consisted of an 8.09M chloride solution (LiCl) acidified to a pH of -1.2 and deaerated with nitrogen. The chemistry of this solution in terms of its chloride ion concentration and pH were based on the results of a mathematical model developed by Gartland<sup>29</sup>. Prior to anodic polarization the specimens were exposed to the simulated crevice solutions and the open circuit potentials were monitored until steady state potentials were reached. Only a few hours were needed to establish steady state. The polarization curves were generated potentiodynamically at a scan rates of 0.005 mV/s and 0.1 mV/s.

For the cathodic polarization experiments conducted in chlorinated seawater sodium hypochlorite, NaOCl, was added to ASTM artificial seawater to achieve a total residual oxidant (TRO) concentration of 1 mg/l. This chlorination level is typical of what might be found in a fouling controlled seawater piping system. A DPD colorimetric method was utilized to verify the total oxidant concentration. For simplicity, chlorinated artificial seawater was used in lieu of chlorinated natural seawater in these experiments. Little error is expected from such a substitution since chlorination of the natural water kills the biological component of the water. Use of the crevice free specimen configuration for these experiments necessitated the use of deaerated solutions in order to discourage waterline attack. Prior to polarization, open circuit potentials were monitored with time until steady state values were reached. The cathodic polarization curves were generated potentiodynamically at a scan rate of 0.1 mV/s.

Cathodic polarization curves were also generated on uncreviced specimens in aerated natural seawater. Prior to cathodic polarization the specimens were exposed to ambient temperature (temperature ranged from 16°C to 13°C), quiescent, natural seawater (Wrightsville Beach, NC) and the open circuit potentials were monitored for a period of 25 days. The cathodic polarization curves were generated potentiodynamically at a scan rate of 0.1 mV/s and a temperature of 22°C.

## Results and Discussion

### Crevice Corrosion in Natural Seawater

In this section crevice corrosion initiation and propagation mechanisms involving the IR drop down the crevice are presented. In order to illustrate these mechanisms mixed potential theory and anodic and cathodic polarization curves generated in environments simulating those inside and outside a crevice were used. The environments inside the crevice corresponded to either the initiation or the propagation phase of crevice corrosion. For the initiation phase, artificial seawater saturated with NaCl ( $[Cl^-] = 6M$ ), acidified to a pH of -0.25, and deaerated with nitrogen was chosen based on the mathematical model results of Oldfield and Sutton. During the early stages of propagation the acidity and chloride ion content of the crevice solution continue to increase and finally after a period of time steady state conditions are established. The chemistry chosen to model the solution found inside the crevice during propagation was an 8.09 M chloride solution with the pH adjusted to -1.2. This choice was made based on Gartland's mathematical model results<sup>29</sup>. The environments outside the crevice (for the cathodic polarization behavior) considered in this research were artificial seawater, natural seawater and chlorinated seawater.

Several investigators<sup>41,42</sup>, have reported positive shifts in the open circuit potentials for metals exposed to natural seawater. The positive shift in open circuit potential with time has been attributed to bacterial slime films which form on metal surfaces in natural water environments. The exact mechanism by which the slime film enhances the reduction kinetics of dissolved oxygen in seawater is still under investigation<sup>43</sup>, but it has been hypothesized that either an increase in the exchange current density for the oxygen reduction reaction or a decrease in the cathodic Tafel constant are responsible. An open circuit potential versus time curve for alloy 625 in quiescent, natural seawater (Wrightsville Beach, NC, temperature ranged for 16 to 18°C) is presented in Figure 1. The potential shifts positively in stages with the first plateau occurring at approximately 50 mV (vs. SCE) and a later plateau occurring at 150 to 200 mV. In a related investigation<sup>70</sup>, Kain observed initiation of crevice corrosion on creviced cylindrical alloy 625 pipe specimens after 18 to 20 days of exposure to flowing natural seawater (Wrightsville Beach, NC, flow rate = 1 m/s, mean water temp. 14.8°C). This time coincides with the first plateau in potential observed on the open circuit potential vs. time curve at 50 mV (vs. SCE). Kain's data establish that 18 to 20 days are necessary in order to develop a crevice solution aggressive enough to initiate crevice corrosion. From the open circuit potential measurements obtained under almost identical conditions it can be seen that the open circuit potential for alloy 625 in natural seawater is approximately +50 mV (vs. SCE) at the time of initiation. Cathodic polarization curves generated after 2 hours, 13 days and 25 days of exposure to natural seawater (temperature ranged from 16 to 13°C) are presented in Figure 2. Again, these specimens were exposed in the same location and at the same time of year as the ones used in Kain's study. These curves clearly illustrate the positive shift in open circuit potential with slime film formation and also reveal that the slime film does not effect the diffusion controlled portion of the reaction. It will be shown that this positive shift in potential plays a significant role in both the initiation and propagation stages of crevice corrosion.

The steady state anodic polarization behavior of alloy 625 in a solution representative of the chemistry present at the time crevice corrosion initiates is presented in Figure 3. For comparison the anodic polarization behavior of alloy 625 in deaerated artificial seawater (pH=8.2,  $[Cl^-]=0.5M$ ), generated in the same manner as the curve in the simulated crevice environment, is also shown in this figure (dashed line). In seawater, alloy 625 is self passivating and exhibits two regions of passivity before the onset of transpassive dissolution at potentials greater than +800 mV. In the simulated crevice environment (pH=-0.25, saturated with NaCl,

$\rho=4.5$  ohm-cm) a small active passive "nose" is observed in the anodic polarization curve. The active nose is visible in the simulated crevice solution and not in the neutral pH artificial seawater because the primary passivating potential shifts positively as the pH of the solution decreases<sup>45,46</sup>. A broad range of passivity was noted between -100 mV and 900 mV in the simulated crevice solution before the onset of transpassive dissolution at approximately 900 mV. The passive current density was found to be potential dependent, increasing a little more than half an order of magnitude over the 1 V passive range. This dependence of  $i_{pass}$  on potential is commonly observed in nickel<sup>47</sup> and nickel containing alloys. Note that the passive current density in the simulated crevice environment is 1 to 1.5 orders of magnitude higher than the passive current density in seawater.

Figure 4 shows the cathodic polarization curve for alloy 625 after 13 days of exposure to natural seawater adjusted for an area of  $100\text{ cm}^2$  and superimposed on the anodic polarization curve in the simulated crevice environment. This cathodic curve was chosen because it coincides most closely with the potential at the time crevice corrosion initiates. This analysis assumes that the slime film shifts the open circuit potential positively prior to the development of the anodic curve pictured in Figure 4. This assumption is supported by Kain's observation that 18 to 20 days were required for crevice corrosion initiation of alloy 625 when the mean water temperature was  $14.8^\circ\text{C}$ . Analysis of the "crevice couple" is based on current rather than current density because the anodic and cathodic areas are not equal. If the IR drop down the crevice is negligible, the cross over point for the two curves would represent the corrosion rate in the crevice at the time of initiation. However, in most cases the IR drop associated with the restricted geometry of a crevice is not negligible and must be accounted for in the mixed potential analysis.

In order to demonstrate how IR drop induces depassivation of the metal within the crevice and initiates crevice corrosion, consider a crevice 1 cm long by 1 cm wide with a  $0.2\text{ }\mu\text{m}$  gap between the metal and the crevice former. This gap is typical of the gap that exists when a deformable material, such as an o-ring, is pressed against a metal surface<sup>48</sup>. A 225,000 ohm resistance is calculated using the 4.5 ohm-cm resistivity measured for the simulated solution and the dimensions listed. Recall that the passive current density in the simulated crevice solution at the time crevice corrosion initiates is 1 to 2 orders of magnitude higher than the passive current density in seawater. Combining the 225,000 ohm resistance of the crevice and the cross-over current density for the anodic and cathodic curves results in an IR drop of 180 mV. This IR drop is larger than  $IR^*$ , the IR drop which can be accommodated between the two curves in the passive region of the anodic polarization curve, as illustrated in Figure 4. As a result, the IR drop causes the metal within the crevice to reside at a potential in the active nose of the anodic polarization curve. At this potential the passive film is no longer stable and active dissolution of the metal initiates crevice corrosion.

After initiation and before steady state propagation the acidity and chloride ion content of the crevice solution continue to increase<sup>29</sup>. The aggressiveness of the crevice solution used in the propagation experiments was altered by increasing the chloride ion content to 8.09 M and decreasing the pH to -1.2. Figure 5 illustrates the evolution of the anodic polarization curve with increasing chloride ion content and decreasing pH. This figure shows that in the 8.09 M chloride solution with a pH of -1.2 a very large active nose is present in the anodic polarization curve. The active nose extends over the first 600 mV of the polarization curve and current densities as high as  $1 \times 10^{-2}\text{ A/cm}^2$  are observed.

Again, a mixed potential approach is used to evaluate the role that the cathodic reactions play in driving crevice corrosion propagation and also to estimate the crevice corrosion propagation rate. Figure 6 shows the "crevice couple" formed by the cathodic polarization curve



in a bulk natural seawater environment after 25 days and an anodic curve generated in a simulated crevice solution corresponding to the more aggressive conditions present during crevice corrosion propagation. A cathode to anode area ratio of 100 to 1 is, again, considered. This figure shows that the diffusion limited portion of the cathodic oxygen reduction reaction crosses the large active nose of the anodic curve at a current of approximately  $1 \times 10^{-3} \text{ A/cm}^2$ . The cathodic hydrogen evolution reaction in the crevice environment crosses the anodic curve at a current several orders of magnitude lower than the cross over current for the oxygen reduction reaction and, therefore, does not play a significant role in crevice corrosion propagation. During the propagation stage the IR drop down the length of the crevice is beneficial and propagation would be reduced with increasing depth into the crevice. Figure 7 illustrates the effects of IR drop on crevice corrosion propagation; assuming a crevice solution resistivity of 4.5 ohm-cm crevice width of 1 cm and a crevice gap of 1  $\mu\text{m}$ . As the depth into the crevice is increased from 0.01 cm to 0.4 cm the current in the crevice is found to decrease from a value of  $3 \times 10^{-4}$  to  $2 \times 10^{-5} \text{ A}$ .

In a related investigation<sup>44</sup> Kain estimated a propagation current density of  $21 \mu\text{A/cm}^2$  for a creviced alloy 625 specimen (crevice gap approximately 1  $\mu\text{m}$ ) after 40 days of exposure to natural seawater flowing at 1 m/s using a remote crevice specimen configuration. The actual attacked crevice area in Kain's investigation was 3.2 cm and a cathode to anode area ratio of 3.9 to 1 was used. The mixed potential analysis estimate can be compared to this data once the effect of flow on Kain's data has been established and subtracted out. This estimate can be made by comparing Kain's current density with the limiting current density for the oxygen reduction reaction under static conditions from Figure 2. Based on a limiting current density of  $1 \times 10^{-5} \text{ A/cm}^2$  for oxygen reduction under static conditions it appears that the 1 m/s flow is responsible for approximately doubling the limiting current density. Reducing Kain's current density by one half and multiplying this value by the area and by a factor of 25, to account for the larger cathode considered in the mixed potential analysis, results in a current of  $8.37 \times 10^{-4}$ . This value is in fairly close agreement with the mixed potential estimates presented in Figure 7. If a cathodic curve generated in artificial seawater had been used instead of the cathodic curve generated in natural seawater the crevice couple presented in Figure 8 would have resulted. In the artificial environment the activation controlled portion of the oxygen reduction reaction crosses the anodic curve instead of the diffusion controlled portion of the curve resulting in an large underestimation of crevice corrosion propagation rates.

Mixed potential analysis of the anodic and cathodic polarization curves representative of those found inside and outside an actively propagating crevice reveal the importance of acidification and increased chloride ion concentration in establishing the large active nose in the anodic polarization curve. Crevice corrosion is driven by oxygen reduction on the outside (cathodic) surface, but the development of this large active region establishes the possibility for very high propagation rates if the cathode area is increased or if flow to the cathode is increased. IR drop plays a beneficial role in the propagation stage of crevice corrosion because it limits propagation rates with increasing depth into the crevice. If truly representative environments are chosen to model the solutions present inside and outside the crevice, then crevice corrosion rates can be estimated using mixed potential theory. Finally, this analysis emphasizes the need to use a biologically active environment when evaluating the oxygen reduction reaction or determining corrosion rates in a seawater environment.

### **Crevice Corrosion in Chlorinated Seawater**

The use of nickel base superalloys in chlorinated seawater cooling systems of power plants, oil refineries and offshore oil platforms has raised concern over the susceptibility of these

alloys to crevice corrosion in oxidizing chlorinated seawater environments. Of specific interest are the possibility of crevice corrosion initiation by a chloride ion induced breakdown mechanism at the high potentials generated in chlorinated environments and the effect of low level chlorination (1 mg/l) in reducing crevice corrosion propagation rates<sup>24,49,50</sup>. Seawater chlorination results in the production of a number of oxidants the composition and concentration of which depend on temperature, pH, and chlorination level. The primary oxidants present in open ocean water at low chlorination levels (a few mg/l or less total residual oxidant) are HOBr and OBr<sup>-</sup>. Chlorination levels of a few mg/l total residual oxidant (TRO) or less are typical in fouling controlled seawater systems. Higher chlorination levels (65 to 100 mg/l total residual oxidant) can be encountered as effluent from an electrolytic chlorinator in a fouling controlled seawater piping system. At these higher chlorination levels HOCl and OCl<sup>-</sup> are present in addition to the HOBr and OBr<sup>-</sup>. In either case these oxidants are responsible for high open circuit potentials measured on alloy 625 in chlorinated seawater. Open circuit potentials of approximately 300 mV are quickly established in seawater chlorinated to a level of 1 mg/l TRO and potentials of 800 mV are quickly established at chlorination levels of 100 mg/l TRO. The crevice solution chemistries at initiation and during propagation are assumed to be the same as those presented in the natural seawater section. The small amount of oxidant present within the crevice is assumed to be quickly reduced and the resulting additional chloride ions are insignificant in comparison to the 0.5 M chloride solution initially present within the crevice.

Potentiodynamic polarization curves generated in the simulated crevice solution at initiation revealed no signs of chloride ion induced breakdown for alloy 625. These curves were generated at a very slow scan rate, 0.005 mV/s, requiring approximately 3 days for the generation of each curve. In order to confirm that breakdown did not occur with long term exposure to high chloride solutions eighteen day potentiostatic polarization experiments were conducted in an 8 M LiCl solution at the highest possible potential attainable at the chlorination levels investigated in this research, +800 mV. Low steady state current densities of 0.7 to 3.4  $\mu\text{A}/\text{cm}^2$  were observed over the course of the 18 days and SEM analysis of the specimen surface at the end of the test revealed no breakdown of the passive film; proving that crevice corrosion of alloy 625 does not initiate by a breakdown mechanism. Mixed potential analyses of the crevice couples formed in both high and low level chlorinated seawater point to initiation of crevice corrosion by either an IR induced mechanism or an acidification mechanism.

Since crevice corrosion of alloy 625 in chlorinated seawater initiates relatively quickly (a number of hours to a number of weeks depending on the bulk environment<sup>71</sup>) the propagation stages is of much greater engineering significance than the initiation stage. As was stated earlier, crevice corrosion propagation is driven by the reduction reaction(s) occurring in the bulk environment and possibly some hydrogen evolution within the crevice. Cathodic polarization curves generated in low level chlorinated seawater reveal that the primary cathodic reactions in the potential range of interest from +300 to -300 mV result from the reduction of HOBr and OBr<sup>-</sup>. The crevice couple formed by the cathodic polarization curve in low level chlorinated seawater, adjusted for an area of 100  $\text{cm}^2$ , and the anodic polarization curve generated in the aggressive propagation environment is presented in Figure 9. This mixed potential analysis reveals that the diffusion controlled limiting current density is, again, the driving force for crevice corrosion propagation. The hydrogen evolution reaction crosses the anodic curve at a current approximately 1 order of magnitude lower than the HOBr/OBr<sup>-</sup> limiting current density and, therefore, contributes little to crevice corrosion propagation. In the chlorinated case the limiting current density for the reduction of HOBr/OBr<sup>-</sup> is 2 orders of magnitude lower than the limiting current density for dissolved oxygen in the natural seawater environment (dashed line Figure 9) and is responsible for the lower crevice corrosion propagation rates observed in low level chlorinated seawater. Again, the IR drop down the length of the crevice would serve to decrease crevice corrosion propagation rates with increasing depth into the crevice. The lower

limiting current density in the chlorinated case is attributed to the lower diffusion coefficient for HOBr in comparison to dissolved oxygen, to the fact that 2 electrons are transferred in the overall reduction of HOBr instead of the 4 electrons needed for dissolved oxygen, and to the lower concentration of oxidant (1 mg/l) in the potential region of interest in the chlorinated case than in the natural seawater case (8 mg/l).

### Conclusions

1. In natural seawater it has been shown that crevice corrosion initiates on alloy 625 by an IR induced mechanism.
2. The open circuit potential for alloy 625 shifts positively in natural seawater as a result of the formation of a bacterial slime film on the surface of the metal. This slime film effects the kinetics of the oxygen reduction reaction resulting in much higher crevice corrosion rates in natural versus artificial environments and emphasizes the importance of using natural seawater in lieu of artificial seawater for determining corrosion propagation rates.
3. After crevice corrosion initiation and before steady state propagation the acidity and chloride ion content of the crevice solution continue to increase, resulting in the formation of a large active nose in the anodic polarization curve. It is the intersection of the diffusion controlled portion of the cathodic curve in the bulk environment and this active nose (incorporating the effects of IR) that drives crevice corrosion propagation.
4. Polarization experiments in a highly concentrated chloride solution rule out the possibility of crevice corrosion initiation on alloy 625 in chlorinated seawater by a breakdown mechanism. In this environment crevice corrosion initiates either as a result of an IR induced mechanism or an acidification mechanism.
5. A mixed potential analysis of the crevice couples in natural and chlorinated seawater reveals that the diffusion controlled portion of the HOBr/OBr<sup>-</sup> reduction reaction has a limiting current density 2 orders of magnitude lower than the limiting current density for oxygen reduction in natural seawater; thus explaining the lower propagation rates observed for this alloy in low level chlorinated seawater.

### Acknowledgements-

The authors gratefully acknowledge the technical assistance of Bob Kain, Susan Erlich, and Bob Janeczko. This work was supported by the David Taylor Research Center and the Office of Naval Research under contract N00014-87-K-0294.

### References

1. F.N. Speller and F.L. LaQue, Corrosion, 6, 209 (1950)
2. D.J. DePaul, Corrosion, 13, 91 (1957).
3. E.V. Kunkel, Corrosion, 10, 260 (1954).
4. J.A. Collins, Corrosion, 11, 27 (1955).
5. H.P. Hack, Mat. Perf., 22, 24 (1983).
6. A.P. Bond and H.J. Dundas, Mat. Perf., 23, 39 (1984).

7. M.A. Streicher, *Mat. Perf.*, 22, 37 (1983).
8. N.G. Feige and R.L. Kane, *Mat. Perf.*, 9, 13 (1970).
9. L.W. Gleekman, *Mat. Prot.*, 6, 22 (1967).
10. L.W. Gleekman, *Localized Corrosion*, (Ed. K.W. Staehle), p. 669. National Association of Corrosion Engineers, Houston (1974).
11. R.S. Sheppard, D.R. Hise, P.J. Gegner and W.L. Wilson, *Corrosion*, 18, 211t (1962).
12. L.S. Remerski, J.J. Eckenrod, and C.W. Kovach, *Corrosion*, 39, 31 (1983).
13. I.L. Rosenfeld, *Localized Corrosion*, (ed. K.W. Staehle), p. 373. National Association of Corrosion Engineers, Houston (1974).
14. L.W. Gleekman, *Corrosion*, 14, 21 (1958).
15. W.D. France, *Localized Corrosion - Casue of Metal Failure*, STP 516, p. 164, American Society for Testing and Materials, Philadelphia (1972).
16. U.R. Evans, *The Corrosion of Metals*, p. 93, Arnold, London (1926).
17. J.M. West, *Electrodeposition and Corrosion Processes*, p. 55. Van Nostrand, London (1965).
18. U.R. Evans, *An Introduction to Metallic Corrosion*, p. 52. Arnold, London (1948).
19. I.L. Rosenfeld and I.K. Marshakov, *Corrosion*, 20, 115t (1964).
20. J.R. Myers and M.F. Obrecht, 27th Annual Conf., National Association of Corrosion Engineers, paper 90, Chicago (1970).
21. M.G. Fontana and N.D. Greene, *Corrosion Engineering*, p. 41. McGraw-Hill, New York (1967).
22. J.W. Oldfield and W.H. Sutton, *Br. Corroso. J.*, 13, 13 (1978).
23. M.H. Peterson, T.J. Lennox, and R.E. Groover, *Mat. Prot.*, 99, 23 (1970).
24. T. Suzuki, M. Yambe and Y. Kitamura, *Corrosion*, 29, 18 (1973).
25. F.D. Bogar and C.T. Fujii, Naval Research Laboratory Report 7690, March 1974.
26. A. Turnbull and M.K. Gardner, *Br. Corros. J.*, 16, 140 (1981).
27. J.W. Oldfield and W.H. Sutton, *Br. Corros. J.*, 15, 31 (1980).
28. M.D. Carpenter, R. Francis, L.M. Phillips, and J.W. Oldfield, *Br. Corros. J.*, 21, 45 (1986).
29. P.O. Gartland, *Corrosion* 88, St. Louis, Research Symposium Abstract (1988).

30. Boyer and Gall, Metals Handbook, Desk Edition, p. 15. 24. American Society for Metals, Metals Park, (1985).
31. R.C. Scarberry, E.L. Hibner and J.R. Crum, paper 245 - Corrosion 79, National Association of Corrosion Engineers, Houston, (1979).
32. S.C. Tjong, Metals Forum, 7, 251 (1984).
33. W.K. Boyd and F.W. Fink, Corrosion of Metal in Marine Environments, Metals and Ceramics Information Center report 78-37, p. 38. (1978).
34. W.Z. Friend, Corrosion of Nickel and Nickel-Base Alloys, John Wiley & Sons, New York, p. 12. (1980).
35. J.R. Crum, Metals Handbook, Volume 13, p. 654. ASM International, Metals Park (1987).
36. Metals Handbook, Desk Edition, p. 15.24. American Society for Metals, Metals Park, (1985).
37. J.M. Kroughman and F.P. Ijsseling, Proceedings of the Fifth International Congress on Marine Corrosion and Fouling, Barcelona, Spain, p.214, (1980).
38. R.J. Ferrara, L.E. Taschenberg and P.J. Moran, Corrosion 85, Boston, National Association of Corrosion engineers, paper 211, (1985).
39. D.B. Anderson, Galvanic Corrosion and Pitting - ASTM STP 576, American Society for Testing and Materials, Philadelphia, p. 231 (1976).
40. R.M. Kain, Corrosion 86, Houston, National Association of Corrosion Engineers, paper 229, (1986).
41. A. Mollica and U. Montini, Rapporto Tecnico 2E/74, Istituto per la Corrosione Marina dei Metalli. Consiglio Nazionale delle Ricerche, Genova (1974).
42. B. Johansen, P.O. Gartland, A. supphellen, R. Tunold, 10th Scandinavian Corrosion Congress, Paper 27 (1986).
43. S. Dexter, Corrosion 87, San Francisco, National Association of Corrosion Engineers, paper 377, (1987).
44. R.M. Kain, private communication, April 1988.
45. H. Kaesche, Metallic Corrosion, p. 225, National Association for Corrosion Engineers, Houston (1985).
46. J.R. Meyers, F.H. Beck and M.G. Fontana, Corrosion, 21, 277 (1965).
47. N. Sato, Passivity of Metals, (R.P. Frankenthal and J. Kruger eds.) p.30, The Electrochemical Society, Princeton (1978).
48. R.M. Kain, Metals Handbook, Vol. 13, p. 111. ASM International, Metals Park (1987).

49. R.M. Kain and T.S. Lee, Laboratory Tests and Standards, ASTM STP 866, American Society for Testing and Materials, Philadelphia, p. 299, (1983).
50. B. Wallen and S. Henrikson, Corrosion 88, St. Louis, National Association of Corrosion Engineers, paper 403, (1988).
51. R.M. Kain, private communication, Sept 1988.

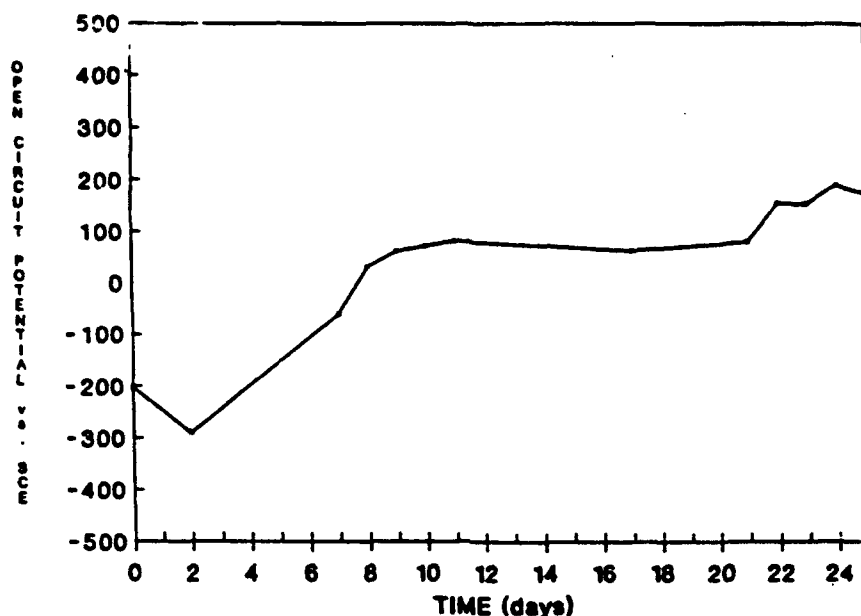


Figure 1 - Open circuit Potential vs. Time Behavior for Alloy 625 in Natural Seawater (Wrightsville Beach, Water Temperature 16 to 13°C)

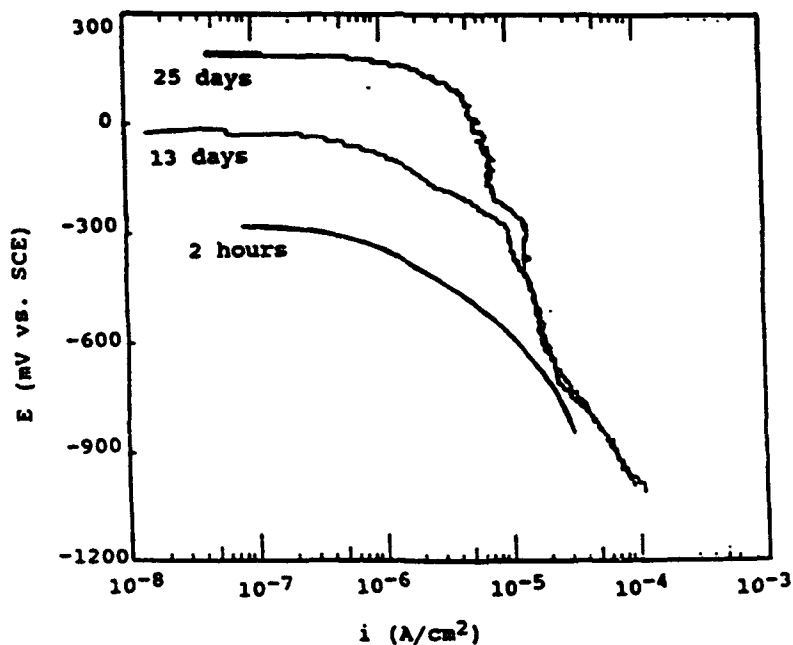
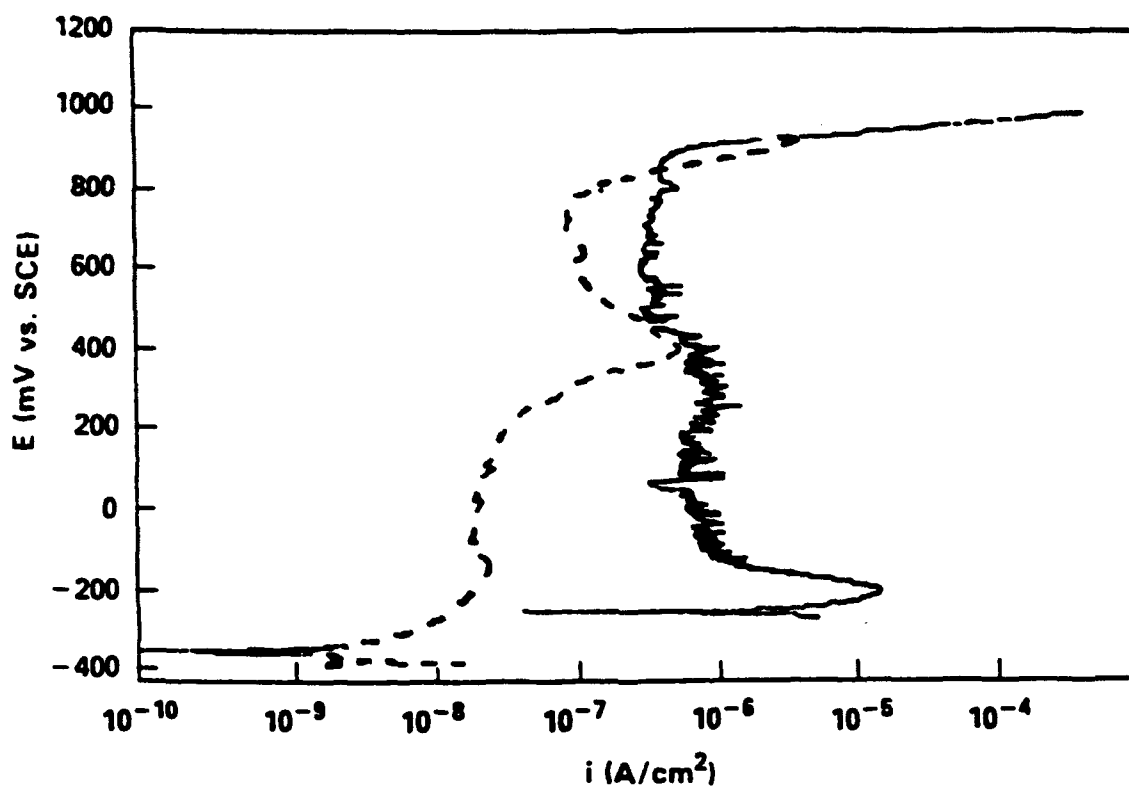
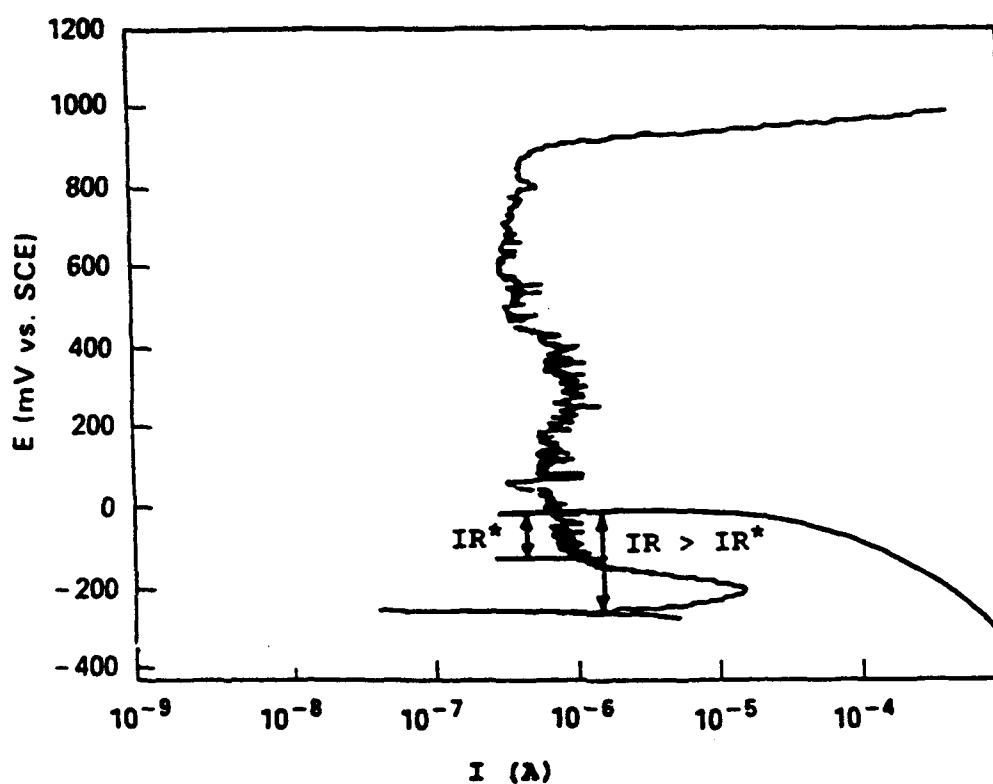


Figure 2 - Cathodic Polarization Behavior for Alloy 625 after 2 Hours, 13 days and 25 days of Pre-exposure in Natural Seawater (Water Temperature 16 to 13°C)



**Figure 3 - Anodic Polarization Behavior of Alloy 625 in Simulated Crevice Solution at Crevice Corrosion Initiation (For Comparison Polarization Behavior in Artificial Seawater is Presented - Dashed Curve).**



**Figure 4 - Mixed Potential Analysis of Crevice Couple in Natural Seawater Illustrating IR Induced Crevice Corrosion**

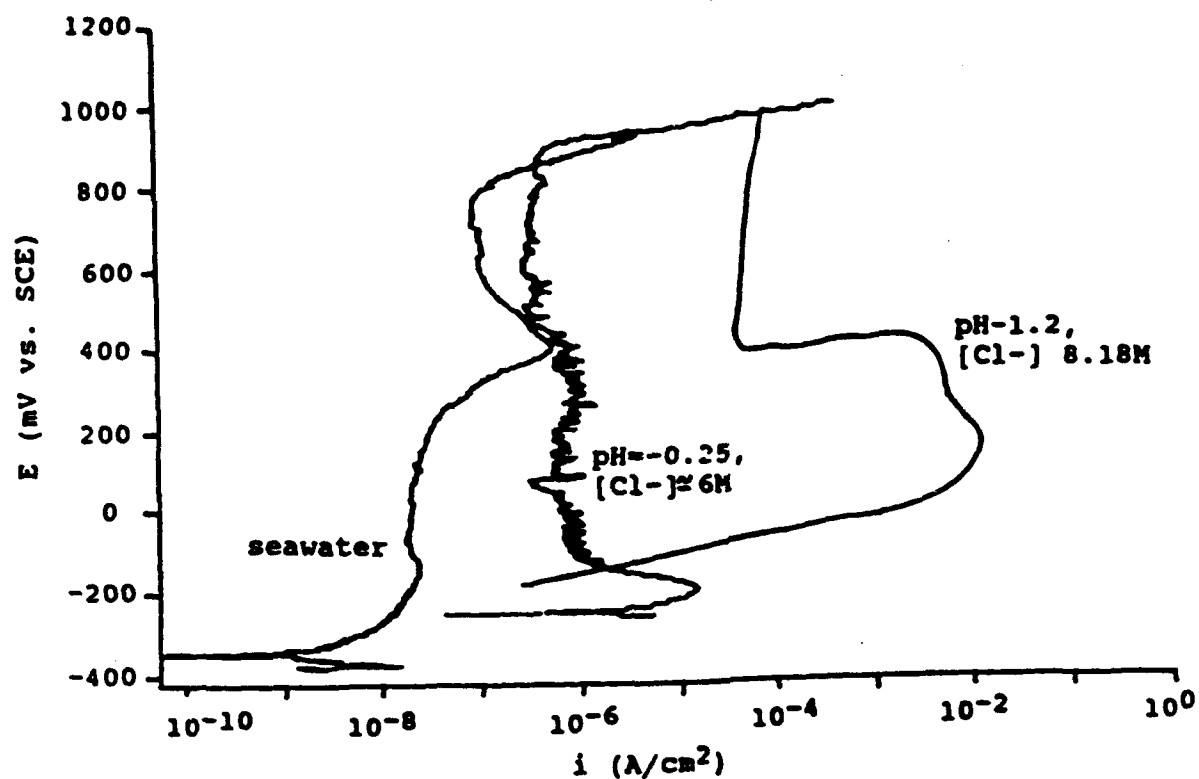


**Figure 5 - Evolution of Anodic Polarization Curve with Decreasing pH and Increasing Chloride Ion Concentration**

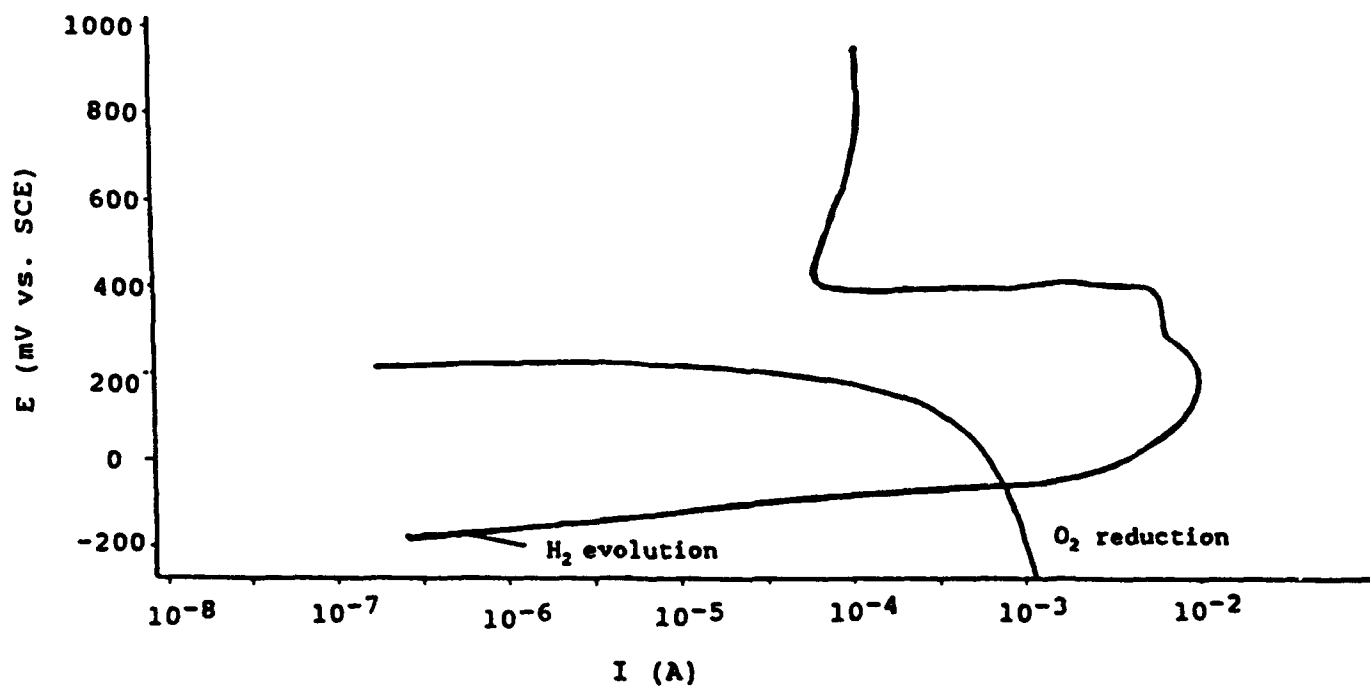


**Figure 6 - Mixed Potential Analysis of Crevice Couple in Natural Seawater During Propagation Stage**



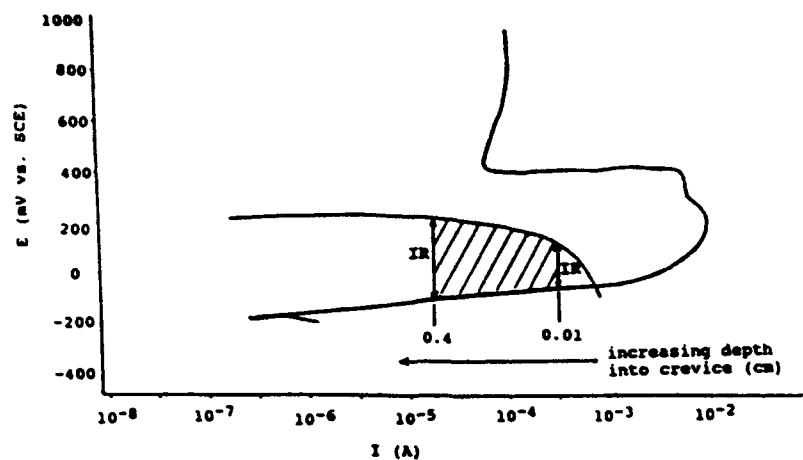


**Figure 7 - Mixed Potential Analysis of Crevice Couple in Natural Seawater During Propagation Stage Including the Effects of IR Drop Down the Crevice**

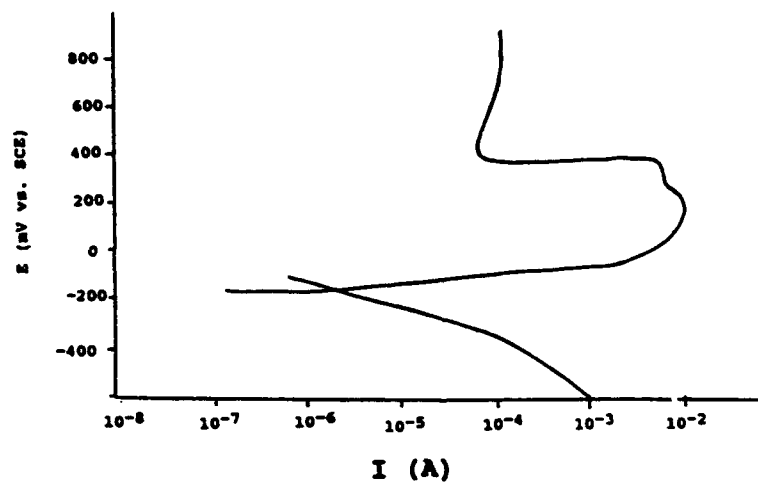


**Figure 8 - Mixed Potential Analysis of Crevice Couple in Artificial Seawater During the Propagation Stage**

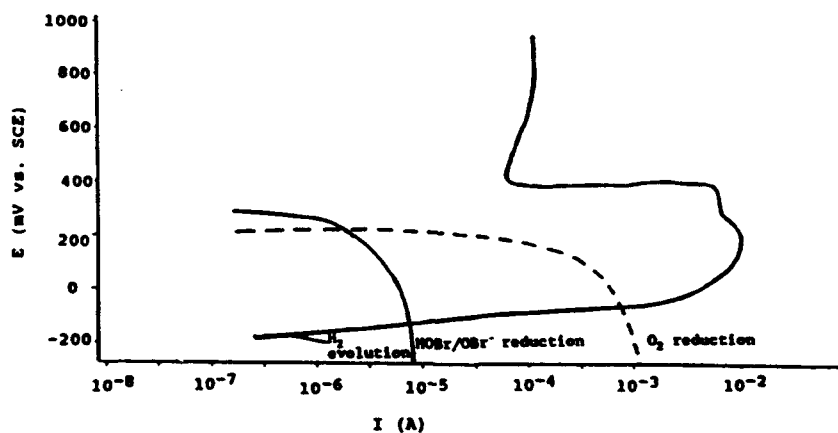


**Figure 9 - Mixed Potential Analysis of the Crevice Couple in Low Level Chlorinated Seawater During the Propagation Stage (Natural Seawater Curve - Dashed Line)**

## **The IR Voltage Mechanism of Localized Corrosion**

**Howard W. Pickering**  
**Department of Materials Science and Engineering**  
**The Pennsylvania State University**  
**University Park, PA**

### **Abstract**

This paper reviews experimental and theoretical results of the past decade at Penn State University that have identified and to a substantive degree revealed how the so called IR mechanism operates to produce localized corrosion. Results from a novel specimen design permitting several parameters to be simultaneously monitored have proved beyond doubt that (i) an IR voltage is the operative parameter defining crevice corrosion in iron and (ii) solution resistivity and other influential parameters, like inhibitors of crevice corrosion, and acidification and chloride ion buildup of the crevice electrolyte, can be understood within the framework of the IR mechanism. A computational model of the IR mechanism based on potential theory and the active/passive transition has been formulated which can predict its occurrence. Other experiments have demonstrated to various degrees that the IR mechanism also operates in pit growth in iron and nickel, in producing lace-like structures around pits and along grain boundaries in steels and stainless steels, in intergranular corrosion of sensitized stainless steel (the chromium depletion mechanism operates initially to produce a groove suitable for the IR mechanism), and in corrosion under an organic coating such as in undercutting (paint film blistering) at an exposed edge of galvanized steel.

**Key terms:** crevice corrosion, potential and current distribution, mathematical model, IR voltage, anodic polarization curve, passive/active transition, separated anode and cathode.

### **Introduction**

In our previous papers, a new mechanism of localized corrosion has been identified and explored in some detail. By far the most extensive and conclusive results are those recently obtained for crevice corrosion.<sup>1-5</sup> In this work, an IR voltage mechanism was proven beyond doubt to operate; was shown in the simplest cases to be the only necessary consideration,<sup>1-4</sup> was shown to be the foundation upon which the roles of important parameters like acidification and chloride ion buildup in the crevice electrolyte could be understood;<sup>3,4</sup> has to date been found to operate in every case (numbering in the tens) of crevice corrosion in iron, steel and stainless steel; and some of the conditions of crevice corrosion (width, depth, aspect ratio) have been shown to be quantitatively predictable for the simplest cases of crevice corrosion in iron<sup>(5)</sup>.

The IR mechanism is based on the IR voltage that exists between the anode and the cathode of a localized corrosion cell. Since, in the case of localized corrosion the anode and cathode sites are separated, the IR voltages can be very large ( $10^2$  to  $10^3$  mV) and when considered in the context of the potential range of stability of the passive film, the anodic sites (within the crevice, pit, grain boundary, etc.) can find themselves outside the potential region of stability of the passive film (i.e., at low overvoltages where the passive film is less stable, often resulting in an active loop in the polarization curve).

Although the suggestion of a possible role of IR in localized corrosion surely goes back to the early days of corrosion science, there are only a few prior research efforts that attempt to understand

what, if any, role IR within cavities may have for an electrode in an electrochemical cell. The most obvious electrochemical conditions involve cathodic polarization processes such as electroplating and cathodic protection, and in these areas the role of IR has been explored. Nevertheless, it is not surprising that insight into the role of IR in localized corrosion is not forthcoming from these studies for the simple reason that there is nothing in the cathodic polarization curve that resembles the passive condition in anodic polarization. Thus, one can find in the literature only a handful of measurements/ observations of large IR voltages in cavities that were focused on localized corrosion, prior to our increased activity in the mid-eighties. Some of these early observations include  $10^2$  to  $10^3$  mV IR voltages within pits and crevices in stainless steel,<sup>6-8</sup> carbon steel,<sup>9</sup> iron,<sup>8</sup> and titanium.<sup>10</sup> These, and other measurements like them (see the writer's other paper in this proceedings for a review of IR voltages under cathodic polarization conditions<sup>11</sup>), were a boost to the idea that large IR voltages shift the potential within cavities out of the region of stable passivity and into a lower overvoltage region of the polarization curve to produce the localized corrosion event.<sup>8</sup>

Within pits, however, the calculated IR is usually much smaller than the measured IR; this led to the explanation by Pickering and Frankenthal,<sup>8</sup> based on their observation that actively growing pits in iron were always largely filled with gas, that the gas in the pits effectively reduces the solution cross section available for carrying the current and increases the resistance and actual IR voltage. The efforts of the last decade in our laboratory were motivated by this earlier research and by the awareness of a possible connection between the occurrence of a stable pitting process and the existence of a large IR voltage in the pit electrolyte.

When the IR mechanism is considered in the context of other localized corrosion processes, it becomes clear, at least in principle, that the IR phenomenon will occur to some extent in all forms of localized corrosion. That it has been found to occur in pit growth in iron<sup>8</sup> and more recently in nickel,<sup>12</sup> in grain boundary corrosion of sensitized stainless steel,<sup>13,14</sup> and under an organic coating on stainless steel,<sup>13</sup> attests to this conclusion. It also is likely the second corrosion process that occurs during undercutting (paint film blistering) at an exposed edge of galvanized or Al-Zn coated steel: Walter<sup>15</sup> has reported that once a crevice is formed by corrosion of the metallic coating at an exposed edge, undercutting continues by a second crevice-type corrosion process.

Since the IR mechanism controls crevice corrosion, it also can be expected that inhibitors of crevice corrosion will function within the framework of the IR phenomenon and that therein will lie a more complete explanation of their inhibiting power, and that likewise so also will promoters of localized corrosion such as acidification and chloride ion buildup in the cavity. In this paper, the IR mechanism is outlined and explained, and the experimental and modeling results which prove its occurrence are presented or cited.

### The IR Mechanism

The IR mechanism of localized corrosion is schematically represented in the cross section of Figure 1 in which the necessary condition for its occurrence is  $|IR| > IR^*$ . This cross section is representative of a localized corrosion process (crevice, pit, grain boundary groove, etc.). The IR mechanism is best understood (and documented) once the localized corrosion event is beyond the initiation stage but the understanding that has emerged from the data obtained during stable crevice corrosion provides also for a partial interpretation of the initiation process. The occurrence of the IR mechanism only requires that the anodes and cathodes are separated which could mean a separation as small as 1-10 nm (e.g., during some initiation events) but usually will be several orders of magnitude larger especially for ongoing localized corrosion in large structures, e.g., of reinforcement in concrete. For separation of the anode and cathode to occur, the metal dissolution reaction has to be suppressed in the surface location where the oxidant is plentiful (cathode). Thus, the anodic reaction, if it is going to occur at an appreciable rate, must occur elsewhere. One

way the anodic reaction is suppressed is by the formation of a passive film at the potential established by the oxidant.

What Figure 1 shows is that the electrode potential,  $E(x)$ , beyond some distance,  $x_{\text{pass}}$ , into the crevice is in a potential region of high metal dissolution currents (active) whereas the external surface (top of crevice) is at more noble (positive) potentials ( $E_{\text{surf}}$ ) in the region of very low (passive) dissolution rates. The crevice electrode potential,  $E(x)$ , is stabilized in the active region by the IR voltage associated with the anodic current flowing from the active anodic site through the crevice electrolyte to the cathodic site at the outer surface<sup>+</sup>:

$$E(x) = E_{\text{surf}} + IR \quad (1)$$

where  $I$  is negative since current flow is in the negative  $x$  direction in the crevice and  $|IR| > IR^*$  (refer to Figure 1). This reasoning is the basis for the  $|IR| > IR^*$  criterion for stable crevice corrosion to occur. In all the experiments conducted to date (mostly on iron but also on steel, stainless steel and nickel) crevice corrosion occurred only when this criterion was met, i.e., the measured electrode potential in the crevice was in the active loop of the crevice polarization curve.<sup>1-4</sup> To ensure that crevice corrosion was, in fact, occurring during potential measurements inside the crevice, a transparent Plexiglas crevice wall (Fig. 2) allowed for independent, insitu, microscopic observation of the iron crevice wall while simultaneously measuring the cell current, the latter being at a high value during active crevice corrosion. For establishment of this basic criterion, many of the experiments on iron were conducted in buffered solutions free of chloride and other aggressive anions, i.e.,  $\text{Cl}^-$  ion was not present in the cell and the pH in the crevice electrolyte remained at the pH of the bulk solution as shown by pH measurements during the experiment.<sup>1,3,4</sup> Thus, neither acidification nor chloride ion buildup in the crevice electrolyte are necessary for crevice corrosion to occur in iron in many electrolytes; on the other hand both parameters are promoters of crevice corrosion and their roles are examined below in the context of the IR framework of localized corrosion.

Since  $E(x)$  shifts to less noble potentials as  $x$  increases (to a limiting value,  $E_{\text{lim}}$ ,<sup>23</sup>) active dissolution occurs at and below a well defined distance into the crevice,  $x_{\text{pass}}$ , corresponding to the  $E_{\text{pass}}$  value of the polarization curve. Also, the shape of the developing cavity is determined by the shape of the active loop of the polarization curve, e.g., the most rapid attack occurs where the potential,  $E(x)$ , is that of the peak anodic current and gradually decreases with further distance  $x$  into the crevice in accord with the decreasing current in the Tafel region. This general shape of the active loop is readily recognizable in cross sections of the corroded region after the experiment.<sup>4,24</sup> In addition, a method has been developed to calculate the current distribution beyond  $x_{\text{pass}}$  (active loop) from the measured potential distribution by Nystrom, et. al.<sup>25</sup> The calculated current distribution between  $x_{\text{pass}}$  and  $x_{\text{lim}}$  agrees well with the observed shape of the corroded crevice wall and resembles the shape of the active loop of the bulk solution (acetic acid/sodium acetate) polarization curve. The distance  $x_{\text{pass}}$  can also be predicted using a recently developed computational model<sup>5</sup> (summarized next) if the conductivity, dimensions of the crevice,  $E_{\text{surf}}$ , and polarization curve are known. Predicted  $x_{\text{pass}}$  values from the model have shown a good agreement with experimentally measured  $x_{\text{pass}}$  values, Table 1, and are a confirmation of the validity of the model.

<sup>+</sup> In previous papers<sup>1-4,16-22</sup>, Equation 1 was sometimes given as  $E_x = E_{\text{surf}} - |IR|$  for open circuit corrosion or anodic protection, and as  $E_x = E_{\text{surf}} + |IR|$  for cathodic polarization except that the absolute magnitude of IR was only implied. Equation 1 as presented above is equivalent but can be used for all three situations since it considers that the current  $I$  is negative when it flows out of the cavity (negative  $x$  direction) as in the case of anodic protection and open circuit corrosion, and is positive when it flows into the cavity as in the case of cathodic protection.

## Modeling the Potential and Current Distributions in an Active/Passive System

The issue of the potential and current distributions within an active crevice is of crucial importance in the quantitative study of crevice corrosion. Prior to the computational model of Xu and Pickering<sup>5</sup>, some modeling efforts had been made to define the potential difference between the outer surface and inside the crevice.<sup>8,27-34</sup> The influence of this potential difference on the electrochemical reactions within the crevice, however, had been largely ignored in the past except for the experimental results reported by France and Greene in the early development stage of anodic protection technology<sup>7</sup> and by Pickering and Frankenthal<sup>8</sup> in a study of pitting corrosion of iron and stainless steel.

In order to define the role of the potential difference in crevice corrosion in more detail than the previous models<sup>8,27-34</sup> and to establish the conditions of IR-induced crevice corrosion so as to be able to predict its occurrence, it was necessary to determine quantitatively the potential and current distributions within a crevice taking into account the active/passive transition. However, the active - passive transition makes routine computation approaches, e.g., the linear polarization approximation or the Tafel kinetics treatment, inadequate.

The computational model of Xu and Pickering enables one to calculate the potential and current distributions in the electrolyte phase and on the electrode surface for a system in which a part of the anode is passivated while the rest remains in the active dissolution state. The computation employs the finite element method allied with a boundary variation and a trial and error technique. From the obtained distributions, the location of the boundary between the active and passive regions on the anode can be predicted. In the case of a crevice, this means that a critical distance into the crevice exists beyond which active corrosion (crevice corrosion) takes place. In addition to the active/passive behavior of the material, solution conductivity,  $\kappa$ , applied potential at the sample's outer surface,  $E_{\text{surf}}$ , crevice gap and depth dimensions, and passive current density,  $i_{\text{pass}}$ , influence this critical distance to different degrees. Thus the occurrence of crevice corrosion may be predicted and the distance into the crevice,  $x_{\text{pass}}$ , at which crevicing starts, as well as the total crevicing current,  $I$ , may be defined.

The developed software package may also be used for (1) IR - induced crevice corrosion under open circuit conditions where the electrode potential at the outer surface is established in the passive region by an oxidant, (2) the design of anodic protection systems, and (3) the design of some corrosion resistant coatings and alloys.

The model has been applied for conditions in which the crevice polarization curve is approximately the same as that of the bulk solutions, a situation that is approached in chloride-free buffered solutions, complexing solutions (e.g., Fe in ammoniacal solution) and in solutions of pH adjusted to the equilibrium pH of the hydrolysis reaction (bearing in mind that pH is a dominating parameter affecting the potential of the active-passive transition). On the other hand the crevice electrolyte polarization curve must be used in place of the bulk solution polarization curve when changes in the crevice electrolyte change the size of the active loop, including pH,  $\text{Cl}^-$  concentration and inhibitor ( $\text{Na}_2\text{CrO}_4$ ) concentration.<sup>1-4</sup> The values of the critical distance into a crevice,  $x_{\text{pass}}$ , for pure iron in buffered ammoniacal (pH 9.7) and acetic acid (pH 4.6) solutions are calculated, and the latter are shown to be in good agreement with available literature values, Table 1.

### Initiation

Whereas in an ongoing (stable) crevice corrosion process, the peak current density,  $i_{\text{peak}}$ , and other currents in the active loop are instrumental in meeting the IR condition, the anodic currents and  $E(x)$  during initiation of the localized corrosion event vary with time and are more difficult to define. Two limiting cases can be considered. If the crevice wall is already covered by a passive film prior to the experiment, as may be the case for many corrosion resistant alloys, only the (low)

passive current and anodic current spikes due to local breakdown and repassivation would be available for meeting the IR condition. If, on the other hand, the passive film has to first form as in the case of iron in acid, currents are high initially and decrease with time. Applying potential theory,<sup>5</sup> the currents are initially highest at the outer surface but as the outer surface passivates the highest currents occur at progressively deeper locations on the crevice wall as the passivation front moves into the crevice. Thus, at some time when  $x_{\text{pass}}$  is at the distance for which the IR condition is met, the passivation front proceeds no further into the crevice and stable crevice corrosion occurs beyond  $x_{\text{pass}}$ . Few data are available to test this scenario in detail but motion of the passivation front into the crevice has been (in-situ) observed in our laboratory during crevice corrosion experiments with iron using the design shown in Figure 2.

Initiation is yet more complicated in the case of pitting corrosion where, in the absence of a preexisting cavity, breakdown of the passive film is the first step in forming the pit cavity. The operation of the IR mechanism just following passive film breakdown is in principle possible<sup>2,5,27,35</sup> since the ratio of the pit depth to diameter (aspect ratio) is a measure of the resulting IR voltage between the anodic site in the pit and the cathodic site on the outer surface,<sup>5,27,30,35</sup> i.e., large IR voltages are predicted for very shallow pits because the diameter of the pit opening is also very small, although the model does not incorporate the complications of the double layer that may become dominant somewhere in the 1 to 10 nm diameter range. Gas bubbles attached to the surface promote IR-induced breakdown of the passive film, e.g., see Figure 13 of Reference 2, where the IR voltage is produced by current flow from the anodic sites under the bubble to the bulk solution. Growth and, on the other hand, waning of the gas bubble may both occur at the locations of different electrode potentials underneath the bubble, as discussed elsewhere.<sup>1</sup>

### Factors That Affect IR

An obvious electrolyte parameter influencing IR is the resistivity. The larger the resistivity is, the larger the IR is for all other conditions the same (i.e., crevice geometry, cell current flowing from the anode sites in the crevice to the cathode sites on the outer surface, outer surface potential, etc.). In such a case the  $|IR| > IR^*$  criterion predicts that  $x_{\text{pass}}$  is smaller for a larger resistivity, exactly as found in experiments on iron.<sup>26</sup> For example, the  $x_{\text{pass}}$  in a crevice in an iron sample anodically polarized (600 mV SCE) in 0.5 M  $\text{CH}_3\text{COOH}$  + 0.5 M  $\text{NaC}_2\text{H}_3\text{O}_2$  (conductance  $\kappa = 0.034 \Omega^{-1} \text{cm}^{-1}$ ) and 0.5 M  $\text{CH}_3\text{COOH}$  + 0.2 M  $\text{NaC}_2\text{H}_3\text{O}_2$  ( $\kappa = 0.015 \Omega^{-1} \text{cm}^{-1}$ ) was 1.8 and 0.8 mm, respectively, illustrating the role of conductivity in modifying IR. These measured  $x_{\text{pass}}$  values are also in good quantitative agreement with computed values using the IR model.<sup>5</sup>

In addition to solution resistivity, various species will be expected to influence the crevice corrosion tendency and rate by changing IR or/and  $IR^*$  in the  $|IR| > IR^*$  criterion, either increasing susceptibility (e.g., acidification and chloride ion buildup within the crevice electrolyte) or decreasing susceptibility (e.g., the addition of inhibitors). The question to be asked then is how do these solution species affect the polarization curve, especially how are  $E_{\text{pass}}$ ,  $i_{\text{peak}}$  and  $i_{\text{pass}}$  modified? Accepting the basic  $|IR| > IR^*$  framework, one or both of the following would be expected to occur when promoters of crevice corrosion, e.g.,  $\text{H}^+$  ion or  $\text{Cl}^-$  ion, increase in the crevice electrolyte: (1) the active loop increases in size, specifically  $E_{\text{pass}}$  shifts to more noble potentials and  $i_{\text{peak}}$  increases and (2) the passive current,  $i_{\text{pass}}$ , increases. In contrast, when an inhibitor is added to the crevice electrolyte (1) or/and (2) would change in the opposite direction. This expected behavior is illustrated in Figure 3, i.e., the  $|IR| > IR^*$  criterion is more easily met when the polarization curve changes from i to ii in Figure 3, and, consequently, localized corrosion more readily occurs. The shift of  $E_{\text{pass}}$  to the more noble value decreases  $IR^*$  (see Figure 1 for definition of  $IR^*$ ) and the increase in  $i_{\text{peak}}$  increases IR by increasing I. Similarly, during initiation of the local cell process, the increase in  $i_{\text{pass}}$  or/and (passivity breakdown) current spikes could be instrumental by increasing IR. Species that affect the polarization curve in just the opposite sense

reduce the likelihood that the  $|IR| > IR^*$  criterion for localized corrosion will be met and are, therefore, inhibitors of localized corrosion.

A decrease in pH is well known to have exactly the effect shown in Figure 3 for many different alloy systems including iron and stainless steel. Thus, in an alkaline solution which is buffered to avoid pH change in the crevice, crevice corrosion may not occur but does if acidification is allowed to occur by removing the buffer or if the solution is replaced by a lower pH solution. For example (see Figure 9 in Reference 2), when a buffered pH9 solution in which crevice corrosion of iron did not occur was replaced with a pH5 solution, crevice corrosion occurred in minutes and the crevice electrode potential decreased dramatically into the active potential region in accord with the IR mechanism. These results were accompanied by a two order-of-magnitude increase in current and formation (in-situ observation) of the corroded region on the crevice wall below the straight  $x_{pass}$  boundary (using the specimen design in Figure 2). In other results for iron in buffered solutions, the measured  $x_{pass}$  decreased with decreasing pH, and the amount of the decrease was in good agreement with the calculated value using the  $|IR| > IR^*$  model by Xu and Pickering<sup>5</sup>.

The change in the polarization curve with addition of chloride ion is not as well documented in the literature as the effect of pH. However, the available results show the behavior indicated in Figure 3, and this behavior was confirmed by our own results for iron in solutions of increasing  $Cl^-$  ion concentration. A schematic of the results for iron is shown in Figure 1 of Reference 4. Hence, chloride ion also promotes crevice corrosion of iron by facilitating the  $|IR| > IR^*$  condition. The results convincingly demonstrate that crevice corrosion that occurs more readily by addition of chloride to the solution does so within the framework of the IR mechanism.<sup>4,24</sup> Photographs of the crevice wall, e.g., see Figure 3 of Reference 4, show clearly the features expected if the  $E(x)$  potential profile on the crevice wall extends over the entire anodic polarization curve. With increasing distance,  $x$ , into the crevice and the outer surface potential more positive than the pitting potential, the crevice wall exhibits: pitting to a certain distance,  $x_{pit}$ , passivity without pitting to another distance,  $x_{pass}$ , and active dissolution to the limiting distance,  $x_{lim}$ .

Sodium chromate is known to inhibit crevice corrosion in iron so the addition of  $Na_2CrO_4$  to the electrolyte must modify the polarization curve as shown (ii→i) in Figure 3. Valdes's results indeed show that  $E_{pass}$  shifts to the left (less noble direction) and  $i_{peak}$  decreases when  $Na_2CrO_4$  is added to the electrolyte.<sup>1,2</sup>

### Lace-like Structure

In IR-induced localized corrosion in crevices,<sup>1</sup> pits<sup>12</sup> and grain boundary grooves,<sup>13</sup> the subsurface attack eventually penetrates the outer surface from underneath since the IR path and hence, the localized corrosion process is not constrained to a particular direction. When penetration occurs the IR path is shortcircuited, resulting in passivation of the subsurface cavity in the vicinity of the new opening to the bulk electrolyte. As this and other penetrations passivate, still more penetrations occur further from the original opening (crevice, pit, grain boundary groove). Eventually, larger and larger rings of small penetrations appear on the surface concentrically located around the original opening to produce a lace-like pattern<sup>1</sup> often seen around pits, grain boundary grooves and crevices, e.g., see Figures 12 and 13 of Reference 8.

### Concluding Remarks

The IR concept of localized corrosion is a direct consequence of potential theory and as such is accepted in principle. The only question is whether or not the IR mechanism operates in practice. What has been found in the past decade using a novel experimental design at the Penn State Corrosion Laboratory is that the IR mechanism is responsible for crevice corrosion in iron. Crevice corrosion was only found to occur when the IR voltage within the crevice takes a part of the crevice wall out of the potential region of stable passivity. This is now a well established fact

for iron in acid and alkaline solution. Furthermore, when considered in the light of the IR mechanism's sound theoretical basis, it raises the very real possibility that the IR mechanism also operates in other forms of localized corrosion and in other metals. This prophecy is being borne out in crevice, pitting, grain boundary, and undercutting corrosion results on steel, nickel and stainless steel where the IR mechanism is being found to cause localized corrosion and to be the exclusive mechanism by which the localized corrosion occurs. In sensitized stainless steel, the chromium depletion corrosion mechanism produces the grooves at the grain boundaries but then the IR mechanism commences and becomes the operative corrosion mechanism.

### **Acknowledgment**

Dr. Yuan Xu and E. A. Nystrom provided helpful comments and Richard Tinsman helped with preparation of the manuscript. Partial support of the Office of Naval Research, Contract No. N00014-91-J-1189 (A. J. Sedriks) is gratefully acknowledged.

### **References**

1. A. Valdes and H. W. Pickering, *Advances in Localized Corrosion*, H. Isaacs, U. Bertocci, J. Kruger and S. Smialowska, Eds., NACE-9, (Houston, TX, National Association of Corrosion Engineers, 1990), p. 393; *ibid.*, p. 77.
2. H. W. Pickering, *Corrosion Sci.*, 29 (1989): p. 325.
3. K. Cho and H. W. Pickering, *J. Electrochem. Soc.*, 137 (1990): p. 3313; *ibid.*, 138 (1991): p. L56.
4. K. Cho and H. W. Pickering, *Critical Factors in Localized Corrosion*, G. Frankel and R. Newman, Eds., Proc. 92-9, (Pennington, NJ, The Electrochemical Society Softbound Proceedings Series, 1992), p. 407.
5. Y. Xu and H. W. Pickering, *J. Electrochem. Soc.*, 140 (1993): p. 658; *ibid.*, *Critical Factors in Localized Corrosion*, G. Frankel and R. Newman, Eds., Vol. 92-9, (Pennington, NJ, The Electrochemical Society Softbound Proceedings Series,, 1992), p. 389.
6. H. H. Uhlig, *The Corrosion Handbook*, (New York, NY, Wiley and Sons, Inc., 1948), p. 165.
7. W. D. France, Jr., and N. D. Greene, *Corrosion*, 24 (1968): p. 247.
8. H. W. Pickering and R. P. Frankenthal, *J. Electrochem. Soc.*, 199 (1972): p. 1297; *ibid.*, p. 1304.
9. G. Herbsleb and H. J. Engell, *Z. Electrochem.*, 65 (1961): p. 881.
10. C. M. Chen, F. H. Beck and M. G. Fontana, *Corrosion*, 27 (1971): p. 234.
11. H. W. Pickering, *This Proceeding*.
12. M. Wang, Y. Xu and H. W. Pickering, in preparation.
13. W. K. Kelly, R. N. Iyer and H. W. Pickering, submitted to *J. Electrochem. Soc.*
14. A. Sehgal, R. N. Iyer and H. W. Pickering, in preparation.



15. G. W. Walter, *Corrosion Sci.*, in press.
16. H. W. Pickering, *Corrosion*, 42 (1986): p. 125.
17. B. G. Ateya, H. W. Pickering, *J. Electrochem. Soc.*, 122 (1975), p. 1018; *ibid*, *J. Appl. Electrochem.*, 11 (1981); p. 453.
18. B. G. Ateya, H. W. Pickering, *Hydrogen in Metals*, I. M. Bernstein, A. W. Thompson, ed., (Metals Park, OH, Am. Soc. Metals, 1974), pp. 207-222.
19. B. G. Ateya, H. W. Pickering, *Stress Corrosion Cracking and Embrittlement of Iron Base Alloys*, R. W. Staehle, J. Hockmann, R. D. McCright, J. E. Slater, ed. (Houston, TX, 1977), pp. 1183-88.
20. B. G. Ateya, H. W. Pickering, *Passivity of Metals*, R. P. Frankenthal, J. Kruger, ed., (Pennington, NJ, The Electrochemical Society, 1978), pp. 350-367.
21. H. W. Pickering, R. P. Frankenthal, *J. Electrochem. Soc.*, 119, (1972): p. 1297.
22. H. W. Pickering, P. J. Byrne, *J. Electrochem. Soc.*, 120 (1973): p. 607.
23. H. W. Pickering, *Corrosion and Corrosion Protection*, R. P. Frankenthal and F. Mansfeld, Eds., Vol. 81-8, (Pennington, NJ, The Electrochem Society Softbound Proceedings Series, 1981), p. 85; *ibid*, *Corrosion*, 42 (1986): p. 125.
24. H. W. Pickering, K. Cho, E. A. Nystrom, *Corrosion Sci.*, in press.
25. E. A. Nystrom, J. B. Lee, A. A. Sagüés and H. W. Pickering, submitted to the *J. Electrochem. Soc.*
26. K. Cho and H. W. Pickering, to be published.
27. B. G. Ateya and H. W. Pickering, *J. Electrochem. Soc.*, 122 (1975): p. 1018.
28. B. G. Ateya and H. W. Pickering, *J. Appl. Electrochem.*, 11 (1981): p. 453.
29. B. G. Ateya and H. W. Pickering, *Passivity of Metals*, R. P. Frankenthal and J. Kruger, Eds. (Pennington, N.J., The Electrochemical society Softbound Proceedings Series, 1978), p. 350.
30. J. C. Walton, *Corrosion Sci.*, 30 (1990): p. 915.
31. P. H. Melville, *Br. Corros. J.*, 14 (1979): p. 15.
32. J. Newman, D. N. Hanson and K. Vetter, *Electrochim. Acta*, 22 (1977): p. 829.
33. G. J. Bignold, *Corrosion*, 28 (1972): p. 307.
34. P. Doig and P.E.J. Flevitt, *Met. Trans.*, 9A (1978): p. 357.
35. M. Wang, Y. Xu and H. W. Pickering, *Oxide Films on Metals and Alloys*, B. MacDougall, R. S. Alwitt and T. A. Ramanarayanan, Eds., (Pennington, NJ, The Electrochemical Society Softbound Proceedings Series, 1993) in press.

TABLE 1

Comparison between the computed<sup>5</sup> and measured<sup>4,26</sup> values of the critical distance into the crevice for breakdown of passivity,  $x_{pass}$ , and the total crevicing current,  $I$ , for iron in 0.5 M acetic acid + 0.5 M sodium acetate solution.

Critical Distance, $x_{pass}$ cm		Total Crevicing Current, $I$ mA	
Computed	Measured	Computed	Measured
0.14	0.12-0.20	1.2	1.2-1.4

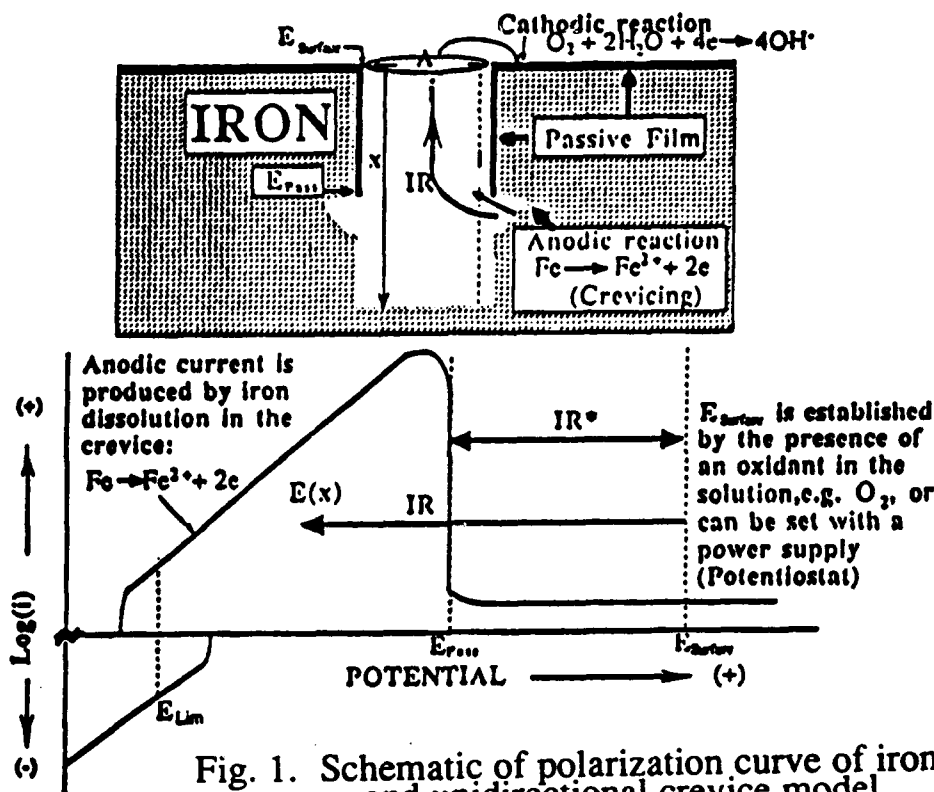


Fig. 1. Schematic of polarization curve of iron and unidirectional crevice model.

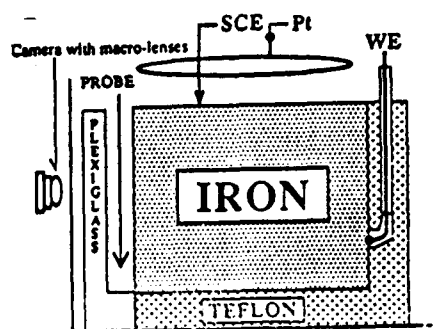


Fig. 2. Experimental crevice corrosion set-up.

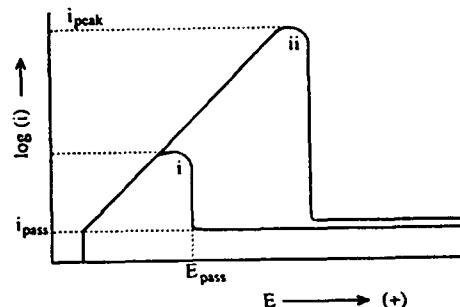


Fig. 3. Increase in active loop and  $i_{pass}$  (i→ii) due to pH decrease or  $Cl^-$  increase, or visa versa (ii→i) due to inhibitor addition.

## Corrosion Behaviour of High Nitrogen Stainless Steels for Biomedical Applications

Alberto Cigada

Politecnico di Milano-Dipartimento di Chimica Fisica Applicata  
Piazza Leonardo da Vinci 32, 20133 Milano (Italy).

Gianni Rondelli, Bruno Vicentini, Giampaolo Dallaspezia.

CNR-Istituto Tecnologia Materiali - Via Bassini 15, 20133 Milano (Italy)

### Abstract

The localized corrosion behaviour of three classes of stainless steels (Ni-austenitic, Mn-austenitic and Duplex) in environment simulating that of human body was evaluated by several electrochemical tests (Potentiodynamic, Critical Pitting Temperature, Scratch and ASTM F746). The results pointed out an increasing order of severity: Potentiodynamic  $\leq$  CPT  $<$  Scratch  $<$  ASTM F746.

By using a particular PRE formula ( $PRE = \%Cr + 3.3\%Mo + 30\%N + 0.5\%Ni - 0.5\%Mn - 30\%C$ ) it is possible to establish a good relationship between PRE of steels and their localized corrosion resistance. The positive effect of nitrogen addition was also evidenced. The Ni-austenitic 26Cr-32Ni-4Mo, the Ni-austenitic high nitrogen 24Cr-18Ni-4Mo-0.50N and the high nitrogen Duplex stainless steel 25Cr-7Ni-4Mo-0.26N can be considered not susceptible to localized corrosion in the human body.

**Key terms:** High nitrogen stainless steels, Localised corrosion, Orthopedic devices, Pitting Resistance Equivalent.

### Introduction

Stainless steels AISI 316L and the corresponding medical grade ASTM F138 have been widely used for biomedical applications in particular for osteosynthesis devices, due to their high generalised corrosion resistance, easy workability, good mechanical properties in the cold worked conditions and relatively low price.

However clinical experience has shown that traditionally used austenitic stainless steels are susceptible to crevice corrosion in the human body<sup>1-2</sup> causing release of metallic ions in the tissues surrounding the implants. This may cause local irritations or systemic effects, that are among the principal causes of clinical unsuccess in this field. In particular the adverse effect of nickel has been outlined, also due to the allergic sensitization of many people to this element<sup>1</sup>. Increase of mechanical properties is also useful for biomedical applications in particular for some high stressed orthopaedic devices such as Harrington rods, Ender nails, etc.<sup>3</sup>. Consequently the development of new steels with reasonable price, low nickel content, high mechanical properties and improved localized corrosion resistance, compared with the steels traditionally used for osteosynthesis devices, are advisable.

High nitrogen stainless steels seem to be interesting for these applications because, as reported in the literature<sup>4-9</sup>, the addition of nitrogen increases localized corrosion resistance. Moreover the nitrogen addition improves the mechanical properties of the material: it has been evaluated an increase in the mechanical properties of about 50 MPa for each 0.1% of added nitrogen<sup>10</sup>.

Therefore a research on high nitrogen stainless steels was carried out to qualify new materials for orthopaedic applications. Three classes of stainless steels were evaluated: nickel containing austenitic stainless steels with nitrogen up to 0.5% (Ni-austenitic), manganese containing austenitic stainless steels with nitrogen up to 1.0% (Mn-austenitic), duplex stainless steels with nitrogen up to 0.3% (Duplex).

### Experimental

Tests were carried out on traditional and high nitrogen stainless steels: five Ni-austenitic stainless steels (AISI 304L, AISI 316L, ASTM F138, 26Cr-32Ni-4Mo, 24Cr-18Ni-4Mo-0.50N), two Mn-austenitic stainless steels (18Cr-19Mn-0.55N and 18Cr-19Mn-2Mo-0.90N) and three Duplex stainless steels (23Cr-4Ni-0.10N, 22Cr-5Ni-3Mo-0.16N and 25Cr-7Ni-4Mo-0.26N). The 26Cr-32Ni-4Mo (SANICRO 28), 23Cr-4Ni-0.10N (SAF 23-04), 22Cr-5Ni-3Mo-0.16N (SAF 22-05) and 25Cr-7Ni-4Mo-0.26N (SAF 25-07) steels were supplied by Sandvik Steel (Sweden), 24Cr-18Ni-4Mo-0.50N (REMANIT 4565S) is produced by Thyssen (Germany), 18Cr-19Mn-0.55N (SAZ 55) and 18Cr-19Mn-2Mo-0.90N (SAKZ 90) were supplied by VSG (Germany). The chemical compositions and the nominal yield strength of the steels are reported in Table 1.

Four different types of corrosion tests were performed to evaluate the resistance to pitting and crevice corrosion of the materials.

Potentiodynamic tests were performed in artificial physiological solution (NaCl 8.74 g/l,  $\text{NaHCO}_3$  0.35 g/l,  $\text{Na}_2\text{HPO}_4$  0.06 g/l,  $\text{NaH}_2\text{PO}_4$  0.06 g/l) at 38°C following the ASTM G61 Standard Practice. The electrode potential was increased at a scanning rate of 600 mV/hour up to an anodic current density value of 100  $\mu\text{A}/\text{cm}^2$  to determine the potential ( $E_{\text{POT}}$ ) at which pitting attack took place, or up to transpassivity range ( $E > 800$  mV vs SCE) if pitting did not start.

Critical pitting temperatures were evaluated in physiological solution using the apparatus suggested by Lau and Bernhardsson<sup>11</sup>. The temperature at which the anodic current reaches the critical value of 10  $\mu\text{A}/\text{cm}^2$  was determined for different electrode potentials, obtaining temperature vs potential curves; the potential ( $E_{\text{CPT}}$ ) corresponding to the onset of localized corrosion at 38°C was then evaluated for each steel.

Stepwise potentiostatic tests with scratch according to the procedure proposed by Pessal and Liu<sup>12</sup> were performed in physiological solution. The passive film was locally damaged with a diamond tip at increasing potential values and the potential ( $E_{\text{SCRATCH}}$ ) at which the specimen does not repassivate was determined; tests were stopped if pitting did not occur at +800 mV vs SCE.

Tests according to ASTM F746 Standard Test Method were conducted in 0.9% NaCl at 37°C. Cylindrical specimens with a PTFE tapered collar were potentiostatically polarised to +800 mV vs SCE; when the current density reached 500  $\mu\text{A}/\text{cm}^2$  the potential was almost immediately decreased to low potential and the highest potential ( $E_{\text{ASTM}}$ ) at which the material repassivates after the stimulation step was determined.

## Results and Discussion

The results of the corrosion tests are summarized in Table 2 and in Figures from 1 to 4, where the localized corrosion potential obtained in each test is reported in each test is reported versus the Pitting Resistance Equivalent (PRE) index proposed by Speidel<sup>13</sup> and defined as follows:

$$\text{PRE} = \% \text{Cr} + 3.3\% \text{Mo} + 30\% \text{N} + 0.5\% \text{Ni} - 0.5\% \text{Mn} - 30\% \text{C}$$

The above formulation of PRE was chosen, among the different ones, because in additions to Cr, Mo, N usually taken into account, considers also the presence of other elements like manganese and nickel, whose amount varies considerably in the studied steels.

The detrimental influence of manganese on the localized corrosion resistance has been reported in the literature<sup>14-16</sup> due to manganese sulphide inclusions, that can act as localized initiation sites. As far as nickel is concerned, it has been observed<sup>16-18</sup> its positive influence on localized corrosion resistance in chloride containing environments. In the Figures 1-4 the range of the corrosion potentials (+200/+350 mV vs SCE) of passive stainless steels in human body<sup>19</sup> is also reported.

From the examination of the results (Figures 1-4), it can be observed that, increasing the PRE, increases the localized corrosion resistance of the steels. Only the 18Cr-19Mn-2Mo-0.90N steel showed in the Scratch and ASTM F746 tests a behaviour worse than that foreseeable on the basis of its PRE.

Concerning the potentiodynamic tests (Figure 1) it can be observed that, on 26Cr-32Ni-4Mo, 24Cr-18Ni-4Mo-0.50N, 18Cr-19Mn-2Mo-0.90N and 25Cr-7Ni-4Mo-0.26N, the onset of pitting can takes place only at potential values corresponding to the transpassivity of the material. The ASTM F138 steel has a better behaviour than AISI 316L according to its higher molybdenum content and higher purity. The 18Cr-19Mn-0.55N and 23Cr-4Ni-0.10N steels have behaviour similar to the AISI 316L, while noticeably worse behaviour was displayed by the AISI 304L, according to its lowest PRE.

The results of CPT tests are shown in Figure 2. The critical potentials ( $E_{\text{CPT}}$ ) are similar to those obtained from potentiodynamic tests ( $E_{\text{POT}}$ ), with the same ranking of the materials. To evaluate the onset of localized corrosion in the potentiodynamic test the electrode potential is increased at constant temperature, while in the CPT test the temperature is increased at constant potential: in both the tests the passivity film is not damaged by external stimulation. Consequently similar results have to be expected.

The results of scratch tests are reported in Figure 3. Also in this case the ranking of the materials is similar to those previously obtained, but the critical potentials ( $E_{\text{SCRATCH}}$ ) are lower than  $E_{\text{POT}}$  and  $E_{\text{CPT}}$ . This may be related to the experimental technique, because in the scratch test the tendency of the material to heal the passive film, mechanical damaged by the diamond tip, is evaluated.

The results of ASTM F746 tests are summarised in Figure 4. The potentials obtained are always lower than those of the other tests. These differences are ascribable to the presence of crevice assembly and to the different way the passivity film is damaged. In the ASTM F746 test a local damage of the passive film is obtained by an electrochemical method during the stimulation step at +800 mV vs SCE. This damage is more severe than that realized by the scratch, because under the collar more severe conditions are achieved due to the lowering of pH and increase in chloride ion concentration, because of the charge flowed. Moreover by the

ASTM F746 test, since attack under the PTFE collar usually took place, the repassivation tendency of the creviced areas and not that of the bare surface is determined, and it is well known that the potential values at which crevice corrosion takes place are lower than pitting potential values<sup>4, 20-22</sup>.

Considering all the test techniques, only 25Cr-7Ni-4Mo-0.26N, 26Cr-32Ni-4Mo and 24Cr-18Ni-4Mo-0.50N steels resulted not susceptible to localized corrosion also at potential values approaching the transpassivity region.

As far as the localized corrosion resistance in the human body is concerned, it should be considered that the higher free corrosion potential that a stainless steel can display in the human body is about 350 mV vs SCE<sup>20</sup>. Therefore, on the basis of our tests, it can be observed that the stainless steels today used, AISI 316L (PRE = 29.1) and ASTM F138 (PRE = 33.4), are susceptible to crevice corrosion in the human body, so confirming the wide clinical evidences<sup>1</sup>.

Susceptible to pitting corrosion are the steels with lower PRE, such as the AISI 304L (PRE = 24.8), confirming the occurrence of this form of attack observed during in vivo tests<sup>23</sup>. Immune to localized corrosion in the human body should be both the Ni-austenitic 26Cr-32Ni-4Mo (PRE = 56.0) the high nitrogen Ni-austenitic 24Cr-18Ni-4Mo-0.50N (PRE = 57.3) steels and the high nitrogen duplex 25Cr-7Ni-4Mo-0.26N steel (PRE = 48.9). Regarding the last steel it should be remarked that its excellent behaviour was also confirmed by clinical experimentation<sup>24</sup>.

Some additional considerations should be made on high nitrogen 18Cr-19Mn-2Mo-0.90N stainless steel. This material appears to be very interesting for biomedical applications owing its very low nickel content, its high mechanical properties in the annealed condition and its non magnetic properties even when subjected to high cold working degree. The 18Cr-19Mn-2Mo-0.90N steel showed good resistance to pitting corrosion and crevice corrosion resistance higher than the presently used ASTM F138 steel; however to achieve completely satisfactory crevice corrosion resistance a further increase in the PRE (3-5 units) is desirable.

### Conclusions

On the basis of localized corrosion tests conducted on three classes of stainless steels (Ni-austenitic, Mn-austenitic and Duplex) in environment simulating that of human body the following conclusions can be drawn:

- an increasing order of test severity can be established: Potentiodynamic  $\leq$  CPT  $<$  Scratch  $<$  ASTM F746;
- the localized corrosion resistance of the steels regularly increases with their PRE given by the formula:  $PRE = \%Cr + 3.3\%Mo + 30\%N + 0.5\%Ni - 0.5\%Mn - 30\%C$ ;
- the beneficial effect of a high nitrogen content was evidenced;
- among the Ni-austenitic and Duplex stainless steel's classes it is possible to select materials (24Cr-18Ni-4Mo-0.50N, 26Cr-32Ni-4Mo, 25Cr-7Ni-4Mo-0.26N) that can be considered not susceptible to localized corrosion in the human body. Regarding the 18Cr-19Mn-2Mo-0.90N austenitic steel it should be remarked that even if it shows a good resistance to pitting and crevice corrosion, a further improvement of its localized corrosion resistance is desirable.

# **Nitrogen bearing austenitic stainless steels - A promising replacement for currently used 316L stainless steel orthopaedic implant material**

**M.Sivakumar**

Department of Analytical Chemistry  
University of Madras  
Guindy Campus  
Madras - 600 025, India.

**U.Kamachi Mudali**

Metallurgy Division  
Indira Gandhi Centre for Atomic Research  
Kalpakam - 603 102, India.

**S.Rajeswari**

Department of Analytical Chemistry  
University of Madras  
Guindy Campus  
Madras - 600 025, India.

## **Abstract**

Potentiodynamic anodic polarization experiments on various nitrogen-bearing austenitic stainless steels (i.e. 316L stainless steel with 680 and 1600 ppm of nitrogen, 317L stainless steel with 880 and 1410 ppm of nitrogen and for comparison the currently used 316L stainless steel), were carried out in Hank's solution at pH 7.4 and 310K. The mean value of critical pitting potential ( $E_{pp}$ ) for the 316L stainless steel was + 365 mV (SCE). The presence of 680 ppm of nitrogen in this steel increased the  $E_{pp}$  value to + 620 mV (SCE), whereas the presence of 1600 ppm of nitrogen increased the  $E_{pp}$  value to + 1117 mV (SCE). A similar influence of nitrogen was also found in the case of type 317L stainless steel containing 880 ppm and 1410 ppm of nitrogen. The pit protection potential ( $E_{prot}$ ) was also found to be higher in the case of 316L stainless steel with 1600 ppm of nitrogen followed by 317L stainless steel with 1410 ppm of nitrogen, 317L stainless steel with 880 ppm of a nitrogen and 316L stainless steel with 680 ppm of nitrogen. It indicates that the increased nitrogen content hinders the development of new pits and also slows down the kinetics of growing pits. The presence of 680 ppm of nitrogen in the 316L stainless steel increased the critical crevice potential ( $E_{cc}$ ) to + 459 mV (SCE) from + 272 mV (SCE) and the presence of 1600 ppm of nitrogen raised the  $E_{cc}$  value to + 730 mV (SCE). Similar, influence of nitrogen addition was also found for the type 317L stainless steel containing 880 ppm and 1410 ppm of nitrogen with respect to the critical crevice potential. Thus the present study has shown the pitting and crevice corrosion resistance were higher in the austenitic stainless steels containing higher amount of nitrogen and the nitrogen-bearing austenitic stainless steels may be considered as alternate materials for the currently used 316L SS orthopaedic implant materials.

**Key terms:** Orthopaedic implants, nitrogen bearing stainless steel, pitting corrosion, crevice corrosion.

## Introduction

Orthopaedic implants are artificial mechanical devices that are mounted to the skeletal system of the human body for various purposes such as supporting bone, replacing bones or joints and reattaching tendons or ligaments. These surgical implants are usually made of one of the three types of materials viz., (i) austenitic stainless steels, (ii) cobalt-chromium alloys and (iii) titanium and its alloys.<sup>(1)</sup> Amongst all these materials titanium and its alloys are found to be most corrosion resistant.<sup>(2)</sup> However, the main disadvantages were their high cost and special welding procedures required for joining.<sup>(3)</sup> The austenitic stainless steels, especially type 316L stainless steel, are the most popular ones because of their relative lower costs and reasonable corrosion resistance.<sup>(4)</sup> However, it has been reported that type 316L SS implants get corroded in the body environment and release iron, chromium and nickel ions.<sup>(5)</sup> These leached chromium and nickel ions have been shown to be powerful allergens and are demonstrated to be carcinogenic in rats.<sup>(1)</sup> Therefore high corrosion resistance is demanded for implants to obtain biocompatibility and acceptability. The failure investigations/survey of failed stainless steel implants removed from human subjects revealed significant localised corrosion attack viz., pitting and crevice corrosion<sup>(6-9)</sup> which are the most frequently observed types of corrosion attack. The above factors necessitated the development of new stainless steel implant materials exhibiting resistance to localised corrosion.

In spite of immense strides made in the development of metals for use in orthopaedic surgery much remains to be improved. Pohler<sup>(10)</sup> and Nielsen<sup>(5)</sup> have suggested the adoption of accelerated tests to simulate the human body environment in tests aimed at identifying alternative stainless steels to type 316L.

Nitrogen is considered as an important alloying addition to austenitic stainless steel in terms of corrosion resistance as it widens the passive range in which pitting is less probable.<sup>(11-13)</sup> Nitrogen-bearing austenitic stainless steels are going to be used in the construction of fast breeder reactors in India, and efforts are now made to produce locally these materials. In the present work an attempt was made to study these materials for their suitability as orthopaedic implant devices, from the corrosion point of view.

## Materials and Methods

### A. Electrode Preparation

The alloys used in this investigations were:

(i)	316L stainless steel	-	316L
(ii)	316L (680 ppm of nitrogen)	-	316LN1
(iii)	316L (1600 ppm of nitrogen)	-	316LN2
(iv)	317L (880 ppm of nitrogen)	-	317LN1
(v)	317L (1410 ppm of nitrogen)	-	317LN2



The elemental compositions of the above alloys are given in Table 1. The alloys were cut into 1cm x 1cm x 0.3cm size specimens and annealed for an hour at 1323K and water quenched. These specimens were soldered to a copper rod to provide electrical contact. They were then doped with epoxy resin in such a way that one of its sides with 1cm<sup>2</sup> surface area gets exposed and this formed the working electrode. In order to avoid severe polishing after the resin mounting (which might cause microcracking at the metal-resin interface), the specimens were wet ground with SiC papers down to 600 grit followed by 6 and 1  $\mu$ m diamond paste before mounting. The edges of the mounted specimens were examined at 100 x (oil immersion) objective lens in an optical microscope for the presence of any gap between the metal and epoxy resin. If any gap was seen, the specimens were remounted. Then the electrodes were ultrasonically cleaned for 3 minutes and passivated in a solution of 30% HNO<sub>3</sub> (V/V) at 60°C for 30 minutes, thoroughly washed in deionised water rinsed in alcohol and dried.

### B. Polarisation Cell Assembly

A three compartment electrochemical cell (borosilicate glass) with a capacity of 500 ml was adopted. A platinum foil was used as the counter electrode and a saturated calomel electrode (SCE) was used as the reference electrode. The electrolyte used was a Hank's solution (whose composition is shown in Table 2) and its pH was adjusted to  $7.00 \pm 0.05$  with sodium bicarbonate and maintained at  $37 \pm 1^\circ\text{C}$  by means of a water bath. The test solution was continuously purged with nitrogen, then the working electrode was introduced into the cell and the potential was allowed to stabilise for 20 minutes.

### C. Pitting Corrosion

In the anodic polarisation study the potential was increased in the noble direction at a rate of 0.166 mV/sec until the breakdown potential ( $E_{pp}$ ) was attained where the alloy entered the transpassive or pitting region. Then the sweep direction was reversed after reaching an anodic current density of 0.5 mA/cm<sup>2</sup> till the reverse scan reaches the passive region. The potential at which the reverse anodic scan meets the passive region is the pit protection potential ( $E_{prot}$ ).

The parameters of interest that were recorded during cyclic potentiodynamic polarisation tests were (i) the corrosion potential  $E_{corr}$ , (ii) the pitting potential  $E_{pp}$ , (iii) the pit protection potential ( $E_{prot}$ ) and (iv) the safe region to corrosion attack ( $\Delta E$ ) and they are illustrated schematically in Fig.1.

### D. Crevice Corrosion

A glass assembly was designed as described by Dayal *et al*<sup>(14)</sup> to create a crevice on the mounted electrodes. The tip of the glass rod was brought into close contact with the electrode surface using the nut and threaded rod arrangements. The angle

between the glass and the electrode surface was maintained at  $1.2^\circ \pm 0.2^\circ$  and the bulk crevice area ratio was  $5.6 \pm 1.5:1$ .

To rule out any possibility of pitting and edge attack on electrode surface soon after the experiment, the electrode surface was thoroughly examined in an optical microscope. The electrodes with edge attack were rejected and those electrodes without edge attack were taken into consideration for the study.

## Results and Discussion

### A. Critical Pitting Potential

The critical pitting potential for 316L, 316LN1, 316LN2, 317LN1 and 317LN2 were determined from the polarisation curves and they are shown in Fig.2. The mean value of critical pitting potential ( $E_{pp}$ ) for the 316L stainless steel was +365 mV. The presence of 680 ppm of nitrogen in this stainless steel increased the  $E_{pp}$  value to +620 mV whereas the presence of 1,600 ppm of nitrogen increased the  $E_{pp}$  value to +1,179 mV. A similar influence of nitrogen was also found in the case of type 317L stainless steel containing 880 ppm and 1,410 ppm of nitrogen (vide table 3).

The present study has shown an increased value of the critical pitting potential for nitrogen-bearing austenitic stainless steels in the presence of molybdenum. A synergistic influence of nitrogen and molybdenum on the pitting corrosion resistance was reported by Truman *et al*<sup>(15)</sup> and Clayton.<sup>(16)</sup> Newman *et al*<sup>(17)</sup> have noticed an enrichment of molybdenum and nitrogen at the passive film/metal interface.

From the foregoing observations the alloys are ranked in the increasing order of pitting corrosion resistance as: 316L < 316LN1 < 317LN1 < 317LN2 < 316LN2

### B. Pit Protection Potential

The pit protection potential was determined for the above alloys from the polarisation curves (Fig.2). The mean value of pit protection potential for the 316L stainless steel increased from +24 mV to +93 mV for 316LN1 whereas for 316LN2 it increased from +24 mV to +137 mV. A similar trend was found for the type 317L stainless steel containing 880 and 1410 ppm of nitrogen. These observations can be interpreted as showing that new pits cannot be initiated above these potentials and hence it can be inferred that the increased nitrogen content hinders the development of new pits and also slows down the kinetics of pit growth.

The role of nitrogen on the pit protection potential can be explained by the following mechanism. Once the passive film is damaged, the formation of pit commences on the metal surface. If the pit grows, the conditions prevailing at the pit site are those of active dissolution. During active dissolution alloying elements such as iron, chromium and nickel dissolve whereas non active elements such as nitrogen can enrich at such

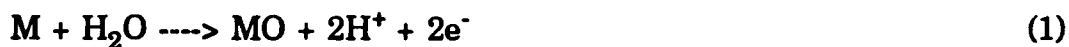
surface. Such a segregation has been reported by Newman *et al*<sup>(16)</sup> and also by Clayton and Martin<sup>(18)</sup> at least to the level of seven times the original concentration. This stage leads to the formation of ammonium ions and subsequently nitrogen compounds or it may provide an inactive layer to improve the pitting corrosion resistance.

The difference between the pit protection potential and the corrosion potential for a given system is defined here as the relative corrosion resistance ( $\Delta E$ ). This value can be used to rank alloys. The mean value of  $\Delta E$  for 316L stainless steel was 132 mV. The presence of 680 ppm of nitrogen in this stainless steel increased the  $\Delta E$  value to 261 mV whereas the presence of 1,600 ppm of nitrogen increased the  $\Delta E$  value to 296 mV. A higher value of  $\Delta E$  reflects an enhanced resistance to pitting or accelerated general corrosion. The presence of 880 ppm and 1410 ppm of nitrogen in 317L stainless steel also showed similar increase in  $\Delta E$  value, as shown in Table 3.

### C. Critical Crevice Potential

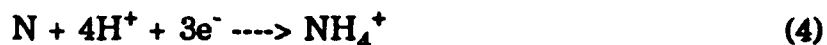
The critical crevice potential  $E_{cc}$  was determined from the polarisation curves of the materials studied by the anodic polarisation method and they are shown in Fig.3. The presence of 680 ppm nitrogen in the 316L stainless steel increased the  $E_{cc}$  value to +459 mV from +272 mV and presence of 1600 ppm of nitrogen raised the  $E_{cc}$  value to +730 mV. Similar influence of nitrogen addition was found for the type 317L stainless steel containing 880 and 1410 ppm of nitrogen with respect to the critical crevice potential. Thus the present study has shown the beneficial effect of nitrogen addition in improving the crevice corrosion resistance of austenitic stainless steels.

The pH of the normal body fluid is 7.4. In this condition oxygen is the principal depolariser and the oxygen present at the implant crevice is consumed quite rapidly either in the cathodic reaction or passivation. This depletion in oxygen concentration leads to the formation of a concentration cell. However, the change in the pH of the medium seems to be of greater importance than the change in the oxygen concentration. Acidification of the crevice area can take place as a result of the anodic reaction and hydrolysis of the metal ions:-



The acidification can accelerate the anodic reaction in the crevices. The addition of nitrogen to austenitic stainless steels improved the crevice corrosion resistance due to the formation of ammonium ions at the pits present in the crevices which increased the pH and slowed down the pit growth kinetics. Clayton<sup>(16)</sup> suggested a chemical rather an electrochemical mechanism for the formation of ammonium ions and pH was controlled by the formation of nitrides formed from the anodically

segregated nitrogen. Kamachi Mudali *et al*<sup>(19)</sup> has suggested that the dissolution of nitrogen at the pit site and subsequent formation of ammonium ions and nitrate compounds, improved the pitting corrosion resistance.



Thus the effect of localised decrease in pH at the crevice area can be avoided by using nitrogen-bearing stainless steel as implant material.

The nitrogen-bearing stainless steels showed a similar trend of both pitting and crevice corrosion resistance. The results of this investigation indicate that the pitting corrosion resistance and the crevice corrosion resistance are interrelated and that an improvement in the pitting corrosion resistance is generally accompanied by an improvement in the crevice corrosion resistance. However, the 317LN2 showed a higher crevice corrosion resistance than 316LN2. This increased corrosion resistance is due to the fact that the 317LN2 contains higher Ni content than that of 316LN2 stainless steel (Table 1). The presence of higher nickel content raises the critical pitting potential in the noble direction, thereby rendering the breakdown of the passive film within the crevice more difficult. In addition, the hydrolysis of  $\text{Ni}^{2+}$  yields essentially a neutral pH so that the dissolved nickel ions are not likely to contribute to the acidification of the solution within the crevice.

The increasing order of crevice corrosion resistance was:



#### **D. Environment of implanted material in fractured bone site**

Though normal body fluids are of neutral pH (7.4), an acidic condition was reported at the implanted site of a bone fracture.<sup>(5)</sup> The pH in the early periods following surgery drops to 4 and only in the course of 10 to 15 days, the pH attains neutrality. If wound healing is delayed, a lower pH will persist. The decrease in pH at such critical sites will induce pitting corrosion.<sup>(6)</sup> Normally the implant placed on the fractured bone is subjected to the unbalanced weight bearing biomechanical forces resulting in bending and torsional stresses and the implant may undergo a cyclic loading.<sup>(10)</sup> So the propagation of stress corrosion and corrosion fatigue cracks and mechanical fatigue fracture can originate from the corrosion pits.<sup>(6,7)</sup> The effect of local decrease in pH on the stainless steel implant at the fractured bone site can be avoided by using nitrogen-bearing austenitic stainless steels as implant materials because the nitrogen released from this alloys at such critical sites can form ammonium ions by utilising  $\text{H}^+$  ions.

## Conclusions

The following conclusions are obtained from the present investigation:

- \* The critical pitting and pit protection potentials of nitrogen-bearing austenitic stainless steels were nobler than those of the presently used 316L stainless steel. The higher pitting and pit protection potentials indicated the beneficial effect of nitrogen in improving the pitting resistance of austenitic stainless steels. The repassivation of actively growing pits are considerably increased in these alloys.
- \* The nitrogen-bearing stainless steels showed higher resistance to crevice corrosion than 316L stainless steel. The nitrogen present in this alloy gives rise to ammonium ions and ammonium nitrates at the pits present in the crevices which slow down the pit growth kinetics owing to the increase in the pH of the solution inside the pits.
- \* The localised corrosion resistance of the 316LN2 (17.4% Cr, 13.2%Ni, 2.57%Mo, 0.16%N and 0.01%C) and 317LN2 (18.47%Cr, 14.18%Ni, 3.58%Mo, 0.141%N and 0.014%C) alloys in the simulated body environment were sufficiently higher to prevent the onset of pitting corrosion and crevice corrosion attack.

## Acknowledgement

The authors express their gratitude to **Shri.J.B.Gnanamoorthy**, Head, Metallurgy Division and **Dr.R.K.Dayal**, Scientist, Metallurgy Division, IGCAR, Kalpakkam for their help during this investigation.

## **Pit-induced corrosion failures in stainless steel orthopaedic implant devices**

**M.Sivakumar**

Department of Analytical Chemistry  
University of Madras  
Guindy Campus  
Madras - 600 025, India.

**U.Kamachi Mudali**

Metallurgy Division  
Indira Gandhi Centre for Atomic Research  
Kalpakkam - 603 102, India.

**S.Rajeswari**

Department of Analytical Chemistry  
University of Madras  
Guindy Campus  
Madras - 600 025, India.

### **Abstract**

The origin and modes of failure have been investigated for a failed compression bone plate and intramedullary nail removed from the femur portion of a patient. The fracture surface of the compression bone plate revealed the presence of combined influence of fatigue and pitting corrosion. The site of fracture on the bone plate showed severe mechanical damage and secondary cracks. The fracture surface of the implant revealed the occurrence of 'beach marks' radiating from the pit present in the inner side of the screw hole. The magnified view of the fracture surface revealed the presence of fatigue striations and secondary cracks. The failed intramedullary nail showed that the edges were severely pitted and many cracks were found associated with the pits. The crack morphology was found to be transgranular, branched and unblunted. This suggests that it could be stress corrosion cracking rather than corrosion fatigue that was involved in the failure of the nail. The anodic polarization studies of the materials in Hank's solution indicated that they were highly susceptible to pitting attack. Moreover, the elemental analysis of the failed implant indicated that it contained lower molybdenum than the recommended limit (2-3 wt.%). In both the cases the inclusion content was found to be 4 (ASTM Unit) and grain size was 3 (ASTM unit), in contrast to the ASTM recommended limit for inclusion content and grain size of 2 and 4 respectively. The failure of the compression bone plate and intramedullary nail was a result of fatigue and stress corrosion cracking, respectively, due to the propagation of cracks from a corrosion pit.

**Key terms:** Orthopaedic implants, fatigue failure, stress corrosion cracking

## Introduction

Orthopaedic devices are artificial mechanical devices that are mounted on the skeletal system of the human body for various purposes such as supporting bone or replacing bone or joints and reattaching tendons or ligaments. These artificial mechanical devices are usually made of one of the three types of materials viz., (i) austenitic stainless steels (ii) cobalt chromium alloys and (iii) titanium and its alloys. Type 316L stainless steel is the most commonly used implant material<sup>(1)</sup>. The artificial mechanical devices are considered to have failed when they have to be prematurely removed from the body because the implant does not accomplish its intended function due to implant corrosion and/or fracture<sup>(2)</sup>. In every failure, the patient is made to experience the trauma of repeated surgeries as well as the severe pain experienced during the process of rejection of the device. The removal of failed implant will cause great expense and hardship to the patient. Therefore, it is highly desirable to keep the number of failures to a minimum. Hence, the determination of the mechanism that caused failure of an implant is necessary. It is also important to explore the event (or) sequence of events which caused that particular mechanism(s) to become operative. Further failure investigation will help to improve the total performance of implant devices as well as revealing the details of the mode and origin of failure mechanisms.

In spite of the recent innovative metallurgical and technological advances and a remarkable progress in the design of implants, failures of implants continue to occur<sup>(3)</sup>. The failures of implants have been reported as due to fatigue<sup>(4)</sup>, corrosion<sup>(5,6)</sup>, other general failure mechanisms but the underlying causes for the initiation of these failures are seldom determined. The question often arises as to whether stress corrosion cracking can take place *in vivo*. Gray<sup>(7)</sup> has reported an example of classical stress corrosion cracking appearance in a stainless steel screw removed from the body. ASTM<sup>(8)</sup> also gives evidences of some low-temperature stress corrosion cracking in 316 stainless steel. Bombara *et al.*<sup>(9)</sup> reported pit-induced stress corrosion cracking in stainless steel removed from the body. However, these occurrences are rare.

The present study reveals that the failure of implants made of stainless steel is typically pit-induced fatigue and stress corrosion cracking. This contributes to the understanding of the failure mechanism of metal fixtures under the action of physiological conditions.

## Materials and Methods

The implants were examined in a stereomicroscope to furnish information on surface scratches, corrosion and other imperfections. In addition, fractographic analysis was carried out on the fracture surface of the failed implant with a scanning electron microscope [SEM].

A portion of the failed area of the implant was metallographically polished and subjected to electrolytic etching [10%  $(\text{NH}_4)_2\text{S}_2\text{O}_8$ ] and the microstructure was studied. The Vicker's hardness of the implant was determined by using a diamond indenter with 5 kg load in a Leitz metallurgical microscope. The specific composition of implant alloys may have a telltale effect on the durability. Hence chemical analysis of the implant was carried out by using inductively coupled plasma spectroscopy.

The potentiodynamic anodic polarization study of the failed implant and 316L stainless steel (ASTM recommended composition for surgical implant) was carried out to evaluate the pitting resistance. The electrode preparation was based on the ASTM recommended practice for surface preparation of surgical implants (ASTM-F-36). After polishing the alloy specimens were degreased in acetone and passivated in a 30% solution of nitric acid at 50°C to 60°C for a period of 30 minutes. The specimens were then sterilized in a steam autoclave for 15 min at 120°C.

The electrolyte used was a Hank's solution (8g NaCl, 0.14g  $\text{CaCl}_2$ , 0.4 g KCl, 0.35g  $\text{NaHCO}_3$ , 1g glucose, 0.19g  $\text{NaH}_2\text{PO}_4$ , 0.19  $\text{MgCl}_2$ , 0.06g  $\text{Na}_2\text{HPO}_4 \cdot 2\text{H}_2\text{O}$ , 0.06g  $\text{MgSO}_4 \cdot 7\text{H}_2\text{O}$ /1000 ml) adjusted to a pH of  $7.00 \pm 0.05$ . The electrolyte was maintained at  $37 \pm 1^\circ\text{C}$  and potentials were measured with respect to a saturated calomel reference electrode (SCE). For anodic polarization the potential was increased in the noble direction at a rate of 0.166 mV/sec, until the breakdown potential was observed or until the alloy entered the transpassive region.

## Results and Discussion

The compression bone plate is currently used as one of the fixing devices for the treatment of fractures. In the present study the above implant was inserted in the right femur of a 27 years old male during January - 1990. Eleven months later the implant was found to have fractured, as shown in the Fig.1, and hence it was removed.

Visual observations on the failed implant revealed several scratches on the surface (Fig.2). The fracture had occurred on the fifth countersunk hole of the implant which coincided with the location of the fracture on the bone of the right femur of the patient. SEM examination of the implant revealed several scratches and secondary cracks in the vicinity of the fractured site of the implant (Fig.3) and severe mechanical damage was noticed in the sixth countersunk hole (Fig.4). The sixth countersunk hole was closer to the site of the bone defect. Hence, it had experienced severe mechanical damage during the patient's movement.

The severe damage that occurred around the sixth countersunk hole of the implant was due to the compression between the screw head and screw hole that might have aggravated the fracture. There was no significant mechanical damage or fretting corrosion observed in the remaining regions of the countersunk holes, whereas slight



mechanical damage was seen on the other side of the sixth countersunk hole of the plate. Examination of the fracture surface of the implant revealed the occurrence of 'beach marks' radiating from the pit present in the inner side of the screw hole (Fig.5). The higher magnified view of the fracture surface revealed the presence of fatigue striations and secondary cracks (Fig.6) which confirm the fatigue failure of compression bone plate. However, in the case intramedullary nail a stress corrosion crack was observed. The intramedullary nail under investigation was inserted in the right from of a 27 years old male during January - 1990. Nine months later, a chronic pain and inflammation in the region necessitated the immediate removal of the device.

Fig.7 shows the roentgenogram of the failed device. The arrow B indicated the hair line crack at the site of the bone fracture. The cracks were not visible upon visual examination of the retrieved device (Fig.8). Stereomicroscopic examination revealed the presence of microcracks (A and C) adjacent to the hair line crack (Fig.9). However, the hairline crack (B) was not visible even under stereomicroscopic examination. The least developed cracks revealed that crack nucleation took place at the edges of the failed device. The SEM micrograph of crack B, present in Fig.9 is shown in Fig.10. It revealed that the edges were severely pitted and most cracks were definitely associated with pits. Typical example of cracks originated from pits are shown in Fig.11.

Magnified view of the cracks A and C in Fig.9 are shown in Figs.12 and 13. The crack morphology was found to be transgranular, branched and unblunted, suggesting at first sight that stress corrosion cracking rather than corrosion fatigue was involved in the failure of the implant.

The Vicker's hardness of the failed compression bone plate and intramedullary nail ranged from 250-260 Hv and 240-250 Hv, respectively. The devices were sectioned near the failed area, polished and etched for microscopic examination. In both the cases the inclusion content was found to be 4 (ASTM Unit) and grain size was 3 (ASTM Unit). In contrast the ASTM recommended limit for inclusion content and grain size were 2 and 4, respectively<sup>(10)</sup>.

The specific elemental composition of the implant material may have a telltale effect on its durability and hence elemental analysis was carried out. The specific elemental composition of the failed implant as well as ASTM standard values are set out in Table - I for an effective comparison. The chromium and nickel contents in the compression bone plate was about 3.6% and 3% higher respectively, and the molybdenum content was about 1.3% lower, than the recommended ASTM limit. The other elements were within the ASTM recommended limit. Intramedullary nail showed a molybdenum content about 0.5% lower than the recommended limit. In the above cases molybdenum content was lower than the recommended ASTM limit (2-3 wt%). The specific purpose of molybdenum in austenitic stainless steel is to improve the pitting corrosion resistance<sup>(3)</sup>.

In the above cases the high inclusion content and low molybdenum content would have reduced the pitting resistance of the implant. The above conclusion was confirmed by the potentiodynamic anodic polarization study of the failed devices. The pitting potential observed for the standard 316L SS was +365 mV (SCE) whereas for the compression bone plate, it was +265 mV (SCE) and for intramedullary nail it was +280 mV (SCE) as shown in Fig.14. From the anodic polarization studies it is inferred that the failed implants were highly susceptible to pitting corrosion.

Generally, body fluids are neutral with pH values of approximately 7.4. However, pH is not neutral in a wound which is in the process of healing. The pH in the early periods following surgery drops to 5 and only in the course of 10 to 15 days it again reaches neutrality. For patients whose wound healing is delayed, a change in pH will persist<sup>(3)</sup>. In both the cases the cracks in the devices exactly coincided with the fractured site of the bone. The presence of pits in devices at such critical sites had resulted in a decrease of pH in the vicinity of implant at the fractured site.

Pohler<sup>(11)</sup> has shown that the implant placed on the fractured bone is subjected to the unbalanced weight bearing biomechanical forces, resulting in bending and torsional stresses and the compression bone plate may undergo a cyclic loading leading to fatigue damage. For fatigue cracks to develop, it is not necessary for the implants to be loaded in the plastic deformation range. Moreover, the local stresses that occur under the conditions of loading in the elastic deformation range of the implant, is sufficient to initiate fatigue cracks on the surface of the implant. Similar biomechanical forces might have aggravated the compression bone plate.

The microscopic observations indicated the involvement of stress corrosion cracking in intramedullary nail. The typical sequence of events in stress corrosion cracking of steel has been aptly depicted by Brown<sup>(12)</sup> as consisting of the following stages.

- (1) Localised breakdown of the oxide film.
- (2) Crack nucleation from the pit.
- (3) Stress corrosion crack propagation.
- (4) Termination of crack by mechanical rupturing.

The incubation period involves steps 1-3, which depends on the specific medium and the physicochemical conditions of exposure. The studies of Harston and Scully<sup>(13)</sup> in  $H_2SO_4/NaCl$  solution confirmed that a critical combination of acidity and chloride ion concentration is conducive to stress corrosion cracking of austenitic stainless steel even at ambient temperature.

The presence of pits in intramedullary nail could be seen as serving two functions:

- (1) Stress-raising although to a lesser extent because of the rather round shape of normal pits.

- (2) The crack in the implant exactly coincided with the fractured site of the bone. The presence of pits in implant at such critical sites had resulted in a decrease of pH in the vicinity of implant at the fractured site.

Therefore the failure of the intramedullary nail was a result of stress corrosion cracking due to the propagation of cracks radiating from a corrosion pit (or) pits.

## **Conclusion**

The failure of compression bone plate and intramedullary nail was a result of fatigue failure and stress corrosion cracking, respectively, due to the propagation of cracks radiating from the corrosion pits. In both cases, the crack propagation was aggravated by high inclusion content, large grain size of the implants and biomechanical forces exerted on the above devices.

## **Acknowledgement**

The authors express their gratitude to **Shri.J.B.Gnanamoorthy**, Head, Metallurgy Division and **Dr.R.K.Dayal**, Scientist, Metallurgy Division, ICCAR, Kalpakkam, for their help during this investigation.

## **References**

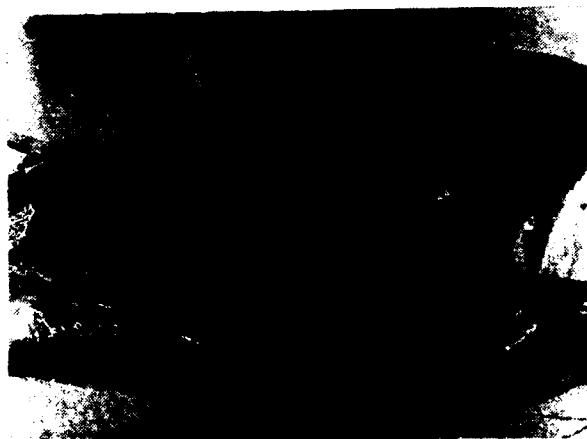
1. R.A. Silva, M.A. Barbosa, G.M. Jenkins and I.Sutherland, *Biomaterials*. **11** (1990): p.336.
2. D.F. Williams. *J. Mater. Sci.*, **22** (1987): p.3421.
3. K.Nielsen, *Br. Corros. J.*, **22** 4 (1987): p.272.
4. O.E.M. Pohler and F. Strumann, *Fatigue and corrosion fatigue studies on stainless steel implant material*, in *Evaluation of Biomaterials*, C.D. Winter, J.L.Leray and K.De Groot Eds., (John Wiley & Sons, 1980) p.89.
5. V.J.Colangelo and N.D. Greene, *J. Biomed. Mater. Res.* **3** (1969): p.247.
6. A Fraker and C.D. Griffin E., *Corrosion and degradation of implant materials*, American Society for Testing and Materials, ASTM Spec. Tech. Publ.859, Philadelphia, (1985).
7. R.J.GRAY, *Biomed. Mater. Res. Symp.*, **5** (1974): p.27.
8. American Society for Testing and Materials, ASTM Spec. Tech Publ.859, Philadelphia, (1960).

9. G.Bombara and M.Cavallini, Corros. Sci., 17 (1977): p.77.
10. J.R.Cahoon and H.W. Paxton, J. Biomed. Mater. Res., 4 (1970): p.223.
11. O.E.M. Pohler, "Metals Handbook", Vol.11, 9<sup>th</sup> Edn. edited by K.Mills (Metals Park, Ohio, American society for metals, 1986) p.670.
12. B.F.Brown, "The Theory of Stress Corrosion Cracking in Alloys", edited by J.C.Scully (Brussels, North Atlantic Treaty Organization, 1971) p.186.
13. J.D. Harston and J.C. Scully, Corrosion, 25 (1969): p.493.

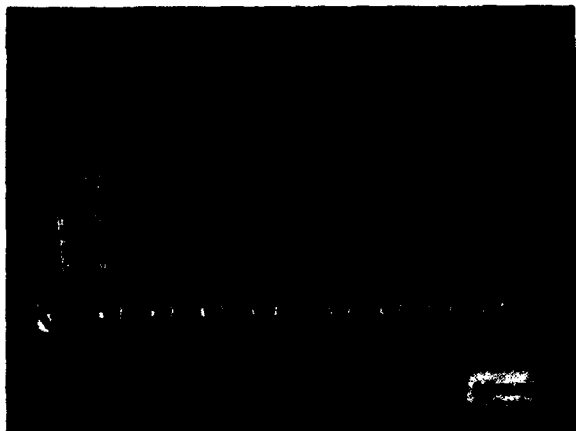
**Table - 1**

**Chemical Composition of the failed implants (% wt. )**

Elements	ASTM standard for surgical implants	Compression bone plate	Kuntscher's clover leaf intramedullary nail
Cr	17.00 to 19.00	22.6	18.1
Ni	12.00 to 14.00	17.0	12.2
Mo	2.00 to 4.00	0.7	1.5
Mn	2.00 Max	2.2	2.1
P	0.03 Max	0.01	0.01
Si	0.75 Max	0.61	0.52
S	0.03 Max	0.03	0.04
C	0.03 Max	0.023	0.03
Fe	Balance	Balance	Balance



1. Photograph shows the fractured compression bone plate and screws with the fractured femur of a 21 years old patient. Notice the fracture at the fifth countersunk hole of the implant which corresponds with the fracture on the femur bone (B-femur bone, F-fracture on the bone, P-bone, S-screw).



2. Photomicrograph of a failed compression bone plate and its screws. Notice a fracture on the fifth countersunk hole and scratches on the surface of the bone plate.



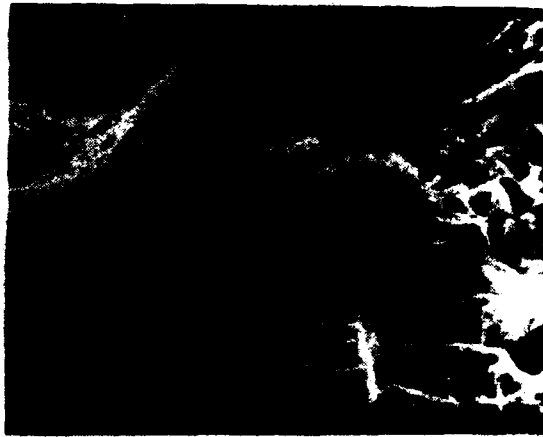
3. Scanning electron micrograph showing the microcracks emanating from the fifth countersunk hole of the failed implant.



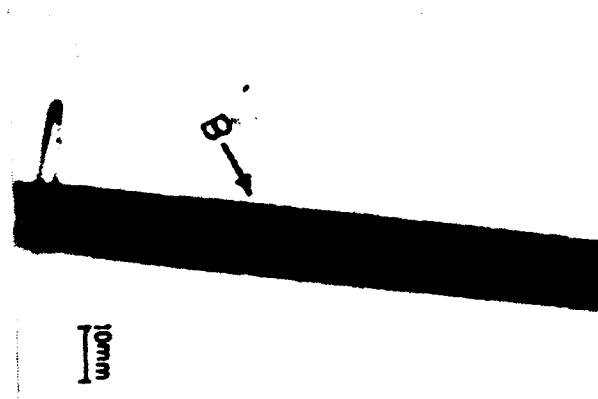
4. Stereomicrograph of the sixth countersunk hole of the failed compression bone plate. Notice the severe damage at the sixth countersunk hole and scratches around the countersunk hole.



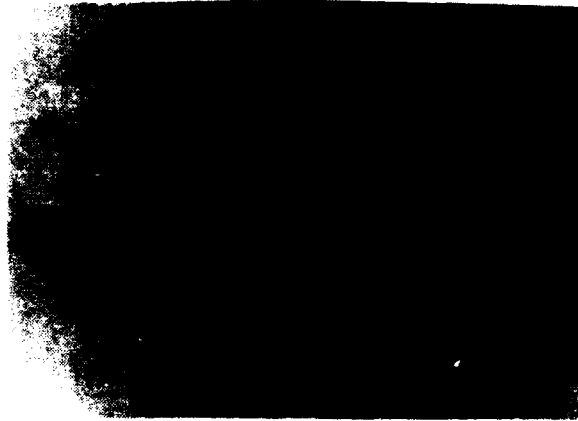
5. Stereomicrograph of the fracture surface of the failed compression bone plate. Notice the 'beach marks' radiating from the countersunk hole of the implant (unlabelled arrow).



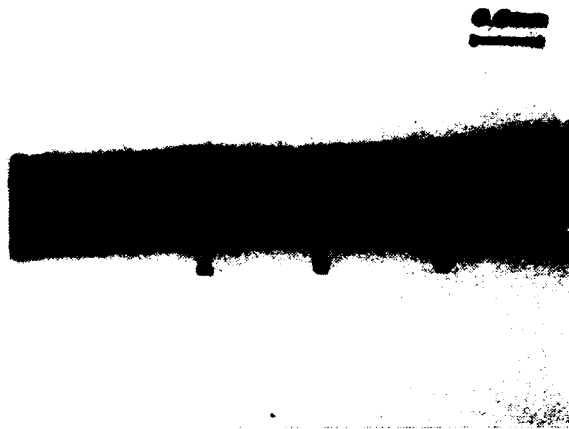
6. Scanning electron micrograph showing fatigue striations.



7. Roentgenogram showing the failed intramedullary nail. Arrow B indicates the hairline crack in the nail which corresponds with the fracture on the femur bone.



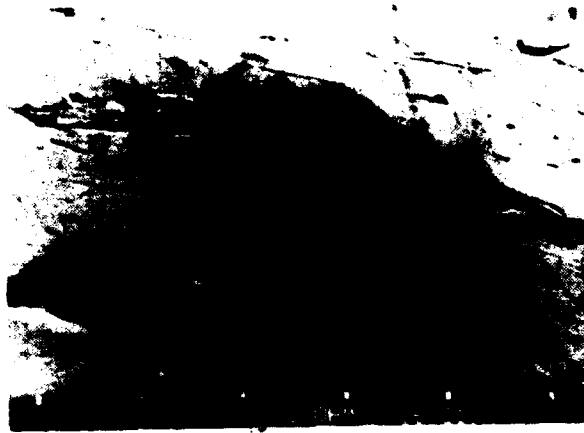
8. Photograph of a failed intramedullary nail removed from body.



9. Stereomicrograph showing the microcracks emanating from the edges of the end of nail. Microcrack A, hairline crack B and microcrack C.



10. Scanning electron micrograph of crack B, indicated in Fig.9, revealing that the crack was associated with the pit.



11. Scanning electron micrograph of crack B, indicated in Fig.9, showing that the crack originated from pits.



12. Scanning electron micrograph of crack A, indicated in Fig.9, showing that the crack morphology was transgranular and branched (unlabelled arrow:).



13. Scanning electron micrograph of crack B, indicated in Fig.9, showing that the crack morphology was unblunted.



## **Studies of the Environmental Degradation of Metal Matrix Composite Materials**

**A.K. Rawat**  
Mechanical & Aerospace Engineering Department  
University of Central Florida,  
Orlando, FL 32816.

**V.H. Desai**  
Mechanical & Aerospace Engineering Department  
University of Central Florida,  
Orlando, FL 32816.

**P. Ramakrishnan**  
Metallurgical Engineering Department  
Indian Institute of Technology,  
Bombay, India 400076.

**R.C. Prasad**  
Metallurgical Engineering Department  
Indian Institute of Technology  
Bombay, India 400076.

### **Abstract**

Studies were performed on a series of Al 6061/SiC<sub>p</sub> and on the corresponding matrix alloy in 3.5% NaCl solution. All the specimens were in T-6 heat treatment condition. The effect of particle size and volume percent of reinforcing SiC phase was studied using Electrochemical Impedance Spectroscopy, D.C. techniques, open circuit potential variation and Optical and Scanning Electron Microscopy (SEM). The effect of the same parameters was studied on the mechanical properties of these materials at room temperature and at elevated temperatures. The results from these studies indicate that in all the cases the corrosion resistance of the composite materials is inferior to that of the corresponding matrix alloys. The pitting and corrosion potential show a small but definite shift in more active direction with increasing the particle size and volume percent of the reinforcing phase. The matrix cracking is observed in some MMC specimens immersed in the electrolyte for few weeks. There is an increase in the strength of the MMC with increasing the volume percent of the SiC particles. The result from these studies are being utilized to develop optimum processing parameters.

**Key Words** : Metal matrix composites, electrochemical impedance spectroscopy, localized corrosion, SiC reinforcement.

## Introduction

Metal matrix composite (MMC) materials are an attractive, relatively new class of engineered materials. They offer attractive properties of high strength and low density. They can be fabricated using varied number of processing techniques such as powder metallurgy, directional solidification, injection molding and casting techniques. Moreover, they can be fabricated to fit a variety of mechanical design requirements. This has given rise to extensive investigation especially in the processing, mechanical properties and fracture behavior. Unfortunately not much work has been done in the corrosion behavior of composite materials. Introduction of reinforcing phase in the form of particles, whiskers and fibers improves the strength to weight ratio but at the same time introduces inhomogeneities in the matrix in the form of crevices, pores and reinforcement/matrix interfaces. Since corrosion is known to start preferentially at the inhomogeneities, MMC materials should be more prone to corrosion, especially the localized corrosion, than the corresponding matrix alloy. In most composite materials, the reinforcing phase is generally more noble than the matrix alloy. This can enhance the corrosion by contributing to the galvanic interaction between the matrix and the reinforcement phase. Even though the literature on the corrosion behavior of MMC is sparse and controversial (in terms of the nature of attack and effect of different phases) almost all of the studies indicate that corrosion resistance is generally poor as compared to the matrix alloy<sup>1-13</sup>. Due to present applications and the possibility of extensive use of MMC materials in the future it is of paramount importance to study the corrosion behavior of these materials. Since there are inherent processing inhomogeneities in MMC, they are very prone to crevice corrosion and pitting corrosion. The mechanism of localized attack is far from being understood. There is controversy regarding the site of initiation of localized attack (at reinforcement/matrix interface or away from the interface). Another area of dispute is the effect of the galvanic coupling on the initiation site of localized attack. According to Sedriks et al<sup>11</sup>, the increased susceptibility of MMC to localized corrosion is due to the increase in the anodic areas in the vicinity of the reinforcement/matrix interface, whereas, Mansfeld et al<sup>12</sup>, ascribe the inferior corrosion resistance of MMC to the increase in cathodic sites due to the presence of SiC particles.

## Experimental Methods and Materials

### Processing and Mechanical Properties of Composite Materials

Al-1%Mg-0.6%Si Corresponding to 6061 alloy and  $\beta$ -SiC (Grindwell Norton Co.) particles of average size 10, 40 and 60  $\mu\text{m}$  were used as reinforcement in the present investigation. SiC<sub>p</sub> constituting 10, 15 and 20 vol% were incorporated in the Aluminum matrix. The alloy was melted in a graphite crucible with a nitrogen atmosphere. Additional Mg was added to the melt to compensate for the magnesium loss during processing. The melt was stirred with a ceramic coated mechanical impeller. SiC particulates were added to the molten metal while the stirring was continued. After complete addition of SiC<sub>p</sub>, the melt was stirred well and poured at a temperature of 700°C into metallic molds. The cast ingots were machined to 45 mm dia x 45 mm height billets, soaked at 525°C and extruded at an extrusion ratio of 1:17 in to circular rods at a ram speed of 2 mm/sec. The extruded rods were solution heat treated at 530°C, water quenched and then aged at 175°C to obtain the maximum matrix hardness. The aging time was first optimized by determining the matrix microhardness at different aging times using a diamond indenter at a load of 10 gms. The tensile testing was conducted on round specimens with 6 mm gauge diameter using a servohydraulic mechanical testing machine (MTS-810) with a cross head speed of 0.17 mm/min.

### Corrosion Studies

The materials studied were MMC Al 6061/SiC<sub>p</sub> which contained different volume fractions and particle sizes of SiC as indicated above. The corresponding matrix alloy Al 6061 was also studied for comparison purpose. All the specimens were given T6 heat treatment at 530-535°C for 6 to 7 hours. The Al 6061/SiC<sub>p</sub> MMC specimens were in the form of cylindrical samples about 2.0 cm long and 1.0 cm in diameter. All the specimens were polished up to 600 grit with SiC paper then polished with alumina suspension of 5.0  $\mu\text{m}$ , 1.0  $\mu\text{m}$ , 0.5  $\mu\text{m}$ , and 0.03  $\mu\text{m}$ . Finally the specimens were degreased in acetone and ultrasonically cleaned in deionized water and blow dried using hot air gun. The electrolyte used was 3.5% NaCl solution of pH 7.0.

The following corrosion tests were conducted :

**O.C.P vs. Time.** Polished specimens were immersed in 3.5% NaCl open to air. The variation of open circuit potential was measured using Saturated Calomel Electrode (SCE) as the reference. The potential was monitored for times till a steady state was reached. In general, the MMC specimens took longer times to attain steady state as compared to the corresponding matrix alloy.

**Potentiodynamic polarization studies.** Polished specimens were immersed in 3.5% NaCl solution for about one hour or till the open circuit potential becomes reasonably stable. The potential was scanned from open circuit to the noble direction (anodic polarization). The scan rate was 0.2 mV/sec.

**Electrochemical Impedance Spectroscopy (EIS).** Impedance studies were performed using EG& G PARC Model 273 Galvanostat/Potentiostat and Model 5210 Lock-in amplifier. The frequency range was 0.01 Hz to  $10^4$  Hz. Perturbation of 5.0 mV was applied. A 30 pF capacitor was connected in series with reference electrode using a platinum wire to eliminate the frequency induced phase shifts at higher frequencies.

### **Optical and Scanning Electron Microscopy**

Optical microscopy was performed on as received specimens and after performing electrochemical testing in NaCl solution. The extent and nature of attack and the homogeneity of SiC particle distribution in the matrix were also investigated. Scanning electron microscopic studies were also performed to for the same purpose.

## **Results and Discussion**

### **Mechanical Properties**

Matrix microhardness variation with aging time is shown in Figure 1. Accelerated aging of the matrix was observed by reinforcing with SiC. The peak aging at 175°C occurred faster with increasing SiC<sub>p</sub> volume percentage in the matrix<sup>14-16</sup>. The peak aging time for the matrix reduced from 8 hours to 6.5 hours by incorporating 15 vol% SiC and the time further reduced to 5.75 hours by increasing the SiC volume to 20%. The mechanical properties of composite investigated are shown in Figure 2 & 3. It was observed that the yield strength of the alloy first increased with increasing SiC<sub>p</sub> volume in the matrix up to 15% and on further increase in the SiC<sub>p</sub> volume fraction, the yield strength tends to decrease. The yield strength of the composite also showed similar trend with increase in SiC particulate size. This may be attributed to the fact that for a constant volume fraction of SiC in the matrix, the interparticle distance increases with increase in the SiC particulate size by which the matrix resistance to deformation is reduced<sup>17,18</sup>.

The effect of SiC<sub>p</sub> reinforcement on the properties of the composites is found to be influenced by the particle size and volume fraction of the reinforcements. With the addition of SiC<sub>p</sub> reinforcement the yield strength is found to increase with increase in volume fraction of the reinforcement (Figure 3). The matrix yield strength increased from 236 MPa to 305 MPa with increasing the SiC<sub>p</sub> to 15 vol%. By using a particle size 10  $\mu$ m the yield strength of the matrix with 10 vol% SiC increased from 236 to 297 MPa while with an increase of particle size of 40  $\mu$ m, the yield strength increased to only 256 MPa. Further increase in particle size to 60  $\mu$ m for the same volume fraction the Y.S. of the matrix decreased from 236 to 234 MPa (Figure 2). While increasing the volume fraction

of  $\text{SiC}_p$  (40  $\mu\text{m}$ ) from 10 to 15% the yield strength decreased from 256 MPa to 225 MPa (figure 2). Considering the influence of  $\text{SiC}_p$  size on the yield strength of the composite the finer size of 10  $\mu\text{m}$  is found to provide the maximum increase in yield strength for the same volume fraction of the reinforcement. While coarser fractions are found to decrease the yield strength with increasing volume fraction of the reinforcement, the finer particle size reinforcement of 10  $\mu\text{m}$  is found to increase the yield strength with increasing volume fraction within the range of this investigation.

## Corrosion Behavior

**O.C.P. vs Time.** Figures 4 and 5 show the variation in open circuit potentials with time. All the specimens were immersed in 3.5% NaCl solution open to air. The open circuit potential shows considerable fluctuation for the first few hours but eventually attains a steady state value. In general, the OCP values for all MMC specimens are very close to that of the corresponding matrix alloys but in all the cases values for MMC are slightly negative to that of the matrix alloy. The OCP becomes more negative with the increase in the size of reinforcing SiC particles and also with increase in their volume percent. This trend is more clearly evident in figures 6 and 7 where the steady state values of OCP are plotted as a function of SiC particle size and increasing volume percent. It is speculated that this trend in the negative direction may be due to the effects on the homogeneity of the oxide film in MMC specimens. It is believed that with increasing size and volume percent of SiC particles the integrity of the film is disrupted which leaves it more prone to the attack by aggressive ions like  $\text{Cl}^-$  and hence a new value of the open circuit potential is attained which will depend on the extent of the discontinuity of the film on the sites where SiC particles are present in the film. This speculation is further reinforced by observation of the variation of pitting potentials with SiC particle size and their volume percent as described in the next section.

**Potentiodynamic Polarization Studies.** Figures 8 and 9 show the potentiodynamic polarization curves of MMC and corresponding matrix alloys in 3.5% NaCl solution open to air. The curves indicate that all these specimens show a very limited passive behavior in this electrolyte. The current density shows a very rapid increase after polarization of only a few millivolts above the free corrosion potential, thus indicating the onset of the localized attack which is later identified to be in the be pitting corrosion. The current density stays very high during the scan reversal (not shown in the figures, for clarity). In all the MMC specimens the repassivation is not observed once the pitting has started. Also the corrosion potentials shifts in more negative directions after the polarization. As indicated above, the pitting potential shows a small but definite trend in the more negative direction with increasing volume percent and size of SiC particles. The pitting potential is determined from the point where a rapid increase in the current density occurs. As shown in figure 6 and 7 the pitting potential of the alloy Al 6061 is -740 mV vs. SCE where as the pitting potential becomes -815 mV vs. SCE when the size of the reinforcing SiC particles is increased to 60  $\mu\text{m}$ . Similarly, increase in the amount of SiC results in shift in pitting potential in more active direction as indicated by figure 7. The definite reason for negative shift in the pitting potential is unknown at this

time but it is believed that discontinuity in the oxide film due to the presence of SiC particles plays a role. The integrity of the film is affected which may initiate localized attack at lower potentials. Furthermore, it is observed that in all the cases the current density increases with the increase in the amount and size of the reinforcement. Since SiC is virtually inert in nature, the anodic current density is mostly due to the dissolution of the matrix phase. Hence the actual dissolution rate of the matrix is higher than that indicated for the total exposed area of the specimens. This is an important factor which is often ignored while reporting the current density for the corrosion of metal matrix composites. The reasons for the increase in the current density with increasing size and amount of SiC are not very clear. Our speculation is that the poor integrity of the passive oxide film plays a role by providing a ready access to the underlying matrix at the particle/matrix interfaces. Although, SiC is virtually inert, even the limited conductivity of these particles may induce some galvanic effects thereby accelerating the attack on the matrix. Most of the pits seem to have nucleated near the particle/matrix interfaces. Other reason for the accelerated corrosion of MMC with increase in the particle size and vol% may be due to the increase in the cathodic areas which result in the higher cathodic currents and consequently increasing the anodic current density. Some of the preliminary cathodic polarization studies on these specimens (not shown in this paper) indicate that there is hardly any effect of the particle size and amount on the cathodic current density. Hence at this stage it appears that there may be more than one single reason for the poor corrosion resulting from the addition of SiC particle to the matrix alloy.

#### **Electrochemical Impedance Spectroscopy.**

Electrochemical Impedance Spectroscopy (EIS) has been used increasingly these days to detect the initiation of localized corrosion and also to study the reaction mechanisms of various electrochemical steps. The figures 10 to 13 show Bode plots for various MMC samples and the corresponding matrix alloys. In general, all the specimens show the scatter in the data towards the low frequency limit. This scatter in data is thought to be associated with the initiation of pitting attack. There are no significant differences in the nature of Bode plots for different MMC samples and the matrix alloys. In all the cases the plots of phase angle vs. frequency show a single time constant associated with a single electrochemical reaction. The values of phase angle at higher frequency are high and there is a tendency towards second time constant but it couldn't be observed in the maximum frequency studied ( $10^4$  Hz). The Bode plots also predict same general behavior as was inferred from the polarization and OCP vs. time studies. The polarization resistance values seem to decrease with increasing the volume percent and the particle size of reinforcing SiC. The variation of the phase angle with frequency shows the same general trend in all the cases.

#### **Optical and Electron Microscopic Studies**

Optical micrographs indicate extensive localized corrosion in the form of pitting (figures 14 and 15). Some of the specimens showed cracking after immersion in the electrolyte for about four weeks. This type of cracking has been reported in Al based MMC by Wheat et al<sup>13</sup> also. The pits seem to be irregular in shape and are closely associated with the SiC particles. When compared to the matrix alloy, the composite materials has more

numerous pits and are more irregularly shaped. Pit depth also seems to be more as determined by optical microscopy. Most of the pits contain SiC particles within indicating that the pits may have nucleated around the particle/matrix interface. Scanning Electron Microscopy (SEM) was performed on some of the specimens after polarization and impedance experiments. Whereas, the visual inspection itself indicated extensive localized damage after polarization test, specimens subjected to impedance tests did not show any visible damage. SEM studies showed severe pitting in the case of polarized specimens and also some pits in the case of specimens subjected to impedance spectroscopy. This may be due to the pitting phenomenon during low frequency measurements where the perturbation is applied for longer time duration. This observation of pits may further explain the fluctuation in the data at low frequency measurements. As observed under optical microscope, a fine network of cracks is observed under SEM also. These cracks are observed only in the case of specimens which had been immersed in the electrolyte solution for times more than two weeks. This is a serious problem since there was no applied external load.

## Conclusions

1. Corrosion potentials of Al 6061 and MMC Al 6061/SiC<sub>p</sub> do not differ significantly in 3.5% NaCl solutions open to air but the steady state values are definitely affected by the volume percent and the size of the reinforcing SiC particles. Potentials tend to move in the more active direction with increasing particle size and volume fraction.
2. Severity of localized corrosion in Al 6061/SiC<sub>p</sub> composites increases with increasing SiC contents. This may be either due to weakening of passive film by incorporation of more and more SiC particles or increased cathodic sites or both. This conclusion is important since the yield strength of MMC increases with increase in volume percent of SiC as long as the particle size is kept near 10  $\mu\text{m}$ . With increase in SiC particle size to 40  $\mu\text{m}$  the yield strength decreases .
3. Composite materials containing coarser SiC particles are least resistant to localized corrosion. From the corrosion studies and mechanical properties of the MMC it is evident that the corrosion resistance and the yield strength decrease with increasing the SiC particle size. MMC containing 10  $\mu\text{m}$  SiC show the highest yield strength and corrosion resistance for same vol% .
4. Pit size and distribution is affected by the presence of SiC<sub>p</sub>. Pits are irregular and more numerous in composite material. Some of the pits contain SiC particles in them suggesting that perhaps the pit nucleation occurs at the particle/matrix interface.

## References

1. D.M. Aylor, Metals Handbook, 9th Ed., (Metals Park, OH: ASM, 1987), p. 859.

2. P.P. Trzaskoma, *Journal of Metals*, Dec. 1988, p. 21.
3. D.H. Aylor, P.J. Moran, *J. Electrochem. Soc.*, 132 6 (1985) p. 1277.
4. D.M. Aylor, P.J. Moran, *J. Electrochem. Soc.*, 133 5 (1986) p. 949.
5. D.M. Aylor, P.J. Moran, *J. Electrochem. Soc.*, 133 5 (1986) p. 868.
6. S.L. Pohlman, *Corrosion*, 34 5 (1978) p. 156.
7. F. Mansfeld, S. Lin, K. Kim, H. Shih, *Corrosion Science*, 27 9 (1987) p. 997.
8. R.C. Paciej, V.S. Agarwala, *Corrosion*, 42 12 (1986) p. 718.
9. P.P. Trzaskoma, *Corrosion*, 46 5 (1990) p. 402.
10. P.P. Trzaskoma, E. McCafferty, *J. Electrochem. Soc.*, 130 9 (1983) p. 1804.
11. A.J. Sedriks et al., *Metall. Trans.*, 2 (1971) P. 871.
12. F. Mansfeld, S. Lin, S. Kim, H. Shih, *Corrosion*, 45 8 (1989) P.615.
13. H. Sun, E.Y. Koo, H.G. Wheat, *Corrosion*, 47 10 (1991) p. 741.
14. T. Christman, S. Suresh, *Acta Metal.*, 36 (1988) P. 1691.
15. P. Appendino et al. *Mat. Sci. & Eng.*, A135 (1991), p. 275.
16. I. Dutta, D.L. Bourall, D. Latimer, *J. Compos. Mat.*, 22 (1988) p. 829.
17. J.J. Stephans, J.P. Lucas, F.M. Hosking, *Scripta Met.*, 22 (1988) P. 1312.
18. P.S. Robi, R.C. Prasad, P. Ramakrishnan, *Conf. Proc. INCAL-91, Bangalore, INDIA*. Ed. E.S. Dwarakadasa, S. Seshan & K.P. Abraham, (1991) p. 835.



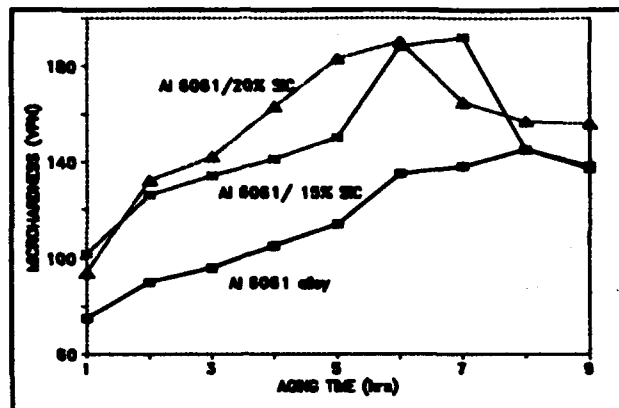


Figure 1 Matrix microhardness variation vs aging time of Al 6061/SiC<sub>p</sub> composite.

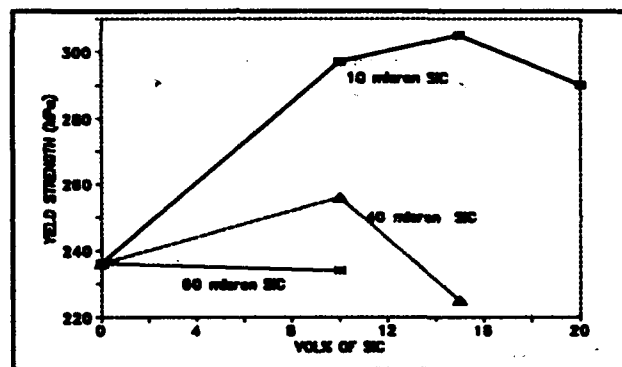


Figure 2 Effect of Vol% of SiC particles on the yield strength of Al 6061/SiC<sub>p</sub> composite .

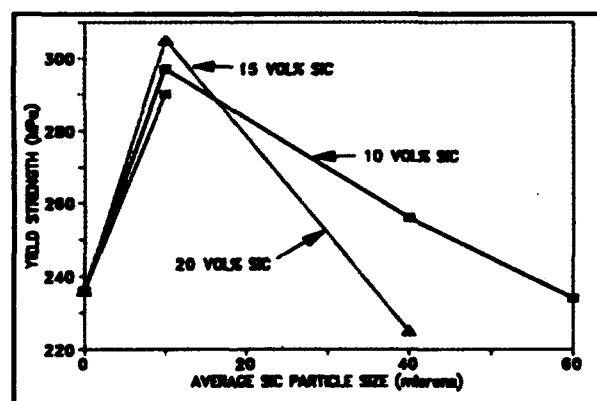


Figure 3 Effect of SiC particle size on the yield strength of Al 6061/SiC<sub>p</sub> composite.

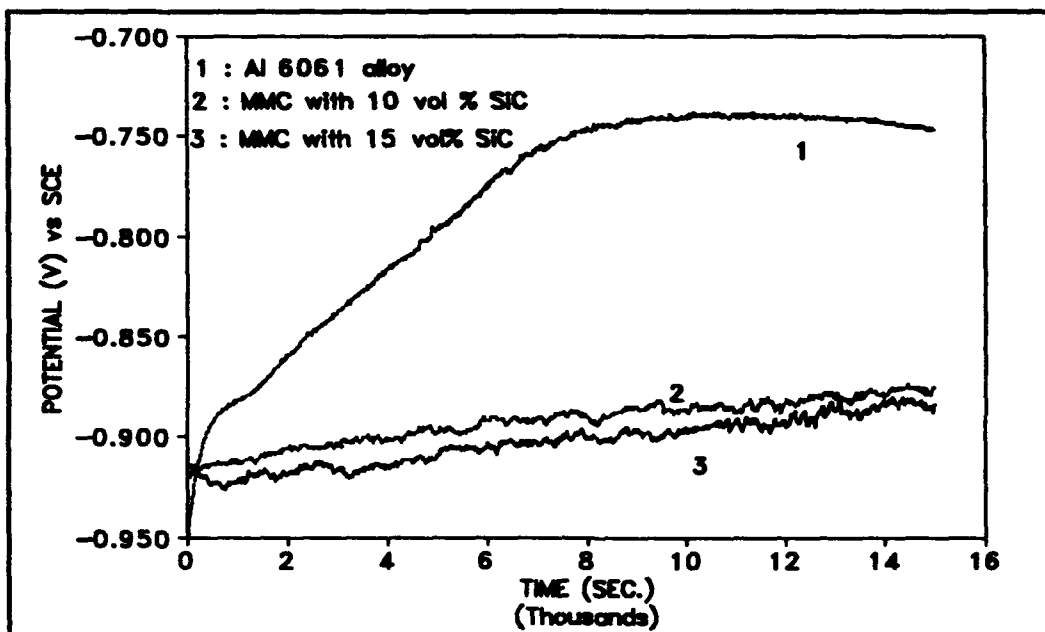
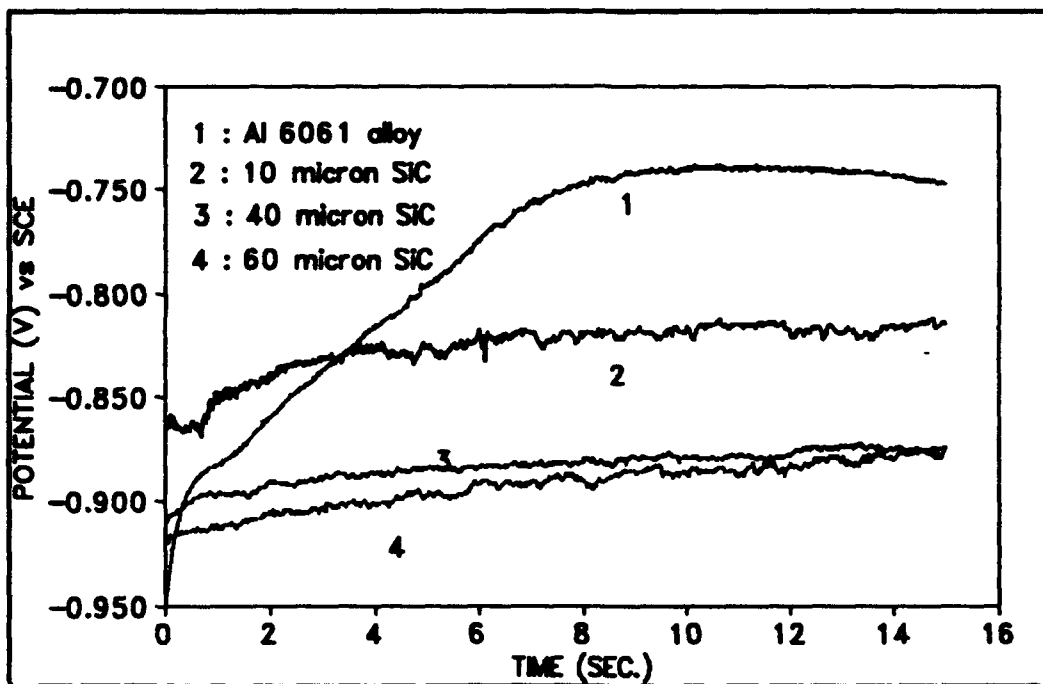


Figure 4-5 Variation of Open Circuit Potential (OCP) vs Time for Al 6061/SiC<sub>p</sub> in 3.5% NaCl solution.

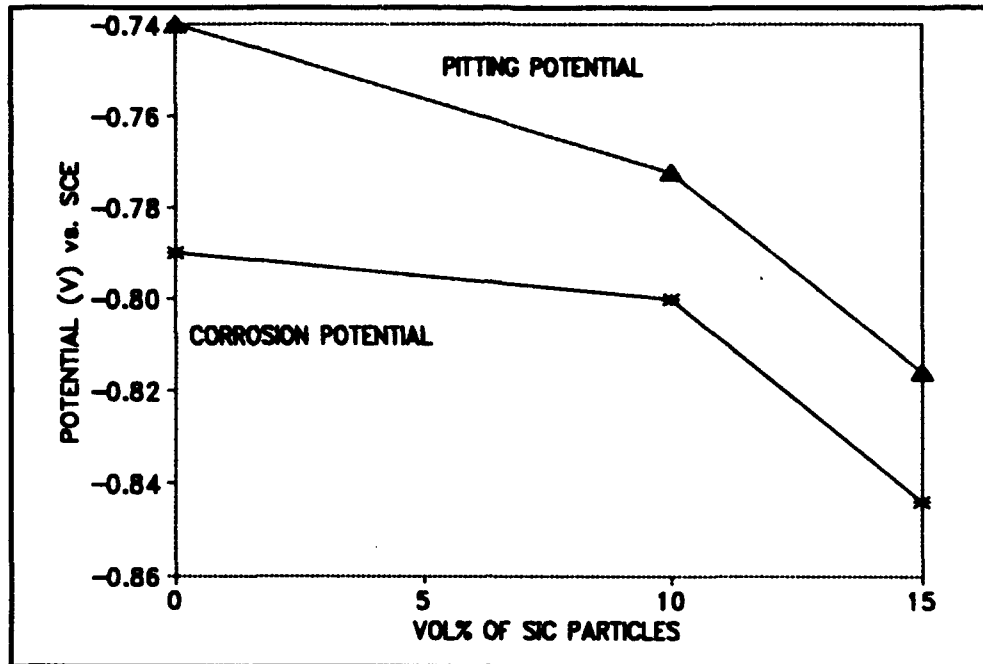


Figure 6 Effect of  $\text{SiC}_p$  Vol% on Corrosion Potential and Pitting Potential of MMC Al 6061/ $\text{SiC}_p$  in 3.5% NaCl solution.

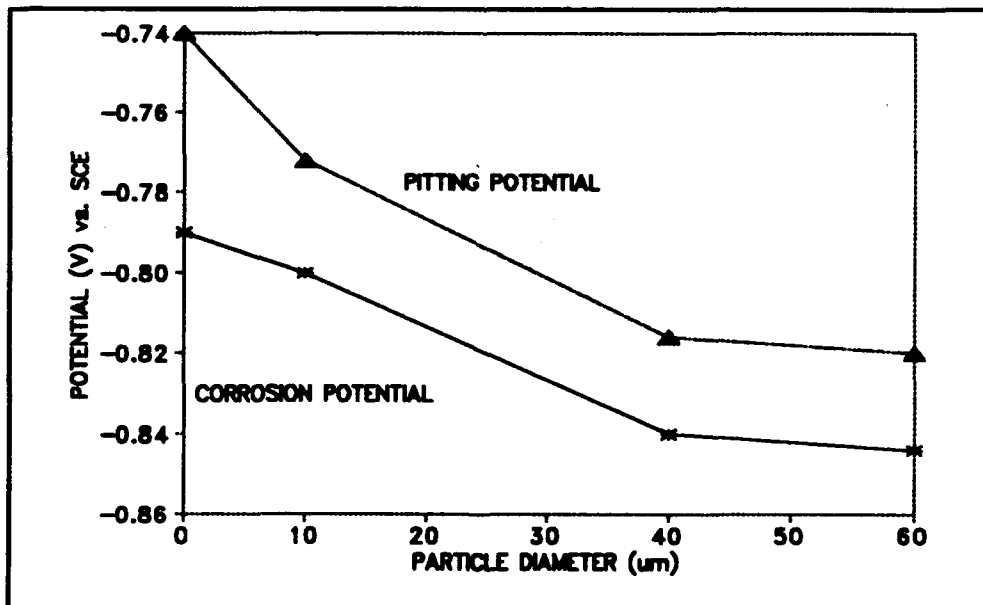


Figure 7 Effect of  $\text{SiC}_p$  diameter on the corrosion potential and pitting potentials of Al 6061/ $\text{SiC}_p$  composite in 3.5% NaCl solution.

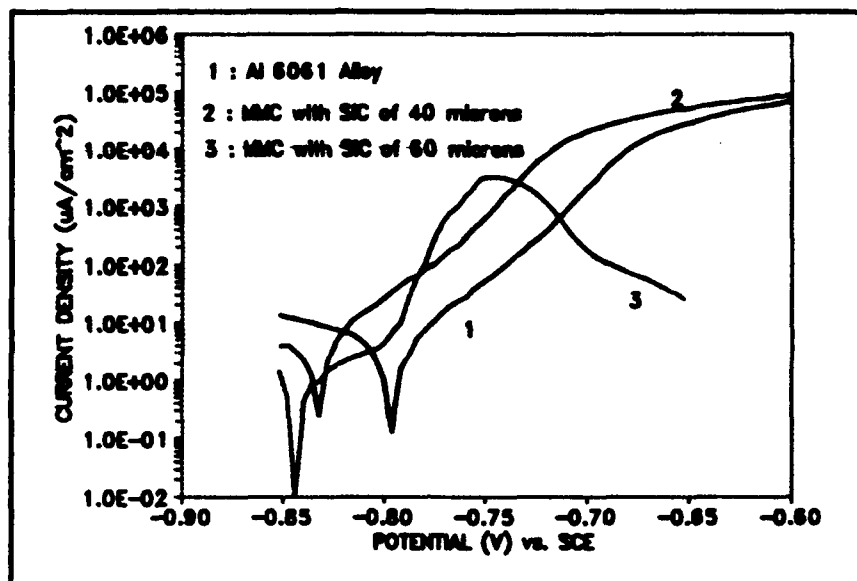


Figure 8 Potentiodynamic polarization curves for Al 6061/SiC<sub>p</sub> in 3.5% NaCl solution, showing the effect of SiC particle size.

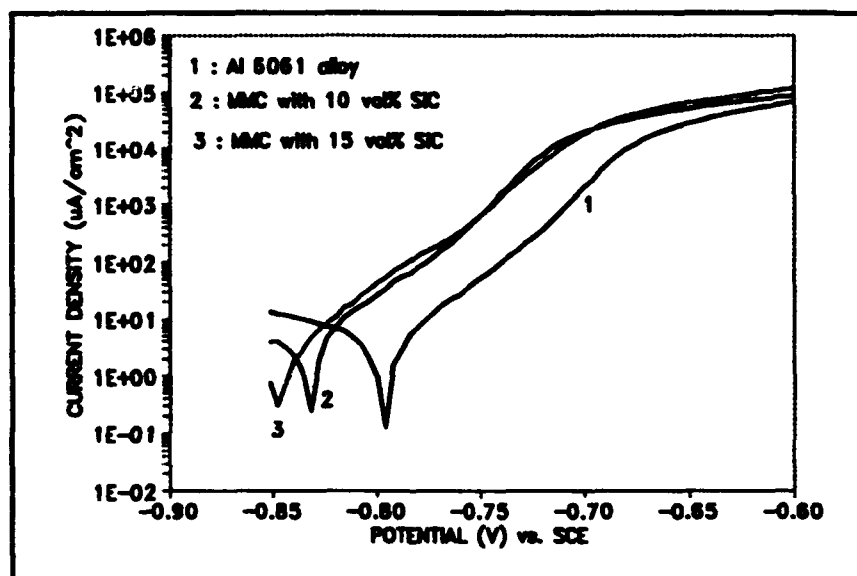


Figure 9 Potentiodynamic polarization curves of Al 6061/SiC<sub>p</sub> composite in 3.5% NaCl solution, showing the effect of SiC vol.%.

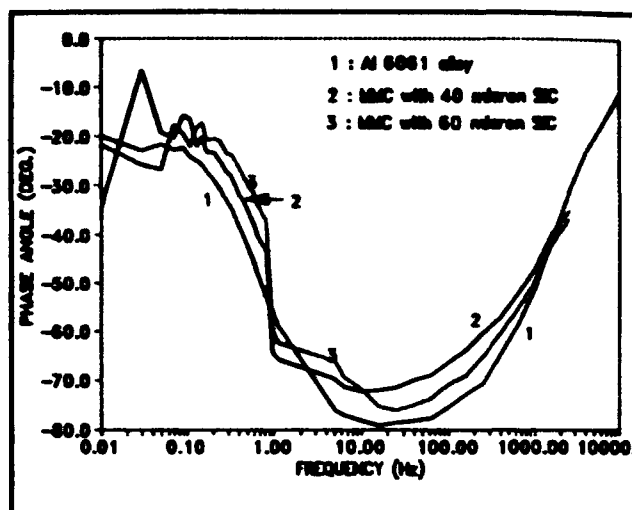
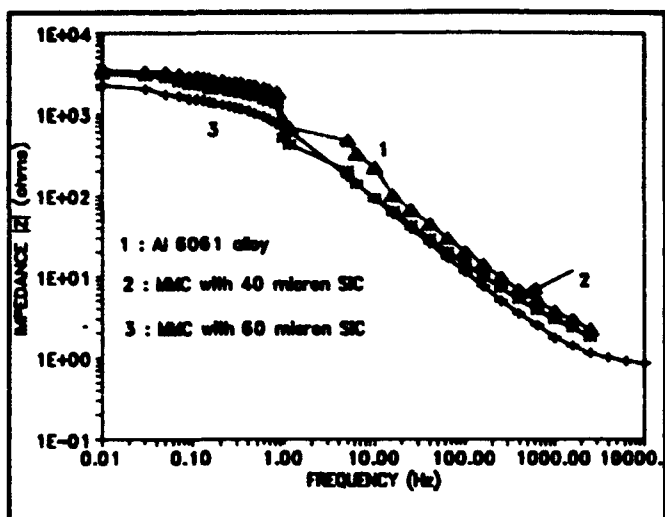


Figure 10-11 Bode plots of Al 6061/ $\text{SiC}_p$  composite in 3.5% NaCl solution showing the effect of SiC particle size.

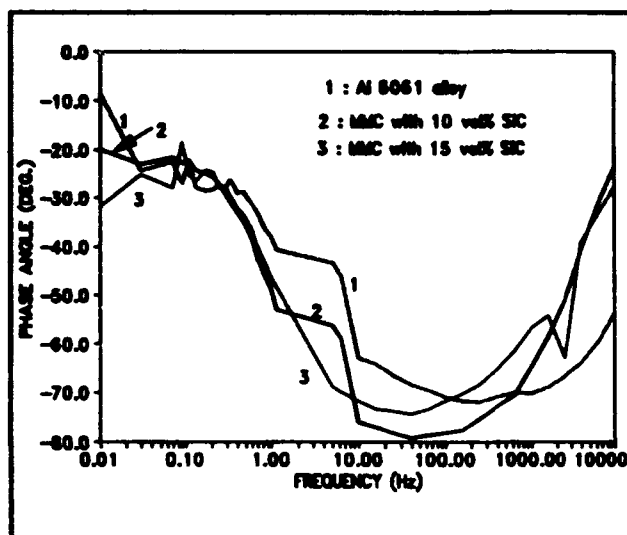
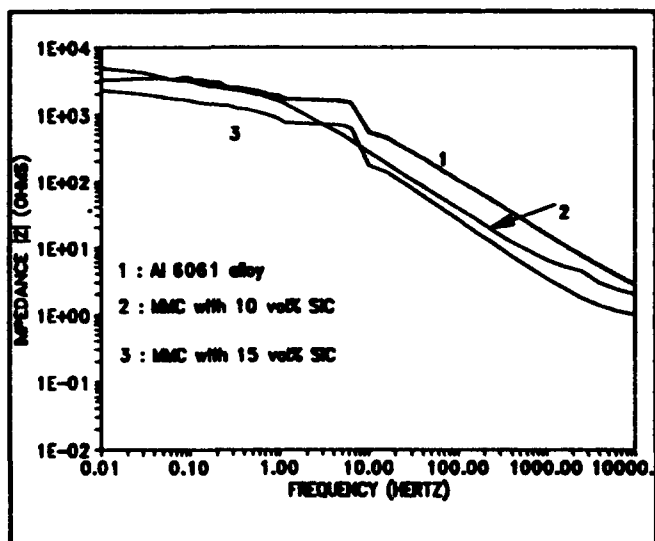


Figure 12-13 Bode plots of Al 6061/ $\text{SiC}_p$  composite in 3.5% NaCl solution, showing the effect of SiC volume percent.

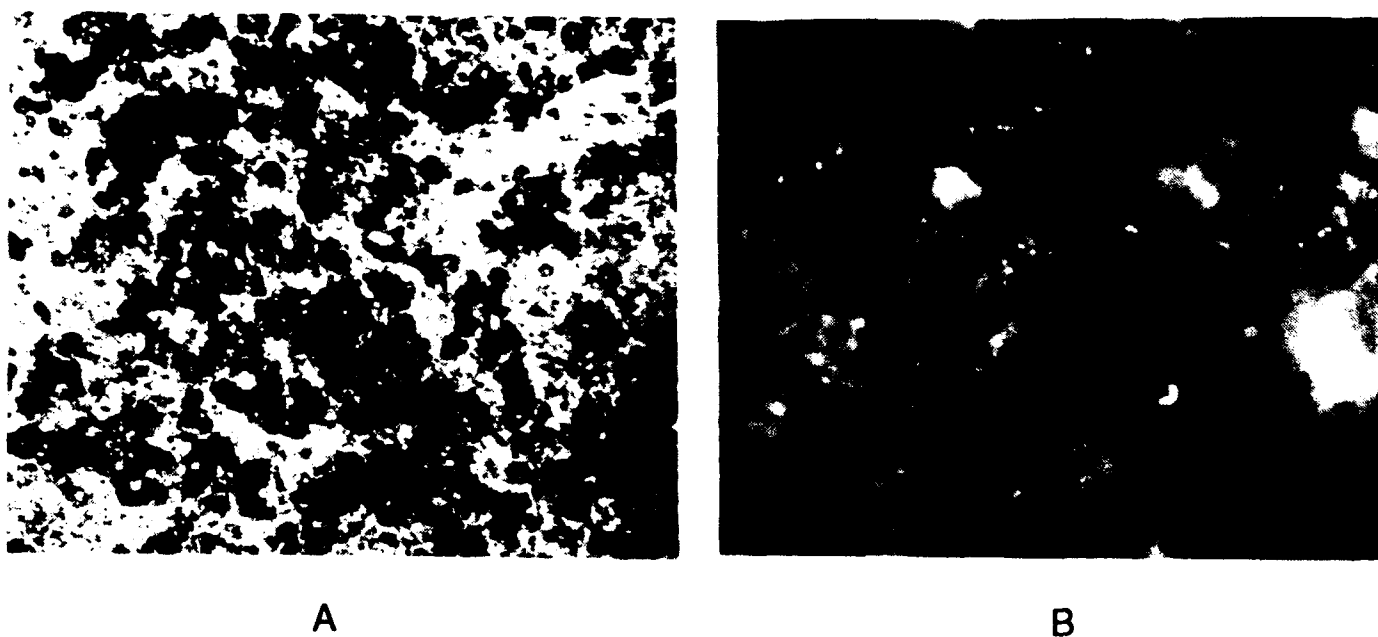


Figure 14 Optical micrographs of Al 6061/SiC<sub>p</sub> after immersion in 3.5% NaCl solution (a) extensive localized corrosion after anodic polarization (b) matrix cracking after 4 weeks immersion.



Figure 15 Scanning Electron Micrograph showing large pit (MMC after anodic polarization in 3.5% NaCl solution).

## Corrosion Behavior of Alumina/Al and SiC/Al Metal Matrix Composites

P.C.R. Nunes,  
Comissao Nacional de Energia Nuclear,  
Instituto de Pesquisas Energeticas e Nucleares,  
C.P. 11049, Cidade Universitaria,  
Sao Paulo 05422-970,  
Brazil.

L.V. Ramanathan,  
Comissao Nacional de Energia Nuclear,  
Instituto de Pesquisas Energeticas e Nucleares,  
C.P. 11049, Cidade Universitaria,  
Sao Paulo 05422-970,  
Brazil.

### Abstract

Particle reinforced Al base metal matrix composites (MMC) are being considered for a range of applications. Their mechanical properties have been investigated in detail but only limited information is available about their corrosion behavior. This paper describes the influence of (a) alloy composition, (b) particle characteristics such as composition, size, volume fraction, pretreatment and (c) anodization of the composites on the aqueous corrosion behavior of Al-matrix composites prepared by the melt stirring process. The corrosion tests consisted of prolonged immersion and anodic polarization measurements. The corrosion potential,  $E_{\text{corr}}$ , and the pitting potential,  $E_p$ , of the alloys and the composites varied by upto 500 mV in deaerated solutions. Particle addition affected  $E_p$  and not  $E_{\text{corr}}$ . Immersion test data revealed significant specimen weight loss for the composites, due mainly to formation of pits or microcrevices in the matrix close to the particle/matrix interface. The pits formed in SiC composites were deeper than those in the alumina composites. This is attributable to the higher cathodic reactivity of the SiC particles. The mechanism by which pit initiation and propagation takes place is related to the presence of weak spots in the air formed film and to oxygen reduction at the particles or precipitates. Anodization improved the pitting resistance of the composites.

Key terms : Metal matrix composites, Al matrix, particle reinforcements, aqueous corrosion, pitting.

### Introduction

Of the various "new" metallic materials, metal matrix composites are anticipated to have a significant niche in industries such as defence, aerospace, automotive and sports equipment. The combination of properties such as high modulus and stiffness, low

density and reduced coefficient of thermal expansion are the main attributes to ensure their place. Presently, a significant amount of data is available about the mechanical properties and correlations between processing route, microstructure and properties of MMCs. However, only limited information is available about their environmental stability. This aspect is closely associated with the presence of heterogeneities, and MMCs have a large quantity of heterogeneities in the form of the reinforcement, microcrevices, voids, porosity as well as precipitates. Although MMCs encompass a very wide range of matrix/reinforcement combinations, the aluminium alloy/SiC (or alumina) particle combination seems to be one of the most interesting for industrial applications. These composites can be produced by a variety of techniques and although the powder metallurgy route has been used quite extensively, the molten metal route is considered to be cost effective for large scale production.

A few corrosion studies on SiC/Al base alloy MMCs have focussed on the effects of reinforcement material on pitting potential, pit morphology and general corrosion susceptibility in chloride solutions (1-3). Trzaskoma et.al. observed that the pitting susceptibility of a number of common matrix alloys did not alter upon addition of SiC (1). They also found the MMCs to be less resistant to pit initiation. Paciej and Agarwala, investigating the effects of processing variables, found that a high extrusion ratio and modified solution heat treatment enhanced the corrosion resistance of alloy AA 7091/SiC composites (4). McIntyre et. al. reported that the precipitation behavior of heat treatable matrix alloys to alter the pitting susceptibility in the presence of SiC (5). It has also been shown that changes taking place at the matrix/reinforcement interface affect mechanical behavior of MMCs (6). These changes are due to a combination of one or more of the following: matrix alloy, particle surface characteristics, processing route and subsequent heat treatment. The interfacial changes are usually in the form of variations in local composition, formation of precipitates, or other reaction products, and these affect corrosion behavior. This paper describes the effects of particle composition, volume fraction, matrix alloy, particle pretreatment, and MMC surface treatment on the aqueous corrosion behavior of Al matrix composites.

## Materials and Methods

### Materials

Alloy AA 2014 (Al-4.5Cu-1Si-0.8Mn-0.5Mg) and Al-7.5Si-1Mg were used for preparing the MMCs. The composites preparation procedure consisted of adding preheated (and where relevant, pretreated) particles of either SiC or alumina to a vigorously stirred bath of the molten alloy. After 10 minutes agitation, the composite was poured into chilled copper molds and allowed to solidify. Particles of varying sizes were used and composites with different particle volume fraction were prepared. The particle pretreatments



consisted of (a) preoxidation of the SiC particles at 1100° C in air for 2 hours, and (b) electroless nickel plating of alumina particles from a chloride bath for 10 minutes followed by rinsing. The composite processing parameters such as melt temperature, stirrer design, stirring rate and duration, which affect reinforcement distribution were maintained at their optimized values to obtain uniform particle distribution (7). The MMC surface treatment consisted of anodization in 16 wt% sulphuric acid at 23°C and 27 mA cm ( ~ 18V) for 30 minutes followed by sealing in boiling water for 30 minutes. Specimens, 10x10x3mm were cut from the prepared composites for corrosion measurements.

### Corrosion Measurements

The corrosion evaluation consisted of (a) long term immersion tests in 3.5% NaCl at 25° C for 28 days and (b) anodic polarization in 3.5% NaCl. Specimens of the various composites listed in Table I were prepared for the long term tests by grinding to 600 grit, degreasing and rinsing. The weighed specimens were suspended within a temperature controlled bath of NaCl. The pH was maintained constant at 7. After the test, the specimens were cleaned in 50vol% HNO<sub>3</sub>, dried and weighed. The specimens for the electrochemical measurements were cut to size (5x5x3mm), cold mounted in epoxy resin, ground to 600 grit, rinsed and introduced into a standard corrosion cell. The specimens were allowed to equilibrate prior to measurement of the corrosion potential,  $E_{corr}$ , and initiation of anodic potentiodynamic polarization scans from -1400mV to +100mV at 10mV/s. The potential vs current curves were recorded. Measurements were carried out in both aerated and deaerated NaCl solutions. Deaeration was achieved by bubbling nitrogen through the electrolyte before and during the measurements. In tests carried out to study pit morphology, the specimens were exposed to 3.5% NaCl at 50mV above the pitting potential for 15 minutes. The specimens were rinsed thoroughly and examined in a scanning electron microscope with analytical attachments.

## Results and Discussions.

### Microstructural Aspects

The as cast microstructures of alloys AlSiMg and AA 2014, and their composites revealed primary dendrites, silicon particles and in the case of the composites the reinforcement particles (figure 1). The reinforcement can be observed to be well distributed. Significant improvements in particle distribution were achieved by controlling the composite processing parameters. Nevertheless, particle clustering could not be completely eliminated.

### Electrochemical Measurements

The anodic polarization curves of alloy AlSiMg, AA 2014 and the composites in aerated and deaerated NaCl solutions were found to

be similar and Figure 2 shows typical curves in aerated and deaerated NaCl. The pitting potential  $E_p$ , denoted by the potential at which the current increases was read from these curves. Tables II and III list  $E_p$  and  $E_{corr}$  of the different specimens. In deaerated NaCl,  $E_p$  of the AlSiMg alloy and its composites were 300-500 mV higher than their corresponding  $E_{corr}$ . This difference in potential was observed for both alumina containing and SiC containing composites. The addition of either SiC or alumina particles to AlSiMg did not alter the corrosion potential in deaerated or aerated NaCl. These observations differ from those of Mahn and Roepstorff, who reported increase in  $E_{corr}$  with addition of and further increase in SiC to Al-SiC composites (3). In aerated NaCl, the difference between  $E_p$  and  $E_{corr}$  reduces to  $\sim 100$  mV. This is due mainly to an increase in  $E_{corr}$  of the alloy and the composites in aerated solutions. Aeration of NaCl brings about only a slight increase in the  $E_p$  of the alloy and the composite. The addition of alumina or SiC to the alloy slightly increased the pitting potential. On the other hand, increase in particle size or quantity did not significantly alter  $E_{corr}$  and  $E_p$ .

Regarding the effects of particle treatments on electrochemical parameters, it can be observed that the composites with nickel plated alumina exhibited  $E_{corr}$  higher than that of the alloy or composites with unplated alumina. The increased  $E_{corr}$  can be attributed to the more noble nickel. Pre-oxidation of SiC particles did not affect the  $E_{corr}$  or  $E_p$  of the composites in both aerated or deaerated solutions.

Table IV lists the  $E_{corr}$  and  $E_p$  values of the as cast and anodized SiC reinforced composites of alloys AlSiMg and AA 2014 in aerated NaCl. It can be observed that both  $E_{corr}$  and  $E_p$  of alloy AA 2014 are higher than those of alloy AlSiMg. Anodization of the alloys increased both  $E_{corr}$  and  $E_p$ . The pitting potential of the anodized composite specimens were significantly higher than those of the as cast composites indicating the increased resistance of the anodized specimens to pit. Improvements in pitting resistance of anodized SiC composites were also reported elsewhere (1).

#### Long Term Immersion Tests

Weight loss data for the alloy and the composite specimens following 28 days immersion in 3.5 NaCl are given in Table V. It can be observed that the extent of corrosion was considerable in all cases, and provoked by pitting of the matrix. The extent of corrosion of the unreinforced alloy decreased upon addition of 5 vol% particles. Increase in SiC particle content increased

corrosion rate, whereas increase in alumina content decreased corrosion rate. This behavior may be attributed to the differences in electrical conductivity of the two types of reinforcements. Preoxidation of the SiC particles did not significantly alter long term corrosion behavior of the matrix. This may be due to loss of the  $\text{SiO}_2$  layer on the SiC particles during specimen preparation. The extent of corrosion of composites containing Ni plated alumina was very high, due to increased galvanic effects.

### Pit Morphology

Two sets of pit morphological studies were carried out. In the first, specimens held for 15 minutes at 50 mV above  $E_p$  in NaCl were examined. In the second, the specimens exposed to 3.5% NaCl for 28 days were examined. The AlSiMg alloy exposed at a fixed potential, revealed both sporadic pits and pit clusters. In the alumina containing composites, microcrevice formation was observed at the interfacial regions and in their vicinity (figure 3a,b). In many respects, the nature of the attack was similar to that observed in the alloy. The cathodic regions in the alloy and in the alumina composites were probably the precipitated second phase particles. The microcrevice formation was more widespread in regions where alumina particle clusters were present. At higher magnifications, crystallographic facetting was also observed in the alloy and in the composite. The pits formed in SiC composites were deeper than those formed in alumina composites formed under identical conditions (figure 3c). Trzaskoma et.al. reported the formation of shallow pits in SiC/6061 composites as compared to those in the unreinforced alloy (1,9). In this investigation, it has been observed that in SiC composites, the pit sizes varied considerably from 5 to  $20\mu\text{m}$ . Crystallographic facetting has been observed in both the alloy and in the composites contrary to observations reported elsewhere (10).

In the as cast alloy exposed for 28 days, the pits, even though few, were deeper as shown in figure 4a. The pits were crystallographic, with no evidence of facetting. The lack of facetting could be attributed to the prolonged exposure during which preferential dissolution of the edges may have taken place. In almost all the cases, in the initial stages, the interdendritic or intergranular Si was unaffected, leading eventually to it dropping out. At higher magnifications, the intergranular regions were found to be smooth and shallow (figure 4b). In the alumina composites also, preferential dissolution of the matrix led to particle dropout. In the SiC composite, smooth hemispherical pits formed around the particles (figure 4c). After 28 days exposure, more alumina particles were in place as compared to SiC particles in the respective composites. This behavior could be attributed to the higher cathodic reactivity of the SiC particles and also to the higher NaCl concentration in this investigation as compared to that used elsewhere (1).

## General Discussions

In chloride ion containing solutions aluminium alloys generally pit. This has been observed, both in the unreinforced alloy as well as in the matrix of the composite. Pits usually initiate at surface heterogeneities and in the as cast alloy or the composite matrix, these heterogeneities are one or a combination of the following: (a) casting defects, due mainly to solidification shrinkage and hydrogen liberation; (b) second phase particles or other precipitates; (c) reinforcements and (d) reinforcement/matrix interaction products. In this investigation the total number of intermetallic precipitates were found to be considerably higher in the composite than in the unreinforced alloy subjected to identical treatments. Similar observations were reported by Trzaskoma (9). Consequently, candidate sites for pit initiation in the composites were significantly higher. In the unreinforced alloy, the intermetallic precipitates were the cathodic sites, whereas in the composites, depending on the composition of the reinforcement, the second phase precipitates or the interfacial reaction products were the cathodic sites for the oxygen reduction reaction.

The extent of pitting of composites reinforced with Ni plated alumina was significantly more than those reinforced with as received alumina. This behavior is attributable to the electrochemically more noble Ni envelope being efficient cathodic sites for oxygen reduction.

### Mechanism

The fact that (a) in quiescent aerated chloride ion containing solutions, unreinforced and reinforced Al alloys pit spontaneously and (b) in aerated NaCl the corrosion potential of the Al alloys is more negative than in deaerated NaCl, the primary driving force in aerated media is the cathodic reduction of oxygen. In the unreinforced alloy, due to the poor conductivity of the oxide film, the oxygen reduction reaction is confined to localized areas of the surface associated with impurities or precipitates. Hence, when unreinforced alloy specimens are exposed to aerated NaCl, they reveal only a few deep pits. The introduction of ceramic reinforcements increase the density of heterogeneities, which in turn affects the electrochemical and corrosion behavior of the alloy. Since SiC is noble to the matrix in NaCl, it acts as a cathodic site. It has also been shown by surface analysis that the surface density of intermetallic precipitates is a factor of two greater for the reinforced alloy as compared to a similarly processed monolithic alloy (10). Consequently, in composites, the increased number of pits are due primarily to the increase in the number of weak spots in the oxide film covering these particles and precipitates.

Specific composite processing conditions also result in alteration of the particle/matrix interface composition and henceforth in the formation of crevices rather than pits. Similar data were reported

by Aylor and Moran for SiC<sub>w</sub>/6061 (PM) composites (3).

Overall, it can be stated that the introduction of the reinforcement into the matrix alloy gives rise to three kinds of corrosion problems. The first are associated with galvanic effects. In SiC composites, the particles are more noble. In alumina composites, galvanic coupling exists to a reduced extent between the precipitated second phases and the matrix. The second are those associated with particle/matrix reaction products. These products are generally intermetallic precipitates and the oxide on the composite surface covering these precipitates are the preferred or weak spots for pit initiation. The third involve the formation of microcrevices at the interfaces and voids. Certain interfacial defects arise from incomplete cohesion between reinforcement and matrix. At these defects local chemistry necessary to retard local repassivation is easily achieved and results in formation of crevices or trenches. In this investigation, all three forms of defects induced by particle addition have been observed, either singly or jointly. Reduction in pitting of composites can be achieved by anodization of the composite or by application of reactive element impregnated coatings.

### Conclusions

1. In NaCl solutions the corrosion potential,  $E_{\text{corr}}$  of the alloys and the composites increased in the presence of dissolved oxygen.
2. The pitting potential,  $E_p$  of the alloys and the composites were not affected significantly by aeration of the solution.
3.  $E_p$  of the composites were higher than those of the alloys in aerated NaCl.
4. The particle/matrix interfacial regions were the preferred sites for pitting.
5. In the presence of the reinforcement, a significant increase in the number of precipitate particles were observed.
6. The SiC particles and the precipitated phases were the sites for cathodic oxygen reduction in the SiC and alumina composites, respectively.
7. The pits were crystallographic in nature and those in SiC composites were deeper than those formed in the alumina composites.
8. Microcrevice formation was also observed, due possibly to particle/matrix decohesion.

9. Particle addition gives rise to three kinds of corrosion related problems: galvanic effects; particle/matrix reaction product induced effects; and interfacial microcrevicing.
10. Anodization of composites increases pitting resistance.

#### References

1. P.P. Trzaskoma and E. McCafferty, J. Electrochem.Soc., 130,9,(1984),p.1804.
2. M.Metzger and S.G. Fishman, Ind. Eng. Chem. Prod. Res. Dev., 22, 2,(1983),p. 296.
3. D.M. Aylor and P.J. Moran, J. Electrochem.Soc., 132,6,(1985), p.1277,
4. R.C. Paciej and V.S. Agarwala, Corrosion, 44, 10,(1988),p. 680.
5. J.F. McIntyre, R.K. Conrad and S.L. Golledge, Corrosion, 46,11, (1990),p.902.
6. D.J. Llyod, H.P. Legace and A.D. McLeod in "Controlled Interphases in Composite Materials, ICCI-III", Ed. H. Ishida, Elsevier,(1990),p. 359.
7. L.V. Ramanathan, Proc. 12th Riso Int. Symp. on "Metal Matrix Composites", Ed. N. Hansen et.al.,(1990),p. 611.
8. E. Maahn and S. Roepstorff, Proc. 12th Riso Symp on "Metal Matrix Composites", Ed. N. Hansen et. al,(1990),p. 497.
9. P.P. Trzaskoma, Corrosion, 46, 5,(1990),p. 402.
10. A. Turnbull, British Corr. J., 27, 1,(1992),p. 27.
11. L. Salvo, M. Suery, G.L. Legoux and G. l'Esperance, Mat. Sci nd Engg., A135,(1991),p.129.

Table I. AlSiMg alloy composites designation and characteristics.

Designation	Reinforcement			
	Type	Volume %	Size( $\mu\text{m}$ )	Treatment
CA-05-20	Alumina	5	20	-----
CA-05-100	Alumina	5	100	-----
CA-20-100	Alumina	20	100	-----
CNA-05-50	Alumina	5	50	Ni plated
CC-05-50	SiC	5	50	-----
CC-10-50	SiC	10	50	-----
CC-05-100	SiC	5	100	-----
CC-10-100	SiC	10	100	-----
COC-05-50	SiC	5	50	oxidized

Table II Corrosion and pitting potentials of AlSiMg alloy and its alumina composite specimens in aerated and deaerated 3.5% NaCl. All potentials vs SCE.

Specimen	Aerated		Deaerated	
	$E_{\text{corr}}$ (mV)	$E_p$ (mV)	$E_{\text{corr}}$ (mV)	$E_p$ (mV)
Alloy	-760	-695	-1140	-719
CA-05-20	-736	-608	-1220	-688
CA-05-100	-740	-675	-1240	-625
CA-20-100	-760	-620	-1070	-599
CNA-05-50	-770	-690	-729	-685

Table III. Corrosion and pitting potentials of alloy AlSiMg and its SiC containing composite specimens in aerated and deaerated 3.5% NaCl. All potentials vs SCE.

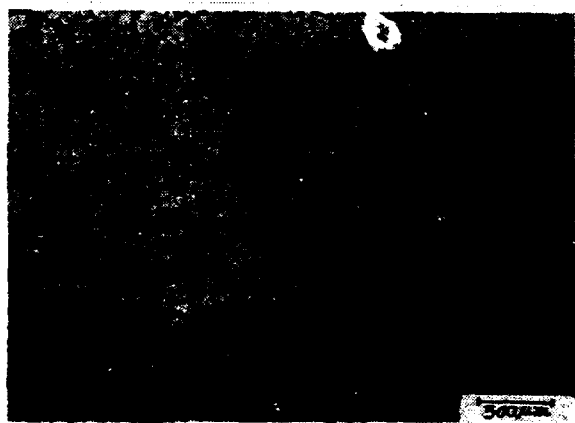
Specimen	Aerated		Deaerated	
	$E_{\text{corr}}$ (mV)	$E_p$ (mV)	$E_{\text{corr}}$ (mV)	$E_p$ (mV)
Alloy	-760	-695	-1140	-719
CC-05-50	-735	-639	-1030	-659
CC-10-50	-733	-688	-1130	-678
CC-05-100	-755	-600	-930	-713
CC-10-100	-744	-721	-1100	-728
COC-05-50	-764	-650	-885	-746
Anodized	-890	-813		
CC-05-20				
Anodized	-725	-458		
CC-10-50				

Table IV. Corrosion and pitting potentials of alloy AlSiMg and AA 2014 composites in the as cast and anodized conditions in aerated 3.5% NaCl (vs SCE).

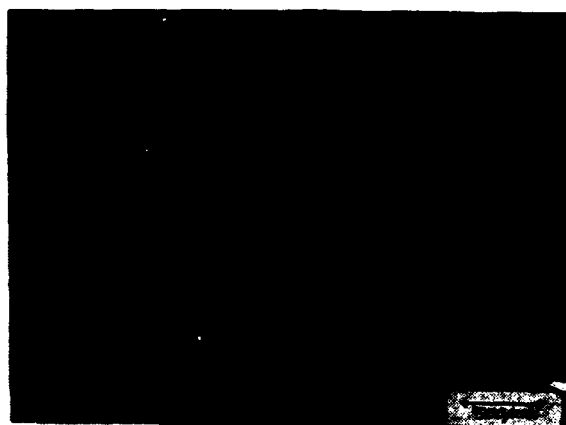
Specimen	$E_{corr}$		$E_p$	
	as cast	anodized	as cast	anodized
AlSiMg +CC-05-100	-755	-725	-600	-458
Alloy 2014 +CC-05-100	-700	-644	-500	-440

Table V. Average corrosion weight loss in 3.5% NaCl, pH 7.0 after 28 days.

Specimen	weight loss m.d.d.	Specimen	weight loss m.d.d.
Alloy AlSiMg	5.28	CA-05-20	4.75
CC-05-20	2.37	CA-05-50	6.95
CC-05-50	3.41	CA-05-100	4.45
CC-05-100	5.6	CA-10-50	4.61
CC-10-50	4.67	CA-10-100	4.38
CC-10-100	6.12	CNA-05-100	12.05
COC-05-50	5.58		



A



B

Figure 1. Optical micrographs of as cast (a) AlSiMg alloy and (b) alumina composite.



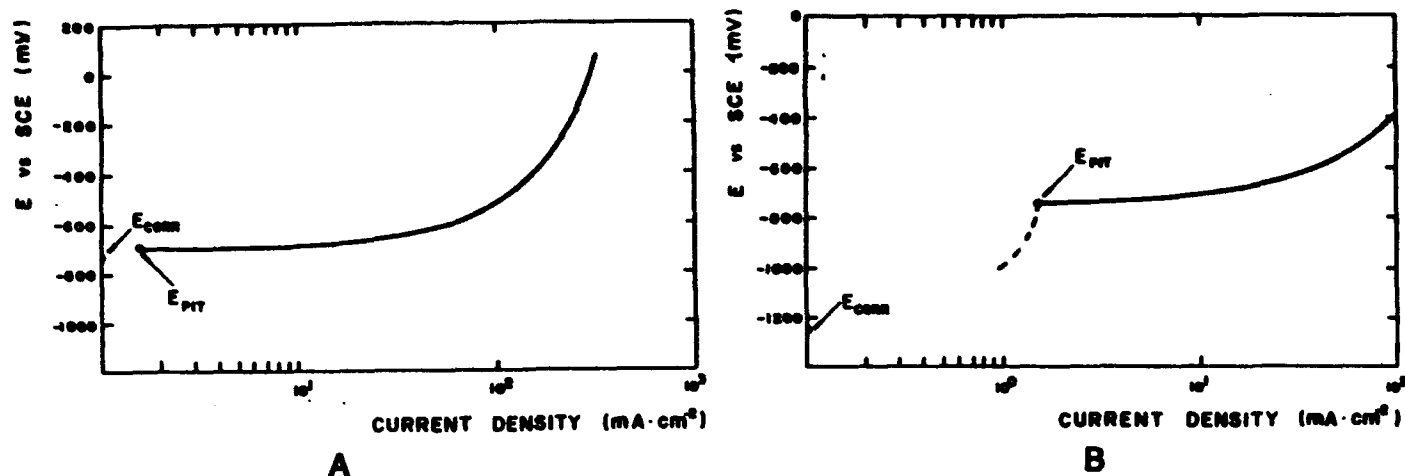


Figure 2. Anodic potentiodynamic polarization curves of alloy AlSiMg in 5% NaCl. (a) aerated (b) deaerated.

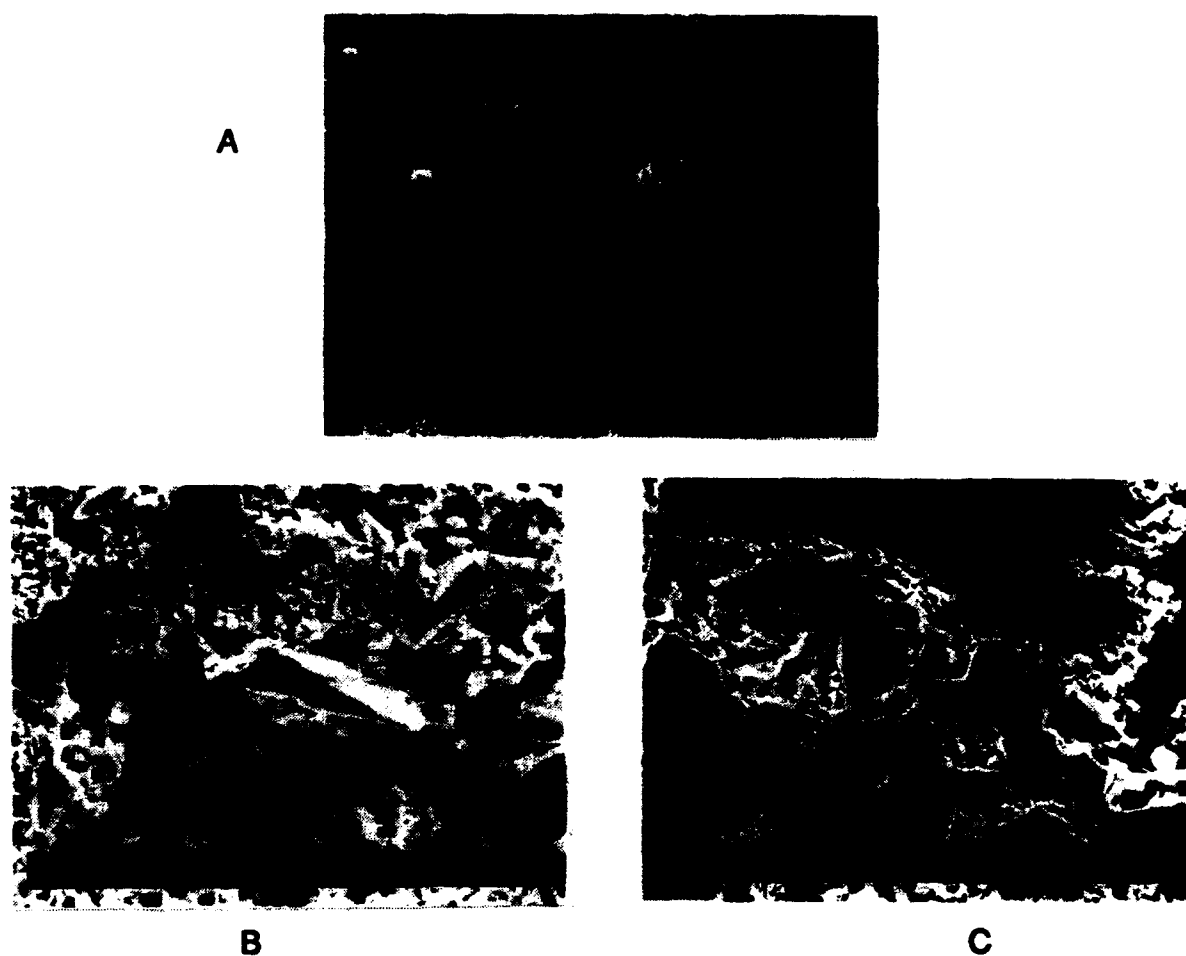


Figure 3. Scanning electron micrographs of (a), (b), alumina composite and (c) SiC composite surfaces exposed for 15 minutes at 50mV above  $E_p$  in 3.5% NaCl.

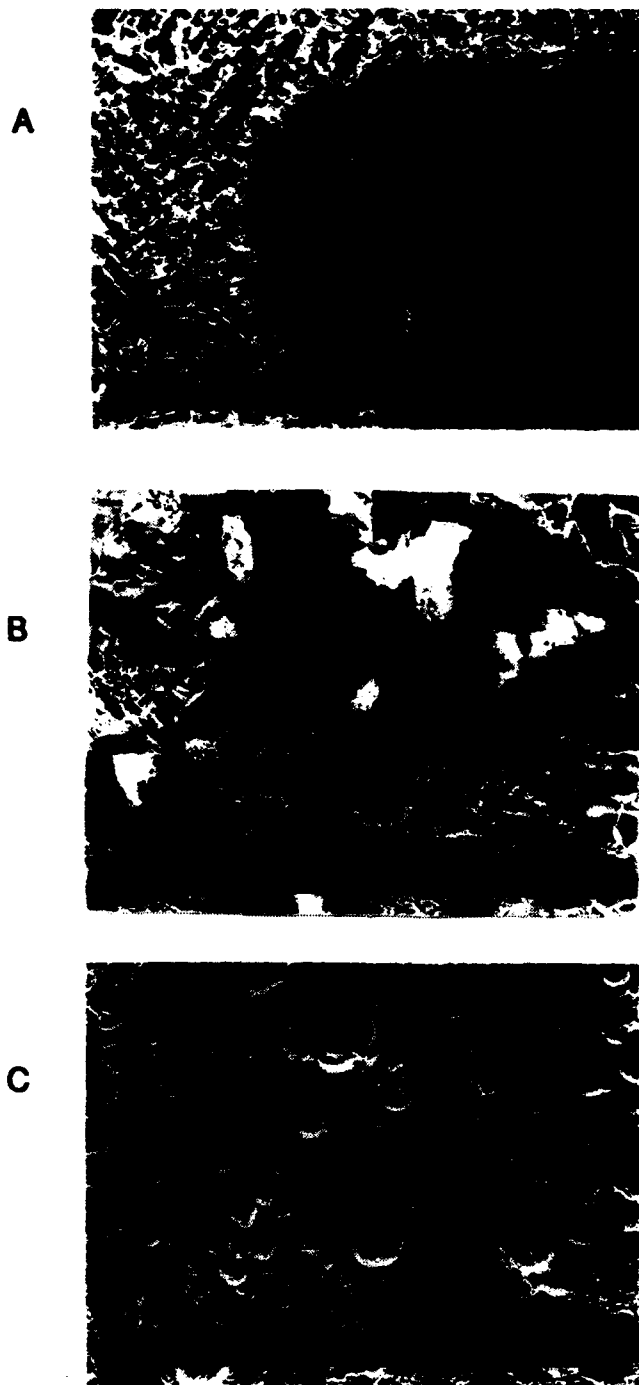


Figure 4. Scanning electron micrographs of (a) (b) AlSiMg alloy, (b) alumina composite and (c) SiC composite exposed to 3.5% NaCl for 28 days.

## Effect of Cold-Working on the Crevice Corrosion of Austenitic Stainless Steels

**Takao Handa**

Nippon Telegraph and Telephone Corporation  
Technical Assistance and Support Center  
9-11 Midori-cho 3-chome, Musashino-shi, Tokyo, 180 Japan

**Yoshimori Miyata**

Nippon Telegraph and Telephone Corporation  
Technical Assistance and Support Center  
9-11 Midori-cho 3-chome, Musashino-shi, Tokyo, 180 Japan

**Hisayoshi Takazawa**

Nippon Telegraph and Telephone Corporation  
Technical Assistance and Support Center  
9-11 Midori-cho 3-chome, Musashino-shi, Tokyo, 180 Japan

### Abstract

Stainless steels such as type 304 are affected by localized corrosion such as crevice corrosion when used in environments with solutions containing high chloride ion concentration. It was found that extensive crevice corrosion of cold-rolled type 304 stainless steels occurred within a year in solution with about  $0.020\text{--}0.50\text{ kgm}^{-3}$  chloride ion concentration in outdoor telecommunication plants. The cause of this corrosion was investigated from the viewpoint of cold-working. Solution-treated metastable austenite forms strain-induced martensite. It has been pointed out that special phases such as martensite accelerate pitting corrosion. However, the effect of the transformation phase on crevice corrosion has not been studied systematically.

To investigate the effect of cold-working on the crevice corrosion of austenitic stainless steels, their repassivation potentials were measured in solutions with chloride ion concentrations equivalent to those of fresh water and sea water. The repassivation potential is believed to be an important parameter in determining resistance to crevice corrosion.

It was found that the repassivation potential of type 304 stainless steel, a typical metastable austenitic stainless steel, tended to move in the active direction, because of the formation of martensite during cold-working. Furthermore, especially at low chloride ion concentration, there was significant dependence of repassivation potential on cold-working. Stainless steel with more than 20% reduction experienced crevice corrosion in dilute NaCl solution with  $0.020\text{ kgm}^{-3}$  chloride ion concentration (tap water).

Crevice corrosion of stainless steels in freshwater has been given little attention. However, we showed that there was a need to investigate the effects of cold-working of stainless steels particularly in solution environments with low chloride ion concentration.

**Key terms:** austenitic stainless steels, crevice corrosion, cold-working, chloride ion, type 304, type 310S, repassivation potential, martensite

## Introduction

Stainless steel possesses excellent corrosion resistance, mechanical properties, heat resistance, and processability. It is therefore used extensively in a variety of fields. However, it suffers from problems of localized corrosion such as crevice corrosion when subjected to solutions with high chloride ion concentration such as seawater. When exposed to freshwater solutions with low chloride ion concentration, stainless steel is considered to have excellent corrosion resistance. However, the authors have observed crevice corrosion occurring in metals immersed in solutions with a chloride ion concentration of several hundred  $\times 10^{-3}$   $\text{kgm}^{-3}$ <sup>1</sup>. Stainless steel is often processed by rolling, for example, before use. In widely used metastable austenitic stainless steels such as type 304, a strain-induced  $\alpha'$  martensite phase is formed<sup>2</sup>. Although it has been pointed out<sup>3</sup> that such special phases promote crevice corrosion, few systematic studies have been conducted into its effect. In particular, it is extremely important to understand the influence of cold-working on crevice corrosion of stainless steel in freshwater solutions with low chloride ion concentration.

The authors studied crevice corrosion in cold-worked austenitic stainless steels in solutions with chloride ion concentrations equivalent to those of freshwater and seawater. In this paper, we report the effect of cold-working by comparing a typical metastable austenitic stainless steel (type 304) and stable austenitic stainless steel (type 310S) in which the martensitic transformation does not occur even when cold-worked. In particular, we show the effect of cold reduction ( $\alpha'$  martensite formation) on repassivation potential which is an important measure of crevice corrosion.

## Example of Crevice Corrosion

Figure 1 shows an example of crevice corrosion in type 304 formed in a freshwater environment. Table 1 shows the analysis of the solution in which the corrosion occurred. It is seen that the chloride ion concentration that greatly promotes crevice corrosion is almost the same as that of general-purpose groundwater, that is a freshwater environment. The example in Figure 1 was observed in 20% cold-reduced type 304 material, that was immersed in the freshwater solution of the composition shown in Table 1, for approximately one year. The corrosion pits evident along the rolling direction are distinctive. It is thus clear that stainless steel does not always have excellent corrosion resistance even in solutions with low chloride ion concentration.

## Experimental Procedures

### Chemical Composition of Test Pieces

Table 2 shows the chemical composition of the test pieces. It shows the equivalent chemical compositions for typical metastable austenitic stainless steels AISI type 304 and stable austenitic stainless steel AISI type 310S.

## Preparation of Cold-worked Test Pieces

The cold reduction (%) given was within the range 0 to approximately 60%. The processes of cold-working and solution treatment were combined in order to exclude the influence of plate thickness. The final thickness of all the test pieces was 0.5 mm.

When metastable austenitic stainless steel is processed by cold-working, martensite is formed with HCP and BCC crystalline structure<sup>2</sup>. The amount of alpha' martensite in the rolling material was calculated by jointly using a Ferritescope (Helmut Fisher GMBH)(using magnetic detection), and X-ray diffraction. Figure 2 shows the relationship between the cold reduction (%) of the type 304 and type 310S test pieces, and the amount of alpha' martensite. In the case of type 304, the amount of alpha' martensite increases with increase in the cold reduction (%). The martensite phase is not detected in rolled type 310S.

## Measurement of Repassivation Potential

Preparation of Test Pieces for the Measurement of Repassivation Potential. Test pieces were prepared as follows. Stainless steel was cut into 10 x 20 x 0.5 mm billets and degreased with ethanol. The area where the connecting lead was to be connected was insulated and cleaned ultrasonically with acetone. A surface area of 2 cm<sup>2</sup> was sandwiched between two acrylic plates to form two crevices and was exposed to the solution. Figure 3 shows a schematic view of the test piece.

Test Solution. NaCl test solutions were prepared having chloride ion concentrations of 0.020, 0.20, 2.0, and 20 kgm<sup>-3</sup>.

Measurement Method. The test piece was immersed in the solution at 298 K, and exposed to air. The reference electrode was a saturated calomel electrode. The repassivation potential was measured by the potential scanning patterns shown in Figures 4 and 5. The potential was scanned at a speed of 0.1 mV/s towards the noble direction from the 100 mV base potential of the natural immersion potential ( $E_c$ ). At the point where the potential was normally +500 mV (but sometimes up to +1000 mV due to progression of corrosion), the potential was held for  $1 \times 10^4$  s to promote crevice corrosion. The potential was then scanned towards the active direction at a slow scanning speed of 0.01 mV/s. As this potential was scanned towards the base direction, the potential that caused the current from the test piece to change from plus to minus was taken as the repassivation potential (Figure 5, arrow Er).

## Experimental Results and Discussion

### Locations where Crevice Corrosion Occurred

Corrosion occurred at the crevice (Figure 3) formed between the stainless steel test piece and acrylic plates. Corrosion was observed only in the crevices and none was detected on the other immersed parts of the test piece.

## Occurrence and Growth of Crevice Corrosion

Figure 5 shows the results for the repassivation potential of a 50% cold-reduced Type 304 test piece in a NaCl solution with chloride ion concentration of  $2.0 \text{ kgm}^{-3}$ . If the potential, (Figure 5, arrow(1)), at which the anodic current starts to increase suddenly from the passivation region, is plotted against cold reduction (%), the relationship between the potential and cold reduction (%) can be found. Figure 6 shows this relationship. This figure shows the measurement of potential in a solution with chloride ion concentration of  $0.20 \text{ kgm}^{-3}$ . In the case of type 304, the potential tends to depend on cold reduction (%), and to move towards the active direction.

The movement of the pitting potential of type 304 in the active direction due to cold-working has been reported by Tsujikawa et al.<sup>4</sup>. Also, Sunada et al.<sup>5</sup> reported that pitting in type 304 in an  $\text{H}_2\text{SO}_4$ -NaCl solution is often observed at the boundary between the austenite and martensite phases or in the martensite phase, whereas it is only slightly observed in the austenite phase. The potential shown in Figure 6 is the crevice corrosion start potential. Although we did not make a direct comparison with pitting potential, the changes in Figure 6 are believed to be in agreement with the phenomena reported in Ref.4.

In the case of type 310S, there is little dependence of potential on cold reduction (%). It has been pointed out that localized corrosion starts in areas where defects (such as grain boundaries and dislocations) and inclusions exist<sup>6-10</sup>. However, we believe that the results put forward in this paper demonstrate that the martensite transformation contributes considerably more than surface defects to localized corrosion.

## Influence of Cold-Working on Repassivation Potential

Repassivation potential, the focus of this study, is the most active potential at which crevice corrosion is completely repassivated. It is believed that this is independent of conditions during formation and growth of crevice corrosion such as the geometrical conditions of the crevice, and that it is an important indicator in the evaluation of crevice corrosion resistance.

Figure 7 shows the changes in repassivation potential in type 304 and type 310S caused by cold reduction (%). These two kinds of test pieces were compared using a solution with chloride ion concentration of  $0.020 \text{ kgm}^{-3}$ . With the type 304 test piece, there was a tendency for repassivation potential to depend on cold reduction (%), and to move towards the active direction. At 20% cold reduction or more, the repassivation potential reaches a very active value of approximately -300 to -400 mV. In the case of the type 310S test piece, there were few changes in repassivation potential with respect to cold reduction (%).

It is also conceivable that differences in the chemical composition of type 304 and type 310S, such as the amount of Cr, influence the repassivation potential. However, for values of cold reduction of approximately 10% or less, the repassivation potential of both test pieces is almost the same. We believe that type 304 possesses crevice corrosion resistance equivalent to that of type 310S if the type 304 is not cold-worked, and that the influence of differences in chemical composition is not significant.

From these results we conclude that martensitic transformation, which does not occur in type 310S, causes the repassivation potential in metastable austenitic stainless steel type 304 to move towards active values.

#### Dependence of Repassivation Potential on Chloride Ion Concentration

Figure 8 shows the relationship between the repassivation potential and chloride ion concentration of solution-treated type 304 and type 310S, and 50% cold-reduced materials. The figure shows approximate linearity for these materials, and indicates that the repassivation potential moves in the active direction at high concentrations. If solution-treated and cold-reduced type 304 test pieces are compared, it is found that although there is no major difference between the repassivation potentials of the test pieces in solutions with high chloride ion concentration of  $20 \text{ kgm}^{-3}$ , there is a difference of some several hundred mV in freshwater solutions with chloride ion concentration of  $0.020 \text{ kgm}^{-3}$ . The dependence of repassivation potential on chloride ion concentration in type 310S indicates a linear relationship, almost the same as that of solution-treated type 304. With type 310S test pieces, all cold-reduced and solution-treated test pieces show overlapping values in Figure 8, and significant differences are seen between solution-treated and cold-reduced type 304.

#### Possibility of Crevice Corrosion

From the standpoint of practical use of type 304, let us consider the possibility of crevice corrosion by referring to the relationship between cold reduction (alpha' martensite) and chloride ion concentration. The natural corrosion potential of type 304 was approximately 0 plus or minus 100 mV as shown by previous experimental data. Therefore, one possible way to predict crevice corrosion is to determine whether the repassivation potential is towards the noble or active directions from 0 mV. The results in Figure 7 show that, in the case of cold-worked materials, the repassivation potential is 0 mV or less if, for example, rolling of approximately 20% (amount of martensite 40%) is applied, and that it is difficult for the occurrence of crevice corrosion to cause repassivation even in tap water solutions with chloride ion concentration of  $0.020 \text{ kgm}^{-3}$ . These results agree with the results for crevice corrosion in type 304 used in a normal outdoor environment. Also, the results in Figure 8 indicate that the repassivation potential of solution-treated type 304 or type 310S moves towards the noble direction from 0 mV in a freshwater solution with chloride ion concentration of several hundred  $\times 10^{-3} \text{ kgm}^{-3}$ , and that repassivation is obtained when immersed.

#### Appearance of Crevice Corrosion of Type 304

When the appearance of crevice corrosion in type 304 cold-worked materials and type 304 solution-treated materials is compared, the main feature is the directional corrosion observed in the cold-worked materials (Figure 1). Figure 9 shows corrosion in 20% cold-reduced type 304 in which relatively mild crevice corrosion was induced by a solution with chloride ion concentration of  $0.20 \text{ kgm}^{-3}$  and under electrolytic conditions of constant-current electrolysis  $5.0 \times 10^{-5} \text{ A} \times 200 \text{ h}$ . Corrosion similar to that in Figure 1 was observed. This corrosion is different in form from the grain boundary or transgranular cracking seen in SCC. A similar form of corrosion has been observed in copper piping, as reported in references 11 and 12. The potential of the type 304 cold-worked materials when

crevice corrosion was formed under the above electrolytic conditions gradually moved towards the active direction from a relatively noble value immediately after start of electrolysis, and moved further towards the active direction as corrosion progressed. The state in Figure 9, that is, the potential after electrolysis for 200 hours was approximately -100 mV. When this current density was increased to  $2.5 \times 10^{-4}$  A, the potential became approximately +50 mV, and the directional crevice corrosion was not observed.

If a chloride ion concentration of  $0.20 \text{ kgm}^{-3}$  is considered in Figure 8, it is seen that the -100 mV potential (condition for Figure 9) lies within a difficult-to-repassivate range for cold-worked materials, whereas repassivation is possible in the case of solution-treated materials (austenite phase). It has been pointed out that more pitting corrosion occurs in the martensite phase and at the boundaries of both phases than in the austenite phase<sup>5</sup>. There is a difference between the anode electrolytic properties of the austenite phase, the martensite phase and the boundaries of both phases. Accordingly, it is assumed that directional appearance in Figure 9 is formed as a result of accelerated corrosion with the martensite phase and boundaries of the austenite and martensite phases in a non-passivated state even though the austenite phase is passivated. We believe that differences in phases can be easily determined when corrosion is induced comparatively mildly in cold-worked material due to immersion without any electrolysis over a prolonged period of time.

The development of crevice corrosion is determined by the balance of the diffusion of chloride ions towards and away from the crevice. One reason for the acceleration of crevice corrosion by cold-working even in relatively mild environments, is believed to be obstruction of the diffusion of concentrated chloride ions by the small corrosion pits observed in cold-worked materials (e.g. Figures 1 and 9).

### Conclusions

A comparative study of the crevice corrosion of the metastable austenitic stainless steel, type 304, and stable austenitic stainless steel, type 310S, in the annealed and cold-worked states revealed the following:-

- (1) The repassivation potential of the metastable austenitic stainless steel, type 304, in crevice corrosion is made to move towards the active direction by cold-working.
- (2) The repassivation potential of the stable austenitic stainless steel, type 310S, is not influenced by cold-working.
- (3) Martensitic transformation induced by cold-working causes the repassivation potential to move toward the active direction, and its influence is large, particularly in solutions with low chloride ion concentration.
- (4) Directional crevice corrosion morphologies are sometimes observed in type 304 cold-worked material.



## References

1. N. Yamauchi, Y. Miyata, S. Mitani, H. Takazawa, Proceedings of 37th Joint Symp. Corros. and Tech., (1990): A203.
2. Z. Nishiyama, K. Shimizu, S. Morikawa, Nihonkinzokugakkai-shi, 27(1963): p.497.
3. T. Suzuki, Boshoku Gijutsu, 28(1979): p.38.
4. S. Tsujikawa, Y. Ishihara, T. Shinohara, Zairyo-to-Kankyo, 42(1993): p.20.
5. S. Sunada, H. Maezato, Y. Yokoi, H. Notoya, S. Sanuki, K. Arai, Nihonkinzokugakkai-shi, 54(1990): p.1078.
6. J.R. Galvele, Passivity of Metals: p.285.
7. J. Kruger, J. Electrochem. Soc., 106(1959): p.736.
8. A.P. Bond, G.F. Rolling, H.A. Domain, ibid., 113(1966): p.773.
9. A. Szummer, Z. Szklarska-Smialowska, M. Janik-Czachor, Corros. Sci., 8(1968): p.827.
10. Z. Szklarska-Smialowska, A. Szummer, M. Janik-Czachor, Br. Corros. J., 5(1970): p.159.
11. T. Notoya, T. Ishikawa, Proceedings of Fushoku-Boshoku '91: B106.
12. T. Takahashi, M. Watanabe, Y. Salto, H. Ogawa, Proceedings of Fushoku-Boshoku '91: B107.

Table 1 Analysis of the solution in which crevice corrosion occurred.

( $10^{-3}\text{kgm}^{-3}$ )	$\text{Cl}^-$	$\text{NO}_3^-$	$\text{SO}_4^{2-}$
Figure 1	20	2	15
General	10	2	20

Table 2 The chemical composition of the test materials (mass%)

Material	C	Si	Mn	P	S	Ni	Cr	Mo	N
Type 304	0.05	0.46	1.30	0.03	0.006	8.23	18.06	0.10	0.05
Type 310S	0.05	0.48	0.83	0.03	0.008	19.46	24.86	0.31	0.02

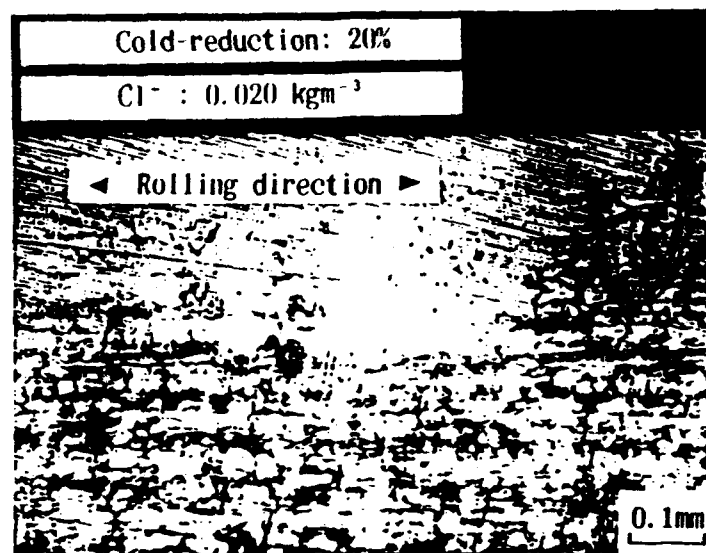


Figure 1 Crevice corrosion in type 304 formed in a fresh water environment.

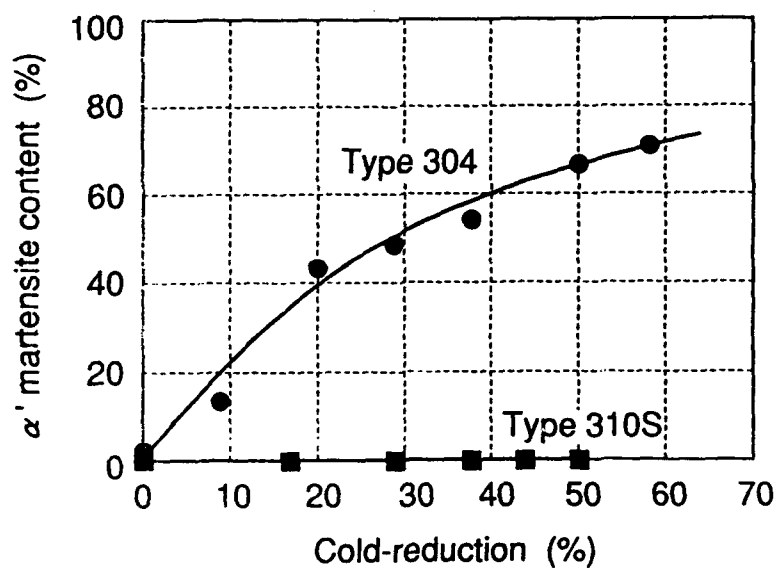


Figure 2 The  $\alpha'$  martensite content versus the degree of cold-reduction.

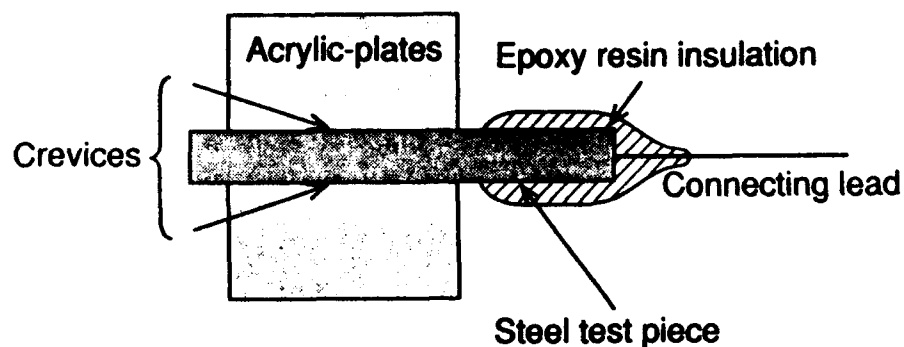


Figure 3 Schematic view of the measurement test piece.

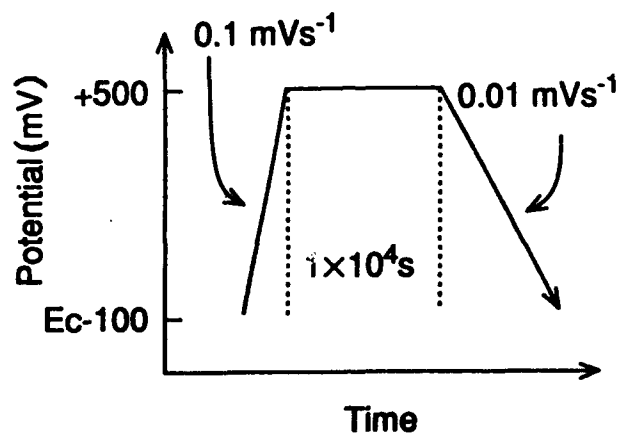


Figure 4 The potential scanning pattern for measuring the repassivation potential.

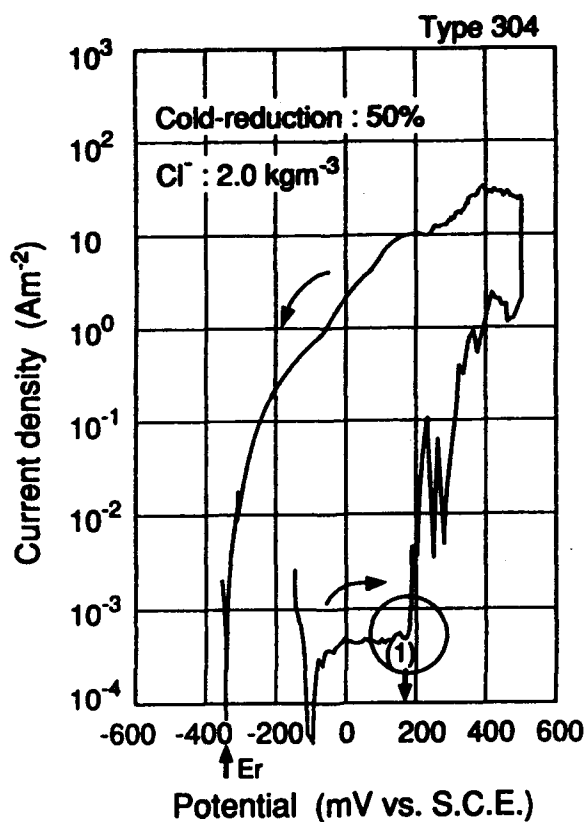


Figure 5 Measurement of repassivation potential.

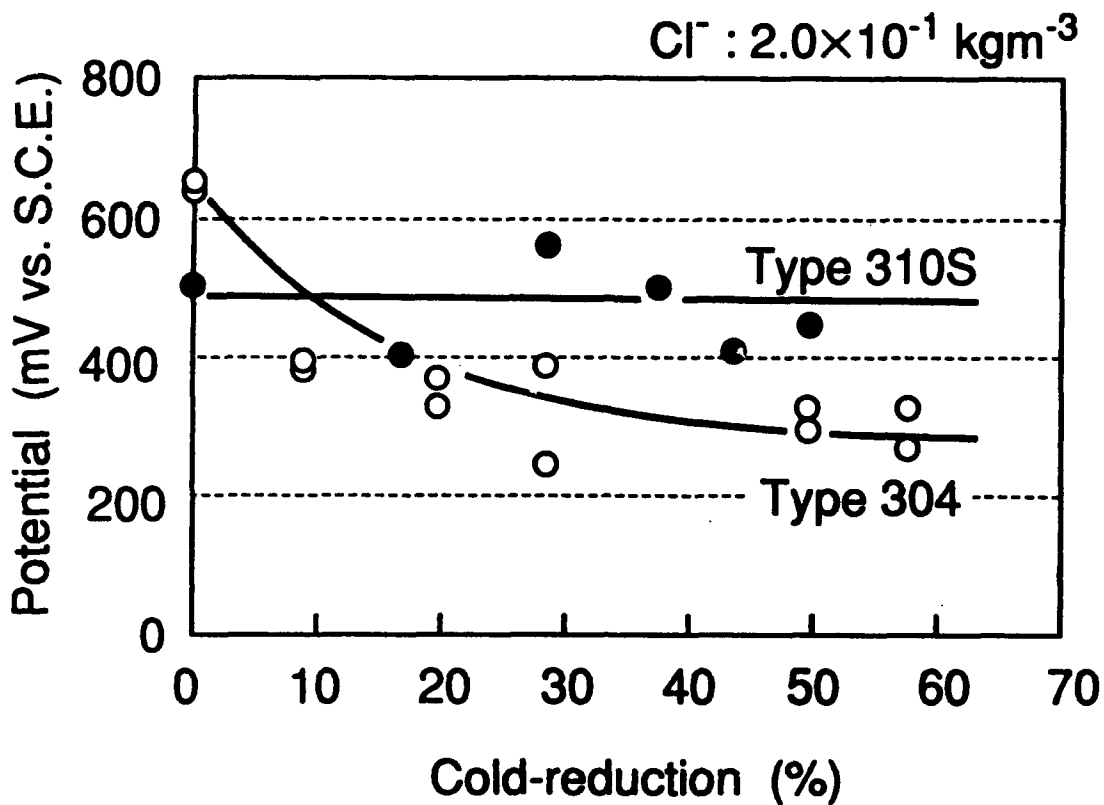


Figure 6 Potential at which the anodic current starts to increase versus cold-reduction.

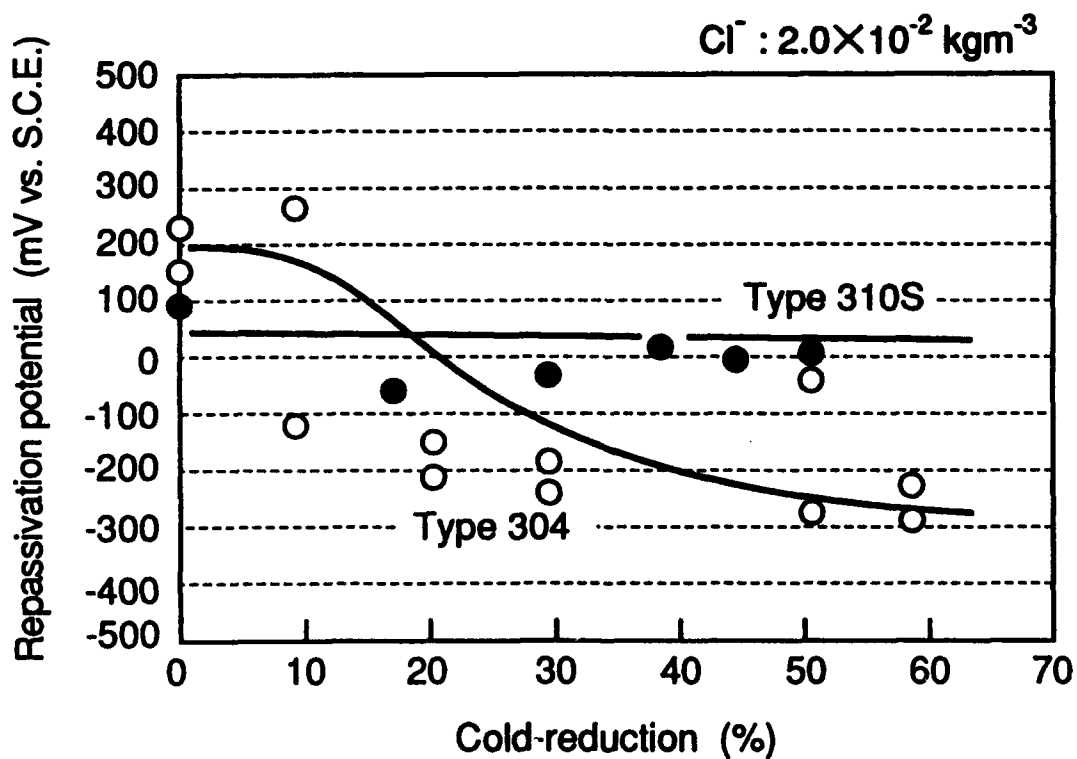


Figure 7 Repassivation potential versus cold-reduction.

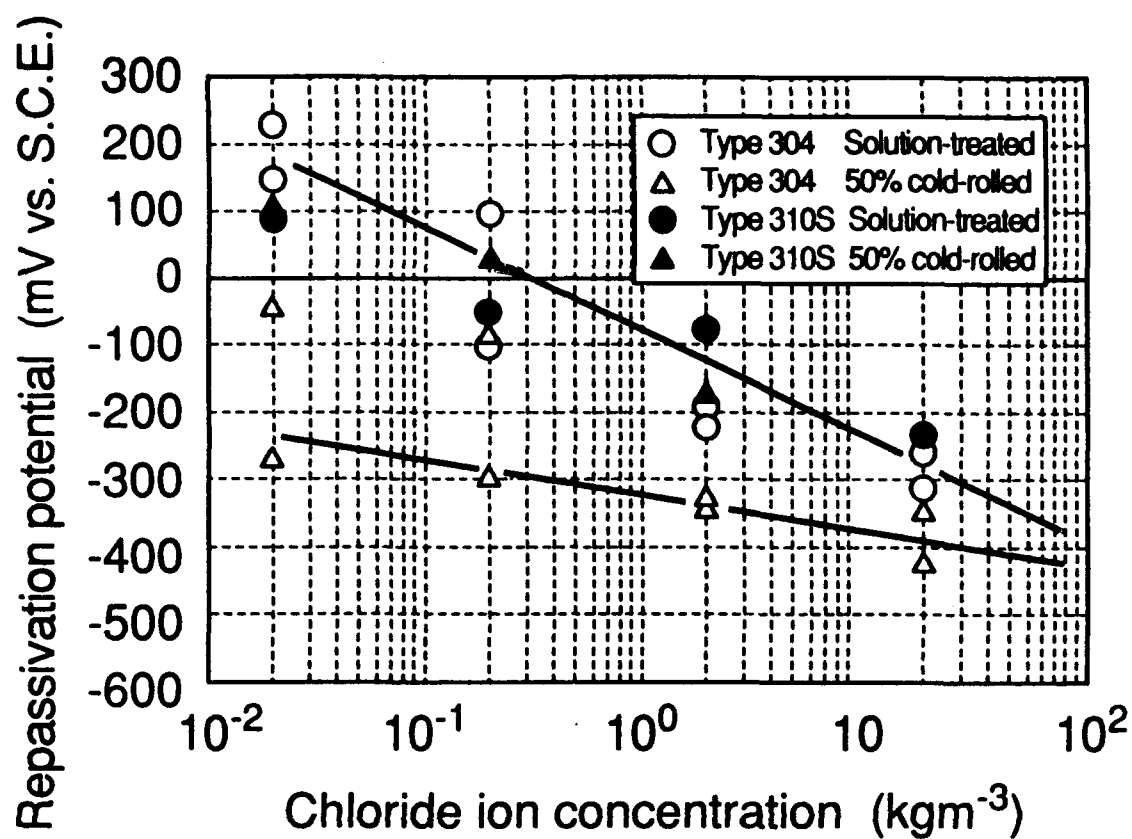


Figure 8 Repassivation potential versus chloride ion concentration.

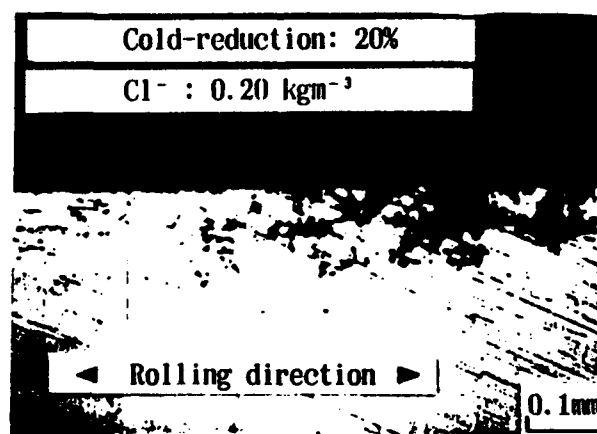


Figure 9 Crevice corrosion in 20% cold-reduced type 304 in electrolytic experiments.

Application of *In situ* Scanning X-ray Fluorescence to Study  
the Concentration of Metal Ions in Simulated Pits

H. S. Isaacs  
Brookhaven National Laboratory  
Upton, NY 11973

Jeong-Hwan Cho  
Department of Chemistry  
Yonsei University  
Seo-Dae-Moon Gu, Shinchon Dong 143  
Seoul 120-749  
Korea

A. J. Davenport  
Brookhaven National Laboratory  
Upton, NY 11973

M. L. Rivers  
Department of Geophysical Sciences  
University of Chicago, Chicago IL 60637

S. R. Sutton  
Department of Geophysical Sciences  
University of Chicago, Chicago IL 60637

### Abstract

X-ray energy-dispersive spectroscopy has been used to study the compositions of metal ions in solutions developed during localized corrosion. An electrochemical cell was designed to simulate a corrosion pit, maintaining one-dimensional diffusion and fulfilling the requirements for x-ray fluorescence measurements. The working electrode consisted of a dissolving thin foil of Type 304 stainless steel sealed between Mylar sheets through which the x-ray beam passed. Concentration gradients within the artificial pit were quantitatively determined.

### Introduction

X-ray fluorescence measurements offer a powerful method for the *in situ* study of chemical and physical changes during electrochemical and corrosion processes<sup>1</sup>. The measurements offer a non-destructive *in situ* technique for analysis. In contrast to other surface analytical techniques, e.g. Auger and x-ray photoelectron spectroscopies, that require a vacuum and can induce chemical changes<sup>2,3</sup>. High photon intensity monochromatic synchrotron x-rays have been used for x-ray absorption measurements of a number of corrosion systems in air<sup>4</sup>

and under controlled electrochemical conditions<sup>4</sup>. The major contribution of this technique is information as to the chemical nature of the elements, but the concentrations of individual elements can also be obtained.

Concentration variations and the associated chemistry within a pit or a crevice have been the subject of theoretical calculations<sup>7,11</sup>. However, due to difficulties in performing *in situ* measurements of such solutions, the accuracy of the calculations are hard to assess. Consequently, uncertainties arise as to the nature of the solutions within an actively dissolving metal site. Several investigations of pit and crevice solutions have been appeared in the literature<sup>12-15</sup>. Ives and Luo<sup>12</sup> measured the concentration of chloride ion, potential and pH as a function of depth within a pit using *in situ* micro-electrode measurements and clarified the conditions for a steady growing pit during pitting corrosion. Tsuru *et al.*<sup>13</sup> estimated apparent transport numbers of anions and cations in an occluded cell from chemical analysis of the solution. The measured transport numbers were different from those calculated from known mobility data and inferred the presence of the metal-chloride complex ion  $\text{FeCl}^+$ . Complex formation is also supported by x-ray scattering studies of solutions<sup>14</sup>. Nash and Kelly<sup>15</sup> used ion chromatography to obtain compositions of solutions extracted from stainless steel artificial pits. Their data indicated preferential dissolution of chromium and manganese.

Methods for analyzing the chemical composition and nature of the solutions within pits and crevices during active dissolution have been developed. In the present report, *in situ* fluorescence microanalysis using white x-rays and an energy-dispersive spectrometer<sup>16-18</sup> was carried out in order to determine the chemical compositions of the solutions within a one-dimensional artificial pit. This enabled simultaneous counting of the x-ray fluorescence from all the elements in stainless steel at each position of the sample and reduced the time required to obtain concentration gradients. Measurements of the concentration gradients of the major constituents of the alloy could be made more rapidly than with x-ray absorption measurements using monochromatic x-rays that must scan over the separate energy range for resolving each element. However, unlike x-ray absorption data fluorescence data contain no information on the chemical states of the elements.

## EXPERIMENTAL

The electrochemical cell shown in Fig.1 was designed to simulate one-dimensional diffusion processes taking place in pitting or crevice corrosion. It consisted of a thin foil strip 2 mm wide and 0.016 mm thick of stainless steel sandwiched between Mylar sheets and sealed using an epoxy glue. The composition of the stainless steel is given in Table 1. The sandwich adhered to a Teflon tape that formed the window to the cell and through which the x-ray beam entered. The upper cross-section of the steel strip was exposed to the solution. A 0.5 M HCl + 0.5 M NaCl solution was used. The steel was dissolved at a constant potential of 600 mV (vs. SCE) leaving a rectangular shaped crevice. Helium gas was bubbled into the bulk solution to stir it and thus avoid the concentration build-up of diffusing species at the mouth of the cavity.

The measurements presented here were carried out with high intensity white x-rays at the National Synchrotron Light Source Beamline X26A<sup>16-18</sup>. A schematic diagram of the X26A x-ray microprobe beamline is shown in Fig. 2. The beam size was collimated down to a pin-hole size of 0.02 mm. The cell was positioned with the plane of the foil at 45° to the beam. The cell was held on a motorized stage and area or linear scans were made from the stainless steel to the bulk solution via the artificial pit. After the experiment was completed the solution in the cell and crevice was replaced with a standard solution of 0.5 M NiCl<sub>2</sub> + 0.8 M CrCl<sub>3</sub> was used for calibration and to examine the uniformity of the thickness within the artificial pit. Measurements were also carried out using a 0.1 mm Kapton sheet with sputtered titanium about 500 Å thick placed against the cell in the x-ray beam. The counts from the titanium were used to normalize the effective x-ray intensity as described below.

### Data Analysis

It takes a finite time for the electronics of the solid state detector to process a signal from a single photon. During this time, any other photons which are incident on the detector will not be collected. For high photon fluxes, this gives a significant "dead-time" so that counting only takes place for a fraction of the total time available. The consequence of this is that the total "live-time" during which counting is carried out is the difference between the total counting time or "real-time" and the "dead-time". The number of counts are therefore normalized to the "live-time". This value is further normalized to account for changes in the incoming x-ray beam by dividing by the current in the storage ring or the counts from the ion chamber detector (see Figure 2). In order to overcome statistical variations associated with these required normalization, the counts from the thin layer of titanium placed in the beam was used instead.

Quantitative x-ray fluorescence analysis has been well established for many years<sup>19</sup> and a number of possible methods of calibration are available. The principles of quantitative analysis by synchrotron radiation-induced x-ray fluorescence (SRXRF) data are presented by Lu et al.<sup>18</sup> Two main methods are used for quantitative analysis. The first is an empirical method exemplified by the multiple regression treatment of Lucas-Tooth and Pyne<sup>20</sup>. This method calculates the absorption and scattering effects of each element present in a sample from the fluorescent intensities measured. Standards are required which are similar to the sample. The second method calculates the expected intensities based on a fundamental-parameters method<sup>21</sup>. This method derives the expected intensities from a given sample composition, geometry and three sets of basic information: the x-ray spectral distribution of the incoming beam, the mass absorption coefficients for each element in the sample, and their fluorescence yields. In this study, the fundamental-parameters method was employed to obtain calibration curves, and the reliability of this approach was investigated using known standards. A modified NRLXRF Fortran program<sup>22</sup> was used and referenced to the stainless steel and the standard solution in order to convert the measured normalized fluorescent intensities of Fe, Cr and Ni to solution concentrations. The minor elements such as C, P, Si, Cu, Mn and Mo were not included.



## Results and Discussion

An investigation of the dissolution characteristics of the sandwich type cell was carried out to ensure that a flat dissolving edge parallel to the mouth resulted from the mass transport-controlled dissolution process. The crevice was observed to be filled by a gel. Subsequent analysis using a scanning electron microscope and EDX showed only silicon. The gel was formed from the silicon in the steel which expanded to occupy the volume of the metal as it dissolved. Similar effects were observed with an Fe-3% Si alloy. Here, because the five times greater amount of Si, the gel was seen to be extruded from the crevice as dissolution proceeded. Ultrasonic cleaning of the crevice to remove the gel did not produce an observable difference in the concentration gradients across the boundary between first and second dissolution sequences. However, with or without removal of the gel, if the applied potential was turned off and the dissolving steel repassivated, subsequent dissolution often left remnants of steel under the passive surface that was undermined when the adjacent surface was reactivated. The remnants acted as an obstacle to diffusion with major perturbation in the measurements. Generally the gradients were therefore measured during a single continuous dissolution of the foil.

Figure 3 shows a fluorescent spectrum of the solution inside the cavity immediately above the metal for real-time counting of 600 s. The counts under the  $K\alpha$  energy peak for each element (except Cu) were integrated and used to determine the concentration of each element. The  $K\beta$  peak was used for Cu because of the interference with the Ni  $K\beta$  peak. The Ar  $K\alpha$  peak was from argon in the air. The source of the As and Br peaks could be due to their presence as impurities in the plastic, the Teflon window or the epoxy glue. These possibilities were not pursued as they were only observed after long counting times (600 s) and were not seen when counting for real-time 30 seconds. This does however show the application of x-ray fluorescence microscopy to quantitative analysis of trace impurities down to extremely small quantities<sup>16,17</sup>.

The concentrations of Fe, Cr and Ni with distance were derived from the results in Figure 3 using the NRLXRF program and the data from the stainless steel foil as a reference. The total metal ion concentration was 4.75 M with a calculated chloride concentration of 10.6 M deduced from the metal concentrations. This value is in agreement with the value of Hakkarainen<sup>23</sup> who observed that approximately 10 M chloride ions were required to give a saturated metal chloride solution on dissolving Type 304 stainless steel in HCl.

The relative Fe:Cr:Ni weight per cent ratios in the saturated solution at the metal interface were 67 : 22 : 11 compared to ratios of 68.7 : 18.2 : 13.1 in the metal. The differences in the ratios resulted from unequal the mass trans rate for the ions in solution. The mass transfer include an electromigration contribution in addition to diffusion, but as the contribution is not known, the results have been treated in terms of an effective diffusion rates. The effective intergral diffusion rates calculated from the concentrations at the metal/solution interface, the depth of the crevice and the current density. The valuse obtained were 6.0, 5.2 and 4.7  $10^6$  cm<sup>2</sup>/s for the ions or chloride salts of nickel, iron and chromium respectively. These values are close to published results for nickel chloride diffusion<sup>24</sup> and indicate that only a small electromigration contribution is present.

The concentration gradients in Figure 4 were clearly non-linear with increased slopes close to the dissolving metal interface and close to the mouth of the crevice. This behavior shows that the differential diffusion coefficients have a maximum at intermediate concentrations around a total metal ion concentration of about 2.5 M. Once again this behavior is consistent with diffusion coefficients of many salts<sup>2</sup>. The results for nickel chloride solutions show a maximum diffusion coefficient but at a lower concentration of 1.5 M<sup>24</sup>.

### ACKNOWLEDGEMENTS

The x-ray fluorescent microanalysis were carried Beamline X26A of the National Synchrotron Light Source at Brookhaven National Laboratory. This work was performed under the auspices of the U.S. Department of Energy, Division of Materials Sciences, Office of Basic Energy Sciences under Contract No. DE-AC02-76CH00016.

### References

1. A. Davenport, J. G. Gordon II, ed., "X-ray Methods in Corrosion and Interfacial Electrochemistry," Vol 92-1, (Pennington, NJ, The Electrochemical Society Inc.,1992)
2. K. Asami and K. Hashimoto, Corrosion Sci., 17, (1977): p. 559.
3. A. G. Schrott, G. S. Frankel, A. J. Davenport, H. S. Isaacs, C. V. Jahnes, and M. A. Russak, Surf. Sci., 250, (1991):p. 139.
4. M. W. Kendig A. J. Davenport, H. S. Isaacs, Corrosion Sci., 34 (1993): p. 41.
5. A. J. Davenport, H. S. Isaacs, G. S. Frankel, A. G. Schrott,C. V. Jahnes, M. A. Russak, J. Electrochem. Soc., 138 (1991): p. 337.
6. J. A. Bardwell, G. I. Sproule, B. MacDougall, M. J. Graham, A. J. Davenport, H. S. Isaacs, J. Electrochem. Soc., 139 (1992): p. 371.
7. J.R. Galvele, Corrosion Sci., 21 (1981): p. 551.
8. B.G. Ateya and H.W. Pickering, "Passivity of Metals" Edited by R.P. Frankenthal and J. Kruger, the Electrochemical Society, NJ, p.350 (1978).
9. S.M. Sharland, C.P. Jackson and A.J. Diver, Corrosion Sci., 29 (1989): p. 1149.
10. M. Watson and J. Postlethwaite, Corrosion, 46 (1990): p. 522.
11. A. Turnbull, Corrosion Sci., 23 (1983): p. 833.
12. M.B. Ives and J.L. Luo, 11th ICC, Paper No. 88, Firenze, April (1990).

13. T. Tsuru, K. Hashimoto, A. Nishikata and S. Haruyama, Material Science Forum, 44&45 (1989): p. 289.
14. M. Magini, J. Chem. Phys., 74 (1989): p. 2523.
15. B. K. Nash, R. G. Kelly, J. Electrochem. Soc., 139 (1992): p. L47.
16. K. W. Jones et al, Advances in X-Ray Analysis, (New York, NY: Plenum Publishing Co., 1988).
17. Y. Wu, A. C. Thompson, J. H. Underwood, R. D. Gaiuque, K. Chapman, M. L. Rivers and K. W. Jones, Nucl. Inst. and Methods, A291, (1990): p. 146.
18. F-Q. Lu, J. V. Smith, S. R. Sutton, M. L. Rivers, A. M. Davis, Chem. Geol., 75 (1989): p. 123.
19. B. Dziunikowski, Energy Dispersive X-ray Fluorescence Analysis, (Amsterdam, Holland: Elsevier, 1989)
20. H. S. Lucas-Tooth and E. C. Pyne, "Advances in X-Ray Analysis", Vol. 7, Plenum Press, New York, p. 523 (1964).
21. J. W. Criss and L. S. Birk, Anal. Chem., 20, 1080 (1968).
22. J. W. Criss, "NRLXRF, A FORTRAN program for X-ray Fluorescence Analysis", Naval Research Laboratory, Washington, D.C. (1977).
23. T. Hakkarainen, "Corrosion Chemistry within Pits, Crevices and Cracks", Edited by A. Turnbull, (London, England: HMSO, 1987): p. 17.
24. R. H. Stokes, P. Phang, R. Mills, J. Solution Chem., 8 (1979): p 489.
25. R. A. Robinson, R. H. Stokes, "Electrolyte Solutions" (London, England: Butterworths Scientific Publications, 1959), p. 290.

Table 1. Chemical composition of a commercial stainless steel foil.

element	wt%	atom%
C	0.11	0.50
Mn	1.70	1.70
P	0.01	0.02
S	0.002	0.003
Si	0.54	1.06
Cr	17.73	18.75
Ni	12.81	12.01
Cu	0.12	0.10
Mo	0.28	0.16
Fe	66.70	65.69

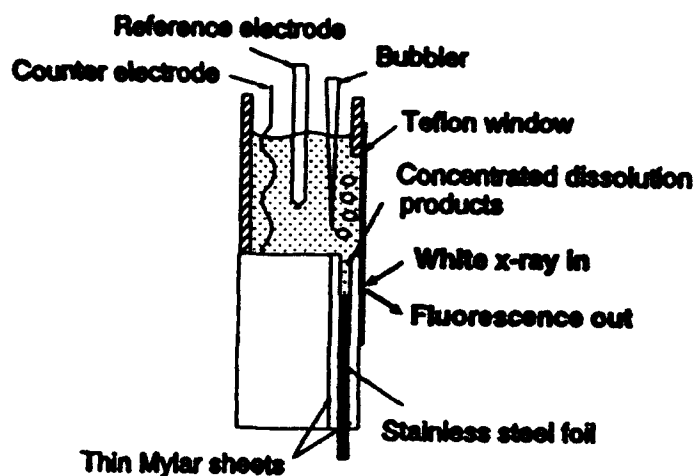


Figure 1. A simulated one-dimensional pit used for x-ray fluorescence microscopy.

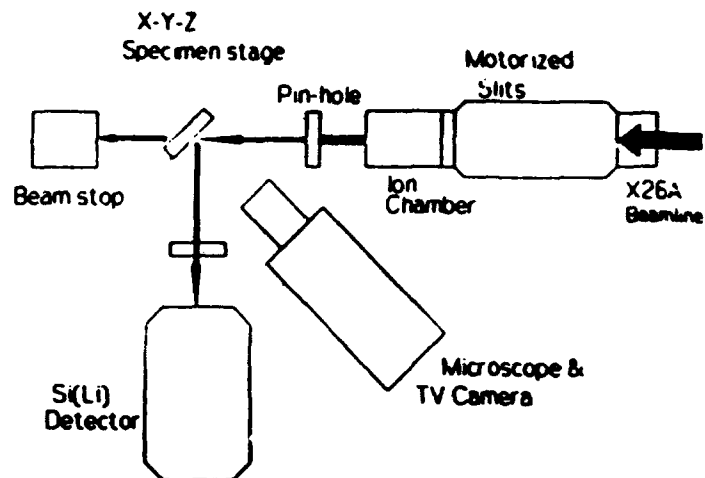


Figure 2. A schematic diagram of beamline X26A.

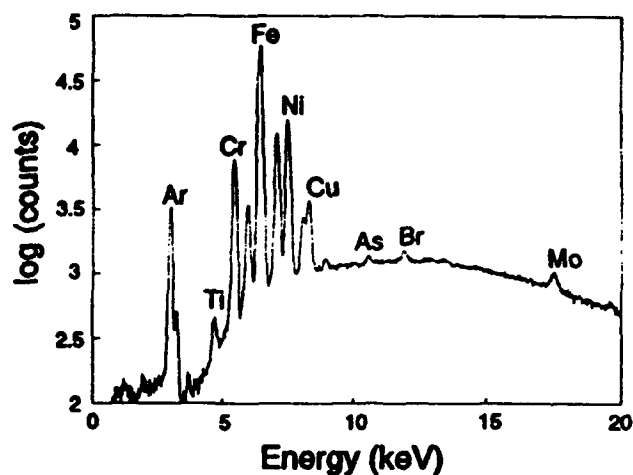


Figure 3. X-ray fluorescence spectrum taken immediately above the metal foil during steady state dissolution (Counted for 600 seconds of real-time).

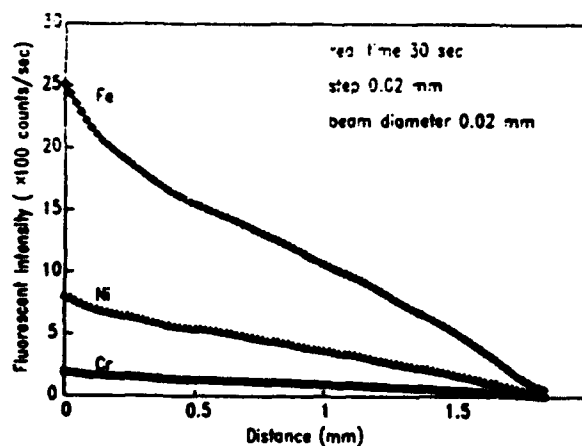


Figure 4. Normalized fluorescence counts as a function of position above the metal surface during dissolution of the Type 304 stainless steel foil.

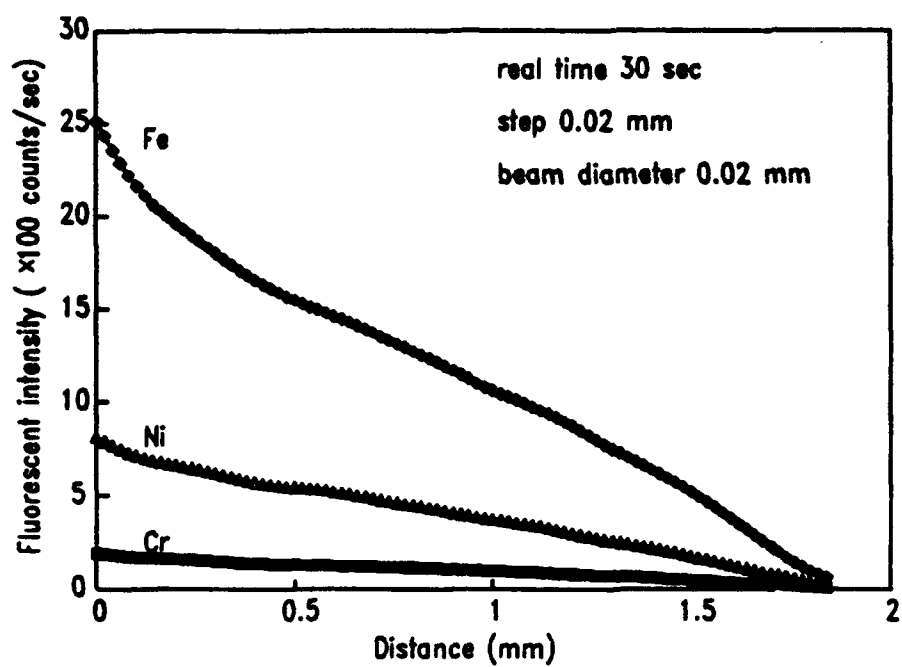


Figure 5. Concentrations of metal ions in an artificial cavity above the metal surface calculated from the results in Figure 4.

**Pitting Conditions Evolution of 316L Stainless Steels  
During Aging in Sea Water : a Statistical Approach**

**M. Ghiazza**  
ICMM - Torre S. Benigno,  
Via Scarsellini  
16149 GENOVA - Italia

**Dominique Festy**  
IFREMER - Centre de Brest  
BP 70  
29280 PLOUZANE - France

**Johanès Léonard**  
LG2mS, URA n° 1505 du CNRS  
Université de Compiègne, BP 649  
60206 COMPIEGNE CEDEX - France

**Christian Lemaître**  
LG2mS, URA n° 1505 du CNRS  
Université de Compiègne, BP 649  
60206 COMPIEGNE CEDEX - France

**Abstract**

The pitting resistance of stainless steels in neutral chloride media is classically measured by the value of the pitting potential. In marine media, the immersion time plays also a role because the aging conducts to have an increase in the open circuit potential, and when the value of this parameter is equal to pitting potential, one have the initiation of pits. But during that aging, the pitting potential can also change because the passive film is modified.

We have measured the pitting potential evolution with immersion time in two different media : a natural sea water and a synthetic sea water. For that, we have performed statistical measurements by using a potentiokinetic technique. We have compared the values of the pitting potentials and of rest potentials for different immersion times.

Our results confirm that the rest potential values increase with the immersion time, but show also that the pitting potentials shift after an induction period, and then the steels resistance to pitting increases : when the localized corrosion is occurring the mechanism of that corrosion is modified by the changes in the passive film.

**Key terms :** Pitting Corrosion, Stainless steels, Passivity, Marine corrosion, Microbially Influenced corrosion, Aging, Statistics

**Introduction**

The use of stainless steels in sea water leads to study the localized corrosion of these alloys, and to perform measurements concerning for example the pitting corrosion. The pitting resistance of stainless steels in neutral chloride media is classically measured by the value of the pitting potential [ 1 ]. For long immersion times, the passive films of stainless steels can be modified by species proceeding from the medium, and then the conditions of the equilibrium between this medium and the metal surface can evolve [ 2 ]. In marine media, the aging conducts to have an increase in the open circuit potential, and when the value of this parameter is equal to the pitting potential, one have a large risk to observe the initiation of pits [ 3 ]. But during that aging, the pitting potential

can also change. It is necessary to compare at each time the equilibrium and the pitting conditions. Thus, the evolution of the open circuit potential and the pitting potential versus the immersion time must be considered [ 4 ]. To measure this risk of pitting, we have used the stochastic technique called " multipits" suggested by SHIBATA and TAKEYAMA [ 5, 6 ] and developed by BAROUX [ 7, 8 ]. To separate the role of chemical and biological parameters, we have performed the tests respectively in synthetic and natural sea water.

## Experimental

### I - Material and Media

The tested material was a commercial AISI 316L stainless steel. The used natural sea water was drawn in Brest ( France), filtered, and used at 15°C. It contains NaCl 35,5 g/l, and its pH is equal to 8,2. During the immersion periods before the tests, this medium circulated in the cell and returned to the sea. The synthetic sea water was an ASTM standardized medium ( ASTM standard D 1141-52, 1971 ), adjusted to pH 8,2 with NaOH.

### II - Pitting Potentials measurements

The experimental procedure was previously described, using a multichannel electrochemical device [ 7 ], and a potentiokinetic mode ( with in our case  $v = 150$  mV/min ). The threshold current on each specimen is equal to 50  $\mu$ A. From the experimental data, the survival probability  $P_E$  is deduced as a function of the electrode potential  $E$ . The "elementary pitting probability" per unit area is then :

$$\omega_E = (1/S) \cdot \ln P_E$$

The value of this parameter depends on the potential sweep rate. Then, from  $\omega_E$  one can determine the " pit generation rate" :

$$g_E = \frac{d\omega_E}{dt} = \omega \cdot v \cdot \frac{d\omega_E}{dE}$$

This later parameter does not depend on potential sweep rate used for the potentiokinetic tests [ 7 ]. A "conventional pitting potential"  $E_{pit}$  is defined as  $g(E_{pit}) = \text{Constant}$

## Results

### I - In synthetic sea water

The evolution of the open circuit potential versus the immersion time shows an increase in the value of this potential ( Fig. 1 ), with a 150 mV shift approximatively, corresponding to an ennoblement of the material-medium couple for this time of immersion.

Concerning the pitting initiation potentials, the Fig. 2 shows that the pit generation rate varies greatly with the imposed potential, when the value of that later corresponds to the risk of the local breakdown of the passive film. We have chosen two constants to determine the evolution of the conventional pitting potential versus the immersion time :

- $g = 0,01 \text{ cm}^{-2} \cdot \text{s}^{-1}$  where the risk of pitting initiation is low
- $g = 0,1 \text{ cm}^{-2} \cdot \text{s}^{-1}$  where this risk is high

The obtained results with these two conventions are reported in the Fig. 3 ; it appears that the pitting potentials change also after 4 weeks of immersion, with an ennoblement of that potential

## II - In Natural Sea Water

We have performed two measurements of the open circuit potential ( OCP ) by using two samples of the same steel. There is also in this case an ennoblement in this potential values during the immersion, but the shift is important ( Fig. 4 ) : it corresponds to 200 or 300 mV after 2 weeks.

The multipits results obtained with the same conventions than in the synthetic medium to determine the pitting potential are reported in the Fig. 5 : there is an ennoblement during the first two weeks, and a stabilization after this period.

## Discussion

For the natural and the synthetic media, the potentials evolution of the OCP and the Epit are similar, with an ennoblement of their values, but the critical times are not identical in the two media : there are changes in the potential evolutions after 4 weeks in the synthetic sea water, and after two weeks in the natural one.

In synthetic sea water, the OCP is always low behind the conventionnal pitting potential, and the risks to initiate pits are practically equal to zero. After 4 weeks, the pitting potential increases largely, and it is then very difficult to initiate pitting. The passivity is improved. In natural sea water, the comparison between OCP and Epit permits to observe that, when the conventions are modified to obtain  $g_E = 10^{-4}$  or  $10^{-5} \text{ cm}^{-2} \cdot \text{sec}^{-1}$ , the values of these potentials are in the same domain ( Fig. 6 ) between 10 and 15 days approximatively. Then, the pitting initiation is possible. After this period, the pitting initiation risk decreases, but it is more important than one obtained in synthetic sea water.

Thus, it appears that in the ASTM medium the passive film properties of the stainless steel are improved by the immersion, and this improvement , due to physico-chemical reasons, increases with the duration of that immersion.

In the natural used sea water, bacteria are present in the medium, and the variations of the potential are more important than in synthetic one, and for shorter times : the bacteria modify the passive film properties and also the OCP, by the biofilm formation. Then, the equilibrium conditions at the interface and the pitting resistance change simultaneously.

## Conclusion

In synthetic sea water, OCP and Epit are increasing : the equilibrium potential of the NERNST's equation evolutes versus the immersion time, then the passive film is modify during this immersion. In natural sea water, the OCP increases more rapidly and with a larger shift than in synthetic one. Epit varies also more rapidly, but the shift is smaller than in ASTM medium.

It appears that the passive film resistance decreases when bacteria are present in the medium in correlation with a change in the interface equilibrium, and that a critical period can exist, where the risk of pitting is maximum : in our case, it corresponds to a period of 10 - 15 days after the begining of the immersion.

Then, this is the evolution versus the time of the passive films which leads the corrosion resistance of the stainless steels.



## References

- [ 1 ] BIRD H.E.H. ; PEARSON B.R. ; BROOK P. A.; Corr. Sci.28,1 ( 1988 ), p. 81
- [ 2 ] SMIALOWSKA Z.S. ; " Pitting Corroison of metals" NACE Ed.( Houston),1986
- [ 3 ] BAROUX B. ; LEMAITRE C ; DABOSI F. ; in " Les aciers inoxydables "  
Editions de physique ( Paris ), 1990, Chap. 9, p. 305
- [ 4 ] LEMAITRE C. ; HERNANDEZ G. ; BERANGER G. ; GUEZENNEC J.  
Materiaux et Techniques ( France ), 12 ( 1990 ) p. 25
- [ 6 ] SHIBATA T. ; TAKEYAMA J. ; Corrosion, 33,7 ( 1977), p.243
- [ 6 ] SHIBATA T. ; TAKEYAMA J. ; 8th ICMC, Franckfurt/Main ( 1981 )  
Proceed. Dechema, Vol. 1 ( 1981 ), p. 146
- [ 7 ] BAROUX B. Mem. Sci. Rev. Met. ( Fr ) 12 ( 1988 ), p. 684
- [ 8 ] BAROUX B. Corr. Sci. 28, 10 ( 1988), p. 968

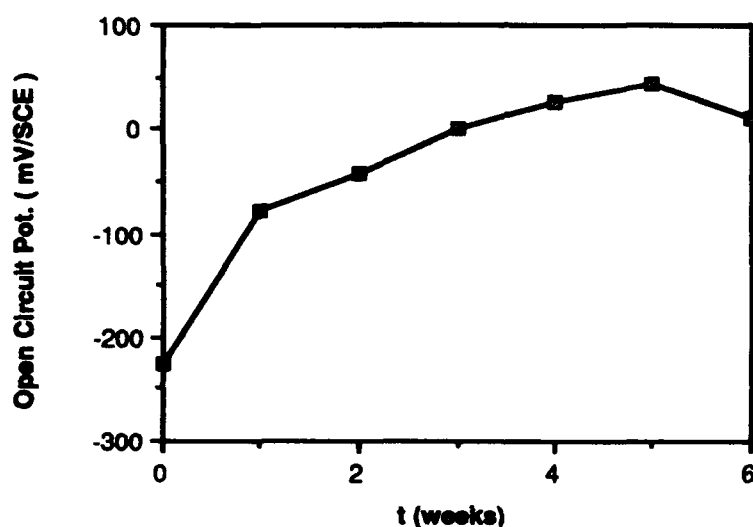


Fig. 1 : Open circuit potentials in synthetic sea water

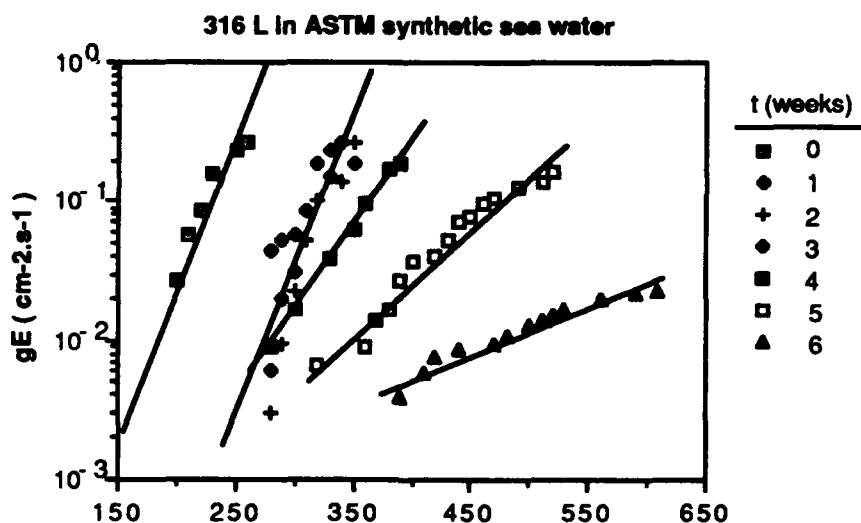


Fig 2 : Pit generation rates after different times of immersion in synthetic medium

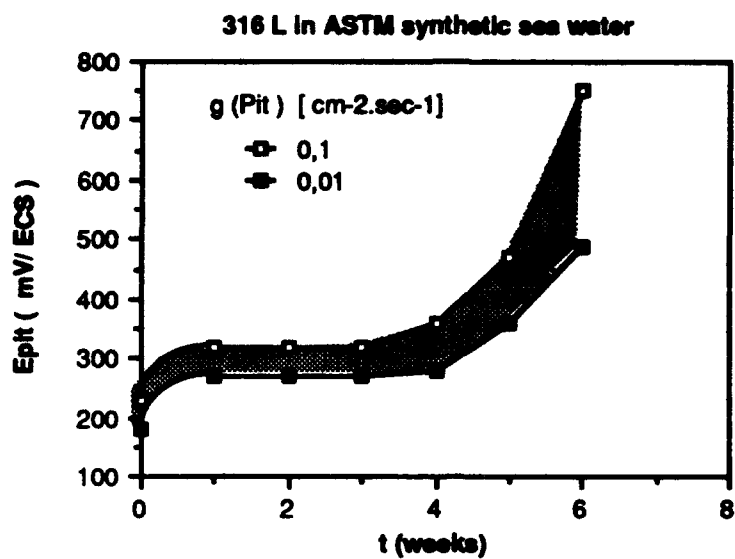


Fig 3 : Influence of the time of immersion on the conventional pitting potential`

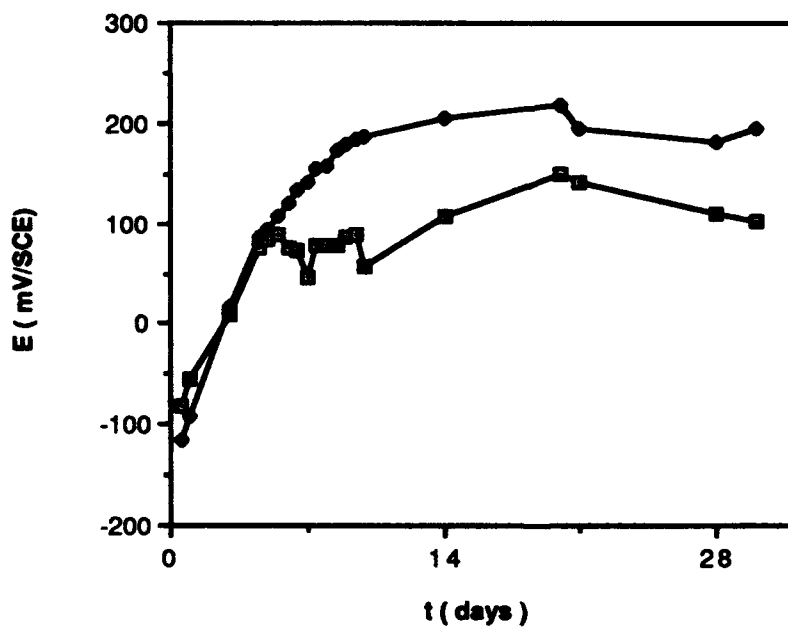


Fig. 4 : Open circuit potential in natural sea water for two specimens of the used stainless steel

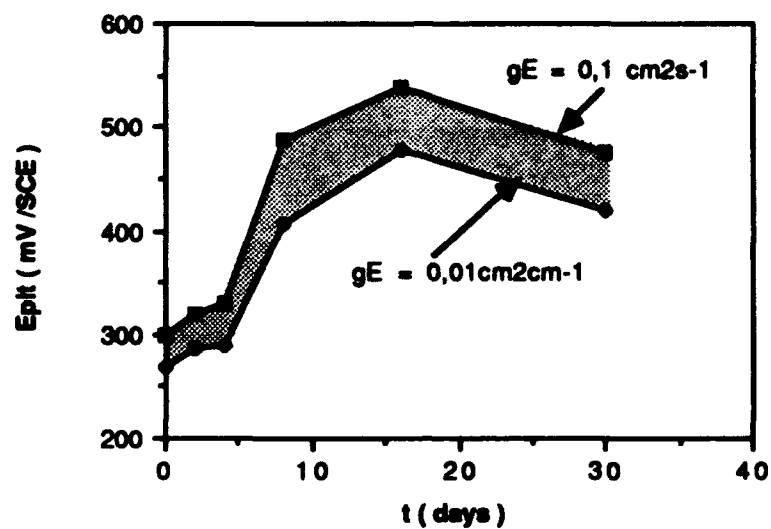


Fig 5 : 316 L in natural sea water.  
Open circuit potential evolution versus the immersion time

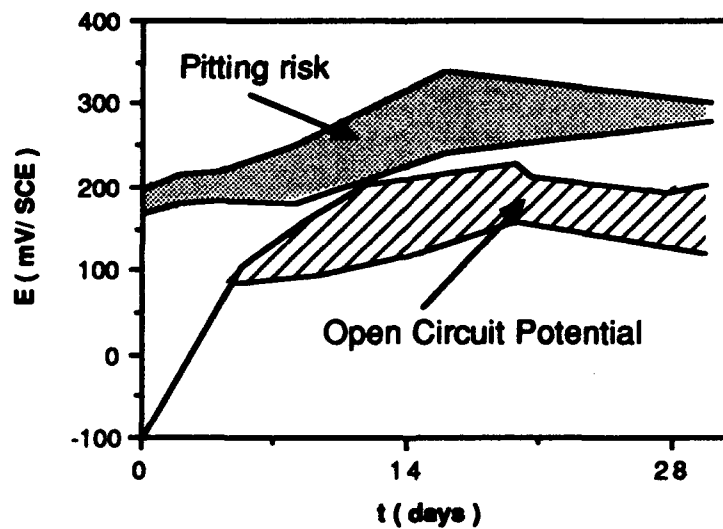


Fig 6 : Pitting risks during the immersion in natural sea water

## Pitting Behaviour of UNS NO8904 Stainless Steel in Salt Solutions

V.K.Gouda and E.A. Abd El Meguid

Department of Electrochemistry and Corrosion

National Research Centre, Dokki, Cairo, Egypt

### Abstract

Pitting corrosion studies were performed on UNS<sup>(1)</sup> NO8904 (904L) stainless steel (SS) in aqueous chloride media. Potentiodynamic anodic polarization and scanning electron microscopic (SEM) techniques were utilized. The effects of environmental factors such as temperature, presence or absence of air, pH value and chloride ion concentration on the pitting corrosion behaviour of 904 L SS have been investigated.

The results indicate that in aerated 0.6 M NaCl in absence or in presence of 0.1 M Na<sub>2</sub>SO<sub>4</sub> or in sea water, the critical temperature for pitting is 40°C. However, in nitrogen saturated solutions the critical temperature is 50°C. All pitting potentials (E<sub>pit</sub>) determined in nitrogen saturated solutions are significantly shifted in the noble direction by 160 - 280 mV while the corresponding protection potential (E<sub>prot</sub>) values are not greatly affected.

The presence of sulphate ions causes a noble shift in both E<sub>pit</sub> and E<sub>prot</sub> that amounts to about 40 and 140 mV, respectively. Changing the pH values of the solutions does not change significantly E<sub>pit</sub> or E<sub>prot</sub> in the acid range while in the alkaline range E<sub>pit</sub> increases by 40 mV/ unit pH increase. At 60°C the critical chloride ion concentration for pitting occurrence is found to be 0.6 M NaCl in aerated or deaerated solutions. Below 0.6 M NaCl pitting occurs only in the transpassive region. Above 0.6 M NaCl, E<sub>pit</sub> values are linear with log chloride concentration. The slopes are found to be 320 and 135 mV for nitrogen saturated and air saturated solutions, respectively.

**Key terms:** stainless steel, seawater, chloride, pitting, temperature, pH

### Introduction

Scarce data is available in the literature regarding localized corrosion behaviour of type 904L SS (UNS NO8904) in salt solutions. The alloy has been developed for severe aggressive environments and especially for marine applications as heat exchangers. However, there have been incidence of premature failures of heat exchangers made of 904L SS in North Africa<sup>1</sup> and in the Middle East<sup>2</sup>, and in these cases seawater was used as a coolant. In both cases

---

<sup>(1)</sup>UNS numbers are listed in the Unified Numbering System for Metals and Alloys, published jointly by the Society of Automotive Engineers (SAE) and ASTM.

failures were attributed to sulphate reducing bacteria. Crevice corrosion attack for 904L SS heat exchangers resulting from deposited micro - organisms was also reported. <sup>3,4</sup> Rujini et al <sup>5</sup> as well as Ives <sup>6,7</sup> reported that pitting of 904L SS takes place in deaerated chloride/sulphate solutions only above 60C. Tromans and Frederick<sup>8</sup>, demonstrated that crevice corrosion of 904L SS can take place in 1 M NaCl at 55C. The electrochemical behaviour of 904L SS in deaerated enriched seawater in absence or in presence of sulphate reducing bacteria at 30C has been reported recently. <sup>9</sup> Pitting corrosion was detected only under bacterial colonies after anodic polarization of specimens that were exposed for at least 14 days.

This paper presents a study on the effect of environmental factors such as temperature, pH and the presence or absence of air on the pitting corrosion behaviour of 904 L SS in pure chloride and chloride / sulphate solutions as well as seawater. In another publication the effect of the presence of chloride or hypochlorite on pitting corrosion of the same alloy is given <sup>10</sup>. The aim of the present study is to establish the characteristic pitting conditions for 904 L SS in chloride containing solutions that may serve as guidelines for its use in practice.

### Experimental Method

The material used was type 904L ( UNS NO8904 ) commercial stainless steel. The % average chemical compositions is : C : 0.015 Mn: 1.55, S : 0.01, P : 0.028, Si : 0.58, Ni : 23.5, Cr : 20, Mo : 4.5 , V : 0.24 and W : 0.6. Specimens were cut from a 2 mm thick sheet. Those used for electrochemical tests were mechanically polished with emery paper down to 600 grit, while specimens to be examined metallographically were fine- polished with 0.3 and 0.05  $\mu\text{m}$  alumina paste, ultrasonically cleaned and finally rinsed with acetone and double distilled water. The back and edges of the specimens were coated with epoxy resin, allowing 1  $\text{cm}^2$  to be exposed to the test solution.

All salt solutions were prepared from analytical grade reagents and double distilled water. The pH of the solutions was adjusted to give values between 3 and 12 by adding HCl or NaOH. Depending on the need of the test the solutions were either air saturated or deaerated by bubbling nitrogen gas into the cell for one hour before the test. The experiments were conducted at the desired thermostated temperature. Non - treated seawater was used that was brought from the same location in Alexandria. Its analysis is given in Table I.

Potentiodynamic anodic polarization experiments were conducted using a scan rate of 600 mV/h, commencing at the open circuit potential after the sample has been immersed for 30 minutes in the solution. The potential of the working electrode was referred to a saturated calomel electrode ( SCE ) . The counter electrode was a platinum wire. All electrodes were placed vertically in the cell .

The pitting potential was determined from the anodic polarization curves where a stable increase in current density occurs. The protection potential was determined from the reverse cyclic polarization at the intersection point with the forward polarization curve.

All potentials quoted in the text are with respect to SCE .

For morphological examination of pitting corrosion a two - step potentiostatic treatment was applied; first, the specimen was polarized at a constant potential value above the critical pitting potential ( a value chosen after determining  $E_{pit}$ ) until  $10 \text{ mA / cm}^2$  is reached then the potential was reduced to a value above the protection potential . The change of current density was followed up to 10 minutes. The morphology of pits after the tests was examined using optical and scanning electron microscopes.

## Results and Discussion

### I - Critical Temperature for Pitting Corrosion in Aqueous Salt Solutions.

#### A- In Aerated Solutions

The potentiodynamic reverse polarization scans of 904L SS in seawater and in 0.6 M NaCl in absence or in presence of  $0.1 \text{ M Na}_2\text{SO}_4$  at different temperatures were determined. The results obtained in seawater are shown in Fig.1. At 30C no breakdown of passivity nor hysteresis loop is seen but at temperatures  $\geq 40\text{C}$  breakdown of passivity is evident. The passive current (  $I_{pass}$  ) is  $2 \mu\text{A / cm}^2$  for all temperatures tested . The increase of temperature causes a decrease in  $E_{pit}$ , while the protection potential (  $E_{prot}$  ) is found to be independent on temperature and amounts to about -30 mV. The pitting and protection potentials depicted from the reverse scans for 0.6 M NaCl and 0.6 M NaCl + 0.1 M  $\text{Na}_2\text{SO}_4$  are given in Table II. At 30 and 35C in pure chloride solutions, pitting corrosion occurred in the transpassive region while in chloride / sulphate solutions no pitting was detected and the behaviour was similar to that obtained in seawater at 30C, ( Fig.1, curve1).  $I_{pass}$  in all tests was constant, but  $E_{pit}$  dropped significantly above 40C. Values of  $E_{pit}$  and  $E_{prot}$  obtained in chloride/ sulphate solutions are shifted in the noble direction by about 40 mV and 100 mV, respectively. It is worth noting that  $E_{pit}$  at 40C in seawater is close to that obtained in aerated 0.6 M NaCl. However, the increase of temperature caused a remarkable negative shift in  $E_{pit}$  values in aerated pure chloride or chloride / sulphate solutions compared to that obtained in seawater. while,  $E_{prot}$  is almost the same in seawater and in chloride / sulphate solution. Above 60C  $E_{pit}$  becomes less dependent on temperature in seawater.

#### B- In Nitrogen Saturated Solutions

The effect of temperature on pitting corrosion of 904L SS in nitrogen saturated chloride or chloride/ sulphate solutions was also studied. These series of experiments were conducted for comparative purposes with data reported in nitrogen saturated solutions by other workers<sup>5</sup> and to gain further insight into the influence of the presence of air or nitrogen on the pitting

behaviour. Table III indicates that the critical temperature for pitting in nitrogen saturated solutions is 50C. Below this temperature pitting in the transpassive region is only noticed in pure chloride solutions. A critical pitting temperature of 60C was reported by Ruijini et al <sup>5</sup> for a similar system .

The relationship between  $E_{pit}$  and temperature for all solutions tested is given in Fig.2. It is interesting to observe that  $E_{pit}$  values obtained in nitrogen saturated salt solutions are significantly shifted in the noble direction compared to that obtained in air saturated solutions. In general,  $E_{pit}$  decreases with the increase in temperature for all types of stainless steel. This is most probably due to the fact that the majority of chemical and electrochemical reactions proceed more rapidly at higher temperatures. The particular dependence of  $E_{pit}$  on temperature depends on several factors such as grade, heat treatment and presence of inclusions in the alloy. However, the present results indicate that aerated salt solutions have a strong temperature effect on  $E_{pit}$  for 904L SS in comparison to nitrogen saturated salt solutions or aerated seawater .

The fact that when the salt solutions were saturated with air the pitting potentials became more active is difficult to interpret. In spite of the vast literature related to pitting corrosion of stainless steels , data concerning the effects of the presence of gases in solutions are scanty. Most of the data available in the literature is related to nitrogen saturated solutions . According to Leckie and Uhlig,<sup>11</sup> the pitting potentials should not be affected by aeration of the electrolyte provided crevice corrosion is avoided. It is known that crevice corrosion takes place at more active values than that for pitting corrosion. Thus in order to be sure that what we are determining is the pitting potential and not a breakdown due to crevice corrosion, an anodic polarization experiment was conducted in 0.6 M NaCl at 60C on a specimen having a crevice ( intentionally created) . The polarization curve obtained for the creviced specimen ( Fig.3) is different than that obtained for crevice- free specimen. Thus a reduction of the passive region takes place and the breakdown potential is -20 mV as compared to + 260 mV for crevice- free specimen ( c.f. Table. II ). Further, microscopic inspection revealed the occurrence of localized attack but no pits were detected. These results agree with that reported by Wilde<sup>12</sup> who noticed that when polarizing a creviced 30Cr-3Mo- Fe steel in 1M NaCl, the passive region was diminished. Also Atrens<sup>13</sup> reported the absence of the passive region when a 12% Cr SS specimen having a crevice was anodically polarized in chloride solution and the polarization curve displayed a pseudo - Tafel region.

Thus it may be concluded that the presence of oxygen in the aerated solutions caused a significant enhancement of pitting corrosion. Streicher<sup>14</sup> reported that when 304 SS was exposed to an aerated NaCl solution pitting corrosion occurred. However, pitting was suppressed under fully oxygenated conditions and also under deaerated conditions. In other words, oxygen plays a dual role in relation to pitting corrosion; at low concentrations oxygen may enhance pitting corrosion by accelerating the cathodic reaction while at high concentration pitting corrosion may be inhibited by stifling the anodic reaction through film formation <sup>14</sup>.

Based on the present results, for testing alloy / environment systems simulating heat exchangers, the results of the experiments conducted in air saturated solutions would be more realistic for such practical applications than that obtained in nitrogen saturated solutions.

## II- Effect of pH on Pitting Potential

The effect of pH on pitting corrosion of 904L SS has been investigated in pure chloride and chloride/ sulphate solutions in air or nitrogen saturated solutions at 60°C. The results are shown in Fig. 4. It is clear that in all solutions E<sub>pit</sub> is not affected in acidic salt solutions in the range of pH 3 - 7.5 for aerated solutions, and pH 3 - 5.8 in nitrogen saturated solutions. However, in all alkaline solutions whether aerated or deaerated a linear relationship holds between E<sub>pit</sub> and pH, with a shift of 40 mV/ unit pH increase. Ruijini et al.<sup>15</sup> showed a well-defined pH effect for 904LSS in deaerated chloride / sulphate solutions, in the acidic as well as in the alkaline range at 70°C. However, the independence of E<sub>pit</sub> on pH in acid solutions has been reported by several investigators (e.g.<sup>11,15,16</sup>). Fokin et al.<sup>15</sup> demonstrated that E<sub>pit</sub> in 3% NaCl was independent on pH in the range of 3 to 8 for three SS alloys (13 Cr, 17 Cr and 18 Cr- 8 Ni-Ti). Further, Leckie and Uhlig<sup>11</sup> showed that E<sub>pit</sub> of 18-8 SS was not significantly affected in 0.1 M NaCl in the pH range 1 to 7. The present results confirm the independence of E<sub>pit</sub> on pH in the acid solutions. This behaviour may be explained on the premise that the hydrolysis reaction in the pits generates its own characteristic acidity which is most probably slightly influenced by the pH of the bulk solution. The fact that in alkaline solutions E<sub>pit</sub> is significantly displaced in the noble direction is in line with the well established pitting inhibition effect of higher concentrations of OH<sup>-</sup> ions on different iron base alloys<sup>11,16</sup>.

It is worthy to mention that values of E<sub>prot</sub> in nitrogen saturated solutions did not change significantly with the increase of pH while in aerated solutions E<sub>prot</sub> did shift considerably in the noble direction.

## III -Critical Chloride Concentration for Pitting Corrosion

Figure 5 shows the effect of chloride concentration on the anodic behaviour of 904L SS in aerated chloride solutions in the range of 0.4 M - 2.4 M NaCl at 60°C. It is clear that in 0.4 and 0.5 M NaCl solutions pitting occurs only in the transpassive region while at concentration  $\geq 0.6$  M pitting corrosion occurs in the passive region. E<sub>pit</sub> and E<sub>prot</sub> shift in the active direction with the increase of Cl<sup>-</sup> concentration ( $C_{Cl^-}$ ). I<sub>pass</sub> also increases with the increase of chloride concentration reaching 6  $\mu A / cm^2$  at 2.4 M NaCl.

The relationship between log  $C_{Cl^-}$  and E<sub>pit</sub> in aerated and in nitrogen saturated salt solutions at 60°C is shown in Fig.6.

It is clear that under the present experimental conditions the effect of deaeration is considerably greater than the effect of SO<sub>4</sub><sup>2-</sup> ions on the pitting corrosion behaviour in



chloride solutions. However, in all solutions a linear relationship holds between  $E_{pit}$  and  $\log C_{Cl^-}$  as follows :

$$E_{pit} = A - B \log C_{Cl^-}$$

This kind of relationship has been verified experimentally and theoretically for various alloys . e.g. <sup>11,13 & 16</sup> . It is interesting to observe that B value in aerated salt solutions amounts to 135 mV while in nitrogen saturated salt solutions B= 320 mV. The values obtained in nitrogen saturated solutions are close to that produced by Ruijini et al <sup>5</sup>. B value obtained in other types of stainless steel amounts to 130 mV for 316 SS <sup>17</sup> in aerated pure chloride solution at 60C or 30C, 88 mV for 304 SS<sup>11</sup> in deaerated NaCl solutions and 183 mV for 12% Cr martensitic SS<sup>13</sup> in deaerated chloride solutions. It is clear that high values of B are obtained in Mo-containing SS in nitrogen saturated solutions. However, the presence of air causes considerable reduction of B value and thus it becomes close to that obtained for 316 or 304 SS. It can be concluded that the value of B for 904 L SS is essentially dependent on the presence or absence of air in the salt solution while the critical chloride concentration for pitting is not affected whether the solutions are aerated or deaerated.

### Metallographic Examination

Microscopic inspections were conducted to confirm the occurrence of pitting corrosion of 904 L SS as well as to examine pit morphologies under the different environmental conditions tested. SEM micrographs of Fig. 7 are typical examples of pitting corrosion obtained after anodic pretreatment in aerated pure chloride solutions of pH 5.7 ( Fig.7, micrograph a) and of pH 12 ( Fig.7, micrograph b). It is clear that the pits are almost spherical in shape and the diameter is in the range of 25-75  $\mu m$  and about 25  $\mu m$  for pH 5.7 and 12, respectively. In aerated chloride/ sulphate solution or in nitrogen saturated solutions ( Fig.8, micrographs a & b, respectively), the pits produced are similar but relatively smaller and fewer in number than that obtained in pure aerated chloride solutions. Thus it seems that under the present test conditions the pit morphology of 904 L SS is not significantly influenced by the bulk- solution chemistry nor the absence or presence of air in the test environment.

### Conclusions

From the results of the present study the following conclusions may be drawn :

- 1- In air saturated salt solutions pitting corrosion of 904L SS is greatly enhanced as compared to nitrogen saturated solutions.

- 2- The effect of nitrogen on pitting inhibition is much more significant than that produced by  $\text{SO}_4^{--}$  or  $\text{OH}^-$ .
- 3- Below 0.6 M NaCl no pitting corrosion occurs in aerated or deaerated solutions.
- 4- pH does not have a significant effect on Epit in the acidic solutions while in alkaline solutions Epit increases by 40 mV/ unit pH increase.
- 5- The critical temperature for pitting corrosion is 40C in seawater or air saturated salt solutions and 50C in nitrogen saturated salt solutions.

### References

- 1- P.J.B.Scott and M.Davies, Corrosion / 89, paper no.86. ( Houston, Tx : National of Corrosion Engineers, 1989).
- 2- V.K.Gouda and A.Al. Hashem, International Conference on " Advances in corrosion and protection " , UMIST, UK, 1992.
- 3- V.Scotto, R.Di Cintio and G.Marcenaro, Corros. Sci. 25 (1985): p. 185 .
- 4- B.Johansen, P.O.Gartland, G. Hagen, A.Supphellen and R.Tunold, Proceedings 10th Scandinavian Corrosion Congress, Stockholm (1986): p. 135.
- 5- G.Ruijini, S.C. Srivastava and M.B. Ives, Corrosion, 45 (1989): p. 874.
- 6- M.B. Ives, Application of Stainless Steels " 92", Sweden, June 9-11 (1992).
- 7- M.B.Ives, G.Ruijini and S.C.Srivastava, Proc. 10th ICMC (1987): p. 3225.
- 8- V.K. Gouda, H.M.Shalaby and I.M. Banat, International Conference on " Advances in Corrosion and Protection " , UMIST, UK. 1992
- 9- D.Tromans and L. Frederick, Corrosion, 39 (1983): p. 305.
- 10- V.K. Gouda and E.A. Abd El Meguid, to be published.
- 11- H.P.Leckie, H.H.Uhlig, J. Electrochem. Soc. 113 (1966): p. 1261.
- 12- B.E. Wilde, Localized corrosion, ( Houston, Tx : National Association of Corrosion Engineers, 1974 ), p 342.

- 13- A.Atrens, Corros. Sci, 39 (1983): p. 483.
- 14- M.A.Streicher, J. Electrochem. Soc. 103 (1956): p. 375.
- 15- M.N.Fokin, M.M. Kurtepov, V.I.Bochkareva, Sborrik Po Korozii, Moscow (1965).
- 16- Z.Szklarska-Smialowska, Pitting Corrosion of Metals, (Houston, Tx : National Association of Corrosion Engineers ,1986 ).
- 17- V.K.Gouda, E.A. Abd El Meguid and N.A.Mahmoud, 13th Egyptian Chemical Conference , Cairo, 1993.

**Table I. Aanalysis of seawater**

Parameter	Concentration (ppm)
Chloride	20850
Sulfate	2700
Total Alkalinity	170
Sodium	11000
Potassium	370
Calcium	400
Magnesium	1542
Nitrate	0.25
Nitrite	0.04
Oxygen	6.5
T.D.S.	41800
pH	7.3

**Table II. Influence of temperature on the pitting and protective potentials in air saturated salt solutions ( pH 5.7 )**

Temp C	0.6 M NaCl		0.6 M NaCl + 0.1 M Na <sub>2</sub> SO <sub>4</sub>	
	Epit, mV	Eprot, mV	Epit, mV	Eprot, mV
30	730*	600	no pitting **	
35	700*	580	745*	520
40	660	-100	700	40
50	440	-100	480	40
60	260	-140	300	0
70	220	-160	260	-20

\* Pitting in the transpassive region.

\*\* No hysteresis loop.

**Table III . Influence of temperature on the pitting and protective potentials in nitrogen saturated salt solutions ( pH 5.7 )**

Temp C	0.6 M NaCl		0.6 M NaCl + 0.1 M Na <sub>2</sub> SO <sub>4</sub>	
	Epit, mV	Eprot, mV	Epit, mV	Eprot, mV
40	750*	500	no pitting **	
50	600*	120	640	140
60	560	140	580	140
70	540	120	560	130

\* Pitting in the transpassive region.

\*\* No hysteresis loop.

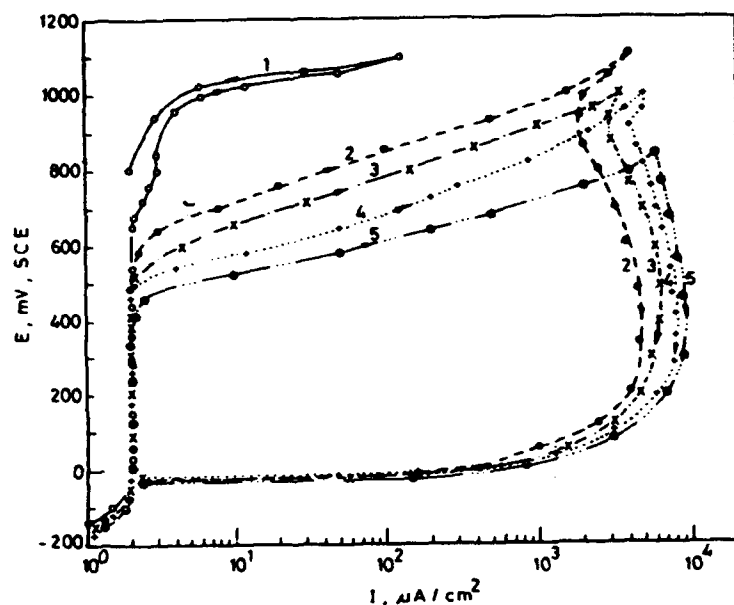


**Fig.1 Potentiodynamic cyclic anodic polarization curves of UNS NO8904 SS in aerated seawater at different temperatures.**

1) 30C, 2) 40C, 3) 50C, 4) 60C, 5) 70C

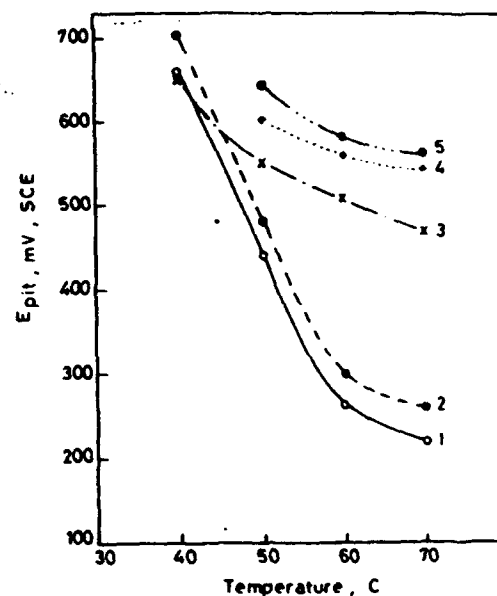


**Fig. 2 Temperature dependence of critical pitting potential of UNS NO8904 SS in salt solutions.**

1) aerated 0.6M NaCl  
2) aerated 0.6M NaCl + 0.1 M Na<sub>2</sub>SO<sub>4</sub>  
3) aerated seawater  
4) deaerated 0.6 M NaCl  
5) deaerated 0.6M NaCl + 0.1 M Na<sub>2</sub>SO<sub>4</sub>

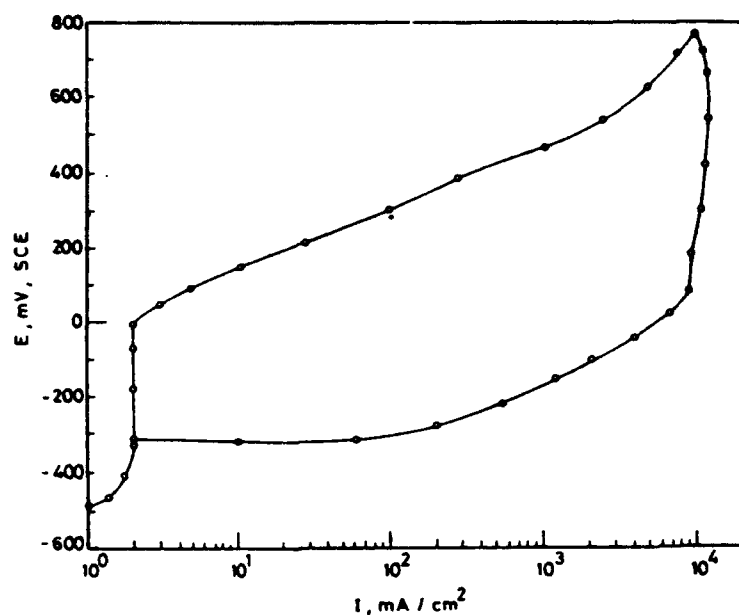


Fig.3 Potentiodynamic cyclic anodic polarization of UNS NO8904 SS, creviced specimen in 0.6 M NaCl at 60C and pH 5.7

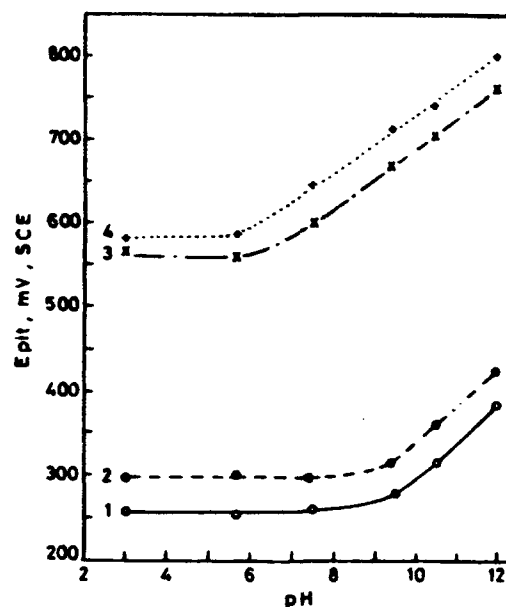


Fig.4 Effect of pH on critical pitting potential of UNS NO8904 SS in aerated and deaerated salt solutions at 60C.

- 1) aerated 0.6M NaCl
- 2) aerated 0.6M NaCl + 0.1 M Na<sub>2</sub>SO<sub>4</sub>
- 3) aerated seawater
- 4) deaerated 0.6 M NaCl

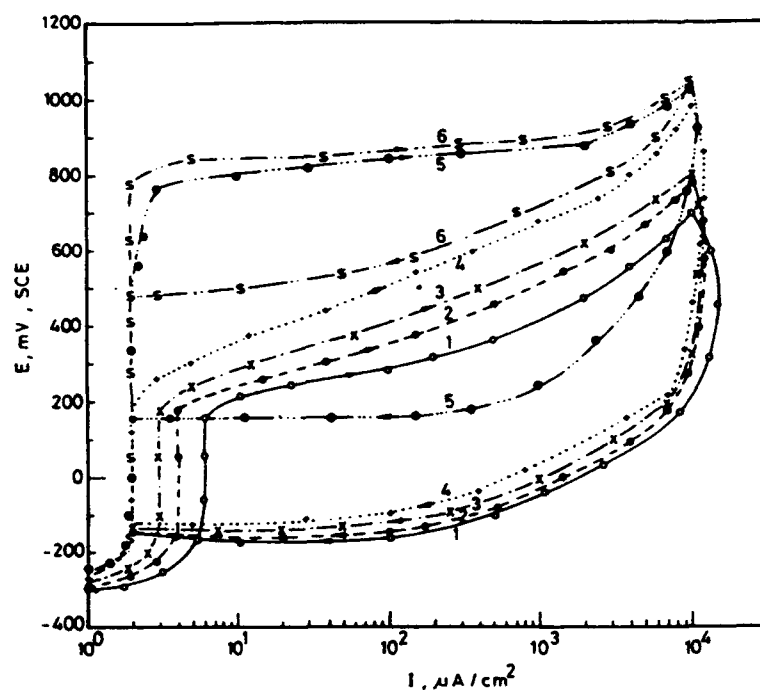


Fig.5 Potentiodynamic cyclic anodic polarization of UNS NO8904 SS in aerated NaCl solutions of different concentrations at 60C and pH 5.7.

- 1) 2.4 M NaCl
- 2) 1.8 M NaCl
- 3) 1.2 M NaCl
- 4) 0.6 M NaCl
- 5) 0.5 M NaCl
- 6) 0.4 M NaCl

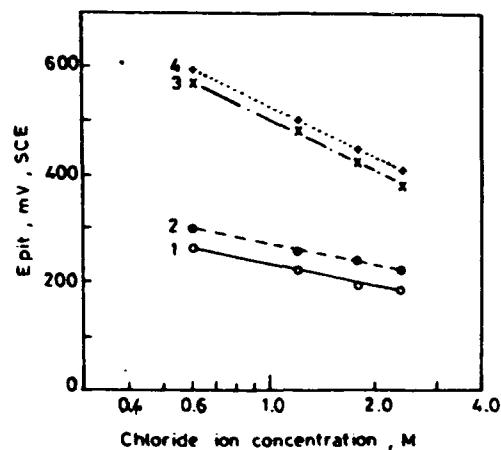
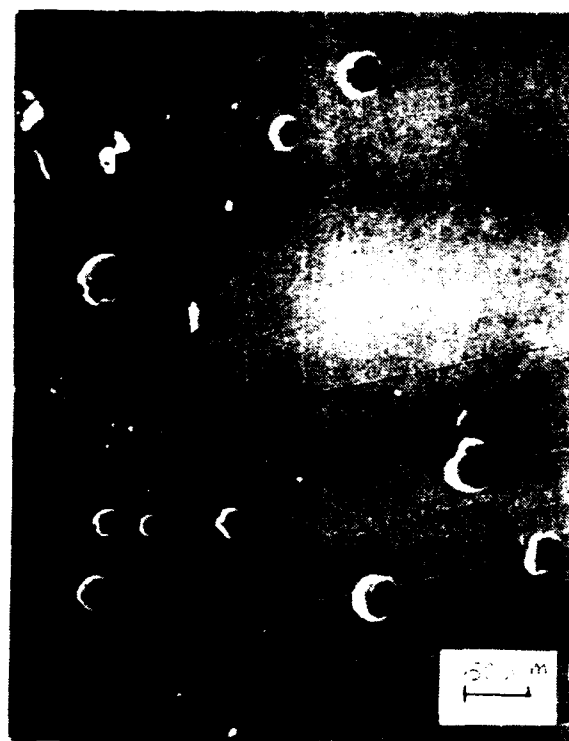


Fig.6 Effect of chloride ion concentration on Epit in aerated and deaerated salt solutions at 60C and pH 5.7.

- 1) aerated 0.6M NaCl
- 2) aerated 0.6M NaCl + 0.1 M Na<sub>2</sub>SO<sub>4</sub>
- 3) aerated seawater
- 4) deaerated 0.6 M NaCl

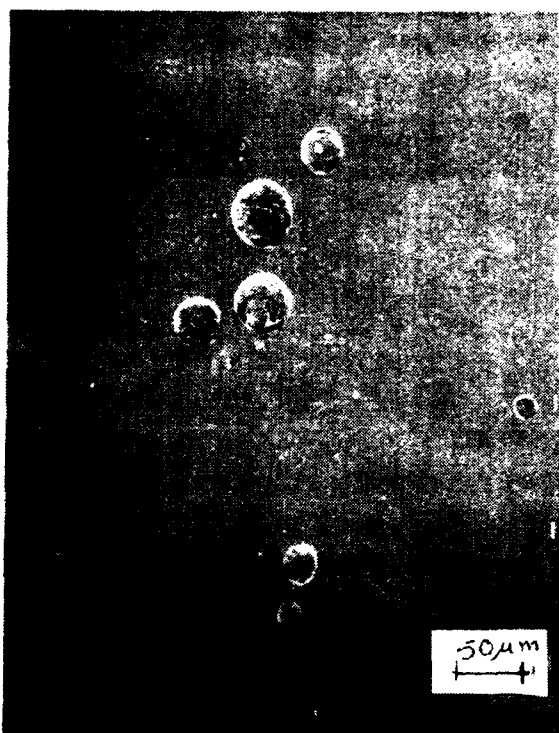


a ) pH 5.7

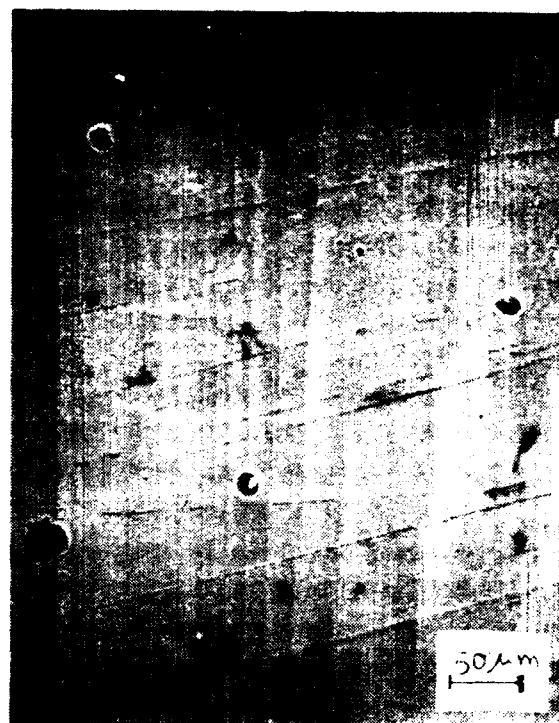


b ) pH 12

Fig.7 SEM micrographs showing pits produced in UNS NO8904 in aerated chloride solutions.



a) aerated chloride / sulphate  
solution, pH 5.7



b) deaerated chloride  
solution, pH 12

Fig.8 SEM micrographs showing pits produced in UNS NO8904.

# Corrosion Monitoring of Aluminum Easy-Open Ends by Area Polarization Technique

Osami Seri and Kazunao Furumata  
Muroran Institute of Technology  
27-1, Mizumoto, Muroran  
Hokkaido, 050, JAPAN

Yoshimasa Matsumura  
Daiwa Can Co., Ltd., Central Research Laboratories  
5-5-1 Nishihashimoto, Sagamihara  
Kanagawa, 229, JAPAN

## Abstract

Developments have been made on monitoring system in order to easy-detect the occurrence of pitting attacks in scored aluminum alloy 5182 end of easy-open end. The sign of pitting attacks on the aluminum alloy 5182 which is galvanically coupled to commercial-purity copper in a kind of beverages in Japanese market is observed as the change of the value of the anodic polarization resistance by the area polarization technique. The monitoring of the anodic polarization resistance by the area polarization technique enables an easy detection of pitting attacks on aluminum alloy used beverage.

Key terms: aluminum alloy, pitting-attack, can beverage, monitoring

## 1. Introduction

Easy open ends (EOEs) are widely used as the lids of food and drink cans. One of the most preferred material is aluminum due to its safety and easy opening. In Japan, cans have a tendency to have a high-strength aluminum alloys such as 5182, because of reducing the thickness of material. The aspect of the electrochemical series tells us that pitting attacks may occur on the 5182 aluminum alloy, because of it has large electromotive potentials between noble potential alloy-elements such as copper or iron and less noble potential alloy-elements such as magnesium or manganese. Some sport drink solution containing chloride ion and low pH ions may lead to pitting attacks in aluminum EOEs.

The can-pack-test is well known as a shelf life test and is widely used in estimating corrosion of can material<sup>1), 2)</sup>, but it has a number of faults: the large number of possible combinations

of can materials and contents, the long period required, and the many man-hours of labor needed to observe the corrosion attacks. Can makers have desired an alternative that would offer an easy, rapid and accurate technique for measuring can life.

This paper introduced a technique of electrochemical measurement which is named "area polarization technique"<sup>3),4)</sup> in order to compensate or reduce these faults. This technique is effective, simple and facilitates the prediction of pitting attacks in aluminum EOE's.

## 2. Experimental Method

### 2.1 Specimens

Specimens measuring 20 by 80 mm were cut from high-purity copper (99.99% Cu) and 5182 aluminum alloy in Japanese can market. They were cleaned ultrasonically in acetone. The exposed areas of the samples are denoted as  $S_a$  for the 5182 aluminum anode and  $S_c$  for the copper cathode. It was determined that the areas of  $S_a$  and  $S_c$  are  $6.0\text{cm}^2$  and  $0.1\text{cm}^2$ , respectively. Enamel shielding was used to regulate the area of electrode exposed.

### 2.2 Test Solutions

A beverage solution (approximate contents are glucose, citric acid, sodium chloride, potassium chloride, sodium bicarbonate, potassium phosphate, sodium phosphate) consumed in Japanese market was used as the test solution. Deaerated solution was made by bubbling with 99.999% nitrogen gas.

### 2.3 Measurement

In all measurements, the reference potential was provided by an Ag/AgCl electrode in saturated KCl solution; potentials quoted simply as  $V$  relate to Ag/AgCl unless otherwise stated.

In the apparatus for the area polarization technique<sup>4)</sup>, the main galvanic circuit between the  $S_c$  and  $S_a$  electrodes is set up in the same cell at room temperature (about 25°C). The mixed potential of  $S_a$  and the galvanic current are obtained by a personal computer through an electrometer and a zero-drop ammeter. They are denoted as  $E_m$  and  $I_g$ , respectively. The area polarization technique characteristically shows that the  $S_c$  electrode has a branch electrode,  $dS_c$ , a smaller area than  $S_c$ . The area of  $S_c$  to be exposed should be decided by trial and error, and in this paper  $0.1\text{cm}^2$  was selected. The  $dS_c$  electrode is connected to the  $S_c$  by a shorting switch. When  $dS_c$  is shorted to  $S_c$  in the main galvanic circuit, small increments of cathodic reaction will occur. This increment shifts the galvanic current from  $I_g$  to



$I_g + dI_g$  and moves the mixed potential of  $E_m$  to a more noble potential of  $E_m + dE_m$ . The differential value of  $dE_m/dI_g$  corresponded directly to the value of the anodic polarization resistance of 5182 in the corroded state. Changes in anodic polarization resistance over time is obtained by selecting the time of the interval between open/short condition. The interval time of open/closed circuit was 20 min. The data-sampling time was 1 min. The analysis was continuously controlled and calculated by a personal computer.

### 3. Experimental results

#### 3.1 $E_{corr}$ -time curve of 5182 in beverage solution

The variation of corrosion potential,  $E_{corr}$  of 5182 with time in the beverage solution was measured. It is shown in Fig.1. The  $E_{corr}$  shows the value of -0.77V at the immersion time 1 min. and increases with time. At the immersion time of 30 min, it shows the peak value of -0.59V and decreases with time. At more than the immersion time of 1500 min,  $E_{corr}$  shows the constant value of -0.67V.

#### 3.2 Anodic Polarization Curves of 5182

The three anodic polarization curves of 5182 at the immersion time of 3 min, 30 min and 3000 min, at which  $E_{corr}$  characteristically shows the values for the immersion periods, in the beverage solution were measured. They are shown in Fig.2.

The each curve shows a typical and simple shape, with potential monotonously related to the current. There is a knee in each curve at the pitting potential,  $E_{pit}$ . The  $E_{pit}$  show the values of -0.57V at 3 min and 30 min immersion, and -0.58V at 3000 min immersion.

From  $E_{corr}$  to  $E_{pit}$ , the anodic polarization resistance ( $H_a(Al/Al_2O_3)$ ) may be approximately calculated to:

At 3 min immersion,

$$H_a(Al/Al_2O_3) = 267 \times 10^3 \text{ ohm} \quad \dots(1)$$

At 30 min immersion,

$$H_a(Al/Al_2O_3) = 44 \times 10^3 \text{ ohm} \quad \dots(2)$$

At 3000 min immersion,

$$H_a(Al/Al_2O_3) = 12 \times 10^3 \text{ ohm} \quad \dots(3)$$

Above  $E_{pit}$ , a linear relation between potential and current give us the approximate values of the anodic polarization resist-

ance,  $H_a(Al/Al^{3+})$  to:

At 3, 30 and 300 min immersion,

$$H_a(Al/Al^{3+}) = 3 \times 10^3 \text{ ohm} \quad \dots(4)$$

The potentiodynamic polarization measurement leads to the fact that the occurrence of pitting attacks causes the value of anodic polarization resistance to be reduced to 3/267 - 3/12.

### 3.3 Cathodic polarization curve of copper

Figure 3 shows the polarization curve for copper in a deaerated beverage solution. The rest potential of the copper specimen shows the value of -0.13V. The large cathodic polarization resistance is observed.

### 3.4 Area Polarization technique

The variations with time of potential and galvanic current,  $I_g$  of 5182,  $E_m$  by the area polarization technique are shown in Fig.4. The behavior of the  $E_m$ -time curve is the same as that of the  $E_{corr}$ -time curve in Fig.1. Up to an immersion period of 500 min, variations occur irregularly, but at more than 1500 min immersion, the values are stationary at -0.67 - -0.68V and  $0.05 \times 10^{-6}$  A, respectively. When the branch copper electrode,  $dS_c$  is shorted to the main electrode,  $S_c$ , the  $E_m$  shifts to a more noble potential of  $E_m + dE_m$ , and the value of  $I_g$  increases to  $I_g + dI_g$  due to an increase in the cathodic reaction.

The  $dE_m/dI_g$  term represents the anodic polarization resistance of 5182 aluminum alloy,  $H_a$ :

$$H_a = dE_m/dI_g \quad \dots(5)$$

Figure 5 plots the variations in the value of  $H_a$  with time as calculated from Fig.4 by a personal computer. The  $H_a$  shows the value of  $3.8 \times 10^5$  ohm at the first immersion. It decreases with time. At more than 2400min immersion, the scattered values of the  $H_a$  are about  $5 \times 10^3$  -  $8 \times 10^3$  ohm.

After the experiment shown in Fig.4, many pitting cavities are observed.

## 4. Discussion

### 4.1 Galvanic Coupling between 5182 and Copper

The table of electrochemical series shows that when 5182 is galvanically coupled to copper in a corrosive environment, 5182

and copper will act as the anode and cathode, respectively. In galvanic coupling, the potential of 5182 indicates the mixed potential of  $E_m$  and the galvanic current indicates  $I_g$ . Above  $E_{pit}$ , it is obvious that the value of anodic polarization resistance decreases, because of being low anodic resistance polarization reaction (pitting attack reaction).

#### 4.2 Linear Relationship Between Potential and Current for 5182

As shown in Fig.2, the anodic polarization curve for 5182 aluminum alloy shows a simple shape on which the potential monotonously related to current. There is no active/passive transition behavior like a stainless steel.

In the restricted range of the curve, it may be lead to the assumption that the anodic potential is linearly related to the anodic current as:

$$E_a = A_0 + A_1 \times I_a \quad \dots(6)$$

where,  $A_0$ : Potential at  $I_a=0$ , (V)  
 $A_1$ : gradient, (ohm)

The determination of the anodic polarization resistance by potentiodynamic technique is the same procedure as that measured by the area polarization technique in terms of the gradient in Equation(6). When no pitting occurs (i.e., at potentials below  $E_{pit}$ ):

$$A_1 = H_a(Al/Al_2O_3) = (dE_m/dI_g) \quad \dots(7)$$

When pitting occurs (above  $E_{pit}$ ),

$$A_1 = H_a(Al/Al^{3+}) = (dE_m/dI_g) \quad \dots(8)$$

The experimental fact that the anodic polarization resistance at which localized attack such as pitting attack is smaller than when no localized attack occurs applies not only to the potentiodynamic technique but also the area polarization technique.

$$H_a(Al/Al_2O_3) = (dE_m/dI_g) < H_a(Al/Al^{3+}) = (dE_m/dI_g) \quad \dots(9)$$

The change in value of Equation(9) by area polarization technique indicates the occurrence of pitting attacks in the case of whether or not an experimental corrosion state or a realistic

corrosion state. In terms of detecting the sign of pitting attack initiation, if the value of  $H_a$  varies in satisfying the following relation,

$$H_a(t_1) \gg H_a(t_2) \quad \dots(10)$$

where,  $H_a(t_1)$ : value of anodic resistance at immersion time  $t_1$   
 $H_a(t_2)$ : value of anodic resistance at immersion time  $t_2$   
( $t_1 < t_2$ ).

Then, the possibility of the pitting attack of 5182 may tend to decrease and vice versa. The monitoring of the value of  $H_a$  in the realistic corrosion state by area polarization technique leads to one of the most effective techniques by which an indicator of impending localized attacks such as pitting attacks can easily be obtained.

## 5. Conclusion

An effective electrochemical measurement called area polarization technique has been introduced to detect the occurrence of pitting attack in 5182 aluminum alloy specimens that are galvanically coupled to copper specimen in a beverage solution. The area polarization is an effective technique and is easy to handle. The monitoring of the change of the value of the anodic polarization resistance by the area polarization technique enables an easy technique of detection of localized attacks such as pitting attacks.

## References

- 1) M. Tsurumaru: Boshoku Kanri, No.11, 42(1981).
- 2) T. Miyazaki: Tetsu to Hagane, 73, 427(1987).
- 3) O. Seri, N. Ohtani and K. Tagashira: Boshoku Gijutu, 38, 224(1989).
- 4) O. seri and S. Furuya: Corrosion, 48, 5(1992)

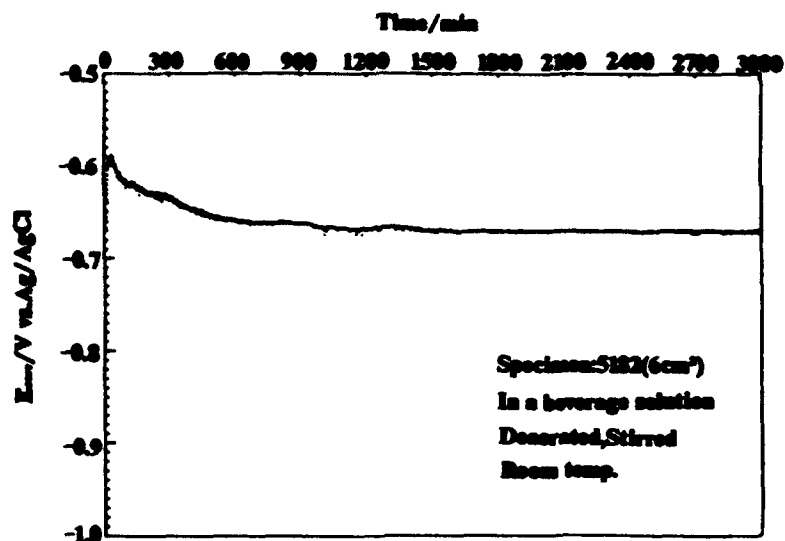


Fig.1  $E_{corr}$ -time curve of 5182 aluminum alloy in a beverage solution.

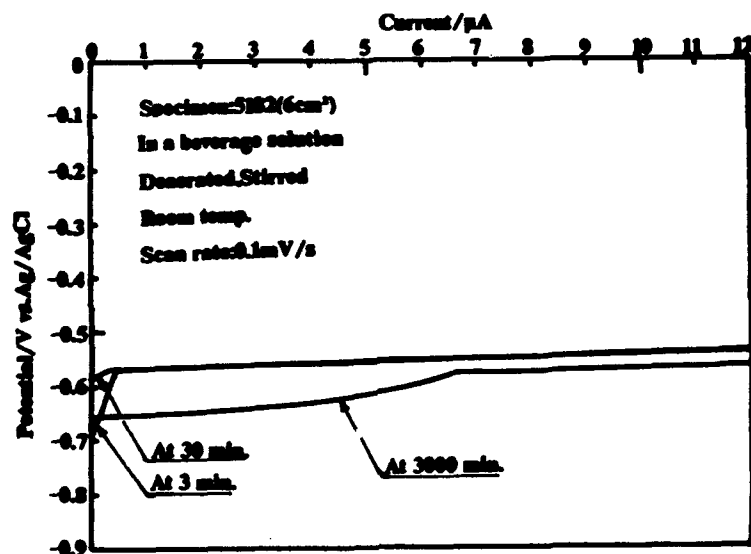


Fig.2 Anodic polarization curves for 5182 aluminum alloy in a beverage solution.

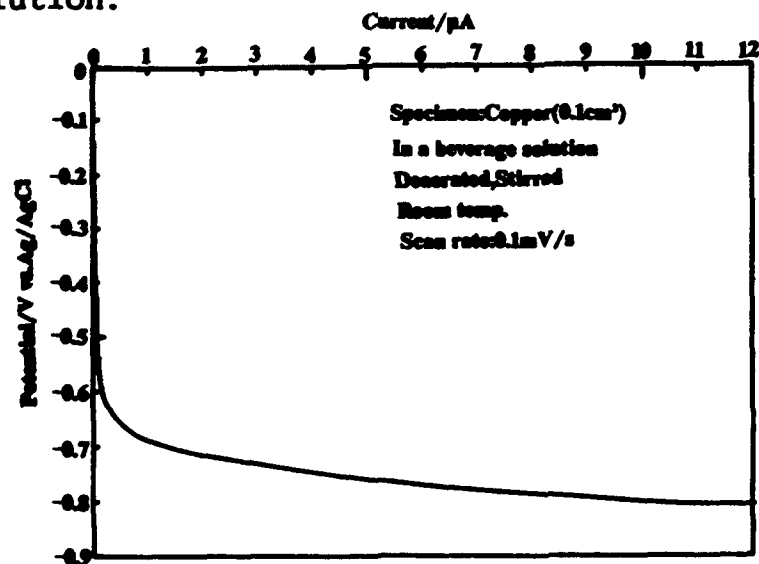


Fig.3 Cathodic polarization curve for copper in a beverage solution.

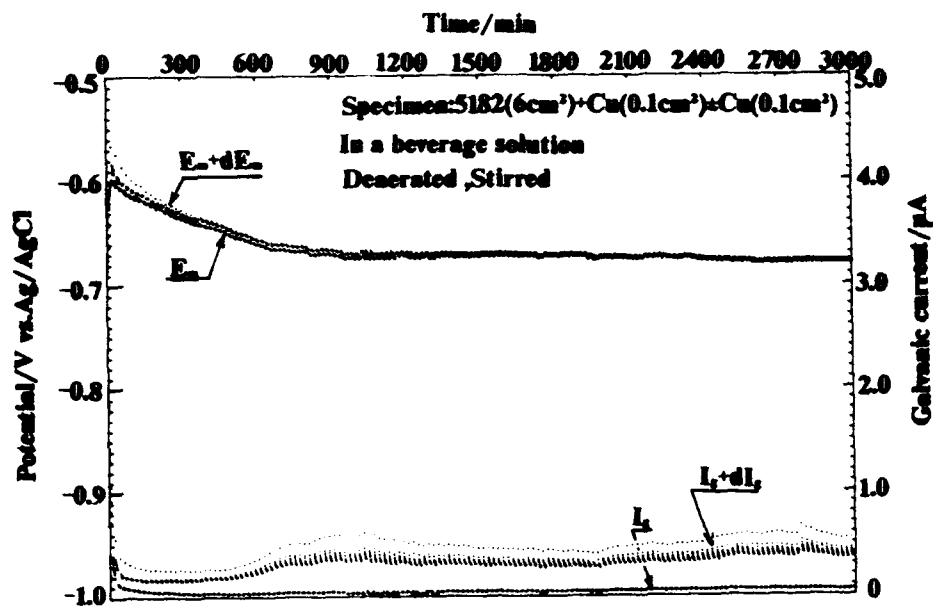


Fig.4 Variation of potential and galvanic currents between 5182 and copper in a beverage solution by area polarization technique.

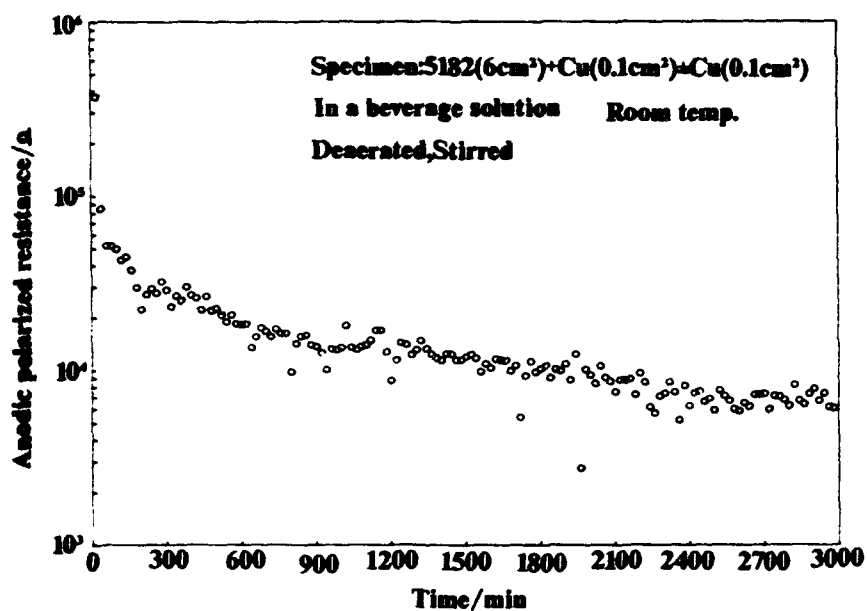


Fig.5 Calculated values of anodic resistance for 5182 from Fig.4.

## **Passivity and Passivity Breakdown in Sputtered Aluminum and Iron Alloys**

**Z. Szklarska-Smialowska**  
Department of Materials Science and Engineering  
The Ohio State University  
Columbus, OH 43210

**R. Inturi**  
Department of Materials Science and Engineering  
The Ohio State University  
Columbus OH 43210

### **Abstract**

Pitting potentials of sputtered Al-Cr, Al-Ta, Fe-Cr, Fe-Ta and Fe-W in chloride solutions were determined. The higher the concentration of alloying element, the higher the pitting potential of the alloys. A correlation was found between the pitting potential and experimental determined solubility of hydroxides of alloying elements in aluminum and iron in acid solution with a pH corresponding to that within the pits. A model is proposed to explain the influence of the alloying elements on the pitting potentials of Al- and Fe-base alloys.

**Key terms:** pitting, sputtered films, Al-alloys, Fe-alloys

### **Introduction**

Several Researchers have found (1-7) that the pitting potential of aluminum can be substantially increased by the addition of certain alloying elements such as W, Ta, Mo and Cr. The high pitting resistance of these alloys has been correlated with 1/ the low pH of a zero charge ( $\text{pH}_{\text{Zch}}$ ) of the alloying element oxide; the lower the  $\text{pH}_{\text{Zch}}$  the higher the pitting potential (1), 2/ the enrichment of oxidized alloying elements and structural modifications in the passive films, i.e., hindrance to chloride ion penetration (2-4); and 3/ the low solubility of the oxidized alloying elements in acidic solutions (8).

Although a good correlation was found between  $\text{pH}_{\text{Zch}}$  of hydrated oxides of alloying elements and the pitting potential of aluminum alloys in a 1N NaCl solution, several experimental results, listed below, cannot be explained by the  $\text{pH}_{\text{Zch}}$  concept.

1. From the anodic polarization curves of co-sputtered (9) and ion-implanted alloys (10) it follows that the passive current density is similar for Al and all supersaturated Al-alloys even though the pitting potentials of the alloy vary over a wide potential range.
2. The same current density was observed for Al-Ta, Al-Mo, Al-Zr and Al-Cr alloys in spite of the fact that the concentration of the oxidized solute increase five fold (9,11) from the corrosion potential to the pitting potential.
3. Even though Al-W alloys (both co-sputtered and ion-implanted) exhibited the highest pitting potentials, the oxidized species of W was not observed in the interior nor at the surface of the passive film (12).
4. Mo is not enriched in the passive film at the open circuit potential (4). However, at applied anodic potentials the Mo concentration in the passive film first increases and close to the pitting potential decreases.

On the basis of the above experiments, it was concluded (8) that 1/ the passive films on the sputtered alloys are electrochemically identical to the passive film on Al; 2/ the defect nature and endurance of the passive film on the alloys toward aggressive anions is about the same as that on the passive film of Al; 3/ the rate determining step in pitting may not be associated either with the bulk characteristics of the passive film or with the chloride anion adsorption characteristics of the passive film.

It has been stated in a previous paper (8), that the rate determining step is the establishment of a localized solution composition in pre-existing defects at the metal/passive film interface causing stable pit growth. This conclusion was withdrawn from the data showing the existence of the correlation between the pitting and solubility of the oxide (hydroxide of the alloying elements in acid solutions (8).

The purpose of this work is to explain from the mechanistic point of view the effect of alloying elements such Ta, Cr, W on the pitting potential of aluminum and iron alloys. Because of the very low solubility of those elements in aluminum it is not possible to keep these elements in solid solutions using conventional methods for the alloys production. Therefore, the sputtering technique for production of metastable, supersaturated Al-alloys was used by many researchers and by the authors of this paper (1-7). In order to compare the effect of alloying elements in Al and Fe, Fe-alloys were also prepared by the sputtering technique.

#### The Dependence between the Pitting Potential and Experimentally Determined Solubility of Hydroxides of Alloying Elements in Aluminum

It is well established that a pit can develop in a chloride solution only when acidic conditions are established within the pits. Therefore, it is obvious that pit growth can proceed only when the oxide film formed on the metal surface is soluble in the acidic pit electrolyte but is only slightly soluble in the bulk solution. Figures 1 and 2 are compilations of the results of  $E_{np}$  of aluminum alloys with various alloying elements in a NaCl solution, obtained by several authors as a function of the solubility of the oxide of the alloying elements at pH 7 and 0 (calculated from the thermodynamic data) (13, 3, 4). The lower the solubility of the oxidized species the higher the pitting potential at pH 0. However, the results of  $E_{np}$  vs the solubility for an alloy containing W deviate significantly at pH 7. It should be noted that the solubility of a W oxide is higher at pH 7 than at pH 0. This is the reason for a lack of W in the oxide film on W-Al alloys. Therefore, even at high anodic potentials as the pH in the occluded cell decreases, the oxide of this element remains stable resulting in a superior pitting resistance.

Even though the correlation between the pitting potential and the calculated solubility of the alloying element's oxide is very good, it is more appropriate to correlate the pitting potential to the experimental solubilities which can be substantially different.

The solubilities of the alloying element oxides determined experimentally (14) differ from those calculated from thermodynamic data. This can be seen by comparison of Figure 2 with Figure 3. The electrolyte within the pit is close to zero where saturated  $AlCl_3$  probably exists. The pH of saturated  $AlCl_3$  is 0.3 (15). Both of these figures indicate that the pitting potential of the alloy increases as the solubility of the alloying element decreases. The increase in the pitting potential is highest for alloys containing alloying elements whose oxides exhibit the lowest solubilities. The solubility range is much narrower in Figure 3 when compared to that in Figure 2. It is also observed that there



is a great discrepancy between the calculated and the experimental solubility of certain alloying elements (W, Nb, Mo) oxides. However, the trend of the dependence of the pitting potential is similar. The correlation in Figure 3, which is based on the experimental solubilities, is better than in Figure 2.

#### The Dependence between the Pitting Potential and Experimentally Determined Solubility of Hydroxides of Alloying Elements in Iron

Anodic polarization curves of the bulk Fe, Fe-film and Fe-alloys film determined in a deaerated 0.02 M  $\text{H}_3\text{BO}_3$  + 0.005 M  $\text{Na}_2\text{B}_4\text{O}_7 \cdot 10 \text{H}_2\text{O}$  + 0.02 M NaCl solution are presented in Figure 4. The open circuit potentials of the bulk Fe, Fe-alloys films, except for the Fe-18 Cr film were almost the same. All of the samples exhibited an active/passive transition behavior except the Fe-18% Cr film which did not undergo active dissolutions. The passive current density of all of the film samples was found to be similar. The pitting potential of the Fe-18%Ta film is taken from the plot of the pitting potential of the Fe-Ta alloy films versus a concentration of Ta (Figure 5). The increase in the pitting potential of Fe with an increase of a Cr addition is given in Figure 6.

The dependence of the pitting potential of Fe and Fe-alloys containing approximately the same concentration of alloying elements on the experimental solubility of alloying elements oxides in acid solution is plotted in Figure 7. This figure shows the relationship between the pitting potential of the Fe-alloys and the experimental solubility of the alloying element oxide in a HCl solution of pH 2 (pH observed within the pits of the iron (16)). The oxidized species of W, Ta, Cr and Fe considered for the solubility in acidic solutions are  $\text{WO}_3$ ,  $\text{Ta}_2\text{O}_3$ ,  $\text{Cr}(\text{OH})_3 \cdot n\text{H}_2\text{O}$ , respectively. The solubilities of these species were collected from references (14 and 18). There are no solubility data available at pH 2, therefore, extrapolated values of solubility from the values reported in the above paper are given in Figure 7. The correlation between  $E_{np}$  and the solubility seems to be very good. The pitting potential of Fe-alloys increases with a decrease in the solubility of the alloying element oxide which is similar to the case of the Al-alloys.

To check the validity of the model (1, 18) based on surface charge considerations and a pH of zero charge of the alloying element oxide, the pitting potentials of Fe alloy films were plotted as a function of  $\text{pH}_{zch}$  of the alloying element oxide. (Figure 8). According to the papers (1-18), the pitting potential should increase continuously with a decrease in the  $\text{pH}_{zch}$  of the alloying element oxide and the W should give the greatest improvement in the pitting potential of Fe compared to other alloying elements. However, the highest pitting potential was obtained for the Fe-Cr and Fe-Ta films, not for the Fe-W film. Therefore, the  $\text{pH}_{zch}$  model suggested for Al-alloys is not applicable to Fe-base alloys. The findings of this study suggest that an explanation for the effect of alloying elements on pitting, proposed earlier, based on the solubility of alloying element oxides for Al-alloys is also applicable to Fe-base alloys.

#### Model of Action of Alloying Elements in Pitting Corrosion

This interpretation is based on the Galvele (19) model of pitting corrosion. It is assumed that the pitting potential is determined by events occurring at the metal/oxide interface. It is believed that a passive film contains different defects (pores, cracks, flaws) through which  $\text{Cl}^-$  ions and water can migrate relatively rather easily and reach the metal surface. Occluded cells are formed as a result of localized dissolution of the metal; because of hydrolysis of the metal cations, the pH of the pit solution decreases. Stable pits are

formed when the pH became lower than a critical value. This critical value of pH depends on the composition of the alloys. The effectiveness of the alloying elements in increasing the pitting potential of metals is related to the stability and solubility of the oxidized species of the alloying element in the acidic solution present in the occluded cell. For example, at pH 0 the solubility of molybdenum oxide, chromium hydroxide, hydrated zirconium oxide, and vanadium oxide is lower than that of aluminum hydroxide. Hence, alloying elements such as Zr, Mo, Cr and V increase the pitting potential of Al by forming a protective film in the occluded cell through oxidation. As the anodic potential increases, the Al dissolution rates increases and the local cell pH continuously decreases by hydrolysis. Under these conditions, due to the increased solubility of the oxidation products of these alloying elements, the alloy undergoes pitting. The oxides of Ta and W are more stable than the oxides of Mo, Cr, Zr, and W at zero pH and therefore the increase in the pitting potential of Al due to a W and Ta addition is higher than the pitting potential of Al-Mo, Al-Cr and Al-Zr alloys.

The same is true for Fe-alloys. The solubility of the oxides (hydroxides) of Cr and Ta in a chloride solution with pH 2 is lower than the solubility of the tungsten oxide and as a result the alloys Fe-Cr and Fe-Ta exhibit a much higher pitting potential than the iron and Fe-W alloy film.

### Conclusion

The model proposed to explain the influence of the alloying elements in pitting corrosion of aluminum alloys applies also in the case of pitting corrosion of iron alloys. A very good correlation was found between the pitting potential of Al and Fe base alloys and the solubility of the alloying element's oxide in acid solutions with a pH corresponding to that within the pits (at pH 0 for Al and pH 2 for Fe). The pitting potential of the Al or Fe alloy is found to increase with a decrease in the solubility of the alloying element's oxide in an acid solution.

### References

1. P.M. Natishan, E. McCafferty and G.K. Hubler, *J. Electrochem. Soc.* 133, (1986): p. 1061.
2. B.A. Shaw, W.C. Moshier, G.D. Davis, T.L. Fritz and B.J. Rees, *Annual Report, MML TR 91-10c, Martin Marietta Laboratories* (1991);
3. G.D. Davis, W.C. Moshier, T.L. Fritz and G.O. Cote, *J. Electrochem. Soc.*, 137, (1990): p. 422.
4. W.C. Moshier, G.D. Davis and G.O. Cote, *J. Electrochem. Soc.* 136, (1989): p. 356.
5. G.S. Frankel, M.A. Russak, C.V. Jahnes, M. Mirzamaani, and V. Brusic, *J. Electrochem. Soc.* 133, (1986): p. 1061.
6. M. Fass, D. Itzhak, D. Elieser and F.H. Froes, *J. Mat. Sci. Lett.*, 6, (1987): p. 1227.
7. R. Inturi and Z. Szklarska-Smialowska, submitted to *Corrosion Science*;
8. Z. Szklarska-Smialowska, *Corr. Sci.* 33, (1992): p. 1193.
9. G.D. Davis, W.C. Moshier, T.L. Fritz, G.O. Cote, *J. Electrochem. Soc.*, 137, (1990): p. 422.

10. E. McCafferty, G.K. Hubler, P.M. Natishan, P.G. Moore, R.A. Kant and B.D. Saltwell, *J. Electrochem. Soc.* 135, (1988): p. 321.
11. W.C. Moshier, G.D. Davis, G.O. Cote, *J. Electrochem. Soc.* 136, (1989): p. 356.
12. G.D. Davis, T.L. Fritz, B.J. Rees, B.A. Shaw and W.C. Moshier, Annual Rep. MML TR 91-10, Martin Marietta Laboratories 1991:
13. M. Pourbaix, *Atlas of Electrochemical Equilibria in Aqueous Solutions*, NACE, CEBELCOR, 1974:
14. *Solubilities of Inorganic and Organic Compounds*, Ed. by H.C. Silcock, Vol. 3, Ternary & Multicomponent Systems of Inorganic Substances, Part I to III (1963);
15. D.A. Vermilyea, *J. Electrochem. Soc.*, 118, (1971): p. 529.
16. G. Butler, H.C.K. Ison and A.D. Mercer, *Brit. Corr.J.*, 16, (1971): p. 31.
17. M. Seo, R. Fururichi, G. Okamoto, N. Sab, *Trans. Japan Institute of Metals*, 16, (1975): p. 519.
18. E. McCafferty, G.K. Hubler, P.M. Natishan, P.G. Moore, R.A. Kant and B.D. Saltwell, *Corr. Sci.* 32, (1991): 721.
19. J.R. Galvele, *J. Electrochem. Soc.* 123, (1976): p. 464.

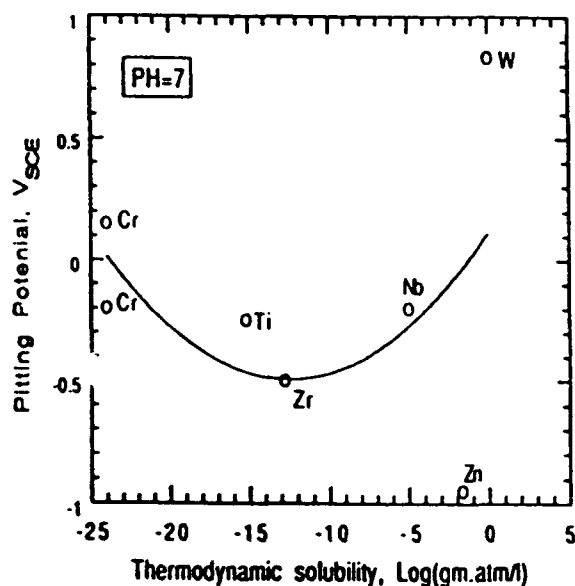


Fig 1: Pitting potential for non-equilibrium Al alloys in chloride solutions vs the solubility of the hydrated oxide of the alloying elements at pH7.

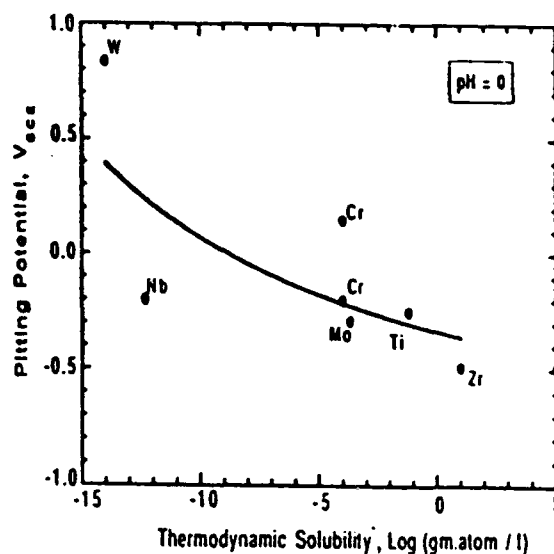


Fig 2: Relationship between the pitting potential of the Al alloy and the thermodynamic solubility of alloying element oxide at pH 0 (5, 12, 8). Alloying element concentration is approximately 4 at%.

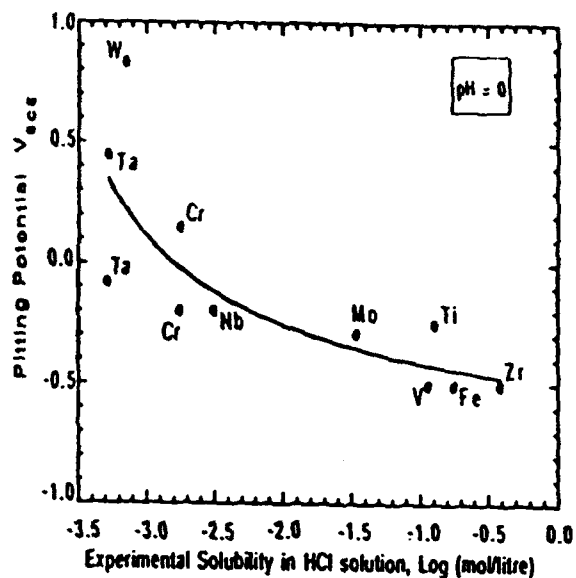


Fig 3: Relationship between the pitting potential of the Al alloy and the experimental solubility of alloying element oxide in HCl solution at pH 0 (5, 12, 8). Alloying element concentration is approximately 4 at% except for Al-Ta alloy, where Ta conc. is 8-10 at%.

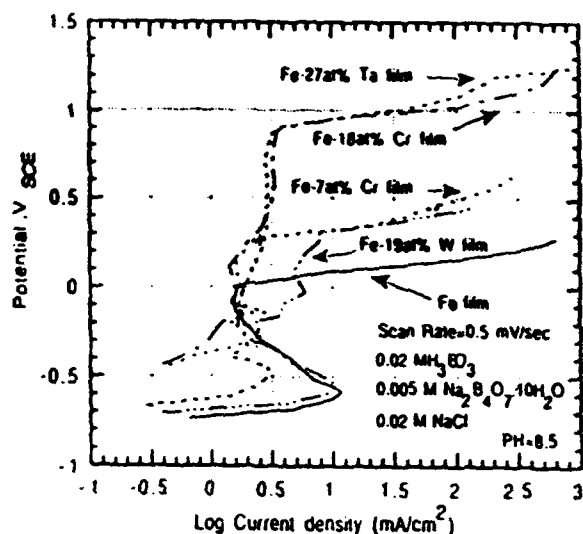


Fig 4: Anodic polarization curves for sputtered Fe film and Fe alloy films in deaerated 0.02 M  $\text{H}_3\text{BO}_3$  + 0.005 M  $\text{Na}_2\text{B}_4\text{O}_7 \cdot 10 \text{H}_2\text{O}$  + 0.02 M NaCl solution (pH = 8.5).

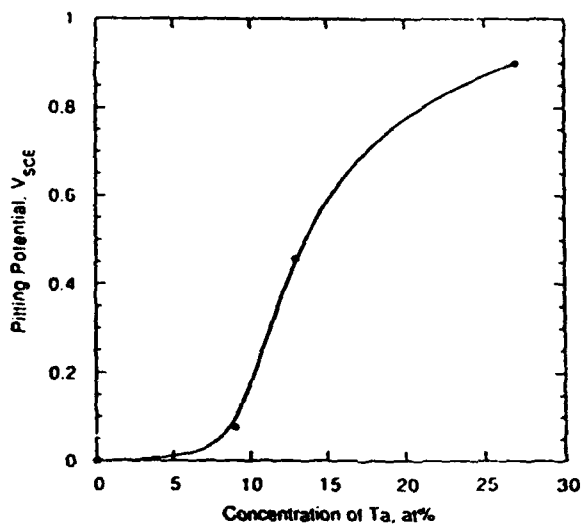


Fig 5: Relationship between the pitting potential and the concentration of Ta for Fe-Ta alloy films.

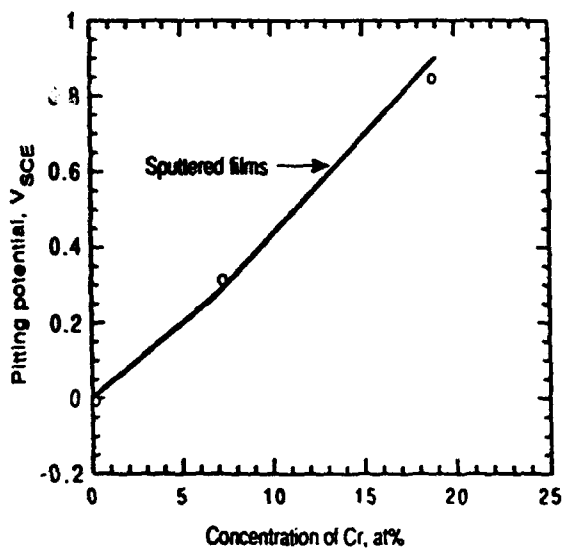


Fig 6: Relationship between the pitting potential and the concentration of Cr in Fe-Cr alloys.

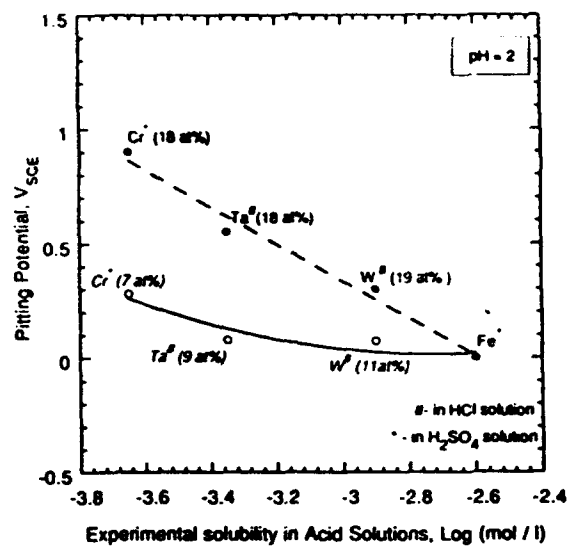


Fig 7: Relationship between the pitting potential of the sputtered Fe alloy and the experimental solubility of the alloying element oxide in acidic solutions at PH2.

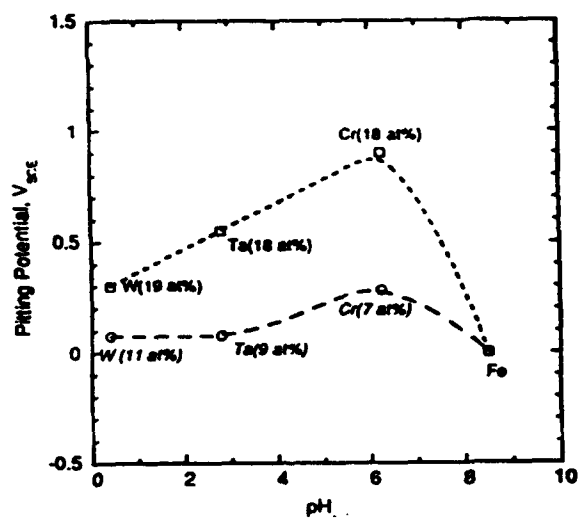


Fig 8: Relationship between the pitting potential of the sputtered Fe alloy and the pH of zero charge ( $pH_{Zch}$ ) of the alloying element oxide.

**LOCALIZED CORROSION PHENOMENA STUDY IN AISI 304L  
AND 316L STAINLESS STEELS PREPARED BY POWDER  
METALLURGY.**

**E. Otero**

Departamento de Ciencia de Materiales  
Facultad de Ciencias Químicas  
Universidad Complutense  
28040-Madrid, Spain.

**A. Pardo**

Departamento de Ciencia de Materiales  
Facultad de Ciencias Químicas  
Universidad Complutense  
28040-Madrid, Spain.

**V. Utrilla**

Departamento de Ciencia de Materiales  
Facultad de Ciencias Químicas  
Universidad Complutense  
28040-Madrid, Spain.

**E. Sáenz**

Laboratorio de Corrosión  
Pontificia Universidad Católica del Perú  
Lima 32, Perú.

**F. J. Pérez**

Departamento de Ciencia de Materiales  
Facultad de Ciencias Químicas  
Universidad Complutense  
28040-Madrid, Spain.

**Abstract**

The corrosion behavior of austenitic stainless steel 304L and 316L obtained by powder metallurgy was studied. The material was exposed to ferric chloride solution following the ASTM G48-76 method A (reapproved in 1980). The influence of  $\text{FeCl}_3$  concentration and dissolution temperature in the kinetic of these materials was

also studied. A mechanism is proposed to explain the localized attack in certain areas where the contact between particles was not completed in the sintering cycle.

**Key Terms:** Ferric chloride, stainless steel, 304L, 306L, powder metallurgy, general corrosion, crevice corrosion.

## **Introduction**

The use of stainless steels obtained by powder metallurgy has grown noticeable in recent years due mainly to their cost. The automatic production of components of complex geometry and good mechanical properties is possible while avoiding finishing processes.

<sup>1</sup> The main applications are in the petrochemical, food and nuclear industries, as well as in medical and environmental devices. <sup>2</sup>

The main restriction to the use of these stainless materials as compared with similar ones obtained by casting or rolling is their low corrosion resistance, although there is little data in the literature on the behavior of the powder metallurgy stainless steels. <sup>3,4</sup> The processes that are used to obtain sintered stainless steels need to be improved to increase their resistance to aggressive media. <sup>5</sup> Moreover, a better control of sintering parameters should be carried out during the addition of elements such as tin and copper. <sup>6,7</sup>

A previous study <sup>8</sup> demonstrated that powder metallurgy stainless and conventional steels behave differently under ASTM G48-76 test. Pitting corrosion was obtained in the casting and rolling steel and general corrosion was obtained in the powder metallurgy steel.

In the present study, the behavior of powder metallurgy steel is studied in different  $\text{Cl}^-$  concentration solutions at two temperatures.

## **Experimental Method**

Stainless steels 304L and 316L obtained by powder metallurgy (PM) were tested. The chemical composition is given in Table I. Disc-shaped samples (25 mm diameter and 4.9 mm thick) were prepared by uniaxial compacting at 700 MPa. Zinc stearate was used as

lubricant. The green density was 6.4 g/cm<sup>3</sup> for 304L and 6.43 g/cm<sup>3</sup> for 316L powder steels. The samples were sintered in a vacuum furnace for 30 min. at 1603K (heating rate 5K/min.). Subsequently, a solubilization treatment was applied at 1573K for 10 min. in an argon atmosphere followed by water quenching. The final densities were 6.9 g/cm<sup>3</sup> for 304L and 7.0 g/cm<sup>3</sup> for 316L. Finishing was conducted by abrasion with 120 grit emery paper.

The corrosion behavior study was conducted following the ASTM G48-76 standard, <sup>9</sup> *i.e.* a ferric chloride solution treatment was used for 72 h. To determine the influence of the electrolyte concentration and temperature, 0.05, 0.10, 0.21, and 0.41 M FeCl<sub>3</sub> solutions were utilized at 323K and 295K. The corrosion rate, in cm/month, was calculated in each case and the attack morphology was determined by scanning electron microscopy.

### Experimental Results and Discussion

At 323K 304L PM steel showed generalized attack in each tested solution. The attack was preferential in pore areas due to a crevice corrosion process. Higher the electrolyte concentration and the higher the temperature the higher the attack. In the case of 316L PM steel the attack is mainly circumscribed to pores, that is, general corrosion is not observed.

The powder metallurgy product presents a level of porosity that allows the contact of occluded areas with the electrolyte. A crevice corrosion process is possible to develop. The same behavior was detected in rolled steels <sup>10</sup> where 'crevice areas' appeared. The process mainly consists of a desoxygenation of the solution inside the pores with an increase in the Cl<sup>-</sup> concentration which promotes an increase in the local acidity. As a consequence, the breakdown of the passive film occurs in the pores (Fig. 1). The attack can be extended to other areas of the sample, namely to the contact area between particles where a protective film does not form due to the rubbing process during the vacuum sinterization. The corrosion between the particles will undermine the union among them ensuing a partial crumble of the structure (Fig. 2). Therefore, the weight loss process is part due to electrolytic corrosion and part due to mechanical stability. The above mechanism is occurring everywhere in the sample surface, due to the small size of the particles that constitute the powder metallurgy product. The overall process is a severe and generalized attack of the material.



Figure 3 shows that by increasing the electrolyte concentration and the temperature the corrosion rate increases. The higher corrosion resistance of the 316L PM steel as compared to 304L PM steel is mainly to its higher molybdenum concentration. The effect of the temperature on the 316L PM corrosion rate is higher at higher electrolyte concentrations. On the other hand, for the 304L PM steel the effect of the temperature is noticeable at all ferric chloride concentrations. For both materials, by increasing the ferric chloride concentration from 0.05 M to 0.41 M, the corrosion kinetics increases one order of magnitude.

Figures 4 and 5 show the attack morphology of the 304L PM and 316L PM steels, respectively. 304L PM steel showed a crevice and general attack in all the tested solutions. 316L PM steel only showed general attack at 323K and 0.41 M ferric chloride solution (normalized test); in all other solutions, crevice attack was observed. This dissimilar behavior of 316L PM steel is a consequence of its better passivation properties. Only at the highest ferric chloride concentration the transpassive potential is reached and, therefore, general corrosion occurs. In the case of 304L PM steel the transpassive potential is reached at all tested electrolyte concentrations, consequently general corrosion was always detected. Presently this hypothesis is being verified.

In the powder metallurgy products no pitting corrosion is observed. This phenomena is common in casting materials of similar composition in identical environments. It is speculated that the crevice corrosion masks the pitting corrosion.

### Conclusions

- 1 For all tested environments, 304L PM showed generalized corrosion and severe crevice corrosion attack in areas close to the pores and in areas in contact between particles.
- 2 316L PM steel only showed generalized attack in the normalized test (323K and 0.41M  $\text{FeCl}_3$ ). In all other tested environments localized attack was observed.

3 In the powder metallurgy products no pitting corrosion was detected in the tested environments. The same materials prepared by casting exhibit pitting corrosion.

### Acknowledgments

The authors express their gratitude to the CICYT for the financial support of this work. Project MAT 90-0980-C03-01.

### References

- 1 M. A. PAO and E. KLAR "On the corrosion resistance of PM austenitic stainless steels," PM 82 European International Powder Metallurgy Conference, Florence, Italy (1982), p. 359.
- 2 T. RAGHU et al, "Corrosion behaviour of sintered stainless steel in sulphuric acid and sodium chloride solutions," 10th International Congress on Metallic Corrosion, Vol. 1, Madras. Trans. Tech. Publications (1987), p. 441.
- 3 O. W. REEN and G. O. HUGHES, Precision Metal, July 1977, pp. 38-40.
- 4 R. GOLD, Precision Metal, March 1982, p. 31.
- 5 W. E. JONES, Powder Metallurgy, 2 (1981), p. 101.
- 6 G. H. LEI and R. M. GERMAN, Modern Developments in Powder Metallurgy, 16 (1984), pp. 261-275.
- 7 S. K. CHATTERJEE et al., Modern Developments in Powder Metallurgy, 16 (1984), pp. 277-293.
- 8 E. OTERO et al., "Pitting Corrosion Behaviour of the 304L stainless steel obtained by pulvimetallurgy," 10th European Corrosion Congress, Paper 002, Barcelona, Sociedad Española de Química Industrial (1993). In press.
- 9 ASTM Standard G48-76 (reapproved in 1980), method A.
- 10 J. W. OLDFIELD, T. S. LEE and R. W. RAIN, "Crevice corrosion of stainless steels in marine environments," Stainless Steel 84, London, The Institute of Metals (1985), pp. 57-58.

**Table 1:** Chemical composition of stainless steels studied.

Material	Elements (wt %)							
	C	Si	Mn	Cr	Ni	S	P	Mo
304L P/M	0,017	0,62	≤0,05	18,15	11,5	0,007	0,024	-
316L P/M	0,023	0,82	2,18	16,27	13,8	0,007	0,018	2,15

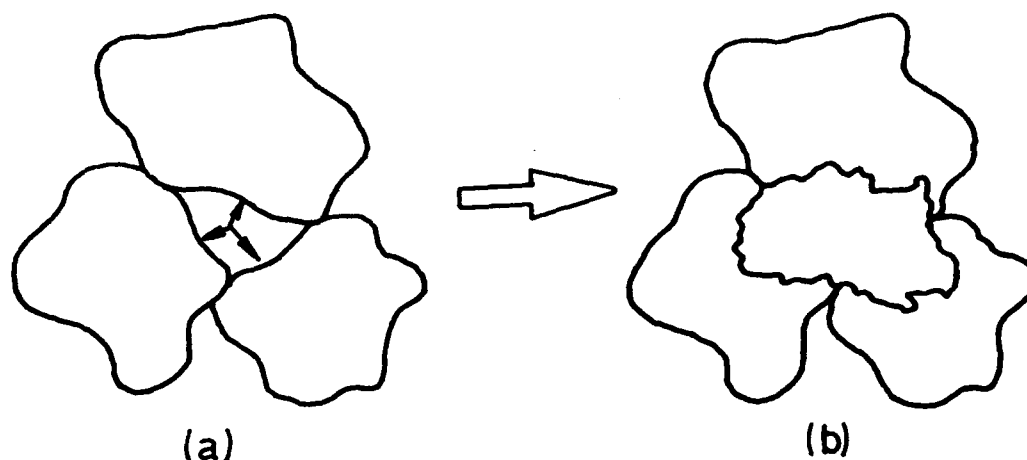


**Figure 1 :** Crevice corrosion attack and local concentration of oxidized chlorine

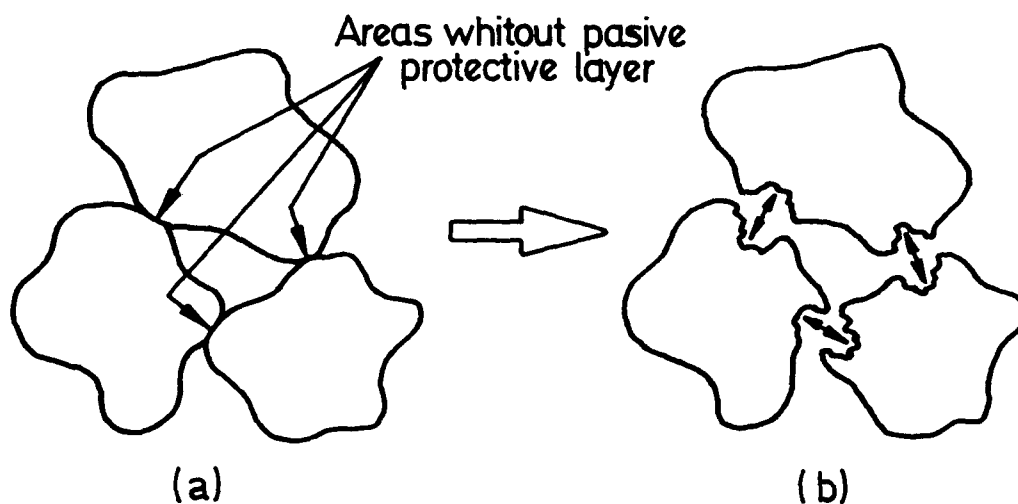


**Figure 2 :** Attack due to the formation of active-passive areas and the crumble of the material structure.

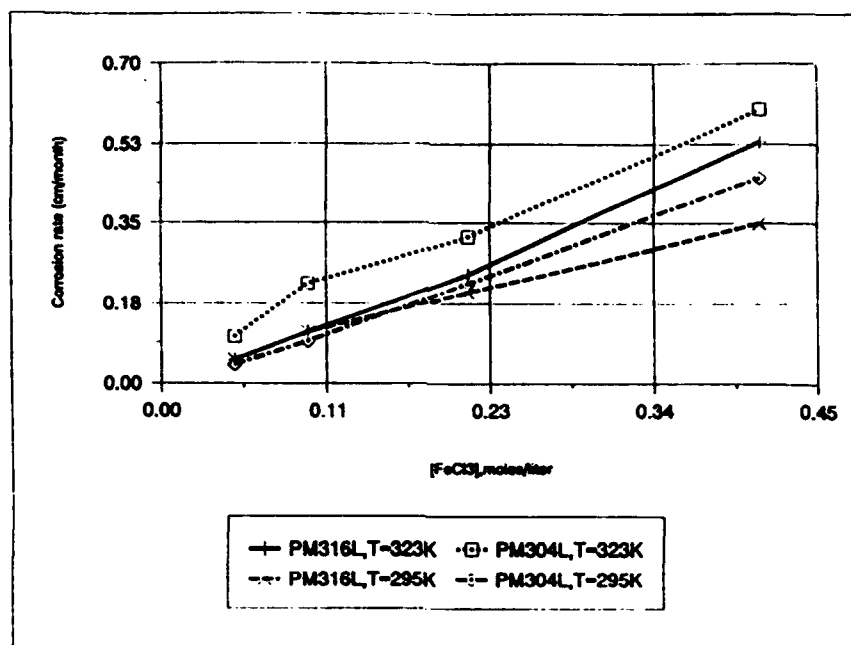
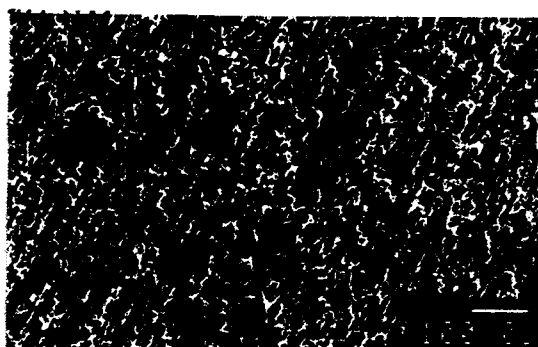
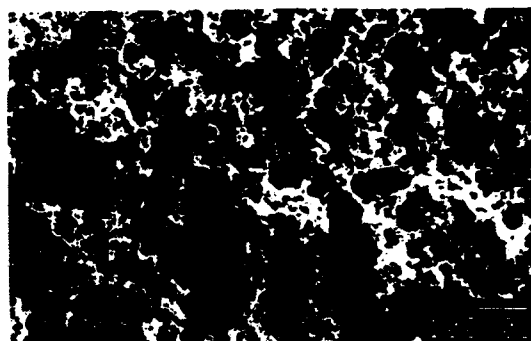


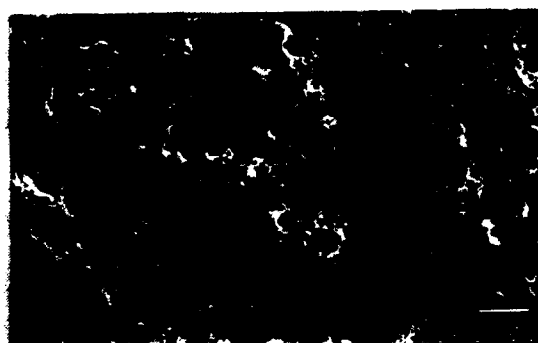
**Figure 3 :** Influence of concentration and electrolyte temperature in the corrosion rate of the 304L and 316L stainless steels obtained by powder metallurgy.



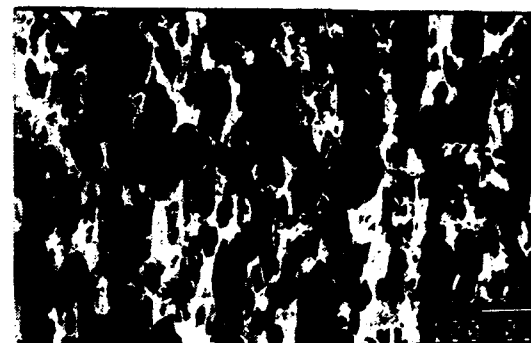
(a)



(b)



(c)



(d)

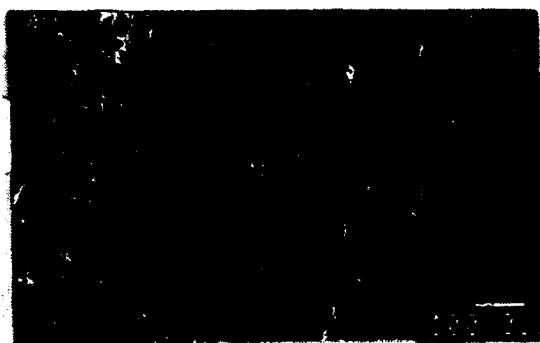
**Figure 4 :** 304L (P/M) steel microstructure tested at different temperatures and concentrations of FeCl<sub>3</sub>: (a) 0,05 M, T=295 K, (b) 0,41 M, T=295 K, (c) 0,05 M, T=323 K, (d) 0,41 M, T=323 K



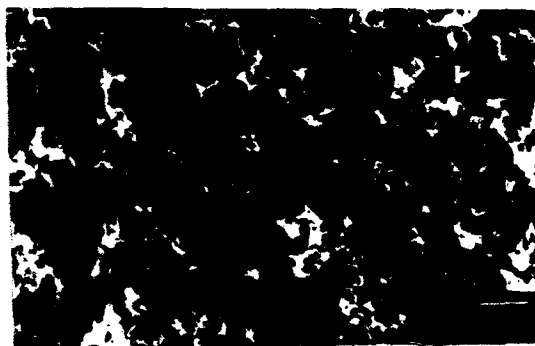
(a)



(b)



(c)



(d)

**Figure 5 :** *316L (P/M) steel microstructure tested at different temperatures and concentrations of  $\text{FeCl}_3$ : (a) 0,05 M,  $T=295$  K, (b) 0,41 M,  $T=295$  K, (c) 0,05 M,  $T=323$  K, (d) 0,41 M,  $T=323$  K.*

# **MEASUREMENT IN SITU OF THE $\text{Cl}^-$ CONCENTRATION DISTRIBUTION IN TWO DIMENSIONS OF METAL SURFACE.**

Changjian Lin

State Key Laboratory for Physical Chemistry of the Solid Surface

Department of Chemistry

Xiamen University

Xiamen, Fujian, 361005 China.

## **Abstract**

A micro-combination Ag/AgCl electrode and a micro-combination  $\text{Cl}^-$  sensitive liquid membrane were designed and constructed. The performance of the two micro  $\text{Cl}^-$  sensitive probes was examined in situ by measuring the  $\text{Cl}^-$  concentration distribution in two dimensions of metal surface for a localized corrosion system. The  $\text{Cl}^-$  concentration at the metal/electrolyte interface can be sensitively determined by using the combined micro probes. This system is a promising tool in studying the role of  $\text{Cl}^-$  ion in the micro areas of the metal surface where localized corrosion initiates and propagates.

## **Introduction**

The chloride ion plays a relevant role in various types of localized corrosion such as pitting corrosion, crevice corrosion and stress corrosion cracking. Therefore, the examination of the influence of  $\text{Cl}^-$  on the local passivity breakdown is one of the most critical subjects in corrosion science. Several theoretical models relating the effect of the  $\text{Cl}^-$  aggressiveness to the passivity breakdown have been proposed [1-6]. However, what is most important is a direct experimental evidence of the  $\text{Cl}^-$  behavior in a micro area close to metal/electrolyte interface. Micro-electrode techniques have been developed to measure the  $\text{Cl}^-$  concentration in the occluded area of localized corrosion [7-8]. However, by inserting a single Ag/AgCl micro electrode into the tip of a localized corrosion region, serious error in the  $\text{Cl}^-$  determination may result because of the simultaneous variation of  $\text{Cl}^-$  concentration and potential. It is also

difficult to determine accurately the  $\text{Cl}^-$  concentration in a micro area if the tip of the probe is not small enough and the reference electrode is set far away from the probe. On the other hand, ex-situ measurements of  $\text{Cl}^-$  distribution in two dimensions of metal surface using surface techniques such as SAM, EDAX, etc. [9] will stop the corrosion process and can not provide a dynamic information of the  $\text{Cl}^-$  behavior at the interface metal/solution.

In the present work a micro combination Ag/AgCl electrode and  $\text{Cl}^-$  selective liquid membrane were designed and constructed. The assemblage was tested in a two dimension metal surface for a localized corrosion system. The vital role of  $\text{Cl}^-$  in initiation and propagation of localized corrosion is discussed.

## Experimental

### *Micro Ag/AgCl Combination Electrode*

The micro combination electrode has two compartments; one serves as the reference electrode and the other acts as the  $\text{Cl}^-$  selective electrode. A thick wall double-barreled 1.5/0.8 mm (OD/ID) borosilicate glass capillary was shaped into a pointed micropipette using electrical heating. One of the two barrels was truncated at the tip to insert the  $\text{Cl}^-$  ion selective electrode and the other (10  $\mu\text{m}$  tip) was filled with 0.5 M KCl containing agar gel as a micro Lugging bridge to the Ag/AgCl electrode. The  $\text{Cl}^-$  selective electrode was made of a 0.1 mm diameter high purity (99.9%) silver wire shaped at one end to 10  $\mu\text{m}$  and electrodeposited with AgCl. The body of the Ag/AgCl wire was coated with epoxy except by the exposed tip. This wire was inserted into the shorter barrel and secured with wax at both ends. The micro Luggin bridge was connected with a 3 mm ID Pyrex glass and sealed with wax at the joint. The glass tube was filled with 0.5 M KCl as an internal reference solution. Finally, a 250  $\mu\text{m}$  diameter Ag/AgCl electrode was placed in the glass tube and the top of the compartment was sealed with silicone rubber. The arrangement is shown in Fig. 1.

### *Micro Combination $\text{Cl}^-$ Ion Selective Liquid Membrane Electrode*

Ion selective micro membrane electrodes have been well developed in the biological and medical sciences [10-12]. A micro-combination  $\text{Cl}^-$  ion selective electrode was designed for imaging the  $\text{Cl}^-$  concentration in localized corrosion. This electrode (Fig. 2)

contains two compartments, one operates as the reference electrode and the other as the  $\text{Cl}^-$  ion sensitive liquid membrane electrode. A double barreled 1.5/0.8 mm borosilicate glass capillary (WPI) was point-shaped under electrical heating leaving two holes of 1-2  $\mu\text{m}$  inner diameter. Subsequently the glass capillary was exposed to 5% dimethyldichlorosilane xylene solution for 1-2 min. and baked at  $100^\circ\text{C}$  for 1 h. Following silanization, one of the tips was filled with a  $\text{Cl}^-$  ion selective exchanger (WPI, IE 170) to a 200  $\mu\text{m}$  in length. A Ag/AgCl electrode was inserted into each barrel after filling with 0.5 M KCl. All the fabrication process was carried out under an optical microscope. The body of the  $\text{Cl}^-$  ion selective liquid membrane electrode was fixed with a 4 mm diameter glass tube for the scanning measurements.

#### *Measuring System for Scanning Micro Electrode*

The scanning reference electrode technique has been well developed for in situ imaging of potential distribution in localized corrosion systems. The principles and measuring devices of SRET is described by Isaacs and Vyas [13]. An improved system, controlled by a computer, was setup in our laboratory [14] for imaging the ion concentration distribution. The system is shown schematically in Fig. 3.

#### *Measurement Procedure*

The experiments were carried out using commercial 18/8 stainless steel with a chemical composition of 18.40% Cr, 9.55% Ni, 0.85% Si, 1.38% Mn, 0.091% C, 0.04% P, 0.01% S and balance Fe. The specimens were fabricated as cylinders of 6 mm diameter and 20 mm long, sealed in a Teflon holder with epoxy. The testing surface was finished by polishing with 0.5  $\mu\text{m}$  diamond paste. After polishing the specimens were degreased with methanol and rinsed several times in triple distilled water. The specimens were connected to the Teflon container through a especially designed screw. A platinum wire was arranged in a coil shape around the specimen to act as a counter electrode to maintain a uniform applied current distribution on the surface. A low-noise home-made potentiostat was used. The micro combined  $\text{Cl}^-$  ion selective electrode was located carefully to 10  $\mu\text{m}$  from the surface using an optical microscope. The test solution was later introduced by means of a syringe. The test solutions were 0.1 M NaCl, 0.5 M  $\text{FeCl}_3$  and 0.02 M  $\text{K}_2\text{HPO}_4$ . The



solutions were exposed to air at room temperature throughout the experiments.

## Results and Discussion

### *Calibration*

In order to examine the feasibility and sensitivity of the two  $\text{Cl}^-$  ion selective probes, a simulated arrangement consisting of an anode and a cathode of different area was constructed. A 1 mm hole was drilled in the center of a 8 mm diameter and 10 mm long copper cylinder. A 0.08 mm diameter platinum wire was inserted into the hole and isolated by epoxy from the copper cylinder. The assembled cross section was polished and then inserted into the Teflon cell. The copper and platinum were connected from the back through a battery and an adjustable resistance to a micro-ammeter. The polarity and activity of the electrodes of the simulated galvanic cell was controlled and monitored after addition of 20 ml of 0.02 M  $\text{K}_2\text{HPO}_4$  to the cell. The designed  $\text{Cl}^-$  ion sensitive probes were used to measure the  $\text{Cl}^-$  distribution on the surface under different conditions.

It is very difficult to obtain a stable image of  $\text{Cl}^-$  concentration distribution using the  $\text{Cl}^-$  sensitive electrode when no  $\text{Cl}^-$  ion is contained in the electrolyte. When a 0.5 ml 1 M NaCl solution was added to the 20 ml 0.02 M  $\text{K}_2\text{HPO}_4$  and a 61  $\mu\text{A}$  external current was applied to keep the platinum wire as the anode, a higher  $\text{Cl}^-$  concentration was sensed near the platinum wire than in the surrounding areas (Fig. 4a). When the platinum electrode was controlled as the cathode and a 122  $\mu\text{A}$  current was passed the  $\text{Cl}^-$  distribution imaging indicated no difference in the concentration over the scanned surface (Fig. 4b). The same results were obtained using the Ag/AgCl combination electrode for the scanning procedure.

It was shown that the  $\text{Cl}^-$  ion in the solution migrated and accumulated near the anode. Therefore, when a metal is immersed in a solution containing  $\text{Cl}^-$  ions, their accumulation may expedite the development of various types of localized corrosion. The non-uniform  $\text{Cl}^-$  distribution near the interface is called a "chloride-island" [9] and results from the non uniformity of the electric field on the metal surface. The latter results from the presence of inhomogeneities on

the metal surface, which may be one of the important reasons for localized corrosion. When the simulated anodic area was much larger than the cathodic area, the  $\text{Cl}^-$  ion was not accumulated on the surface, therefore a more uniform  $\text{Cl}^-$  concentration was measured.

#### *Crevice Corrosion*

The  $\text{Cl}^-$  imaging concentration for 18/8 stainless steel immersed in 0.1 M NaCl solution is presented in Fig. 5. The distribution was measured by scanning using the micro combination Ag/AgCl micro electrode after polarizing 0.2 V vs. Ag/AgCl. The  $\text{Cl}^-$  concentration is higher along the junction between the stainless steel and the epoxy coating, that is, where crevice corrosion occurred. The  $\text{Cl}^-$  concentration at the open corroding crevice surface was estimated to be three fold higher than in the bulk solution. It is reported that the  $\text{Cl}^-$  ion concentration in the occluded region might be as high as ten fold the bulk concentration [15]. The accumulation of  $\text{Cl}^-$  ions may be one of the necessary conditions for crevice corrosion propagation. The increase of  $\text{Cl}^-$  concentration at the opening region of the crevice is a result of  $\text{Cl}^-$  migration from the bulk to keep electrical neutrality in the anodic crevice.

#### *Pitting Corrosion*

The  $\text{Cl}^-$  distribution for pitting corrosion of 18/8 stainless steel immersed in 0.5 M  $\text{FeCl}_3$  solution is shown in Fig. 6. The profile was measured by the  $\text{Cl}^-$  ion selective liquid membrane probe. When pitting corrosion occurred a non uniform distribution of  $\text{Cl}^-$  was detected in the solution near the metal surface. The higher the activity of pitting corrosion the higher the concentration of  $\text{Cl}^-$ . It is possible to monitor in situ the pitting propagation process by determining the  $\text{Cl}^-$  ion distribution.

### **Conclusions**

The preliminary conclusions are: (1) A micro combination Ag/AgCl electrode and a micro combination  $\text{Cl}^-$  ion selective liquid membrane electrode were designed and constructed for studies of localized corrosion. (2) The feasibility of these probes was demonstrated by determining the  $\text{Cl}^-$  distribution in simulated

galvanic and actual corroding systems. (3) The  $\text{Cl}^-$  ion migrate towards the anode and accumulate in the micro area under the influence of an electric field. (4) The accumulation of  $\text{Cl}^-$  ions in the anodic region of crevice and pitting may be one of the most important factors to maintain the propagation of localized corrosion.

## References

1. Z. SZKLARSKA-SMIALOWSKA, *Corrosion*, **27**, 223 (1971).
2. J. R. GALVELE, *Passivity of Metals*, The Electrochemical Society Inc., Princeton, NJ (1978), p. 285.
3. M. JANIK-CZACHOR, G. C. WOOD and G. E. THOMPSON, *Br. Corros. J.*, **15**, 154 (1980).
4. J. KRUGER, *International Materials Reviews*, **33**, 113 (1988).
5. M. JANIK-CZACHOR, *J. Electrochem. Soc.*, **128**, 513 (1981).
6. H. BOHNI, *Langmuir*, **3**, 924 (1987).
7. T. NGUYEN and C. LIN, NIST Technical Note 12664 (1989).
8. J. A. DAVIS, *Localized Corrosion*, National Association of Corrosion Engineers, Houston TX (1974) p. 168.
9. M. JANIK-CZACHOR, *Corrosion Science*, **15**, 775 (1975).
10. L. A. GEDES, *Electrodes and the Measurement of Bioelectric Events*, Wiley-Interscience, New York (1971) p. 10.
11. R. C. THOMAS, *Ion-Selective Intracellular Microelectrodes - How to Make and Use Them*, Academic Press Inc., London (1978) p. 56.
12. D. AMMAN, *Ion-Selective Microelectrodes - Principles, Design and Application*, Pringer-Verlag, Berlin (1986), p. 97.
13. H. S. ISAACS and B. VYAS, *Electrochemical Corrosion Testing*, ASTM STP 727 (1981) p. 3.
14. CHANGJIAN LIN, Ph. D. Thesis, Xiamen University (1985).
15. R. M. KAIN, T. S. LEE and J. W. OLDFIELD, *Electrochemical Techniques for Corrosion Engineering*, National Association of Corrosion Engineers, Houston TX (1986) p. 261.

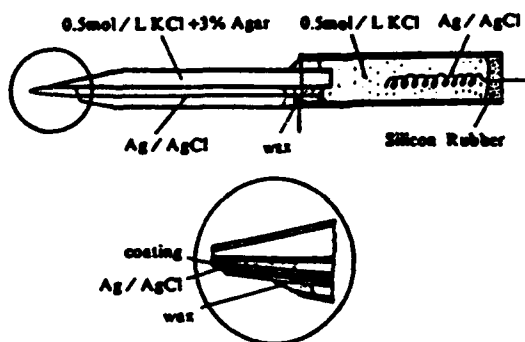


Fig.1 Structure of micro-combination Ag/AgCl electrode.

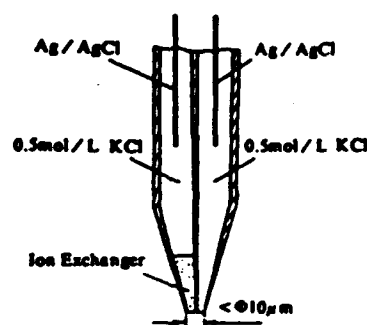


Fig.2 Structure of micro-combination  $\text{Cl}^-$  sensitive liquid membrane electrode.

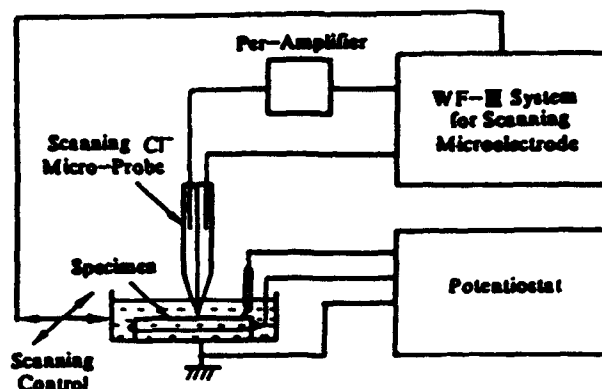


Fig.3 Schematic diagram of measurement stem for in situ  $\text{Cl}^-$  imaging at the interface of metal/electrolyte.

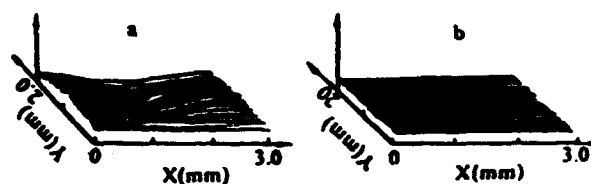


Fig.4  $\text{Cl}^-$  concentration imaging on the simulated galvanic system when controlling Pt, at electrode center, as an anode (a), and controlling Pt as a cathode (b), in 20ml 0.02mol/l  $\text{K}_2\text{HPO}_4$  + 0.5ml 1.0mol/l NaCl solution, by micro-combination liquid membrane electrode.

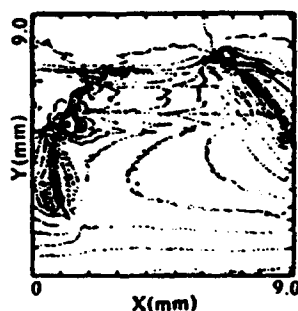


Fig.5  $\text{Cl}^-$  concentration imaging on 18/8 stainless steel surface in 0.1 mol/l NaCl solution, when crevice corrosion happened along the edge of metal/epoxy, by micro-combination Ag/AgCl electrode

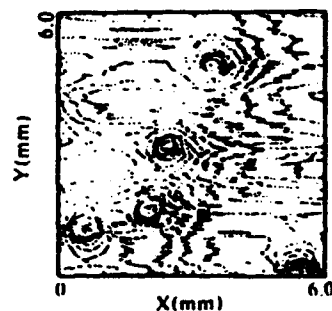


Fig.6  $\text{Cl}^-$  concentration imaging on 18/8 stainless steel surface in 0.5mol/l  $\text{FeCl}_3$  solution, when pitting corrosion happened, by micro-combination  $\text{Cl}^-$  liquid membrane electrode.

# INFLUENCE OF ANIONS ON THE SURFACE ENHANCED RAMAN SPECTRA OF PASSIVE FILMS FORMED ON IRON

Jing Gui and T.M. Devine

Department of Materials Science and Mineral Engineering  
University of California  
Berkeley, CA

## Abstract

*In situ* surface enhanced Raman spectra were obtained for the passive films formed on iron in 5 different aqueous solutions: 0.3M NaNO<sub>3</sub>, 0.15M Na<sub>2</sub>CO<sub>3</sub> + 0.15M NaHCO<sub>3</sub>, M K<sub>2</sub>HPO<sub>4</sub> + 0.02M KH<sub>2</sub>PO<sub>4</sub>, and 0.3M Na<sub>2</sub>SO<sub>4</sub> at pH 10 and pH 5. The results indicate that in the nitrate, carbonate and sulfate (pH 10) solutions the passive films are similar, independent of potential (over the range -400 mV to +100 mV), and consist of Fe(OH)<sub>2</sub> + (Fe<sub>3</sub>O<sub>4</sub> and/or  $\gamma$ -Fe<sub>2</sub>O<sub>3</sub>). In the sulfate solution (pH 10) sulfate anions adsorbed on the surface of the passive film. The passive films formed in the phosphate electrolyte were unlike those formed in any of the other solutions. Little if any Fe(OH)<sub>2</sub> was present in the films formed in phosphate; the films appeared to contain phosphate in the bidentate C<sub>2v</sub> configuration and/or other orthophosphates. Finally, the passive film formed on iron in sulfate at pH 5 was similar to that formed in the same solution at pH 10 except for the very strong presence of sulfate that was covalently bonded in the bidentate C<sub>2v</sub> configuration to iron in the passive film.

## Introduction

Earlier work reported the use of surface enhanced Raman spectroscopy (SERS) to obtain the *in situ* vibrational Raman spectra from passive films formed on iron in aqueous borate-buffer solution (pH=8.4).<sup>1-3</sup> These measurements enabled identification of the species that make up the films.<sup>2</sup> More recently, SERS has been used to obtain the vibrational Raman spectra from the passive films formed on nickel, chromium and stainless steel.<sup>4-6</sup> SERS, as opposed to conventional Raman scattering, is employed because of the extremely weak Raman intensities that are generated from very thin passive films. Surface enhancement increases the strength of the Raman scattered radiation by many orders of magnitude, thereby producing a signal of measureable intensity.<sup>7</sup> The experimental procedure has been described in detail elsewhere.<sup>3</sup> Suffice it to say, silver particles (~ 50 nm in diameter) are spaced ~ 600 nm apart on the surface of the material of interest. The sample is then illuminated with a laser and the incident photons excite surface plasmons in the silver particles. The result is a magnification in the optical field that falls off exponentially with distance from the surface of the silver. Consequently, the Raman spectrum from species on the surface of the metal of interest, such as its passive film, is enhanced. Briefly stated, the silver particles act as electrochemically-inert Raman antennae.

In the present study SERS is used to investigate the influence of anions other than borate (which was the subject of an earlier study<sup>2</sup>) on the identities of the passive films formed on iron.

## Experimental Procedure

The electrochemistry and surface enhanced Raman spectroscopy experiments were performed using procedures that have been described in detail elsewhere.<sup>2,3</sup> Briefly, the working electrode was a disc of polycrystalline iron (99.99% purity) that was cut from a rod measuring 12mm in diameter by 60 mm in length and which was obtained

from Johnson Matthey Chemicals LTD. Prior to each test the iron electrode was mechanically polished to 1  $\mu\text{m}$  diamond compound finish and then, in order to obtain SER spectra from the passive films of iron, an array of tiny ( $\approx 50\text{nm}$  in diameter) silver particles were electrodeposited onto the iron from a bath of  $1\text{mM AgNO}_3 + 1\text{mM HNO}_3$  at a potential of  $-0.6\text{V (SCE)}$ . Reference #3 contains scanning electron micrographs that illustrate the size and distribution of silver particles on the iron surface. All potentials are reported with respect to the saturated calomel electrode (SCE). The sample was then immersed in the test solution and cathodically polarized at a potential of  $-0.9\text{ V (SCE)}$  for 10 minutes. This removed most, if not all, of the films present on the iron as confirmed by a nearly featureless Raman spectrum. The potential of the sample was then stepped to the value of interest and the Raman spectra of the films forming on the electrode were obtained.

5 different solution chemistries were tested:  $0.3\text{M Na}_2\text{SO}_4$  with pH of 10.0 and 5.0,  $0.15\text{M Na}_2\text{CO}_3 + 0.15\text{M NaHCO}_3$  (naturally buffered at pH 10),  $0.3\text{M NaNO}_3$  (pH 10) and  $\text{M K}_2\text{HPO}_4 + 0.02\text{M KH}_2\text{PO}_4$  (naturally buffered at pH 8.3). The pH of the 2 sodium sulfate solutions and that of the nitrate solution were unbuffered. The pH of each of the pure sulfate solutions was adjusted through additions of NaOH or  $\text{H}_2\text{SO}_4$  and that of the nitrate solution by the addition of  $\text{HNO}_3$ .

Detailed information describing the Raman facility is described in earlier works.<sup>2,3</sup> Succinctly stated, the Raman spectra were taken on a Jobin-Yvon U1000 Ramanor double monochromator with  $1800\text{ grooves mm}^{-1}$  holographic gratings. Spectral slit widths of  $6\text{ cm}^{-1}$  were used. All spectra were acquired at  $2\text{ cm}^{-1}$  intervals with a 0.2 second integration time. Samples were illuminated with the  $647.1\text{ nm}$  line of a Krypton ion laser. This radiation is below the optical band gap of the passive film formed on iron in aqueous solutions and low intensity was used to avoid heating the sample ( $200\text{mW}$  laser output intensity incident on the sample at an angle of  $\approx 45^\circ$  and focussed to a spot of  $\approx 0.6\text{ mm}^2$ ). Because it is not practically possible to measure the absolute intensity of a Raman line, the intensity is usually measured with respect to that of another line in the same spectrum. Consequently, the results of the SERS experiments are presented as graphs of relative Raman intensity versus the shift in energy of the inelastically scattered radiation.

## Results

Quasi-steady-state anodic polarization curves were measured for iron in each of the 5 solutions. The passivation potentials were  $\leq -600\text{ mV}$  for sulfate (pH 10), phosphate (pH 8.3), carbonate-bicarbonate (pH 10) and nitrate (pH 10), and  $\approx -300\text{ mV}$  for sulfate (pH 5). SER spectra were first obtained at  $-900\text{mV}$  after the samples had been cathodically polarized at  $-900\text{ mV}$  for 10 min. The spectra at  $-900\text{ mV}$  were generally featureless and this initial condition of the sample's surface is referred to as film-free or nearly film-free.

Figure 1 illustrates the influence of potential on the SER spectra of the passive films formed on iron in  $0.3\text{M NaNO}_3$  (pH = 10). The spectrum of the passive film that forms when the potential is stepped from  $-900\text{ mV}$  ( $\approx$  film-free state) to  $-400\text{ mV}$ , a potential that is within the passive region, is shown in figure 1a. It consists of 3 predominant features: a strong peak centered at  $\approx 550\text{ cm}^{-1}$ , a broad shoulder that extends from  $\approx 640$  to  $670\text{ cm}^{-1}$ , and a number of low intensity peaks in the range of  $300$  to  $480\text{ cm}^{-1}$ . The existence of the latter is inferred from the relatively high intensity of the "background" measured in this region of the spectrum (i.e., compare the measured intensity of the spectrum in the range  $300\text{--}480\text{ cm}^{-1}$  to the height of the curve formed by

extrapolating into this region the "Rayleigh Tail" that appears at the far-left hand end of the spectrum). The assignments of all the spectral features will be presented in the Discussion. As shown in figure 1b when the potential is held at -400 mV for 24 hrs., the SER spectrum of the resulting passive film is changed: the relative intensity of the peak at  $\approx 550\text{ cm}^{-1}$  decreases and that of the shoulder in the range  $640\text{ to }670\text{ cm}^{-1}$  increases. When the potential is then stepped to +100 mV, little change occurs in the spectrum of the passive film as shown in figure 1c.

The series of spectra presented in figure 2 were obtained at potentials of -400 mV and 0 mV in aqueous carbonate-bicarbonate which is naturally buffered at a pH of 10.0. When the potential is stepped from -900 mV ( $\approx$  film-free state) to -400 mV the spectrum of the passive film that forms is shown in figure 2a. It consists essentially of a strong, broad peak at  $\approx 550\text{ cm}^{-1}$  and several weak peaks in the ranges  $\approx 600 - 700\text{ cm}^{-1}$  and  $320 - 480\text{ cm}^{-1}$ . The existence of the latter is inferred from the relatively high intensity of the "background" in the range  $320 - 480\text{ cm}^{-1}$  as was mentioned above in the description of figure 1a. The spectrum of the passive film that results from holding the potential of the sample at -400 mV for 24 hrs. is presented in figure 2b. In comparison to figure 2a, the low intensity peaks in the range of  $600\text{ to }700\text{ cm}^{-1}$  have increased significantly in intensity while those in the range of  $200 - 400\text{ cm}^{-1}$  have decreased. When the potential is then stepped to 0 mV the intensity of the peaks in the range  $600 - 700\text{ cm}^{-1}$  decrease relative to that at  $\approx 550\text{ cm}^{-1}$  and the peaks in the range  $200 - 400\text{ cm}^{-1}$  increase as shown in the spectrum in figure 2c. Very little changes occur in the spectrum as the potential of the sample is held at 0 mV for 24 hrs. as seen by comparing the spectra in figures 2c and 2d. The spectrum that results when the potential of the sample is again stepped down to -400 mV results in few changes as is shown in figure 2e. The intensity of the peak at  $550\text{ cm}^{-1}$  has increased slightly. However, as shown in the spectrum presented in figure 2f, after 24 hrs. at -400 mV the intensities of the peaks in the ranges  $200 - 400\text{ cm}^{-1}$  have decreased and those in the range  $590\text{ to }700\text{ cm}^{-1}$  have increased noticeably.

Figure 3 presents the influence of applied potential on the SER spectra of the passive films formed on iron in 0.3M  $\text{Na}_2\text{SO}_4$  (pH 10). Figure 3a is the spectrum that was obtained after the potential of the sample was stepped from -900 mV ( $\approx$  film-free state) to -400 mV, a potential that is within the passive region. There is in figure 1a a broad, rather intense peak at  $\approx 550\text{ cm}^{-1}$ , a broad, shallow shoulder at  $\approx 670\text{ cm}^{-1}$ , a sharp, reasonably intense peak at  $\approx 980\text{ cm}^{-1}$ , and a number of fairly weak peaks in the range of  $\approx 300 - 480\text{ cm}^{-1}$ . After the spectrum in figure 3a was obtained, the potential of the sample was stepped from -400 mV to 0 mV and the spectrum in figure 3b was measured. The change in potential caused a shift in the position of the most intense peak from  $554\text{ cm}^{-1}$  to  $563\text{ cm}^{-1}$  as well as a decrease in its intensity; in addition, the peak at  $980\text{ cm}^{-1}$  grew in intensity relative to background and the shoulder at  $\approx 670\text{ cm}^{-1}$  became more intense. If instead of first stepping the potential from -900 mV to -400 mV and then stepping to 0 mV as was done before obtaining the spectrum in figure 3b, the potential of the sample is immediately stepped from -900 mV (the "film-free" state) to 0 mV the resulting SER spectrum of the passive film is that shown in figure 3c. Essentially the spectrum is the same as that shown in figure 3b. Finally, if the potential is now stepped from 0 mV to -400 mV the SER spectrum that results is presented in figure 3d. The only major change is a shift in the center of the most intense peak from  $563\text{ cm}^{-1}$  to  $550\text{ cm}^{-1}$ . In summary, the biggest difference between the SER spectra of the passive films formed on iron at potentials of -400 mV and 0 mV in pH 10 sulfate is a shift in energy of the most intense peak from  $550\text{ cm}^{-1}$  to  $563\text{ cm}^{-1}$ . It bears noting that the spectrum at a

particular potential (e.g., -400 mV and 0 mV) is relatively independent of the path taken to arrive at that potential (i.e., the spectra in figures 3a and 3c are nearly identical as is true of the spectra in figures 3b and 3d).

Figure 4 illustrates the influence of applied potential on the passive films formed on iron in phosphate that is naturally buffered at pH 8.3. Figure 4a was obtained after the potential of the sample was stepped from -900 mV to -400 mV. In comparison to the spectra obtained in the 2 sulfate solutions and presented in figures 1 and 2, that obtained in the phosphate solution at -400 mV does not exhibit a readily discernable peak at  $\approx 550\text{ cm}^{-1}$ . Instead there appears to be a large number of fairly intense peaks in the range 350 to  $600\text{ cm}^{-1}$ . In addition, there appears to be a peak at  $\approx 670\text{ cm}^{-1}$  and several in the range of  $900\text{--}1100\text{ cm}^{-1}$ . The spectrum that results following a 24 hr. hold at -400 mV is shown in figure 4b. Now a peak at  $570\text{ cm}^{-1}$  is apparent as are peaks at 605, 653, 726 and multiple peaks in the range of  $923\text{--}1150\text{ cm}^{-1}$ . When the potential is stepped to +100 mV the measured spectrum, shown in figure 4c, consists of a nearly horizontal, straight line between 370 and  $625\text{ cm}^{-1}$  plus a wide, shallow peak or series of peaks between 900 and  $1140\text{ cm}^{-1}$ .

Unlike the relative insensitivity to potential of the SER spectrum in 0.3M  $\text{Na}_2\text{SO}_4$  pH 10, that in pH 5 was fairly dependent on potential. This is at least partially caused by the higher passivation potential in pH 5 which results in some of the spectra being obtained in the active region such as the spectra in figures 5a and 5b. Figure 5a is the spectrum of the film on iron at a potential of -700 mV. It consists of a very broad and shallow peak at  $\approx 550\text{ cm}^{-1}$ , a shoulder at  $\approx 600\text{ cm}^{-1}$ , a weak peak at  $\approx 980\text{ cm}^{-1}$  and several, low intensity peaks in the range of  $250\text{--}480\text{ cm}^{-1}$ . When the potential of the sample was then stepped from -700 mV to -500 mV the spectrum presented in figure 5b was measured. A strong, broad peak occurred at  $\approx 550\text{ cm}^{-1}$  and it possessed a shoulder that began at  $\approx 579\text{ cm}^{-1}$ . In addition, there was a peak of moderate intensity at  $980\text{ cm}^{-1}$ , a highly asymmetric peak with its maximum at  $866\text{ cm}^{-1}$ , and a number of low intensity peaks in the range of  $250\text{--}480\text{ cm}^{-1}$ . Finally, when the potential of the sample was stepped to -100 mV, which is above the passivation potential, the spectrum presented in figure 5c was measured. In relation to the spectrum shown in figure 5b, the intensities of the peak at  $978\text{ cm}^{-1}$  and the broad, asymmetric peak at  $863\text{ cm}^{-1}$  have increased while that of the peak at  $550\text{ cm}^{-1}$  has decreased but still remains strong. In addition, the fine structure of the spectrum suggests that a number of overlapping peaks are responsible for the broad shoulder in the range of  $590\text{ cm}^{-1}$  to  $690\text{ cm}^{-1}$ .

## Discussion

Before considering individually the SER spectra obtained from the passive films formed on iron in each solution it is instructive to note the significant differences that exist between the spectra obtained in the different solutions. In this section the causes of these differences will be addressed.

Typically, in deconvoluting conventional (as opposed to surface enhanced) Raman spectra the most intense peaks are considered first and initially assigned to the  $A_1$  modes of suspected species. In deconvoluting SER spectra it is necessary to take into account the fact that the Raman scattered radiation associated with different vibrational modes of a particular species are in general not enhanced to the same extent.<sup>8,9</sup> This is the result of the fact that close to the surface of a metal that is illuminated by an unpolarized optical laser, the magnitude of the electric field vector that is parallel to the surface is significantly less than that of the component of the electric field that is



perpendicular to the surface. Consequently, if the molecule is oriented with its major axis of symmetry perpendicular to the surface of the metal then the intensity of its  $A_1$  mode can be further increased by a factor of  $\sim 4$  to  $\sim 16$  times greater than the intensity enhancements of other vibrational modes.<sup>8</sup> Thus, a first approach to the assignments of peaks is to associate them with the  $A_1$  vibrational modes of constituents in the film.

The most dominant feature in the SER spectra of the passive films formed on iron in 0.3M  $\text{NaNO}_3$  (pH 10) is the intense peak that is centered at  $\approx 550 \text{ cm}^{-1}$ . This peak is also found in the spectra of the passive films formed in all of the other solutions except the phosphate solution. Consequently it is unlikely to be caused by any of the specific anions present in the different solutions and based on the Raman spectra listed in Table I for bulk crystals of oxides, hydroxides and oxyhydroxides of iron, this peak is assigned to the  $A_1$  mode of  $\text{Fe}(\text{OH})_2$ , although for reasons cited elsewhere this species may best be referred to as  $\text{Fe}(\text{II,III})(\text{OH})_y$ .<sup>2</sup> There are 2 other features in the spectra of the passive films formed in the nitrate solution that are worth discussing. First, there is a broad shoulder centered at  $\approx 670 \text{ cm}^{-1}$  and second there appear to be a number of weak, overlapping peaks in the range of  $\approx 300\text{--}480 \text{ cm}^{-1}$ . The Raman spectrum of the nitrate ion (point group  $D_{3h}$ ) which is listed in Table II as well as the Raman spectra that have been recorded for nitrate that is bonded in the bidentate configuration (point group  $C_{2v}$ ) to various metal cations indicates that the lowest energy vibrational mode occurs at  $\approx 720 \text{ cm}^{-1}$  and this is for the doubly degenerate  $E'$  mode in  $D_{3h}$  which splits into  $A_1 + B_1$  modes in  $C_{2v}$ .<sup>10</sup> From the results of several researchers it appears that the magnitude of the splitting is small and 2 individual peaks may not be resolvable. At any rate, the shoulder in the spectra in figure 1 is rather intense and located at  $\approx 670 \text{ cm}^{-1}$ . Both of these suggest that it is unlikely that the shoulder is associated with the nitrate ion. The presence of  $\text{Fe}_3\text{O}_4$  and/or  $\gamma\text{-Fe}_2\text{O}_3$  in the passive film would produce a reasonable amount of scattered intensity in the range of  $600\text{--}700 \text{ cm}^{-1}$  as well as a number of lower intensity peaks in the range of  $\approx 300\text{--}500 \text{ cm}^{-1}$ . In summary, it is concluded that the passive film that forms on iron in 0.3M  $\text{NaNO}_3$  consists of  $\text{Fe}(\text{OH})_2 + (\text{Fe}_3\text{O}_4 \text{ and/or } \gamma\text{-Fe}_2\text{O}_3)$ . It should be noted that there is no evidence for adsorption of nitrate on the surface of the passive film. Of course, since the most intense vibrational mode of nitrate occurs at  $\approx 1050 \text{ cm}^{-1}$  and since our spectra were stopped at  $1000 \text{ cm}^{-1}$ , it is quite possible that nitrate has adsorbed but that the intensity of the  $E$  mode at  $\approx 720 \text{ cm}^{-1}$  is too weak to be observed.

As was the case for the passive films formed on iron in 0.3M  $\text{NaNO}_3$  (pH=10), the most dominant feature in the spectra of the films formed on iron in 0.15M  $\text{Na}_2\text{CO}_3 + 0.15\text{M NaHCO}_3$  is a strong peak centered in the vicinity of  $\approx 550 \text{ cm}^{-1}$ . As discussed above, this peak is assigned to the  $A_1$  mode of  $\text{Fe}(\text{OH})_2$ . In comparing figures 2a and 2b it is seen that as the time spent at  $-400 \text{ mV}$  is increased from  $\approx 15$  minutes (figure 2a) to 24 hrs. (figure 2b) a substantial shoulder in the range  $600\text{--}700 \text{ cm}^{-1}$  and centered at  $\approx 635 \text{ cm}^{-1}$  appears on the main peak. In addition, another change occurs that is not as readily apparent. Namely, intensity is lost in the range of  $200\text{--}400 \text{ cm}^{-1}$ , as though a single, broad peak or several more narrow ones had all decreased in strength. When the potential was then stepped to  $0 \text{ mV}$ , the shoulder in the range  $600\text{--}700 \text{ cm}^{-1}$  disappeared and the intensity in the range of  $200\text{--}400 \text{ cm}^{-1}$  increased as shown in figure 2c. In fact, stepping the potential from  $-400 \text{ mV}$  to  $0 \text{ mV}$  approximately wiped out the changes that had been produced in the spectrum by holding at  $-400 \text{ mV}$  for 24 hrs. The only differences between the 2 spectra in figures 2a and 2c is the slightly lower intensity of the peak at

550  $\text{cm}^{-1}$  and a more defined shoulder centered at  $\approx 689 \text{ cm}^{-1}$  in the spectra obtained at 0 mV. A comparison of figures 2c and 2d indicates that the only change that occurred during a 24 hr. hold at 0 mV was additional sharpening of the shoulder centered at 689  $\text{cm}^{-1}$ . It is worth noting that although the changes in the spectra that occurred as a result of holding the potential at -400 mV for 24 hrs. were somewhat subtle, they were reproducible. That is, a shoulder appeared in the range of 600-700  $\text{cm}^{-1}$  and intensity was lost in the range of 200-400  $\text{cm}^{-1}$  during 24 hr. hold-time at -400mV and when the potential was stepped to 0 mV the changes were reversed. Similarly, if the potential was first stepped from -900 mV to 0mV and then decreased to -400 mV and held for 24 hrs. the same results occurred. In assigning the spectral features to particular constituents in the passive film it is first noted in Table III that the lowest energy vibrational mode of the carbonate ion ( $\text{D}_{3h}$ ) occurs at 680  $\text{cm}^{-1}$  for an E mode and that when the carbonate ion is bonded in the bidentate configuration the E mode is split into an  $\text{A}_1$  mode at  $\approx 770 \text{ cm}^{-1}$  and a  $\text{B}_2$  mode at  $\approx 670 \text{ cm}^{-1}$ . Depending on the orientation of the carbonate ion on the surface of the film, the surface enhancement factor for the  $\text{A}_1$  mode will be at least equal to and probably greater than that of the  $\text{B}_2$  mode.<sup>8</sup> Since the more intense  $\text{A}_1$  mode does not appear in the spectrum, it is unlikely that the shoulder in the range of 600-700  $\text{cm}^{-1}$  is caused by the  $\text{B}_2$  mode. Thus, it is unlikely that the shoulder in the range of 600-700  $\text{cm}^{-1}$  is indicative of the presence of carbonate ion either in or on the surface of the passive film. Furthermore, the appearance of the shoulder in the range 600-700  $\text{cm}^{-1}$  appears to coincide with a loss of intensity in the range of 200-400  $\text{cm}^{-1}$  and it does seem likely that the same component in (or on the surface of) the film is responsible for both features. Since increased time at -400 mV drives these spectral changes it seems that they might be associated with further oxidation of  $\text{Fe}(\text{OH})_2$ , however, since these changes are reversed by stepping to a higher potential (0 mV), this explanation also seems unlikely. Consequently, it is not possible at this time to account for these changes. Comparing the spectrum of the passive film formed in carbonate at 0 mV to that in nitrate at +100 mV indicates that the shoulder that is centered at 689  $\text{cm}^{-1}$  in the carbonate spectrum (note: this shoulder is distinct from the feature that forms during 24 hr.-long hold-times at -400 mV) is a little lower in intensity than that in the nitrate solution. Otherwise the 2 spectra are fairly similar: both consist of a strong peak at  $\approx 550 \text{ cm}^{-1}$ , both have a shoulder centered at 670-690  $\text{cm}^{-1}$  and both contain a number of low intensity, overlapping peaks in the range of 300-480  $\text{cm}^{-1}$ . The lower intensities of the spectra in the carbonate solution compared to those in the nitrate suggests that the films are thinner in the carbonate solution. In summary, the passive film that forms on iron in 0.15M  $\text{Na}_2\text{CO}_3$  + 0.15M  $\text{NaHCO}_3$  is thought to consist of  $\text{Fe}(\text{OH})_2$  + ( $\text{Fe}_3\text{O}_4$  and/or  $\gamma\text{-Fe}_2\text{O}_3$ ).

As shown in figure 3 the spectra of the passive films formed on iron in 0.3M  $\text{Na}_2\text{SO}_4$  (pH 10) are very similar to those measured in 0.3M  $\text{NaNO}_3$ . The only differences are the higher intensity of the peak assigned to  $\text{Fe}(\text{OH})_2$  and the presence of a sharp peak at 978  $\text{cm}^{-1}$  which, based on the information presented in Table IV is assigned to the  $\text{A}_1$  symmetric stretching vibration of the sulfate ion (point group  $\text{T}_d$ ). In a separate investigation the SER spectra of the passive films formed on iron in 0.3M  $\text{Na}_2\text{SO}_4$  at pH 10 and pH 5 are analyzed in detail and compared to calculated spectra.<sup>11</sup> the results are the same as reported here but there is greater support provided for the peak assignments. It is concluded that the passive films formed on iron in the sulfate solution at pH 10 consist of  $\text{Fe}(\text{OH})_2$  + ( $\text{Fe}_3\text{O}_4$  and/or  $\gamma\text{-Fe}_2\text{O}_3$ ) + sulfate ions adsorbed on the surface.

The most distinctive difference between the spectra of the passive films formed on iron in  $M K_2HPO_4 + 0.02M KH_2PO_4$  and the spectra obtained in all the other solutions is the absence of a strong peak at  $\approx 550\text{ cm}^{-1}$  in the phosphate solution. As shown in figure 4a, there are several weak peaks in the range of  $640\text{--}720\text{ cm}^{-1}$ . The Raman spectra of various orthophosphates are listed in Table V and it seems unlikely their vibrational modes are the source of these peaks. Based on the Raman spectra listed in Table I for various oxides, etc. of iron, these peaks are tentatively assigned to  $Fe_3O_4$  and/or  $\gamma\text{-Fe}_2O_3$ . Although the SER spectra of these 2 species is expected to contain several peaks in the range of  $300\text{--}560\text{ cm}^{-1}$ , these will be of lower intensity than the peaks in the range of  $600\text{--}700\text{ cm}^{-1}$  and hence it is clear that additional species must be present in the film to account for the relatively high scattered intensity in the range of  $400\text{--}600\text{ cm}^{-1}$ . Examining the list of peaks found in the Raman spectra of the orthophosphates presented in Table V indicates that the degeneracy of the  $T_2$  mode of phosphate is removed in the mono- and di-hydrogen phosphates present in solids. These vibrational modes along with the E modes which occur in the range of  $380\text{--}461\text{ cm}^{-1}$  are tentatively identified as the source of the scattered radiation in the range of  $360\text{--}600\text{ cm}^{-1}$  in the spectra obtained at  $-400\text{ mV}$  and  $+100\text{ mV}$ . In addition, there appears to be a large number of relatively weak and overlapping peaks in the range of  $\approx 900\text{--}1180\text{ cm}^{-1}$  in all 3 spectra obtained in phosphate. These are ascribed to a variety of modes including  $A_2$  ( $\approx 880\text{ cm}^{-1}$ ),  $A_1$  symmetric stretching of phosphate and mono- and di- hydrogen phosphate ( $936\text{--}1069\text{ cm}^{-1}$ ), and the triply degenerate  $T_2$  mode of phosphate ( $1014\text{ cm}^{-1}$ ) and its correlated non-degenerate modes that occur in mono- and di- hydrogen phosphate ( $1068\text{--}1150\text{ cm}^{-1}$ ). Succinctly stated, the passive films formed on iron in buffered phosphate (pH 8.3) appear to consist predominantly of iron orthophosphates with some evidence for the presence of  $Fe_3O_4$  and/or  $\gamma\text{-Fe}_2O_3$ . In comparison to the passive films formed on iron in the other aqueous solutions, those formed in the phosphate solution were also distinguished by their lack of a significant quantity of  $Fe(OH)_2$ .

In some respects the spectra from the passive films formed on iron in  $0.3M Na_2SO_4$  (pH 5) are the most interesting. Based on the peak assignments applied to the spectra of the films formed in the solutions discussed above, the strong peak that is centered at  $\approx 550\text{ cm}^{-1}$  in the 3 spectra presented in figure 5 is identified as the  $A_1$  mode of  $Fe(OH)_2$ . Since potentials of  $-700\text{ mV}$  and  $-500\text{ mV}$  are below the passivation potential of  $-300\text{ mV}$  it is clear that films form on the electrode at potentials in the active region. A somewhat sharp peak centered at  $\approx 980\text{ cm}^{-1}$  appears in each of the spectra and its intensity increases with applied potential. Consistent with the assignment of this peak in the spectra obtained in the sulfate solution at pH 10, the peak at  $\approx 980\text{ cm}^{-1}$  is associated with sulfate ( $T_d$ ) that is adsorbed onto the surface of the films. A broad, asymmetric peak with its maximum at  $\approx 865\text{ cm}^{-1}$  is also present in each of the spectra and, like the peak at  $980\text{ cm}^{-1}$ , its intensity also increases with applied potential. As discussed in detail elsewhere, this peak is assigned to the symmetric stretch mode of sulfate which is covalently bonded in the bidentate configuration to iron in the passive film. In this bonding arrangement the sulfate ion now belongs to the point group  $C_{2v}$ . In this arrangement the triple degeneracy of the  $T_2$  mode of  $T_d$  sulfate is completely broken and 3 peaks are formed in the range of  $593\text{--}704\text{ cm}^{-1}$  as is listed in the Table IV. These peaks are responsible, in part, for the large asymmetry in the peak in figure 5c with its maximum at  $\approx 550\text{ cm}^{-1}$ . Detailed analyses shows that these 3 peaks can not completely account for all of the scattered radiation that occurs in the range of  $590\text{--}700$

$\text{cm}^{-1}$  and therefore it is also suggested that there is also a mixture of  $\text{Fe}_3\text{O}_4$  and  $\gamma\text{-Fe}_2\text{O}_3$  in the film as well.<sup>11</sup> These 2 constituents can also account for the number of low intensity, overlapping peaks that appear in the spectrum from 300–480  $\text{cm}^{-1}$ . In summary, the passive film formed on iron in sulfate at pH 5 consists of  $\text{Fe}(\text{OH})_2$  + ( $\text{Fe}_3\text{O}_4$  and/or  $\gamma\text{-Fe}_2\text{O}_3$ ) + bidentate sulfate ( $\text{C}_{2v}$ ) covalently bonded to iron in the film + sulfate ( $\text{T}_d$ ) adsorbed on the surface of the passive film.

### Summary

The surface enhanced Raman (SER) spectra were measured for the passive films formed on iron in 0.3M  $\text{NaNO}_3$  (pH 10), 0.15M  $\text{Na}_2\text{CO}_3$  + 0.15M  $\text{NaHCO}_3$ , 0.3M  $\text{Na}_2\text{SO}_4$  (pH10), M  $\text{K}_2\text{HPO}_4$  + 0.02M  $\text{KH}_2\text{PO}_4$ , and 0.3M  $\text{Na}_2\text{SO}_4$  (pH 5). In the nitrate, carbonate, and sulfate (pH 10) solutions the passive films consisted of  $\text{Fe}(\text{OH})_2$  + ( $\text{Fe}_3\text{O}_4$  and/or  $\gamma\text{-Fe}_2\text{O}_3$ ). There was no evidence of adsorption of either nitrate or carbonate ions on the passive film but this can not be stated too strongly since the spectra did not include the regions where the most intense modes for both nitrate and carbonate are located. Sulfate ions were found to adsorb on the surface of the passive film. The passive films formed on iron in the phosphate solution were markedly different from the films formed in the other solutions. In the phosphate solution,  $\text{Fe}(\text{OH})_2$  was only weakly present, if at all. In addition, the complex spectra appeared to contain either phosphate in the bidentate  $\text{C}_{2v}$  configuration and/or several other orthophosphates which because of their lower symmetries would also have a large number of peaks in the ranges of 400–600  $\text{cm}^{-1}$  and 900–1100  $\text{cm}^{-1}$ . Finally, the passive film formed on iron in the sulfate solution at pH 5 was distinguished by the presence of sulfate ions in the bidentate configuration ( $\text{C}_{2v}$ ) that were covalently bonded to iron in the passive film. The incorporation of sulfate into the passive film is apparently dependent on pH since it occurred in films formed in 0.3M  $\text{Na}_2\text{SO}_4$  with pH 5 but not with pH 10.

### Acknowledgements

It is a pleasure to thank the Electric Power Research Institute of Palo Alto, CA, and in particular, Dr. Wylie Childs for their financial support and interest in this research.

### References

1. J.C. Rubim and J. Dunnwald, *J. Electroanal. Chem.*, **258**, 327 (1989).
2. J. Gui and T.M. Devine, *Corrosion Science*, **32**, 1105–1124 (1991).
3. J. Gui and T.M. Devine, *J. Electrochem. Soc.*, **138**, 1376–1384 (1991).
4. C.A. Melendres and M. Pankuch, *J. Electroanal. Chem.*, **333**, 103–113 (1992).
5. C.A. Melendres, M. Pankuch, Y.S. Li and R.L. Knight, *Electrochimica Acta*, **37**, 2747–2754 (1992).
6. C.A. Melendres and M. Ferr, *J. Electrochem. Soc.*,
- 7 J. Gui and T.M. Devine, *Corrosion '91*, Cincinnati, paper#, National Association of Corrosion Engineers, Houston, TX (1991).
8. J.A Creighton, *Corrosion Science*, **124**, 209–219 (1983).
9. M. Moskovits and J.S. Suh, *J. Phys. Chem.*, **88**, 5526–5530 (1989).
10. E.B. Wilson, J.C. Decius and P.C. Cross, "Molecular Vibrations," Dover Publications Inc., NY (1980).

11. J. Gui and T.M. Devine, "Surface Enhanced Raman Spectra of Passive Films Formed on Iron in Aqueous Sulfate Solutions," submitted for publication in Corrosion Science.
12. G. Nauer, P. Strecha, N. Brinda-Konopik, and G. Liptay, J. Thermal Anal., **30**, 813 (1985).
13. I.C.G. Thanos, Electrochim. Acta, **31**, 811 (1986).
14. J. Dunnwald and A. Otto, Corros. Sci., **29**, 1167 (1989).
15. I.R. Beatties and T.R. Gilson, J. Chem. Soc., A, 980 (1970).
16. T. Ohtsuka, K. Kudo and N. Sato, Corros., **42**, 476 (1986).
17. J.L. Verble, Physical Review B, **9**, 5236-5248 (1974).
18. K. Nakamoto, J. Fujita, S. Tanaka and M. Kobayashi, J. Am. Chem. Soc., **79**, 4904 (1957).
19. G. Hertzberg, "Infrared and Raman Spectra of Polyatomic Molecules," p.178, D. Van Nostrand Co., NY (1945).
20. B.M. Gatehouse, S.E. Livingstone and R.S. Nyholm, J. Chem. Soc., p.4222 (1957).
21. J.R. Ferraro and A. Walker, J. Chem. Phys., **42**, 1278 (1965)
22. K. Nakamoto, "Infrared and Raman Spectra of Inorganic and Coordination Compounds," 4th ed., p.255, John Wiley & Sons (1986).
23. R.W. Horn, E. Weissberger and J.P. Collman, Inorg. Chem., **9**, 2367 (1970).
24. J.R. Ferraro and A. Walker, J. Chem. Phys., **42**, 1278 (1965)
25. T.J. Hanwick and P. Hoffman, J. Chem. Phys., **17**, 1166 (1949).
26. A.C. Chapman and L.E. Thirlwell, Spectrochim. Acta., **20**, 937 (1964).

Table I

Locations of Peaks in the Raman Spectra of Selected Iron Oxides, Hydroxides and Oxyhydroxides ( $\text{cm}^{-1}$ )<sup>12-17</sup>

The  $A_1$  modes and other lines of high intensity are underlined.

$\beta$ -FeOOH	330	415	<u>745</u>						
$\gamma$ -FeOOH	<u>255</u>	380	528	654	1054	<u>1307</u>			
$\delta$ -FeOOH	663 (broad)								
Fe(OH) <sub>2</sub>	460	<u>550</u>							
Fe(OH) <sub>3</sub>				692 (broad)					
$\alpha$ -Fe <sub>2</sub> O <sub>3</sub>	<u>225</u>	245	<u>295</u>	415	500	615	1320		
$\gamma$ -Fe <sub>2</sub> O <sub>3</sub>	265	300	345	395	515	<u>645</u>	<u>670</u>	<u>715</u>	1440
Fe <sub>3</sub> O <sub>4</sub>	300	320	420	560	<u>680</u>				

Table II

Locations of Vibrational Modes ( $\text{cm}^{-1}$ ) of Nitrate and Nitrate Complexes<sup>18-20</sup>

Symmetry (D <sub>3h</sub> )	A <sub>1</sub> '	[A <sub>2</sub> ]	E'	E'
Carbonate (D <sub>3h</sub> )	1063*	879**	1415**	680**
Symmetry (C <sub>2v</sub> )	A <sub>1</sub>	B <sub>2</sub>	A <sub>1</sub> - B <sub>2</sub>	A <sub>1</sub> - B <sub>2</sub>
Carbonate (C <sub>2v</sub> )*	1060	840	1370-1480	770-670

Note: A<sub>2</sub>' is Raman Inactive

**Table III**  
Locations of Vibrational Modes ( $\text{cm}^{-1}$ ) of Carbonato and Nitrate Complexes<sup>21,22</sup>

Symmetry ( $D_{3h}$ )	$A_1'$	$A_2'$	$E'$	$E'$
Nitrate ( $D_{3h}$ ) <sup>o</sup>	1050	831	1390	720
Symmetry ( $C_{2v}$ )	$A_1$	$B_2$	$A_1 - B_2$	$A_1 - B_2$
Nitrate ( $C_{2v}$ ) <sup>o</sup>	1020	800	1300-1425	760

**Table IV**  
Locations of Vibrational Modes ( $\text{cm}^{-1}$ ) of Sulfate and Sulfato Complexes<sup>23,24</sup>

Symmetry ( $T_d$ )	$A_1$	$E$	$T_2$	$T_2$
Sulfate (free ion)	983	454	1140	613
Symmetry ( $C_{3v}$ )	996-970	438	1140-1100	645
Unidentate			1050-1030	604-632
Symmetry ( $C_{2v}$ )	996-752	549-515	1400-1211	704-645
Bidentate			1200-1125	604-632
			1075-875	598-593

**Table V**  
Locations of Vibrational Modes ( $\text{cm}^{-1}$ ) of Orthophosphates<sup>25,26</sup>

Symmetry ( $T_d$ )	$A_1$	$E$	$T_2$	$T_2$	$A_2$
Phosphate ( $T_d$ ) <sup>3</sup> ( $K_3PO_4$ )	936	420	1014	573	--
<hr/>					
Aq. $K_2HPO_4$	976	394	1081	537	865
Sol. $Na_2HPO_4$	948	461	1150 1388 1068 1352	590 860 570 547 520	
Aq. $KH_2PO_4$	1069	380			880
Sol. $NaH_2PO_4$	1053	422	1166 1280 1120 1240 1098	567 820 540 527 510	

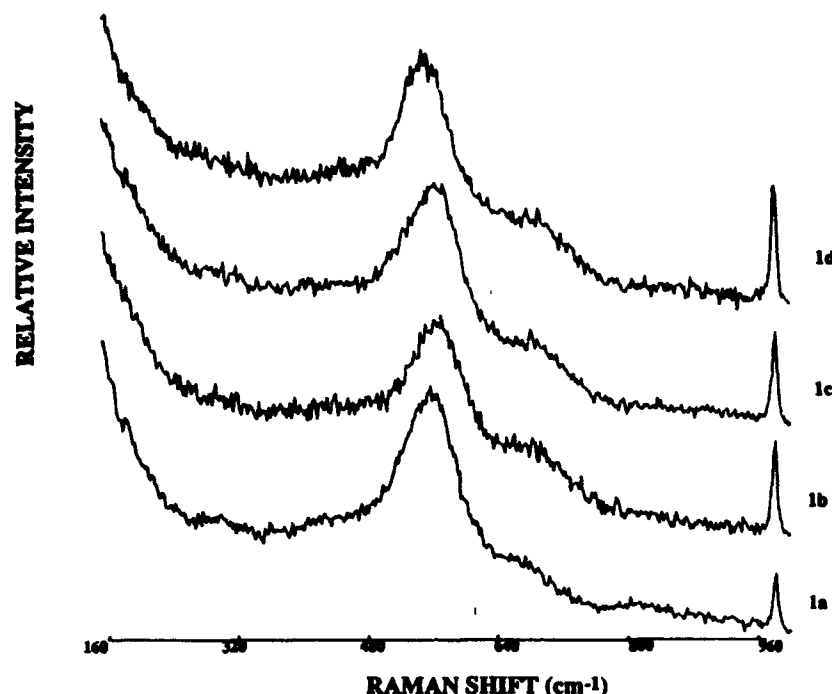


Figure 1. *In situ* surface enhanced Raman spectra of passive films on iron in 0.3M  $\text{NaNO}_3$  (pH 10.0). (a) sample was polarized to  $-0.9\text{V}(\text{SCE})/10$  min. and then the potential was stepped to  $-0.4\text{V}(\text{SCE})$  and the SER spectrum was obtained; (b) potential was held at  $-0.4\text{V}$  for 24 hrs. and then the spectrum was measured; (c) potential was stepped from  $-0.4\text{V}(\text{SCE})$  to  $+0.1\text{V}(\text{SCE})$  and the SER spectrum was measured; (d) potential was stepped from  $+0.1\text{V}$  to  $-0.9\text{V}$  and held at  $-0.9\text{V}$  for 10 min. then the potential was stepped to  $+0.1\text{V}$  and the spectrum was measured.

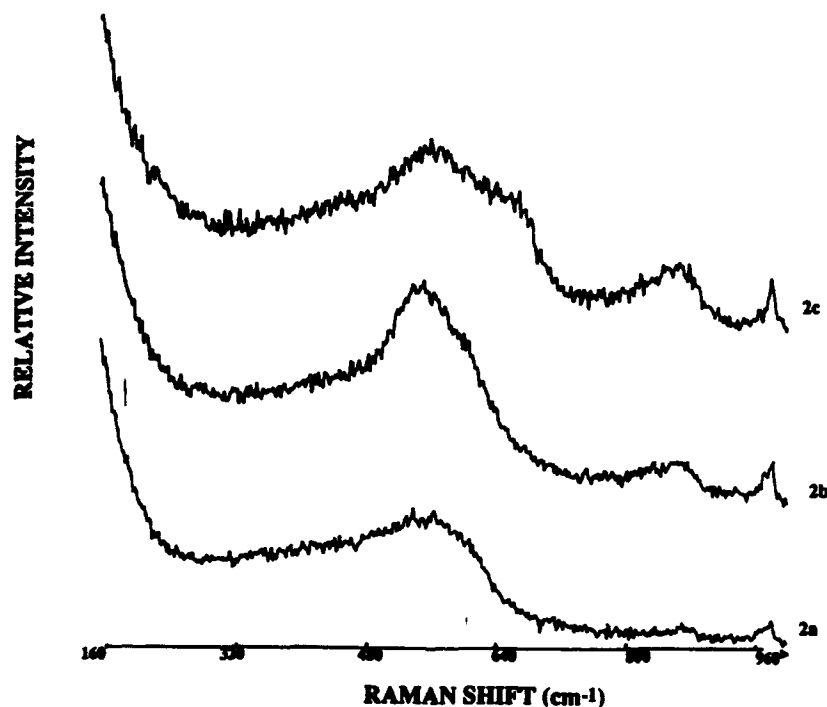


Figure 2. *In situ* surface enhanced Raman spectra of passive films on iron in 0.15M  $\text{Na}_2\text{CO}_3 + 0.15\text{M NaHCO}_3$  (pH 10.0). (a) sample was polarized to  $-0.9\text{V}(\text{SCE})/10$  min. and then the potential was stepped to  $-0.4\text{V}(\text{SCE})$  and the SER spectrum was obtained; (b) potential was held at  $-0.4\text{V}$  for 24 hrs. and then the spectrum was measured; (c) potential was stepped from  $-0.4\text{V}(\text{SCE})$  to  $0\text{V}(\text{SCE})$  and the SER spectrum was measured; (d) potential was held at  $0\text{V}$  for 24 hrs. and then the spectrum was measured; (e) potential was stepped from  $0\text{V}(\text{SCE})$  to  $-0.4\text{V}(\text{SCE})$  and the SER spectrum was measured; (f) potential was held at  $-0.4\text{V}$  for 24 hrs. and then the spectrum was measured;

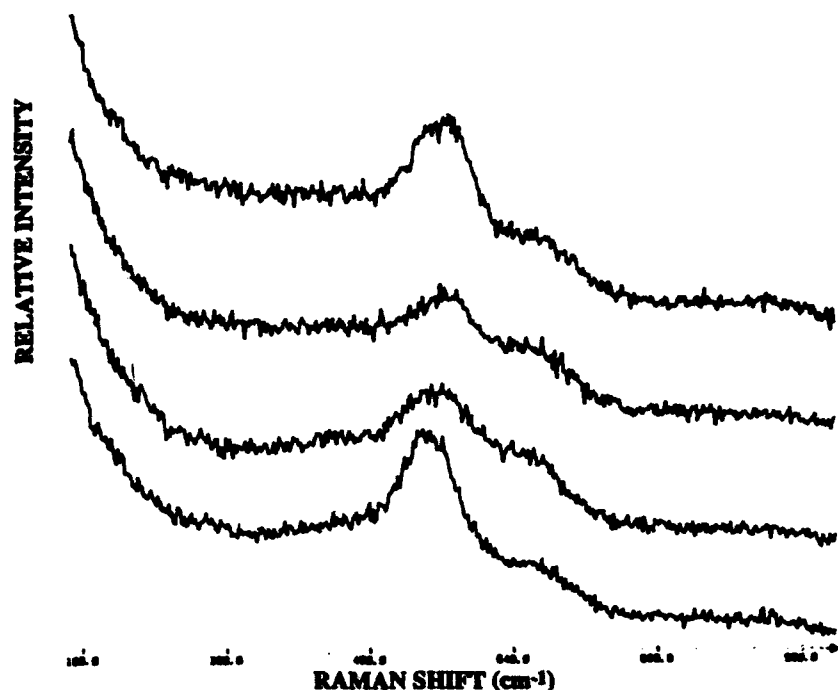


Figure 3. *In situ* surface enhanced Raman spectra of passive films on iron in 0.3M  $\text{Na}_2\text{SO}_4$  (pH 10.0). (a) sample was polarized to  $-0.9\text{V}(\text{SCE})/10$  min. and then the potential was stepped to  $-0.4\text{V}(\text{SCE})$  and the SER spectrum was obtained; (b) potential was stepped from  $-0.4\text{V}(\text{SCE})$  to  $0\text{V}(\text{SCE})$  and the SER spectrum was measured; (c) potential of sample was stepped from  $0\text{V}$  to  $-0.9\text{V}$  and sample was polarized at  $-0.9\text{V}(\text{SCE})/10$  min. and then the potential was stepped to  $0\text{V}(\text{SCE})$  and the SER spectrum was obtained; (d) potential was stepped from  $0\text{V}(\text{SCE})$  to  $-0.4\text{V}(\text{SCE})$  and the SER spectrum was measured.

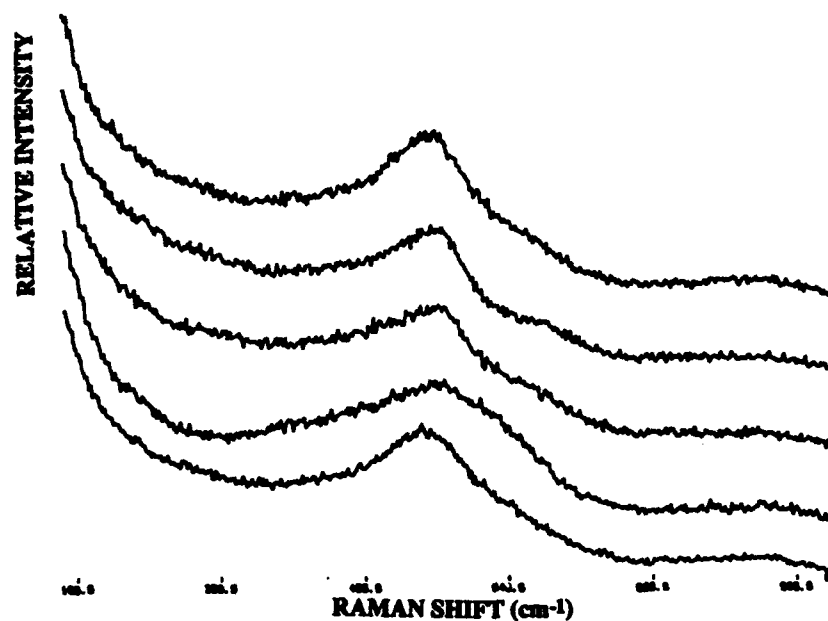


Figure 4. *In situ* surface enhanced Raman spectra of passive films on iron in  $0.02\text{M K}_2\text{HPO}_4 + 0.02\text{M KH}_2\text{PO}_4$  (pH 8.3). (a) sample was polarized to  $-0.9\text{V}(\text{SCE})/10$  min. and then the potential was stepped to  $-0.4\text{V}(\text{SCE})$  and the SER spectrum was obtained; (b) potential was held at  $-0.4\text{V}$  for 24 hrs. and then the spectrum was measured; (c) potential was stepped from  $-0.4\text{V}(\text{SCE})$  to  $+0.1\text{V}(\text{SCE})$  and the SER spectrum was measured.





Figure 5. *In situ* surface enhanced Raman spectra of passive films on iron in 0.3M  $\text{Na}_2\text{SO}_4$  (pH 5.0). (a) sample was polarized to -0.9V(SCE)/10 min. and then the potential was stepped to -0.7V(SCE) and the SER spectrum was obtained; (b) potential was stepped from -0.7V(SCE) to -0.5V(SCE) and the SER spectrum was measured; (c) the potential was stepped from -0.5V(SCE) to -0.1V(SCE) and the SER spectrum was obtained.

## Vacancy Condensation as the Precursor to Passivity Breakdown

Digby D. Macdonald  
Center for Advanced Materials  
The Pennsylvania State University  
517 Deike Building  
University Park, PA 16802

### Abstract

This paper outlines the events that are envisaged to occur, according to the Point Defect Model (PDM), during "chemically-induced" breakdown of the barrier layer on passivated metals and alloys in aqueous environments. The essential hypothesis of the model is that the local generation of cation vacancies at the barrier layer/environment interface, due to the autocatalytic adsorption of a damaging species such as chloride ion into the oxygen vacancy structure, leads to an enhanced flux of cation vacancies across the film. If the vacancies that arrive at the metal/film interface cannot be annihilated by cation ejection from the metal, the vacancies will condense leading to the local decohesion of the barrier layer from the metal. A combination of film dissolution at the barrier layer/environment interface and residual stresses in the oxide film leads to the physical rupture of the film, marking a passivity breakdown event. The PDM accounts for a variety of empirically-established relationships for the nucleation of pits, including the fact that the breakdown voltage ( $V_c$ ) and induction time ( $t_{ind}$ ) are distributed quantities; that  $V_c = V_c^0 - b \log(a_{Cl^-})$ , where  $b > 2.303RT/F$ ; and that  $\log(t_{ind}) \propto 1/\Delta V$ , where  $\Delta V = V$  (applied voltage) -  $V_c$ . Also, the model has been extended to account for alloying effects and, indeed, new alloys are now being designed on the basis of rules that have been derived from the PDM.

### Introduction

Passivity breakdown is the necessary precursor to localized corrosion of industrially-important metals and alloys. While extensive research has been carried out to ascertain the fundamental aspects of the breakdown phenomenon<sup>1-5</sup>, no universally accepted mechanism has been devised. In this paper, the events that occur within the barrier layer leading to "chemically-induced" breakdown, as envisaged in the Point Defect Model (PDM) and the Solute-Vacancy Interaction Model (SVIM)<sup>6-14</sup>, are reviewed. We show that the PDM and SVIM are able to account for many of the phenomenological aspects of passivity breakdown and that they lead to a set of rules for designing alloys of enhanced passivity. To our knowledge, these rules represent the first theoretically-inspired procedure for designing new, pitting-resistant alloy systems.

### Passivity Breakdown and Pit Nucleation

#### Structure of Passive Films

The bulk of the experimental evidence indicates that passive films, which form on metals and alloys in contact with aqueous environments, consist of at least two layers, as depicted in Figure 1. The inner or "barrier" layer forms by movement of the metal/film interface into the metal phase, due to the inward movement of oxygen via the outward movement of oxygen vacancies<sup>1</sup>. On the other hand, the outer layer forms by the hydrolysis of cations ejected from the barrier layer at the film/solution interface. Because the barrier layer forms by a solid-state reaction, it is expected to consist of a disordered oxide containing both anion (oxygen) and cation (metal) vacancies, the relative concentrations of which depend on the thermodynamics of vacancy formation and on the kinetics of the vacancy generation and the annihilation reactions (Figure 2).

**Key terms:** vacancy condensation, passivity breakdown, pitting corrosion, alloy design

Assuming that ions from the environment cannot readily enter the barrier layer via the oxygen vacancy structure, one would not expect the barrier layer to incorporate species from the solution. On the other hand, the outer layer can readily incorporate ions from the environment via coprecipitation, so that the oxide, oxyhydroxide, or hydroxide that comprises the outer layer is expected to contain extraneous species from the environment. This is perhaps best seen in the case of aluminum when anodized in borate buffer solutions, where borate ions are found to be incorporated into the outer layer but are absent from the inner layer<sup>15</sup>.

**Pitting Corrosion.** The best known causative agent of "chemically-induced breakdown" is chloride ion, which shows a remarkable ability to cause pitting on many metals and alloys of industrial interest<sup>16-18</sup>. Assuming that an ion, like chloride, must interact physically with the barrier layer to cause passivity breakdown, and hence to nucleate pits, it is of interest to explore, for the moment, how this might happen on an atomistic scale. Accordingly, it is necessary to envisage oneself as a hydrated chloride ion ( $\text{Cl}^- \cdot n\text{H}_2\text{O}$ ,  $n \approx 6$ ) approaching the film/solution interface of the barrier layer (after moving through the precipitated, outer layer). From this vantage point, the barrier layer appears as an undulating surface of charge with positive potentials occurring over cations and negative potentials over anions, with the difference between the peaks depending on the degree of covalent (vs. ionic) bonding in the lattice (the greater the extent of covalent bonding the lower the difference between peaks). Occasionally, however, the chloride ion will experience vacancies, with cation vacancies appearing as sites of high negative charge (corresponding to a formal charge of  $-Xe$ ) and oxygen vacancies appearing as sites of high positive charge (formally  $+2e$ ). Thus, the chloride ion is presented with a number of attractive sites to attack, but which will be favored? This is a very difficult question to answer unequivocally, because other processes must be considered. For example, a chloride ion could absorb into a surface oxygen vacancy, but this must be done at the expense of considerable dehydration. However, the high coordination afforded by neighboring ions is a positive factor (favoring absorption), although any expansion of the vacancy to accommodate the ion would be energetically costly. On the other hand, the anion could interact electrostatically with a positive center in the film surface represented by a surface cation; in this case, the interaction might be weaker (because of significant covalent bonding) but, because less dehydration is required in that the ion would not penetrate into the surface, the overall effect might favor absorption at a cation site. These two scenarios could lead to quite different mechanisms for localized attack.

In the first case (anion absorption into a surface oxygen vacancy), the film may respond in a number of different ways, as depicted in Figure 3. In one way (Case I), the system responds to the loss of oxygen vacancies by generating cation vacancy/oxygen vacancy pairs via a Schottky-pair type of reaction. The oxygen vacancies in turn react with additional anions (e.g. chloride) at the film/solution interface to generate yet more cation vacancies. Importantly, the generation of cation vacancies is autocatalytic, but whether or not the film breaks down depends on the relative rates with which the cation vacancies are transported across the barrier layer and are annihilated by emission of cations from the metal into the film. If this annihilation reaction is incapable of consuming the cation vacancies arriving at the metal/film interface, the excess vacancies will condense and lead to the local detachment of the film from the underlying metal, as depicted in Figure 4. Consequently, provided the local tensile stresses are sufficiently high and/or the film dissolves locally, the barrier layer will rupture, marking the initiation of a pit. The evidence for this mechanism is discussed elsewhere<sup>1</sup>.

This particular case was considered in detail by Lin et al<sup>6</sup>, who assumed that the enhanced flux of cation vacancies across the barrier layer could not be accommodated by Reaction (1) in Figure 2, thereby leading to the formation of a cation vacancy condensate. Once the condensate (Figure 4) has grown to a critical size, dissolution of the film at the film/solution interface and the tensile stresses in the barrier layer induce a mechanical or structural instability, resulting in rupture of

the film and hence in rapid localized attack. These ideas were assembled by Lin et al<sup>6</sup> to derive expressions for the critical breakdown voltage and induction time for a single breakdown site as

$$V_c = \frac{4.606RT}{\chi F \alpha} \log \left[ \frac{J_m}{J^0 u^{-\chi/2}} \right] - \frac{2.303RT}{\alpha F} \log (a_{X^-}) \quad (1)$$

and

$$t_{ind} = \xi' \left[ \exp \left( \frac{\chi F \alpha \Delta V}{2RT} \right) - 1 \right]^{-1} + \tau \quad (2)$$

where  $\Delta V$  is the breakdown overvoltage ( $\Delta V = V - V_c$ ),  $a_{X^-}$  is the activity of  $X^-$  in the solution,

$$\xi' = \xi / J^0 u^{-\chi/2} (a_{X^-})^{\chi/2} \exp \left( \frac{\chi \alpha F V_c}{2RT} \right) \quad (3)$$

and  $\xi$  is the critical areal concentration of cation vacancies at the metal/film interface. Other parameters are as defined in the original publication<sup>6</sup>. Equations (1) and (2) account for many of the phenomenological characteristics of pitting attack; (i) that the "pitting potential" ( $V_c$ ) varies linearly with  $\log(a_{X^-})$  with a slope greater than  $2.303RT/F$  (i.e.  $> 0.05916V/\text{decade}$  at  $25^\circ\text{C}$ ) because  $\alpha < 1$ , (ii) that  $\log(t_{ind}) \propto 1/\Delta V$  for sufficiently large overvoltages, and (iii) that  $t_{ind}$  is an inverse function of the activity of the aggressive anion.

In deriving Equations (1) and (2), we have assumed that the critical concentration of cation vacancies at breakdown ( $\xi$  mol. vacancies/cm<sup>2</sup>) is independent of the applied voltage and hence thickness of the barrier layer. This assumption was made because transmission of cation vacancies through the film can occur only as long as the film is attached to the base metal in order that the vacancies can be annihilated by Reaction (1), Figure 2 (see also Figure 4). Thus, growth of the condensate normal to the interface cannot occur once the film has separated from the substrate and, since separation occurs by condensation of a single layer of vacancies, our assumption of  $\xi \neq f(V, L)$  is justified.

**Distribution Functions.** On any real surface, a large number of potential breakdown sites exist corresponding to a distribution in the properties of the "weak spots". Perhaps the most graphic illustration of this property is the data of Shibata and co-workers<sup>19,20</sup>, who showed that the "pitting potential" is near normally distributed and that the induction time follows a distribution that is skewed towards short times. Assuming that the breakdown sites on a surface are normally distributed with respect to the cation vacancy diffusivity, we derived distribution functions for the breakdown voltage and induction time of the form<sup>10,11†</sup>

$$\frac{dN}{dV_c} = -\frac{\gamma D}{\sqrt{2\pi} \sigma_D} e^{-(D-\bar{D})^2/2\sigma_D^2} \quad (4)$$

and

$$\frac{dN}{dt_{ind}} = \left[ \frac{\xi u^{\chi/2}}{\sqrt{2\pi} \sigma_D \hat{a}} \right] e^{-(D-\bar{D})^2/2\sigma_D^2} \cdot \frac{e^{-\gamma V}}{a_x^{\chi/2} (t_{ind} - \tau)^2} \quad (5)$$

† Equations [6] and [7] are given in slightly different form in Refs. 10 and 11.

where  $\gamma = \alpha\chi F/2RT$ ,  $\sigma_D$  is the standard deviation for the diffusivity for the population of breakdown sites, and the other quantities are as previously defined<sup>10,11</sup>.

For comparison with experiment, we define the cumulative probability in the breakdown voltage and the differential cumulative probability in the induction time as

$$P(V_c) = 100 \int_{-\infty}^{V_c} \left( \frac{dN}{dV_c} \right) dV_c \quad (6)$$

and

$$\Delta N \Big|_{t_j}^{t_{j+1}} = \int_{t_j}^{t_{j+1}} \left( \frac{dN}{dt_{ind}} \right) dt_{ind} \quad (7)$$

The latter quantity is defined in this manner so that direct comparison can be made with experimental pitting induction time data, which are commonly presented as histograms of the number of pits nucleating in successive increments of time.

A fit of  $P(V_c)$  to the experimental data of Shibata et al<sup>19,20</sup> for pitting of Fe-17Cr in 3.5% NaCl solution at 30°C is shown in Figure 5. This fit was accomplished by adjusting groups of unknown or poorly-known parameters, which affect the location of  $P(V_c)$  on the potential axis but not the shape, such that the experimental and calculated distribution functions coincide for a mean diffusivity for cation vacancies of  $5 \times 10^{-20}$  cm<sup>2</sup>/s (this is approximately the value indicated by electrochemical impedance spectroscopy). Without adjusting any additional parameters, the distribution (histogram) in induction time is found to agree very well with the experimental data for the same system, as shown in Figure 6. It should be noted that the model described thus far does not consider the "death" or repassivation of pits; however, its omission is appropriate because, in Shibata's analyses, each specimen was taken out of the population once breakdown had occurred. We should also note that similar distributions in  $V_c$  and  $t_{ind}$  are obtained if we assume other distribution functions (e.g. the student-t and  $\chi^2$  distributions) for the breakdown sites with respect to cation vacancy diffusivity.

The analysis outlined above has permitted us to identify factors that make for "good passivity." Besides lowering the total number of potential breakdown sites per unit area of the surface, the parameter that may be manipulated to impact the susceptibility of a passive film to chemically-induced breakdown is the cation vacancy diffusivity. Thus, a decrease in the cation vacancy diffusivity results in an increase in the "pitting potential" (i.e.  $\bar{V}_c$ ), because a higher voltage is required to produce the same flux of cation vacancies across the barrier layer. Note that metals that have inherently low cation vacancy diffusivities (e.g. Ti, Zr, Ta) are quite resistant to pitting.

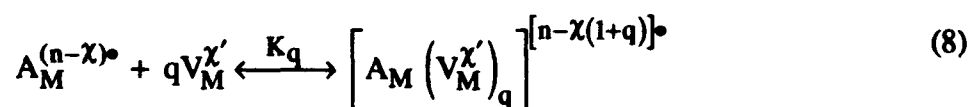
### The Theory of Alloys

The development of a successful theory for the effects of alloying on corrosion resistance would have an enormous impact on how alloys are designed, particularly if the theory is quantitative and, hence, deterministic. Significant progress has been made towards that goal with the development of the Solute-Vacancy Interaction Model (SVIM) by Urquidi-Macdonald and Macdonald<sup>1,13</sup> some years ago. Although this model has now been extended to account for the effects of alloying elements on the distributions in  $V_c$  and  $t_{ind}$ , it is currently limited to dilute binary alloys. Nevertheless, the SVIM has led to the derivation (to our knowledge) of the first theoretically-inspired set of rules for choosing an alloying element, as discussed later in this paper.

**Segregation of Alloying Elements.** In the analysis that follows, we assume that the alloying element is uniformly distributed throughout the metal phase. Accordingly, the reactions that occur within the metal/solution interphase (as depicted in Figures 1-3) lead to non-uniform distributions of the elements within the metal (but close to the interface), the barrier layer, and perhaps even in the precipitated outer layer normal to (but not laterally across) the surface. That alloying elements are segregated into the barrier layer (but not necessarily into the upper, precipitated layer) is shown unequivocally by the SALI (Surface Analysis by Laser Ionization) data presented in Figure 7<sup>21</sup>. These data show that, for a series of Ni-A alloys, with A = Al, Ti, and Mo, the extent of segregation of the alloying element into the barrier layer increases with increasing charge on the solute (i.e. Ni-Al < Ni-Ti < Ni-Mo, for which the solutes may be represented as  $\text{Al}_{\text{Ni}}^{\bullet}$ ,  $\text{Ti}_{\text{Ni}}^{2\bullet}$ , and  $\text{Mo}_{\text{Ni}}^{4\bullet}$ ). Furthermore, it is evident from the existence of the diffusion gradient of the alloying element in the alloy phase that segregation occurs via a solid state reaction at the metal/film interface, as discussed below. The greater segregation of more highly charged solutes into the barrier layer can be explained in terms of the more favorable free energy of these species in the high dielectric film (for example, experimental measurements indicate that the dielectric constant for the passive film on Cr is  $\approx 56$  whereas that on Type 304SS is 68-107, see citations in Ref. 11), compared with that for a less highly charged species.

Extensive work on the segregation of chromium into the passive films that form on Fe/Cr alloys in acidic and alkaline solutions has been reported by Strehblow and coworkers<sup>22-24</sup> and by others<sup>25-27</sup>. Using a combination of XPS (X-ray Photoelectron Spectroscopy) and ISS (Ion Scattering Spectroscopy), Strehblow et. al<sup>22-24</sup> found that the inner ("barrier") layers of the passive films formed on Fe-XCr (X = 5-20%) were substantially enriched in chromium, whereas the outer layers were enriched in Fe(III). For passive films formed under identical conditions (mechanical polishing followed by passivation in 0.5M  $\text{H}_2\text{SO}_4$  for 3 hours at 0.9 V vs. SHE) the segregation factor [ $S = (\text{X}_{\text{Cr}}^{\text{film}}/\text{X}_{\text{Fe}}^{\text{film}}) / (\text{X}_{\text{Cr}}^{\text{alloy}}/\text{X}_{\text{Fe}}^{\text{alloy}})$ ] decreases from  $\sim 14$  for the Fe-5Cr alloy to  $\sim 8$  for Fe-20Cr, as calculated from the data given in Figure 3 of Ref. 22. Furthermore, for passive films formed for 5 minutes on Fe-15Cr in 1M NaOH, the segregation factor was found to decrease slightly with increasing formation voltage, from  $\sim 3$  at  $-0.86\text{V}$  (SHE) to  $\sim 2.2$  at  $0.34\text{V}$  (SHE). A similar trend with formation voltage was found in our work<sup>21</sup> for the Ni-A (A=Al, Ti, Mo) alloys referred to above, although no clear trend in the segregation factor with concentration of A in the alloy could be discerned. A comprehensive theory for the segregation of alloying elements into the barrier layers formed on alloys, on polarization in aqueous systems, has yet to be developed, so that a quantitative interpretation of the findings discussed above is not possible. In the analysis that follows, we will accept segregation as an experimentally demonstrated phenomenon, with the caveat that it is not yet possible to calculate, on an *a priori* basis, the concentration of alloying element in the barrier layer from the composition of the alloy. Accordingly, all "compositions" referred to in the remainder of this paper will be those for the barrier layer.

**Solute-Vacancy Interaction Model.** Returning now to the role of alloying elements in passivity breakdown, we proposed<sup>12</sup> that the interaction between the substitutionally present (immobile) solute and mobile cation vacancies can be represented as a chemical equilibrium,



where  $n$  is the oxidation charge of the solute (e.g.  $+6$  for  $\text{Mo}^{6+}$ ), and  $K_q$  is the equilibrium constant. For 1:1 complexes, Urquidi-Macdonald and Macdonald<sup>11</sup> derived the modified vacancy diffusivity as

$$D^* = \frac{D}{2} \left[ 1 \mp \frac{(\hat{\alpha} - n_A)}{(\hat{\alpha}^2 - n_A n_V)^{1/2}} \right] \quad (9)$$

and a modified  $K^*$  ( $= \epsilon F/RT$ ) as

$$K^* = 2K \frac{\left[ 1 - \hat{\alpha} / n_V \mp (\hat{\alpha}^2 - n_A n_V)^{1/2} / n_V \right]}{\left[ 1 \mp (\hat{\alpha} - n_A) / (\hat{\alpha}^2 - n_A n_V)^{1/2} \right]} \quad (10)$$

where  $\hat{\alpha} = (n_A + n_V + K_1^{-1})/2$ , and  $n_A$  and  $n_V$  are the stoichiometric concentrations of the solute and cation vacancies in the film. By applying ion-pairing theory, as used in solution theory and in solid state physics, we can express the equilibrium constant,  $K_1$ , as

$$K_1 = \left[ 4\pi(t/kT)^3 \int_a^\infty e^{-\gamma} \gamma^2 d\gamma \right] \quad (11)$$

where  $a$  is the distance of closest approach,  $t = z_1 z_2 e^2 / \hat{\epsilon} \hat{\epsilon}_0$ ,  $z_1$  and  $z_2$  are the charges (including signs) on the interacting species,  $e$  is the electron charge,  $\hat{\epsilon}$  is the dielectric constant,  $\hat{\epsilon}_0$  is the permittivity of free space, and  $\gamma$  is the variable of integration. The equilibrium constant,  $K_1$ , needs to be corrected for screening by the mobile vacancies. This correction is expressed through Debye-Huckel theory as<sup>12</sup>

$$K_1^{\text{corr}} = K_1 f_A f_M \quad (12)$$

where  $f_A$  and  $f_M$  are activity coefficients given by

$$f_A = \exp \left\{ -\frac{e^2 z_2^2}{2\hat{\epsilon} \hat{\epsilon}_0 T \ell_D (1 + b' / \ell_D)} \right\} \quad (13)$$

and

$$f_M = \exp \left\{ -\frac{e^2 z_1^2}{2\hat{\epsilon} \hat{\epsilon}_0 kT \ell_D (1 + b' / \ell_D)} \right\} \quad (14)$$

The parameter  $\ell_D$  is the Debye length

$$\ell_D = \left\{ \frac{\hat{\epsilon} \hat{\epsilon}_0 kT}{e^2 4\pi [n_V z_1^2 + n_A z_2^2]} \right\}^{1/2} \quad (15)$$

and  $b'$  is the distance at which the coulombic interaction energy is equal to  $kT$  (the thermal energy)

$$b' = -\frac{z_1 z_2 e^2}{2\hat{\epsilon} \hat{\epsilon}_0 kT} \quad (16)$$

Although the SVIM is currently quite crude, in that it does not consider the complexing of more than one cation vacancy per solute and does not employ exponential distributions of vacancies across the film, the model is surprisingly successful in accounting for the effect of molybdenum, for example, on the pitting characteristics of stainless steel. Thus, by combining the SVIM with the distribution functions for passivity breakdown, we calculated  $P(V_c)$  as a function of molybdenum concentration in the alloy, assuming that the solute is in the +6 oxidation state (we have also considered the +4 state but it will not be discussed extensively here), and that preferential segregation of Mo into the barrier layer did not occur (i.e. the concentration of Mo in the barrier layer was assumed to be the same as that in the base alloy). The distribution functions are shown in Figure 8. In deriving these data, we selected model parameters so that the molybdenum-free case coincided with the experimental data of Shibata<sup>19,20</sup> for Fe-17Cr in 3.5% NaCl at 30°C; these parameters were then maintained constant for all molybdenum-containing alloys. Accordingly, as far as the latter are concerned, there are no arbitrarily adjustable parameters in the model.

The  $P(V_c)$  data plotted in Figure 8 predict that small additions of molybdenum (e.g. 1%) have only a modest impact on the pitting characteristics of stainless steel, but that additions of greater than 2% have a large impact. However, additions of more than 3% have incrementally smaller effects, at least for the parameter values chosen for these calculations. In this regard, it is interesting to note that experience has shown that 2 - 2 1/2% Mo is optimal for protecting Type 304SS against pitting in seawater systems with the modified alloy being the well-known Type 316SS. Perhaps a better test of the SVIM is afforded by the data plotted in Figure 9, where a comparison of  $\bar{V}_c$  (breakdown voltage at the 50th percentile) is made with experimental data from the literature. Although the experimental data do not display the sigmoid shape predicted by theory (and probably could not because of their limited precision), the agreement between experiment and theory is surprisingly good. Also shown is the prediction of the SVIM assuming that molybdenum is in the +4 state; clearly, the former ( $\text{Mo}^{6+}$ ) provides a better description of the experimental data than does the latter ( $\text{Mo}^{4+}$ ), although the actual oxidation state of molybdenum in the barrier layer on stainless steel has not been established unequivocally. The major impact of shifting  $P(V_c)$  in the positive direction is to greatly increase the induction time for passivity breakdown (i.e. the time required to accumulate a critical concentration of cation vacancies at the metal/film interface). Although we do not show the calculations here, this is precisely what is predicted by the model.

Other data also support the predictions of the model. For example, various studies<sup>3-5</sup> on supersaturated aluminum alloys of the type Al-A (A = 0-8 at/o Mo, Cr, Ta, W) have shown that elements such as molybdenum and, in particular, tungsten, can displace the critical potential for pitting in chloride solution in the positive direction by as much as 2500mV(4). Both elements form species in the +6 oxidation state, which should complex mobile  $V_{\text{Al}}^{3'}$  vacancies, although the extensive segregation of the alloying element into the barrier layer has not been demonstrated. However, in the presence of a thick outer layer (relative to the barrier layer), even when using a glancing radiation technique (e.g. EXAFS), as employed in those studies<sup>3-5</sup>, it is difficult to establish the extent of segregation into the barrier layer alone, and it is likely that techniques with much higher depth resolution, such as SALI, will be required to fully characterize the composition of the interfacial region.

## Alloy Design

What makes a good alloy? An answer to this question is of enormous scientific, technological, and economic importance, given that the annual cost of corrosion in any industrial society is about 4.5% of the GNP (about \$230 billion for the US in 1990). The work outlined above



provides clear guidance on this question and, recognizing that the models are still quite crude, we have formulated a set of principles to aid the alloy designer in devising new systems of superior resistance to passivity breakdown. The rules are as follows:

- (i) The alloying element must segregate into the barrier layer, preferably preferentially with respect to the host cation.
- (ii) The alloying element must exist in a "dissolved" (substitutional) state in the barrier layer in as high an oxidation state as possible, and certainly in an oxidation state that is higher than that of the host cation.
- (iii) The alloying element should be uniformly distributed throughout the layer or at least should not form a second phase that might introduce heterogeneities into the barrier layer that could act as sites for the nucleation of localized attack.

Other factors also affect the theoretical effectiveness of an active alloying element, according to the SVIM. For example, a decrease in the dielectric constant (Figure 10) and a decrease in the distance of the closest approach [Equation (13)] will both shift Reaction (8) to the right, signifying stronger interaction between the ionized alloying element ( $A_M^{(n-x)^+}$ ) and the mobile cation vacancies. However, neither of these parameters are readily manipulated, so that their optimization is not included in the rules outlined above.

We have tested these principles by measuring distribution functions,  $P(t_{ind})$ , for a series of Ni- $x$ Al, Ni- $x$ Ti, and Ni- $x$ Mo alloys ( $x = 0-8$  atomic %) in NaCl/borate buffer solutions at 25°C<sup>29</sup>. In these experiments, the specimens were held at a constant potential above the "pitting potential," and the number of pits nucleated on the surface were counted as a function of time. Although these experiments are complicated by the observation that existing active pits protect the remaining surface at radii that increase with time (and for this reason they have not yet been published), the data are in good qualitative agreement with the predictions of the model, in that the Ni-Mo alloys were the most resistant and the Ni-Al alloys were the least resistant to passivity breakdown, with the effect being roughly as expected from the charge on the solute (i.e. 4: 2: 1 for  $Mo_{Ni}^{4+} : Ti_{Ni}^{2+} : Al_{Ni}^{+}$ ).

#### Acknowledgements

The authors gratefully acknowledge the support of this work by the U.S. Department of Energy, Division of Basic Energy Sciences, under Grant No. DE-DG03-84ER45164.

#### References

1. D.D. Macdonald, J. Electrochem. Soc., **139**, 3434 (1992).
2. A.J. Sedriks, Corrosion of Stainless Steels, The Electrochemical Soc., Princeton, NJ (1979).
3. B.A. Shaw, G.D. Davis, T.L. Fritz, B.J. Rees, and W.C. Moshier, J. Electrochem. Soc., **138**, 3288 (1991).
4. G.D. Davis, W.C. Moshier, G.G. Long, and D.R. Black, J. Electrochem. Soc., **138**, 3194 (1991).
5. P.M. Natishan, E. McCafferty, and G.K. Hubler, J. Electrochem. Soc., **133**, 1061 (1986); **135**, 321 (1988).

6. C.-Y. Chao, L.-F. Lin, and D. D. Macdonald, *J. Electrochem. Soc.*, **128**, 1187 (1981); **128**, 11 (1981); **129**, 1874 (1982).
7. D. D. Macdonald and M. Urquidi-Macdonald, *J. Electrochem. Soc.*, **137**, 2395 (1990).
8. D. D. Macdonald, S. Biaggio, and H. Song, *J. Electrochem. Soc.*, **139**, 170 (1991).
9. D. D. Macdonald, S. I. Smedley, *Electrochim. Acta*, **35**, 1949 (1990).
10. D. D. Macdonald and M. Urquidi-Macdonald, *Electrochim. Acta*, **31**, 1070 (1986).
11. M. Urquidi-Macdonald and D. D. Macdonald, *J. Electrochem. Soc.*, **134**, 41 (1987).
12. M. Urquidi-Macdonald and D. D. Macdonald, *J. Electrochem. Soc.*, **136**, 961 (1989).
13. D. D. Macdonald and M. Urquidi, *J. Electrochemical Soc.*, **132**, 555 (1985).
14. S. Lenhart, M. Urquidi-Macdonald, and D. D. Macdonald, *Electrochim. Acta*, **32**, 1739 (1987).
15. G.C. Wood and J.P. O'Sullivan, *J. Electrochem. Soc.*, **116**, 1351 (1969).
16. "Passivity and Its Breakdown on Iron and Iron-Based Alloys," R. W. Staehle and H. Okada (Editors), NACE, Houston, TX (1976).
17. "Passivity of Metals and Semiconductors," M. Fromout (Editor), Elsevier, Amsterdam (1983).
18. "Passivity of Metals," R. P. Frankenthal and J. Kruger (Editors), the Electrochemical Society, Princeton, NJ (1978).
19. T. Shibata, *Trans. ISIJ*, **23**, 785 (1983).
20. T. Shibata and T. Takeyama, *Corrosion*, **33**, 243 (1977).
21. D.D. Macdonald, M. Ben-Hain, and J. Pallix, *J. Electrochem. Soc.*, **136**, 3269 (1989).
22. C. Calinski and H.-H. Strehblow, *J. Electrochem. Soc.*, **136**, 1328 (1989).
23. S. Haupt and H.-H. Strehblow, *Corr. Sci.*, **29**, 163 (1989).
24. S. Haupt, C. Calinski, U. Collisi, H.W. Hoppe, H.-D. Speckmann, and H.-H. Strehblow, *Surf. Interf. Anal.*, **9**, 357 (1986).
25. R.P. Frankenthal and D.L. Malm, *J. Electrochem. Soc.*, **123**, 186 (1976).
26. S. Storp and R. Holm, *Surf. Sci.*, **68**, 10 (1977).
27. K. Asami, K. Hashimoto, and S. Shimodaira, *Corr. Sci.*, **16**, 387 (1976).
28. E.A. Lizlovs and A.P. Bond, *J. Electrochem. Soc.*, **122**, 720 (1975).
29. D.D. Macdonald, C. English, and S.J. Lenhart, unpublished data (1985).

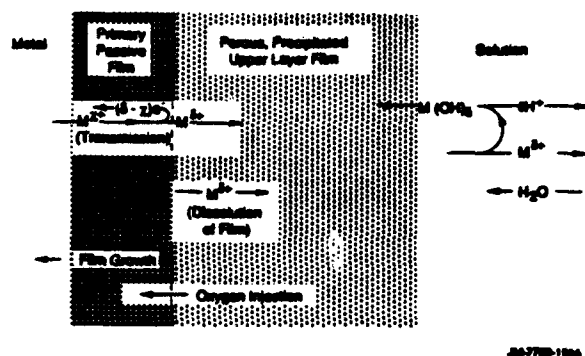


Figure 1. Schematic of processes that lead to the formation of bilayer passive films on metal surfaces.

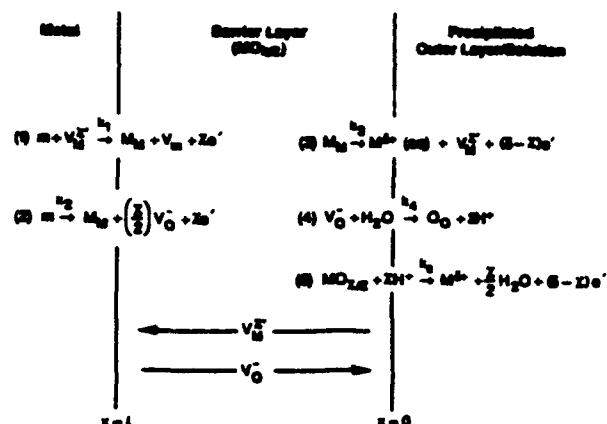


Figure 2. Schematic of physico-chemical processes that occur within the barrier layer according to the point defect model.

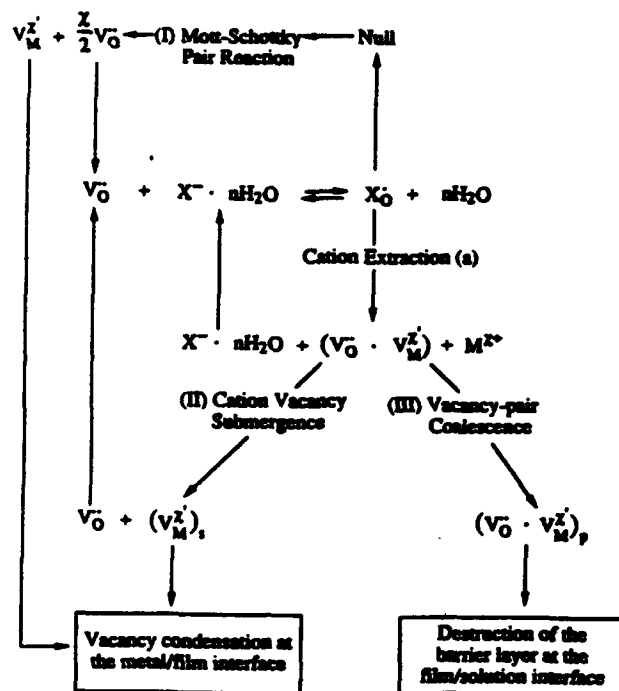


Figure 3. Summary of proposed reactions leading to passivity breakdown.

$m$  = metal atom,  $M_M$  = metal cation in cation site,  $O_O$  = oxygen ion in anion site,  $V_M^X$  = cation vacancy,  $V_O$  = anion vacancy,  $V_M$  = vacancy in metal phase.

During film growth, cation vacancies are produced at the film/solution interface, but are consumed at the metal/film interface. Likewise, anion vacancies are formed at the metal/film interface, but are consumed at the film/solution interface. Consequently, the fluxes of cation vacancies and anion vacancies are in the directions indicated. Note that Reactions [1], [3], and [4] are lattice conservative processes, whereas Reactions [2] and [5] are not.

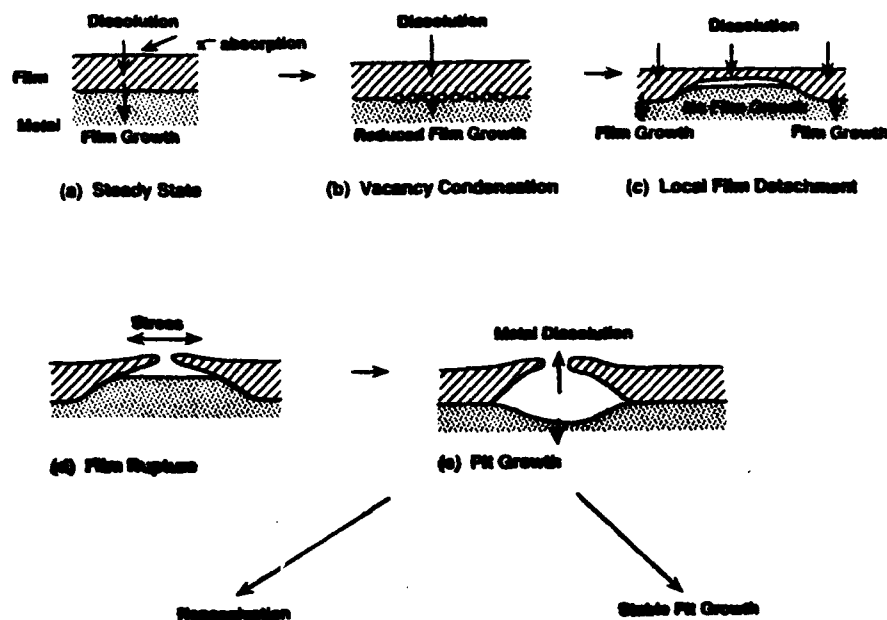


Figure 4. Cartoon outlining various stages of pit nucleation according to the Point Defect Model

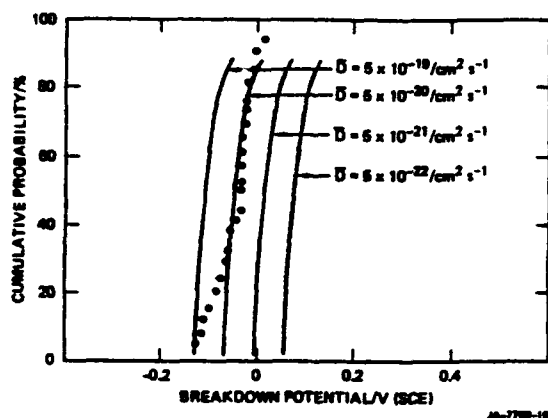


Figure 5. Cumulative probabilities for the breakdown voltage as a function of  $\bar{D}$  for normal distributions in the diffusivity  $D$ .

$\sigma_D = 0.75$ . \*Data for Fe-17Cr in 3.5% NaCl solution at 30°C from Shibata [19,20].  $\bar{V}_c = -0.046$  V (SCE).

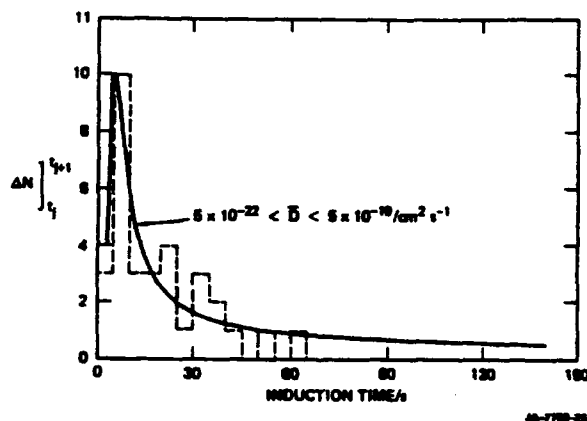


Figure 6. Differential cumulative probabilities for the induction time as a function of  $\bar{D}$  for normal distributions in  $D$ .

$\sigma_D = 0.75 \bar{D}$ . (—) Data for Fe-17Cr in 3.5% NaCl solution at 30°C from Shibata [19,20].  $\bar{V}_c = -0.046$  V (SCE),  $V = 0.020$  V (SCE),  $t = 7.5$  s,  $\tau = 0$ .

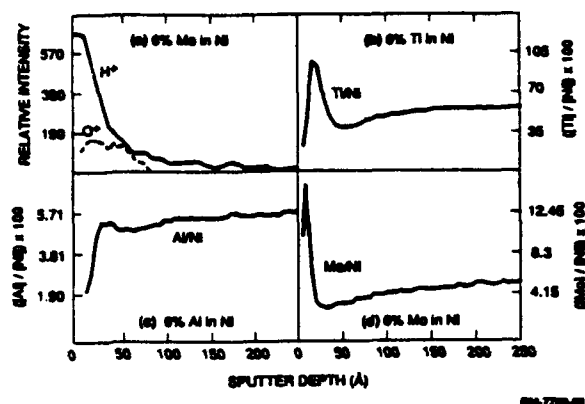


Figure 7. Concentration profiles of H, O, Al, Ti, and Mo in passive films formed on Ni-6% Al, Ni-6% Ti, and Ni-6% Mo in 0.1N H<sub>3</sub>PO<sub>4</sub>/NaOH, pH = 12, at 25°C as determined by surface analysis by laser ionization.  $V = 0.30V$  vs. SCE, growth time = 12 h (21).

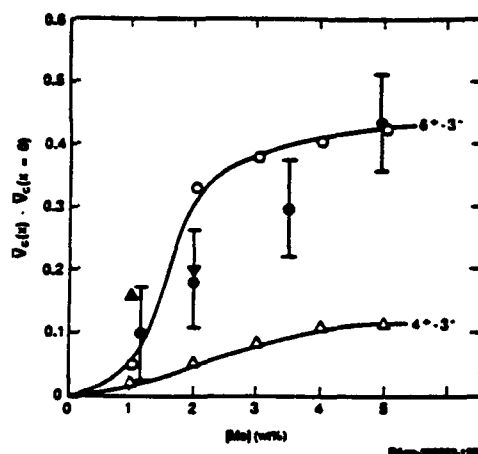


Figure 9. Effect of molybdenum concentration on  $V_c(x) - V_c(x=0)$  for  $6^{+}-3^{-}$  (O) and  $4^{+}-3^{-}$  (Δ) complexes in the film.

$n_V = 5 \times 10^{20} \text{ cm}^{-3}$ ,  $K_1 = 1.13 \times 10^{-16} \text{ cm}^3$  (O),  $K_1 = 9.05 \times 10^{-21} \text{ cm}^3$  (Δ).

- Lislovs and Bond [28]: Fe-18Cr in 1M NaCl at 25°C
- ▲ Shibata [19]: Fe-17Cr in 3.5% NaCl at 30°C
- ▼ Shibata [20]: Fe-18Cr in 3.5% NaCl at 30°C

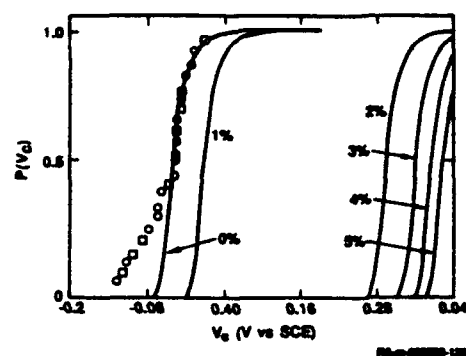


Figure 8. Effect of solute (Mo) concentration ( $n_{\text{Mo}} \cdot \text{wt}\%$ ) on the cumulative distribution function for  $V_c$  for a passive film containing  $6^{+}-3^{-}$  complexes.

$n_V = 5 \times 10^{20} \text{ cm}^{-3}$ ,  $K_1 = 1.13 \times 10^{-16} \text{ cm}^3$ . O, □ Data of Shibata [19,20] for Fe-17Cr in 3.5% NaCl at 30°C.

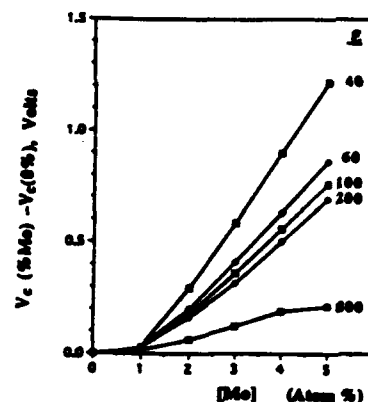


Figure 10. Calculated shift in the mean critical breakdown potential with molybdenum concentration in the barrier layer as a function of the dielectric constant.

$[\Omega = 30 \text{ cm}^3/\text{mol}$ ,  $\Delta G_{A-1} = -4 \times 10^4 \text{ J/mol}$ ,  $\phi_{f/s}^0 = -0.5V$ ,  $\Delta G_s^0 = -4 \times 10^4 \text{ J/mol}$ ,  $\tau = 0$ ,  $D = 5 \times 10^{-20} \text{ cm}^2/\text{s}$ ,  $n_V = 5 \times 10^{20} \text{ cm}^{-3}$ ,  $\epsilon = 1.1 \times 10^6 \text{ V/cm}$ ,  $T = 303.15 \text{ K}$ ,  $\alpha = 0.65$ ,  $\beta = -0.01$ ,  $\text{pH} = 7$ ,  $a_{X-} = 0.402$ ,  $\xi = 1.0 \times 10^{16} \text{ cm}^{-2}$ ,  $J_m = 1.587 \times 10^{13}/\text{cm}^2 \cdot \text{s}$ ,  $N_0 = 5000 \text{ cm}^{-2}$ ]

# Passivity of FeCr alloys

J.H.W. de Wit

Delft University of Technology

Materials Institute Delft

Division of Corrosion Technology, Electrochemistry and Spectroscopy Rotterdamseweg 137,  
2628 AL Delft, The Netherlands

## Abstract

The mechanism for breakdown of passive films on Fe-Cr alloys depends on many parameters including the composition of the alloy and the electrolyte, the existence of different phases in the alloy, stresses in the alloy, the composition and morphology of the film and the film potential during breakdown. The composition and the morphology of the passive film depend also on the mechanism of formation and therefore the history of the film, which in turn depends on the same parameters concerning the alloy and electrolyte. Moreover these parameters are often strongly interrelated.

After a summary of literature data and an overview of some models for the passive film, including a semiconductor model it is shown in this paper how impedance spectroscopy and cyclic voltammetry in conjunction with in situ ellipsometry give important information on the formation and the stability of the film. Together with XPS data and current transients, this information is shown to be useful for a more detailed description of the film properties, including mechanistic information on the initiation of localized corrosion phenomena. A preliminary semiconductor model for the passive film on Fe-Cr alloys is given.

Key terms: Passivity, FeCr alloys, Impedance Spectroscopy, Cyclic Voltammetry, Ellipsometry, XPS, Pitting, Semiconductor model.

## Introduction

### Electrodepotential and Passive Film Formation.

The passive film on Fe-Cr alloys consists of a Cr rich (hydr-)oxide layer. The film thickness and composition depend strongly on the Cr content of the alloy, on the thermal history and electrochemical pretreatment of the alloy, the pH of the electrolyte and the potential of observation. The film-thickness in 0.5 M H<sub>2</sub>SO<sub>4</sub> varies from 1-2 nm<sup>1-3</sup>. A high Cr content of the alloy and a relatively cathodic potential within the passive region result in the lowest layer thickness. In this paper only pure Cr and Fe-17Cr will be discussed.

It is now generally accepted that the formation of a passive film is a very dynamic process. The passivation process during slow potential scanning from the active to the passive region can be described as a slow transition from the active dissolution of the metal (Cr and Fe) through enrichment of the electrolyte with metal ions near the metal surface, the formation of complex M(OH)<sub>x</sub><sup>y-</sup> ions, adsorption at the metal surface of these ions to the formation of a gel-like film. This overall process is different in details for various metals. For Fe the reaction can be described as a dissolution precipitation process, while for Cr the formation of the film takes place by a direct reaction of the metal with the solvent. This process is not taking place uniformly over the whole metal surface, and is of course influenced by local variations in alloy composition, e.g. at grain boundaries, impurities and structural discontinuities.

Griffin and Sato<sup>3,4</sup> describe the passivation potential as the potential, where dehydration of the gel-like film takes place, because the bridge-formation energy for the neighbouring adsorbed complex ions becomes big, while the dissolution current density is small. This dissolution current density would indeed be small if the whole surface were covered. This description is incomplete, since the surface of the alloy is only partially covered with a film, when the

passivation reaction is gradually taking over from the dissolution reaction. At that stage the average dissolution current density is still considerably higher than the passive current density. Careful analysis of stationary polarisation measurements showed a clear deflection in the polarisation curve well before the maximum current was attained, while at the same time the relative phase-retardation of the ellipsometer signal changes <sup>1,2,5,6</sup>, due to the formation of some patches of oxide at the most stable sites. This is clearly visible in figure 1.

The potential where the dissolution current shows a deflection point should therefore preferably be called the initial passivation potential. The potential of maximum current density is indicative of the onset of full coverage of the surface, whereafter the current density reaches the very low value for a passive surface within a very narrow potential region. Alternatively after a potential jump, from the potential of maximum current density to high anodic potentials it only takes a very short time of the order of some milliseconds before full passivation is obtained. Moreover, for Cr and high Cr alloys the initial film immediately after the active-passive transition will probably still be an amorphous hydroxide, which is further dehydrated at higher potentials.

## Models For The Passive Film

### Introduction

A survey of different models for passive films was recently given by Sato<sup>3</sup>. Most models describe the film in a stationary situation, where the film is studied under potential control. The transport of ions through the film is the central issue. When a fully protective barrier layer has been formed, the stationary situation can only remain when dissolution of the layer is fully compensated by renewal of the layer through the formation and incorporation of new cations in the film, irrespective of the type of majority ionic defects responsible for the materials transport through the film. However, the transport of electronic charge carriers is as important. Therefore some models focus on the semiconductor properties of the passive films. A close look at the various models shows that these are not really conflicting, but only differ in the starting position, which depends mostly on the background of the author.

The transport properties of ions and electrons through the passive film are closely related with the breakdown mechanisms, be it under anodic or cathodic potential control or under seemingly stationary conditions, of the film, which is very relevant for mechanistic interpretation of local corrosion phenomena. Both the ionic bilayer model and the semiconductor model are relevant for Cr and Fe-Cr alloys in sulphuric acid. Another model describing the steady state properties of the passive film was recently published by D.D. MacDonald<sup>7</sup>, building on the original PDM of 1981 by Chao et al. <sup>8</sup>.

### The ionic bilayer model

If the initially formed passive film is considered, to be a bipolar membrane with an anion selective inner layer due to the adsorbed metalions and a cation selective outer layer (e.g. due to adsorbed sulphate ions) separated by a thin neutral water rich layer, high anodic polarisation results in a high electric field in the neutral layer. The water molecules in this neutral layer will dissociate resulting in a flow of  $H^+$  to the electrolyte and eventually resulting in an inner oxide barrier layer covered with a hydrated outer layer at least for neutral solutions as is indicated in figure 2. In acid solution this outer layer will quickly dissolve. The initial bilayer passive film for Cr-oxide formers is thus quickly transformed into an oxide-like barrier layer by deprotonation. This oxide layer itself, however, can also be described as a bipolar layer with excess metal ions in the inner layer and excess oxygen in the outer layer. In terms of the ionic transport models it would again result in a anion selective inner layer and a cation selective outer layer; this is clearly visible in figure 3. The transport of cations from the metal-oxide interface would thus be restrained, which results in a well protecting barrier layer. However, the overall thickness of the layer on FeCr alloys is, depending on alloy composition, only 1-2 nm, making this model less realistic.

### The semiconductor model

A better approach would be the semiconductor description of the film. Starting with the initial passive film in analogy with the ionic bilayer model, the passive film can be described as an inner n-type semiconducting layer and an outer p-type semiconducting film. See also figure 3. The n-type character of the inner film would result from the high concentration of electron donor levels provided by the excess of metal ions (either in the form of oxygen vacancies or in

the form of interstitial metal ions), while the metal ion vacancies act as acceptor levels in the p-type outer layer. In fact the passive film would be a p-n junction, which provides a high potential barrier for the electrons. The electric field in this type of very thin (1-2 nm) passive films under potential control is as high as  $10^6$ - $10^7$  V/cm. In a somewhat simpler and because of the extreme thin layer thickness more realistic approach the passive film is considered to be either n-type or p-type. Most passive oxide films are n-type semiconductors as for Fe with a very high donor concentration above  $10^{19}$  cm<sup>-3</sup>. The oxide film on Ni normally is p-type while the film on Cr may be either p-type or n-type<sup>9,10</sup>. The actual behaviour depends on the departure from stoichiometry and the impurity level.

If the passive film is amorphous, like for Cr, with a high concentration of localised donor or acceptor states, which may be of intrinsic or extrinsic nature, the band gap between the conductivity and the valence band must be replaced by the mobility gap, which effectively results in a change of about 10% of the  $E_g$  value. The bandgap of  $\text{Cr}_2\text{O}_3$  is not well known, but at least 3.6 eV<sup>9,10</sup>.

The most marked difference between a metal- and a semiconductor-electrode is the distribution of the potential across the electrode solution interface. For metal electrodes the potential is distributed only at the Helmholtz layer. A linear relation exists between the Helmholtz potential at the film solution interface and the electrode potential. For semiconductors the potential distribution also occurs in the film in the space charge region. The Helmholtz potential ( $\phi_H$ ) remains constant with changing electrode potential, and is only pH dependent, as long as no degeneracy of the electronic charge carriers exists. See figure 4. In the latter case the film obtains semimetallic properties due to overlap of the Fermi level with either the conduction band or the valence band at the film surface. This may also result from anodic polarisation, which lowers the Fermi-level, and results in an upward bending of the energy bands. Anodic polarisation thus results in overlap with the valence band and tunnelling of the electrons from the surface of the film into the metal-substrate. In this way the rate of metal ion transfer to the solution is increased, resulting in transpassive behaviour.  $\phi_H$  is now again potential dependent, because of the positive charge accumulated at the outer surface of the film. See figure 5.

Cathodic polarisation of the electrode would result in a negative charge accumulated at the outer surface of the film, due to overlap of the Fermi level with the conduction band at the surface as a result of the downwards bending of the conduction band. The rate of oxygen ion transfer from the film is now potential dependent, resulting in fast cathodic reduction (= breakdown) of the film. Clearly for n-type semiconductors higher anodic polarisation is necessary to obtain overlap between the higher Fermi-level and the valence band, resulting in the situation where electrons can tunnel through the film. Therefore n-type films are more stable in as much as anodic dissolution or in other words transpassivity, is concerned.

For Cr also higher valencies do exist, which influence the transpassive dissolution. The formation of Cr(IV) or even Cr(VI) either in the film or in solution as Chromate, can take place at lower anodic potentials as soon as the Fermi-level of the film is lower than the electron-level of the oxidation reaction, or as soon as the electrode potential is more anodic than the redox potential of the reaction as is indicated in figure 6.a. The cathodic depassivation is given in figure 6b. Therefore the passive region of Cr and high Cr-alloys is more narrow than would be expected based on the stability and semiconductor properties of  $\text{Cr}_2\text{O}_3$  itself.

The model by D.D. Macdonald for the steady state conditions of the passive film based on the point defect model published earlier, assumes that there is no potential gradient in the film, while the film thickness is potential dependent. We did not observe any significant increase of the film thickness with potential in the passive region, as to be discussed in Table 10, which was confirmed by new interferometric ellipsometry and new XPS measurements recently<sup>6,11</sup>. Therefore this model was not further taken into account in this paper.

### Conclusion

It is obvious from this short discussion on passivity, that we need very detailed information on the character of the passive film during formation, in stationary condition, and during transpassive dissolution in order to obtain a detailed model for the passive film and its breakdown under various conditions.

It is also very important to keep in mind that even in the stationary passive region under potentiostatic control the film should be regarded as a dynamic layer, which is continuously



dissolving and growing, and not in a laterally uniform way. This is also clearly evidenced by current transients measured in the passive region <sup>12,13</sup>. Moreover, because the stationary situation is always preceded by active or transpassive behaviour, these stages are as useful to give us relevant information on the breakdown of passive films as the passive region itself.

### The Passivity of Pure Cr

Because we can expect, based on the general description of the film as a semiconducting film, that the breakdown of the passive film is closely related with the morphology, structure and composition of the film, since these all influence the electronic and ionic properties of the film surface, a thorough analysis of the mechanism of formation, the stationary behaviour under potential control, and the transpassive dissolution is necessary in order to find detailed mechanistic information on localised corrosion problems. This information can be obtained from a combination of electrochemistry, in situ ellipsometry and XPS measurements.

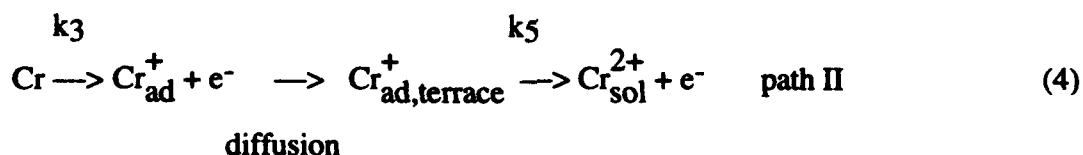
A logic start would be the passive film on pure poly- and single-crystalline Chromium. The relatively simple case of the formation of the passive film on pure Chromium in sulphuric acid was therefore studied with impedance spectroscopy <sup>14,15</sup>. An extensive analysis of the impedance data, including the deduction of a complete transfer function, describing all possible processes at the surface, resulted in a reaction mechanism as given in the following equations 1-6, and schematically given in figure 7. The fitted equivalent circuit is given in figure 8.

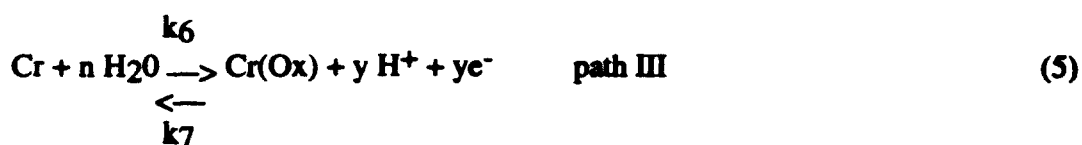
The model can be described in compact form as follows:

Cr<sup>2+</sup> is formed during the corrosion reaction. This can occur by direct dissolution of chromium atoms from "active" sites without the aid of OH<sup>-</sup> or water. This is visualized in figure 7 by path

I. The dissolution of chromium, however, is most likely to occur in two steps. When Cr<sub>ad</sub><sup>+</sup> is

formed it can diffuse over the surface on the terrace and then dissolve as Cr<sup>2+</sup>. This can explain the diffusion controlled process, found in the impedance measurements. These processes are denoted by path II. Path III represents the formation of the passive film which can both occur at the terrace and at the kink and ledge sites. In figure 7 only the formation of the passive film at the terraces is shown. Since the exact composition of the passive film is unknown it is represented as Cr(Ox). Chromium can still dissolve through the passive film, which gives rise to the passive current in the passive region. Hydrogen is evolved, both at the bare metal surface and at the passive film solution interface, in two steps of which the first step is supposed to be rate determining. The most likely place for hydrogen evolution to occur is at the terraces since they make up the largest surface area.





Coming from the active region, at the beginning of the passive region two time constants were found. This means that beside the dissolution of chromium through the passive film and the hydrogen evolution, a new process appears. This process can be described as the change of the "character" of the passive film, due to e.g. film growth, dehydration etc.

This example shows that even for a very simple pure metal the description of the film formation is complicated. Various partly interdependent reactions take place at the surface simultaneously. In the passive region the situation is simpler with a purely capacitive impedance; however, this does not give very much information on the stability of the film as such. Moreover, it just gives an impression of the average behaviour of the film.

#### The Passivity of Binary Fe-Cr Alloys.

For binary alloys of Fe and Cr the situation is even more complicated. The passive film now also contains some Fe, the amount of which depends on the composition of the alloy and on the electrode potential. The Fe contents of the film may influence the stability of the film in several ways: it may dissolve selectively from the film at potential changes, it may act as a dopant in the semiconductor, it may concentrate in a thin surface layer of the film, with different electronic properties and it can contribute to passive behaviour due to secondary passivation at relatively high anodic potentials, where Cr tends to become transpassive.

Therefore we undertook experiments to evaluate the thickness, the composition and the electrochemical behaviour of the film. A more detailed description of experimental details was published before 2,5,6,11.

Figure 9 shows two successive cyclic voltammograms of a 17%Cr alloy in 0.5 M sulphuric acid. It exhibits in anodic direction a current maximum with a shoulder between -1000 and -500 mV (SSE) in the first scan, which is less pronounced in the second scan. Also a maximum around +450 mV and a shoulder at +650 mV can be observed. In cathodic direction for both scans the current decreases slowly at -50 mV resulting in a small cathodic peak, while at lower potential two anodic peaks can be observed.

The composition of the passive film depends on the potential as can be seen in table I.

Polarisation in the active region at -940 mV results in a thin oxide layer with the same concentration of chromium as in the bulk metal. At 200 mV 66% of the metal in the oxide film is Cr. At 600 mV the Chromium concentration has increased to 76%. In a static polarisation curve the current increases between +200 and +600 mV. Obviously the beginning of transpassivity, generally believed to be due to the formation of a higher valency of Cr like Cr(IV) and Cr(VI) does not result immediately in a decreasing amount of Cr in the film, due to dissolution. This depletion takes place at higher potentials. At +900 mV the chromium content has decreased to 40%. The anodic current peak at +450 mV is therefore believed to be due to oxidation of Fe(II) to Fe(III) in the film without a change in concentration of Fe in the film. The shoulder at +650 mV can be attributed to the oxidation of Cr. As we have seen initially it does not lead to a depletion of Cr in the film, on the contrary a small increase to 76% at +600 mV takes place. Also it does not lead to major changes in the optical properties as can be seen in figure 10a. Consequently it is obvious that the film can contain a certain amount of Cr(VI) or perhaps also Cr(IV). The increasing instability of the Cr in the film above +650 mV, results in initiation of the transpassive breakdown of the film for alloys with Cr concentration above 17%. For the 17% alloy secondary passivation due to the formation of a Fe rich film can be observed in figure 9 above +750 mV. The transformation of a chromium-rich to a iron-rich oxide film results in a small change in the relative phase retardation  $\Delta$  of the ellipsometer. According to the thickness calculated from the XPS data an increase of the layer thickness took place. It should be noted that the film at +900 mV still contains 40% of Cr which is significantly more than in

the metal (surface 26%, bulk 17%). It confirms the idea that the film can contain higher valent Cr. This is an important conclusion, since the incorporation of Cr(VI) and also (MoVI) is thought to be responsible for the inhibitive character of chromates and molybdates <sup>16</sup>.

Careful analysis <sup>2, 5</sup> of all data showed that the cathodic peak between -50 and -500 mV can be attributed to the reduction of Fe(III) to Fe(II) in the film. Furthermore, also some Fe(III) in the vicinity of the surface contributes to the current response. According to the ellipsometric data (especially the value of  $\Delta$ ) as given in figure 10b, the reduction and additional depletion of iron in the film is accompanied by a transformation of the film. The XPS results as given in table I show a Cr content of 81% in a film which was taken out of the solution after open circuit decay to -600 mV. Thus a depletion of iron takes place during this decay from +20 to -600 mV. Also this sustains the idea that the cathodic peak between -50 mV and -500 mV is due to Fe(III) reduction. For a 9% alloy (not given in this paper) this reduction leads to complete breakdown of the film during scanning. For the 17% alloy as given in figure 3 breakdown took place at slower scan rates in the same potential region. This reduction process therefore is important for the cathodic breakdown mechanism of the film. Addition of Mo to the alloy may have the function of stabilizing the Fe(III) in the film, resulting in a slower cathodic breakdown.

From this discussion it follows that the valencies of Cr and Fe and also the iron content play an important role in the potential dependent stability of the passive film. A detailed description of the passive current density in terms of variables determining the alloy composition, environment and interface would be of great importance for corrosion protection measures to be taken, especially for corrosion initiated by localised breakdown. It would also be vital to obtain quantitative information on the relation between the ionic and electronic current density, regardless whether hole injection (thicker layers) or electron-tunneling (thinner layers) would be responsible for the corrosion process. The number of parameters in practical applications is enormous, which makes such a description difficult. If all environmental and surface state parameters are fixed, the problem is simplified. Therefore the study of the polarisation curves of a Fe17%Cr alloy in 0.5 M sulphuric acid as described above is useful, especially if extended by impedance measurements, which in principle can reveal more detailed information, since impedance data reflect the contribution of all potential dependent processes governing the passive current density. As already discussed, impedance measurements for the passivation process of pure Chromium indeed proved to be successful. However, for the alloy we have to take into consideration the following potential dependent processes: film growth, compositional changes, dehydration, oxidation state changes, lateral inhomogeneity in composition and morphology.

All these processes contribute to the impedance measured in a frequency range of  $10^5$  to  $10^{-3}$  Hz, which results in a large overlap in time constants, making it difficult to separate them.

However, it proved possible <sup>17,18</sup> to determine the number of time constants in the impedance diagrams, by assuming that all processes were parallel. A reasonably good fit of the data was obtained with three or four time constants. Unfortunately it was not possible to identify the time constants based on impedance measurements alone. Other techniques should be used to pin the various time constants to processes. If strong coupling exists between the different processes the impedance can possibly never be fitted to any equivalent circuit. In order to evaluate this major problem, a fundamental description in terms of a transfer function will be needed. Because no detailed quantitative information on the processes occurring during the passivation and in the passive state is as yet available, no detailed description of the passive film as for pure Cr is possible for FeCr alloys.

New quantitative angle resolved XPS measurements using the most recent available curve analysis and background subtraction software <sup>11</sup>, in combination with potential modulated reflectometry <sup>6</sup> have recently provided more detailed information on potential and environment dependent composition and film thickness. More details will be published shortly.

#### **Implications For A Semiconductor Model For The Passive Film On FeCr**

Because the film thickness proved to be hardly potential dependent in the passive region under potential control, the semiconductor approach seems obvious.

A tentative semiconductor model for the passive film on FeCr alloys is given in figure 11.

In this stationary polarisation plot the Flat-band potentials for Cr<sub>2</sub>O<sub>3</sub> and Fe<sub>2</sub>O<sub>3</sub> have been indicated, using values for  $E(\text{gap})$  based on literature data <sup>3,8,10</sup>. For Fe<sub>2</sub>O<sub>3</sub> extrinsic n-type

behaviour was assumed. For  $\text{Cr}_2\text{O}_3$  the Fermi-level is unknown, but probably above 1.8 eV, which would be intrinsic. Also the standard potential in acid solution for the redox couple  $\text{Cr(III)/Cr(VI)}$  was incorporated in the figure. It is clearly observed that due to the oxidation of  $\text{Cr(III)}$  to higher valencies it can be expected that an anodic current increase takes place well before normal transpassivity is observed. This is in striking accordance with the polarisation plot and also in accordance with very recent XPS data <sup>11</sup>. Moreover  $\text{Cr}_2\text{O}_3$  is shown to have a much wider passive region than  $\text{Fe}_2\text{O}_3$ , due to the extension of the passive region in cathodic direction, till the flat band potential is reached. At anodic potentials Cr is reaching normal transpassivity before Fe, due to the formation of chromate, initially at the reversible potential for the  $\text{Cr(III)/Cr(VI)}$  couple (1.3 eV) in the layer and irreversibly at somewhat higher potentials when the layer is further oxidised while dissolving.

Taking into account the uncertainties in the used data, and even more important the fact that the passive film is not crystalline, the agreement between the semiconductor picture and the electrochemical approach is quite good.

### Implications For Localised Corrosion Phenomena

The above discussion shows the complicated nature of a detailed description of the passive film, even for assumed lateral homogeneity. For pitting corrosion of stainless steels, however, localised impurities (inclusions) of MnS play an important role in the initiation mechanism <sup>12,13</sup>. This fact alone is enough to make the usefulness of "the pitting potential" as a material property doubtful. But even for special stainless steels or simple binary alloys as discussed, with a very low amount of these inclusions, the pitting potential will remain dependent on lateral inhomogeneities in the alloy as precipitates near grain boundaries of impurities and second phase alloy particles with lower Cr content <sup>18</sup>. Both examples of lateral discontinuities are very much dependent on the thermal history of the materials <sup>11</sup>. Also the specific role of chloride-ions should be mentioned here.

The phenomenon of pitting is intrinsically dependent on coincidental lateral inhomogeneities, where the passive film is weak. A better approach to this kind of localised corrosion is the study of potential and time dependent variations of the passive current density. For a more detailed description of current transients as a function of alloy composition and pretreatment I refer to ref. <sup>12,13</sup>. It is important to relate the knowledge on the transpassive breakdown of passive films with localised attack at weak spots in the film. The growth of metastable pits and repassivation phenomena in the pits is linked with the ionic and electronic transport properties of the film as discussed in this paper.

### General Conclusions

The phenomenon of the breakdown of passive films, either by cathodic reduction, or by anodic processes as localised corrosion and transpassivity, can only be understood, when detailed quantitative information on all possible processes during formation and in the stationary situation, is available. Even for relatively simple model systems including elemental single crystals, this information can only be obtained by combination of various chemical and physical analysis techniques. These include dc electrochemistry, ac impedance, chemical analysis with XPS and AES, characterisation of the semiconductive properties of the film with dielectric and photocurrent measurements, in situ potential modulated ellipsometry and reflectometry and a complete structural and morphological description of the alloys. In this paper the first attempts to combine the results from various techniques in a mixed semiconductor model for FeCr alloys were presented. It was shown that such a model gives valuable information on passivity. Future work on these alloys will hopefully increase the quality of the model, which should become the base for our understanding of many practical corrosion phenomena of stainless steels.

### References

1. J.H. Gerretsen, and J.H.W. de Wit: Proc. 9th European Congress on Corrosion, Utrecht, The Netherlands, October 1989, FU-056.
2. J.H. Gerretsen, J.H.W. de Wit and J.C. Rivière: Corrosion Science, **31**(1990) 545.
3. N.Sato, Corrosion, May 1989, pp. 354-368.  
and: Sato, N.: Corrosion Science, **31**(1990) pp.1-21.

4. G.L. Griffin, J. Electrochem. Soc., 131(1984) pp.18.
5. J.H. Gerretsen, Thesis, 1990, T.U. Delft, The Netherlands.
6. L. Jacobs, K. Hemmes and J.H.W. de Wit, Proc. 2nd int. symposium on Electrochemical Impedance Spectroscopy, July 12-17 1992, Santa Barbara, USA.
7. D.D. Macdonald and M. Urquidi-Macdonald, J. Electrochem Soc. 137(1990)2395-2402.
8. C.Y. Chao, L.F. Lin and D.D. Macdonald, J. Electrochem. Soc., 128,6(1981)1187-1198
9. E.W.A. Young, P.C.M. Stiphout and J.H.W. de Wit: J. of the Electrochem. Soc., 132, 4(1985) pp. 884-886.
10. E.W.A. Young, J.H. Gerretsen and J.H.W. de Wit: J. of the Electrochem. Soc., 134, 2,(1987)pp. 2257-2260.
11. S. Norgren, M.A.J. Somers, W. Sloof and J.H.W. de Wit: Proceedings of the 12th Scandinavian Corrosion Congress & Eurocorr '92, Vol. 1 (1992) 139, Espoo, Finland.
12. E.F.M. Jansen and J.H.W. de Wit: Proceedings of the 12th Scandinavian Corrosion Congress & Eurocorr '92, Vol. 1 (1992) 91, Espoo, Finland.
13. E.F.M. Jansen, W.G. Sloof, J.H.W. de Wit, Eur. Symp. on Mod. of Passive Films, Paris 15-17 Febr. 1993.
14. J.A.L. Dobbelaar and J.H.W. de Wit: J. Electrochem. Soc., 137, 7(1990) pp. 2038-2048.
15. J.A.L. Dobbelaar and J.H.W. de Wit: J. Electrochem. Soc., 139, 3(1992) pp. 716-724.
16. Corrosion Inhibitors, Ed. C.C. Nathan, NACE, Houston, Texas, 1979.
17. J.A.L. Dobbelaar, E.C.M. Herman and J.H.W. de Wit: Corrosion Science, 33, 5(1992) 779.
18. J.A.L. Dobbelaar, E.C.M. Herman and J.H.W. de Wit: Corrosion Science, 33, 5,(1992)765.

**Table I**

E(mV)	Cr(alloy)%	Cr(oxide)%	d(nm)	Fe <sup>2+</sup> /Fe <sup>3+</sup>
-940	18	20	0.8	0.7
+200	28	66	1.1	0.7
+600	25	76	0.9	0.7
+900	26	40	1.5	0.4
-600	25	81	0.8	0.8

Cr(alloy)% : at % of Cr in alloy at interface with film

Cr(oxide)% : at % of Cr in film with respect to total metal concentration

d : thickness of film

Fe<sup>2+</sup>/Fe<sup>3+</sup> : ratio of Fe species in the film

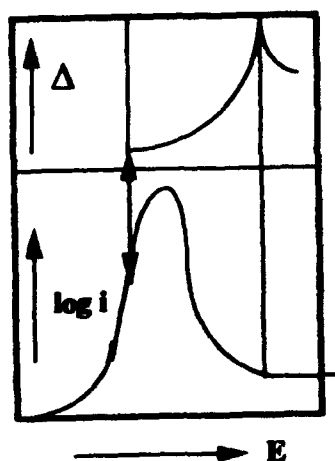


Figure 1.

The relative phase retardation ( $\Delta$ ) (upper part) and the log of the current density ( $\log i$ ) as a function of the electrode potential during passivation of pure Cr metal, starting at cathodic potentials. The picture has been schematised.

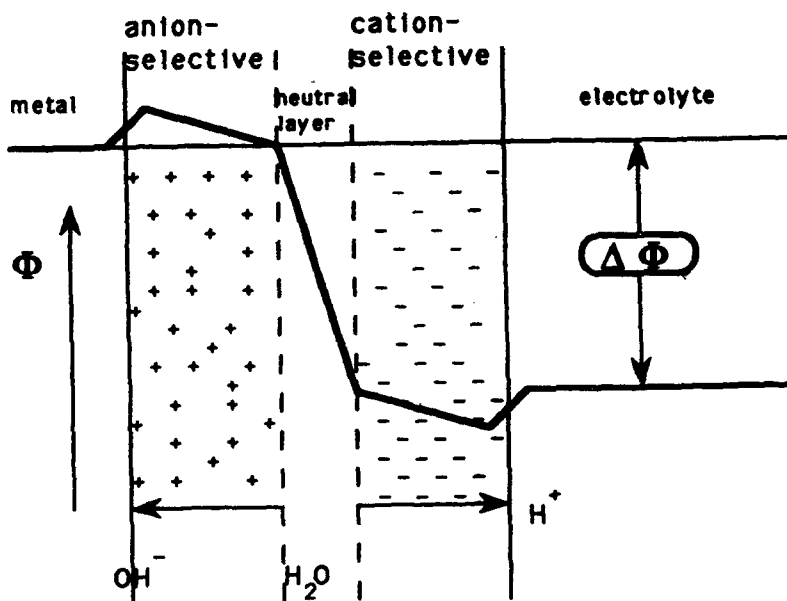


Figure 2.  
Schematic potential distribution across bipolar membrane under anodic polarisation.

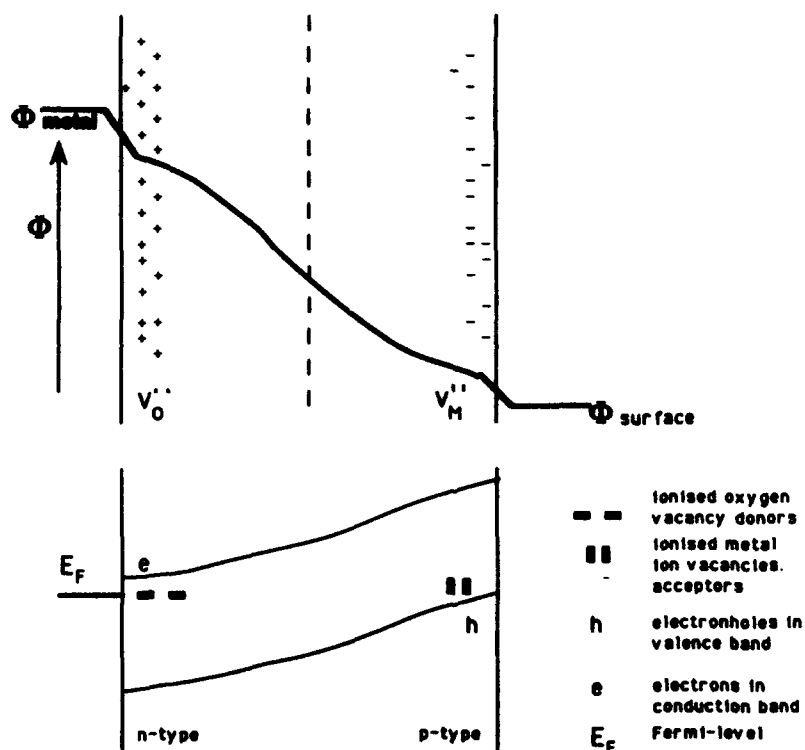


Figure 3.  
bipolar oxide layer anion-selective, donor rich n-type inner  
layer and cation selective, acceptor rich p-type outer layer.

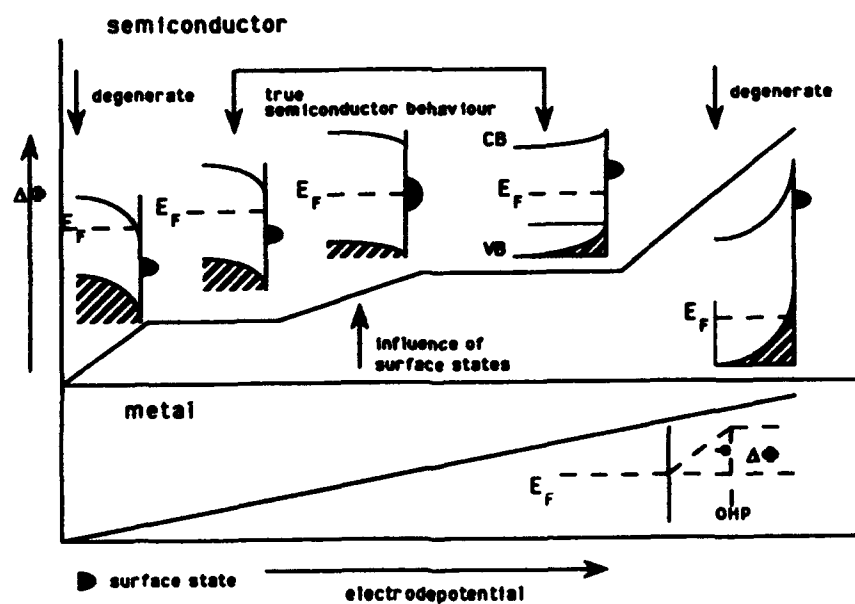
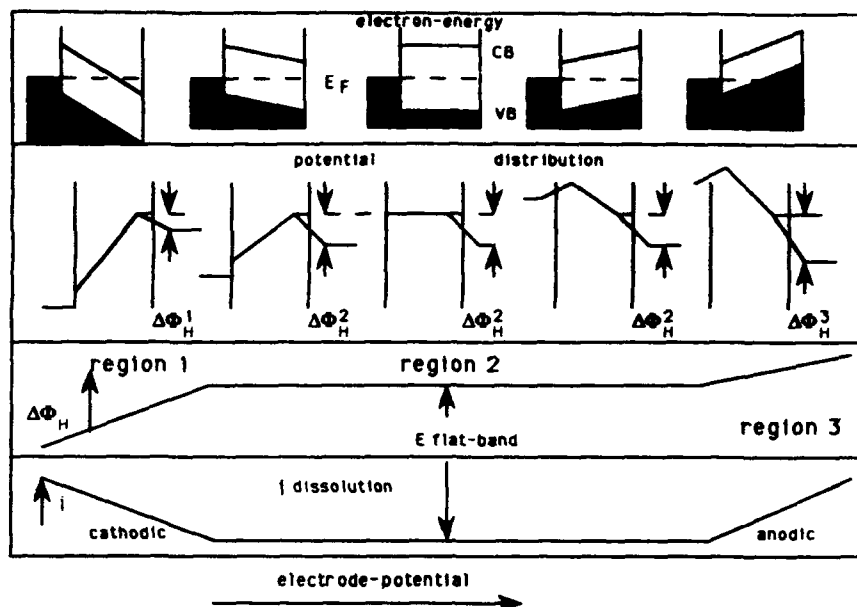
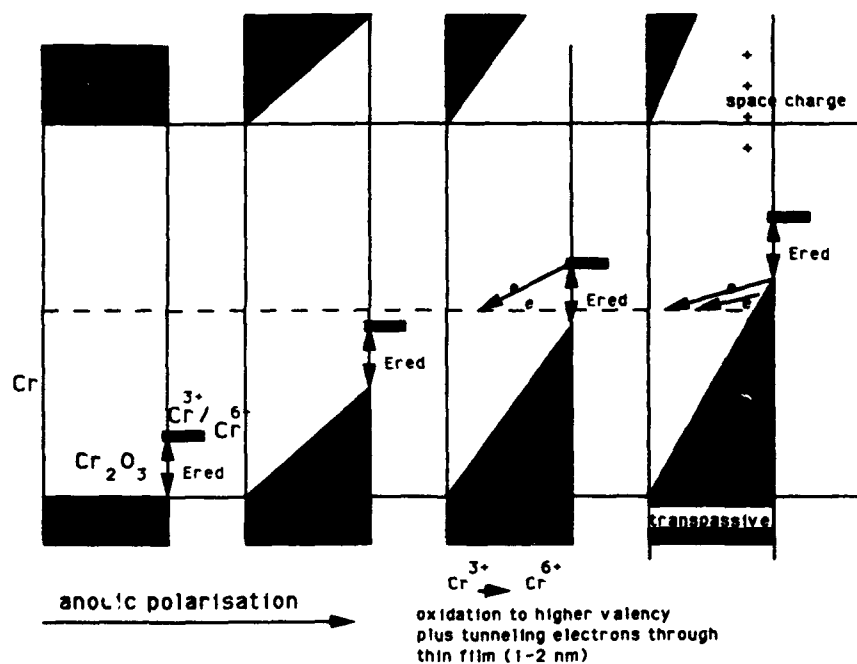


Figure 4.  
Relation between Helmholtz potential and  
electrodepotential for  
metals and semiconductors, including surface  
states.



**Figure 5.**  
Schematic diagram of electron energy levels, potential distribution  
Helmholtz potential, and film dissolution rate for a thin passive film  
as a function of electrode potential



**Figure 6 a.**  
Anodic dissolution of passive film on  
Cr  
pre-transpassive and transpassive  
behaviour



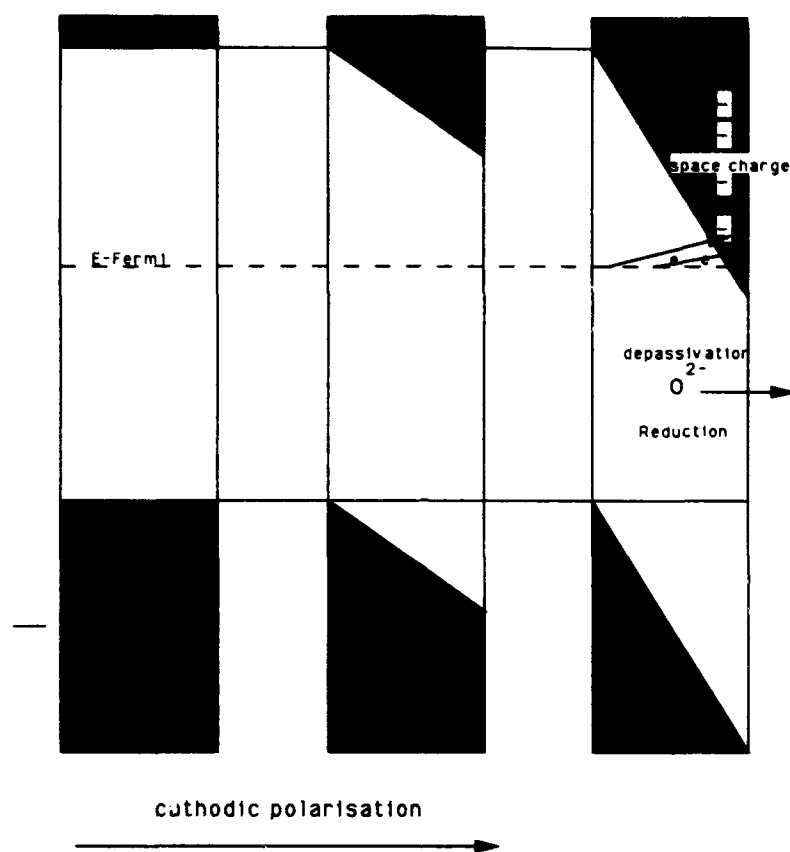


**Figure 6b.**  
Cathodic reduction of passive  
film on Cr.

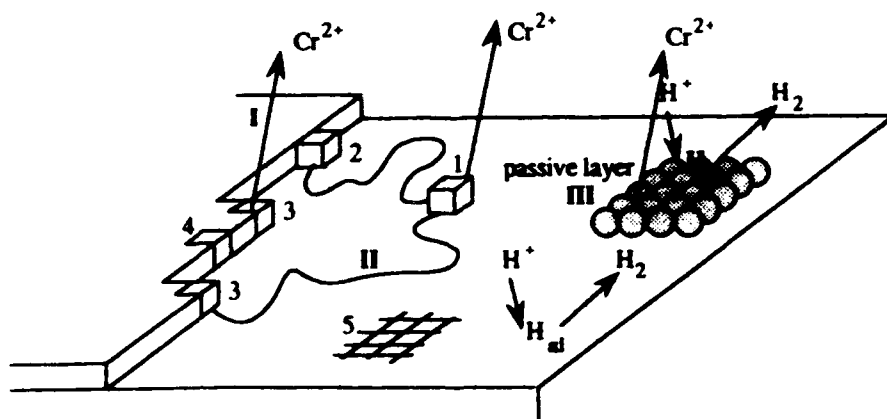


**Figure 7.** The corrosion process occurring at a chromium-sulphuric acid solution interface.

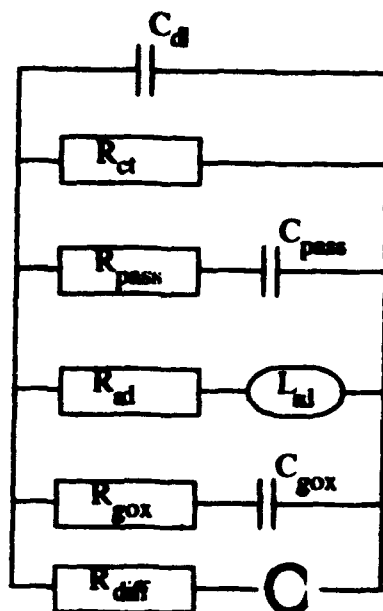


**Figure 8:** The equivalent circuit representing the model in equations 1-6.

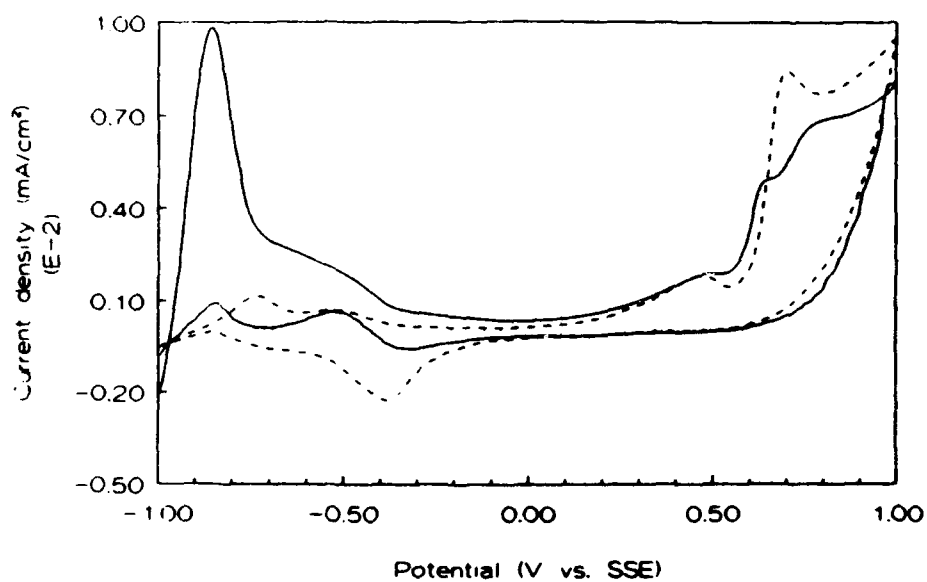


**Figure 9:** Two successive cyclic voltammograms of a Fe17%Cr alloy in 0.5 M sulphuric acid. —: first scan, - - : second scan.

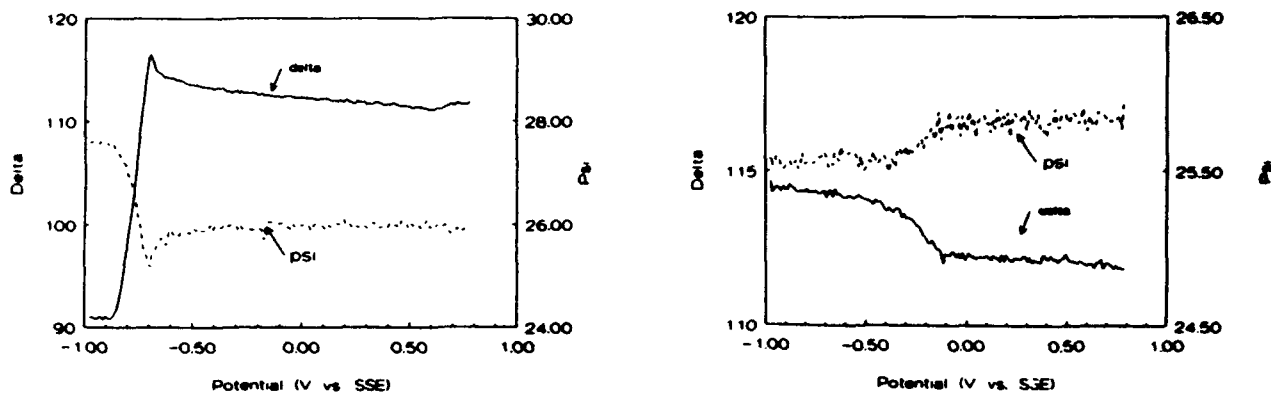


**Figure 10:** Variation of Delta and Psi as measured during a cyclic potential scan. Scan rate 20 mV/s. top: a: during anodic scan, bottom: b: during cathodic scan.

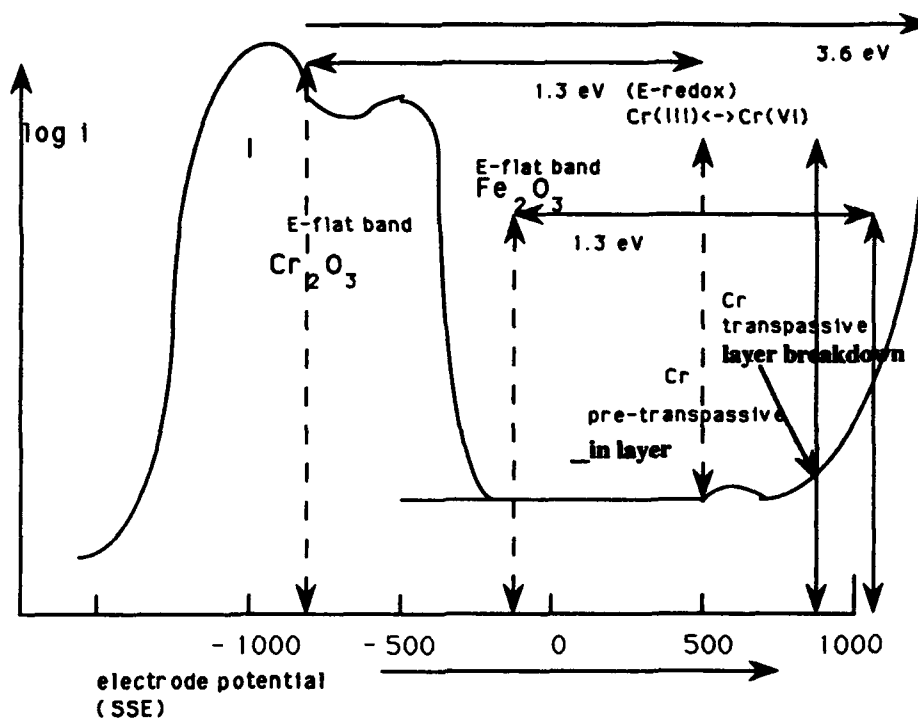


**Figure 11.** Semiconductor model for passive behaviour of Fe-Cr alloys. Schematised.  
Used data and assumptions:  
 $E_g(\text{Cr}_2\text{O}_3) = 3.6 \text{ eV}$ ,  $E(\text{Fermi}) > 1.8 \text{ eV}$  (intrinsic) n-type  
 $E_g(\text{Fe}_2\text{O}_3) = 1.6 \text{ eV}$ ,  $E(\text{Fermi}) = 1.3 \text{ eV}$  (extrinsic) n-type  
 $E(\text{redox}) \text{ Cr(III)/Cr(VI)} = 1.3 \text{ eV}$

# Passive Oxide Films on Well-Defined Nickel Surfaces: An Examination of Film Growth on Ni(100) with *Ex Situ* Scanning Tunneling Microscopy

Carissima M. Vitus  
Department of Applied Science  
Brookhaven National Laboratory  
Upton, NY 11973

Alison J. Davenport  
Department of Applied Science  
Brookhaven National Laboratory  
Upton, NY 11973

## Abstract

The surface morphology and atomic structure of air-formed and passive oxide films on a Ni(100) single crystal is presented. The passive oxide film was formed in a 0.15N Na<sub>2</sub>SO<sub>4</sub> solution (pH = 2.8) anodized at 0.0 V vs. Hg/Hg<sub>2</sub>SO<sub>4</sub> reference.

## Introduction

The exact nature of the passive oxide film on metals in aqueous environments and the role it plays in breakdown of passivity is not fully understood. The corrosion behavior of various metals may be linked to the nature of the oxide film breakdown itself, *i.e.* breakdown from selective localized points of attack (pitting) or generalized breakdown from a defective (disordered) oxide film. In recent years there has been considerable debate as to whether passive films are crystalline or glassy. This is important in understanding the mechanisms of passivity breakdown. Whether or not the film is crystalline, breakdown is likely to occur at defects in the film. The nature of these defects is even less well-defined than the structure of the film itself. Access to the structure of films and their defects on an atomic scale is now possible using the recently-developed scanning probe techniques of scanning tunneling microscopy (STM) and atomic force microscopy (AFM).

While a variety of electrochemical systems have been examined and reported using *in situ* STM and AFM<sup>1-5</sup>, direct application to metal corrosion processes in aqueous environments has only occurred within the last few years. Earliest reports include the *in situ* STM examination of the anodic dissolution of nickel in sulfuric acid media by Lev *et al.*<sup>6</sup> and corrosion processes of 304L stainless steel in aqueous chloride solutions by Fan and Bard<sup>7</sup>. Localized corrosion of copper in varying HClO<sub>4</sub> concentrations was observed using STM by Zhang and Stimming<sup>8</sup>. In this study, the corrosion rates compared using STM and SEM were in agreement. Preferential low index etching observed during copper corrosion on the micron scale was monitored using STM by Pickering *et al.*<sup>9</sup>. Silver dealloying from Au-Ag alloys in perchloric acid solutions was observed under potential-controlled conditions using STM by Oppenheim *et al.*<sup>10</sup>. At potentials where silver could undergo selective dissolution from the alloy, monolayer-deep pits formed within the terrace structure, eventually diffusing towards terrace ledges with subsequent surface reannealing. More recently, *in situ* AFM has

been used to study the corrosion behavior of polycrystalline copper electrodes during anodic dissolution in sulfuric acid by Cruickshank *et al.*<sup>11</sup>. In this report, overlayer dissolution on a mechanically polished electrode exposed underlying grain boundaries by applying a small anodic potential. Overlayer dissolution was not observed for chemically polished surfaces. The effects of a corrosion inhibitor was monitored at higher potentials. In the absence of the inhibitor, bulk copper dissolution was observed whereas in the presence of benzotriazole (BTA), dissolution did not take place. Finally, Cruickshank *et al.* have reported atomic images of oxygen adsorption on Cu(100) in low molar acid solutions. A  $(\sqrt{2} \times \sqrt{2})R45^\circ$  lattice was imaged throughout the passive region in both perchloric and sulfuric acid using either electropolished or mechanically polished electrode pretreatments. Images obtained negative of the cathodic oxide reductive peak reveal the underlying  $(1 \times 1)$  square lattice of Cu(100). The reported structure is similar to the oxygen adlattice observed at low temperature in vacuum<sup>12</sup>.

In this study, images will be presented showing the passive oxide film growth on Ni(100) using STM. Previous investigations by others indicate the film consists of near stoichiometric NiO with thickness between 9 - 12 Å<sup>13-15</sup>. Electron diffraction data by MacDougall *et al.* indicate the NiO forms a face-centered cubic lattice with a (111) face parallel to the metal surface and aligned along all possible substrate directions<sup>14</sup>.

### Experimental

The microscope used was a Nanoscope II STM purchased from Digital Instruments, Inc.<sup>16</sup>. In STM, current variations induced by a bias potential set between a rastering atomically-sharp metallic tip a few atomic layers above a conductive surface is translated into real space atomic corrugation. Atomic calibration of the STM A head (~700nm maximum scan size) was performed on freshly-cleaved graphite or Au(111)  $(1 \times 1)$  using tips of either etched tungsten (1M KOH, 15V a.c.) or Pt/Ir (80:20) (etched in 2:1 mixture of H<sub>2</sub>O: sat. CaCl<sub>2</sub> at 40V a.c.). Atomic scale images were acquired with different STM A heads with different calibrations. Experimental parameters used to acquire individual images are indicated in the figure captions.

The Ni(100) single crystal disk, 99.999% pure, was obtained from Monocrystals, Inc.<sup>17</sup>. The orientation was determined to be within 0.5° by x-ray diffraction. Prior to use, the crystal was electropolished in 57% sulfuric acid<sup>14,15</sup>. The crystal was then transferred to a deaerated electrochemical cell and immersed in 0.15N Na<sub>2</sub>SO<sub>4</sub> (T. J. Baker, Inc.) pH = 2.8. The reference electrode used in this cell was a Hg/Hg<sub>2</sub>SO<sub>4</sub> reference (+0.665 vs. NHE). The air-formed oxide layer was removed by applying a cathodic potential at -1.35 V for 5 minutes. A passive oxide film was subsequently formed by anodic polarization at 0.0 V for varying times. Open circuit decay profiles of NiO layers formed in such a manner are consistent with those reported by MacDougall under similar conditions<sup>15</sup>. STM experiments were carried out on air-formed and passive films.

An unaccountable drift is always observed during imaging on this surface even after several hours. Very low drift images of the atomic structure of graphite using similarly made tips acquired on the same day suggest that this drift is associated with the crystal itself. One

possible source of this drift is a magnetic interaction of the nickel crystal with the magnetized course and fine adjustment screws on the microscope. Similar drift problems were observed using different STM A heads.

## Results and Discussion

*Ex situ* STM atomic images of air-formed and passive films on Ni(100) are shown in Figure 1 and 2, respectively. Direct comparison of the two images indicate that similar oxide films form under both conditions. A distorted hexagonal lattice was observed in both images. Measured nearest neighbor lattice parameters are  $0.25 \pm 0.1\text{nm}$  and  $0.29 \pm 0.02\text{nm}$  in Figure 1 and  $0.27 \pm 0.05$  and  $0.32 \pm 0.02\text{nm}$  in Figure 2. These values are consistent with one another within experimental error introduced by drifting problems. They deviate from the calculated nearest neighbor distance of  $0.295\text{ nm}$  for Ni-Ni or O-O surface atoms in a (111) NiO structure by  $\pm 10\%$  due to the distortion. The interatomic distance for nickel is  $0.245\text{nm}$ , somewhat shorter than the measured distance along the shorter axis. However, the underlying nickel has square symmetry which is clearly not observed in these images. It is possible that the distortion may be associated with commensurate growth of the oxide along one direction of the substrate. This requires confirmation by other non-vacuum techniques such as x-ray scattering.

Previous RHEED experiments performed by MacDougall *et al.*<sup>14</sup> observed that an air-formed oxide layer grown on Ni(100) after electropolishing in  $\text{H}_2\text{SO}_4$  solutions was similar to the passive oxide layer formed in a  $\text{Na}_2\text{SO}_4$  solution. In both cases, a near stoichiometric face-centered cubic lattice of NiO in the (111) orientation is observed. The measured lattice parameter of NiO formed after air exposure of an electropolished crystal was ca. +2% expanded from stoichiometric NiO compared to an expansion of ca. +0.3% for anodized NiO films. It was suggested that this expansion was due to water, hydroxyl or hydrogen species on the surface of the metal that are trapped within the oxide film during air exposure after electropolishing<sup>18-19</sup>. Further evidence for trapped species within the lattice was found in the open-circuit decay profiles of air-formed NiO in  $\text{Na}_2\text{SO}_4$  solution in which film breakdown was more rapid compared to anodized NiO films. It was concluded that these species act as preferred sites of rapid breakdown of the film. Oxide films on nickel after cathodic reduction of the air-formed oxide produce films which closely resemble stoichiometric NiO. The distorted hexagonal pattern of the NiO layer reproducibly imaged by STM, under differing preparations and on three different Ni(100) single crystals, suggests that a different NiO structure is observed from the one studied in vacuum. A possible explanation of this discrepancy may be that local heating during RHEED experiments induces an ordering to near stoichiometric NiO in vacuum: such rearrangement would not be seen with the STM.

## Summary

Scanning tunneling microscopy has been used to probe the structure and formation of oxide films on nickel in air. A distorted hexagonal pattern of the oxide layer was obtained on the air-formed or anodized surfaces. Measured lattice parameters indicate the structure resembles a distorted (111)NiO lattice.

### Acknowledgement

The authors would like to thank Peter Eng for useful discussions on Ni preparation. This work was supported by the U.S. Department of Energy, Office of Basic Energy Science, Division of Materials Science under Contract No. DE-AC02-76CH00016.

### References

1. S-L. Yau, C. M. Vitus and B. C. Schardt, *J. Am. Chem. Soc.* **112**, 3677 (1990).
2. H. Honbo, S. Sugawara and K. Itaya, *Anal. Chem.* **62**, 2424 (1990).
3. X. Gao, A. Hamelin and M. J. Weaver, *Phys. Rev. B* **46**, 7096 (1992).
4. C. C. Chen, S. M. Vesecky and A. A. Gewirth, *J. Am. Chem. Soc.* **114**, 451 (1992).
5. M. P. Green and K. J. Hanson, *J. Vac. Sci. Technol. A* **10**, 3012 (1992).
6. O. Lev, F-R. Fan and A. J. Bard, *J. Electrochem. Soc.* **135**, 783 (1988).
7. F-R. Fan and A. J. Bard, *J. Electrochem. Soc.* **136**, 166 (1989).
8. X. G. Zhang and U. Stimming, *Corros. Sci.* **30**, 951 (1990).
9. H. W. Pickering, Y. C. Wu, D. S. Gregory, S. Geh and T. Sakurai, *J. Vac. Sci. Technol. B* **9**, 976 (1991).
10. I. C. Oppenheim, D. J. Trevor, C. E. D. Chidsey, P. L. Trevor and K. Sieradzki, *Science* **254**, 687 (1991).
11. B. J. Cruickshank, A. A. Gewirth, R. M. Rynders and R. C. Alkire, *J. Electrochem. Soc.* **139**, 2829 (1992).
12. B. J. Cruickshank, D. D. Sneddon and A. A. Gewirth, *Surf. Sci. Lett.* **281**, L308 (1993).
13. P. B. Sewell, B. MacDougall, D. Mitchell and M. Cohen, *Proceedings of Sixth International Congress on Metallic Corrosion*, Sydney, Australia, p. 706 (1975).
14. B. MacDougall and M. Cohen, *Passivity of Metals*, R. P. Frankenthal and J. Kruger, Editors, The Electrochemical Society, Princeton, N.J., p. 827 (1978).
15. B. MacDougall, D. F. Mitchell and M. J. Graham, *Corrosion* **38**, 85 (1982).
16. Digital Instruments, Inc. 520 E. Montecito Street, Santa Barbara, CA 93103  
Phone: (805)899-3380
17. Monocrystals, Inc. 1721 Sherwood Boulevard, Cleveland, OH 44117
18. H. T. Yolken, J. Kruger and J. P. Calvert, *Corros. Sci.* **8**, 103 (1968).
19. J. Siejka, C. Cherki and Y. Yahalom, *J. Electrochem. Soc.* **119**, 991 (1972).

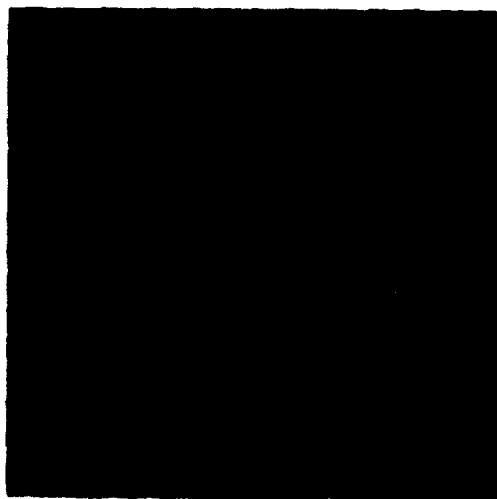


Figure 1. Atomic image of an air-formed oxide layer on Ni(100) after electropolishing. 2nm x 2nm image,  $V_s = 50.0$  mV,  $I_s = 2.0$  nA.



Figure 2. Atomic image of a passive film on Ni(100). 2nm x 2nm image,  $V_s = 600.0$  mV,  $I_s = 22.0$  nA.



## **Passivity and Pitting Corrosion**

**M.B. Ives**  
**Institute for Materials Research**  
**McMaster University**  
**Hamilton, Ontario, L8S 4L7**  
**Canada**

### **Abstract**

The conventional view of the role of passivity in pitting corrosion is that pitting is initiated by the breakdown of passivity. A consequence of this view is that pitting susceptibility can be controlled by ensuring that passive films are not ruptured. But from the engineering viewpoint localized corrosion is only a problem if some kind of failure results. This generally requires macroscopic changes in surface morphology which involve much more than the breaching of passive films. Detailed observations of growing pits, including microelectrode surveys to deduce the local distributions of potential, ionic species and pH, has lead to an appreciation of the competition between local conditions which favour or deny the opportunity for repassivation. This is the more relevant connection between passivity and pitting.

A review of particular pit morphologies, including the role of perforations in pit covers, permits the conclusion that pit growth morphology is determined by both local chemistry and the transport of participating ionic species within active pits. Those such species which originate within the corrosive environment cannot be controlled, leading to the notion that the only means of inhibiting the growth of pits is through blocking the local anodically dissolving metal sites with species present in the alloy. More continued efforts are required to determine alloying additions which effectively block anodic dissolution in the extremely aggressive local environments present within pits. Such additions are not necessarily those which promote passivity in less aggressive natural (e.g. less acidic) environments. It is also suggested that methods of reducing cathodic reaction kinetics would also contribute to the reduction of pit growth rates.

**Key terms:** pitting; passivity; stages of pitting; salt films

## Introduction

At the 9th. International Congress on Metallic Corrosion, an attempt was made<sup>1</sup> to define and rationalize the various stages of the pitting process in a passivable metal surface. It is understood that the development of a pit involves both nucleation and growth phases. Considered in more detail, these phases should properly be considered as a series of distinct stages, from the localized breaching of a passive film, through the rapid active dissolution of metal, to the establishment of a localized chemistry within the pit, sufficient either to stabilize its further growth or to permit repassivation. From the engineering point of view such an initiated and developed pit may be significant in that it could (i) represent a local stress raiser should the pitted metal be subjected to an applied load, or (ii) continue to grow in depth until it perforates the section producing a leak if the metal structure is designed to contain fluid. Furthermore, and in the context of the topic of this specific symposium, the role of passivity may not be primary to the pitting process *when considered as a phenomenon prejudicial to engineering performance*.

In consideration of these stages, it is appropriate to address pit development in terms of the factors relevant to each stage of growth.

**Stage 0** The very first step in the pitting process involves the localized breakdown of an otherwise protective surface ("passive") film. A full understanding of the mechanics of this breakdown has not been obtained, but it is clear that the film is either thinned locally or breaks at "weak spots" and these processes are assisted by the presence in the environment of a supply of "aggressive" ions. This is clearly a breakdown of passivity, and the process is primarily determined by the properties of the passive film. It is therefore entirely appropriate that the study of this breakdown be included in any consideration of the passivity of a given metal.

**Stage 1** Once the passive film is locally unable to protect the surface, the metal at that site is free to dissolve anodically. In the case of a naturally passivated metal in an oxidizing environment, this newly revealed surface will "see" a highly anodic potential<sup>2</sup> and extremely high local metal dissolution results. There is reason to suppose that this condition does not last long, but in the process extremely high local concentrations of dissolved cations are produced. Passivity plays no part in this stage.

**Stage 2** The future of the pit is determined at this most critical stage, and the terms "metastable pit" and "micropit" have been coined for pits while in it<sup>3</sup>. At this point, the pit may either repassivate, or it will permit the establishment of a continuously aggressive local environment, leading to an "autocatalytic" condition of continued growth. While the condition for repassivation is clearly a property of the appropriate passive film, whether this condition is created depends on what other chemical situations are possible. A major contribution to the understanding of this competition between repassivation and continued, stable, pitting was provided by Vetter<sup>4,5</sup>, who showed that the presence of an ionically conducting corrosion product film, a *salzdeckschichten* ("salt film"), could explain the close proximity of both passive and active surfaces at the edge of a growing (open) pit.

The fate of a "Stage 2" pit is thereby determined by the result of a competition between the formation of a protective passive film and an ionically-conductive salt film. If the salt film prevails, the pit can continue into the next Stage. It could be argued, therefore, that the fate of a pit in Stage 2 is determined as much by the stability of the salt film as by that of the passive film.

Stages 3 and 4 envisage<sup>1</sup> the growth of the pit from atomic size to microscopic and ultimately macroscopic dimensions. Within these stages, local ionic compositions are stabilized, usually significantly reducing the pH, and profoundly changing the local solution chemistry. In many real pitting situations, undercutting of the metal surface leads to covered pits, further enhancing the opportunity to stabilize significant different chemistries than exist in the nominal general surface environment. While the passive film will tend to protect further attack of the pit cover, passivity has little to do with what transpires beneath those covers.

The concept of pitting "stages" should, in principle, greatly assist in the comparison of pitting corrosion experimental studies from laboratory to laboratory. It would only require authors to clearly state the Stage of pitting considered in any given piece of research. But no operating definition has been generally adopted, and the term "pitting" in the research literature can refer to any or all of the Stages. This makes the development of coherent pitting theories difficult, since each proponent is likely to have an independent concept of what constitutes pitting. This is unfortunate, because it tends to confuse the precise role played by passivity in the pitting process.

The recent definition provided by Staehle<sup>6</sup>, in reviewing what he has usefully described as the "intrinsic modes" of corrosion, clarifies the difference between "pitting", depicted as attack which tends to be deeper than it is wide, and "general corrosion", which may be in the form of isolated shallow depressions. This is shown schematically in Figure 1. While shallow depressions [Figure 1(a)] are certainly regions of localized corrosion, it is not helpful to call this "pitting", since the Stages described above are not relevant to this form of corrosion. It would clearly be helpful to define *only* the dissolution geometries depicted in Figure 1 (b) and (c) as "pitting".

### Pit Nucleation

To consider first pit *nucleation*, it should be realised that until the recent development of extremely clean stainless steels and superalloys, pit nucleation in commercial alloys could be expected to be primarily associated with inhomogeneities in the metallurgical structure of the alloy. The most significant inhomogeneities would be non-metallic inclusions, at the sites of which any passive film would be interrupted or significantly different to that on the general alloy surfaces. This was realised many years ago, and the attack at sulphide inclusions in low alloy steels capably codified by Wranglén<sup>7</sup>. More recently the influence of a range of inclusions on the pitting corrosion of stainless steel was discussed by Ives and Srivastava<sup>8</sup>.

However, to obtain pitting on a passivable "clean" metal the local breakdown of

passivity is required. But it is a necessary, and not a sufficient condition, for the subsequent degradation of the properties or performance of an engineering structure. Smialowska has pointed out *"that pitting is, ironically, a detrimental side effect of the beneficial phenomenon of passivity."*<sup>9</sup>

A remarkable observation on real structures fabricated of metals prone to pitting is that the density of pits that represent engineering problems are extremely few and far between. Stainless steel tubes will perforate by pitting through their walls, but the density of such pits, including those that have not fully penetrated, is typically less than 10/m<sup>2</sup>. No model of passivity breakdown can rationalize such a small density. In this light, a more productive way to consider passivity in the context of pitting attack would be to concentrate on why many pits nucleate, but only a very few continue to grow and cause problems. Most pitted surfaces appear to retain their passive condition over the non pitted areas. This is unfortunate, since if there were more corroded area, it would require the removal of significantly more metal into solution before perforation of the wall. The most likely microscopic process is one in which large numbers of pits are indeed nucleated, by passive film breakdown, but the vast majority do not progress beyond Stage 2.

### Transport Processes within Pits

Luo et al. have recently described the application of microelectrodes<sup>10</sup> to probe the details of active pits. Figure 2 shows the profiles of chloride concentration, pH, and electrical potential within a simulated one-dimensional ("lead in pencil") pit in nickel, as determined by the microelectrodes<sup>11</sup>. Similar profiles may be assumed for real pits in corroding alloy surfaces, although an accurate measurement of the profiles is more difficult<sup>12</sup>. The significant conclusion from these measurements is that the chemical conditions close to the actively dissolving metal surface are extremely severe. The pH approaches a value less than 1, and chloride ion concentration rises to approximately 6 molar.

It has also been clearly demonstrated<sup>11,13</sup> that the conditions for stable salt film formation are developed only once a critical pit depth has been realised. The type of measurement shown in Figure 2 also permits the investigation of the salt film existing at the corroding surface. Figure 3 shows the electric potential distribution through such a film<sup>14</sup>, permitting the conclusion that the film is about 8 to 9  $\mu\text{m}$  thick, with an effective conductivity of  $(1.6 \pm 0.3) \times 10^{-4} \Omega^{-1} \cdot \text{cm}^{-1}$ .

### Covered Pits

The types of pit amenable to measurement with microelectrodes are open pits. However, many pits in commercial alloys are known to be covered, as depicted schematically in Figure 1(c). Figure 4 demonstrates the complexity which can be exhibited by pits in stainless steels<sup>15</sup>. This type of "wandering" attack is assisted by the undercutting of the pit cover at numerous sites.

The above common observation is in sharp contrast to the pits obtained on a stainless steel which have been ion-implanted with molybdenum<sup>16</sup>. Figure 5 shows an array of uniform

spherically-shaped pits produced on the implanted alloy. Many of the covers in this example have been torn or removed completely by the subsequent processing of the sample, but those that did survive were found to be metallic, presumably comprising the thin molybdenum-rich implanted alloy layer. Because of the large quantity of molybdenum in this layer (approximately 18 wt%), it has been protected from undercutting and additional perforation of the cover. It was concluded that such pits typically exhibit one central hole. Hemispherical covered pits were also observed during the early stages of pitting of a UNS S30200 stainless steel<sup>17</sup>, although in this case the covers were assumed to be porous, but with the pores microscopically unresolvable.

However, a porous cover may not be necessary, in that pit covers with a central hole (Figure 5) produce smooth spherically-shaped pits, and those with multiple perforations (Figure 4) have very irregular internal shapes. This indicates that the dissolution processes at the metal surface are transport controlled. The environment in a covered pit cannot be treated as homogeneous, but supports significant concentration gradients which ensure chemical conditions at the dissolving surfaces which are quite different to those exterior ones on which passive films are formed.

### **Persistent Pits**

Clearly, those pits which lead to engineering failure (perforation), must be able to persist. Mechanisms which would aid such persistence have been discussed above in terms of the maintenance of local aggressive chemistries which mitigate against repassivation. An additional mechanism, which has been shown<sup>8</sup> to exist in alloys, involves the anodic dissolution along the boundaries between inclusions and matrix. If the inclusions are elongated, large deep pits can be formed, thereby assisting in the establishment of a stable aggressive chemical environment.

Metallographic observations of sections through persistent pits in stainless steels invariably show pit profiles which suggest that pits deepen through a mechanism of "pitting within pits". Figure 6 shows sketches of successive sections through individual large pits formed in two austenitic stainless steels after exposure to seawater.

### **Alloying to Reduce Local Anodic Dissolution**

To inhibit the continued growth of a pit in the local aggressive environment it is necessary to block anodic dissolution. Mechanisms to achieve this have recently been discussed by Lu et al. after a series of studies to determine the specific roles of the alloying elements constituent in the modern "super" stainless steels. In particular, it has been shown<sup>18</sup> that there is a definite synergism of action among the elements chromium, molybdenum and nitrogen, most of which results in the blocking of the dissolution of the major alloying element, iron. This is supported by the evidence of Figure 6, wherein there is more "pitting within the pit" in UNS S30403 than in the molybdenum-containing modification, UNS S31603.

## **Alloying to Inhibit Cathodic Reactions**

No matter what type of anodic dissolution takes place within growing pits, if this involves metal ions passing into solution, electrons are released which must be consumed somewhere by a corresponding cathodic reaction. Such cathodic reactions might occur within the pit, thereby comprising an "occluded cell", or outside the pit on the surrounding exterior passive surface. The common observation that pits are frequently found to be spaced over a given metal surface has been used as evidence for the cathodic reactions occurring in each pit vicinity, thereby blocking the nucleation of a nearby new pit. However, the observation of the formation of gas (hydrogen?) bubbles within growing pits<sup>19,14</sup> is evidence for at least some cathodic reaction inside pits.

Whatever the rationale, if the cathodic reaction does occur outside the pits, it must take place on the passive film. It has been shown by Lu<sup>20,21</sup> that various alloying treatments can inhibit the cathodic reactions occurring on stainless steels. It will be interesting to see if such treatments are able to inhibit pitting corrosion.

## **Conclusions**

The role of the breakdown of passivity during the process of "serious" pitting corrosion (i.e. that which degrades the performance of the metal in which it occurs) has been demonstrated to be minor. The serious aspects of pitting involve the continued *growth* of pits, and this is determined by the local chemistry and ionic transport within pits. Continued development of pits is determined also by the properties of ion-transporting "salt films", and not by the ability of the metal or alloy to repassivate locally.

From the alloy development viewpoint, the challenge is to determine those alloying elements which can successfully inhibit either anodic dissolution in the extremely aggressive local environments present within active pits or the cathodic processes occurring on surrounding passive surfaces. A continued search for specific *synergistic* effects between alloying elements would appear to be appropriate in this context, in order that only small additions will be necessary, which improve corrosion resistance without degrading the mechanical properties of commercial alloys.

It would be helpful in future discussions of experiment and theory of pitting processes if the relevant "stages" of pitting were clearly addressed.

## **Acknowledgments**

Much of the research on which this paper is based was supported by grants from Chemetics International Company Ltd., the Natural Sciences & Engineering Research Council (Canada) and the University Research Incentive Fund (Province of Ontario). The contributions of members of the Corrosion Laboratory, McMaster University are gratefully acknowledged, and in particular the input and advice of Yucheng Lu and Jingli Luo.

## References

1. J. Kruger et al., in Proceedings, 9th. International Congress on Metallic Corrosion, NRC, Ottawa, 1984, Vol.2 p. 180
2. H.-H. Strehblow and M.B. Ives, *Corrosion Science* **16**, 317 (1976).
3. G.S. Frankel, in *"Advances in Localized Corrosion"*, H. Isaacs et al., eds., NACE-9, Houston, 1990, p. 137
4. K.J. Vetter, *Ber. Bunsenges. phys Chem.*, **69** 589 (1965)
5. K.J. Vetter and H-H. Strehblow, in *"Localized Corrosion"*, ed. B.F. Brown et al., NACE, Houston, 1974, p. 240
6. R.W. Staehle, in *"Fundamental Aspects of Stress Corrosion Cracking"*, S.M. Bruemmer et al., eds., The Minerals, Metals & Materials Soc., 1992, p.457
7. G. Wranglén, in *"Localized Corrosion"*, ed. B.F. Brown et al., NACE-3, Houston, 1974, p. 462
8. M.B. Ives and S.C. Srivastava, in *"Advances in Localized Corrosion"*, (NACE-9), NACE, Houston, 1991, p. 295
9. Z. Sklarska-Smialowska, *"Pitting Corrosion of Metals"*, NACE, Houston, 1986, p.1
10. J. L. Luo, Y.C. Lu and M. B. Ives, *J. Electroanalytical Chem.* **326** (1992): p.50
11. J.L. Luo and M.B. Ives, in *"Critical Issues in Localized Corrosion"*, Electrochem. Soc., Pennington, NJ, Proceedings Vol. 92-9, 1992 p.134
12. J.L. Luo, Y.C. Lu and M.B. Ives, in *Techniques for Corrosion Measurement* A. Bronson, G. Warren, eds., NACE, Houston, 1992, p. 22-1.
13. T. Hakkarainan, in *"Advances in Localized Corrosion"*, H. Isaacs et al., eds., NACE-9, Houston, 1990, p.277
14. J.L. Luo, PhD Dissertation, *"Salt Film Development during Pitting of Nickel"*, McMaster University, 1992
15. Guo Ruijin, S.C. Srivastava and M.B. Ives, *Corrosion*, **45**, (1989): p.874.
16. U.G. Akano et al., *Corrosion Science*, **31**, (1990) p. 367.
17. G.S. Frankel et al., *Corrosion* **43** (1987) 429
18. Y.C. Lu, M.B. Ives and C.R. Clayton, *"Synergism of Alloying Elements and the Pitting Corrosion Resistance of Stainless Steel"*, *Corrosion Science*, in press
19. F.W. Pickering and R.P. Frankenthal, in *"Localized Corrosion"*, ed. B.F. Brown et al., NACE-3, Houston, 1974, p. 261
20. Y.C. Lu and M.B. Ives, *"Improvement by Cerium of the Localized Corrosion Resistance of Stainless Steel"* *Corrosion Science*, in press.
21. Y.C. Lu and M.B. Ives, *"Chemical Treatment with Cerium to Improve Crevice Corrosion Resistance of Stainless Steels"*, this conference, Paper 371B.

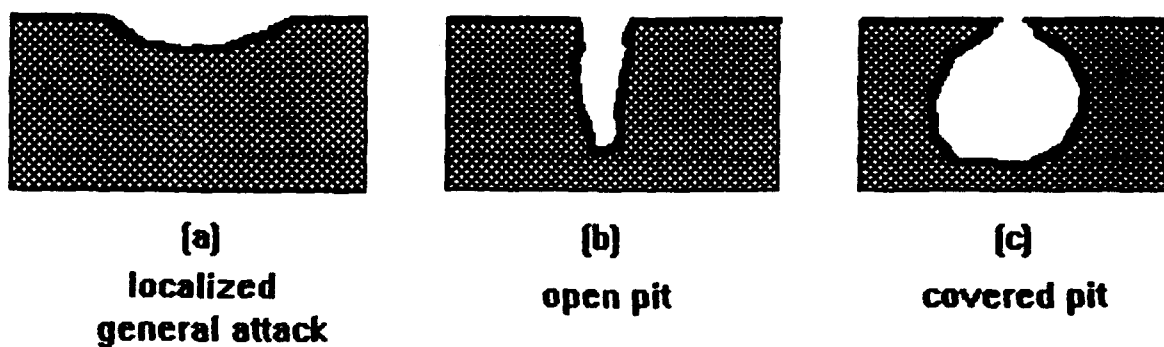


**Figure 1** Schematic form of selected Localized Corrosion phenomena.

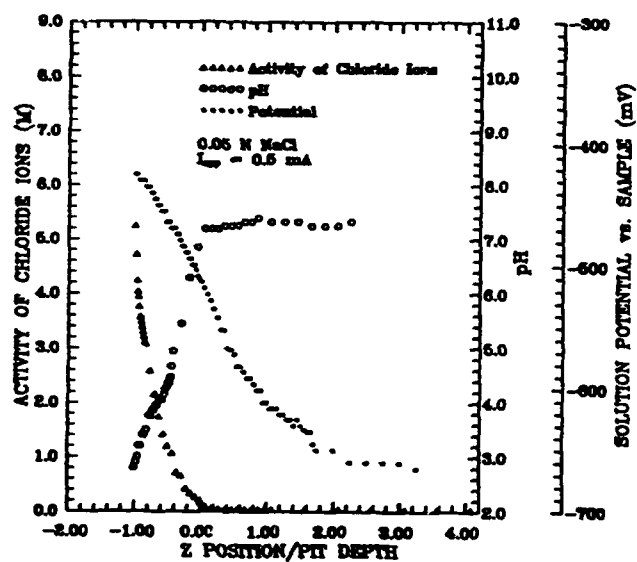


**Figure 2** Solution potential, pH and chloride activity outside and within a simulated pit galvanostatically driven in nickel in 0.05N sodium chloride.

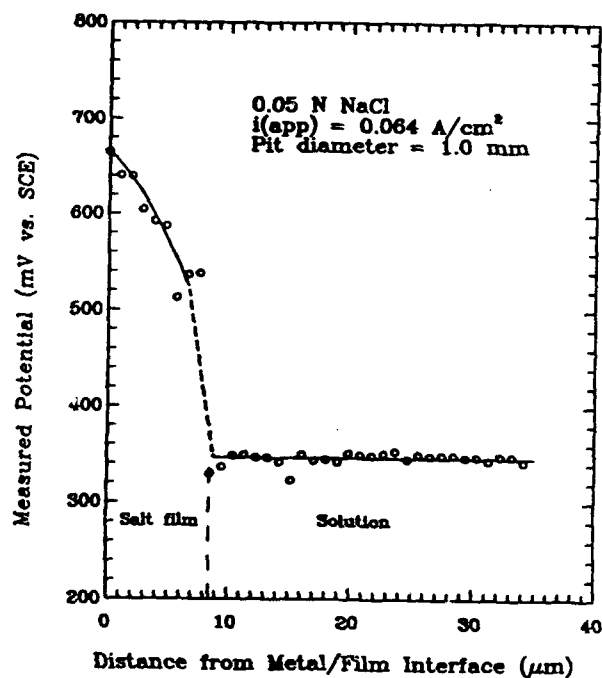


**Figure 3** Potential distribution through the salt film at the bottom of a simulated pit in nickel.



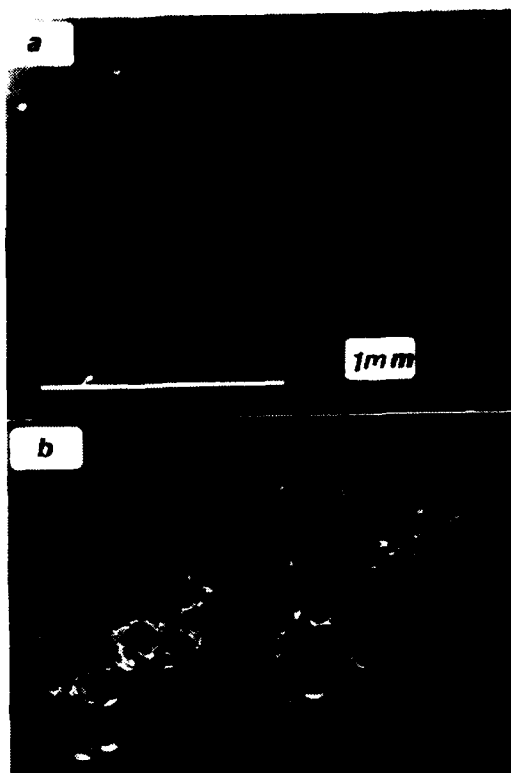
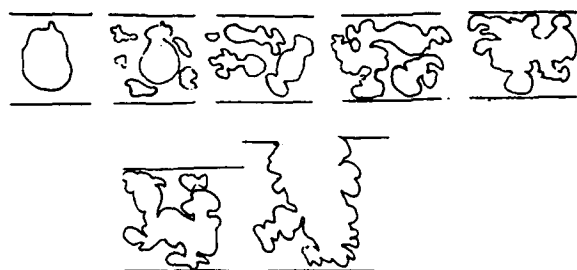


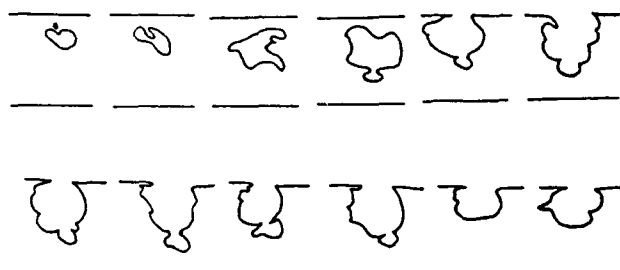
**Figure 4** Complex pit formation in UNS S90403 (a) after potentiostatic dissolution; (b) same region following ultrasonic cleaning.



**Figure 5** Pits on UNS S30100 implanted with molybdenum and anodically polarized in a sodium sulphate/sodium chloride solution. Pit sizes are from 20 to 40  $\mu\text{m}$ .



(a)



(b)

**Figure 6** Profiles through successive sections of through-wall pits produced in tubes exposed to flowing seawater: (a) UNS S30403; (b) UNS S31603

## Atomic Structure of Passive Films on Nickel

P. Marcus

Laboratoire de Physico-Chimie des Surfaces  
CNRS (URA 425) - Université Pierre et Marie Curie  
Ecole Nationale Supérieure de Chimie de Paris  
11 rue Pierre et Marie Curie  
75231 Paris Cedex 05, France

H. Talah

Laboratoire de Physico-Chimie des Surfaces  
CNRS (URA 425) - Université Pierre et Marie Curie  
Ecole Nationale Supérieure de Chimie de Paris  
11 rue Pierre et Marie Curie  
75231 Paris Cedex 05, France

V. Maurice

Laboratoire de Physico-Chimie des Surfaces  
CNRS (URA 425) - Université Pierre et Marie Curie  
Ecole Nationale Supérieure de Chimie de Paris  
11 rue Pierre et Marie Curie  
75231 Paris Cedex 05, France

### Abstract

Scanning tunneling microscopy has been used to study *ex situ* Ni(111) electrodes passivated in 0.05 M H<sub>2</sub>SO<sub>4</sub> at + 550, +650 and + 750 mV/SHE. Roughening with respect to the unpassivated surfaces is observed on a submicroscopic scale and on the atomic scale. Atomic resolution imaging demonstrates the crystalline character of the passive oxide film and the epitaxy with the substrate. The roughening on the submicroscopic scale increases with higher passivation potentials. The observed roughness is attributed to the result of the competition between metal dissolution and nucleation and growth of the passive film. The roughening on the atomic scale is evidenced by the formation of stepped surfaces of the passive film which suggests a tilt of the surface of the film with respect to the interface between the film and the metal substrate. Local variations of the film thickness are likely to result from this tilt. The chemical nature of the atomic structure which is resolved is discussed.

Key terms: nickel, passivity, passive film, atomic structure, roughening, scanning tunneling microscopy

### Introduction

The relationships between, on one side, the extent of ordering and the nature of the defects within passive films and, on the other side, the electrochemical behaviour and the corrosion resistance remain to be investigated in details. A bilayer model is generally admitted to describe the chemical distribution of material in passive films with the inner part of the film being an oxide component and the outer part being an hydroxide or oxihydroxide component<sup>1</sup>. The extent of ordering within passive films is a more controversial topic although the amorphous character has been emphasized<sup>2</sup>. The case of pure nickel is a typical example. The thickness of the oxide inner part of the film has been reported to range from 0.4 to 1.2 nm, and that of the hydroxide outer part has been reported to range from fractions of a monolayer to a complete monolayer (0.6 nm thick)<sup>3-6</sup>. The extent of ordering within the passive film on nickel, which is possibly related to the *ex situ* or *in situ* conditions of investigation of the structure, is still a subject of debate<sup>7,8</sup>.

We have undertaken a Scanning Tunneling Microscopy (STM) investigation of the structure of the passive film formed on pure nickel substrate in acid electrolyte. In the previously reported *in situ* STM investigations related to passive films, the lateral resolution that would be requested to provide information on the atomic structure of the film was not achieved<sup>9-15</sup>. Our choice of a (111) oriented Ni single crystal substrate was mainly dictated by the concern of selecting a system for which the passive film had previously been reported as being crystalline<sup>7</sup> in order to facilitate atomic resolution imaging. Preliminary experiments confirmed the possibility of achieving lateral atomic resolution in *ex situ* investigations of passive films<sup>16</sup>. This paper reports further *ex situ* investigations where the influence of the passivation potential was studied.

## Experimental

Sample preparation from a Ni single crystal rod (purity 99.999%) involved successively: orientation within  $\pm 1^\circ$  by X-ray diffraction, spark machining, mechanical and electrochemical polishing and annealing at 1275 K for a few hours in a flow of purified hydrogen at atmospheric pressure. The sample was then transferred at room temperature and under the hydrogen atmosphere into a nitrogen-containing glove box where the electrochemical experiments were performed. Sulfuric acid (0.05 M) was prepared from reagent grade  $\text{H}_2\text{SO}_4$  and ultrapure water (resistivity of 18 M $\Omega$ .cm). After immersion of the electrode in the electrochemical cell, the potential was stepped from the open circuit value to the passivation potential. Three values were selected: +550, +650 and +750 mV/SHE. After 12 minutes of anodic polarization and completion of the formation of the passive film, the experiment was stopped by emersing the Ni(111) electrode at the applied potential. The sample was then rinsed with ultrapure water, dried in nitrogen gas and finally transferred to air for STM imaging.

STM imaging was performed with the Nanoscope II and III from Digital Instruments (Santa Barbara, CA) operating in atmospheric conditions. Maximum scan range both in X and Y axis of the scanner used for atomic resolution imaging was about 12  $\mu\text{m}$  or 0.7  $\mu\text{m}$  depending on the scanner used. Images were recorded for the most part in the constant current topographic mode of the STM. All reported topographic images have had a least square plane subtracted in order to remove any tilt of the scanning head relative to the sample surface. Sample bias voltages used for atomic resolution imaging were in the range from 30 to 200 mV, positive or negative, and setpoint currents were in the range from 0.5 to 1 nA. Tunneling probe tips were made from W wire etched in 1M KOH.

## Results and Discussion

STM observations of the metal substrate before the passivation treatment revealed the presence of the steps and terraces of the surface. Steps of monolayer to multilayer height could be imaged which were all aligned along the  $\langle -101 \rangle$  directions of the substrate, as determined from a crystal alignment performed by X-ray back diffraction measurements. The width of the terraces was frequently found to exceed 100 nm. A typical example is shown on fig. 1a where two merging step edges along the  $[-101]$  and  $[1-10]$  directions have been imaged. The roughness which was measured on the terraces as it can be seen on fig. 1a is supposedly resulting from the formation of the native oxide. Atomic resolution was not achieved on these surfaces.

After the passivation treatment, two major levels of structural modifications were observed. On a submicroscopic scale (0.2  $\mu\text{m}$ ), a higher density of terraces was observed. The density and the shape of these new terraces depend on the passivation potential. On the atomic scale ( $< 20$  nm), a lattice forming stepped surfaces has been resolved. The parameters of this lattice and the characteristics of the stepped surfaces are found to be independent of the passivation potential.

### I. Submicroscopic scale observations

Examples of the terraces that have been observed on the passivated surfaces can be seen on the topographic images shown on fig. 1b, c and d. On the image shown on fig. 1b recorded after passivation at + 550 mV/SHE, trigonal terraces are resolved. The largest dimension of these terraces is about 90 nm and their density is about

$2 \times 10^{10} \text{ cm}^{-2}$ . The ledges of these terraces are oriented along the  $\langle -101 \rangle$  and  $\langle 1-21 \rangle$  main crystallographic directions of the substrate. On the image shown on fig. 1c recorded after passivation at + 650 mV/SHE, hexagonal terraces are resolved. The largest dimension is about 40 nm and the density is about  $6 \times 10^{10} \text{ cm}^{-2}$ . In this image, the ledges are oriented along the  $\langle 1-21 \rangle$  directions of the substrate. Hexagonal terraces of about the same size and density but with ledges oriented along the  $\langle -101 \rangle$  directions of the substrate could be found after passivation at + 650 mV/SHE. On the image shown on fig. 1d recorded after passivation at + 750 mV/SHE, unsymmetrical terraces are resolved. The largest dimension of these terraces is about 30 nm and their density is about  $1 \times 10^{11} \text{ cm}^{-2}$ . Non-oriented ledges are associated to the unsymmetrical shape. The different shapes of these terraces which are imaged after passivation at different potentials clearly evidence a roughening effect which increases with the passivation potential. At + 550 and + 650 mV/SHE, the ledges are formed along the main crystallographic directions of the substrate. More ledges are formed when increasing the potential from + 550 to + 650 mV/SHE. At + 750 mV/SHE, a more severe roughening causes a loss of symmetry with non oriented ledges. The density of the terraces is also found to increase with the passivation potential.

Two competitive phenomena both depending on the potential take place during a passivation experiment: metal dissolution and formation of the passive film. One effect of increasing the passivation potential is to increase the rate of metal dissolution. The dissolution reaction is activated and the concentration of defect sites acting as preferential sites of dissolution is increased<sup>17</sup>. Increasing the passivation potential is also expected to increase the rate of formation of the passive film by activating the reaction of oxide formation and by increasing the number of nucleation centers as defect sites are also preferential sites for nucleation of the oxide<sup>18</sup>. The variations of topography between the passivated and the not yet passivated surfaces are likely to result from the competition between metal dissolution and formation of the passive film. The highest terraces could correspond to the areas where the fastest passivation took place. Such areas are surrounded by areas which have undergone active dissolution for a longer time and where the metal surface is more corroded. The lowest terraces could correspond to the most corroded areas where the slowest passivation took place. The roughening which is found to increase with the passivation potential thus possibly reflects the effect of the activation of the metal dissolution. The density of the terraces which is measured to increase at higher potential possibly reflects the effect of the potential on the concentration of defect sites which are preferential sites of oxide nucleation. The density of the terraces would then relate to the density of the passivation nucleation centers.

## II. Atomic scale observations

Zooming in down to atomic scale in the large terraces described in the above section revealed a second level of structural modifications of the passivated surfaces with respect to the unpassivated surfaces. Figure 2 shows a typical image recorded on the atomic scale after passivation. Stepped surfaces were imaged over large areas without noticeable defects. A corrugated lattice is resolved on the terraces which has the following parameters:  $0.32 \pm 0.02 \text{ nm}$  and  $117^\circ \pm 5^\circ$ . The agreement is excellent with the lattice parameters of a (111) oriented NiO structure:  $0.295 \text{ nm}$  and  $120^\circ$ . The images indicate that the passive film is crystalline and the following epitaxial relationship is deduced:  $\text{NiO}(111) // \text{Ni}(111)$  and  $\text{NiO}[-101] // \text{Ni}[-101]$ . The step edges of these passivated surfaces are disoriented within  $5$  to  $10^\circ$  from the main crystallographic directions:  $\langle -101 \rangle$  and  $\langle 1-21 \rangle$  with the presence of kinks as it can be seen on fig. 2. The (111) oriented terraces have a width which ranges locally from  $2$  to  $5 \text{ nm}$ . The step height also varies locally but remain consistent with monolayer or double layer NiO spacings. This amounts to an average tilt of  $8 \pm 5^\circ$  for these stepped surfaces with respect to the (111) orientation of the terraces. Figure 3 shows a higher magnification image of these stepped surfaces. The fine structure of a step locally oriented along the  $[-101]$  direction has been resolved. It shows a two stage transition between the upper and lower terraces with an intermediate terrace being resolved as indicated on the figure. This intermediate terrace is characterized by a higher corrugation.

The relation between the chemical nature of the passive film and the STM image is dependent on the tunneling mechanism taking place for such thin film systems. A direct mechanism that would involve tunneling from the metal substrate through the passive film is not likely. Such mechanism would probably require the penetration of the tip into the passive film because the overall thickness of the film is large with respect to the usual width

of tunneling barrier (about  $0.5 \text{ nm}^{19}$ ). In addition, the measured lattice parameters are consistent with those of nickel oxide ( $0.417 \text{ nm}$ ) but not with those of metallic nickel ( $0.352 \text{ nm}$ ). Two other mechanisms can be invoked which differ depending on the role of the hydroxide outer layer. In the case of the mechanism involving electron transfer from the metal substrate to the conduction band of the oxide inner part followed by tunneling through the hydroxide outer part, the structural information in the images would be relative to the oxide inner part of the passive film. In such a case, the thickness of the hydroxide outer layer should not exceed the width of the tunneling barrier. The image shown in fig. 3 where a two stage transition between upper and lower terraces has been resolved, could then be explained by a transition between two O planes (or Ni) via a Ni plane (or O) in the (111) oriented NiO structure which alternates O planes and Ni planes. In the case of a mechanism involving electron transfer through the oxide inner part to surface hydroxyl groups which would act as centers for tunneling to the tip, the structural information of the images would be relevant to the hydroxide outer part of the passive film. The recorded images would then suggest that the surface hydroxyl groups form a complete ordered monolayer of (1x1) periodicity with respect to the underlying nickel oxide. The image shown in fig. 3 could then be explained by a transition between two hydroxyl monolayers covering terraces of the underlying oxide. The intermediate area could correspond to a terrace not covered by hydroxyl groups in the vicinity of a step edge. The structural information contained in the recorded images does not allow us to favor any of these two possible mechanisms.

The average tilt of  $8 \pm 5^\circ$  with respect to the (111) oriented terraces is associated with the presence of steps at the surface of the passive film. The interface between the metal substrate and the passive film cannot be directly resolved in STM experiments. We believe that the orientation of the substrate surface remains (111) and thus the tilt which is measured is assigned to a partial relaxation of the stress resulting from the lattice misfit (expansion of 16.5 % of bulk NiO with respect to bulk Ni) between the metal substrate and the oxide inner part of the film.  $10^\circ$  is the exact amount of disorientation which is required in order to have a perfect coincidence between 7 unit cells of the metal substrate and 6 unit cells of the oxide component of the film. This suggests a possible accommodation of the lattice misfit by a site coincidence growth model. The mechanism for the accommodation of the lattice misfit in the direction parallel to the steps, where no tilt is observed, is not elucidated.

A major consequence of the tilt of the terraces of the passive film with respect to the interface, as illustrated on fig. 4, would be local variations of the thickness of the film. Taking into account an average thickness of  $1 \text{ nm}$ , the presence of steps at the surface of the film would induce variations of thickness of about 25 %. The thickness could even decrease by about 45 % in the case of the presence of monolayer substrate steps at the interface. The bottom of the steps could constitute preferential sites for the breakdown of the passive film where the barrier effect of the film on cation diffusion would be drastically decreased. Considering the average width of  $3.5 \text{ nm}$  for the terraces and one of such sites per step, the density of these preferential sites of breakdown would be about  $3 \times 10^6 \text{ cm}^{-1}$ . It is suggested that the most critical breakdown sites are the sites where a step of the passive oxide coincide with a step of the substrate giving a film thickness estimated to  $0.56 \text{ nm}$  in fig. 4. The density of such sites is evidently much lower than the density of steps on the oxide surface.

### Conclusion

After passivation of Ni(111) single crystal surfaces in  $0.05 \text{ M H}_2\text{SO}_4$ , STM observation in air shows an epitaxial crystalline film. The roughness of the surface is increased with respect to that of the unpassivated surface on two different scales. On a submicroscopic scale, the roughening results in the formation of large terraces. This is assigned to a mechanism of competition during passivation between metal dissolution and formation of the passive film. This roughening increases with the passivation potential and results in higher density of terraces with non oriented edges at higher potential. On the atomic scale, stepped surfaces are imaged. Their characteristics are independent of the passivation potential. The measured lattice parameters of  $0.30 \pm 0.02 \text{ nm}$  and  $117 \pm 5^\circ$  fit those of NiO(111), the inner component of the passive film. The epitaxial relationship of the film to the substrate surface is: NiO(111) // Ni(111) and NiO[-101] // Ni[-101]. The stepped surface of the passive film is attributed to a tilt of  $8 \pm 5^\circ$  of the surface of the film with respect to the interface between metal substrate and passive film. This tilt may result from the accommodation of the lattice misfit at the

interface. A major consequence of this tilt would be local variations of the thickness of the film which would constitute preferential sites of breakdown.

#### References

1. see e.g. P. Marcus, in *Electrochemistry at Well-Defined Surfaces*, eds. J. Oudar, P. Marcus and J. Clavilier, Special Volume of *J. Chimie Physique* 88 (1991), p. 1687.
2. J. Kruger, in *Advances in Localized Corrosion*, eds. H. Isaacs, U. Bertocci, J. Kruger and S. Smialowska, NACE (1987), p. 1, and references therein.
3. P. Marcus, J. Oudar and I. Olefjord, *J. Microsc. Spectrosc. Electron.* 4 (1979): p. 63.
4. B.P. Lochel and H.-H. Strehblow, *J. Electrochem. Soc.* 131 (1984): p. 713.
5. F.T. Wagner and T.E. Moylan, *J. Electrochem. Soc.* 136 (1989): p. 2498.
6. D.F. Mitchell, G.I. Sproule and M.J. Graham, *Appl. Surf. Sci.* 21 (1985): p. 199.
7. J. Oudar and P. Marcus, *Appl. Surf. Sci.* 3 (1979): p. 48.
8. R. Cortes, M. Froment, A. Hugot-Legoff and S. Joiret, *Corrosion Sci.* 31 (1990): p. 121.
9. O. Lev, F.R. Fan and A.J. Bard, *J. Electrochem. Soc.* 135 (1988): p. 783.
10. F.R. Fan and A.J. Bard, *J. Electrochem. Soc.* 136 (1989): p. 166.
11. R.C. Bhardwaj, A. Gonzalez-Martin and J. O'M. Bockris, *J. Electrochem. Soc.* 138 (1991): p. 1901.
12. R.C. Bhardwaj, A. Gonzalez-Martin and J. O'M. Bockris, *J. Electrochem. Soc.* 139 (1992): p. 1050.
13. K. Sashikata, N. Furuya and K. Itaya, *J. Vac. Sci. Technol.* B9(2) (1991): p. 457.
14. M. Szklarczyk and J. O'M. Bockris, *Surf. Sci.* 241 (1991): p. 54.
15. J.S. Chen, T.M. Devine, D.F. Ogletree and M. Salmeron, *Surf. Sci.* 258 (1991): p. 346.
16. V. Maurice, H. Talah and P. Marcus, *Surface Sci.* 284 (1993): p. L431.
17. W.J. Lorenz and K.E. Heusler, in *Corrosion Mechanisms*, ed. F. Mansfeld, Marcel Dekker Inc. (1987), p. 1, and references therein.
18. M. Bäumer, D. Cappel, H. Kühlenbeck, H.-J. Freund, G. Wilhemi, A. Brodde and H. Neddermeyer, *Surf. Sci.* 253 (1991): p. 116.
19. G. Binnig, H. Rohrer, Ch. Gerber and E. Weibel, *Phys. Rev. Lett.* 49 (1982): p. 57.

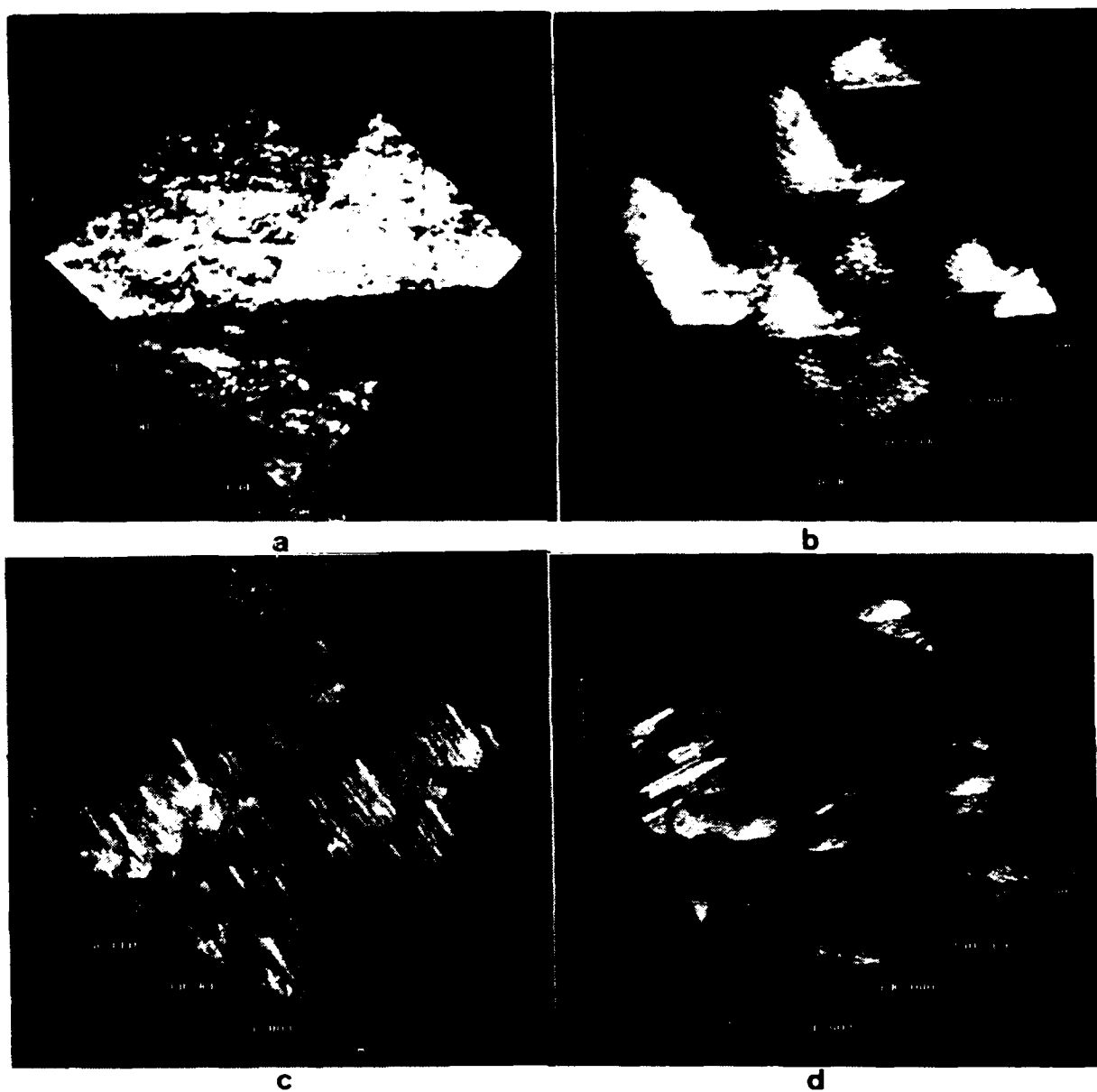


Fig. 1.  $(200 \times 200) \text{ nm}^2$  topographic images<sup>a</sup> (Z range of 5 nm) of the Ni(111) surface recorded: (a) before passivation, tunneling conditions: sample bias voltage,  $V_t = + 582 \text{ mV}$  and setpoint current  $I_t = 0.7 \text{ nA}$ ; (b): after passivation at  $+ 550 \text{ mV/SHE}$  in  $0.05 \text{ M H}_2\text{SO}_4$ ,  $V_t = - 300 \text{ mV}$ ,  $I_t = 0.5 \text{ nA}$ ; (c): after passivation at  $+ 650 \text{ mV/SHE}$  in  $0.05 \text{ M H}_2\text{SO}_4$ ,  $V_t = + 50 \text{ mV}$ ,  $I_t = 0.5 \text{ nA}$ ; (d): after passivation at  $+ 750 \text{ mV/SHE}$  in  $0.05 \text{ M H}_2\text{SO}_4$ ,  $V_t = + 60 \text{ mV}$ ,  $I_t = 0.5 \text{ nA}$ .

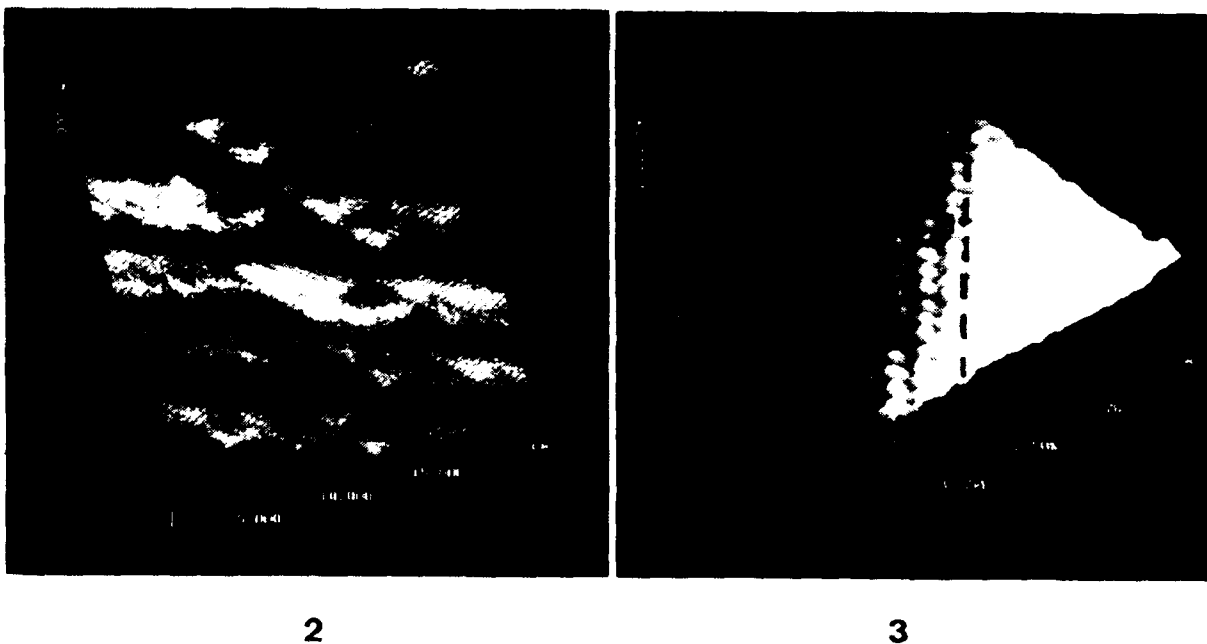


Fig. 2.  $(20 \times 20) \text{ nm}^2$  topographic image of the stepped surface of the passive film formed on Ni(111) at + 750 mV/SHE, sample bias voltage  $V_t = +135 \text{ mV}$ , and setpoint current  $I_t = 0.8 \text{ nA}$ . The kinked structure of the step edges and the atomic lattice on the terraces are evidenced.

Fig. 3.  $(5 \times 5) \text{ nm}^2$  topographic image of the fine structure of a step edge along the  $[-101]$  direction of the surface passivated at + 750 mV/SHE,  $V_t = +113 \text{ mV}$ ,  $I_t = 0.5 \text{ nA}$ . The lines indicate a two stage transition between the upper terrace (right) and the lower terrace (left). The hexagonal lattice assigned to NiO is marked.

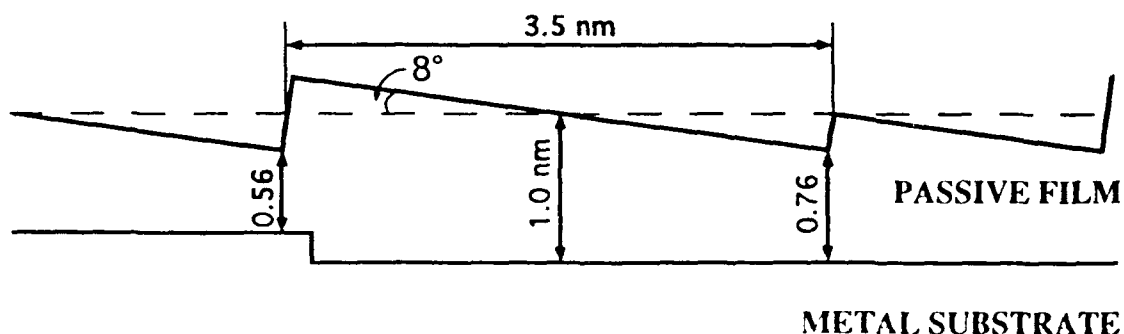


Fig. 4. Schematic representation of the orientation of the surface of the passive film with respect to the orientation of the interface between metal substrate and film. A thickness of 1 nm and a tilt of  $8^\circ$  have been considered. Monolayer oxide steps (0.24 nm) and double layer oxide steps (0.48 nm) are represented at the surface as well as a monolayer substrate step (0.20 nm) at the interface.



# THE EFFECT OF THE TEMPERATURE ON THE PASSIVE $\text{Ni(OH)}_2$ GROWTH ON NICKEL IN 1.0 M $\text{NaOH}$ USING THE HOPPING-MOTION MODEL

C. V. D'Alkaine

Group of Electrochemistry and Polymers

DQ/UFSCar - C.P. 676 - 13565-905 São Carlos (SP)

BRAZIL

M. A. Santanna

Group of Electrochemistry and Polymers

DQ/UFSCar - C.P. 676 - 13565-905 São Carlos (SP)

BRAZIL

## ABSTRACT

The influence of the temperature on the voltammetric transient of the  $\text{Ni(OH)}_2$  film growth on nickel has been study using the equations of the hopping motion model previously developed. The results seems to be in agreement with the model and permit to calculate the ions jump distance, the exchange current density and the activation energy inside the film, at the peak conditions. The jump distance decrease with the increase of the temperature.

**Key terms:** hopping motion model, nickel oxidation, passivation.

## I. Introduction

The electrochemistry of nickel in alkaline solution has been the subject to an extended literature which covers battery electrodes [1,2], precipitate electrodes [3,4], special electrochemical studies for the high potential region [5-8], or general ones including the whole potential region [9-15], principally due to the necessity of a deep understanding of the  $\text{Ni(OH)}_2/\text{NiOOH}$  system for alkaline batteries. On the other side, the  $\text{Ni}/\text{Ni(OH)}_2$  system in this medium has also been the objective of special works [16,17]. From the point of view of its morphological constitution it seems that there is a complet agreement about that it is  $\text{Ni(OH)}_2$ , even when some measurements [12] point out the existence of some  $\text{NiO}$  in the metal/film region. The existence of the  $\text{NiO}$  in that region will depend on the preparation and electrochemical history of the electrode [18]. For the case of  $\text{Ni(OH)}_2$  it seems that at the more cathodic potentials it is the  $\alpha\text{-Ni(OH)}_2$  which growth and at higher potentials the  $\beta\text{-Ni(OH)}_2$ . The  $\alpha\text{-Ni(OH)}_2$  seems to undergo a slow transformation (dehydration) to  $\beta\text{-Ni(OH)}_2$  [9,11,18].

The kinetic of  $\text{Ni(OH)}_2$  growth at the potential region of  $\text{Ni}/\text{Ni(OH)}_2$  system was only treated in the works of Guzman et al. [16] and Pyung and Hong [17]. In the work of Guzman et al. [16] the results are interpreted in terms of a complex reaction pathway involving different hydroxide adsorbed species even

when it will imply a roughness factor of about 6 due to the fact that the related charge is of the order of  $3 \text{ mC/cm}^2$  for the oxidation peak. In the work of Pyun and Hong [17] the potentiostatic transient are interpreted on the base of a modification of the point defect model, taken into account fickian diffusion and field migration and, as a consequence, only valid for low current densities.

From a theoretical point of view it must be pointed out that two different conditions could be present in any electrochemical growth. Those corresponding to high field, that means high current density (Verwey [19], Mott [20] Dewald [21] and D'Alkaine [22], when the hopping motion model is taken into account) and those corresponding to low field (then low current density) and, specially for nickel, where the concentration gradients must be taken into account (MacDonald [23], Shultze and Lohrengel [24], Pyun and Hong [17]).

In the present paper the growth of the  $\text{Ni(OH)}_2$  will be studied by voltammetric techniques following the general treatment of D'Alkaine et al. [22]. Due to the fact that the kinetic experimental data come from the first voltammetric peak we are in the case of high fields where we can disregard the concentration gradient flux. In the present paper we have use the equations for the hopping motion model and a special attention has been given to the influence of the temperature on the kinetic parameters.

## II. Experimental

The nickel electrode was 99.99% purity, included in an epoxy resin and polished up to 600 emery paper before each measurement. The reference electrode to which all potentials are referred, was  $\text{Hg/HgO/NaOH}$  1.0 M. The reference electrode was also submitted to the temperature change.

The sweep rate ( $v$ ) was change from 5 to 350  $\text{mV/s}$  and always only the first cycle was registred. Typical results at  $15^\circ\text{C}$  could be seen in Figure 1. The temperatures employed were 45, 35, 25, 15 and  $5^\circ\text{C}$ . All the measurements were beginning at the inicial potential of  $-1.1 \text{ V}$ , at which the electrode was held up to an initial cathodic current density of  $0.40 \text{ mA/cm}^2$ , before to initiate the potential sweep. This procedure was repeated before each measurement together with the polishing. The solution was 1.0 M NaOH prepared from A.G. reagent and the water was bidestillated.

## III. Results and Discussions

When the differential equation of a voltammetric transient is analysed at the peak conditions for the case of the hopping motion model for the film and a Tafel relation for the

metal/film interface [22] the following equation must be valid:

$$\ln i_p = \frac{\alpha_f f a r v}{C i_p} + \ln i_f^0 \quad (1)$$

where  $\alpha_f$ ,  $C$  and  $a$  are the transfer coefficient, volume per coulomb and the jump distance inside the film, respectively;  $i_p$  and  $i_f^0$  the peak current and exchange current densities for the film, respectively;  $f = F/RT$ ;  $r$  the roughness factor of the surface and  $v$  the sweep velocity.

This equation must be followed for peak conditions at different sweep velocities when the peak charge becomes constant, that means that there is no more change in the film due to aging [22]. This will happens at high sweep velocities like it is shown in Figure 2 in a typical result for the different temperatures for the system Ni/Ni(OH)<sub>2</sub>, NaOH in this case at 15°C.

The corresponding representation of the eq. (1) also for 15°C is shown in Figure 3, which is also a typical result when compared with the other temperatures.

The departure from a stright line due to the aging occurs at higher  $v$  for higher temperatures, which is consistent with the fact that the aging must happen faster with higher temperature. If the departure is taken as a variation of  $i_f^0$  in the slow  $v$  region, then it is possible to obtain from Figure 3 and eq. (1) the Figure 4, which is also typical for all the studied temperatures. The decrease of  $i_f^0$  at low  $v$  shows that the aging promotes defect recombination and then reduce the preexponential factor of  $i_f^0$  inside the film.

From the slope of all the figures equivalent to Figure 3 at the different temperatures, using a calculate value of  $C$  of  $1.2 \times 10^{-4} \text{ cm}^3/\text{C}$ ; under the hypothesis that the energetic barrier inside the film must be symmetric and then  $\alpha_f$  must be equal to 1 and considering a roughness factor of 1.4 [18], in Figure 5 it is given the variation of  $a$  with the temperature.

Due to the fact that those values seems to correspond to the higher constant lattice parameters, if we consider that the lamellar organization of the Ni(OH)<sub>2</sub> is parallel to the metal surface, perhaps the  $a$  reduction with the temperature is related with a dehydration process [25].

From the region of high velocities ( $i_f^0$  constant with  $v$ ), it is possible to calculate the activation energy through an Arrhenius plot for this condition. This result is given in Figure 6.

From this plot it was possible to obtain a value of 13.5 kcal/mol for the activation energy in this region. The value calculated for the pre-exponential factor due to the fact that the  $i_0$  give practically the same value like that for other systems, but with an activation energy 2 or 3 times higher, gives a very high value ( $1.7 \times 10^6$  A/cm<sup>2</sup>). Because this is the first case for an hydroxide film (the other was oxide films), it is necessary to wait for studies on other hydroxides in order to try to understand this last result.

#### IV. Conclusion

As a result of the application of the hopping motion model to the charge movement of the ion inside the Ni(OH)<sub>2</sub> film during its voltammetric transient growth, and due to the fact that the parameters obtained from the calculations seems to be reasonable, it is possible to consider that the film growth could be seen as a normal continuous film growth perpendicularly to the metal surface. The exchange current density inside the film at the peak conditions increases with the sweep velocity coming to be constante at a given critical  $v$ , showing that for higher  $v$  the film is always the same, in agreement with the fact that the peak charge density becomes also constant. Interesting results in these conditions are: (a) the jump distance decrease with the increase of the temperature possibly due to dehydration; (b) the activation energy results to be 13.5 kcal/mol. These results show a normal behaviour against the temperature during the transient growth of Ni(OH)<sub>2</sub> film.

*Acknowledgments:* M.A. Santanna is grateful to CAPES for her PhD scholarship. Both authors are grateful do FAPESP for the financial support to the program to which this work belongs.

#### REFERENCES

1. B.C. CORNILSEN, X. SHAN and P.L. LOYSELLE, "J. Power Sources", 29, (1990), 453-466.
2. D. GUAY, G. TOURILLON, E. DARTYGE, A. FONTAINE, J. MCBREEN, K.I. PANDYA and W.E. O'GRADY, "J. Electroanal. Chem.", 305, (1991), 83-95.
3. P. BERNARD, C. GABRIELLI, M. KEDDAM, H. TAKENOUTI, J. LEONARDI and P. BLANCHARD, "Electrochim. Acta", 36, (1991), 743-746.
4. J.O. ZERBINO, C. DE PAULI, D. POSADAS and A.J. ARVIA, "J. Electroanal. Chem.", 330, (1992), 675-691.

5. C. A. MELENDRES and S. XU, "J. Electrochem. Soc.", 131(10), (1984), 2239-2243.
6. C. ZHANG and S.M. PARK, "J. Electrochem. Soc.", 134(12), (1987), 2966-2970.
7. C. A. MELENDRES, W. PADEN, B. TANI, W. WALCZAK, J. Electrochem. Soc.", 134, (1987), 762-763.
8. DESILVESTRO, D. A. CORRIGAN and M. J. WEAVER, "J. Electrochem Soc.", 135(4), (1988), 885-892.
9. L. D. BURKE and T. A. M. TWOMEY, "J. Electroanal. Chem.", 162, (1984), 101-119.
10. B. BEDEN, D. FLONER, J. M. LÉGER and C. LAMY, "Surface Science" 162, (1985), 822-829.
11. F. HAHN, D. FLONER, B. BEDEN and C. LAMY, "Electrochim. Acta", 32(11), (1987), 1631-1636.
12. H. W. HOPPE and H. H. STREHBLOW, "Surface and Interface Analysis", 14, (1989), 121-131.
13. H. W. HOPPE and H. H. STREHBLOW, "Corrosion Science", 31, (1990), 167-177.
14. G. LARROMONO and C. GUTIÉRREZ, "J. Electrochem. Soc.", 137(2), (1990), 428-435.
15. Z. JIANG, Y. XIANG and J. WANG, "J. Electroanal. Chem.", 316, (1991), 199-209.
16. R. S. S. GUZMÁN, J. R. VILCHE and A. ARVIA, "Corrosion Science", 18, (1978), 765-778.
17. S. I. PYUN and M. H. HONG, "Electrochim. Acta", 37(2), (1992), 327-332.
18. M. A. SANTANNA, PhD Thesis, Chemistry Department, Federal University of São Carlos - Brazil (1993).
19. J. W. VERWEY, "Physica", 2, (1967), 1059.
20. N. CABRERA, N. F. MOTT, "Rep. Prog. Phys.", 12, (1949), 163.
21. J. F. DEWALD, "J. Electrochem. Soc.", 102, (1955), 1.
22. C. V. D'ALKAINE, L. M. M. DE SOUZA and F. C. NART, "Corrosion Science", 34(1), (1993), 129-149.
23. C. Y. CHAO, L. F. LIN and D. D. MACDONALD, "J. Electrochem. Soc.", 128, (1981), 1187.

24. J.W. SCHULTZE and M.M. LOHRENGEL, "Electrochim. Acta", 28, (1983), 973.
25. B. MANI and J.P. NEUFVILLE, "J. Electrochem. Soc.", 135(4) (1988), 800-803.

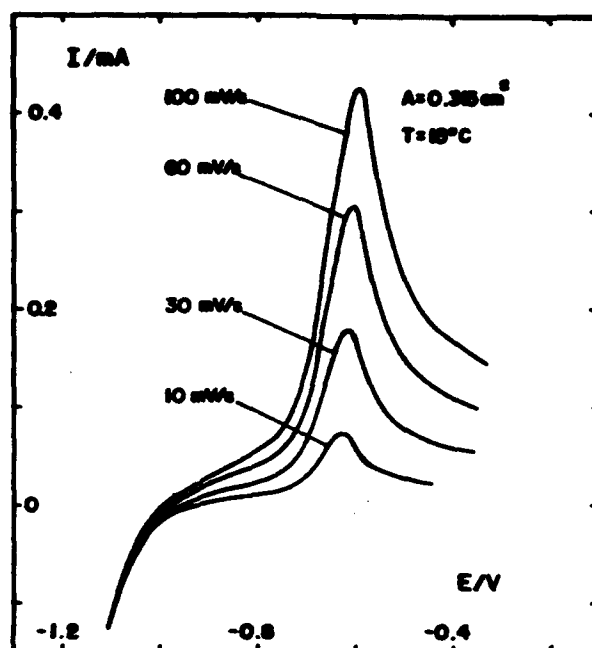


Figure 1. Typical first sweeps for Ni in 1.0 M NaOH in this case at  $15^\circ\text{C}$ .

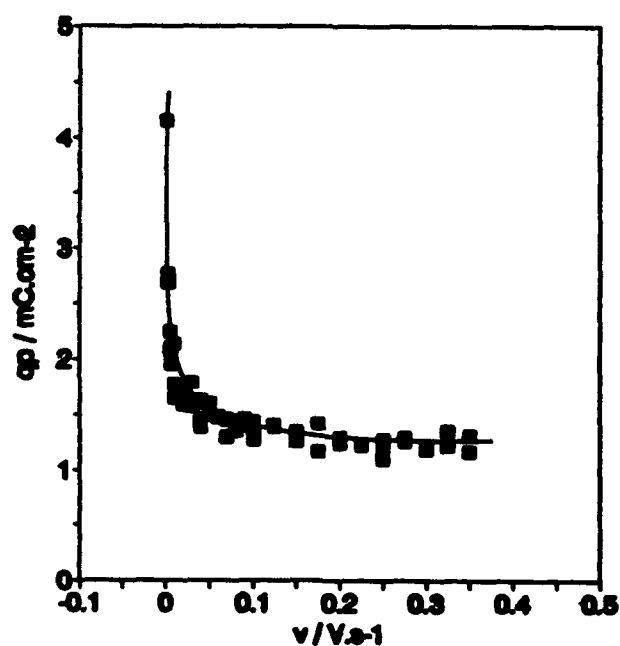


Figure 2. Typical peak charge density against sweep velocity for the Ni/Ni(OH)<sub>2</sub>, NaOH system in this case at  $15^\circ\text{C}$ .

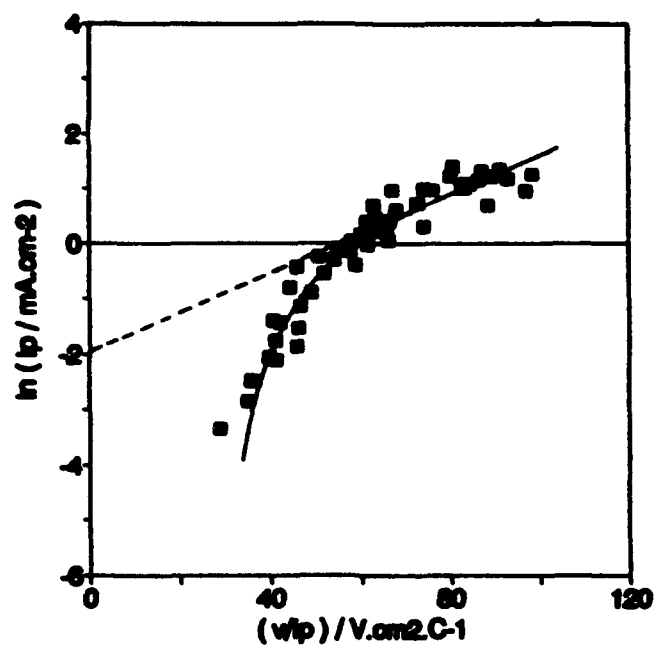


Figure 3. Typical result of eq. (1) for the  $\text{Ni/Ni(OH)}_2$ ,  $\text{NaOH}$  system in this case at  $15^\circ\text{C}$ .

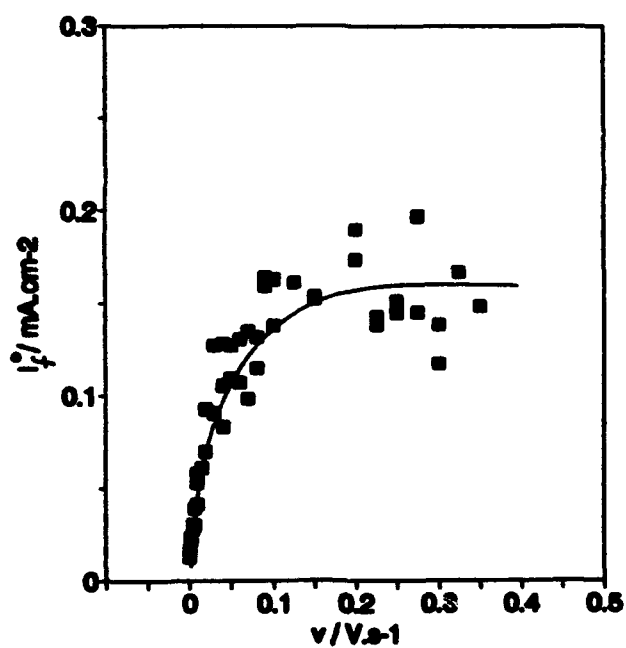


Figure 4. Typical exchange current density inside the film ( $i_f^0$ ) against the sweep velocity for the  $\text{Ni/Ni(OH)}_2$ ,  $\text{NaOH}$  system in this case at  $15^\circ\text{C}$ .

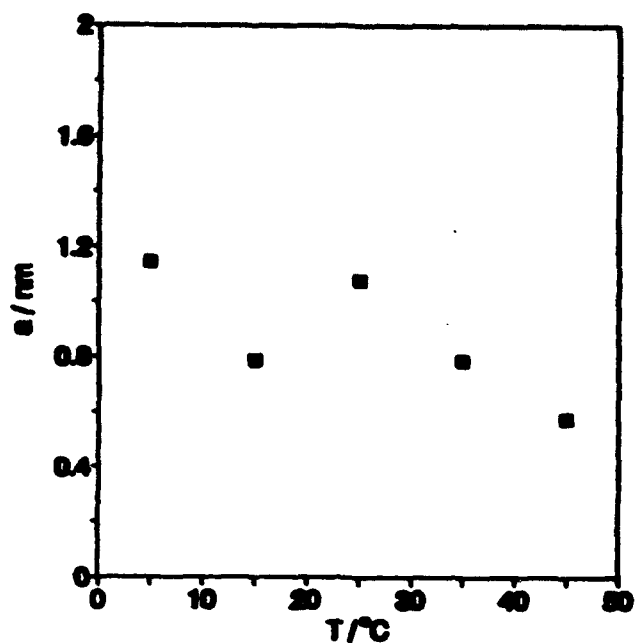


Figure 5. Variation of the jump distance with the temperature for the film of the Ni/Ni(OH)<sub>2</sub>, NaOH system.

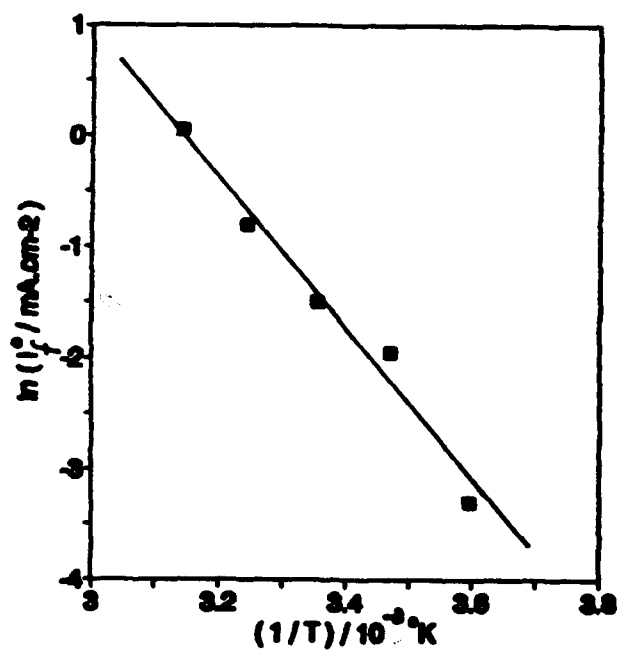


Figure 6. Arrhenius plot of the exchange current density in the region of  $v$  of constant  $i_0^0$ , for the Ni/Ni(OH)<sub>2</sub>, NaOH system.



# **XPS Study of Passive Films on Stainless Steels in Neutral Solutions**

**Antonella Rossi**

Dipartimento di Chimica e Tecnologie Inorganiche e Metallorganiche,  
Università di Cagliari, Via Ospedale 72,  
I-09124 Cagliari, Italy

**Bernhard Elsener**

Institute of Materials Chemistry and Corrosion,  
Swiss Federal Institute of Technology, ETH Hönggerberg,  
CH-8093 Zurich, Switzerland

## **Abstract**

XPS results on the passive film thickness and composition of conventional (1.4301, AISI 304) and high alloyed stainless steel with 6% molybdenum (1.4529) at different polarization potential in neutral sulfate solutions are presented. The thickness of the passive film increases linearly with the passivation potential, on the high alloyed 1.4529 SS it is lower. The composition of the passive film changes with the applied potential, the content of chromium (III) oxyhydroxide is highest at low potentials and decreases with increasing potential. In agreement with the similar bulk chromium content the chromium(III) oxyhydroxide content in the passive films of both stainless steels is similar. On the 1.4529 SS (25% nickel and 6% molybdenum in the alloy) about 10% oxidized nickel and oxidized molybdenum in the valence state +VI are incorporated into the passive film resulting in a much lower iron oxide content in the film. The substrate underneath the passive film is strongly enriched in metallic nickel (twice the bulk content) and depleted in iron. The low iron oxide content in the passive film, the presence of oxidized molybdenum with a high valence state and the strong nickel enrichment beneath the passive film may be responsible for the outstanding stability against localized corrosion attacks of the high alloyed 1.4529 stainless steel.

**Key words:** passivity, stainless steel, surface analysis, molybdenum

## **Introduction**

Stainless steels are of great importance in many areas of present technology. It is well known that stainless steels owe their good corrosion resistance to the formation of a thin adherent surface oxy-hydroxide, the passive film. The study of passive films, their chemical composition, structure and electronic properties is thus an important subject of basic corrosion research [1,2]. Growth and breakdown of passive films on metals and alloys are found to be strongly related to the structure,

the presence of defects [3] or vacancies [4] and the composition of the alloy / passive film interface. In contrast to the passive film itself there is only few information in the literature about changes of this interface. Surface analytical methods such as x-ray photo-electron spectroscopy (XPS) can provide informations about the composition and the chemical state of surface films with minimum amount of induced damage [5]. The application of this technique to the study of passive films in the order of some nanometer thickness is not without problems [6 - 8]. The passive film thickness and composition as well as the composition of the interface alloy / passive film can be estimated applying mathematical models that take into account the attenuation due to the presence of a contamination layer [9 -14].

Passive films of cristalline and amorphous Fe-Cr alloys, ferritic and austenitic stainless steels have been studied mainly in acidic solutions. Generally a marked enrichment of chromium in the passive films and an increase of the film thickness with potential is found [6, 8, 14]. The enrichment of molybdenum [15] or the presence of nickel in the passive films is a subject of controversy. Only very few papers refer to the behaviour in neutral solutions [16 - 18]. Recent in situ studies using ellipsometry and potential-modulated UV visible reflection spectroscopy on high purity Fe-Cr alloys [19] and Fe-Cr-Ni alloys [20] show that in neutral sulfate solutions (pH 6) the cationic mass fraction of  $\text{Cr}^{3+}$  ions decreases gradually with increasing potential. The thickness of the films increased with increasing potential and at a given potential it decreased with increasing Cr content in the film [20].

In this work results of XPS analysis of passive films formed on the conventional 1.4301 SS and the high alloyed 1.4529 stainless steel at different polarization potentials in neutral sulfate solutions are reported. The changes of thickness and chemical composition of the passive films, the differences in the metal/film interface and the role of molybdenum are discussed refering to the outstanding resistance against localized corrosion of the high alloyed 1.4529 stainless steel.

## **Experimental**

### ***Sample preparation***

The compositions of the two stainless steels are given in table 1. The samples - already fixed on the XPS sample holder - were mechanically polished in water (up to 1000 grit) and in ethanol to 1  $\mu\text{m}$  diamond paste ("mirror like"). They were washed with p.a. ethanol, dried under a nitrogen stream and mounted in the electrochemical cell [21]. The deaerated electrolyte was filled in the cell immediately. The samples were hold 15 minutes at the open circuit potential and then polarized in one step to the passivation potential and hold there for one hour. The passivated samples were removed from the cell under applied potential, carefully rinsed with bidistilled water, dried in a stream of nitrogen and held under nitrogen flux until the sample was transferred to the fast entry lock (usually within two minutes). The untreated part of the sample was masked by a gold ring.

### ***Electrochemical experiments***

The experiments were performed in the electrochemical cell previously described [21]. The solutions were prepared from analytical grade  $\text{Na}_2\text{SO}_4 \cdot 10\text{H}_2\text{O}$  and bidistilled water. They were deaerated with argon at least 4 hours prior and during the measurements. Potentiostatic polarization at potentials in the passive range was started after 15 min exposure at the open circuit potential. All the potentials were measured and referred vs the saturated calomel electrode (SCE) at room temperature.

### ***X-ray photoelectron spectroscopy***

XPS analyses were performed with an ESCALAB MkII spectrometer (Vacuum Generator Ltd., U.K.). The vacuum system consists of a turbomolecular pump, fitted with a liquid nitrogen trap, and a titanium sublimation pump. The residual pressure in the spectrometer during the data acquisition was always lower than  $5 \cdot 10^{-7}$  Pa. The x-ray source was Mg K $\alpha$  (1253.6 eV) run at 20 mA and 15 kV. The spectra were obtained in the digital mode (VGS 1000 software on APPLE IIe). The electron analyzer was operated in Fixed Analyzer Transmission (FAT) mode with a pass energy of 20 eV (FWHM Ag 3d $_{5/2}$  = 1.1 eV).

The instrument was calibrated according to [22]. The spectra were resolved into their components after iterative background subtraction according to Shirley [23] and Sherwood [24]. Sputtered stainless steel samples were used as reference for the curve fitting parameters of all the metallic signals, the parameters for the oxidized components were determined on standards. For iron and chromium only the 2p $_{3/2}$  signals were taken into account for the quantitative analysis. The energy differences, height ratios and the FWHM ratios of the Mo3d $_{3/2}$  and Ni2p satellite were determined on standards and hold constant during the curve fitting. The gaussian / lorentzian ratio and the FWHM were hold constant and the energy of the peaks and their height were fitted using a least square algorithm. To compensate for sample charging during the analysis all the binding energies were referred to the carbon 1s signal at 285.0 eV.

### ***XPS quantitative analysis***

The quantitative evaluation of the XPS data was performed as described in [13, 14]. The determination of the thickness and composition of the passive films is based on the three-layer model (contamination, oxide film, substrate) [13, 14] assuming that each of the layers is homogeneous in thickness and composition. Electrons originating from the metal substrate (taken as semi infinite) are attenuated exponentially by the oxide layer and the contamination layer, whereas the electrons originating from the oxide layer (with limited thickness  $t$ ) are attenuated only by the contamination. The basic equations for each component and the solution of the system of equations is given in [13,14].

The mean free-path values  $\Lambda(E_{\text{kin}})$  of the electrons were calculated as  $\Lambda_i = B\sqrt{E_{\text{kin}}}$  with  $B=0.054$  for elements in their formal oxidation state zero,  $B=0.096$  for the oxidized forms and  $B=0.087$  to take into account the attenuation due to the contamination layer [25]. The values for the photoionization cross-section  $\sigma(h\nu, \gamma, i)$

were taken from [26] and corrected for the angular asymmetry function  $L(\gamma)$  with  $\gamma=49.1^\circ$ . The model accounts for the different densities of the alloy ( $\rho^m = 7.9 \text{ gcm}^{-3}$ ) and of the passive film ( $\rho^{ox} = 5 \text{ gcm}^{-3}$ ).

## Results

### *Electrochemical Results*

The open circuit potential of all the samples tested decreased with time of exposure to the deaerated solutions. After 15 minutes a value of  $-400 \pm 20 \text{ mV}$  was reached for the 1.4301 steel at pH 5.8. For the 1.4529 steel at pH 5.8 values of  $-280 \pm 20 \text{ mV}$  were found. The current density during the 3600 sec potentiostatic polarization at all potentials from  $-0.2$  to  $+0.6 \text{ V SCE}$  decreased with time according to the expected power law ([figure 1](#)). A steady state current density after one hour of polarization is nearly reached only for the passivation potential  $+600 \text{ mV}$ , while at all the other potentials the current continues to decrease.

### *XPS Results*

High resolution spectra: The high-resolution XPS spectra after background subtraction [23, 24] and curve fitting of iron  $2p_{3/2}$ , chromium  $2p_{3/2}$ , nickel  $2p_{3/2}$  and molybdenum  $3d$  of a 1.4529 stainless steel sample polarized for one hour at  $+0.2 \text{ V SCE}$  in  $1 \text{ M Na}_2\text{SO}_4$  solution (pH 5.8) are shown in [figure 2](#). The spectra of all the alloy constituents show contributions from the oxidized states (ox) in the passive film and the metallic state (met) immediately beneath the film. The  $\text{Mo}3d$  spectra show contributions from two oxidized species, identified as  $\text{Mo(VI)}$  and a lower oxidation state, in addition to the metallic signal from the substrate.  $\text{Ni}2p$  shows the typical satellite structure for both the metal and the oxide peaks. The  $\text{O}1s$  signal is not a single peak, the curve fitting shows always three components respectively attributed to  $\text{M-O-M}$  ( $530 \text{ eV}$ ),  $\text{M-OH}$  and adsorbed  $\text{H}_2\text{O}$ .

Binding energies: With increasing passivation potential the binding energy ([figure 3](#)) of oxidized iron increases from  $710.1 \text{ eV}$  to  $710.8 \text{ eV}$  reflecting the increasing  $\text{Fe(III)}$  content. The  $\text{Cr}2p_{3/2}$  (ox) signal tends towards lower binding energy values reaching  $576.8 \text{ eV}$  at  $+0.6 \text{ V SCE}$ . This behaviour may be attributed to the presence of a higher chromium(III) hydroxide content in the passive film at lower potential values as it can also be observed from the  $\text{MO}/\text{O}_{\text{tot}}$  ratio. The binding energy of  $\text{Ni(ox)}$  remains constant at  $855.8 \text{ eV}$ , on the 1.4301 steel they are slightly lower. In the 1.4529 SS with molybdenum, two oxidized species were detected:  $\text{Mo(VI)}$  at a nearly constant binding energy of  $232.4 \pm 0.2 \text{ eV}$  and the intermediate oxidation state  $\text{Mo(hy)}$  [27] with a binding energy increasing from  $230.5$  to  $231.6 \text{ eV}$ . The binding energies of the metallic components in the substrate immediately underneath the film remain constant at  $707.0 \pm 0.1 \text{ eV}$  for iron on both steels, for Cr  $573.9 \text{ eV}$  (1.4529) and  $574.0 \text{ eV}$  (1.4301) and for nickel  $852.7 \text{ eV}$  (1.4529) and  $852.9 \text{ eV}$  (1.4301). Molybdenum shows a binding energy of  $227.5 \text{ eV}$ .

**Thickness of the passive film:** The thickness of the passive film (calculated according to the three layer model as described above with correction for the attenuation due to the contamination layer) after 1 hour of polarization increases linearly with the passivation potential (figure 4). On the high alloyed stainless steel 1.4529 the passive film thickness is lower. The slope  $dt/dU$  is approx. 3.3 nm/V.

**Composition of the passive film:** The composition of the passive film vs the applied potential is shown in figure 5. The Cr(III) oxyhydroxide content in the film is nearly the same for the two stainless steels and decreases with higher potential values whereas the Fe(ox) content increases. Only about 3-5% of oxidized nickel is detected on the 1.4301 SS, on the 1.4529 stainless steel about 10% are measured. About 10% of oxidized molybdenum is incorporated in the passive film of the 1.4529 SS regardless of the passivation potential.

**Composition of the substrate:** The composition of the alloy beneath the oxide film for the 1.4529 stainless steel is shown in figure 6. In agreement with results from acidic solutions the interface is strongly enriched in metallic nickel (up to 48%) and depleted in iron (only 30% compared to 52% in the bulk) and to minor extent in chromium. Molybdenum is present with about the same concentration as in the passive film but enriched compared to the bulk composition. For the 1.4301 stainless steel about 20% of nickel are found beneath the passive film.

## **Discussion**

Electrochemical results and the behaviour under practical conditions in aggressive near neutral to acidic chloride containing environments [28] show that the 1.4529 stainless steel is practically resistant against pitting and crevice corrosion even at very high chloride contents whereas the 1.4301 SS is very susceptible to localized attacks - and this despite a similar bulk chromium content of the two stainless steels. Different reasons may be responsible for this fact:

### ***1. Passive film thickness and composition***

The XPS investigations of this work on the two stainless steels (1.4301 without, 1.4529 with 6-7% Mo) show that thickness (figure 4) and composition of the passive films (figure 5) formed in neutral 1 M sulfate solutions (pH. 5.8) strongly depend on the formation potential. It has to be pointed out that for each potential freshly prepared samples had been used. As is shown in figure 3 the binding energies of the oxidized components in the passive film depend on the potential but are identical for both stainless steels under study. Furtheron the *Cr(III) oxy-hydroxide* content is similar on both stainless steels: it decreases from 60-70% at -0.2 V SCE to only 25% at +0.6 V SCE (figure 5). *Oxidized nickel* is depleted in the passive films: on the 1.4301 SS (with 10% Ni in the bulk) only 3 - 5%, on the 1.4529 (25% Ni in the bulk) about 10% Ni(ox) are present in the passive films independent of the potential. On the 1.4529 SS (6-7% Mo in the bulk) about 10-12% *oxidized molybdenum* are found in the passive films, thus oxidized molybdenum definitely

is incorporated in the passive films. For both Ni(ox) and Mo(ox) the pH of the solution will have a great influence, oxidized nickel being favoured in alkaline [29]. This might be the reason that oxidized nickel is not revealed in passive films studied in acidic solutions [6, 30, 31]. The "ex-situ" XPS data of this work are in very good agreement with the chromium content of the passive film determined "in-situ" by Sugimoto [20] (potential modulated UV visible reflection spectroscopy) on the similar alloy Fe-20Cr-25Ni. The quantitative evaluation of the passive film composition assumes a single, homogeneous layer. The results obtained - an increase in iron oxide and correspondingly the decrease of the Cr(III) oxyhydroxide with increasing potential (figure 5) - do not contradict the bilayer model for passive films [4] proposed for stainless steels [30], too.

From the above results it can be ruled out that the content of Cr(III) oxy-hydroxide is responsible for the huge discrepancy in the stability of the passive films on the two stainless steels. A major difference between the two stainless steels is found in the iron oxide content: on the 1.4301 SS the value of 50% Fe(ox) is reached at ~0.2 V SCE, at potentials > 0.4 V it reaches values around 70% whereas, as a result of the presence of Cr(III), Ni(ox) and Mo(ox) in the passive film of the high alloyed 1.4529, the content of iron oxide remains below 50% even at the most positive potentials of 0.6 V SCE. This low iron oxide content together with a smaller film thickness (figure 4) and a higher content of hydroxide M-OH content stabilizes the passive film. Defects created by  $\text{Fe}^{2+}$  are compensated by  $\text{Mo}^{n+}$  present in the passive film [31].

## *2. Composition of the substrate beneath the passive film*

In agreement with XPS studies on passive films formed on austenitic stainless steels in acidic solutions [6, 30, 31] a marked enrichment (about twice the bulk content) of metallic nickel underneath the passive film is found in this work. This corresponds to the low tendency of nickel to oxidation. A slight enrichment of molybdenum is noted, too (figure 6). This results in a iron content of only 30% in the outermost metal layers of the 1.4529 SS whereas about 60 - 65% Fe are found for the 1.4301 stainless steel. This difference might be another reason for the elevated resistance to localized corrosion of the 1.4529: the high content in nickel and molybdenum strongly shifts the anodic polarization curve into more noble direction and reduces the (local) dissolution current, the acidification of the pit embryo and thus facilitates the repassivation.

Summarizing, the lower iron oxide content and the presence of a high valence state of molybdenum in the passive film of the 1.4529 SS may be responsible for the much lower pit initiation rate, the enrichment of nickel and molybdenum in the alloy beneath the passive film facilitates repassivation. The combination of these facts explains the outstanding resistance against localized corrosion of the 1.4529 SS compared to the conventional 1.4301 SS with a similar chromium content. Further work to study the effect of longer passivation time is in progress.

## Conclusions

This XPS study on passive films of stainless steels formed in neutral sulfate solutions has shown

1. The thickness of the passive films on stainless steels in neutral solutions increases linearly with the applied potential. Passive films on the high alloyed 1.4529 SS are thinner than on the conventional 1.4301 SS.
2. The Cr (III) oxihydroxide content is similar on both stainless steels and decreases with more positive potentials. This is in agreement with literature data from in-situ studies performed with UV visible reflection spectrometry.
3. The incorporation of oxidized nickel and molybdenum in the passive film of the high alloyed stainless steel 1.4529 reduces the content of oxidized iron in the film. The presence of oxidized molybdenum with a high valence state can compensate defects created by  $\text{Fe}^{2+}$  and reduce the pit initiation frequency.
4. The strong enrichment of nickel and molybdenum beneath the passive film of the high alloyed 1.4529 SS reduces the (local) dissolution current and acidification of the pit embryo electrolyte, thus the repassivation is facilitated

## References

- [1] R.P. Frankenthal and J. Kruger (Eds.), *Passivity of Metals*, Electrochemical Society, Princeton (1978)
- [2] M. Froment (ed. ), *Passivity of Metals and Semiconductors*, Elsevier Science Publishers, Amsterdam (1983)
- [3] C. Cohen, D. Schmaus, A. Elbiache and P. Marcus, *Corr. Sci.* 31 (1990) 207
- [4] D.D. Macdonald, in Critical Factors of Localized Corrosion, G.S. Frankel and R.C. Newman eds., Proc. Vol 92-9, The Electrochemical Society Pennington NJ (1992) p. 1 - 35
- [5] D. Briggs and M.P. Seah (Eds), *Practical Surface Analysis*, Second Edition. John Wiley and Sons (1990)
- [6] H. Fischmeister and U. Roll, *Fresenius Z. Anal. Chem.* 319 (1984) 639 - 645
- [7] D. Landolt, S. Mischler, A. Vogel and H.J. Mathieu, *Corrosion Science* 31 (1990) 431
- [8] K. Asami and K. Hashimoto, *Langmuir* 3 (1987) 897 - 904
- [9] K. Asami and K. Hashimoto, *Corros. Sci.* 24 (1984) 83
- [10] I. Oleffjord, Application of Surface Analysis Methods to Environmental / Material Interactions, D.Baer, C.R. Clayton and G.D. Davis eds, Proc. Vol. 91-7, The Electrochemical Society Pennington NJ (1991) p. 22
- [11] H.W. Hoppe and H.H. Strehblow, *Corros. Sci.* 31 (1990) 167

- [12] P. Marcus and J. Herbelin, Application of Surface Analysis Methods to Environmental / Material interactions, D.Baer, C.R. Clayton and G.D. Davis eds, Proc. Vol. 91-7, The Electrochemical Society Pennington NJ (1991) p. 222
- [13] A. Rossi and B. Elsener, *Surface Interface Analysis* 18 (1992) 499 - 504
- [14] B. Elsener and A. Rossi, *Electrochimica Acta* 37 (1992) 2269 - 2276
- [15] R. Goetz and D. Landolt, *Electrochimica Acta* 29 (1984) 667 - 676
- [16] K. Sugimoto and S. Matsuda, *Mater. Sci. Eng.* 42 (1980) 181
- [17] W.P. Yang, D. Costa and P. Marcus, in "Oxide Films on Metal and Alloys, B.R. MacDougall, R.S. Alwitt and T.A. Ramanarayanan (eds), Proc. Vol. 92-22 p. 516 - 529, The Electrochemical Society, Pennington NJ (1992)
- [18] B.O. Elfström, *Mater. Sci. Eng.* 42 (1980) 173
- [19] N. Hara and K. Sugimoto, *Corrosion Science* 31 (1990) 197 - 206
- [20] N. Hara and K. Sugimoto, *J. Electrochem. Soc.* 138 (1991) 1594
- [21] S. Virtanen, B. Elsener and H. Böhni, *J. less-common Metals* 145 (1988) 581
- [22] M.P.Seah, *Surface and Interface Analysis* 14 (1989) 488
- [23] D.A.Shirley, *Phys.Rev. B* 5 (1979) 4709
- [24] P.M.A.Sherwood, "Practical Surface Analysis", ed. Briggs and M.P.Seah, Appendix 3, p.445, J. Wiley N.Y. 1983
- [25] M.P. Seah and W.A. Dench, *Surface Interface Analysis* 1 (1979) 1
- [26] J.H.Scofield, *J.Electron Spectroscopy*, 8 (1976) 129
- [27] I. Olefjord and B. Brox, Passivity of Metals and Semiconductors, ed. M. Froment, Elsevier Science Publishers Amsterdam (1983) p. 561
- [28] H. Haslmair, R. Morach and H. Böhni, High alloyed Steels and Nickel Alloys for Fastenings in Road Tunnels, submitted to CORROSION NACE
- [29] H.W. Hoppe and HH. Strehblow, *Surface Interface Analysis* 14 (1989) 121
- [30] I. Olefjord, B. Brox and U. Jelvestam, *J. Electrochem. Soc.* 132 (1985) 2854
- [31] I. Olefjord and C.R. Clayton, *ISIJ International* 31 (1991) 134

Table 1: Ccompositions of the stainless steels (mass%)

Material	Fe	Cr	Ni	Mo	Mn	S	P	other
1.4301	bal	18.1	8.7	0.06	1.3	0.003	0.029	Si 0.58
1.4529	bal	20.8	24.9	6.42	0.82	0.002	0.016	N 0.19



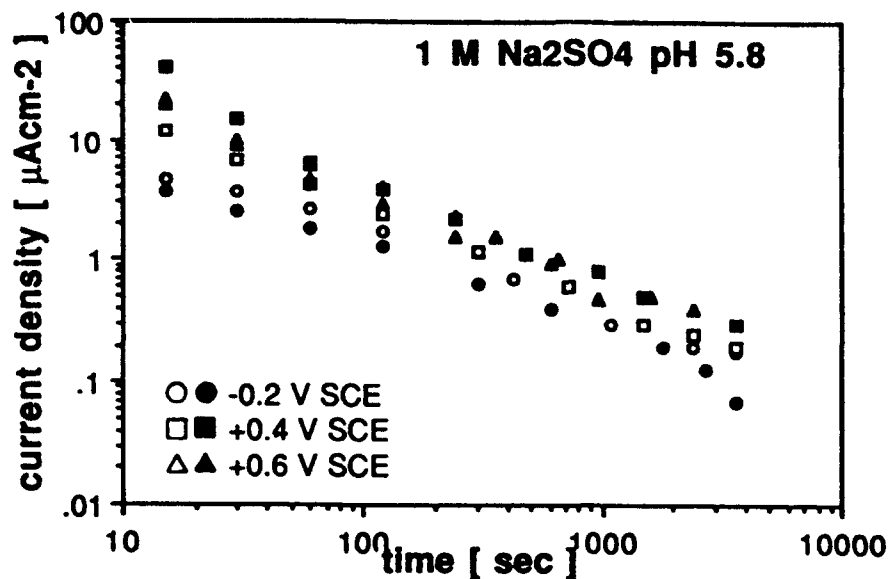


**Figure 1:**  
Current density during potentiostatic passivation in 1 M  $\text{Na}_2\text{SO}_4$  at different potentials in the passive range (open symbols 1.4301, closed symbols 1.4529).

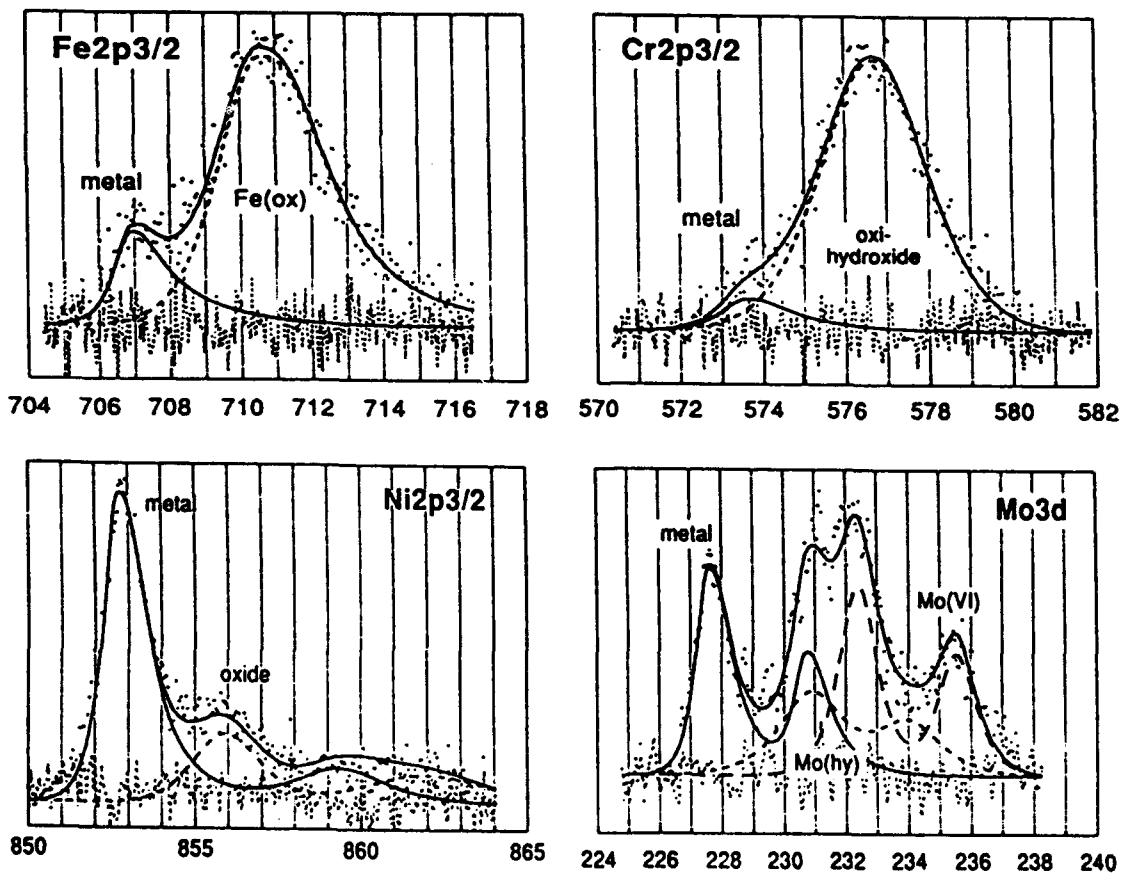


**Figure 2:**  
Detailed XPS spectra of 1.4529 SS polarized for 1 h at +0.2 V SCE in 1 M  $\text{Na}_2\text{SO}_4$  solution (pH 5.8) after background subtraction and curve fitting

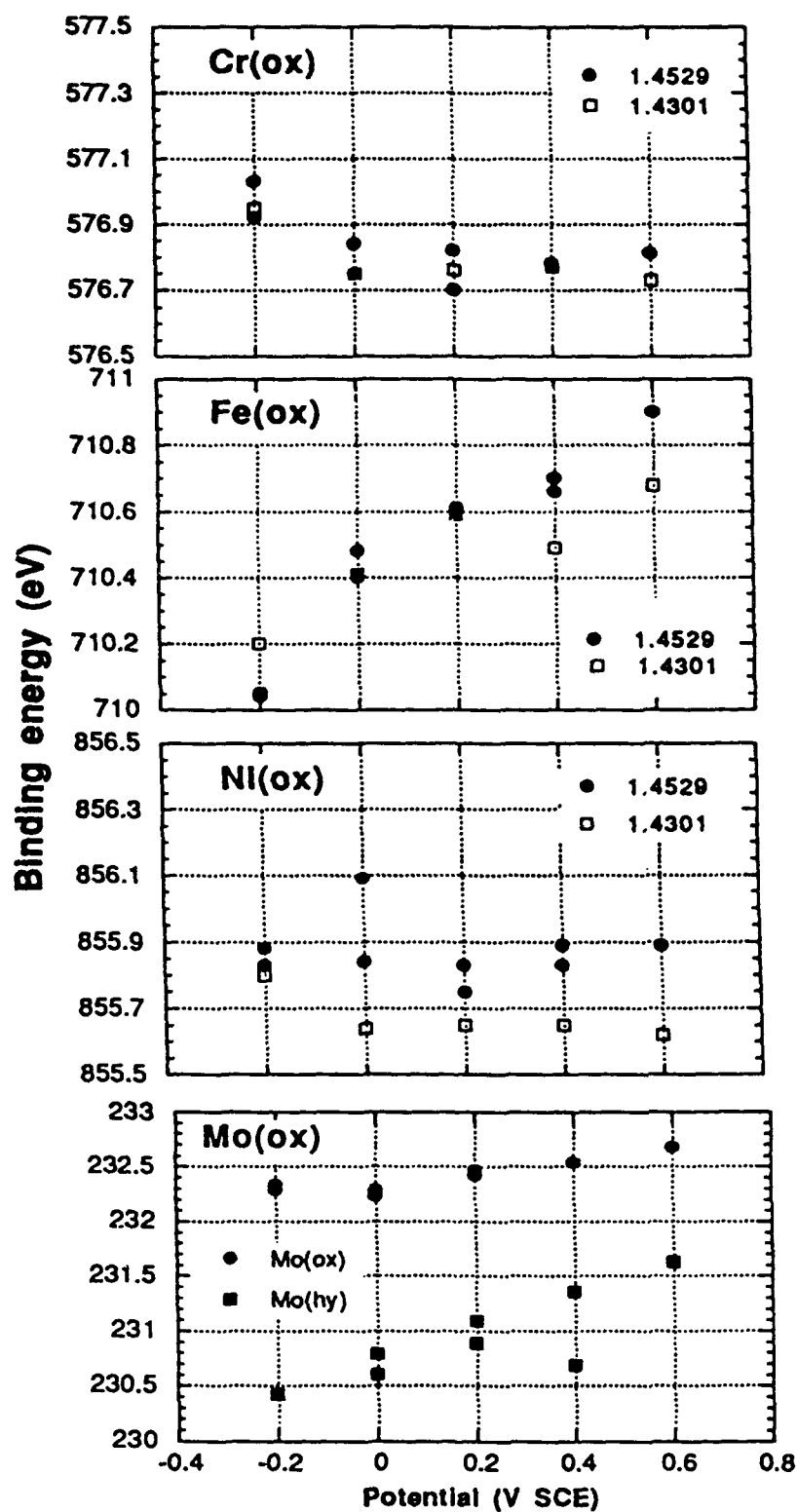


**Figure 3:** Binding energies of the oxidized metals in the passive films of the 1.4529 (closed symbols) and 1.4301 SS (open symbols) as a function of the potential (1 hour passivation in 1 M Na<sub>2</sub>SO<sub>4</sub> solution at pH 5.8)

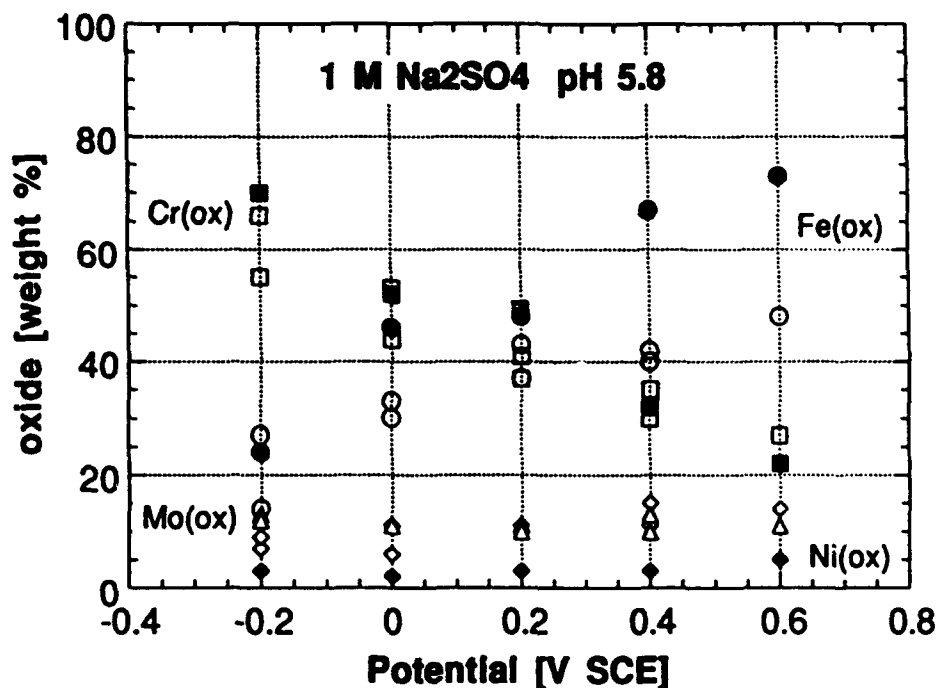


**Figure 5:**  
Composition of the passive films on the 1.4529 and 1.4301 SS formed after 1 hour passivation in 1 M Na<sub>2</sub>SO<sub>4</sub> solution (pH 5.8) as a function of the potential. Open symbols: 1.4529 SS, closed symbols 1.4301 SS

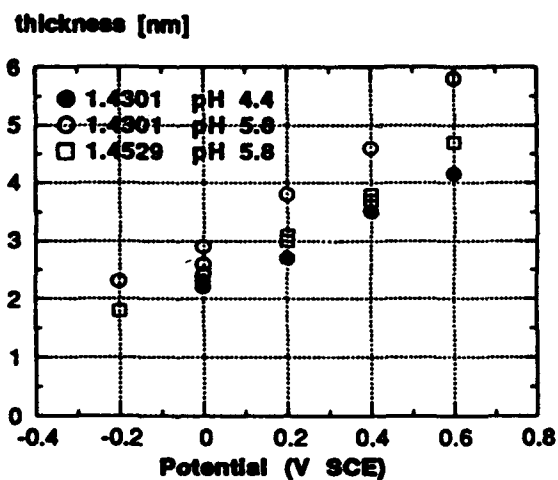


**Figure 4:**  
Thickness of the passive films on the 1.4529 and 1.4301 SS formed after 1 h passivation in 1 M Na<sub>2</sub>SO<sub>4</sub> solution (pH 5.8) as a function of the potential.

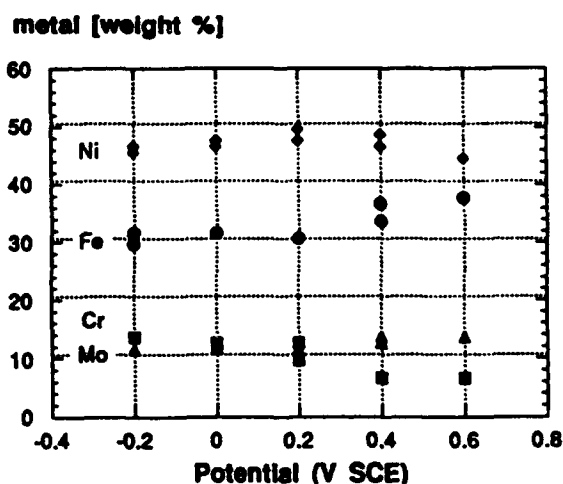


**Figure 6:**  
Composition of the substrate beneath the passive film of the 1.4529 SS (1 h of passivation in 1 M Na<sub>2</sub>SO<sub>4</sub> solution, pH 5.8) as a function of the potential

## **The Passivity of Carbon Steel in Organic Solutions**

David A. Shifler  
Department of Materials Science & Engineering  
The Johns Hopkins University  
Baltimore, MD 22218  
USA

Patrick J. Moran  
Department of Mechanical Engineering  
United States Naval Academy  
Annapolis, MD 21402  
USA

Jerome Kruger  
Department of Materials Science & Engineering  
The Johns Hopkins University  
Baltimore, MD 22218  
USA

### **Abstract**

The passivation and breakdown behavior of 1018 carbon steel in anhydrous solutions of propylene carbonate (PC) or dimethoxyethane (DME) containing 0.5M LiAsF<sub>6</sub> were studied. Results have indicated that for anodic potentials several passivation mechanisms (e.g. air-formed film, solvent adsorption, salt film formation, electropolymerization, and oxide formation) are operative. Each passivation mechanism is strongly dependent on the metal or alloy composition, the potential, the solvent, and the electrolyte. The addition of small amounts of water to PC or DME changes the character of the passive film and the balance between competing mechanisms.

Keywords: passivity, organic solvents, electropolymerization, sulfide inclusions, hexafluoroarsenate, carbon steel

### **Introduction**

The role of passive films in aqueous solutions has been studied fairly extensively<sup>1</sup>, but comparatively little work has been done on passivity in non-aqueous solutions. The formation and the stability of passive films on metals and alloys in non-aqueous organic and mixed organic solvents are of increasing importance in a variety of applications such as high-energy lithium batteries. Long-term integrity of container and structural components in lithium batteries can be achieved by understanding the nature of the passive film and the factors and conditions which cause breakdown of this protective film that leads to localized corrosion in the aprotic solvents commonly employed in these high-energy cells.

This paper compares the passivity and breakdown behavior of AISI 1018 carbon steel in anhydrous propylene carbonate (PC), C<sub>4</sub>H<sub>6</sub>O<sub>3</sub>, an aprotic cyclic ester solvent and dry 1,2-dimethoxyethane (DME), (C<sub>4</sub>H<sub>10</sub>O<sub>2</sub>) an aliphatic ether containing 0.5M LiAsF<sub>6</sub>. Lithium hexafluoroarsenate is a highly soluble electrolyte in polar aprotic solvents such as PC, tetrahydrofuran (THF), and DME and is widely used in lithium battery applications. Previous studies have explored the passive behavior of 99.995% iron in propylene carbonate (PC) solutions<sup>2-5</sup> and in PC-H<sub>2</sub>O mixtures<sup>3,6</sup>. Other examinations have observed the passive behavior of 1018 carbon steel in anhydrous PC solutions<sup>4,5</sup> and mixed PC-H<sub>2</sub>O solutions, nickel-200 in PC and mixed PC-H<sub>2</sub>O solutions<sup>5</sup>, 304 stainless steel in PC solutions<sup>7</sup>, and high purity iron<sup>8</sup> and 1018 carbon steel<sup>9</sup> in DME solutions. Our work has

attempted to examine the fundamental processes and mechanisms for the passivation of structural alloys and the manner in which these passive films degrade in organic solutions commonly utilized in lithium battery systems. A more complete discussion on organic passivity is given elsewhere <sup>2,4,10</sup>.

The mechanisms by which a metal can passivate have been classified into four types: (a) air-formed film, (b) salt film formation, (c) chemisorption of the solvent, and (d) oxide/oxyhydroxide formation<sup>11-13</sup>. Mechanisms (a,b, and c) are operative in organic solvents, while oxide/oxyhydroxide formation, the primary passivation in aqueous systems, is discouraged in most truly deaerated, anhydrous organic solvents. The results of 1018 carbon steel in DME/LiAsF<sub>6</sub> solutions have led to the proposal of another passivation mechanism to be discussed later in this paper.

## Experimental

AISI 1018 carbon steel samples were prepared by a procedure reported by Kelly *et al.*<sup>2</sup>. The steel samples were polished to an 800 grit finish, rinsed with water, acetone, and methanol and dried in warm air prior to mounting the specimens in a Teflon test holder. As reported by Kelly *et al.*<sup>2</sup> this procedure leaves a thin (3 to 4 nm) air-formed film on the surface. Platinum electrodes (0.15mm diameter) were used as one working electrode to assess the stability of the solutions over a wide potential and as a counter electrode during all electrochemical tests. The reference electrode used in this paper is the saturated calomel electrode (SCE). The SCE electrode potential is +3.3 V versus Li<sup>+</sup>/Li.

Solutions of the highest purity commercially available were used. Propylene carbonate and DME were received from Burdick and Jackson with a water content of 60-140 ppm. LiAsF<sub>6</sub> (99.5% min.) and with a maximum water content of 100 ppm was obtained from Lithium Division of FMC and used without further purification. To reduce water impurities in the PC and purge oxygen from PC or DME solutions, a vacuum line technique as described in previous papers<sup>2,4,6-9</sup> was employed. Preparation of PC/0.5M LiAsF<sub>6</sub> solutions and DME/0.5M LiAsF<sub>6</sub> solutions were handled in a glove bag after properly evacuating and backfilling with VUHP N<sub>2</sub> (O<sub>2</sub> and H<sub>2</sub>O content less than 1 ppm). Molecular sieves were added to the organic solutions and allowed to stand for at least 48 hours. After this period, PC or DME solutions were transferred from the storage vessel to the deoxygenation flask and deaerated with VUHP N<sub>2</sub>. Use of this procedure reduced water to 2-5 ppm in PC/0.5M LiAsF<sub>6</sub> and 50-100 ppm in DME/0.5M LiAsF<sub>6</sub>.

Electrochemical measurements were performed using a PAR Model 342 Corrosion Measurement System. All experiments were conducted at room temperature (25 ± 2°C) after allowing the electrodes to come to a steady state open circuit potential which generally required about 2 hours. Potentiodynamic scans utilized a scan rate of 0.5 mV/sec and the data were IR-corrected via automatic current interruption. A number of constant potential experiments were conducted at specific potentials of interest to examine the steady state behavior (i.e. passivity or corrosion). In some experiments, part of the 1018 carbon steel electrode surface was bared by scratching in-situ with a sharp-tipped glass rod while holding the steel at a constant potential to determine repassivation behavior. Water (100-2000 ppm) was intentionally added to several anhydrous PC/0.5M LiAsF<sub>6</sub> or "dry" DME/0.5M LiAsF<sub>6</sub> solutions prior to conducting various electrochemical tests to study its effects on passivity and the breakdown of passivity. Samples were examined and analyzed by scanning electron microscopy and X-ray microanalysis.

## Results

### Potentiodynamic Scans

Slow potentiodynamic scans were conducted on platinum over a potential range of -500 to +2200 mV(SCE) to evaluate the effect of potential on PC and DME solution chemistry and their regions of stability. Polarization scans of platinum in PC/0.5M LiAsF<sub>6</sub> and DME/0.5M LiAsF<sub>6</sub> are shown in Figure 1. Three anodic reactions are observed during the Pt scan in DME/0.5M LiAsF<sub>6</sub>. The first anodic reaction occurs at +850 mV(SCE) from the oxidation of the dimethoxyethane solvent molecules, DME<sub>ox</sub>. A second anodic reaction occurs at ca. +1100 mV(SCE). This reaction has not

been identified. A third reaction develops at ca. +1850 mV(SCE) which is due to oxidation of the lithium hexafluoroarsenate electrolyte. This electrolyte oxidation agrees closely with the work of Ossala *et al.*<sup>14</sup>.

In the PC/hexafluoroarsenate solutions on platinum the PC oxidized at around 900 mV(SCE),  $PC_{ox}$ . A second anodic reaction is observed at about 1850 mV(SCE) from the oxidation of  $AsF_6^-$ . One possible oxidation reaction postulated by Abraham *et al.*<sup>15</sup> in ether/ $LiAsF_6$  solutions is:



The polarization behavior of 1018 carbon steel with its air-formed film intact in neutral anhydrous solutions of PC/0.5M  $LiAsF_6$  and DME/0.5M  $LiAsF_6$  are shown in Figure 2. During slow scans in PC/0.5M  $LiAsF_6$  solutions, the first apparent deterioration of the passive film on carbon steel in PC solution during slow scans occurs about 100-200 mV negative to that observed on high purity iron<sup>4</sup>. This may be related to the relative purity of the metal. In carbon steel, sulfide surface inclusions are common. The role that sulfides assume in pit initiation will be discussed later. During scans the potentials above  $PC_{ox}$  lead to sharply increased current densities until at about 10 mA/cm<sup>2</sup> a limiting process begins. In this limiting region, a brown salt film, presumably  $Fe(AsF_6)_2$  or  $Fe(AsF_6)_3$ , is formed on the metal surface. Subsequent to a test where the presumed  $Fe(AsF_6)_2$  has formed, the salt slowly dissolves from the iron or steel specimen during open circuit decay. Such salt film dissolution is not observed in PC/0.5M  $LiClO_4$  solutions<sup>4</sup>. The passivation mechanism operative in PC solutions above  $PC_{ox}$  is salt film formation; the behavior of the steel above  $PC_{ox}$  is related to the apparent solubility of the precipitated salt composed of metal cations and solution anions. Pitting of the carbon steel is observed by optical microscopy on specimens scanned above  $PC_{ox}$  in PC/0.5M  $LiAsF_6$  solutions.

The potentiodynamic behavior of 1018 carbon steel in a "dry" DME/0.5M  $LiAsF_6$  solution (Figure 2) shows that the current density remains under 10  $\mu A/cm^2$  until a potential of +1050 mV(SCE) is reached. Above +1050 mV, the current density increases by 3 orders of magnitude during the slow scan when 1400 mV(SCE) is reached. Subsequent microscopic examination of the steel surface reveals pitting. No visual or x-ray analytical examination of these pits showed evidence of a developing inorganic salt film. The carbon steel breakdown potential in dry DME/0.5M  $LiAsF_6$  solutions is 200 mV above the DME oxidation potential,  $DME_{ox}$ . Scanlon *et al.*<sup>8</sup> has also observed behavior of this type for high purity iron in dry DME/0.5M  $LiAsF_6$  solutions. This extended passive range above the solvent oxidation potential was not observed in earlier studies of iron or carbon steel in propylene carbonate with  $LiAsF_6$  as the supporting electrolyte<sup>2-5</sup>. This extended passive range was unique when compared to DME/ $LiClO_4$  and DME/TBAP solutions<sup>9,16</sup>.

The effects of small water additions on the polarization behavior of 1018 carbon steel in PC/0.5M  $LiAsF_6$  is shown in Figure 3a. Additions of 100 and 200 ppm water to the anhydrous PC/ $LiAsF_6$  solutions introduces surface activation and increasing current densities below  $PC_{ox}$  from the competitive adsorption of PC and water on the carbon steel surface and local acidification due to water. Small water additions to dry DME/ $LiAsF_6$  solutions (Figure 3b) affect the 1018 carbon steel passive domain and the breakdown potential. The breakdown potential of the steel in "dry" DME/0.5M  $LiAsF_6$  is 1050 mV(SCE). The addition of 100 ppm water to the dry DME solution extends the passive region and elevates the breakdown potential to 1300 mV. An addition of 250 ppm water further extends the passive range to 1450-1500 mV(SCE). No surface activation of the carbon steel below  $DME_{ox}$  was observed in DME/0.5M  $LiAsF_6$  solutions. Added water levels of 500 to 2000 ppm to DME/ $LiAsF_6$  solutions do not markedly boost the protective region beyond the 250 ppm potential range. The added water does not activate the steel surface below the "dry breakdown potential, suggesting that water does not compete with DME for adsorption sites on the carbon steel surface.

### Potentiostatic Holds

At constant potentials below  $PC_{ox}$ , the passivity of the air-formed film on the 1018 carbon steel is stable for at least 4000 seconds in either PC solution. In order to verify the potentials at which the salt film can form and evaluate its protective capability, potentiostatic holds followed by scratching while maintaining the potential were conducted. Figure 4a shows the hold and scratch of 1018 carbon steel in 0.5M  $LiAsF_6$  solutions below  $PC_{ox}$ . The scratch causes a sharp anodic transient with a relatively fast (ca. 10 sec) recovery to the same current level prior to scratching. The charge passed before repassivation is about  $7 \text{ mC/cm}^2$  (correcting for the scratch area) indicating that some dissolution may have occurred. Inspection of the carbon steel surface (Figure 4b) by SEM revealed no apparent electrochemical dissolution in the scratch. Since the air-formed oxide film has been removed and cannot reform in anhydrous organic solutions, and since no salt film is observed, the passivation in hexafluoroarsenate solutions occurred by the chemisorption of PC molecules. The passivity of carbon steel, promoted by this adsorption, is stable below  $PC_{ox}$ .

At constant potentials above  $PC_{ox}$ , the air-formed film over the steel is not stable with PC. In PC/hexafluoroarsenate solutions, scratches on 1018 carbon steel during potentiostatic holds above  $PC_{ox}$  cause huge anodic spikes relative to the magnitude of the pre-scratch current. At potentials above  $PC_{ox}$  where the current density is typically  $6\text{--}7 \text{ mA/cm}^2$  at steady state, scratching through the salt film and the air formed layer causes about a  $200\text{--}400 \text{ mA/cm}^2$  anodic transient in the scratched area which does not return to the pre-scratch condition even after 2000 seconds. Though the salt film does form, the high solubility of the presumed iron hexafluoroarsenate,  $Fe(AsF_6)_2$  or  $Fe(AsF_6)_3$ , precludes adequate protection of either the iron or the carbon steel. The air-formed film is not stable at potentials above  $PC_{ox}$  in hexafluoroarsenate solutions. As shown in Figure 5 for carbon steel in PC/0.5M  $LiAsF_6$  held above  $PC_{ox}$ , removal of the air-formed film by scratching results in general dissolution and pitting within the scratched area and pitting outside the scratched region.

SEM examination of the 1018 carbon steel surface has shown many surface inclusions. These inclusions were confirmed by XRM to consist primarily of sulfides. In PC/0.5M  $LiAsF_6$  solutions, sulfide inclusions found on the carbon steel surface provide pit initiation sites  $100\text{--}200 \text{ mV}$  negative to the breakdown potentials found on high purity iron. At potentials above  $PC_{ox}$ , other defects in the air-formed film can become activated and serve as pit initiation sites. In PC/ $LiAsF_6$ , with the absence of a protective salt film by reason of the higher hexafluoroarsenate salt solubility, dissolution at these other sites leads to a higher concentration of pits on carbon steel than found in PC/ $LiClO_4$  solutions<sup>4</sup>.

In several DME/0.5M  $LiAsF_6$  experiments the 1018 carbon steel was held at selected constant anodic potentials while the steel surface was scratched with a glass rod. After scratching, the current was monitored as a function of time to assess repassivation kinetics and determine the mode of repassivation. At a potential of  $+600 \text{ mV(SCE)}$  (below  $DME_{ox}$ ) surface repassivation occurred within 7 seconds following the scratch. A charge of  $25 \text{ mC/cm}^2$  (corrected for scratch area) passed before currents returned to pre-scratch  $1 \mu\text{A/cm}^2$  conditions. SEM examination of the scratched surfaces of carbon steel were similar when the potential was held below the respective PC or DME solutions. It is presumed that passivation below  $DME_{ox}$  occurs from the adsorption of DME solvent molecules. This is based on past studies<sup>2,9,16</sup> where solvent adsorption was the predominant passivation mechanism for potentials below the solvent oxidation.

At potentials slightly above  $DME_{ox}$  ( $+900\text{--}1000 \text{ mV(SCE)}$ ), the stable passive currents are  $2\text{--}3 \mu\text{A/cm}^2$  prior to scratching the steel surface with the glass rod. Abrading the surface causes an anodic current spike which decays to the pre-scratch condition after 20 seconds. The return of the anodic currents to the pre-scratch state signifies repassivation of the surface. The charges passed during repassivation are  $29 \text{ mC/cm}^2$  at  $900 \text{ mV(SCE)}$ , and  $66 \text{ mC/cm}^2$  during a  $1000 \text{ mV(SCE)}$  hold and scratch test. SEM and x-ray analysis exhibited no apparent film formed within the scratches.

In the presence of small amounts (100-2000 ppm) of water added to dry DME/0.5M LiAsF<sub>6</sub> solutions, passivity is observed above the "dry" breakdown potential of 1050 mV(SCE). In contrast to the behavior in PC/0.5M LiAsF<sub>6</sub>, potentiostatic holds at potentials from 1050-1500 mV in DME/0.5M LiAsF<sub>6</sub> solutions result in low stable currents on the 1018 carbon steel surface. Table I also lists the charges passed during the initial transient when the anodic potentials between 600 and 1400 mV(SCE) were first applied and the charges passed during repassivation of the scratched region at these potentials. The charge values measured at potentials below 1050 mV are independent of the water concentration; however, in order to achieve passivation or repassivation above 1050 mV approximately 100-2000 ppm water is required to be added to "dry" DME/LiAsF<sub>6</sub> solutions. The currents and charges passed during repassivation of the scratches on 1018 carbon steel increase significantly above 1050 mV over those observed at lower potentials before complete repassivation. The large values of charge above approximately 1050 mV suggest that a different passivating mechanism is operative. Figure 6a shows the repassivation of scratch held above 1050 mV(SCE). Examination of this scratch by SEM reveals the formation of a film within the abraded site (Figure 6b) for potentials above approximately 1050 mV. X-ray elemental analysis did not indicate the presence of any elements above carbon in the passivating film found in scratches at 1100-1200 mV(SCE). This shows that an inorganic salt film was not formed, although passivity by salt film had been found in other organic/electrolyte systems<sup>2-5</sup>. XPS analysis of a steel specimen with several scratches repassivated at 1200 mV(SCE) was compared to an unscratched steel sample. Results indicate that the arsenic, oxygen, and fluorine structure have been altered. Although the exact composition of the film has not been determined, Scanlon *et al.*<sup>16</sup>, found using normalized Auger analysis, that a polymer formed in scratches on high purity iron in this same system was enriched in carbon and arsenic but depleted in iron, as compared to the unscratched surface. XPS analysis of the repassivated carbon steel scratches at 1200 mV indicated modified bonding structure for arsenic, oxygen, and fluorine unlike the unscratched region.

At higher potentials (+1300-1400 mV(SCE)) in DME/0.5M LiAsF<sub>6</sub> solutions containing at least 250 ppm water, the repassivation and the accompanying current decay required 300-400 seconds. The passivating film appeared thicker at higher potentials. Generally, no evidence of any element above carbon was found in this film.

## Discussion

The possible passivation mechanisms available to anhydrous organic solvents are: (a) air-formed film, (b) salt film and (c) chemisorption of the solvent molecules. Carbon steel in neutral anhydrous solutions of PC/0.5M LiAsF<sub>6</sub> have demonstrated that each of these three mechanisms has a region of dominance. However these regions may be influenced by such factors as the cleanliness of the metal surface or the physical and chemical properties of the electrolytes.

Stable passivity below PC<sub>ox</sub> is observed on carbon steel even if the air-formed film is removed. Repassivation times are about 5-10 seconds. The repassivation is presumed to be caused by the adsorption of the PC solvent. Above PC<sub>ox</sub>, chemisorption of PC is no longer possible because it oxidizes. The air-formed film also does not appear to be protective above PC<sub>ox</sub>. In hexafluoroarsenate solutions, scratching carbon steel above PC<sub>ox</sub> results in a huge anodic transients which corrected for area are about 200-300 mA/cm<sup>2</sup>. While the currents decrease from these high values due to salt film formation, the films do not render the surfaces passive. In fact, at steady state, the corrosion currents are still about 10 mA/cm<sup>2</sup>. When salt film formation is the dominant passivation mechanism above PC<sub>ox</sub>, the solubility and the chemical properties of the salt determine whether this mechanism will actually passivate.

The carbon steel samples in PC/LiAsF<sub>6</sub> solution show deterioration of the adsorbed PC/air-formed passive film at about 100-200 mV negative to that observed in high purity iron when PC begins to oxidize. It is possible that the lower "breakdown" potential for steel versus iron in both electrolytes is related to the sulfide surface inclusions. Although it has been established that sulfides act as pit initiation sites on carbon steel in aqueous solutions, there has been much debate about the role of sulfides in this preferential corrosion. Reviews by Janik-Czachor<sup>17</sup> and Szklarska-Smialowska<sup>18</sup> discuss factors including surfaces inclusions that lead to pit initiation.



From the observations of the passive behavior and breakdown of 1018 carbon steel in DME/0.5M LiAsF<sub>6</sub> solutions, it appears that several mechanisms are responsible for the passivation of the steel; (1) solvent adsorption at potentials below 850 mV(SCE), (2) formation and adsorption of a complex (to be discussed further) at potentials between 850 and 1050 mV(SCE), and (3) polymerization on the carbon steel surface in the potential range 1050 to about 1500 mV(SCE) in "wet" DME/0.5M LiAsF<sub>6</sub> solutions.

At potentials below +850 mV(SCE) steel passivation is provided by the adsorption of DME solvent molecules. The degree of protection by the air-formed film is obscured since defects in the film will repassivate by DME adsorption. The initial transient charge passed is far below the 200  $\mu\text{C}/\text{cm}^2$  generally considered to be the charge necessary to form a monolayer, but the air-formed film and steric effects would cause less charge to be needed. In scratch tests below DME<sub>ox</sub> the abraded carbon steel surface is repassivated in 5-7 seconds. An anodic charge of 25 mC/cm<sup>2</sup> is passed before the steel repassivates by DME solvent readsorption at 600 mV(SCE). Above ca. +850 mV(SCE) DME oxidizes. The neutral solvent molecules can no longer provide protection. In the 850-1050 mV(SCE) potential range, examination of scratches on the steel surface revealed no inorganic salt film. Yet disruption of the steel surface leads to rapid repassivation. The amount of charge passed during scratch tests is similar to observations below DME<sub>ox</sub> which would suggest an adsorption process.

The initial transient charges and the repassivation charges passed on the carbon steel surface in DME/0.5M LiAsF<sub>6</sub> solutions containing more than 150 ppm water and above 1050 mV increase by 1-2 orders of magnitude. Further, repassivated scratches exhibit film formation. A different passivation mechanism is clearly operating. Glugla<sup>19</sup> describes a cationic polymerization process that initiates upon oxidation of the cyclic ether dioxolane and incorporates LiAsF<sub>6</sub> electrolyte. Dioxolane upon ring opening is similar in structure to DME. Although oxidation could form a free radical, Glugla attributed dioxolane oxidation primarily to cation formation. Other organic systems have also credited solvent oxidation to the formation of a cation intermediate<sup>20,21</sup>. The LiAsF<sub>6</sub> electrolyte was an essential ingredient for the polymerization process along with the particular ether solvent<sup>9,16,19</sup>. In the experiments involving independent dry solutions of DME/LiAsF<sub>6</sub>, DME/TBAP, and DME/LiClO<sub>4</sub><sup>8</sup>, and containing similar water levels (50-100 ppm), carbon steel existed in the passive state above DME<sub>ox</sub> only in the LiAsF<sub>6</sub> solution. This indicates that the LiAsF<sub>6</sub> salt participates in enhancing the passive range. Glugla found that the anodic potential for initiation of dioxolane polymerization is related to the LiAsF<sub>6</sub> concentration<sup>19</sup>. John and Wallace<sup>20</sup> also observed that the concentration of monomer would alter the potential at which polymerization would commence. They also suggested that a critical concentration was required before polymerization could begin<sup>20</sup>.

Water additions cause the passive range to increase above the dry DME/LiAsF<sub>6</sub> (+1050 mV(SCE)) breakdown potential. The addition of water to DME/LiAsF<sub>6</sub> increases the concentration of available acidic hydrogen which can also react with the organic cation intermediate to form complexes. Ethers do not participate in hydrogen bonding, but water can assist in such bonding<sup>22</sup>. It is likely that water assists in complex growth, and assists in enhancing coverage and adsorption on the steel surface. The observed increase in the passive range caused by water additions is completely consistent with the explanation that the passivity is caused by the formation of a cation-electrolyte complex oligomer.

Above 1050 mV scratching the carbon steel surface results in steep jumps in the anodic currents and longer times before repassivation is complete. The scratch event removes the passivating complex and/or the air-formed film from the surface resulting in ferric or ferrous cations leaving the surface. The iron cations appear to be essential for a visible film to form<sup>9,16</sup>. SEM examination reveals the presence of a substantial film within the scratch on carbon steel above 1050 mV(SCE). Koch<sup>23</sup> suggests that a polymer film formed during electroreduction on lithium in THF/LiAsF<sub>6</sub> solutions was composed of (-As-O-As-) <sub>n</sub> polymer and LiF. The present investigation suggests that a similar polymer is formed within the carbon steel scratched surface above 1050 mV(SCE).

## Conclusions

The possible passivation mechanisms available to anhydrous organic solvents are: (a) air-formed film, (b) salt film and (c) chemisorption of the solvent molecules (d) electropolymerization of passive film. Each passivation mechanism has a region of predominance that is strongly dependent on the metal or alloy composition, the potential, the solvent, and the electrolyte. The addition of small amounts of water to PC or DME changes the character of the passive film and the balance between competing mechanisms. In PC, water causes deterioration of the passive film on carbon steel while in DME solutions, water extends the passive range and forms a polymer film.

## Acknowledgements

This work was sponsored by the Assistant Secretary for Conservation and Renewable Energy, U.S. Department of Energy under Contract No. DE-AC03-7600098, subcontract no. 4539610, with Lawrence Berkley Laboratory. David Shifler would also like to thank Sheppard T. Powell Associates for granting him the time to pursue this work.

## References

- 1 - J. Kruger, Ninth International Congress on Metallic Corrosion, 1, 78, National Research Council of Canada, (1984)
- 2 - R.G. Kelly, P.J. Moran, J. Kruger, *J. Electrochemical Society*, **136**, 3262 (1989)
- 3 - R.G. Kelly, PhD thesis, The Johns Hopkins University, Baltimore, MD, (1989)
- 4 - D.A. Shifler, P.J. Moran, J. Kruger, *Corrosion Science*, **32**, 475 (1991)
- 5 - D.A. Shifler, M.S.E. Essay, The Johns Hopkins University, Baltimore, MD, (Oct. 1989)
- 6 - R.G. Kelly, P.J. Moran, E. Gileadi, J. Kruger, *Electrochimica Acta*, **34**, 823 (1989)
- 7 - D.A. Shifler, P.J. Moran, J. Kruger, *J. Electrochemical Society*, **139**, 54 (1992)
- 8 - J.F. Scanlon, P.J. Moran, J. Kruger, Proceedings on the Symposium on Critical Factors in Localized Corrosion, G.S. Frankel, R.C. Newman, eds., **92-9**, 525, The Electrochemical Society, Pennington, NJ (1992)
- 9 - D.A. Shifler, P.J. Moran, J. Kruger, *Electrochimica Acta* (In Press)
- 10 - R.G. Kelly, P.J. Moran, *Corrosion Science*, **30**, 495 (1990)
- 11 - U.R. Evans, *Electrochimica Acta*, **16**, 1825 (1971)
- 12 - T.P. Hoar, D.C. Mears, G.P. Rothwell, *Corrosion Science*, **5**, 279 (1965)
- 13 - T.R. Agladze, Ya.M. Kolotyrkin, T.G. Malysheva, O.O. Denisova, *Protection of Metals*, **22**, 404 (1987)
- 14 - F. Ossola, G. Pistoia, R. Seeber, P. Ugo, *Electrochimica Acta*, **33**, 47 (1988)
- 15 - K.M. Abraham, J.L. Goldman, D.L. Natwig, *J. Electrochemical Society*, **129**, 2404 (1982)
- 16 - J.F. Scanlon, P.J. Moran, J. Kruger, submitted to *J. Electrochemical Society*
- 17 - M. Janik-Czachor, *J. Electrochemical Society*, **128**, 513C (1981)
- 18 - Z. Szklarska-Smialowska, Pitting Corrosion of Metals, National Assoc. of Corr. Engr., Houston, 69 (1986)
- 19 - P.G. Glugla, in Power Sources for Biomedical Implantable Applications and Ambient Temperature Lithium Batteries, B.B. Owens and N. Margalit, eds., **80-4**, 407, The Electrochemical Society, Pennington, NJ (1980)
- 20 - R. John, G.G. Wallace, *J. Electroanalytical Chemistry*, **306**, 157 (1991)
- 21 - A. Diaz, A. Martinez, K.K. Kanizawa, *J. Electroanalytical Chemistry*, **130**, 181 (1981)
- 22 - R.J. Fessenden, J.S. Fessendum, Organic Chemistry, 2nd ed, Willard Grant Press, Boston, 257 (1982)
- 23 - V.R. Koch, *J. Electrochemical Society*, **126**, 181 (1979)

TABLE I

Initial Current Transients and Repassivation Charge Passed vs. Potential

Potential mV(SCE)	Initial Transient Charge	Repassivation Charge
600	4.3 $\mu\text{C}/\text{cm}^2$	25 mC/cm <sup>2</sup>
900	39 $\mu\text{C}/\text{cm}^2$	29 mC/cm <sup>2</sup>
1000	94 $\mu\text{C}/\text{cm}^2$	66 mC/cm <sup>2</sup>
1100	1600 $\mu\text{C}/\text{cm}^2$	186 mC/cm <sup>2</sup>
1200	2090 $\mu\text{C}/\text{cm}^2$	1934 mC/cm <sup>2</sup>
1300	5410 $\mu\text{C}/\text{cm}^2$	1822 mC/cm <sup>2</sup>
1400	29760 $\mu\text{C}/\text{cm}^2$	6640 mC/cm <sup>2</sup>

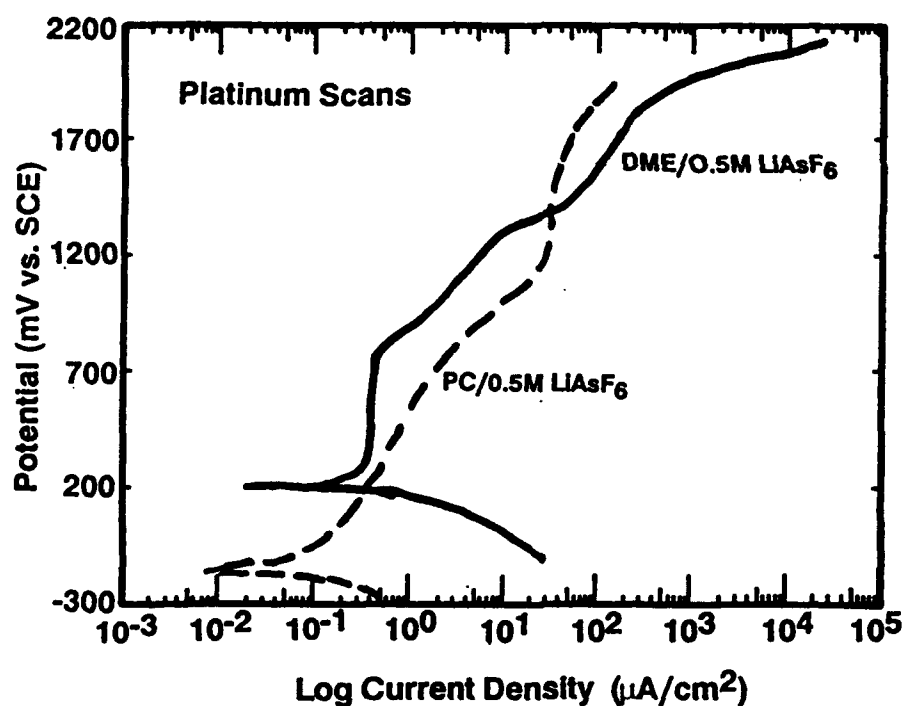


Figure 1 - Slow potentiodynamic scans on platinum in "dry" DME/0.5M LiAsF<sub>6</sub> and anhydrous PC/0.5M LiAsF<sub>6</sub>. DME oxidation occurs at 850 mV(SCE). A second reaction appears at 1100 mV. A possible reaction at this potential will be discussed later. A third reaction at about 1850 mV(SCE) is caused by the oxidation of the LiAsF<sub>6</sub> electrolyte. In the PC/0.5M LiAsF<sub>6</sub> solution on platinum the PC oxidized at around 900 mV(SCE). A second anodic reaction is observed at about 1850 mV(SCE) from the oxidation of AsF<sub>6</sub><sup>-</sup>.

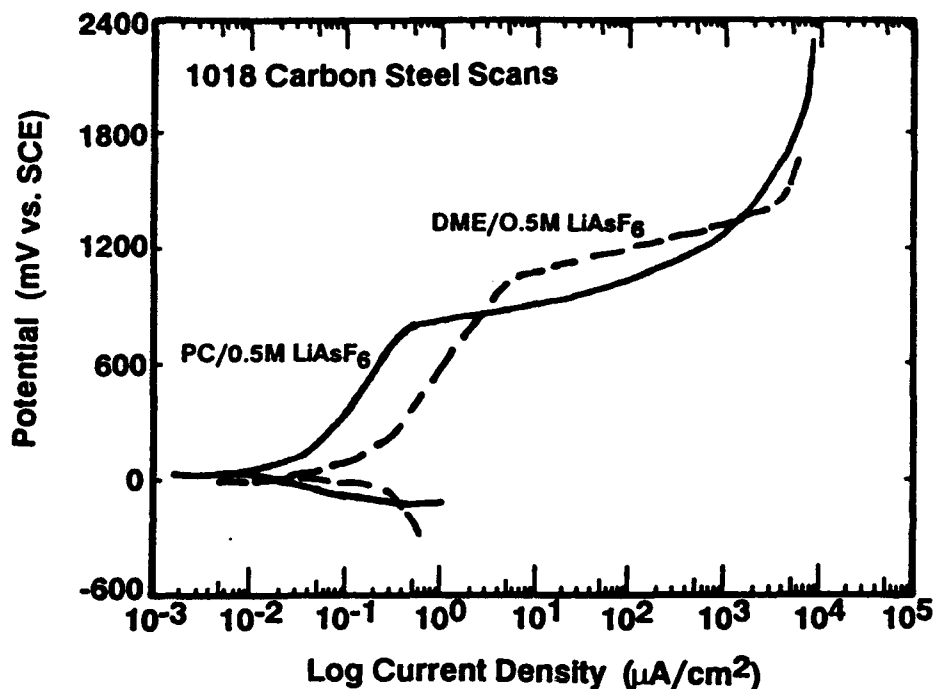


Figure 2 - Slow potentiodynamic scans of 1018 carbon steel in DME/0.5M LiAsF<sub>6</sub> and PC/0.5M LiAsF<sub>6</sub> solutions. (a) In PC/0.5M LiAsF<sub>6</sub> solutions, the 1018 carbon steel anodic currents are low until breakdown 100-200 mV below PC<sub>ox</sub>. (b) In DME/0.5M LiAsF<sub>6</sub> solutions, the currents are low until breakdown at 1050 mV(SCE). Breakdown is 200 mV above DME<sub>ox</sub>.

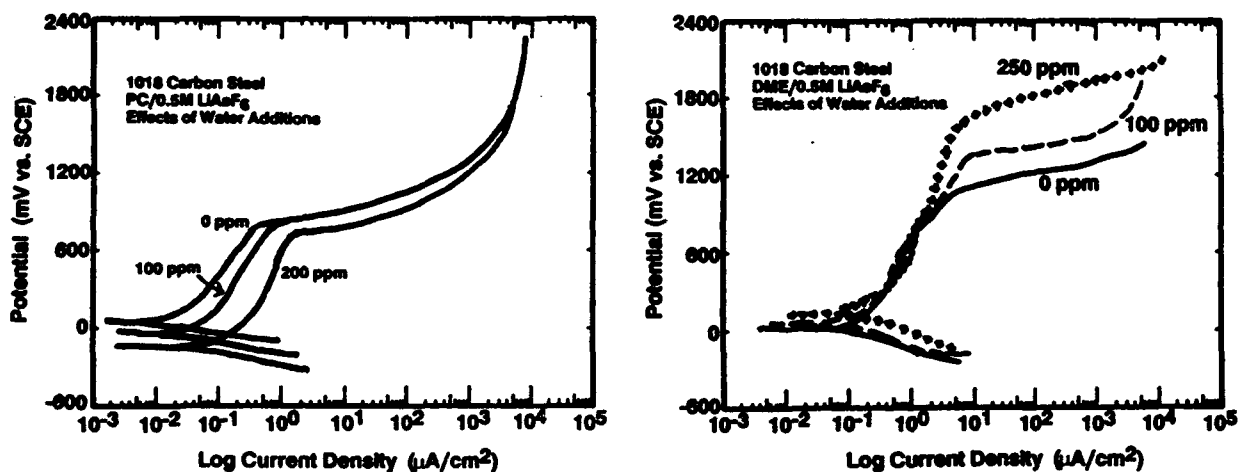


Figure 3 - (a) Slow scans on 1018 carbon steel in PC/0.5M LiAsF<sub>6</sub> with small water additions. The addition of 100 ppm water or more to the anhydrous PC solution activates the steel surface below PC<sub>ox</sub> and does not significantly alter the breakdown potential. (b) In DME/0.5M LiAsF<sub>6</sub> solutions, the addition of 100 ppm water raises the breakdown potential 200 mV. Additions of 250-2000 ppm water raises the breakdown potential to 1450-1500 mV(SCE). No activation of the steel surface occurs below DME<sub>ox</sub>.

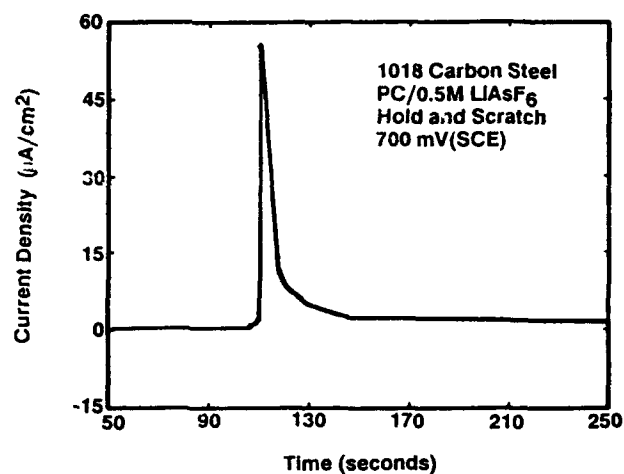


Figure 4 - (a) Potentiostatic hold of 1018 carbon steel in PC/0.5M LiAsF<sub>6</sub> below the oxidation potential of PC followed by a scratch of the surface to remove the air-formed film. The anodic spike upon scratching is followed by rapid repassivation by PC adsorption. (b) SEM photomicrograph of a scratch on 1018 carbon steel held below the PC oxidation potential in a PC/0.5M LiAsF<sub>6</sub>. The scratch is 150  $\mu\text{m}$  wide. No evidence of a film is noted.

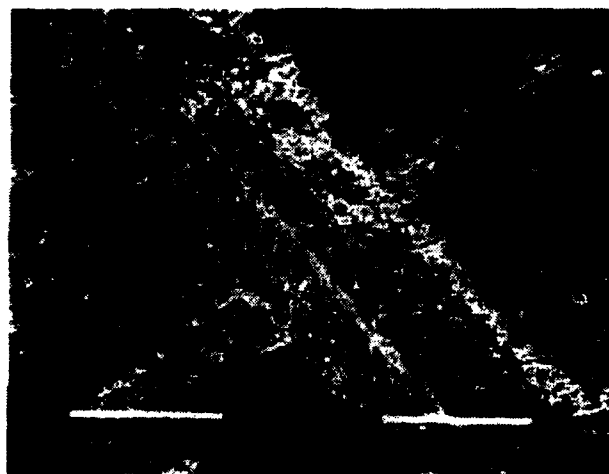


Figure 5 - SEM photomicrograph of a scratch on 1018 carbon steel in PC/0.5M LiAsF<sub>6</sub> held at a constant potential above PC<sub>ox</sub> (+1.1 V(SCE)). General dissolution was confined within the scratch. Pitting was observed both within and outside the scratched area. The scratch running from upper left to lower right is about 100  $\mu\text{m}$  wide.

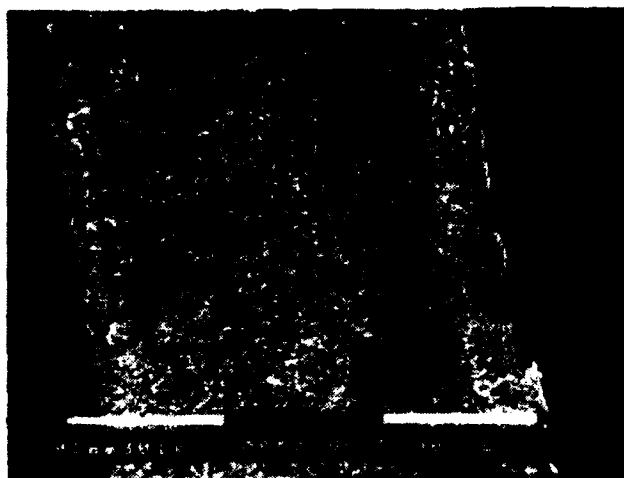
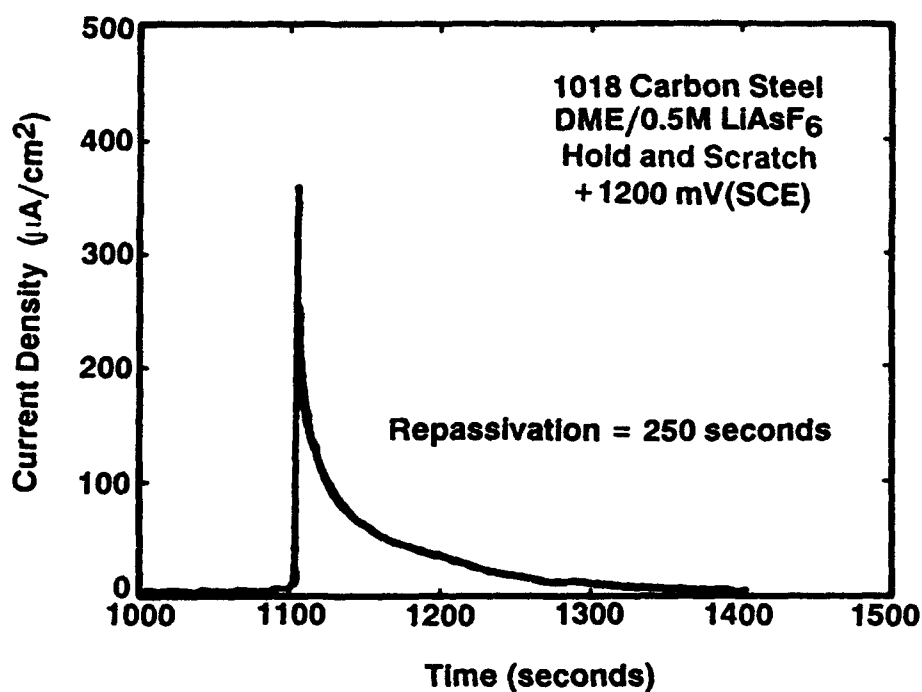


Figure 6 - (a) Potentiostatic hold of 1018 carbon steel in DME/0.5M LiAsF<sub>6</sub> above 1050 mV(SCE) followed by a scratch of the surface to remove the air-formed film. The anodic currents and charges as well as the time to repassivate increase by several orders of magnitude over similar experiments below DME<sub>ox</sub>. (b) SEM photomicrograph of the scratch on 1018 carbon steel held above 1050 mV in DME/0.5M LiAsF<sub>6</sub>. The scratch is about 300  $\mu\text{m}$  wide. An colorless opaque film within the scratch is observed.

# **In-situ STM and AFM characterization of passivity on stainless steels**

**S. Virtanen**

Swiss Federal Institute of Technology  
Institute of Materials Chemistry and Corrosion  
ETH-Hönggerberg, 8093 Zürich, Switzerland

**A. Schreyer**

Swiss Federal Institute of Technology  
Institute of Materials Chemistry and Corrosion  
ETH-Hönggerberg, 8093 Zürich, Switzerland

**H. Böhni**

Swiss Federal Institute of Technology  
Institute of Materials Chemistry and Corrosion  
ETH-Hönggerberg, 8093 Zürich, Switzerland

## **Abstract**

Passive films and breakdown of passivity of stainless steels have been characterized with scanning tunneling microscopy and scanning tunneling spectroscopy. A combination of in-situ STM and AFM measurements were used for the study of the passivation process in order to clarify, if the changes taking place on the surface are purely topographical in nature. The results clearly indicate that on a rougher surface the STM image shows more changes at a potential, where the passive film is formed than on a polished surface. Since these changes could not be seen by AFM, it can be concluded that the changes taking place during the passivation are due to a formation of an electronically heterogeneous passive film - and the heterogeneity is larger on a rougher surface. Since the electronic properties of passive films are mainly determined by their composition and structure, the spatial variation of these properties gives information on the homogeneity / heterogeneity of the films. With help of the scanning tunneling spectroscopy ( $I_T/U_T$ -spectroscopy) local electronic properties of the films can be studied in more detail. Preliminary results of the tunneling spectroscopy confirm the finding from STM/AFM measurements that the mechanical surface pre-treatment influences the electronic properties of passive films formed on differently treated surfaces in solutions and on a rougher surface a more inhomogeneous film is formed.

**Key words:** passivity, passivation, passive film, stainless steel, surface pre-treatment, scanning tunneling microscopy, STM, atomic force microscopy, AFM

## **Introduction**

For stainless steels the effect of many important factors on the pitting corrosion resistance is well known. The effect of various parameters such as alloy composition (e.g. Mo-content), structure (e.g. presence of MnS), solution composition (pH,  $Cl^-$ ) or potential on the pitting corrosion resistance has been summarized by Szklarska-Smialowska [1]. Lately it was shown by Morach [2] that

surface pre-treatment by different mechanical methods can very strongly affect the metastable pitting activity measured as current transients. Similar effects of the surface pre-treatment on the pitting resistance measured as pitting potential have been found by other authors, as well [3-5].

In spite of a lot of effort carried out on studies of passivity and its breakdown, the detailed mechanism of the pit initiation, growth and repassivation has not been clarified. For pit initiation several models exist [1,6], most of which assume the existence of so-called "weak" sites in the passive film to be necessary for the local destruction of the film. In case of the effect of surface pre-treatment a special question arises: Can this effect be explained mainly due to differences in the surface roughness or does the pre-treatment affect the properties of the passive film ?

The development of the scanning tunneling (STM) and atomic force microscopy (AFM) enable the study of metal surfaces with a very high local resolution. A big advantage of these methods is the possibility to study solid/liquid-interfaces with a potentiostatic control of the sample [7,8]. Several authors have shown lately that such investigations can give new insights into topographical changes taking place on metal surfaces during active dissolution or passivation [9-15].

Since the tunneling current depends on the electronic properties of the surface it is further possible to study local variations in the electronic properties with help of so-called tunneling spectroscopy ( $I_T/U_T$ -spectroscopy) [16]. During the last few years many authors have shown by photoelectrochemical methods that passive films on many metals and alloys including stainless steels exhibit a semiconducting behaviour [17-24]. Local photoelectrochemistry with a laser-spot-scanning apparatus has shown that the semiconductive properties of large area measurements of passive films on stainless steels are a sum of a inhomogeneous behaviour of local features [24,25]. Since the semiconductive properties of passive films are mainly determined by their composition and structure, the spatial variation of these properties can give information on the homogeneity / heterogeneity of the films.

A combination of STM and AFM for imaging surfaces enables the separation of changes taking place on the surface into purely topographical and electronical ones. It was the aim of this work to clarify, if such a combination of these two methods can be used to reveal heterogeneities of the passive film during in-situ passivation of stainless steels. Since the pit initiation activity has been found to change very strongly with different surface pre-treatments, these investigations were carried out on samples with different surface pre-treatments. Preliminary studies with the tunneling spectroscopy were carried out to distinguish local variations in the electronic properties of passive films.

## **Experimental**

The material studied was a commercial AISI 304 stainless steel. Prior to the measurements the samples were mechanically grinded (500, 1000 SiC) or polished (1 $\mu$ m diamond), rinsed in ethanol and acetone and dried. As a reference material for the tunneling spectroscopy platinum sheets with identical surface pre-treatment as for the stainless steel were used.



The STM/AFM apparatus used was a Park Scientific Instruments (PSI) combined SFM and STM system (Central control unit SPC-400, STM-SU2-210, SFM-BD2-210) with a bipotentiostat model SA1/BD2-800. In this work the scanning area was large, typically in the  $\mu\text{m}$ -range, in order to have a representative picture of the rough surfaces. The electrochemical cell used in in-situ STM/AFM work was a conventional PSI cell with separate compartments for the reference and the counter electrode. As a reference electrode Ag/AgCl/NaCl(1M) and as a counterelectrode a Pt wire were used. For STM measurements in air tips were prepared by simply cutting a piece of Pt wire. For electrochemical STM measurements commercial insulated tips (Pt/Ir or W) from Longreach Scientific Company were used. During the electrochemical STM measurements the tip and the sample were both individually held under a potentiostatic control. The in-situ STM/AFM work was carried out in 0.1M NaCl at various potentials. During the tip approach the samples were held at a potential of  $E = -600 \text{ mV}$  in order to prevent dissolution prior to the imaging. After the approach the potential of the samples were stepwise increased ( $100 \text{ mV} / 15 \text{ min}$ ) and the surface was continuously imaged. The STM-imaging was in all cases carried out in the constant current mode with a set point tunneling current of 1-5 nA.

The tunneling spectroscopy work was carried out in air on samples which were passivated prior to the measurements in a conventional cell at  $E = +300 \text{ mV SCE}$  in 1M  $\text{Na}_2\text{SO}_4/\text{N}_2$  for 1 h. After this the samples were transported to the STM and the local electronic properties were determined by  $I_T/U_T$ -spectroscopy either at some points after imaging the surface or with so-called current imaging tunnel spectroscopy (CITS). In the latter method an  $I_T/U_T$ -characteristic is measured at each point (64x64 points in one image) of the image. This leads to a poorer image resolution and longer measurements. The advantage of this type of measurement is besides the large number of data the fact that a correlation of the surface site in the image and the corresponding spectrum is not falsified by drifts, since the spectrum is measured immediately at the actual site of imaging. Such measurements were carried out at least at 10 different surface locations. The tunneling voltage for imaging was 500 mV and the tunneling current 1 nA.

## Results

Fig. 1 shows the effect of surface pre-treatment on the potentiodynamic polarization curves of AISI 304 in 0.1M NaCl. It can be seen that the breakdown potential is shifted into the positive direction by polishing the surface. As shown by Morach [2], polishing leads further to a lower number of metastable pitting events at potentials lower than the pitting potential.

In Figs. 2-5 in-situ STM and AFM images at different potentials in 0.1 M NaCl of the 1000 SiC and 1  $\mu\text{m}$  polished surfaces are shown. The 500 SiC surface shows a similar behaviour to the 1000 SiC surface, but it is more difficult to obtain good quality data due to the large surface roughness. In case of the 1000 SiC surface it is clearly to be seen in the STM-images that at a potential of  $E = -200 \text{ mV}$  the surface becomes "rougher" and the initial strong features due to grinding tracks are not as significant as in the beginning of the experiment. The polished surface on the other hand shows much less changes in the studied potential range. In contrast to the STM images in-situ AFM images reveal no significant changes in the same potential range.

Figs. 6-8 show the average roughness of the differently pre-treated and imaged surfaces as a function of potential. The average roughness was determined from area statistics at different surface areas at each potential. In the figure an average value is given. It can clearly be seen that the STM measurements show in the case of the 500 and 1000 SiC surfaces strong potential-dependent changes in the "roughness", which in the corresponding AFM measurements is much less significant.

In Figs. 9 and 10 typical representative STM surface images (a) and corresponding CITS spectra (b) of the passivated AISI 304 stainless steel surface with different surface pre-treatments are shown. In Fig. 9 the spectra measured in CITS mode on the 1000 SiC surface are ordered according to different surface sites. The eight upper spectra correspond to light points of the image - that is to the high parts of the scratches - and the lower eight spectra were measured at the dark points of the image - thus in the bottom of the scratches. It is clearly to be seen that the different regions of the scratched surface exhibit a different  $I_T/U_T$ -behaviour - and thus different electronic properties. On the other hand the spectra measured on the polished surface show at all surface locations an identical shape. Even though these results were not quantified it is clear that the differences between the two types of surfaces are significant.

In order to verify that this behaviour is connected to the passive film formed on differently pre-treated surfaces similar measurements were carried out on Pt. In this case no differences could be seen between the spectra measured on 1000 SiC or polished surface. The spectra measured on Pt shows a nearly ohmic behaviour indicating an almost metallic character of the surface.

## Discussion

It is not the intention of this paper to give a detailed theoretical discussion of the tunneling through oxide films and its interpretation in terms of semiconductor physics. The main point of the comparison of the STM and AFM images on one side and the tunneling spectra on the other side is to reveal the existence of inhomogeneities in the electronic properties of the passive films - and further to show that these inhomogeneities are connected to surface treatment. It has to be pointed out any how that an interpretation of the tunneling current as a measure for the electronic properties of the passive films is only then valid, when the electron transfer does not take place only by direct tunneling from the underlying metal to the tip, i.e. without a contribution of electronic states of the passive film. The mechanism of electron transfer depends on the oxide film thickness and its structure. The direct tunneling probability through the passive film decreases exponentially by increasing film thickness. Since the passive films formed on AISI 304 in a neutral solution have a thickness of approximately 2-3 nm (potential-dependent) and contain a high number of localized states, it can be concluded that direct tunneling through the oxide is not the only mechanism for electron transfer. Therefore the measured tunneling behaviour represents at least partly the electronic properties of the passive films. A detailed theoretical discussion of the tunneling mechanisms is any how beyond the scope of this paper.

A comparison of the results of the in-situ STM and AFM results are a clear indication that the changes taking place on the rough surfaces, which can be seen in the STM images are not due to purely topographical effects, since they cannot

be seen in the AFM images. This finding shows that the tunneling behaviour is influenced by the electronic properties of the surface and these electronic properties are strongly potential-dependent. The strong changes taking place at an potential of -200 mV / -300 mV for the rough surfaces indicate that at this potential a inhomogeneous passive film is formed on the surface, the heterogeneities being seen as an increase of the surface "roughness" when imaging in the tunneling mode. The finding that the changes in the STM surface "roughness" are much less in the case of the polished sample is an indication that on a polished a surface a more homogeneous passive film is formed.

For all cases it is typical that the "roughness" measured by STM decreases at a potential of about 0-100 mV. This indicates that at higher anodic potentials the passive films becomes more homogeneous. Without further work it is not possible to clarify, if this "homogenization" of the film is due to modifications of the film composition or structure. The finding of a potential-dependent inhomogeneity of the passive film is anyhow in good agreement with various literature data according to which the chemical composition of the passive films of iron-chromium alloys and stainless steels is potential-dependent. Changes in the chemical composition (which can on the other side influence the structure of the film) can lead to changes in the tunneling properties. Any how much further work is needed to clarify the origin of the changes in the tunneling behaviour at different potentials.

A comparison of tunneling spectra of the passive films on the differently treated surfaces further suggests that the passive film on the rougher surface shows more electronic inhomogeneities than the passive film on the polished surface. Even though the origin of these inhomogeneities can be various (non-stoichiometric chemical composition, defective structure, different film thickness), this finding means that the surface treatment leads to a modification of the passive film. This can be due to a non-homogeneous potential and current distribution on a rough surface. Thus the influence of mechanical grinding on the pitting resistance is probably not only due to surface roughness - which would lead to a formation of microcrevices on the surface - but directly due to an increased heterogeneity of the passive film on the rough surface.

The results of this work are in good agreement with results obtained on passive films of AISI 304 by in-situ local photoelectrochemical methods [25] showing that the distribution of photocurrents is strongly dependent of the mechanical pre-treatment - a polished surface exhibiting the most even distribution of the photocurrents. A statistical analysis of the photocurrent-maps and a comparison of the effect of mechanical surface pre-treatment on the number of metastable pitting events showed that strong correlations exist between the distribution of local photocurrents and initiation events of pitting corrosion.

Even though these results have to be considered as preliminary, it is clear that scanning tunneling microscopy and atomic force microscopy techniques represent powerful tools for characterizing passivity. In order to clarify the reasons for the different electronical heterogeneties of the differently treated surfaces, further work will be carried out. In order to clarify, if the electronic heterogeneities of the passive films are connected to anionic species in the electrolyte (e.g. to a nonhomogeneous adsorption/incorporation of  $\text{Cl}^-$  onto/into the passive film), similar studies will be carried out in other solutions. Further it has to be pointed out that during this work no pits were detected on the surfaces even though it it well known that at these potentials in 0.1M NaCl metastable pitting takes place. Considering

that the total number of transients detected during 24 h in 0.1M NaCl at 220 mV SCE on an 1000 SiC AISI 304 plate was  $740 \text{ cm}^{-1}$  [2], it can be concluded that the probability of pits being formed at the surface area studied ( $50 \text{ } \mu\text{m} \times 50 \text{ } \mu\text{m}$ ) is rather low. Furthermore in order to image small metastable pits a better resolution is necessary. This will be an object of further studies.

## Conclusions

1. On a rougher surface the STM image shows more changes at a potential, where the passive film is formed than on a polished surface. Since these changes could not be seen by AFM, it can be concluded that the changes taking place during passivation are due to a formation of an electronically inhomogeneous passive film - and the heterogeneity is larger on a rougher surface.
2. The inhomogeneity of the passive film was found to be potential-dependent. At a higher potential in the passive range the heterogeneity is decreased suggesting that changes in the film composition or structure are taking place. The exact reasons for these changes have not yet been clarified.
3. Tunneling spectroscopy measurements ( $I_T/U_T$ -spectroscopy) suggest that significant differences exist in the distribution of local electronic properties of passive films on stainless steels surfaces which were prior to passivation differently mechanically pre-treated (grinding/polishing) - on a rougher surface a more inhomogeneous film is formed.
4. A combination of scanning tunneling microscopy and atomic force microscopy is a valuable tool in characterizing properties of passive films and studying passivation in-situ with a local resolution.

## Acknowledgements:

The authors are pleased to acknowledge the Schweizerischer Nationalfonds zur Förderung der wissenschaftlichen Forschung for financially supporting this research. We also thank Mr. R. Nyffenegger (University of Berne, Institut für Anorganische, Analytische und Physikalische Chemie) for many helpful discussions.

## References

1. S. Szklarska-Smialowaska, Pitting Corrosion, (Houston, TX: National Association of Corrosion Engineers, 1986)
2. R. Morach, P. Schmuki, H. Böhni, Proc. of the 4th Int. Symp. on Electrochemical Methods in Corrosion Research, (Switzerland: Trans Tech Publications, 1992), p. 493
3. P.E. Manning, D. J. Duquette, W.F. Savage, Corrosion 35 (1979): p. 151
4. T. Shibata, T. Takeyama: Corrosion 33 (1977): p. 243
5. W.M. Carroll, T.G. Walsh: Corr. Sci. 29 (1989): p. 1205
6. H. Böhni, Corrosion Mechanisms, (New York: Marcel Dekker Inc., 1987), p. 285

7. H. Siegenthaler, R. Christoph, Scanning tunneling microscopy and related methods, (Netherlands: Kluwer Academic Publishers, 1990), p. 315
8. R. Sonnenfeld, J. Schneir, P.K. Hansma, Modern Aspects of Electrochemistry, Nr. 21, (New York: Plenum Press, 1990), p1
9. O. Lev, F.-R.F. Fan, A.J. Bard: J. Electrochem. Soc. 135 (1988): p. 783
10. F.-R.F. Fan, A.J. Bard: J. Electrochem. Soc. 136 (1989): p. 166
11. X. Zhang, U. Stimming: Corr. Sci. 30 (1990): p. 951
12. H.W. Pickering, Y.C. Wu, D.S. Gregory, S. Geh: J. Vac. Sci. and Technology (1991)
13. R.C. Bhardwaj, A. Gonzalez-Martin, J.O'M. Bockris: J. electrochem. Soc. 138 (1991): p. 1901
14. T.P. Moffat, F.-R: F. Fan, A. J. Bard: J. Electrochem. Soc. 138 (1991): p. 3224
15. R.C. Bhardwaj, A. Gonzalez-Martin, J.O'M. Bockris: J. Electrochem. Soc. 139 (1992): p. 1050
16. R. M Feenstra in Scanning tunneling microscopy and related methods, (Netherlands: Kluwer Academic Publishers, 1990), p. 211,
17. U. Stimming: Electrochim. Acta 31 (1986): p.415
18. C. Sunseri, S. Piazza, A. Di Paola, F. Di Quarto, J. Electrochem. Soc. 134 (1987): p. 2410
19. A. Di Paola, D. Shukla, U. Stimming, Electrochim. Acta 36 (1991): p. 345
20. A.M.P. Simoes, M.G.S. Ferreira, B. Rondot, M. da Cunha Belo, J. Electrochem. Soc. 137 (1990): p. 82
21. M.J. Klopppers, F. Bellucci, R. Latanision, Proc. of the Symp. on the Applications of Surface Analysis Methods to Environmental/Material Interactions, (Pennington, NJ: The Electrochemical Society, 1991), p. 287
22. D. Gorse, B. Rondot, M. da Cunha Belo, Corr. Sci. 30 (1990): p. 23
23. P. Schmuki, H. Böhni: J. Electrochem. Soc. 139 (1992): p. 1908
24. P. Schmuki, H. Böhni, Oxide Films on Metals and Alloys, Proc.-Vol. 92-22, (Pennington, NJ: The Electrochem. Society, 1992), p. 326
25. P. Schmuki, H. Böhni, to be published in Proc. 12th ICC, Houston, TX, 1993

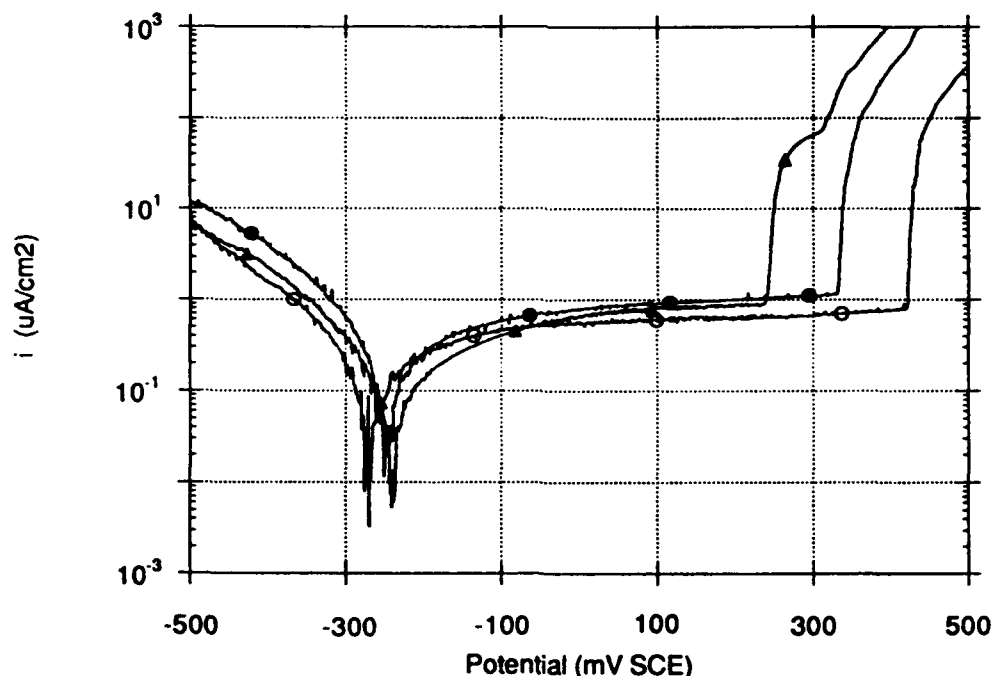


Figure 1. Polarization curves in 0.1M NaCl for AISI 304 with different surface pre-treatments (sweep rate = 0.2 mV/s)

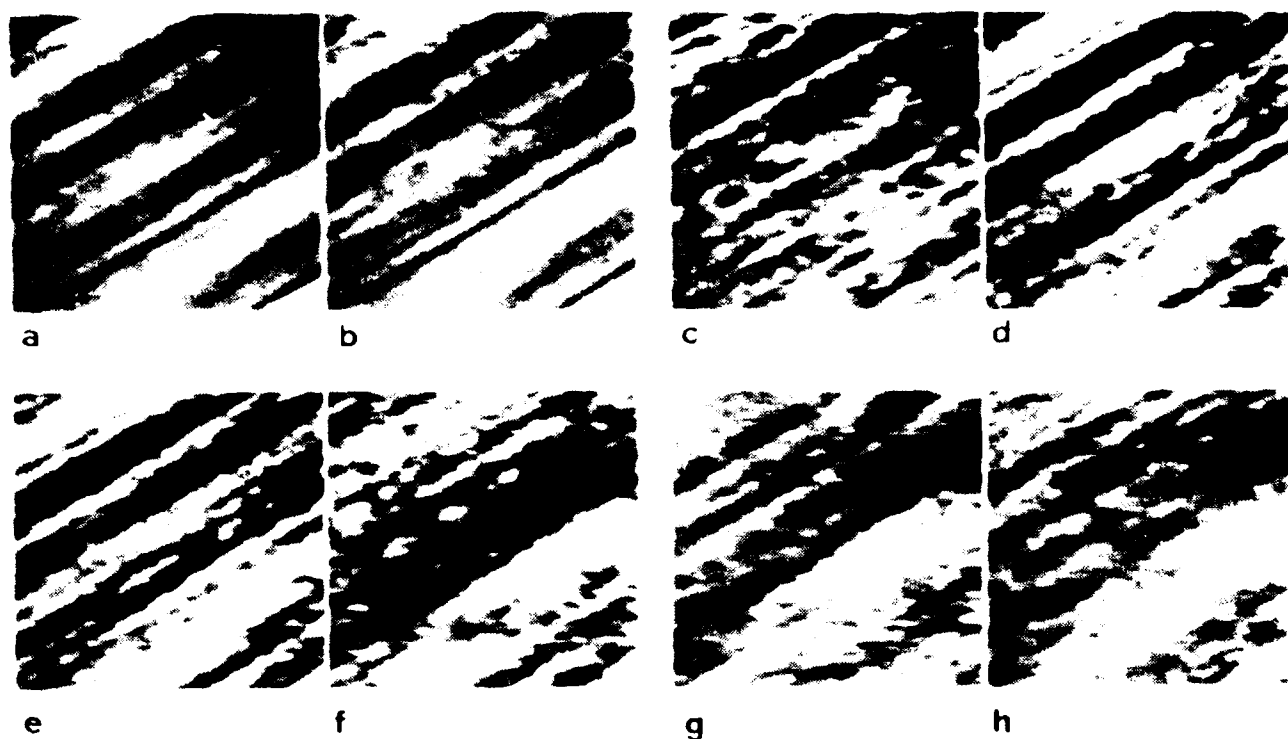


Figure 2. In-situ STM images of AISI 304 / 1000 SiC in 0.1M NaCl  
a) -600 mV, b) -400 mV, c) -200 mV, d) 0 mV, e) 100 mV, f) 200 mV  
g) 300 mV, h) 400 mV side length of the square = 34  $\mu\text{m}$

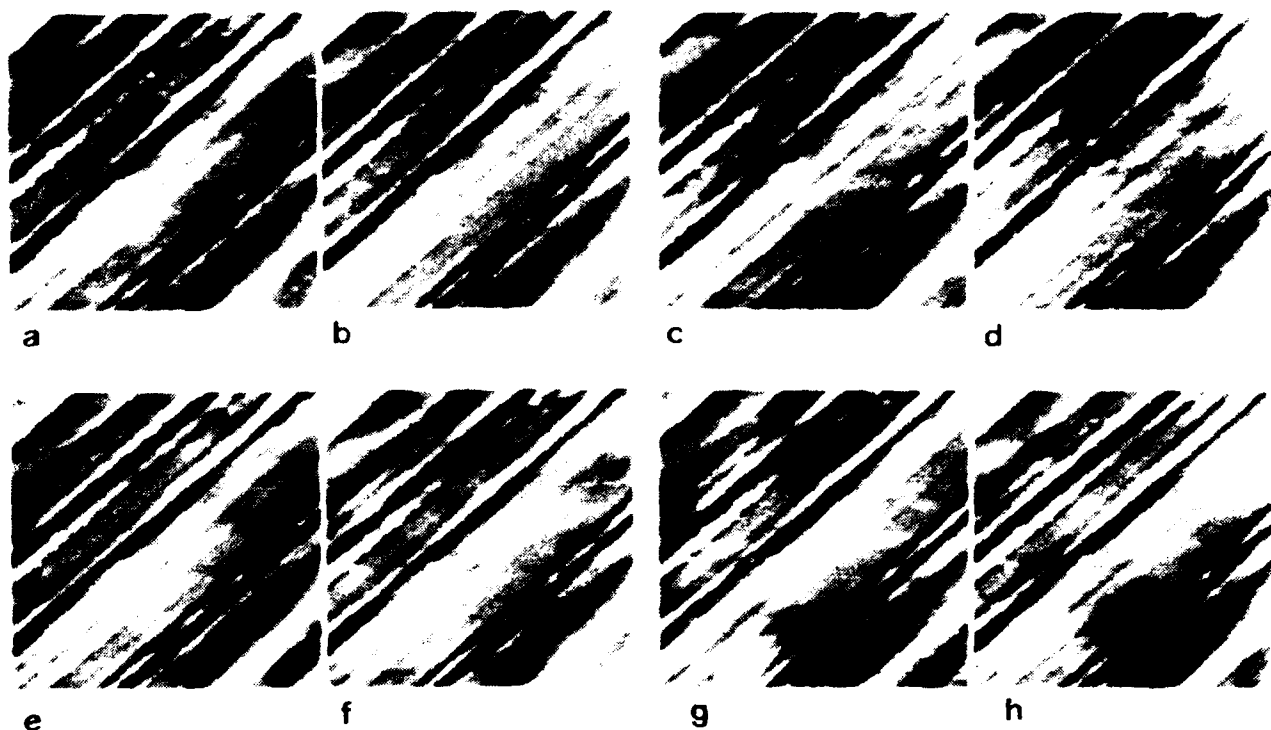


Figure 3. In-situ AFM images of AISI 304 / 1000 SiC in 0.1M NaCl  
a) -600 mV, b) -400 mV, c) -200 mV, d) 0 mV, e) 100 mV, f) 200 mV  
g) 300 mV, h) 400 mV side length of the square = 34  $\mu\text{m}$

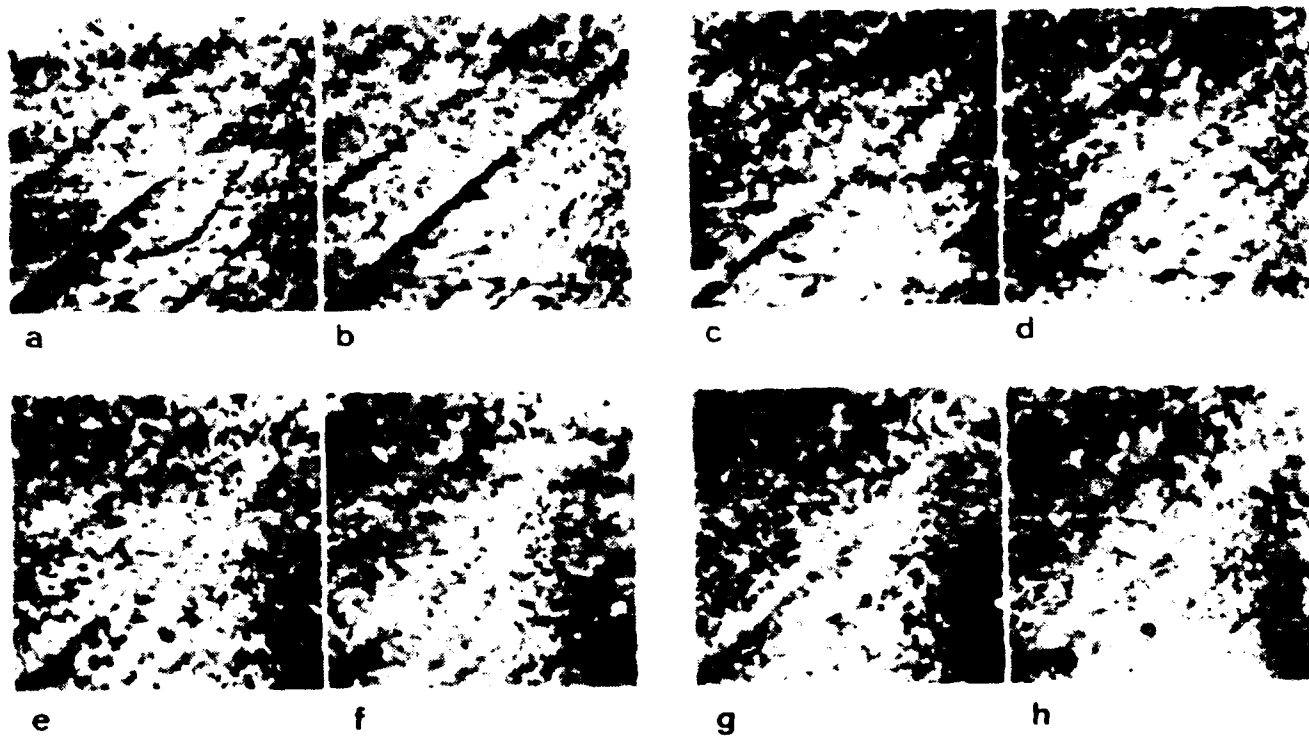


Figure 4. In-situ STM images of AISI 304 / 1  $\mu\text{m}$  polished in 0.1M NaCl  
 a) -600 mV, b) -400 mV, c) -200 mV, d) 0 mV, e) 100 mV, f) 200 mV  
 g) 300 mV, h) 400 mV side length of the square = 34  $\mu\text{m}$

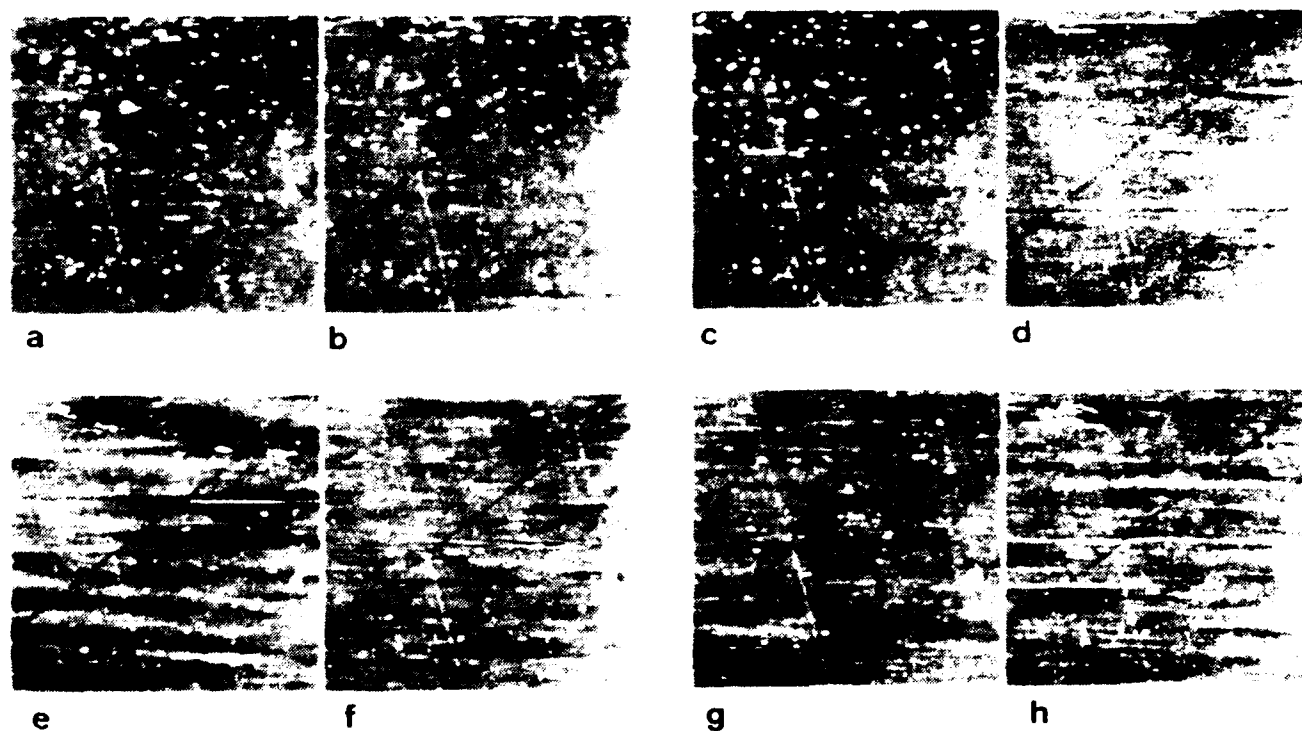
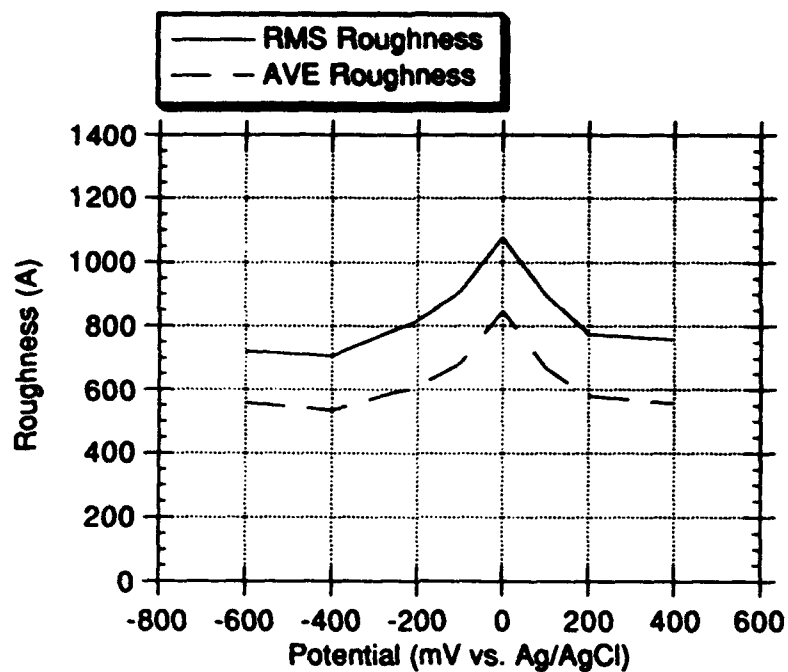
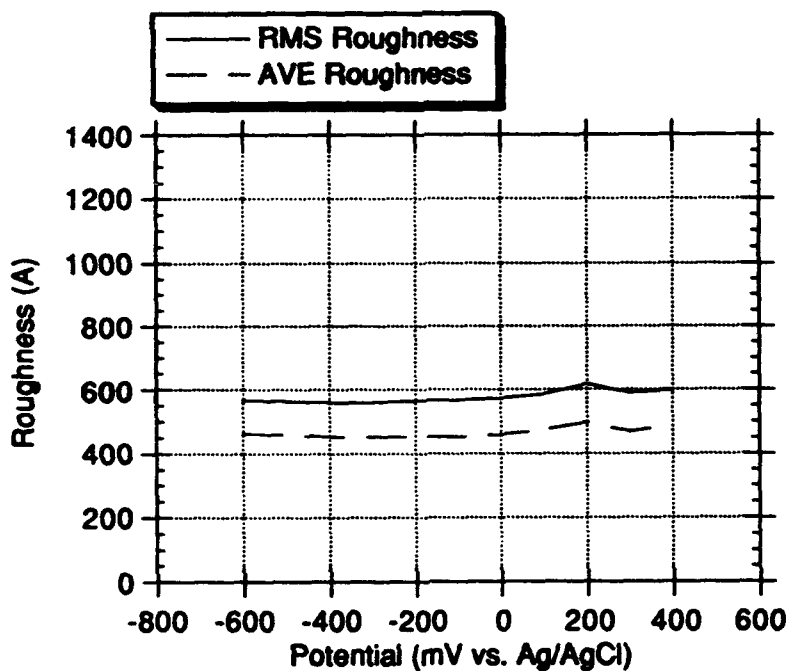


Figure 5. In-situ AFM images of AISI 304 / 1  $\mu\text{m}$  polished in 0.1M NaCl  
 a) -600 mV, b) -400 mV, c) -200 mV, d) 0 mV, e) 100 mV, f) 200 mV  
 g) 300 mV, h) 400 mV side length of the square = 34  $\mu\text{m}$



a)



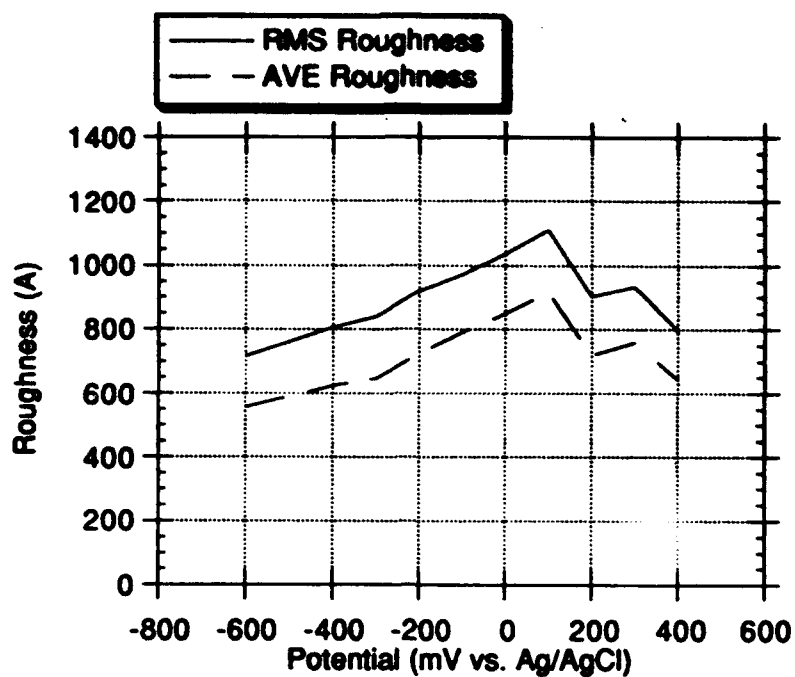
b)

**Figure 6. Average roughness of the surface of AISI 304 / 500 SiC at different potentials in 0.1M NaCl**

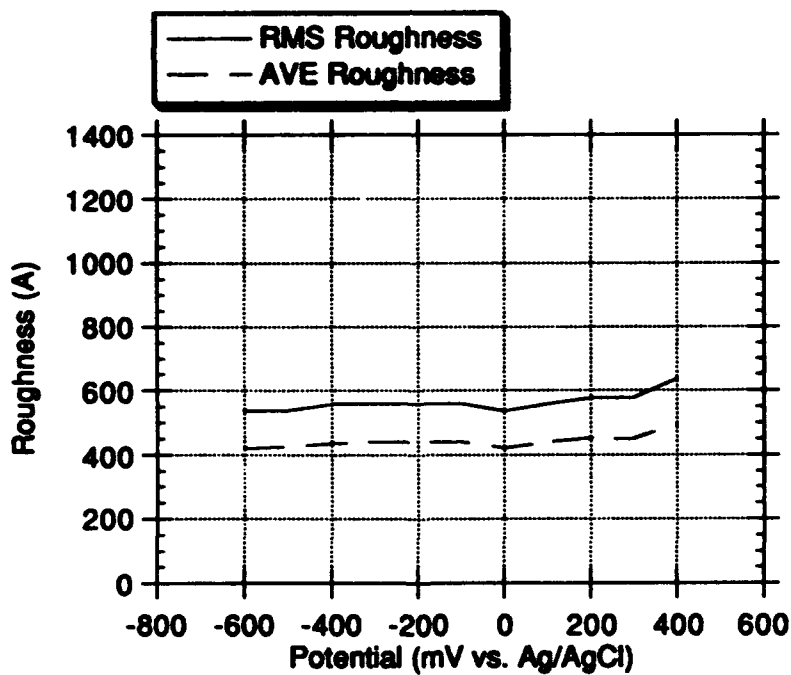
**a) STM measurements, b) AFM measurements**

**RMS = root mean square roughness, AVE = average roughness**





a)

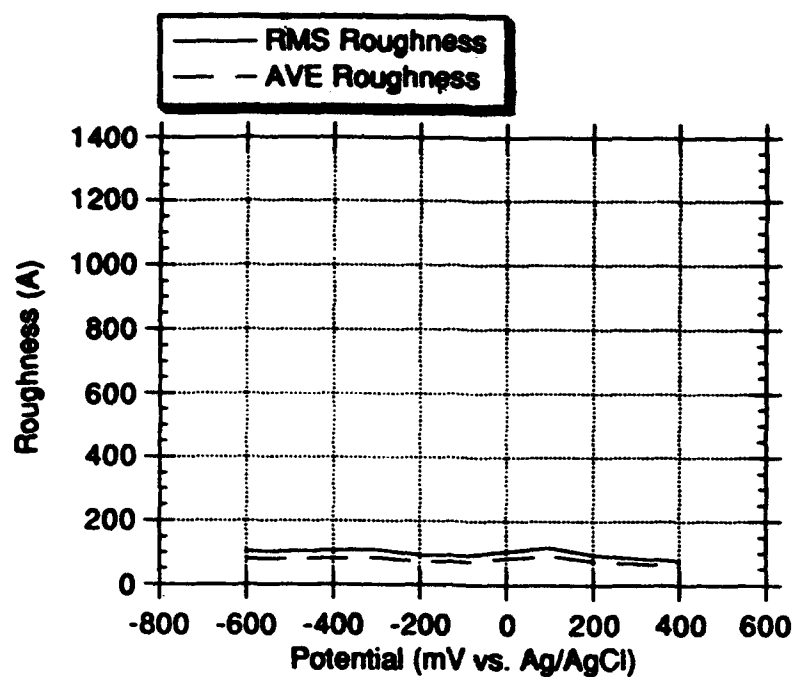


b)

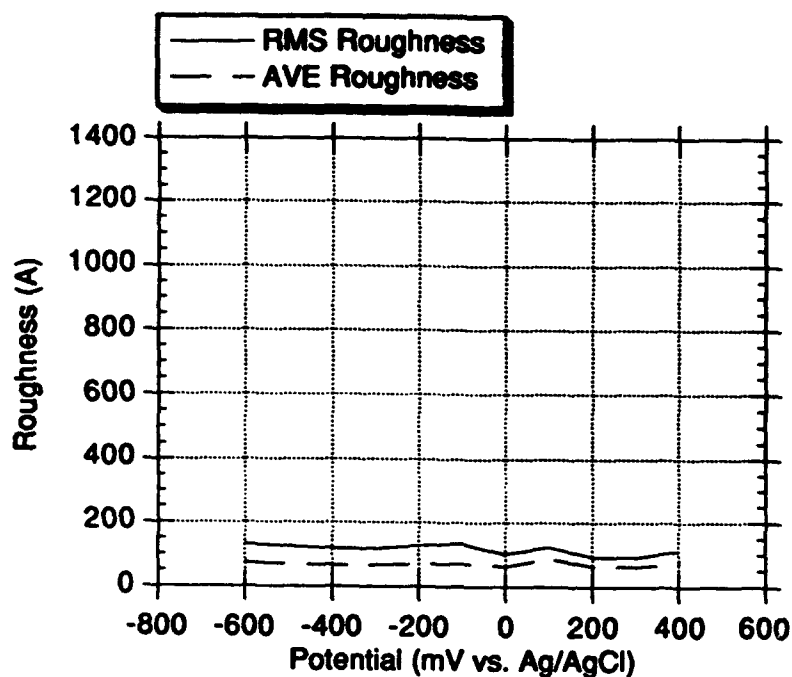
**Figure 7. Average roughness of the surface of AISI 304 / 1000 SiC at different potentials in 0.1M NaCl**

**a) STM measurements, b) AFM measurements**

**RMS = root mean square roughness, AVE = average roughness**



a)



b)

Figure 8. Average roughness of the surface of AISI 304 / 1  $\mu\text{m}$  polished at different potentials in 0.1M NaCl  
a) STM measurements, b) AFM measurements  
RMS = root mean square roughness, AVE = average roughness

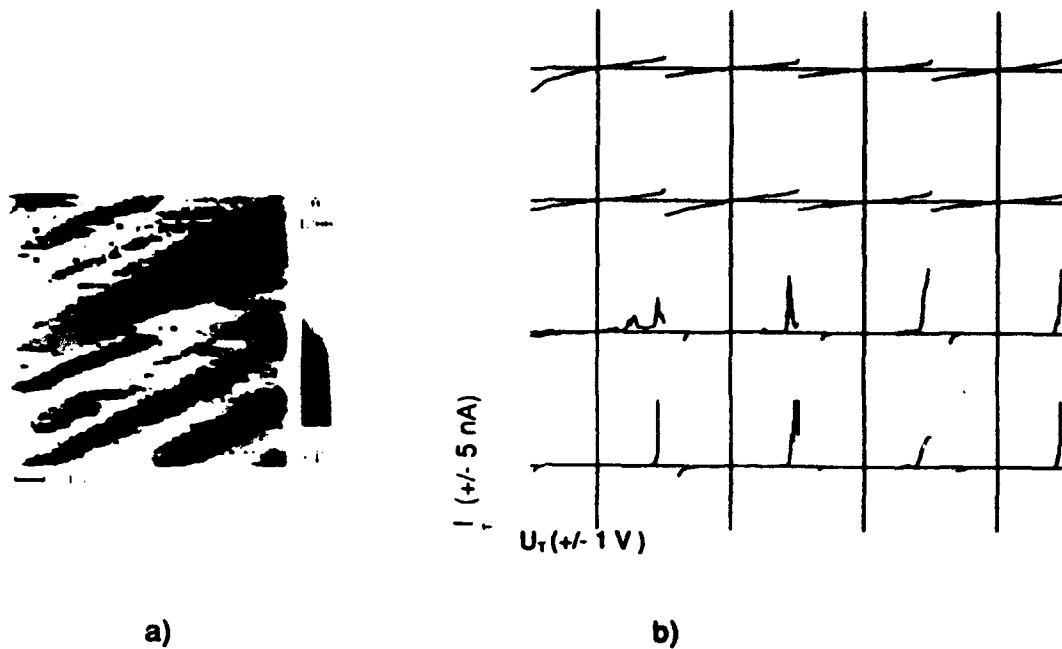


Figure 9. STM-surface image (a) and corresponding CITS spectra (b) of the passivated AISI 304 / 1000 SiC surface (passivation in 1M  $\text{Na}_2\text{SO}_4$  /  $\text{N}_2$ ,  $E=300 \text{ mV SCE}$ , 1 h)

a: side length of the square = 10  $\mu\text{m}$

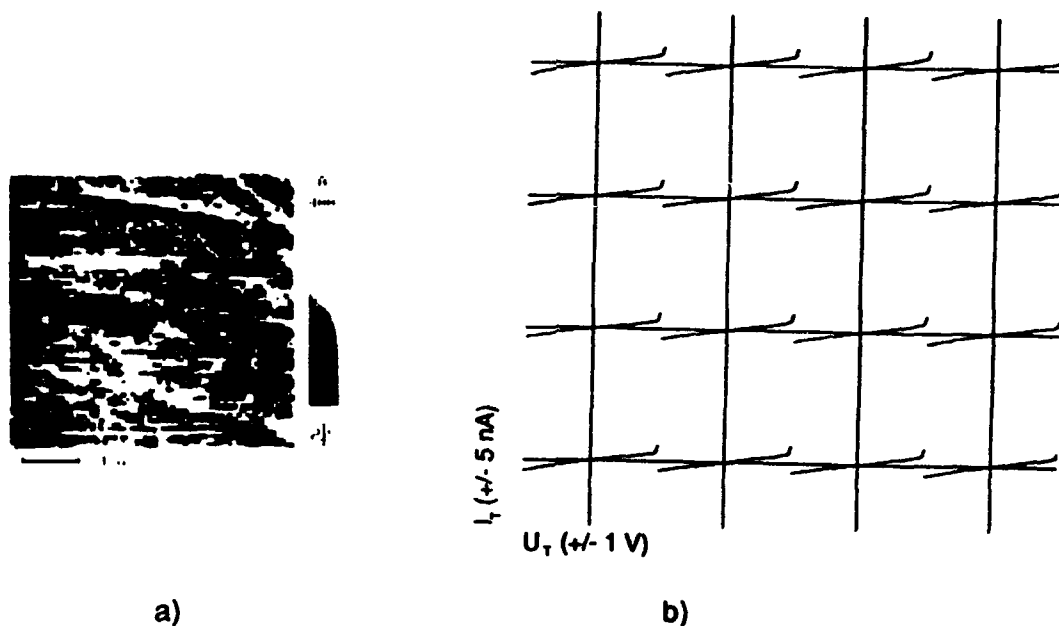


Figure 10. STM-surface image (a) and corresponding CITS spectra (b) of the passivated AISI 304 / 1  $\mu\text{m}$  polished surface (passivation in 1M  $\text{Na}_2\text{SO}_4$  /  $\text{N}_2$ ,  $E=300 \text{ mV SCE}$ , 1 h)

a: side length of the square = 5  $\mu\text{m}$

**An Investigation on The Stability of Transpassivated Film on  
304 Stainless Steel**

**Guang-Ling SONG**

**Corrosion Science Laboratory  
Institute of Corrosion and Protection of Metals  
Chinese Academy of Sciences  
62 Wencui Road, Shenyang 110015, China.**

**Chu-Nan CAO**

**Corrosion Science Laboratory  
Institute of Corrosion and Protection of Metals  
Chinese Academy of Sciences  
62 Wencui Road, Shenyang 110015, China.**

**Hai-Chao LIN**

**Corrosion Science Laboratory  
Institute of Corrosion and Protection of Metals  
Chinese Academy of Sciences  
62 Wencui Road, Shenyang 110015, China.**

**Abstract**

Investigation on stability of transpassivated film on 304 stainless steel was carried out by ellipsometric measurement, AES and XPS analyses and examinations of breakdown potential  $E_b$  and active dissolution time  $t_a$ . It is found that the  $t_a$  of properly transpassivated film is almost of the order of 2 longer than that of normally passivated film, and the  $E_b$  of the film which is post-treated in a molybdate-containing solution much higher than that of the passive film formed in passive region with the same post-treatment. The results of ellipsometric measurement show that the thickness of the film on the stainless steel increases with the positive shift of the anodic polarization potential. Moreover, AES and XPS analyses indicate that the transpassivated film consists of much more  $Fe^{3+}$  and much less  $Fe^{2+}$  than the passivated one, and this film with proper post-treatment contains much more Mo than the film formed in the passive region with the same post-treatment. It is believed that the increase of stability of the surface film obtained by transpassivation and post-treatment is ascribed to the increase of film thickness, the rise of the ratio  $Fe^{3+}/Fe^{2+}$  and the adsorption of Mo into the film during the post-treatment.

**Key terms:** stainless steel, transpassivation, post-treatment

## Introduction

Passivation is an effective measure to improve resistance of a metallic material against corrosion in some environments. Passive film formed in passive region which is believed to be responsible for the corrosion resistance of the material was extensively investigated by means of some surface analysis techniques (such as ellipsometry, XPS and AES, etc.) and some electrochemical methods. However, the transpassivated film formed in transpassivation potential region has not been carefully studied as transpassivation is usually regarded as destroying of a passive film. Nevertheless, some experimental results of alternating-voltage-superimposed passivation of stainless steels obtained in our laboratory<sup>[1-3]</sup> show that some surface films with high stability are formed on condition that the positive part of the superimposed alternating voltage falls in the transpassivation potential region. Thus it is estimated that film formed in transpassive region for a stainless steel may be responsible for its high stability.

## Experimental

Solutions of 0.5mol/L  $H_2SO_4$  (1# solution) and 0.5mol/L  $Na_2SO_4$  (2# solution) are used for passivation/transpassivation. 0.5mol/L  $Na_2SO_4$  + 0.1mol/L  $Na_2MoO_4$  (3# solution) is used for post-treatment. Examination of breakdown potential ( $E_b$ ) of surface film was carried out in 0.02mol/L NaCl (4# solution), while active dissolution of a surface film is tested in 5.6mol/L  $H_2SO_4$  (5# solution). All these solutions were prepared with analytic reagents and distilled water.

Specimen was made of 304 stainless steel (1Cr18Ni9Ti, as received) with a working exposed area  $1cm^2$ . Prior to experiments, the electrode was abraded with emery paper (No.1000#(W10)) and degreased with acetone thoroughly. Then put it into an electrolytic cell under the potential of -800mV vs. a saturated calomel electrode (SCE) in the 1# solution for 5 minutes to remove the oxide film formed in area before experiment. Then anodic polarization treatment of the specimen was performed in twogwifferent ways: (1) The specimen was anodically polarized at different potentials  $E_p$  (which is varied from passive region to transpassive region) in the 1# or the 2# solutions for 30 minutes to obtain a surface film without post-treatment. (2) The specimen was anodically treated just as (1) in the 2# solution for 20 minutes, then immersed into the 3# solution for 10 minutes under the same anodic polarization potential as above-mentioned to obtain a surface film with post-treatment. After that, following tests

were conducted:

1. Measurement of active dissolution time ( $t_a$ ) of the surface film. After the surface film formed in the ways above-mentioned, then put it into the 5# solution. Meanwhile, the corrosion potential ( $E_{corr}$ ) was recorded as a function of time. It was defined as  $t_a$ , at which  $E_{corr}$  dropped sharply and evolution of gas bubble was observed from the electrode surface. The value of  $t_a$  can be used to evaluate the stability of the surface film in the reductive acidic media.

2. Testing of breakdown potential ( $E_b$ ) of the surface film. The specimen was immersed into the 4# solution, and potentiostatic and potentiodynamic measurements were carried out to examine the  $E_b$  of the surface film.

3. Ellipsometrical measurement of thickness ( $d$ ) of the surface film.

The specimen was mounted on a specimen platform of L119 ellipsometer, and the optical parameters of amplitude ratio and phase difference were carefully read, then the film thickness ( $d$ ) of the specimen was calculated by a computer based on these parameters. The wavelength of incident light employed in this experiment is 632.8nm, and the angle between the incident and reflective lights 140°.

4. AES and XPS analyses.

The specimen was moved into a XSAM-800 energy analysis system with a vacuum of specimen chamber being about  $7 \times 10^{-8}$  Pa. The spectra of XPS were decomposed and fitted by a computer, and the AES spectra were revised by relative intensive factors to obtain the concentration of elements contained in the analyzed film.

Except for the  $t_a$  was examined at 50 °C, all of the other experiments were carried out at ambient temperature, and all the potentials presented in this paper are referred to the saturated calomel electrode (SCE)."

## Results and discussion

On Fig.1, following results are schematically presented: the anodic polarization curve ( $\log I_p$ ) of 304 stainless steel in the 1# solution, the active dissolution time ( $t_a$ ) tested in the 5# solution, the breakdown potential ( $E_b$ ) examined in the 4# solution, and the thickness ( $d$ ) of the surface film without post-treatment

obtained by the ellipsometry. In Table 1, the  $t_s$  and the  $E_b$  of surface film formed at different potentials (400mV, 1000mV and 1400mV) in the 2# solution with and without post-treatment are listed.

It can be seen from Fig.1 that the  $t_s$  of the film formed in the transpassive region is much higher than that of the film formed in the passive region, especially, at the transpassivation potential 1500mV, the  $t_s$  is almost of the order of 2 higher than that of the passive film. This is somewhat consistent with the results shown in the Table 1, where the high  $t_s$  is also obtained on condition that the specimen is anodically polarized in transpassive region. It should be noted that the potentials of 400mV, 1000mV and 1400mV are respectively located in the passive region, the lower region of transpassivation and the higher region of transpassivation of 304 stainless steel in 2# solution. Furthermore, some similar results were also observed by authors for 1Cr13 stainless steel in the 1# solution which are not presented in this paper. It is indicated by all of these results that the resistance of stainless steel against active dissolution in an acidic medium can be greatly improved by transpassivation above-mentioned.

On Fig.1 and Table 1, it is shown that, the  $E_b$  of surface film formed in the transpassive region without post-treatment is lower than that formed in the passive region. Nevertheless, if post-treatment was conducted after anodic polarization, then the  $E_b$  of the transpassive film formed in the 2# solution can be considerably increased. It is meant that even though the resistance against pitting breakdown of the surface film is lower by transpassivation, it can be completely recovered and even achieves to a much higher value by suitable post-treatment. Meanwhile, the post-treatment is also beneficial somewhat to the  $t_s$  for the passive film and the transpassive film formed in the lower transpassive region.

Synthetically, the transpassivated film at a suitable potential with the post-treatment in the molybdate-containing solution exhibits wonderful corrosion resistance against the pitting breakdown in  $Cl^-$ -containing medium and the active dissolution in acidic solution, e.g., the synthetic stability ( $E_b$  and  $t_s$ ) of the surface film formed at 100mV in the 2# solution is strikingly increased after the post-treatment.

It is generally believed that under the same condition, the thicker the film is, the longer the  $t_s$ . So the change of the  $t_s$  tested in the 5# solution shown in Fig.1 can be ascribed to the variation of

the thickness of the film. Because in the Fig.1,  $d$  increases with the polarization potential, especially in the transpassive region, it increases much more sharply with the  $E_p$  than in the passive region. However, when  $E_p$  positively exceeds 1500mV, then a loose film can be observed which can be easily scraped off by hand and is definitely different from the film formed at a potential lower than 1500mV. Such a film is obviously less protective, therefore  $t_p$  decreases when  $E_p$  is higher than 1500mV.

Different from  $t_p$ , generally, there is not any correlation between  $E_b$  and the thickness of a surface film, it mainly depends on composition of the film. Therefore, decrease of the  $E_b$  by transpassivation and increase of the  $E_b$  by post-treatment can only be ascribed to the change of the composition and structure of the film, even though the thickness of the film changes after these treatments.

The results of AES and XPS analyses of the surface film formed on 304 stainless steel in 2# solution are shown on Table 2. From the results of AES analysis, it is observed that while Fe and Cr concentrations are lower in the transpassive film formed at the transpassivation potential (100mV and 1400mV), concentration of oxygen is higher than those in the passive film formed at 400mV. It is indicated that the valence of metal ions in oxides in the transpassive film may be higher than that in the passive film. By the XPS analysis is proved the fact that the ratio of  $Fe^{3+}/Fe^{2+}$  in the transpassive film does be higher than that in the passive film. Usually, the trivalent oxide of iron has a higher resistance against chemical dissolution in acidic medium than the bivalent one, so the increase of the ratio of  $Fe^{3+}/Fe^{2+}$  may be another very important factor for the improvement of  $t_p$  by transpassivation in the 5# solution. But the XPS analysis also shows that the ratio of  $Cr^{3+}/Cr^{6+}$  is nearly unchanged by transpassivation. Since the Cr is an effective element for improving the resistance against pitting breakdown of surface film, and the absolute concentration of Cr is increased (according to the AES results) while the ratio of lower valent oxide to higher valent oxide of Cr unchanged (according to the XPS results) by transpassivation, therefore the  $E_b$  of the transpassive film is low in comparing with that of the passive film.

After post-treatment, Mo signal was determined in the film formed in the 2# solution by AES and XPS, and some interesting phenomena are shown in the Table 2 that the concentration of Mo and the ratio of  $Mo^{4+}/Mo^{6+}$  increase with the anodic polarization potential. The



higher amount of Mo in the transpassive film than in the passive film means that the surface film formed in the transpassive region is much easier to adsorb the Mo-containing ion from the 3% solution than the film formed in the passive region. As Mo is also a much effective element for improving stability of stainless steel, increase of Mo concentration in surface film can obviously enhance stability of film. Hence the transpassive film with post-treatment shares higher  $E_b$  than that without post-treatment. And during the transferring process of Mo-containing ion from the 3% solution to the surface film, the transpassive film is furtherly oxidized by the  $\text{MoO}_4^{2-}$ , the  $\text{Mo}^{6+}$  is reduced to  $\text{Mo}^{4+}$  because some  $\text{Mo}^{4+}$  is found in the transpassive film after the post-treatment (table 2).

### Conclusions

In acidic solution, the time for active dissolution of the surface film formed at a proper transpassivation potential is greatly higher than the film formed in the passive region. If post-treatment in molybdate solution is conducted after transpassivation, then the pitting breakdown potential of the transpassive film can be greatly increased, and a wonderful synthetic stability of the stainless steel can be obtained. The improvement of the stability by transpassivation and post-treatment is due to the increase of the film thickness, the higher ratio of  $\text{Fe}^{3+}/\text{Fe}^{2+}$  and the adsorption of Molybdenum into the surface film.

Acknowledgement-- This work was supported by NSF of china. The authors wish to thank Mr. B.J. Xia for his operation of AES and XPS analyses.

### References

1. G.L.Song, C.N.Cao, Y.Wang, H.C.Lin, Journal of Chinese Society of Corrosion and Protection, 11 (1991): p.319.
2. G.L.Song, C.N.Cao, H.C.Lin, Journal of Chinese Society of Corrosion and Protection, 12 (1992): p.36.
3. G.L.Song, C.N.Cao, H.C.Lin, Chinese Journal of Applied Chemistry, 9 (1992): p.79.

Table 1. the  $t_a$  and the  $E_b$  of the surface formed in the 2# solution with and without post-treatment

polarization potential (mV)	$t_a$ (min)	$E_b$ (mV)	
without	400	2	275
post-treatment	1000	153	148
	1400	247	133
with	400	5	225
post-treatment	1000	354	340
in 3# solution	1400	156	250

Table 2. the AES and the XPS analysis results of the surface formed in the 2# solution with and without post-treatment in 3# solution

AES result(atm.%)						XPS result (amt.%)					
Ep(mV)		O	Cr	Fe	Mo	Fe <sup>2+</sup>	Fe <sup>3+</sup>	Cr <sup>3+</sup>	Cr <sup>6+</sup>	Mo <sup>4+</sup>	Mo <sup>6+</sup>
without	400	37.0	9.3	46.0		81.4	22.6	70.6	28.0		
post-	1000	50.2	2.7	44.0		58.4	42.5	70.2	30.6		
treatment	1400	50.1	2.7	41.3		51.7	48.9	69.5	28.3		
with	400	41.7	6.7	45.6	0.2	57.9	43.9	70.2	30.9	0.0	78.7
post-	1000	50.5	3.1	41.3	0.8	53.5	43.3	69.2	31.0	28.0	72.3
treatment	1400	49.9	1.3	39.2	1.5	35.8	58.7	43.3	72.2	55.3	35.8

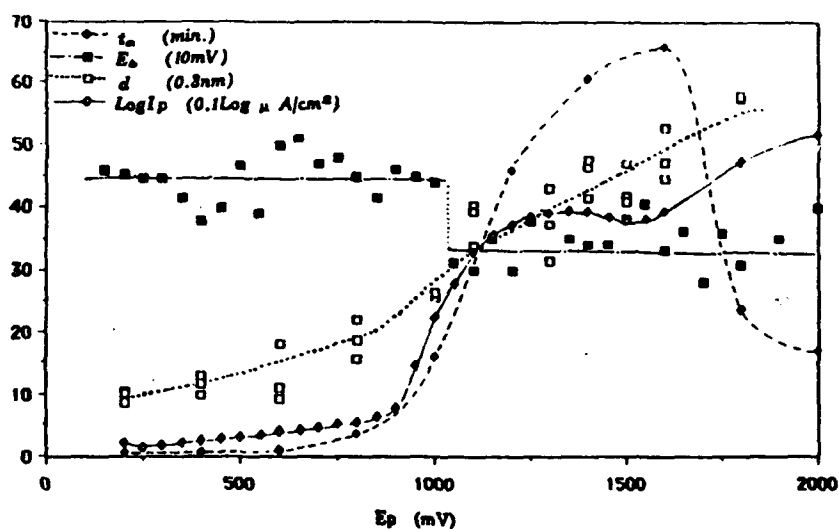


Fig.1 the anodic polarization curve ( $\text{Log} I_p$ ), the active dissolution time ( $t_a$ ), the breakdown potential ( $E_b$ ) and the thickness ( $d$ ) of the surface film formed on 304 stainless steel in the 1# solution.

**Photoelectrochemical Studies of the Passive Films on  
Copper and Brass**

**G. Rajagopal**  
Central Electrochemical Research Institute  
Karaikudi-623006, India

**S. Sathiyarayanan**  
Central Electrochemical Research Institute  
Karaikudi-623006, India

**K. Balakrishnan**  
Central Electrochemical Research Institute  
Karaikudi-623006, India

**Abstract**

The passive films formed on copper and brass in weak alkaline medium exhibit a positive photopotential as the light is shone on them. The qualitative nature of these passive films is analysed with wavelength spectrum of photopotential. The effect of addition of halide ions viz Cl<sup>-</sup>, Br<sup>-</sup>, I<sup>-</sup> and F<sup>-</sup> on the electronic properties of these passive films including band gaps have been determined from the photocurrent measurements.

**Key terms :** Passive film, Photopotential/current, Acceptor concentration, Flat band potential, Band gap.

**Introduction**

The theories and techniques of semiconductors have found wide application in the investigation of passive films. Ex-situ techniques like AES, XPS, ESCA etc. are employed to analyse the structure of the passive films. However, significant changes in structure and composition could occur before such measurements as they require a change of environment. In recent times, photoelectrochemistry, along with the capacitance measurements, is widely employed in understanding the electronic properties of passive films formed on metals and alloys [1-3]. The application of photoelectrochemistry to the study of passive films is based on the assumption that even thin films constitute their own phase with their specific properties and the theories applicable to semiconductors are valid in the case of thin films also. Thus, photoelectrochemistry is used as a

powerful in-situ technique to characterise passive films with respect to their optical and electronic properties.

In this investigation, attempts have been made to study the passive films formed on copper and brass in weak aerated alkaline medium by measuring the photopotential, interfacial capacitance and photocurrent. The influence of halide ions on the electronic properties of these passive films have also been discussed.

### Experimental

The experimental procedures for measuring photopotential and capacitance are briefly described elsewhere [4]. Solutions of AR grade sodium hydroxide, sodium chloride, sodium bromide, sodium iodide and sodium fluoride were made up using triple distilled water. The photocurrents were measured using 173 PAR potentiostat coupled with 5301 PAR lock-in amplifier and is interfaced with a PC-AT through a GPIB.

### Results & Discussion

#### I. Photopotential measurements

The positive potential difference (photopotential) observed for the passive film on copper in 0.1M NaOH as shown in Fig 1 suggests the formation of a p-type semiconducting oxide layer. When the electrode is illuminated, the light of suitable energy  $h\nu$  is absorbed by the passive film resulting in the excitation of electrons from occupied to unoccupied electronic state according to



As a consequence of this, the charge distribution within the film is affected and is very well reflected by the change in the current/potential even at open circuit potential where  $i = 0$ . This has been demonstrated by Oshe and Rozenfeld [5] who determined the type of conductivity for a number of natural oxides of different systems including that of copper under pulsed illumination. Figures 1(a) and 1(b) show the energetic situations in dark and illuminated conditions of oxide layer. The origin of this positive photopotential may be explained in considering these figures as follows :

Irradiation of passive (oxide) film (Fig 1(a)) from the electrolyte side leads to the formation of electron-hole pairs in the Debye region of the film (Fig 1(b)). These electrons and holes may eventually recombine but due to the existence of differential electric field within the oxide film, they are separated. The electrons available in the

conduction band roll down towards oxide/electrolyte interface because of the depletion nature of the film and take part in the following electrochemical kinetics. The holes, on the other hand, move towards the bulk of the oxide [6]. This increased population of electrons in the Debye region results in the shift of Fermi level ( $\Delta E_f$ ) in the negative direction. In other words, the potential difference ( $\Delta V$ ) shifts in positive direction indicative of its p-type semiconducting nature.

As the light is cut off at the end of 120th sec, the potential difference falls much below the initial value. This may be due to back reaction of photo generated species arising because of the presence of surface states, deep traps, dissolved oxygen or some intermediate compounds formed within the film [7].

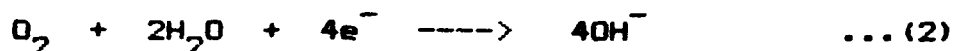
The growth of the passive films on copper with the addition of halide ions in 0.1M NaOH was monitored by measuring the photopotential at regular intervals of time. The logarithmic rise of photopotential of copper in 0.1M NaOH (Fig 2(a)) confirms that the growth of oxide films follows the logarithmic law.

The addition of halide ions slows down the growth of oxide film considerably and this causes the deviation from the logarithmic growth of oxide film. Visual observation, at the end of the experiment shows a thick, adherent, black film over the surface. A marginal increase in photopotential is observed in the case of chloride and fluoride ions. Addition of bromide and iodide ions saturates the photopotential reflecting the involvement of these ions on the retardation of film growth. This observation can be compared with our earlier investigation [4] where the addition of inhibitor saturates the photopotential.

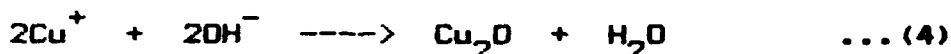
In the case of brass (Fig 2(b)), a linear increase of photopotential with time was observed instead of a logarithmic one. Also the magnitude of the photopotential in the case of brass is less when compared to that of copper. This can be understood in terms of the differences between the copper and zinc oxides. The enrichment of oxides of copper on brass surface results in the positive photopotential. Increase in the photopotential with the addition of halide ions in such a small concentration may be due to the accumulation of negative charges at the oxide/electrolyte interface. The thickness of the film

tends to increase with time. At these concentrations of halide ions, the presence of excess  $\text{OH}^-$  ion dominates the film formation process [8].

Figure 3 shows the spectral distribution of photopotential for copper and brass in 0.1M NaOH for different durations of time. For the case of copper (Fig 3(a)), upto 5th hour, the photopotential peak centres around 500 nm, which is characteristic of  $\text{Cu}_2\text{O}$ . When the electrodes are immersed in the medium, the film formation is facilitated by oxygen reduction



When the intermediates of the reduction processes are also incorporated into the film, the formation of  $\text{Cu}_2\text{O}$  depends on the cupric ion reduction



After 5 hours, this peak at 500 nm disappears and two new peaks around 435 nm and 550 nm appear, indicating that with time, the composition changes from  $\text{Cu}_2\text{O}$  to a mixed oxides of copper. This is in good agreement with the earlier observation of Kruger [9], that irradiation of  $\text{Cu}_2\text{O}$  promotes its own photo-reduction and oxidation.

In the case of brass (fig 3(b)), the photopotential peak centres around 500 nm and persists with time upto 24 hours. Thereafter multiple peaks appear. This indicates that the formation of other oxides of copper takes a longer time on brass.

## II. Capacitance measurements

A simple and versatile method of determining  $V_{fb}$  is by construction and evaluation of Mott-Schottky plots (MS plots). The MS plots i.e., the  $1/C^2$  vs Potential were analysed using the expression for the space charge capacitance of a semiconductor in the depletion range

$$1/C^2 = 2/\epsilon\epsilon_0 q N_A (V - V_{fb} - KT/q) \quad \dots(5)$$

where  $\epsilon$  is the dielectric constant of the film,  $N_A$  the acceptor concentration,  $V$  the applied electrode potential,

$V_{fb}$  the flat band potential and the remaining symbols have their usual meaning. According to the equation (5), the flat band potential of the passive film can be estimated by extrapolating the MS plots to the potential axis i.e.  $1/C^2=0$  and the acceptor concentration can be calculated from the slope of the linear region.

MS plot of copper in 0.1M NaOH for three different frequencies are given in Fig 4. The extrapolation of the linear region of the depletion layer intersects the potential axis at different potentials. According to Dutoit [10], if the set of MS plots are parallel for different frequencies with different potential intercepts then it is classified under A type. In the B-type the MS plots for different frequencies intersects the potential axis at the same point with different slopes. MS plots shown in Fig 4 is a combination of A and B type. Similar results have also been obtained by Dipaulo for stainless steel [11]. In such situations it is not possible to obtain the exact values of  $V_{fb}$  for passive films formed on metal surface and hence it should be restricted to one frequency only. In the forthcoming results, the frequency has been fixed at 100 Hz for further analysis of MS plots.

Table-1 shows the flat band potential and acceptor concentration for the passive films on copper and brass in 0.1M NaOH with the addition of halide ions. Addition of halide ions shifts the flat band potential appreciably in the negative direction for both copper and brass. The acceptor concentration however decreases for copper with the addition of halide ions when compared to that of 0.1M NaOH while it increases for brass. These results agree well with the photopotential measurements where it is observed that the photopotential is lowered with the addition of halide ions for copper and increased in the case of brass.

### III. Photocurrent measurements

For ideal Schottky barrier, Gartner [12] proposed a model which describes the photocurrent behaviour for a metal-semiconductor junction and Butler [13] extended it to semiconductor/electrolyte junction. According to Butler, the absolute value of the photocurrent may be expressed as

$$i_{ph} = e \Phi_0 [1 - \exp(-\alpha W) / (1 + \alpha L_p)] \quad \dots (6)$$

$$W = [2\epsilon\epsilon_0 / eN]^{1/2} [V - V_{fb}]^{1/2}$$

$$\text{and } L_p = (D \tau)^{1/2}$$

where  $e$  denotes the electronic charge,  $\Phi_0$  the incident photon flux,  $\alpha$  the optical absorption coefficient,  $L_p$  the diffusion length of the minority carriers,  $\epsilon$  and  $\epsilon_0$  the dielectric constants of vacuum and semiconductor,  $\tau$  the life time,  $D$  the diffusion coefficient of minority carriers.

#### A. Potential dependance of photocurrent

The photocurrents were measured for copper and brass electrodes immersed in 0.1M NaOH solution after 1st and 5th hour of immersion at 435 nm. The plots of square of the photocurrent vs potential for these electrodes at 435 nm are shown in figure (5). At a constant wavelength, the absorption coefficient ( $\alpha$ ) and the diffusion length ( $L_p$ ) are going to be very small. Hence  $\alpha L_p \ll 1$  and  $\alpha L_p \ll \alpha W$  and the equation (6) will lead to the following approximation :

$$i_{ph} = e \Phi_0 \alpha W = \text{const.} (V - V_{fb})^{1/2} \quad \dots (7)$$

According to this expression, the plot of  $i_{ph}^2$  vs  $V$  should yield a straight line for a constant oxide thickness and the extrapolation of that linear region to  $i_{ph} = 0$  will give the flat band potential. From the figure (5) it is evident that for the passive films on copper at the end of 1st hour only one slope is obtained with the intercept being at +0.115 V (vs SCE). The film grown over 5 hours shows distinctly two slopes with intercepts at +0.076 V and +0.238 V respectively. These results indicate the existence of  $\text{Cu}_2\text{O}$  alone at the end of one hour and mixed oxides of copper at the interface after 5 hours. On the other hand, a single slope, with single intercept, is obtained even after five hours of immersion of brass confirming the existence of single oxide over the surface. This observation is in good agreement with our photopotential spectrum analysis discussed earlier.

#### B. Band gap measurements

The absorption coefficient  $\alpha$  of a crystalline material depends on photon energy and according to Johnson [14]

$$\alpha = A (h\nu - E_g)^{n/2} / h\nu \quad \dots (8)$$



where A is a constant.

For allowed transitions which are likely to be observed,  $n = 1$  describes direct transition and  $n = 4$ , the indirect transition.

For  $\alpha W \ll 1$ , equation (6) becomes

$$i_{ph} h \nu / e \hbar A = (V - V_{fb})^{1/2} (h\nu - E_g)^{n/2} \quad \dots (9)$$

Fig (6) shows the plot of  $(\eta h \nu)^{1/2}$  vs  $h \nu$  for copper and brass in 0.1M NaOH at the end of 1st hour. The best fit of the data is obtained for  $n = 1$  indicating a direct transition. The intersection of such a plot to X-axis yields band gap ( $E_g$ ). In the case of copper, the  $E_g$  is 2.325 eV and for brass it is 2.45 eV.

Table 2 shows the band gap measured for the passive films on copper and brass with the addition of halide ions. As it is evident from the table, the addition of halide ions increases the band gap of the passive layer in the case of copper, the reverse is true with the case of brass. i.e. addition of halide ions decreases the band gap when compared to that in blank (0.1M NaOH). Thus the addition of halide ions decreases the conductivity in the case of copper and increases the same in the case of brass. This may be the reason for the decrease and increase in the photopotential with the addition of halide ion on copper and brass respectively.

Fig (7) shows the effect of applied potential on the  $E_g$  for the passive films on copper and brass in 0.1M NaOH. In both the cases of copper and brass the band gap found with potential decreases and then remains constant. The Higher value of  $E_g$  on brass may arise from the interference due to traces of zinc in the film.

#### Conclusion

The passive films on copper and brass in aerated weak alkaline medium exhibit the properties of a p-type semiconductor. Wave length dependence of photopotential indicates the formation of different oxides of copper within a couple of hours whereas it takes atleast 24 hours for the mixed oxides to form on brass. The capacitance measurements yield a frequency dispersive Mott-Schottky plot. The flat band potential obtained from the fixed frequency MS plot is in good agreement with that obtained from photocurrent

measurements. The formation of different oxides of copper on copper within a few hours of immersion is also confirmed by photocurrent measurements, where two slopes were obtained in  $i_{ph}^2$  vs E plot. The direct band gaps measured for the passive films on copper and brass are 2.325 eV and 2.55 eV respectively.

#### References

1. A. Felske and W. J. Plieth, J. Optical. Soc. Am. B 3 (1986) p815.
2. U. Stimming, Passivity of Metals and Semiconductors, Ed. M. Froment, Elsevier, New York (1983) p477.
3. S. M. Wilhelm and N. Hackerman, J. Electrochem. Soc., 128 (1981) p1668.
4. S. Sathiyarayanan, SP. Manoharan, G. Rajagopal and K. Balakrishnan, Brit. Corros. J., 27 (1992) p72.
5. E. K. Oshe and I. L. Rozenfeld, Elektrokhimiya, 4 (1968) p1200.
6. H. O. Finklea, Semiconductor Electrodes, Ed. H. O. Finklea, Elsevier, New York (1988).
7. K. L. Hardee and A. J. Bard, J. Electrochem. Soc., 124 (1977) p215.
8. N. Sato, Corrosion, 45 (1989) p354.
9. J. Kruger, J. Electrochem. Soc., 106 (1959) p847.
10. E. C. Dutoit, R. L. Vanmeirhaege, F. Cardon and W. Gomes, Ber. Bunsenges. Phys. Chem., 79 (1975) p1209.
11. A. Dipaula, Electrochimica Acta, 34 (1989) p203.
12. W. W. Gartner, Phys. Rev., 116 (1959) p84.
13. M. A. Butler, J. Appld. Phys., 48 (1977) p1914.
14. E. J. Johnson, Semiconductors and Semimetals, Eds. R. K. Willardson and A. C. Beer, Ch. 6, Vol. 3, Academic Press, New York (1967).

Table - 1

Effect of Halide ions on the Flat band potential and  
Acceptor concentration for copper and brass in 0.1M NaOH

Copper :  $V_{fb} = 134 \text{ mV}$  ;  $N_A = 6.68 \times 10^{21} / \text{cm}^3$

Brass :  $V_{fb} = 250 \text{ mV}$  ;  $N_A = 7.8 \times 10^{19} / \text{cm}^3$

Sl. No.	Metal	Conc. (ppm)	Cl		Br		F		I	
			$V_{fb}$	$N_A$	$V_{fb}$	$N_A$	$V_{fb}$	$N_A$	$V_{fb}$	$N_A$
1.	Copper	100	-60.0	0.1200	-56.1	0.0258	40.7	0.0398	-60.0	0.0111
2.		300	-41.2	0.2260	-40.6	0.0626	62.8	0.3580	-76.2	0.0085
3.		500	-31.2	0.2090	-34.4	0.0765	60.9	0.3180	-83.2	0.0074
4.		1000	-26.8	0.0488	-30.0	0.0557	67.5	0.1990	-90.5	0.0424
5.	Brass	100	112.8	0.4100	168.4	0.6000	215.0	0.0360	186.8	0.5600
6.		300	67.4	0.3670	67.9	0.1200	151.0	0.0678	85.6	0.8200
7.		500	61.5	0.1900	75.8	0.2300	75.0	0.0438	97.4	0.3800
8.		1000	61.5	0.3500	70.8	0.2300	78.0	0.0421	86.8	0.4700

Table - 2

Effect of Halide ions on the Band gap of passive films  
on Copper and Brass in 0.1M NaOH

Medium	$E_g, \text{ eV}$	
	Copper	Brass
0.1M NaOH	2.325	2.550
+ 300 Cl	3.020	2.280
+ 300 Br	2.680	2.080
+ 500 F	3.570	2.360
+ 500 I	3.110	2.160

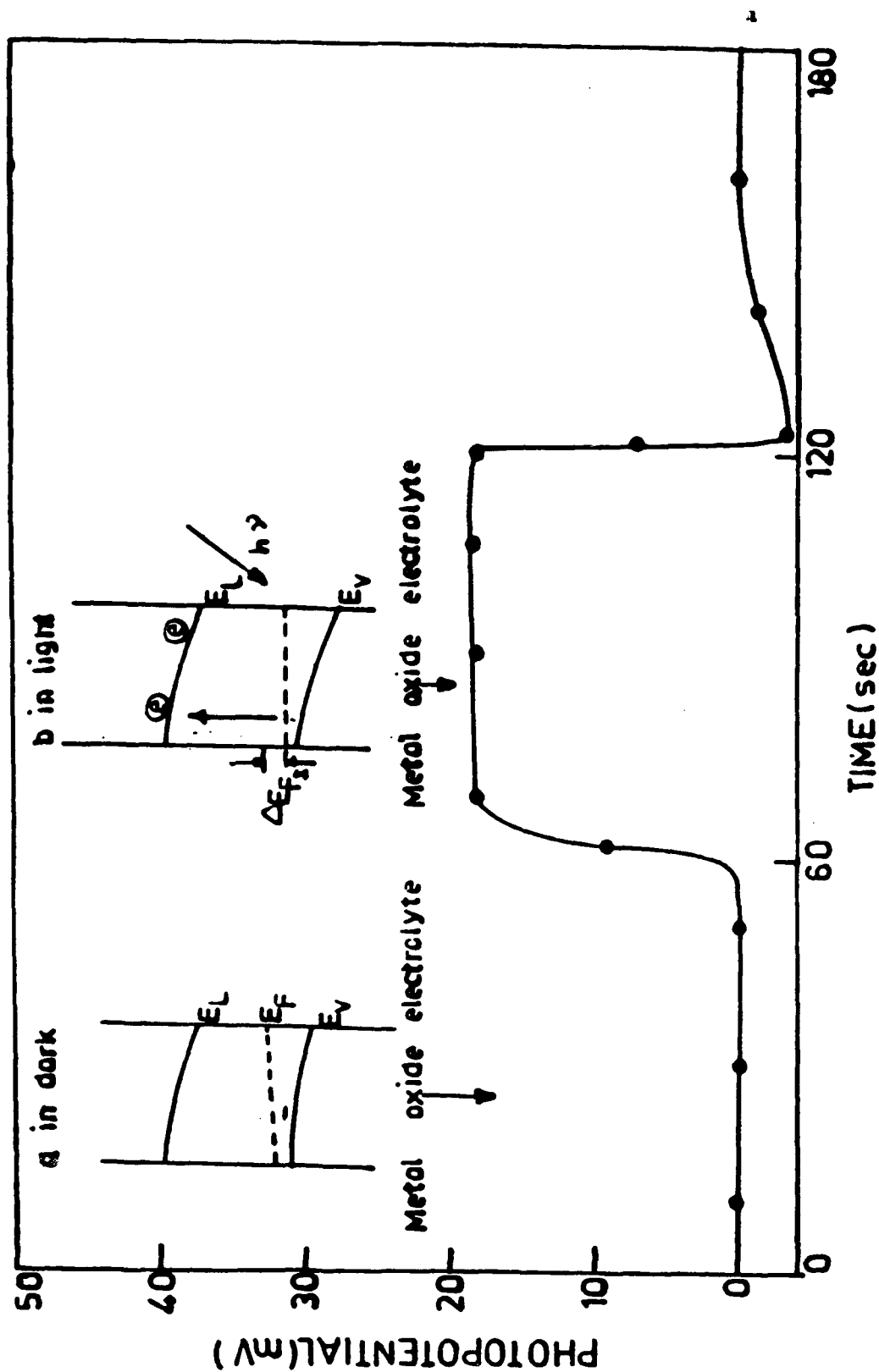


Fig.1 : Photopotential for copper in 0.1M NaOH after 60th min.

(a) Energetic situation in dark

(b) Energetic situation on illumination

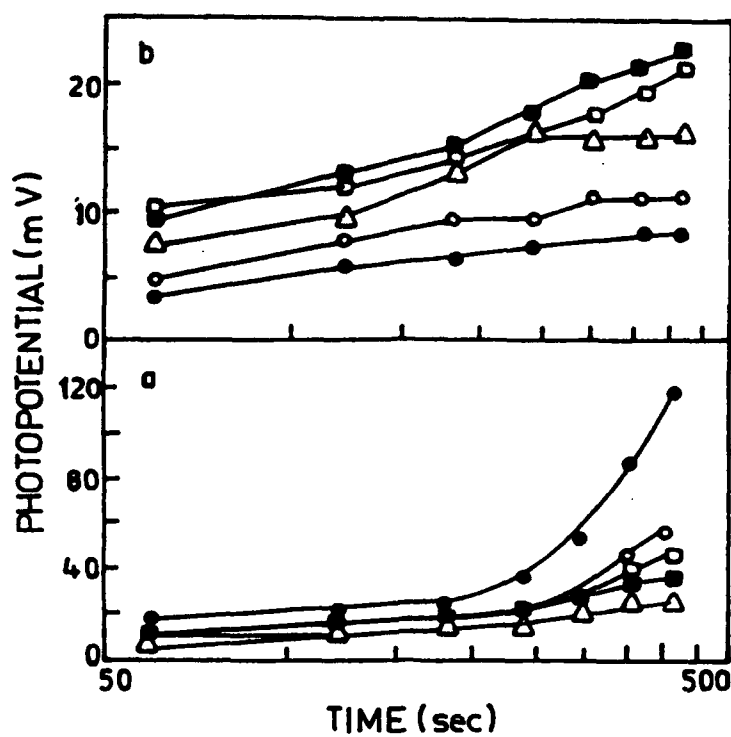


Fig.2 : Effect of Halide ions on the photopotential for (a) Copper and (b) brass in 0.1M NaOH

● Blank ○ 100Cl △ 100Br  
□ 100F ■ 100I

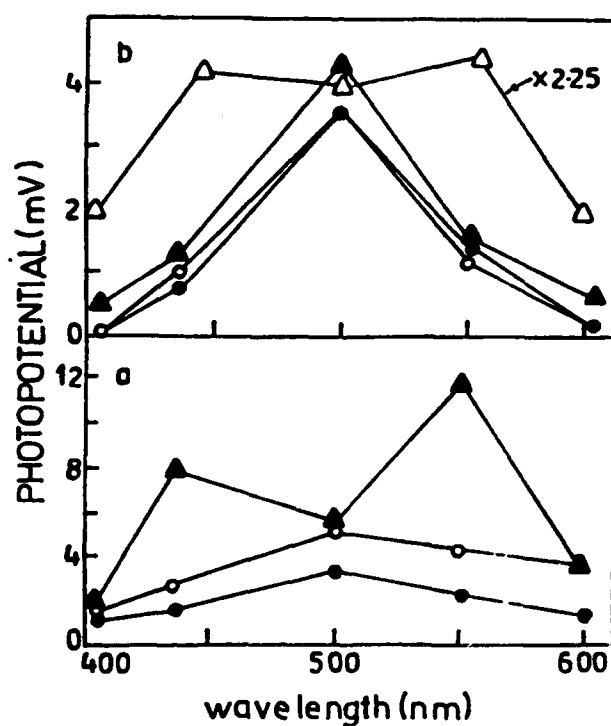


Fig.3 : Wavelength spectrum of photopotential for (a) Copper and (b) Brass on 0.1M NaOH

● 3rd hr ○ 5th hr ▲ 7th hr  
△ 24th hr

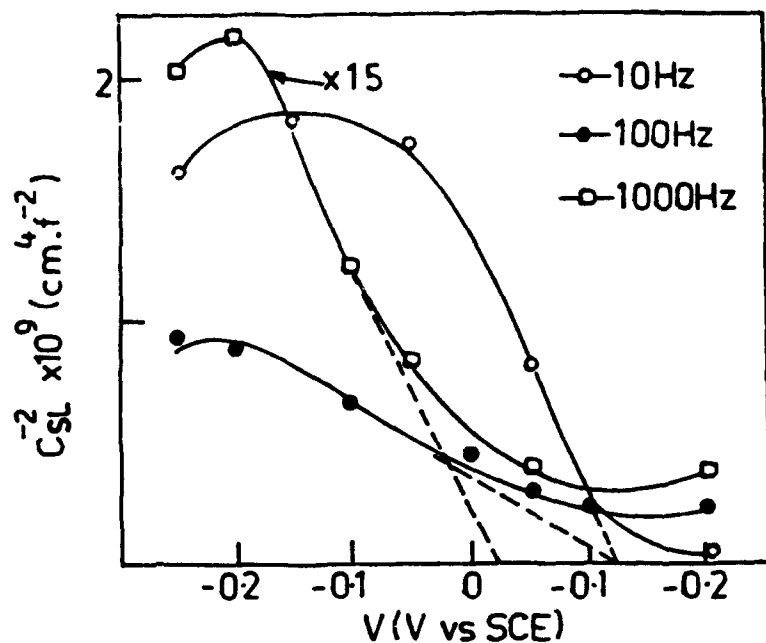


Fig (4) : Mott-Schottky plot for copper in 0.1M NaOH

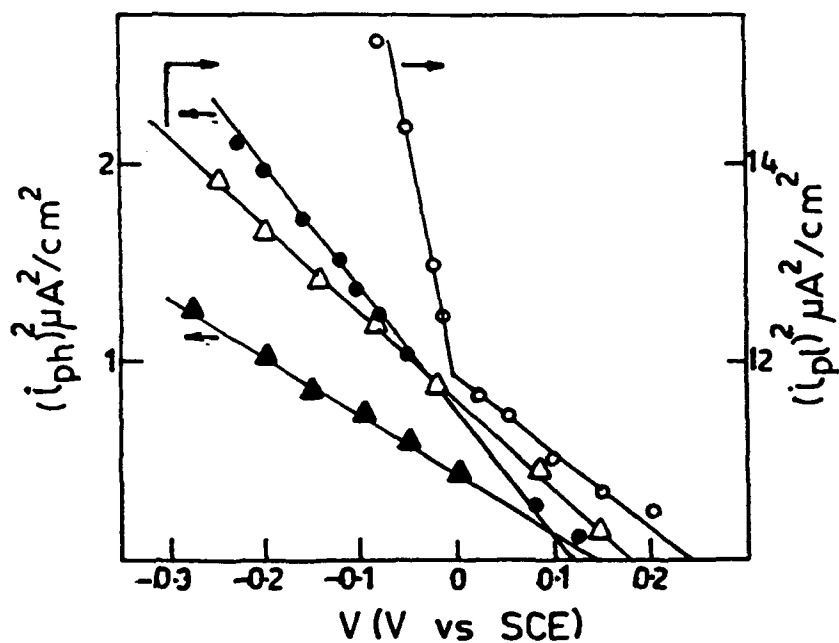


Fig.5 : Plots of  $i_{ph}^2$  vs.  $V$  for copper and brass in 0.1M NaOH.

- |                  |                 |
|------------------|-----------------|
| ● Copper, 1st hr | ▲ Brass, 1st hr |
| ○ Copper, 7th hr | △ Brass, 7th hr |

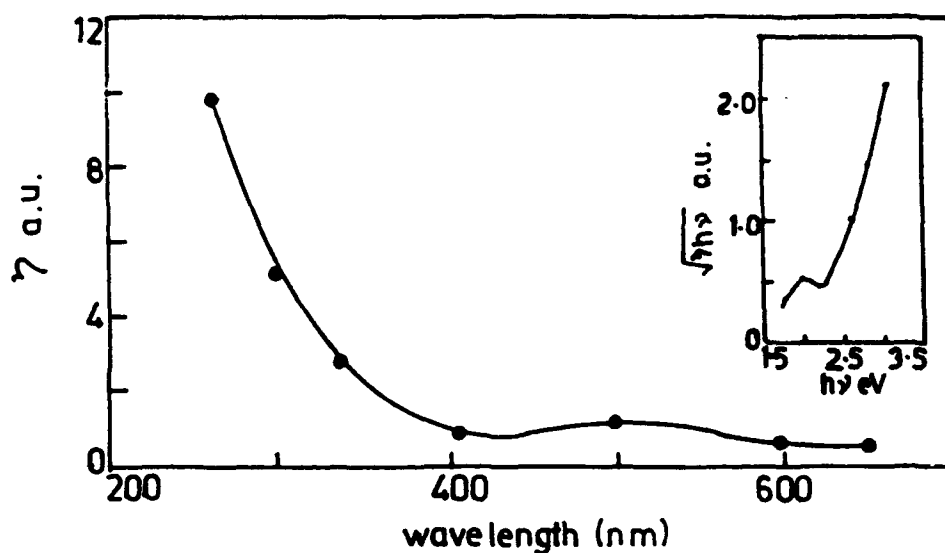


Fig.6 : Relative quantum yield ( $\eta$ ) in dependence on the wavelength for Copper in 0.1M NaOH

(a)  $(\eta h\nu)^{1/2}$  vs.  $h\nu$  plot for copper in 0.1M NaOH

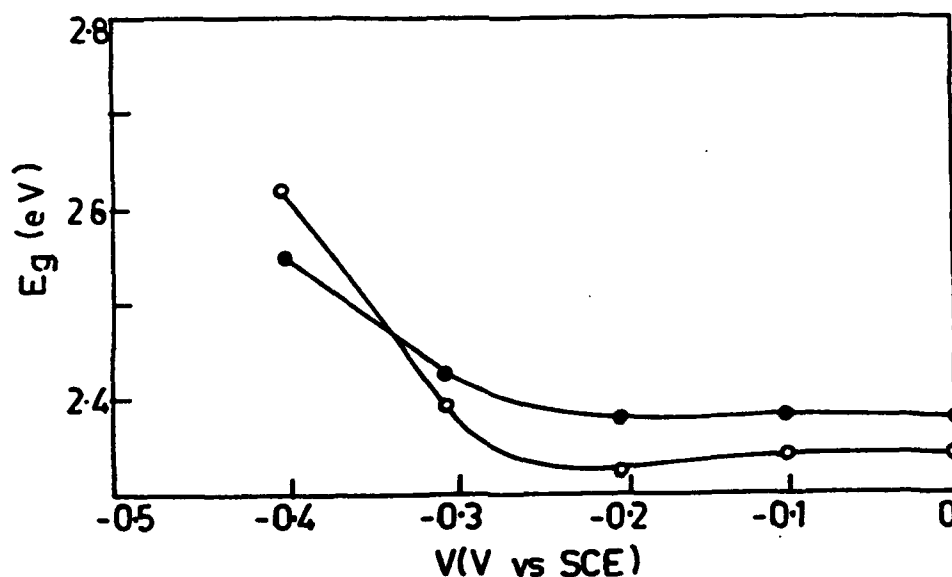


Fig.7 : Dependence of Band gap energy  $E_g$  on the applied potential for copper and brass in 0.1M NaOH

○ Copper

● Brass

(iv)

## 212. The Ion-Exchange Behaviour of the Corrodible Metal Surfaces

A.P. Nazarov,  
Physical Chemistry Institute,  
Russian Academy of Sciences  
31, Leninsky pr., Moscow,  
117915, Russia.

M.A. Petrunin,  
Physical Chemistry Institute,  
Russian Academy of Sciences  
31, Leninsky pr., Moscow,  
117915, Russia.

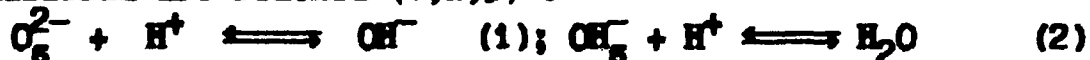
### Abstract

The ion-exchange properties of metal oxide-hydroxide films were reviewed. The cation- and anion-exchangers on the basis of silane modified metal /metal oxides surfaces were formed. The electrochemical and corrosive behaviour of the aluminum, magnesium and carbon steel surfaces with grafted ion-exchanged silanes/siloxanes layers was investigated. A considerable influence of surface siloxane charged layers on the processes of pitting formation was found. The mechanism of local corrosion in terms of interfacial electrostatic interactions is proposed. For the inhibition of local metal failure the formation of negatively charged, cation-exchanged and hydrolytic stable phases is needed.

Key terms: ion-exchangers, silanes, inhibition, pitting corrosion, surface charge.

### Introduction

Metal corrosion in aqueous electrolytes is accompanied by formation of surface hydrated oxide or hydroxide films. The properties of such surface phases with reference to the content of ions in the electrolytes often determine the kinetics of corrosion processes. Particularly, ion-selective and sorption properties of passive films in the presence of ion-activators may be assumed to determine the local corrosion rate of metals. The transfer of  $\text{Cl}^-$  ions through the membrane from iron or nickel hydroxides is determined by the sign of the membrane surface charge [1]. The presence of the negatively charged surface prevents the transfer of  $\text{Cl}^-$  through the membrane (the membrane is of cation-selective type) [2]. Anion-selective properties of surface films accelerate metal corrosion [1] as a result of the transfer of corrosion ion-activators to the metal surface. On the surface of oxide-hydroxide films a number of acid-base and ion-exchange equilibria are reached (1,2,3) :



Selectivity of oxide-hydroxide membranes to different ionic



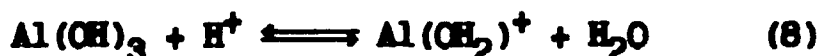
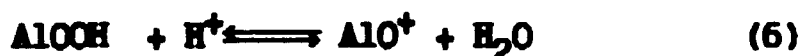
forms in solution is defined by the value and sign of Donnan's potential (4), arising in the interface oxide (hydroxide)-electrolyte. In the case of one ionic form the potential is equal to :

$$\phi_D = \frac{RT}{z_i F} \ln \frac{a_i^{aq}}{a_i^s} \quad (4)$$

where  $z_i$   $a_i^{aq}$   $a_i^s$  is valence, activities of the ion in the electrolyte phase and adsorbed state. If several ionic forms are involved in equilibria (1,2,3), it is necessary that electrical neutrality of the film be preserved :

$$z^+ a_i^+ + z^- a_i^- + wx^- = 0 \quad (5),$$

where  $w$  and  $x$  is the sing and concentration of the fixed charged in the film (membrane). At the interface the following ionic equilibria are possible :



Equilibria (6) and (8) exist mainly in an acid medium where the surface hydrated oxide is an ion-exchanged and (7), (9) exist in an alkali electrolyte, where cation-exchange properties are manifested [3]. Magnesium and iron hydroxides exhibit mainly anion-exchange properties [4]. The equality of positive and negative charges of the fixed groups of the ion-exchanger corresponds to the isoelectrical point of the surface (IEPS). The measurements of electrokinetic potential of aluminum with oxide films of different thickness showed, that in sulphate-containing electrolytes electrokinetic potential equal zero at pH 9.4 [5]. In  $Cl^-$  - containing electrolytes the isoelectrical point of the surface was not reached even at pH > 10. According to the data in [3] the magnesium oxide  $MgO$  has the isoelectrical point at pH  $12.4 \pm 0.3$ , for  $Mg(OH)_2$  at pH 12, for  $Fe(OH)_2$  pH  $12 \pm 0.5$  for  $Fe(OH)_3$  pH 8.5. The above values of the IEPS may indicate that in neutral and weakly alkaline media (pH < pH<sub>IEPS</sub>) oxide-hydroxide passive films on Al Fe and Mg have a positive charge (equilibria 6,8 are shifted to the right-hand side) and possess anion exchange properties. Local corrosion anion-activators can replace coordinated water in the hydroxide matrix (as a result of ion-exchange) and absorb on positive centers of the surface :



A thermodynamic consideration [6] of the adsorption process of different anions (salicilate, chloride, acetate) showed that adsorption occurs in the first place on positively charged

centers of aluminum oxide (eq. 10). The aluminum oxide at  $\text{pH} < \text{pH}_{\text{IEPS}}$  is a weakly alkaline anion exchanger and may be used for chromatographic separation of anions [7]. The row of relative selectivity of the anions on  $\text{Al}_2\text{O}_3$  (pH 5-6 [3]) is:  $\text{OH}^- > \text{PO}_4^{3-} > \text{C}_2\text{O}_4^{2-} > \text{F}^- > \text{SO}_4^{2-} > \text{HCO}_3^- > \text{I}^-; \text{Br}^- > \text{Cl}^- > \text{ClO}_4^- > \text{CH}_3\text{COO}^- > \text{S}^{2-}$ . As shown, selectivity is determined by formation of the most thermodynamically stable and sparingly soluble compounds with  $\text{Al}^{3+}$ . The most active depassivators of aluminum ( $\text{Br}^-$ ,  $\text{Cl}^-$ ,  $\text{ClO}_4^-$ ,  $\text{CH}_3\text{COO}^-$ ) are situated at the end of the selectivity row and have the lowest sorption ability and chemical affinity to the oxide surface. The anions situated at the beginning of the row have an inhibit effect by reference to pitting corrosion Al. According to data [8] on the kinetics of migration of ions of various nature through ion-exchange membranes it may be suggested that mobility of  $\text{L}^-$  is determined by their chemical interaction with fixed ion exchange groups of the oxide matrix. As a result, the anions forming the most thermodynamically stable (complex or sparingly soluble) compounds with the  $\text{Al}^{3+}$  cation have the lowest penetration rate (the highest super voltage) through the oxide-hydroxide membrane  $\text{Al}_2\text{O}_3/\text{Al}(\text{OH})_3$ . The increase in the affinity of the anion to the oxide matrix with the formation of the compounds  $=\text{Al}^+\text{L}^-$  may decrease adsorption and the migration flow of the  $\text{Cl}^-$  anion to the interface  $\text{Me}/\text{MeO}_n$ .

Formation of salt and foreign hydroxide films on the surface of metals (phosphate, oxalate, silicate, chromium hydroxide) change the surface properties of the main metal and are capable of decreasing its tendency to local types of corrosion. Therefore, it is of interest to consider the effect of surface phases on the tendency of metals to depassivation.

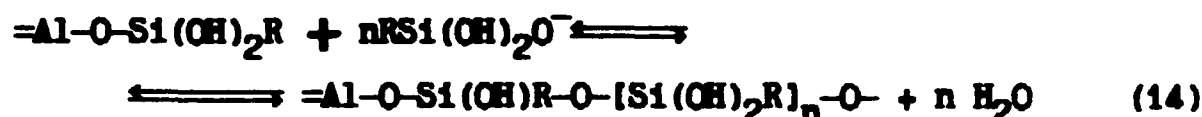
#### Experimental procedure

Aluminum A999, magnesium MG-90, carbon steel St3 were used. The adsorption measurements were made using piezo-quartz micro weighing according to technique [9]. In the vacuum system aluminum was deposited by thermal spraying on the piezo-quartz transducer. The "true" surface area of freshly deposited aluminum was determined by the BET technique using n-octane. Adsorption of silanes on Al was determined in vacuum from the vapor phase and aqueous solutions. The structure and composition of the silanes used are given in Table 1. The corrosion behaviour of modified Al surfaces by piezoquartz microbalance technique and of Mg surfaces by hydrogen realizing method were studied. Electrochemical experiments were made by the potentiodynamic method with the potential sweep speed 0.2 mV/sec. The potential values are given relatively normal hydrogen electrode.

#### Results and Discussion

We have studied the electrochemical behavior of Al, Mg and St3,

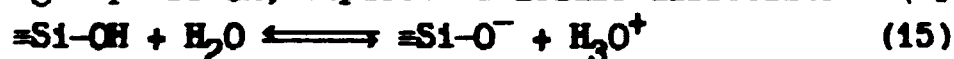
whose surface is modified by silanes [10]. Adsorption of silanes was carried out from aqueous solutions, where silanes are hydrolyzed to silanols  $(\text{OH})_3\text{SiR}$ . Silanols show great surface activity. The vinyltriethoxysilane (VS)  $\text{CH}_2=\text{CHSi}(\text{OC}_2\text{H}_5)_3$  is adsorbed of about 1-2 monolayers at the concentration of solution in water  $5 \cdot 10^{-8} \text{ M}$ . It is observed at  $[\text{VS}] = 0.1 \text{ M}$  a 90-100 Å thick layer of siloxane is formed on the aluminum surface. Aminosilanol  $(\text{OH})_3\text{Si}(\text{CH}_2)_3\text{NH}_2$  (APS) is irreversibly adsorbed to form a 80-100 Å thick siloxane polymer. Adsorption may be described by equations:



The adsorbate consists of siloxane oligomers with the Si-O-Si bonds. About 30% of the silanol groups Si-OH do not enter into the reaction of polycondensation (14) and remain free [10]. The electrochemical behavior of metal surfaces with previously adsorbed siloxane oligomers was considered. It was shown earlier [14] that the tendency of Mg, Al, Sn to local corrosion become less during modification with VS and metals corrosion was activated during modification with APS in the presence of  $\text{Cl}^-$  ions. Adsorption of VS on Al leads to the ennobling of the critical pitting potential ( $\Delta E_{\text{pt}}$ ) by 250 mV.

Fig 1 shows the effect of different amounts of the adsorbate on the anodic behavior of Al in 0.1 M NaCl. Adsorption of 1 monolayer VS from vapor (curve 2) and about 2 monolayers during modification from  $5.7 \cdot 10^{-8} \text{ M}$  aqueous solution (curve 3) leads to an increase in anodic polarization of the electrode. Increasing the VS concentration in the aqueous solution (up to  $2.8 \cdot 10^{-4} \text{ M}$ ) and the amount of the adsorbate on the surface leads to a greater ennobling of  $E_{\text{pt}}$  (curves 4,5). The inhibit effect may be assumed to be due only to the uniformly adsorbed layer of the siloxane oligomer composed of 3-4 monolayers, whose filling leads to a proportional ennobling of  $E_{\text{pt}}$ .

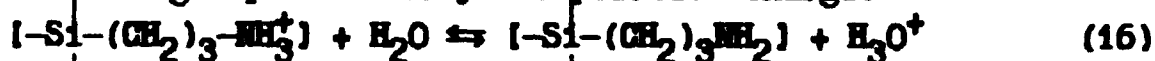
We considered the effect of the electrolyte acidity on the properties of surface siloxane compounds after silane adsorption on Al (from 0.1 M aqueous solution of VS). The electrolyte pH was increased from 3.6 to 10.2. If the changing of pH of the background electrolyte has a little effect on anodic dissolution of aluminum ( $E_{\text{pt}} = -0.4 \text{ V}$ ), the presence of the siloxane polymer leads to the  $E_{\text{pt}}$  ennobling when pH is increased (Fig.2). The greatest increase in  $E_{\text{pt}}$  occurs in passing from a neutral medium to an alkaline one. As it was mentioned above, siloxane oligomers contain about 30% of the silanol groups Si-OH, capable of acidic dissociation (15):



$pK_a$  of Si-OH is more than 8. Thus, changing pH of the electrolyte may lead to the charging of the siloxane layer with formation of fixed negative charges (equilibrium 15) as a result of acidic dissociation of the silanol groups Si-OH in the matrix of the siloxane polymer. This will decrease adsorption and migration of negatively charged  $Cl^-$  ions due to the effect of electrostatic forces.

Trimethylsilanol  $(OH)_3SiOH$  during adsorption from the aqueous phase does not form the siloxane polymer and does not exhibit inhibiting properties (Fig 1, curve 6) with respect to the Al and Mg depassivation process.

The change in the surface charge (to the positive sign) by means of adsorption of silanes could have been expected to lead to easier metal depassivation. Positive charging of the metal surface is observed during preliminary adsorption of amino silanes. According to [12]  $pK_a$  of the amino group in  $(OH)_3Si(CH_2)_3NH_3^+$  is close to 10.2. This means that at  $pH < pK_a$  the amino group will carry the positive charge.



The presence of the positively charged amino groups in the siloxane matrix leads to an increase in the tendency of metals to depassivation. Modification of the aluminum surface with APS is caused to decrease  $E_{pt}$  by 80 mV with respect to  $E_{pt}$  values of the samples without modification in 0.1 M NaCl and by 110 mV in 0.01 M NaCl (pH 6.1) (Fig.3). Increasing of pH electrolyte up to 10.2 leads to a decrease in the activating effect of APS amino groups due to the shift of acid equilibrium (16) to the right-hand side.

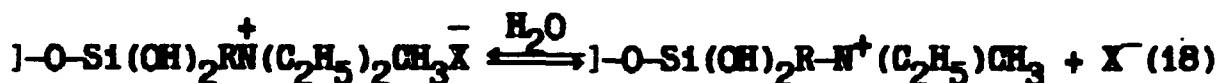
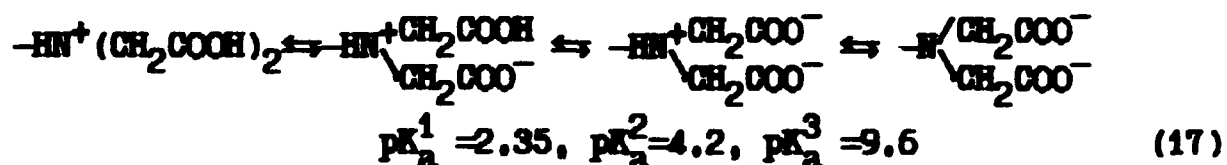
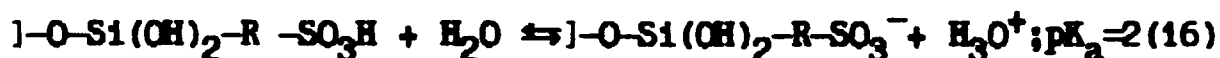
Preliminary adsorption of VS on Mg entirely suppresses corrosion in 0.1 M NaCl (pH 9.1), which leads to a decrease in the corrosion rate by 100 times [10]. If modification of the Mg surface with VS prevents depassivation, then APS initially activates (pH 9.1) and increases the corrosion rate and later amino siloxane oligomers exhibit inhibit properties (pH 10.4) (Fig. 4).

In the 0.1 M NaCl (pH 4) grafted vinylsiloxane oligomers on St3 do not have a marked effect on the anodic behavior of steel (equilibrium (15) is shifted to the left-hand side) (Fig. 5, curve 2). Under these conditions amino siloxane has a marked activating effect on the rate of anodic dissolution of steel ( $i_a$  increases thirty fold) (Fig. 5, curve 3) as a result of the presence of the positively charged amino groups in the siloxane matrix. The change in pH up to 11.5 leads to a large inhibiting effect of VS ( $i_a$  decreases fifty fold) (Fig. 5, curve 2'), moreover amino silane (pH 11.5) not inhibits dissolution of steel markedly (Fig. 5, curve 3'). The increase in the stability of the passive state during adsorption of VS was also observed in sulphate-containing electrolytes [11].

Based on the above reported data it may be suggested that the

effect of grafted siloxane compounds on the process of  $\text{Cl}^-$  adsorption has ion-exchange character. In the case of silanols  $\text{RSi}(\text{OH})_3$ , having the silanol groups  $\equiv\text{Si}-\text{OH}$  capable of acidic dissociation with the formation of  $\equiv\text{Si}-\text{O}^-$  ions, siloxane with properties of a cation exchanger of weakly acid type, which prevents of the sorption of  $\text{Cl}^-$  is formed on the surface. The presence in this layer of positively charged amino groups (weakly alkaline ion-exchanger) increases anion exchange properties of the metal surface and contributes to adsorption of  $\text{Cl}^-$ . In the latter case, due to a different selectivity of the amino-groups  $\equiv\text{Si}-(\text{CH}_2)_3-\text{NH}_3^+$  to anions of different types (in the presence of several types of anions in the electrolyte) the sorption ability of the ion-exchanger with respect to  $\text{Cl}^-$  ions may change. Thus, amino-containing ion-exchange resins have greater selectivity to  $\text{SO}_4^{2-}$  than to  $\text{Cl}^-$  [12]. Introducing  $\text{SO}_4^{2-}$  ions to the chloride-containing electrolyte leads to the change in the activating effect of amino siloxane oligomers with respect to aluminum depassivation by  $\text{Cl}^-$  ions on inhibiting effect. If the 0.01 M NaCl - 0.1 M  $\text{Na}_2\text{SO}_4$  electrolyte aluminum shows the properties of a nonpolarizable anode, then the surface modification by amino silanes lead to the electrode passivation (Fig.3). The prevailing adsorption of  $\text{SO}_4^{2-}$  on amino ion-exchange centers leads to a decrease in anion exchange properties of the surface with respect to  $\text{Cl}^-$ , which is the ion-depassivator of Al.

Based on suggested mechanism we are modified surfaces of aluminum and magnesium by monolayers of silanes with ionogenic groups in organic radicals. The charge of the silane molecules was changed by opening the oxyrane cycle in GPS to form sulphate-, iminodiacetate- and quarternary ammonium groups. The charge of the modified surface may be assumed to be determined by the following equilibria:



where  $\text{R} = (\text{CH}_2)_3-\text{O}-\text{CH}_2\text{CH}(\text{OH})\text{CH}_2$ ;  $\text{X} = \text{Cl}, \text{I}$

At the  $\text{pH} > 2$  grafted sulphate containing silane (SUL) has a negatively charged group. The negative charging of the metal surface upon modification by monolayer of sulphosilane leads to an increase in  $E_{\text{pt}}$  with regard to aluminum modified by non charged GPS (Fig 6). The sulphogroups grafted on the magnesium surface decreased appreciably (in 20 times) the hydrogen

release during corrosion in the 0.1 M NaCl (Fig. 7). The increase in aluminum resistance to pitting formation in the presence of  $\text{Cl}^-$  was also observed upon modification by one monolayer of iminodiacetate-silane. IDA undergoes a number of changes when pH is increased. In a neutral medium it carry one negative charge and in a weakly alkaline medium two negative charges. Increasing pH shifted equilibrium (17) to the side of formation of acetate forms of IDA, which increased the potential of pitting formation. The most appreciable increase in  $E_{pt}$  was observed in passing from the neutral to the weakly alkaline region as a result of the acid dissociation of the nitrogen coordinated proton by IDA (Fig. 8).

We also studied the possibility of the positive charging of the metal surface by silane monolayer, containing quarternary ammonium (TA) group. The modification of aluminum by TA decreased the pitting potential by 110 mV (Fig. 8). The introducing into the GPS molecule of quarternary ammonium group increased the corrosion rate of magnesium in the 0.1 M NaCl with respect to the electrodes modified by GPS (Fig. 7). Moreover, the rate of the hydrogen release was close or somewhat higher than that for pure magnesium. The latter may point to an increase in the adsorption ability of the modified surface with regard to  $\text{Cl}^-$  ions.

In 0.001 M NaCl unmodified Al undergo a pitting corrosion with marked weight loss (Fig. 9 curve 1). This data was obtained by the piezoquartz microweighing. The negative charged silane layer decreases of  $\text{Cl}^-$  adsorption at the interface. The modification of surface by 1 monolayer of IDC (negative charge in organic radical) lead to inhibition of corrosion (curve 2). The positive charging of the surface by adsorption of TA with positive charged ammonium group lead to the increase of corrosion rate of metal (curve 3).

We considered the effect of the adsorption of siloxane oligomers on the structure of the double electric layer. The surfaces of Al, Mg and Fe having hydrated oxide films are charged positively in neutral and weakly alkaline electrolytes ( $\text{pH} < \text{pH}_{IEPS}$ ). Under these conditions the surface has the

properties of weakly alkaline ion-exchangers and is capable of adsorbing the electrolyte anions. During competing adsorption on anion-exchange centers  $\text{M}-\text{OH}_2^+$  it is likely to substitute  $\text{Cl}^-$

depassivator anion by inhibitor ion, having greater selectivity with respect to the above centers is possible. Surface modification by one monolayer of SUL, IDA, TA or several monolayers of siloxane oligomers VS, APS having hydrolysis stable  $\text{Me}-\text{O}-\text{Si}$  bonds can change the charge and ion exchange properties of the surface. The presence of negatively charged groups changes the sign of the surface charge from the positive to negative one. The latter leads to a decrease of the surface concentration of  $\text{Cl}^-$  (equation 19):

$$a_{\text{Cl}^-}^S = a_{\text{Cl}^-} \exp(-zF\phi^s/RT) \quad (19)$$

$$E_{pt} = E_{Al/AlCl_3}^0 - \frac{RT}{F} \ln a_{Cl^-}^s + \eta_{Al} \quad (20)$$

The increase in the positive charge in the presence of protonated amino- or quaternary ammonium groups leads to an increase in the sorption properties on the surface. The value of the surface concentration  $a_{Cl^-}^s$  enters into equation (20) [13] for the pitting potential  $E_{pt}$  and affect it. The value of pitting supervoltage  $\eta_{Al}$  may be assumed to include the abrupt change in the potential in the interface hydroxide - electrolyte which depends on the structure of the double electric layer. The presence of the negative abrupt change in the potential (as a result of the recharging of the surface) will decrease the flow of anion depassivators to the metal surface (increase overvoltage  $\eta_{Al}$ ) due to electrostatic reason. The consideration of the effect of the metal surface charge on the process of pitting formation shows (Fig.9), that for depassivation to be inhibited it is necessary to produce hydrolytic stable phases carrying the negative charge and possessing cation exchange properties.

#### References

1. N.Sato, Corrosion, 45 (1989): p.354.
2. M.Sakashita, N.Sato, Corrosion, 35 18 (1979): p.351.
3. M.J.Fuller, Chromatogr. Rev., 14 (1971): p.45.
4. M.Abe, T.Ito, J.Chem.Soc Jap., 86 (1965): p.817.
5. V.C.P.Macropulus, H.C.Parrieira, Corros.Sci., 7 (1967): p.254.
6. E.Thomas et.al., Colloids and Surfaces., 37 (1989): p.269.
7. R.M. Chioz et. al., J.Chromatogr., 32 (1986): p.359.
8. V.A.Shaposhnik, The Kinetic of a electrolisys, (Nauka, 1989), p.123. (rus.)
9. A.P. Nazarov, Petrunin M.A., Yu.N. Mikhailovski, Zashita metallov, 29 (1993) in press (rus.)
10. A.P. Nazarov, M.A.Petrunin, Yu.N. Mikhailovski, Zashita metallov, 28 4 (1992): p. 976. (rus.)
11. Nazarov A.P., Petrunin M.A., Mikhailovsky Yu.N., "The role of the adsorption of silane coupling agents in the interfacial interactions metal-polymer coatings", 11<sup>th</sup> INT. COR. CON., (Florence, Italy, 1990) V.1, p.225.
12. L.Liberty et.al., Reactive Polymers, 2 (1984): p.111.
13. M. Baumgartner, H. Kaesche, Werkstoffe und Korrosion (1991): p.58

Table 1. The structure formulae of the used silanes.

Name	Chemical formula
MS	$(\text{CH}_3)_3\text{Si}(\text{OC}_2\text{H}_5)$
VS	$\text{CH}_2=\text{CH}-\text{Si}(\text{OC}_2\text{H}_5)_3$
GPS	$\text{CH}_2-\text{CH}(\text{O})-\text{CH}_2-\text{O}-(\text{CH}_2)_3\text{Si}(\text{OC}_2\text{H}_5)_3$
APS	$\text{NH}_2-(\text{CH}_2)_3-\text{Si}(\text{OC}_2\text{H}_5)_3$
SUL	$\text{Na}^+[\text{SO}_3\text{CH}_2-\text{CH}(\text{O})-\text{CH}_2-\text{O}-(\text{CH}_2)_3\text{Si}(\text{OC}_2\text{H}_5)_3]^-$
IDC	$\text{Na}^{2+}[(\text{CH}_2\text{COO})_2\text{NCH}_2-\text{CH}(\text{OH})-\text{CH}_2-\text{O}-(\text{CH}_2)_3\text{Si}(\text{OC}_2\text{H}_5)_3]^{2-}$
TA	$\text{J}^-[ (\text{C}_2\text{H}_5)_3\text{N}^+\text{CH}_2-\text{CH}(\text{OH})-\text{CH}_2-\text{O}-(\text{CH}_2)_3\text{Si}(\text{OC}_2\text{H}_5)_3 ]$



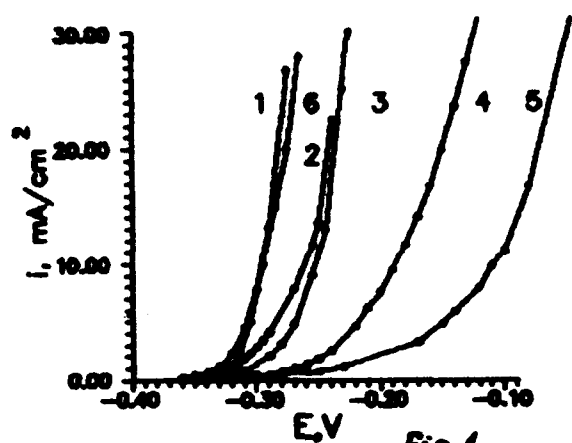


Fig. 1

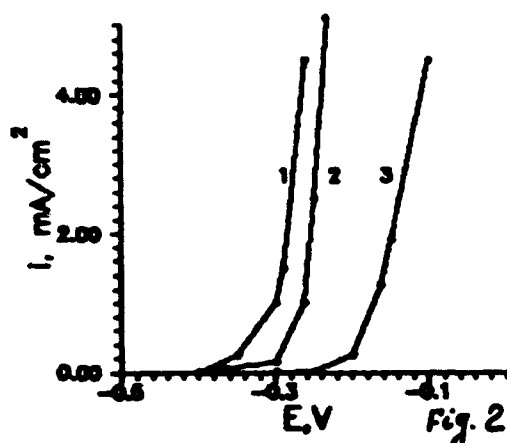


Fig. 2

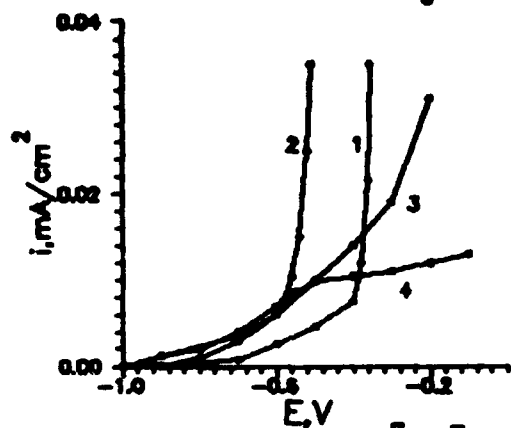


Fig. 3

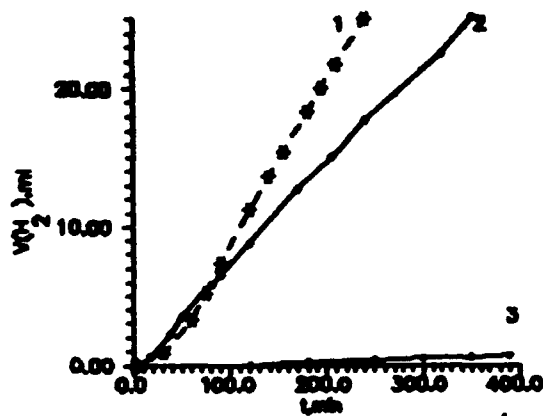


Fig. 4

Fig. 1. Anodic polarization curves of Al (1) in 0.1M NaCl (pH 10.2) Electrodes are modified :2- VS deposited from vapor (1 monolayer), 3.- VS deposited from water solution  $[VS]=5.7 \cdot 10^{-4} M$ , 4-  $[VS]=4.28 \cdot 10^{-4} M$ , 5-  $[VS]=2.8 \cdot 10^{-4} M$ , 6- MS deposited from water solution  $[MS]=0.1 M$ .

Fig. 2. Anodic polarization curves of Al in 0.1M NaCl for different pH of electrolyte : 1.- pH 3; 2.- pH 6.3; 3.- pH 10.2. Electrodes are modified by VS.

Fig. 3. Anodic polarization curves of Al after modification by APS (2,4) and nonmodified (1,3) in 0.01M NaCl pH 6.1 (1,2) and in 0.01 M NaCl + 0.1 M  $Na_2SO_4$  (3,4) pH 6.1.

Fig. 4. Kinetic of hydrogen evolution on Mg in 0.1 M NaCl pH 9.1. Electrodes are modified by silanes 1.- Al; 2.- APS; 3.-VS.

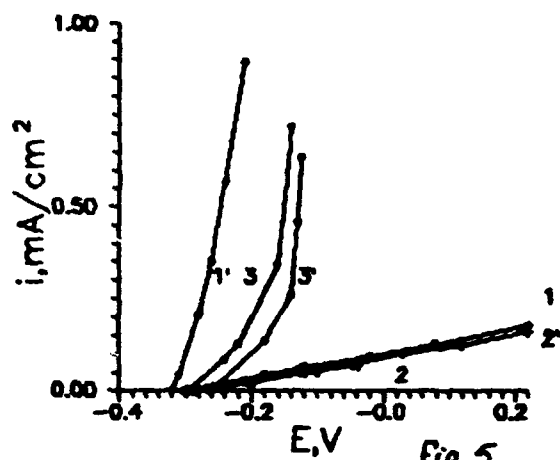


Fig. 5

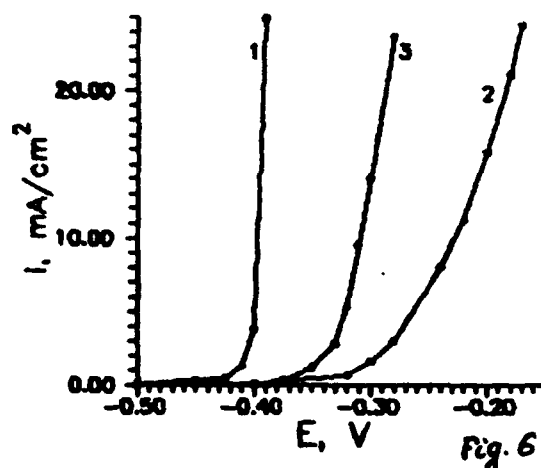


Fig. 6

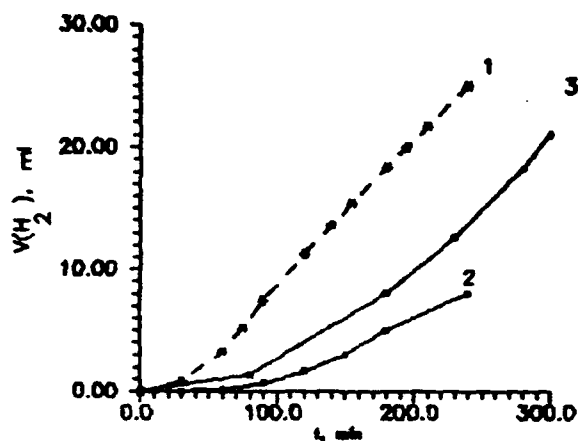


Fig. 7

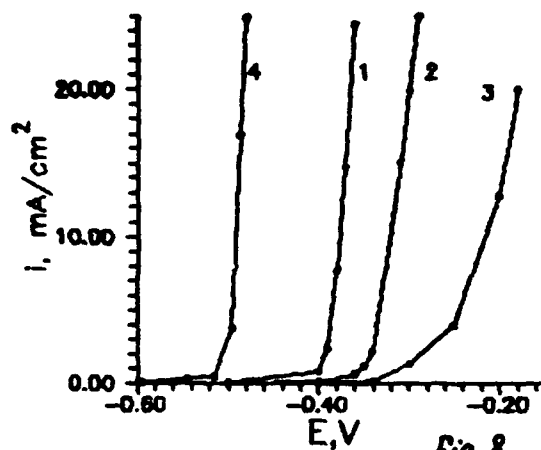


Fig. 8

Fig. 5. Anodic polarization curves of carbon steel (1,1') in NaCl pH 4 (1,2,3) and pH 11.5 (1',2',3') after modification by silanes : VS (2,2') and APS (3,3').

Fig. 6. Anodic polarization curves of Al (1) modified by SUL - 2 and GPS - 3; 0.1M NaCl, pH 6.3.

Fig. 7. Kinetic of hydrogen evolution on Mg in 0.1 M NaCl pH 10.2. Electrodes are modified by silanes 1.- Mg; 2.- sulphosilane; 3.- GPS.

Fig. 8. Anodic polarization curves of Al modified IDC in 0.1M NaCl for different pH of electrolyte : 1.- pH 3; 2.- pH 6.3; 3.- pH 10.2; and Al modified by TA (4), pH 6.1.

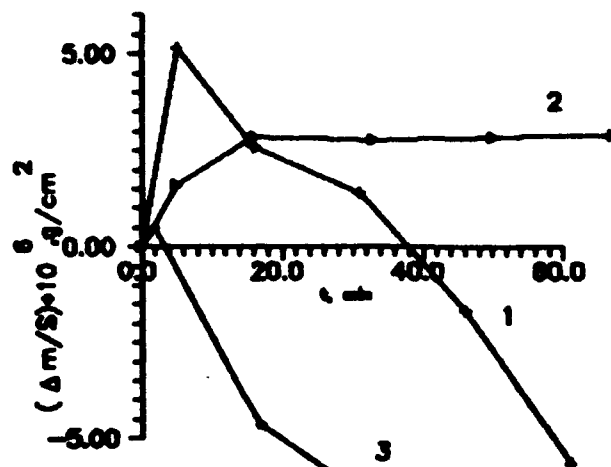


Fig. 9

Fig. 9. Corrosion of Al (1) modified by silanes (1 monolayer)  
1.- Al; 2.- IDC; 3.- TA, 0.001 NaCl, pH 6.

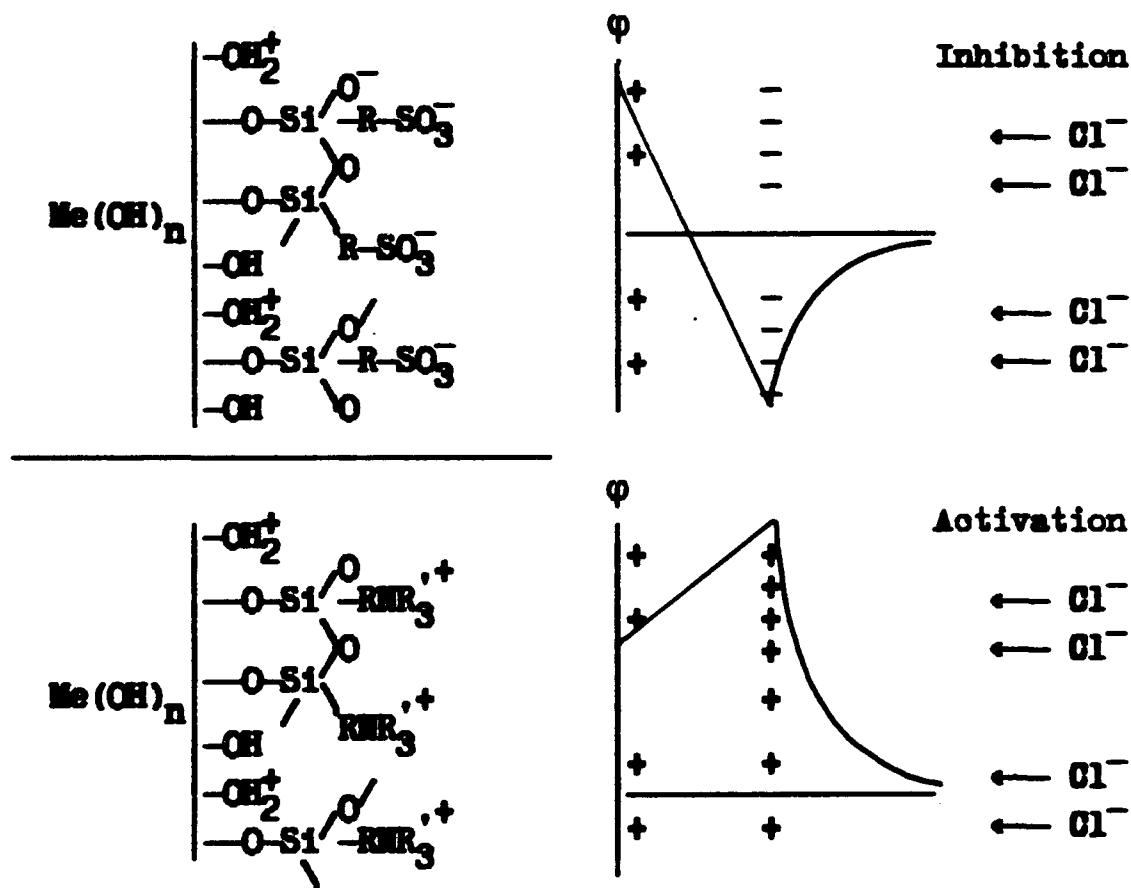


Fig. 10 The scheme of the metal-silane-electrolyte interfaces

## **Nonequilibrium Alloying Studies on Passivity in Chloride Environments**

**E. L. Principe, B. A. Shaw, C. A. Pecile, A. S. Iyengar  
The Pennsylvania State University  
University Park, Pa., 16802**

**G. D. Davis, B. J. Rees  
Martin Marietta Laboratories  
Baltimore, Md. 21227**

### **Abstract**

Results are reported on the electrochemical behavior and film chemistry of nonequilibrium thin film Al-Ta alloys. Studies were conducted at pH 2, 8, and 12 under deaerated conditions in an aqueous 0.1M NaCl environment. Surface analysis of the evolution of the film chemistry as a function of overpotential was performed. Previously, the enhanced passivity of Al-W thin-film alloys in chloride containing environments has been explained by introducing the solute-rich interphase model (SRIM). The SRIM model describes enhanced passive behavior as the result of a rate controlling dissolution process conferred by a layer of enriched solute metal located in an interphase between the oxide layer and the base metal alloy. Formation of the interphase is thought to be caused by preferential dissolution of the aluminum from the solid solution alloy. It is believed that the Al-Ta system is governed fundamentally by the same mechanism. The surface chemistry of the passive film in Al-Ta system is a strong function of pH, particularly in transition from near-neutral to high pH. XPS measurements show that at high pH the passive film is comprised entirely of a hydrated form of Ta oxide at all potentials, including at open circuit. At low and near-neutral pH, the relative amount and composition of Ta oxide in the film is a function of potential.

Early indications on the electrochemical behavior of vapor deposited Al-Ta and Al-W alloys appear promising. Enhanced behavior was noted despite the clear presence of physical defects in the material. The defects can be described as nodules of solute embedded into the bulk. As a result of the inhomogeneities, breakdown occurs earlier than would normally be anticipated. Essentially, this difficulty has been related to a processing parameter and future vapor deposited materials are expected to be improved with respect to the data presented here. These results are, however, significant in that they demonstrate the ability to relate knowledge derived from thin-film alloy studies to bulk materials which share similar enhanced passive behavior.

## Introduction

This research continues to develop nonequilibrium aluminum alloys and conduct mechanistic studies on the enhanced passivity of the thin-film sputter deposited materials in chloride environments. In addition, testing of bulk (or thick-film) materials produced by vapor deposition and plasma spraying has recently been undertaken. With regard to the bulk materials, efforts are concentrated on characterizing the physical and electrochemical behavior of Al-Ta and Al-W alloys. Practical benefits of this research include potential applications in aerospace structures, electronic devices, development of protective coatings with tailored physical and electrochemical properties, and advancements in the realm of aerospace metal-matrix composites.

Aside from the practical, it is rapidly becoming apparent that nonequilibrium alloys possess properties and characteristics which make them attractive for fundamental research. This seems especially true for sputter deposited thin-films. Features of these materials include: an unprecedented control in alloy composition; structures ranging from crystalline to amorphous; the capability to better control the density and type of defects; and surfaces with a mirror quality finish. It is well known that all of these factors contribute significantly to the overall behavior of materials demonstrating passivity.

This program has investigated roles that Cr, Cu, In, Mo, Nb, Si, Ta, V, W, and Y nonequilibrium alloying additions play in promoting passivity in sputter deposited thin-film Al alloys [1-10]. Several other groups have been working with supersaturated aluminum alloys produced by various methods as well [11-28]. Recent efforts in this program have concentrated on more extensive characterization of the alloys exhibiting the most promising performance, Al-W, Al-Mo, and Al-Ta. From the Pourbaix diagrams shown in figure 1, it is reasonable to anticipate that passivity for aluminum based alloys may extend to lower pH values by the addition of W and Ta. This paper will focus on the role that Ta plays in enhancing the corrosion performance of Al over a broad range of pH values.

## Experimental Procedure

### *Thin-film Production*

Thin-film specimens were produced by co-sputter deposition using a 602RS Loadlock thin film deposition system with both DC and RF magnetron sputtering.[29] Four-inch-diameter silicon wafers serve as a convenient substrate for deposition of the films. A rotating substrate holder is employed to eliminate possible concentration gradients during deposition. The films were formed at ambient temperatures (neither heating nor cooling of the stage). Solute concentrations for the alloys were determined by induction coupled plasma (ICP) and all concentrations are given in at.%. After deposition, the wafers were cleaved into smaller sections for testing.

## *Vapor Deposition*

Vapor-deposited specimens were produced by Idaho National Engineering Laboratory (INEL). A schematic of the double source high-rate physical vapor deposition system used for producing the alloys appears in Figure 2. The flux from each source was independently controlled using a Telemark model 272 electron gun to obtain the desired alloy composition. Typical vacuum levels during the deposition process ranged from  $10^{-2}$  to  $10^{-3}$  Pa. To obtain a uniform deposit, the collector plate was rotated during deposition. Pure Al, W, or Ta were used as the sources and glass, aluminum, and silicon single-crystal wafers were used as collector plates.

## *X-ray Diffraction and Microscopy*

Glancing angle x-ray diffraction (GXRD), [30] with a constant angle of  $10^\circ$  between the incident x-ray beam and the film surface, was used to check the thin-film alloys for precipitate formation. The characterization was performed on a Scintag diffractometer using a monochromatic Cu K $\alpha$  x-ray source. The glancing angle was chosen both to optimize the signal from the metal film and to prevent diffraction from the Si single crystal.

All of the specimens were examined under an optical microscope before and after testing. Several specimens were also examined using an ISI SS40 scanning electron microscope to characterize the breakdown morphology.

## *Electrochemical Experiments*

### *Vapor-Deposited Alloys*

Anodic potentiodynamic polarization experiments were performed on the vapor-deposited specimens using EG&G Princeton Applied Research potentiostats controlled by Model 352 corrosion software. The specimens were tested in a flat cell configuration (EG&G flat-cell model K0235). The solutions were open to the atmosphere and were neither aerated nor deaerated. Before polarization, the open circuit potentials were allowed to stabilize for 1 hour. Specimens were dynamically polarized at both the ASTM suggested slow scan rate of 0.2 mV/s as well as a slower scan rate of 0.05 mV/s. All potential given in this paper are versus a saturated calomel reference electrode.

### *Thin-film Alloys*

Individual electrochemical specimens were prepared by attaching a coated lead wire, and masking the back and edges of the specimens with a marine epoxy paint. Anodic potentiodynamic polarization curves were generated at a scan rate of 0.2 mV/s at ambient room temperature ( $23^\circ$  to  $27^\circ$  C). A limited number of experiments were also run at a rate of 0.05 mV/s. Experiments were conducted on duplicate specimens

(minimum) in aerated chloride solutions with pH values ranging from 2 to 12 for the Al-Ta alloys. After immersion, the open-circuit potential,  $E_{OC}$ , was allowed to stabilize for at least 1 hour prior to polarization.

### *Surface Analysis*

The chemistry of the Al-Ta passive film in pH 3 and pH 12 solutions was investigated in the as-sputtered condition, at the open circuit potential, and at various potentials up to  $E_b$ . The same specimens was polarized repeatedly until the breakdown potential was reached. Details of the procedure have been reported previously.[3,4] Changes in the surface chemistry induced by the transfer procedure and by exposure to ultrahigh vacuum have been examined and possible artifacts were shown to be either small (e.g., additional oxidation) or tractable (e.g., adventitious contamination), and differences in the measured surface chemistry were shown to originate in the electrolyte.[2,31]

The x-ray photoelectron spectroscopy (XPS) measurements were made using a Surface Science Instruments Model SSX 100-03 spectrometer with a monochromatized Al  $K\alpha$  x-ray source and a hemispherical electron energy analyzer with multichannel detection. The x-ray source was focused to a spot size of 600  $\mu\text{m}$  and the surface charge was neutralized with low-energy electrons. Binding energies were normalized to that of adventitious hydrocarbon at 284.8 eV. Survey spectra provided a qualitative analysis of the surface, whereas high-resolution spectra of the O 1s, C 1s, Al 2p, and Ta 4f photoelectron peaks were used for quantitative analysis and chemical state determination. Quantitative analysis data were obtained using peak areas and sensitivity factors determined from standards with our spectrometer. Chemical state separation was achieved by curve fitting, the details of which are presented elsewhere [3], with the Ta 4d doublet being constrained with a peak separation of 1.8 eV and an area ratio of 1.333.

## **RESULTS**

### *Material Characterization -- Vapor-Deposited Materials*

When observed under an optical microscope, the vapor-deposited alloys reveal numerous small nodules on their surfaces. The formation of these nodules from small fragments of the solute target was observed during the deposition process. It is believed that defects or impurities in the solute rod stock led to the ejection of these fragments of solute metal during electron-beam melting. These nodules are of concern for two reasons. First, depending on when the particles were ejected and whether they were subsequently coated with the alloy, their presence could establish localized galvanic couples on the surface leading to preferential dissolution of the alloy adjacent to these nodules. Second, the nodules disturb subsequent film growth, leading to misfit and incoherent morphology of the structure. Our earlier work revealed that small discontinuities in the substrate surface or small particles on the surface can have

disastrous effects on alloy growth. Figure 3 shows a cross-section of vapor-deposited alloy that contained a small particle on the surface of the collector plate. This type of defect was observed on the alloy surfaces after deposition by low-magnification optical microscopy, as shown in Figure 4. In addition to promoting formation of occluded cells, these sites may also have a negative influence on electrochemical testing as a result of direct exposure of the underlying collector plate to the test solution. Grain growth in the alloy is obviously influenced by the presence of these nodules, as Figure 5 illustrates.

X-ray diffraction of Al-W PVD alloys revealed the presence of  $WAl_{12}$  and possibly  $WAl_5$  precipitates. At this point, it is uncertain whether these precipitates are associated with the nodules or the alloy itself. Fewer and smaller precipitates which have not yet been identified were also found in the Al-Ta alloys.

## Electrochemical Experiments

### Physical Vapor-Deposited Thin-Film Alloys

Despite the fact that the alloys contained numerous defects, quite promising corrosion performance was observed. The best results were obtained for alloy an Al-2.4 percent W alloy (CD-12 no. 2), which exhibited a breakdown potential of -51 mV. This value is similar to the breakdown potentials reported earlier for our Al-1.5%W thin-film alloys. However, a replicate specimen from this same alloy showed a much lower breakdown potential of -479 mV, as shown in Figure 6. Note that the breakdown potential for pure Al is approximately -690 mV. Similar passive current densities were noted for all of the specimens. The large difference in the breakdown potential between the two replicate specimens is taken as evidence of the influence of defects (probably surface connected) within the second specimen. Differences were also noted between replicate specimens for other compositions and at the slower potentiodynamic scan rate. Figures 7 to 10 show the behavior of replicate specimens for Al-2.2% Ta (CD-13), Al-2.4% Ta (CD-16), Al-1.9%W (CD-17), and Al-3.8%W (CD-25), respectively. A comparison of the behavior of Al-W alloys to that of pure Al is presented in Figure 11. All of the alloys show enhanced passivity in comparison to pure Al with the Al-2.8%W and Al-3.8%W specimens exhibiting the highest breakdown potentials. Because of the significant scatter between replicate specimens, no conclusions could be drawn regarding the influence of collector plate material on alloy performance. However, the smoothness and cleanliness of the surface, no matter what the substrate, were found to be critical factors in the final quality of the deposit.

### Thin-film Alloys

Anodic potentiodynamic polarization was conducted on 24 Al-Ta thin-film specimens. These experiments were carried out at a variety of pH values (2, 8, and 12) and at two different scan rates (0.2 and 0.05 mV/s). Deaerated solutions were used for most of the experiments and the Ta concentration in the alloy was 2.8%.



Polarization curves for duplicate Al-2.8Ta alloys in a pH 12 chloride solution (0.1M NaCl with the pH adjusted with NaOH) generated at a scan rate of 0.2 mV/s are presented in Figure 12. Reproducible behavior was observed with both curves exhibiting similar passive current densities and corrosion potentials. A slight perturbation in the current was observed at low potentials. This may indicate that the specimen had not reached steady state conditions. The most striking feature on these curves is the high breakdown potential of approximately 800 mV. A comparison of the polarization behavior for this alloy with that of pure bulk Al and pure bulk Ta is shown in Figure 13. This comparison reveals that the Al-Ta alloy behavior is more like that of pure Ta than pure Al, suggesting that the passive film chemistry at pH 12 may be closer to that which forms on pure Ta. Indeed, XPS measurements indicate this to be the case.

Similar experiments were also conducted in a pH 2 chloride solution (0.1 M NaCl with the pH adjusted to 2). Replicate curves showed reproducible behavior; however, the behavior was quite different from that observed at the high pH. A comparison of the polarization behavior (generated at a scan rate of 0.2 mV/s) for the Al-Ta alloy with that of the pure metals in the pH 2 solution is shown in Figure 14. In this situation, the alloy curve shows little evidence of passivity. The polarization curve for the Al-Ta alloy at low pH is similar to the curve generated for pure Al.

To confirm the results described above, a series of anodic polarization curves were generated at a lower scan rate of 0.05 mV/s. A comparison of the 0.2 mV/s scan rate data with the data obtained at 0.05 mV/s and at pH 12, is presented in Figure 15. Experiments revealed a much lower breakdown potential for the alloy at the slow scan rate suggesting that the faster scan rate in this case does not reflect a condition close enough to steady state to be a true indication of the alloy behavior. In addition, the scan rate could be expected to have an effect on the formation of the enriched solute layer. One of the three curves generated for the Al-Ta alloy at a pH of 12 appears in Figure 15. Replicate curves at pH 12, generated at the slower scan rate, are presented in Figure 16. Breakdown potentials ranging from 22 mV to 397 mV and passive current densities of 1 to 2 mA/cm<sup>2</sup> were observed for these specimens. Some variation in the breakdown potential is expected due to the stochastic aspects of the pitting process. In addition, small flaws in the alloy film related to the deposition process are believed to contribute to variations in the breakdown potential for these type of alloys. The slight perturbation in current at low overpotentials, which was noted at the faster scan rate, was not observed in any of the specimens tested at the lower scan rate.

At a pH of 2, the slower scan rate data for the Al-Ta alloy actually look better than the faster scan rate data, as Figure 17 illustrates. A more defined passive region and a more distinct breakdown potential are noted at the slower scan rate.

Al-Ta alloy polarization behavior was also evaluated at the 0.05 mV/s scan rate at a pH of 8. Behavior at this pH was similar to that observed at pH 12; however, a slightly

lower breakdown potential was observed at pH 8. Figure 18 shows the polarization curves generated at pH 8 at the slower scan rate. A difference of 270 mV was noted in the breakdown potential and a variation in  $i_p$  from 0.7 to 3.7  $\mu\text{A}/\text{cm}^2$  was observed. Earlier polarization results for this alloy (without deaeration and with a scan rate of 0.2 mV/s) are also included in Table 2 and reveal  $i_p$  values similar to those observed at the faster scan rate and a tendency toward slightly lower breakdown potentials.

A comparison of the Al-Ta alloy polarization behavior as a function of pH is presented in Figure 19. Three observations can be made from these data. First, the open circuit potential increases as the pH decreases. This is expected since the potential of the hydrogen reduction reaction is potential dependent. Second, the breakdown potential increases with increasing pH and constant chloride concentration. Last, the passive current density increases with decreasing pH.

### Surface Analysis

The passive film chemistry of Al-Ta alloys depends strongly on the pH of the solution, especially in the near-neutral to basic solution range (Figure 20). As previously reported [4], in near-neutral solutions, the passive film remains thin (<10 nm) throughout the polarization sequence with the substrate being easily detected by XPS even at the breakdown potential. Considerable amounts of oxidized Ta are present open circuit potential (~20 percent of the oxidized cations); this composition remains essentially constant for the first 600 mV of polarization (Figure 21). Above this potential (corresponding to the potential at which pure aluminum pits), the oxidized Ta increases until the passive film contains nearly equal amounts of oxidized Ta and Al.

The behavior of the passive film in pH 3 solutions is generally similar. The film remains thin until the breakdown potential is reached. Although little Ta is found in the passive film at open circuit and the first polarization, its concentration increases with overpotential (Figure 21). At the breakdown potential, the passive film also contains comparable amounts of oxidized Al and Ta. Nonetheless, at the same overpotential, more oxidized Ta is found in the passive film formed at pH 3 than in that formed at pH 8.

The passive film formed in pH 12 solutions is very different. Even at the open circuit potential, the film is thicker than the information depth of XPS (~10 nm) and is composed entirely of oxidized Ta with no Al detected (Figure 21). Based on XPS quantitative analysis, the film is a hydrated form of  $\text{Ta}_2\text{O}_5$ ,  $\text{Ta}(\text{OH})_5$ . No change in the chemistry is observed during the polarization sequence.

## DISCUSSION

Several possible mechanisms for the interaction of  $\text{Cl}^-$  with the underlying metal and the relation to passivity and breakdown have been proposed. Models include electrostatic repulsion of  $\text{Cl}^-$  by oxidized solute atoms [1-3], oxidized solute barrier layer

formation [3,4], stabilization of the passive film oxide [6], blockage of  $\text{Cl}^-$  transport through the passive film [19], reduction in the level of acidification and reduced dissolution within the pit [17], and inhibition of  $\text{Cl}^-$  adsorption due to modification of the  $\text{pH}_{\text{pzc}}$  [11-15]. In addition, an extension of the point defect model (PDM), referred to as the solute vacancy interaction model (SVIM), has been proposed to explain the effects of alloying elements on the pitting behavior of certain alloys. [32,33]. To explain the enhanced passivity of Al-W alloys over a wide range of pH values despite large changes in the composition of the passive film, we have introduced the solute-rich interphase model (SRIM) [9]. The SRIM requires that the solute exhibit passivity (or, possibly immunity) in the low-pH environment of an occluded cell. Alternatively, synergistic interaction between the solute and aluminum may result in reduced dissolution and promote passivity. In this model, preferential dissolution of the more active aluminum species results in an increase in the normalized solute concentration at the metal-oxide interphase. The stability of the solute enriched layer acts to control the dissolution rate. The kinetics of dissolution through the enriched layer and stability of both the solute and Al oxide(s), are interrelated, and together determine the overall behavior of the system. Further, in the lower pH environment of a nucleating pit, formation of a solute oxide repassivates the site. If a defect in the passive film penetrates to the interphase preferential Al dissolution occurs and acidification begins. The remaining solute forms a continuous protective layer, thereby inhibiting further progress and stabilizing the occluded cell (Figure 22). Adsorption of  $\text{Cl}^-$  would also be less favored in the region according to the pH of zero charge model [11-15], due to the local reduction in the  $\text{pH}_{\text{pzc}}$ . In general, the composition of the passive film formed on the alloy and its behavior as a function of pH and potential is unique to each system but the mechanism for enhanced passive behavior is fundamentally the same.

The Pourbaix diagram for Ta also predicts passivity at low pH, suggesting that the SRIM might be applicable in the Al-Ta case as well. The evolution of the passive film chemistry indicates that this model can indeed explain the enhanced passivity of Al-Ta alloys. The pH 3 data show that  $\text{Ta}(\text{OH})_5$ , a hydrated form of oxidized Ta, is the passivating species under these conditions. As the specimen is polarized, the passive film evolves toward  $\text{Ta}(\text{OH})_5$  as this species replaces the original oxidized Al. In deaerated pH 8 solutions, the passive film initially is a mixture of partially hydrated  $\text{Al}_2\text{O}_3$  and  $\text{Ta}_2\text{O}_5$ , both of which are stable species under these conditions. Little change in the composition is noted until  $E_{\text{b}}^{\text{Al}}$  is approached and the amount of  $\text{Ta}_2\text{O}_5$  increases two-fold. Once breakdown potential of pure aluminum is exceeded the amount of  $\text{Ta}(\text{OH})_5$  increases as it replaces the  $\text{Ta}_2\text{O}_5/\text{Al}_2\text{O}_3$  in the occluded cells and they passivate.

At high pH, the passive film for the alloy is entirely oxidized Ta with no Al detected the same chemistry as would be expected for a pure Ta substrate. However, unlike the case of pure Ta, a breakdown potential is observed for the Al-Ta alloys. This occurs when the  $\text{Cl}^-$  reacts with the substrate (irrespective of whether it is an indirect or direct interaction) and "finds" the metal to be Al and not Ta. At this pH, the passive film is thicker than at the lower pH values and no Al is present. The low passive current

density would be consistent with very limited dissolution of Ta through the  $\text{Ta}(\text{OH})_5$  barrier. At low pH, the passive film chemistry is similar to that observed at neutral pH -- oxidized Al and oxidized Ta are both present and the film is relatively thin ( $< 10\text{nm}$ ).

These findings regarding the mechanism of passivity observed for the nonequilibrium alloys studied in this program correlate with conclusions by other investigators studying the passive films on stainless steels and iron nickel binary alloys [34-38]. Most notably, the work by Olefjord, et al., indicated the Ni, Mo, as well as Cr were enriched in the metallic state below the oxide, with the enrichment of Cr dependent upon the Mo content [34-36]. It was concluded that the enriched layer acted to control the dissolution rate and thereby provoked formation of the passive film. Similar evidence of an enriched metallic state was found by Marcus and Hoppe for Fe-Ni binary alloys [37,38].

## CONCLUSIONS

A dominant factor in the enhanced passivity of Al-Ta alloys is believed to be associated with an enriched solute layer of Ta in the metallic state at the metal-film interphase. The layer of solute in the metallic state complements the outer oxides to determine the overall behavior. The formation of enriched metallic phase is believed to be the result of selective dissolution of the aluminum.

Essentially, the mechanism proposed for the Al-Ta alloys is the same as that proposed for the Al-W system, in which an enriched layer of metallic W at the metal/oxide interphase acts to control the dissolution rate. Each system possesses its own specific passive film chemistry which is dictated by the stability and solubility of the species at the given pH and potential. At pH 12 the passivating film observed for the Al-Ta system is comprised of a hydrated form of Ta oxide,  $\text{Ta}(\text{OH})_5$ , for all potentials. At pH 3 and pH 8 the relative amount and form of Ta oxide present in the film is a function of overpotential.

The passive film composition of the Al-W system follows a different behavior. Very little solute oxide is observed at neutral, regardless of potential. However, at pH 3 comparable amounts of Al and W oxide is present. During pit initiation it is proposed that the W rich interphase is exposed, promoting formation of a stable W oxide and subsequent repassivation of the site.

Research colleagues in this program have previously shown that the Al-Mo and the Al-Cr alloys have similarly been shown to contain a solute rich interphase consisting of the more noble elements in the metallic states [3].

Regarding the early work on vapor deposited materials, thick films of stainless aluminum grown by high-rate physical vapor deposition exhibit enhanced passivity despite nodules and other physical defects. Materials produced in the future are expected to have a greatly reduced number of defects. It is significant that alloying

additions used in thin-film studies have shown similar beneficial effects in vapor deposited Al alloys.

### ACKNOWLEDGMENTS

We gratefully acknowledge the contributions of G. Korth in providing the PVD specimens and of W.C. Moshier and R.G. Wendt in providing the thin-film Al-2.8Ta specimens.

### REFERENCES

1. W.C. Moshier, G.D. Davis, J.S. Ahearn, and H.F. Hough, *J. Electrochem. Soc.* 133, 1063 (1986).
2. W.C. Moshier, G.D. Davis, J.S. Ahearn, and H.F. Hough, *J. Electrochem. Soc.* 134, 2677 (1987).
3. W.C. Moshier, G.D. Davis, and G.O. Cote, *J. Electrochem. Soc.* 136, 356 (1989).
4. G.D. Davis, W.C. Moshier, T.L. Fritz, and G.O. Cote, *J. Electrochem. Soc.* 137, 422 (1990).
5. B. A. Shaw, T.L. Fritz, G.D. Davis, and W.C. Moshier, *J. Electrochem. Soc.* 137, 1317 (1990).
6. G.D. Davis, W.C. Moshier, G.G. Long, and D.R. Black, *J. Electrochem. Soc.* 138, 3194 (1991).
7. B.A. Shaw, G.D. Davis, T.L. Fritz, B.J. Rees, and W.C. Moshier, *J. Electrochem. Soc.* 138, 3288 (1991).
8. B.A. Shaw, G.D. Davis, T.L. Fritz, B.J. Rees, and W.C. Moshier, in *Critical Factors in Localized Corrosion*, G.S. Frankel and R.C. Newman, eds. (The Electrochemical Society, Pennington, NJ, 1992), p. 323.
9. G.D. Davis, B.A. Shaw, B.J. Rees, and M. Ferry, *J. Electrochem. Soc.* 140, 951 (1993).
10. T.R. Schrecengost, B.A. Shaw, and R.G. Wendt, W.C. Moshier, submitted to *Corros.*
11. P.M. Natishan, E. McCafferty, and G.K. Hubler, *J. Electrochem. Soc.* 133, 1061 (1986).
12. E. McCafferty, G.K. Hubler, P.M. Natishan, P.G. Moore, R.A. Kant, and B.D. Sartwell, *Mater. Sci. Eng.* 86, 1 (1987).
13. P.M. Natishan, E. McCafferty, and G.K. Hubler, *J. Electrochem. Soc.* 135, 321 (1988).
14. P.M. Natishan, E. McCafferty, and G.K. Hubler, *Corros. Sci.* 32, 721 (1991).
15. E. McCafferty and P.M. Natishan, in *Critical Factors in Localized Corrosion*, G.S. Frankel and R.C. Newman eds. (The Electrochemical Society, Pennington, NJ, 1992), p. 299.
16. G.S. Frankel, M.A. Russak, C.V. Jahnes, M. Mirzamaani, and V.A. Brusic, *J. Electrochem. Soc.* 136, 1243 (1989).

17. Z. Szklarska-Smialowska, in *Critical Factors in Localized Corrosion*, G.S. Frankel and R.C. Newman, eds. (The Electrochemical Society, Pennington, NJ, 1992), p. 311.
18. R.C. Bhardwaj, A. González-Martín, and J. O'M. Bockris, *J. Electrochem. Soc.* 139, 1050 (1992).
19. J. O'M. Bockris and Lj. V. Minevski, accepted by *J. Appl. Electrochem.*
20. A. González-Martín, R.C. Bhardwaj, and J. O'M. Bockris, accepted by *J. Electrical Anal. Chem.*
21. A.H. Al-Saffar, V. Ashworth, A.K.O. Vairamov, D.J. Chivers, W.A. Grant, R.P.M. Procter, *Corros. Sci.* 20, 127 (1980).
22. M.V. Zeller and J.A. Kargol, *Appl. Surf. Sci.* 18, 63 (1984).
23. R.W. Gardiner and M.C. McConnell, *Met. Mater.* 3, 254 (1987)
24. M. Fass, D. Itzhak, D. Eliezer, F.H. Froes, *J. Mater. Sci. Lett.* 6, 1227 (1987).
25. H. Yoshioka, H. Habazaki, A. Kawashima, K. Asami, and K. Hashimoto, *Corros. Sci.* 32, 313 (1991).
26. H. Yoshioka, A. Kawashima, K. Asami, and K. Hashimoto, in *Proc. Symp. Corrosion, Electrochemistry, and Catalysis of Metallic Glasses* R.B. Diegle and K. Hashimoto, eds. (The Electrochemical Society, Pennington, NJ 1988) p. 242.
27. F.G. Schenk, "The Influence of Heat Treatment on the Performance of Highly Corrosion Resistant Al Alloys," Trident Scholar Report No. 197, U.S. Navy Academy, 1992.
28. C.C. Streinz, "A Microellipsometric Study of the Passive Film Formation on Solid Solution Al-Ta Alloys and the Role of Al<sub>3</sub>Ta Precipitates in Breakdown," The Johns Hopkins University, Baltimore, MD (1992).
29. B. A. Shaw, T. R. Schrecengost, W. C., Moshier, and R. G. Wendt, "Inhibiting Corrosion in Gr/Al and Gr/Mg Metal Matrix Composites Using Nonequilibrium Alloying Techniques," Penn State Report to ONR, June 1992.
30. M. Nathan, *Mater. Lett.* 3, 319 (1985).
31. G.D. Davis, W.C. Moshier, J.S. Ahearn, H.F. Hough and G.O. Cote, *J. Vac. Sci. Technol. A* 5, 1152 (1987).
32. M. Urguidi and D.D. Macdonald, *J. Electrochem. Soc.* 132, 555 (1985)
33. D.D. Macdonald, *J. Electrochem. Soc.* 139, 3434 (1992).
34. I. Olefjord, *Mater. Sci Engr.* 42, 161 (1980).
35. I. Olefjord, B-O. Elfstrom, *Corros.* 38, 46 (1982).
36. I. Olefjord, B. Brox, U. Jelvestam, *J. Electrochem. Soc.* 132, 2854 (1985).
37. P. Marcus, I. Olefjord, *Corros. NACE* 42, 91 (1986).
38. H.W. Hoppe, H.H. Strehblow, *Surf. Interface Anal.* 16, 271 (1990).
31. M. Pourbaix, *Atlas of Electrochemical Equilibria in Aqueous Solutions*, (NACE, Houston, TX 1974) p. 168.
32. N. Bui, A. Irhzo, F. Dabosi, and Y. Limouzin-Maire, *Corros.* 39, 491 (1983).
33. A. Irhzo, Y. Segui, N. Bui, and F. Dabosi, *Corros. Sci.* 26, 769 (1986).
34. H. Habazaki, A. Kawashima, Kasami, and K. Hashimoto, in *The Applications of Surface Analysis Methods to Environmental/Material Interactions (PV 91-7)* D.R. Baer, C.R. Clayton, and G.D. Davis, eds., (The Electrochemical Society, Pennington, NJ, 1991) p. 467.

35. J. Chen and J.K. Wu, Corros. Sci. 30, 53 (1990).

36. B.A. Shaw, T.R. Schrecengost, W.C. Moshier, and R.G. Wendt, "Inhibiting Corrosion in Gr/Al and Gr/Mg Metal Matrix Composites Using Nonequilibrium Alloying Techniques," Penn State Report to ONR, June 1992.

### Pourbaix Diagrams

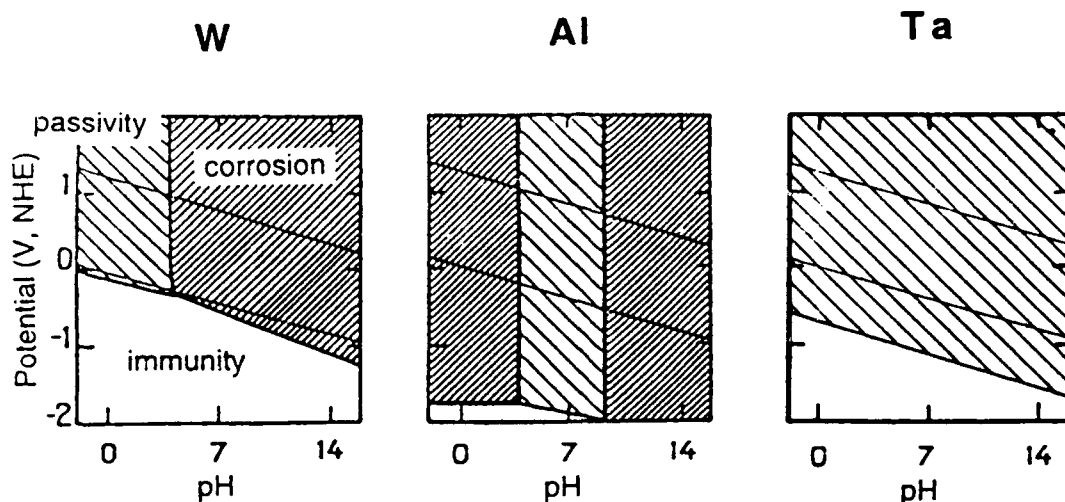


Figure 1. Pourbaix diagrams for Al, W, and Ta

### Schematic of High-Rate PVD System

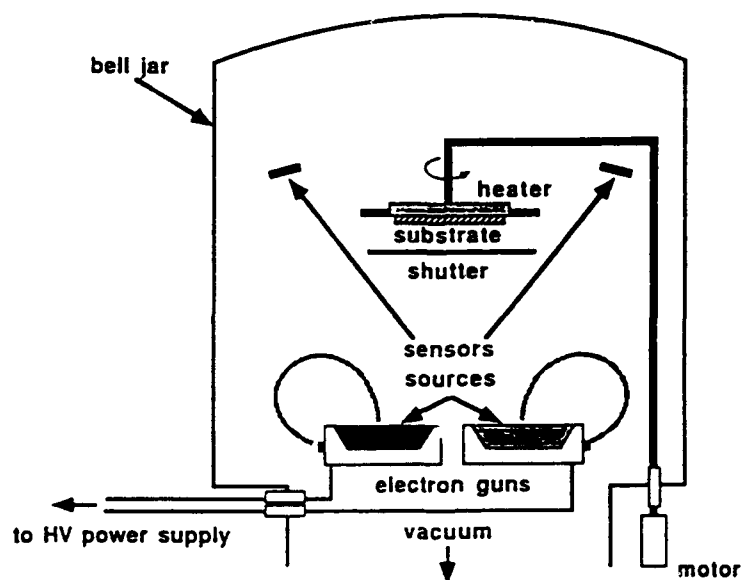


Figure 2. Schematic diagram of High-Rate Physical Vapor-Deposition System.

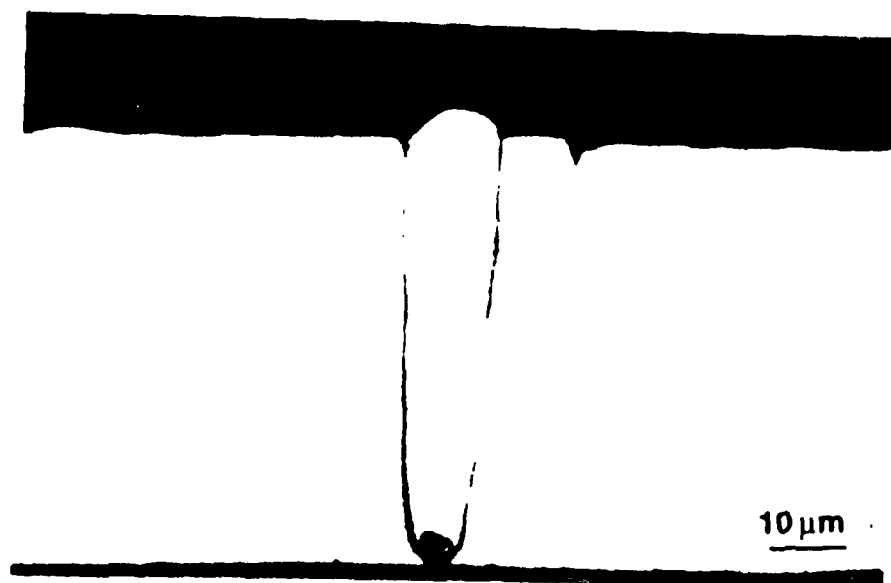


Figure 3. Cross-section through a PVD specimen showing the effect of a small particle on the collector plate on the structure of the deposit.



Figure 4. SEM micrograph of a PVD specimen revealing a nodule and its influence on deposit structure.





Figure 5. SEM micrograph of a PVD specimen showing the effect of a buried nodule on subsequent material growth.

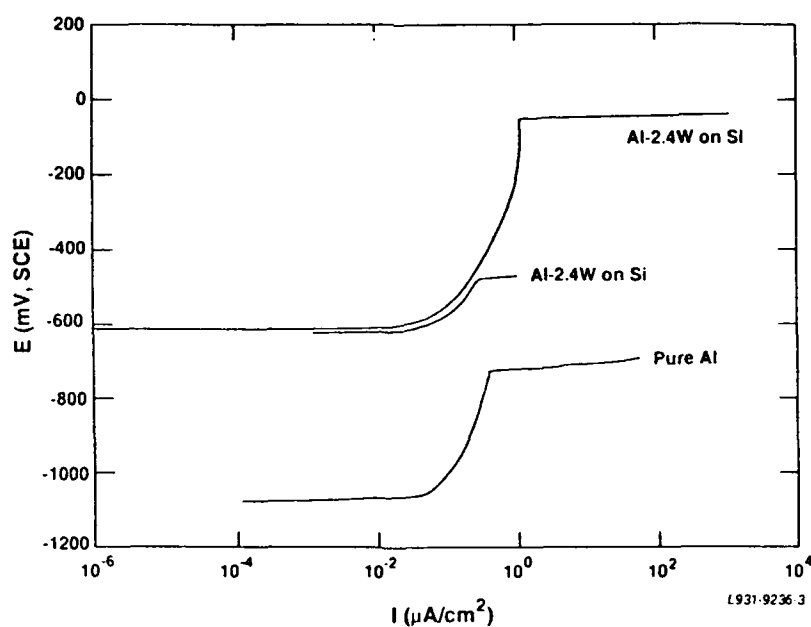


Figure 6. Replicate potentiodynamic scans of CD-12 specimens (Al-2.4W on Si) in 0.1M NaCl solution at pH 8 with a scan rate of 0.2 mV/s. Also shown for comparison is equivalent data for pure Al.

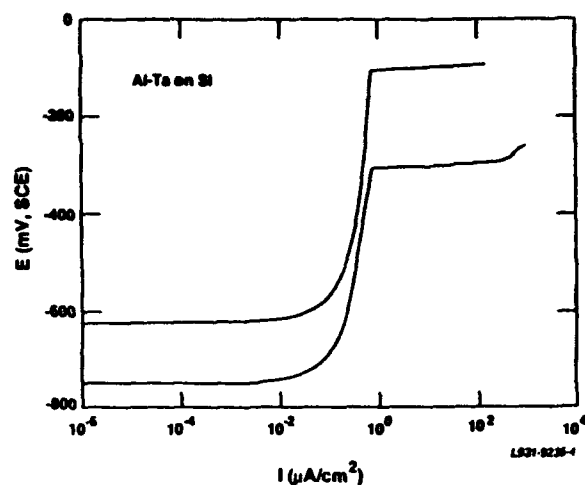


Figure 7. Replicate potentiodynamic scans of CD-13 specimens (Al-Ta on Si) in 0.1M NaCl solution at pH 8 with a scan rate of 0.2 mV/s.

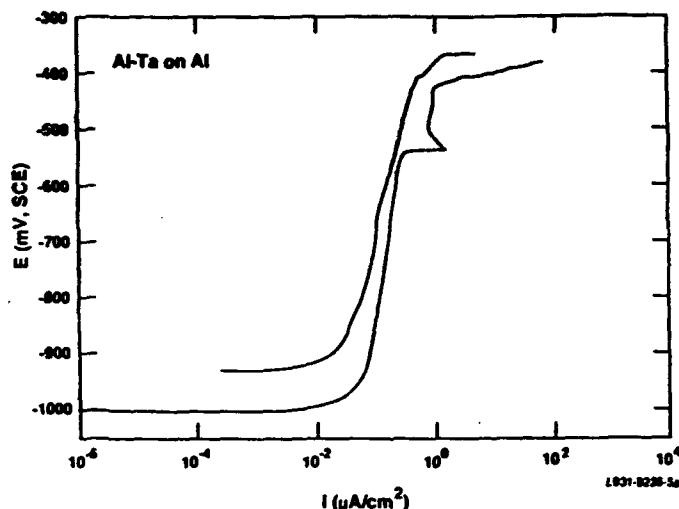


Figure 8. Replicate potentiodynamic scans of CD-16 specimens (Al-Ta on Al) in 0.1M NaCl solution at pH 8 with a scan rate of 0.2 mV/s.

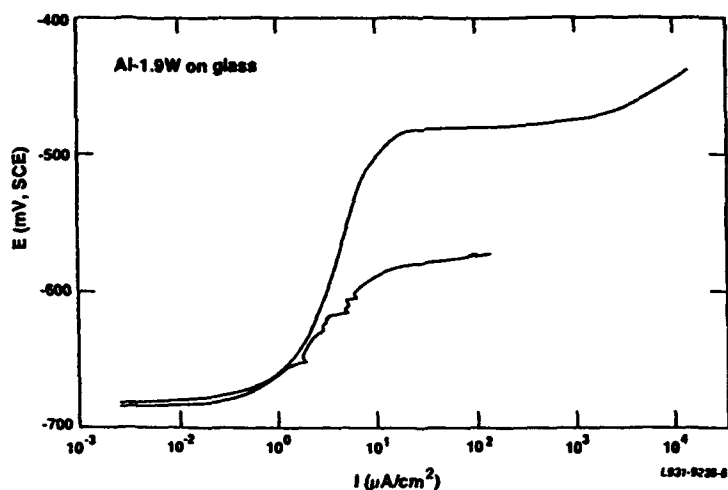


Figure 9. Replicate potentiodynamic scans of CD-17 specimens (Al-1.9W on glass) in 0.1M NaCl solution at pH 8 with a scan rate of 0.2 mV/s.

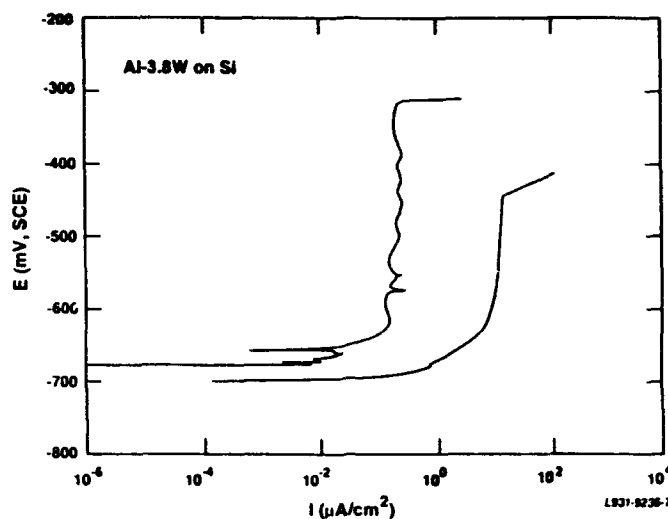


Figure 10. Replicate potentiodynamic scans of CD-25 specimens (Al-3.8W on Si) in 0.1M NaCl solution at pH 8 with a scan rate of 0.05 mV/s.

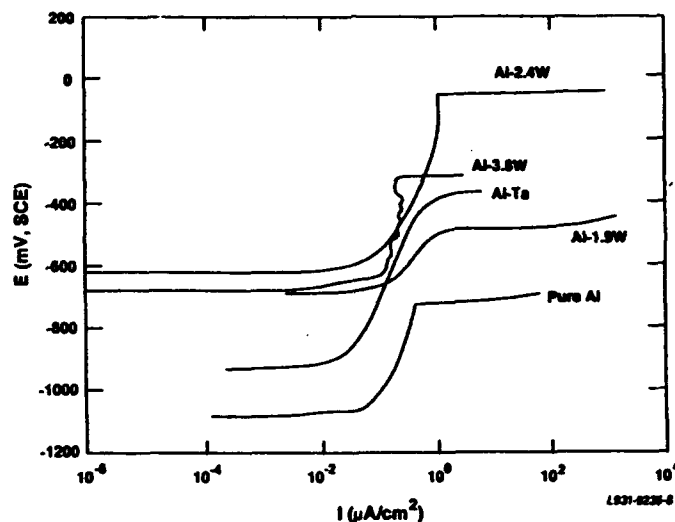


Figure 11. Comparison of potentiodynamic scans of all the vapor-deposited specimens and pure Al. All tests were in 0.1M NaCl solution at pH 8

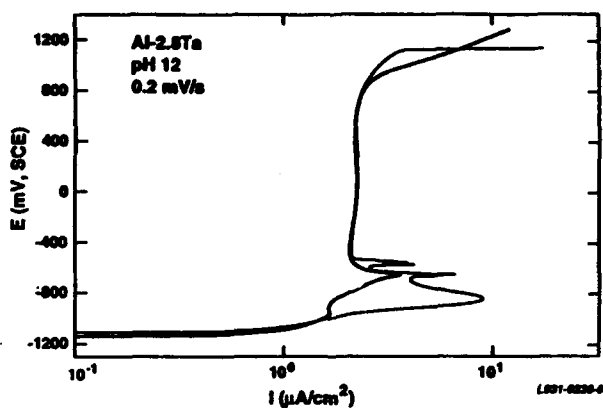


Figure 12. Replicate potentiodynamic scans of Al-2.8Ta specimens in 0.1 M NaCl solution at pH 12 with a scan rate of 0.2 mV/s.

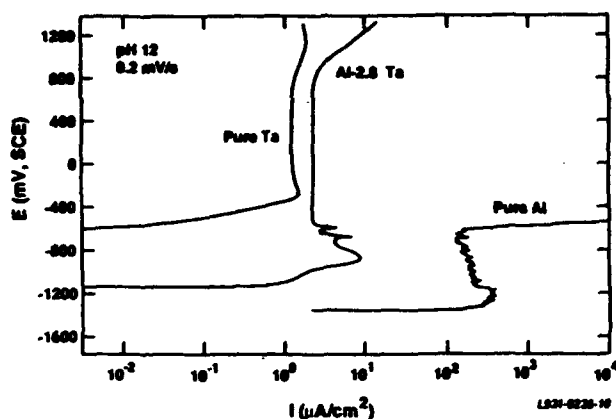


Figure 13. Comparison of potentiodynamic scans of Al-2.8Ta, pure Al, and pure Ta specimens in 0.1 M NaCl solution at pH 12 with a scan rate of 0.2 mV/s.

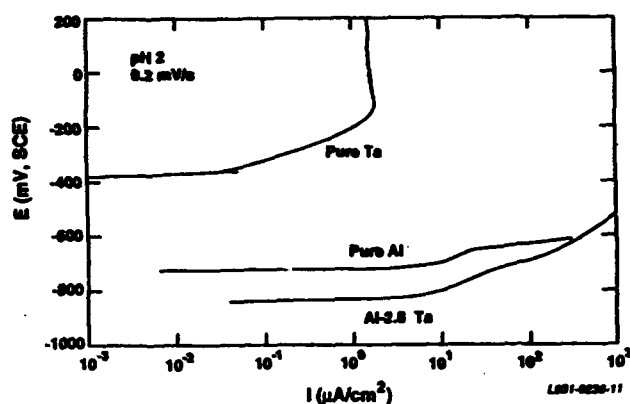


Figure 14. Comparison of potentiodynamic scans of Al-2.8Ta, pure Al, and pure Ta specimens in 0.1 M NaCl solution at pH 2 with a scan rate of 0.2 mV/s.

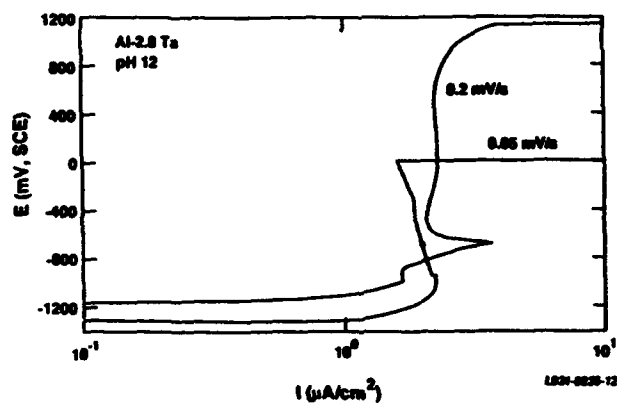


Figure 15. Comparison of potentiodynamic scans of Al-2.8Ta in 0.1 M NaCl solution at pH 12 with scan rates of 0.2 mV/s and 0.05 mV/s.

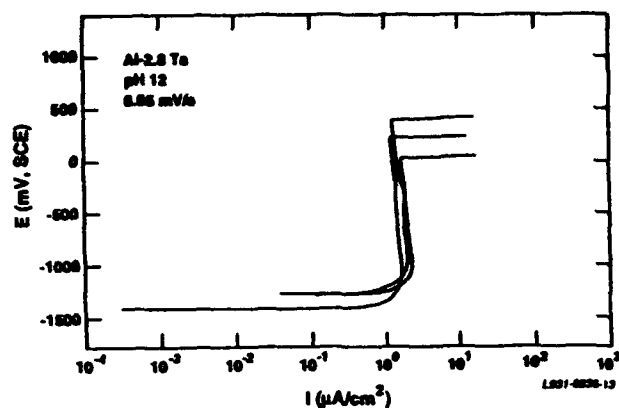


Figure 16. Replicate potentiodynamic scans of Al-2.8Ta specimens in 0.1 M NaCl solution at pH 12 with a scan rate of 0.05 mV/s.

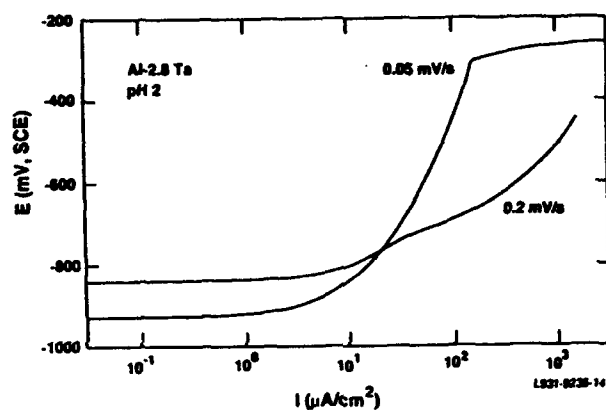


Figure 17. Comparison of potentiodynamic scans of Al-2.8Ta in 0.1 M NaCl solution at pH 2 with scan rates of 0.2 mV/s and 0.05 mV/s.

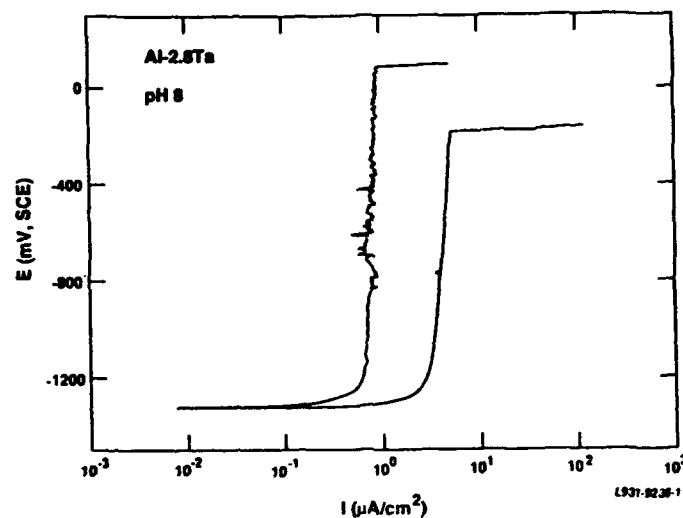


Figure 18. Replicate potentiodynamic scans of Al-2.8Ta specimens in 0.1 M NaCl solution at pH 8 with a scan rate of 0.05 mV/s.

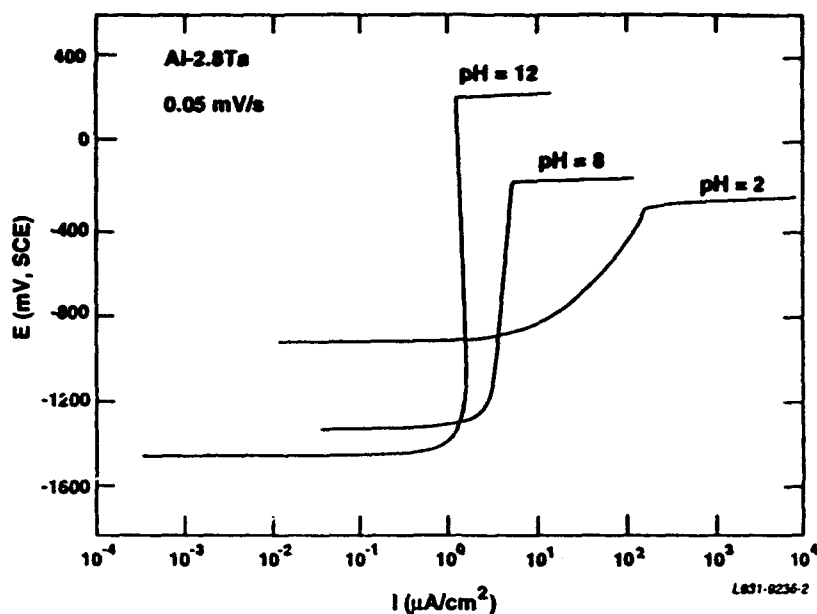


Figure 19. Comparison of potentiodynamic scans of Al-2.8Ta in 0.1 M NaCl solutions at pH 2, 8, and 12 with a scan rate of 0.05 mV/s.

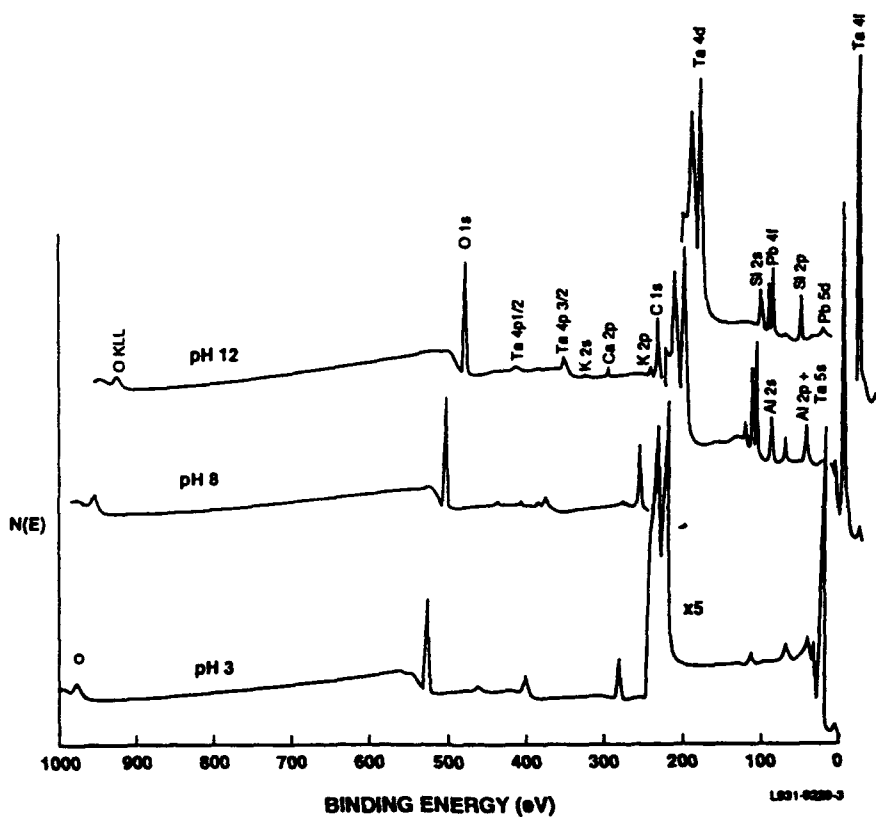
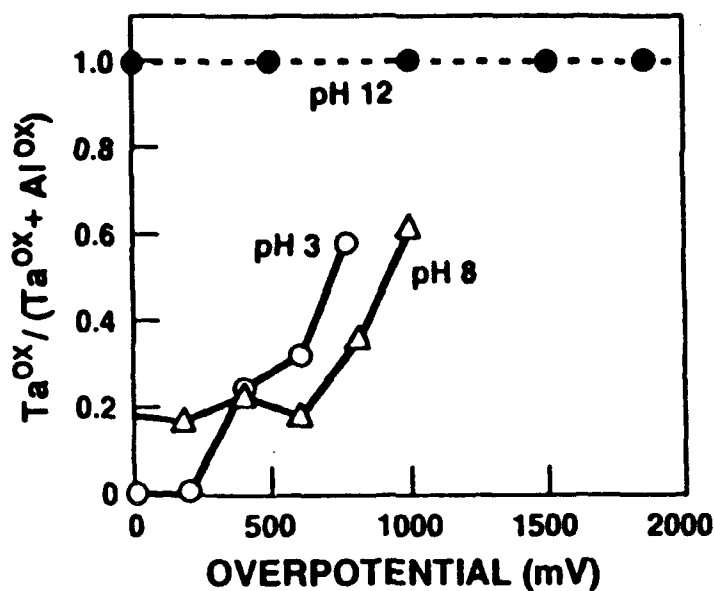


Figure 20. XPS survey spectra of Al-2.8Ta polarized to  $E_b$  in 0.1 M NaCl solutions at pH 2, 8, and 12. (The low binding-energy region of each spectrum was acquired with five times the number of scans of the remainder of the spectrum).



L913-9236-15

Figure 21. Ratio of oxidized Ta to all oxidized cations in the passive film, as measured by XPS, as a function of overpotential in 0.1 M NaCl solutions at pH 2, 8, and 12.

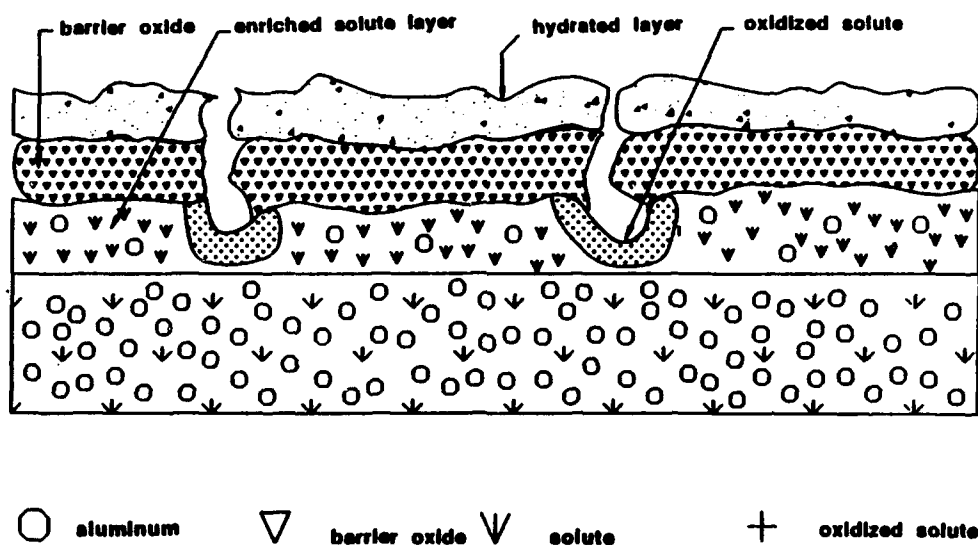


Figure 22. Schematic representation of the Solute-Rich Interphase Model (SRIM). Solute-rich metallic region under the passive film promotes pit repassivation; if a nucleating pit penetrates the outer oxide layer, the exposed solute will subsequently form a more stable oxide and invoke repassivation of the occluded cell.

# **The Effect of Ion Implantation on the Passivation Behavior of Pure Copper**

**E. J. Wright**  
Exxon Production Research Company  
Houston, Texas, U. S. A.

**V. Ashworth**  
Global Corrosion Consultants  
Shifnal, Shropshire, U.K.

**R. P. M. Procter**  
University of Manchester Institute of Science and Technology (UMIST)  
P. O. Box 88, Manchester, U.K.

**W. A. Grant\***  
University of Salford, Salford, U.K.

## **Abstract**

The effect of implanting different ions on the passivation behavior of copper in deaerated alkaline sulfate solutions was examined using potentiokinetic polarization techniques. Glancing-angle Rutherford backscattering and Auger electron spectroscopy were used to study the composition of the surface alloys produced by ion implantation. The microstructure of copper independently implanted with Cu, Cr, Ti and Ta ions was investigated using thin foil transmission electron microscopy. Electron diffraction measurements on these foils showed that the implant elements exist as single-phase, metastable solid solutions in the copper substrate.

The potentiokinetic polarization data for Ar- and Cu-implanted copper show that these inert ion implantations produce no significant effects on the passivation behavior of copper in this test environment. It may be concluded that the ion implantation process itself does not affect passivation. Implantation of chemically active species produces significant improvements in the passivation behavior of copper in the alkaline sulfate solutions. The beneficial effects of these species are attributed to their incorporation in the oxide film, thereby facilitating the active-passive transitions. The effect exerted by each of these elements is different from one to another. This behavior is explained by differences in their chemical and electrochemical properties. For example, polarization of Cr-implanted copper to potentials noble to the active-passive transition results in a rapid increase in the anodic current density. This behavior is related to the transpassive dissolution of the Cr and corresponded to the increase in current density observed at the same potential on the polarization curves for pure Cr. The anodic polarization curves of Ta-implanted copper exhibit active-passive transitions which can be related to the passivation behaviors of both Cu and Ta. The passivation behavior of Ta-implanted copper is superior to that of either pure copper or Ta in this solution. These observed improvements are probably due to the formation of a mixed Ta and Cu passivating phase, which is more readily formed and more protective than those of either pure Cu or pure Ta.

The results demonstrate that elements introduced by ion implantation exert their normal chemical and electrochemical effect when the surface alloys are exposed to a corrosive environment. The work demonstrates that ion implantation can be used for the production of novel, corrosion-resistant alloys and also provides a rational basis for the use of implantation as a surface alloying technique for corrosion control.

**Keywords:** copper, alloying, corrosion, passivation, ion implantation, polarization

---

\* Deceased



## Introduction

A number of techniques is available for the protection of metals from corrosion; among these, the technology of alloying to produce more corrosion resistant materials is well established. However, for an alloy addition to produce improvements in the corrosion resistance of the base metal to either uniform or localized corrosion, it is generally regarded as essential that the addition remains in single-phase solid solution in the base metal at the concentration level needed to provide the required corrosion resistance.

The process of ion implantation consists of bombarding a substrate with energetic ions. The ions penetrate the substrate surface to a depth dependent on many factors, but largely on the incident ion energy and the nature of the ions and the substrate. In a metallic lattice the neutralized ions come to rest very rapidly in the lattice at substitutional or interstitial positions and remain there in solid solution. Due to its grossly non-equilibrium nature, ion implantation offers the possibility of overcoming the solubility limitations imposed by equilibrium phase diagrams, and of producing novel, single-phase surface alloys that are inaccessible by conventional metallurgical techniques. These alloys may exhibit a significantly improved corrosion resistance, provided that suitable implant species are chosen.

Previous studies indicate that ion implantation can be used as a surface alloying tool because the implant elements exhibit their normal chemical and electrochemical properties when the surface alloy is exposed to the corrosive environment. Specific works have examined the effect of ion implantation on iron as a model system<sup>1-3</sup>, aluminum<sup>4</sup> and AISI 304 stainless steel<sup>5, 6</sup>. However, limited work has been carried out on the effect of ion implantation on the aqueous corrosion behavior of copper. Street<sup>7</sup> investigated the effects of boron implantation on the passivation behavior of copper and there are reports that the atmospheric tarnishing of copper can be inhibited by the independent implantation of chromium<sup>8</sup> and boron<sup>9, 10</sup>.

Copper has good corrosion resistance to many environments, attributable, in part, to the nobility of the metal; however, in other environments corrosion resistance often depends on the formation and maintenance of protective passive films on the metal surface. The corrosion resistance of copper is much reduced when such protective films are not formed. Furthermore, the degree of protection provided by these films, compared to other passive metals, is relatively poor<sup>11</sup>. These factors limit the application of copper and therefore any improvement in the protectiveness of the passive films would lead to corresponding improvements in the general corrosion resistance of copper.

The aim of the present work was to investigate the effect of implanting various ion species on the aqueous corrosion behavior of copper. The reader is referred to the original report on this work<sup>12</sup> for further details. The first stage of the work was to characterize the composition and microstructure of the surface alloys produced by implantation. The second stage was to examine the effects of ion implantation on the passivation behavior of copper using electrochemical polarization. The electrolyte solution chosen for the corrosion tests had to be sufficiently conductive to enable the specimens to be correctly polarized by the potentiostat. A dilute, 0.01 M sodium sulfate solution was therefore chosen. The pH of the sulfate solution was adjusted to 12.4 as copper exhibits passivity on anodic polarization in this solution; the effects of ion implantation on the passive film on copper could therefore be examined.

The investigation of the effects of ion implantation on the passivation of copper was divided into two parts: first, an investigation was carried out on the effects of the implantation of the inert ions, Ar and Cu, on the passivation of copper. This was to determine the effects, if any, of the ion implantation process itself on the passivation. Second, an investigation of the effects of the implantation of the chemically active species Cr, Ti and Ta on the passivation of copper in this test environment was carried out. These elements were chosen because of their ability readily to form highly protective passive films and their addition to copper was therefore expected to produce significant improvements in the passivation.

## Experimental

### Materials

The nominal composition of the high purity, vacuum melted copper rod used in this investigation was iron < 1 ppm, sulfur < 1 ppm, silver < 0.5 ppm and total of all other impurity elements < 0.3 ppm. The material was used in the as-received condition and had a grain size of 0.6 mm and a Vicker's hardness of 70. To produce test specimens the rod was skimmed down to 9 mm diameter and then cut into discs 6mm thick. One face of these unmounted specimens was skimmed and ground and metallographically polished down to 1 micron diamond paste. A threaded hole on the other face was used for electrical connection to the electrode holder for polarization tests.

### Ion Implantation

The ion implantation machine used consisted of three units: an ion source chamber, an isotope separator and a target chamber. Low energy 3.2 fJ (20 keV) ions were used together with high doses ( $10^{15}$  ions/mm<sup>2</sup>) to obtain a high concentration of implanted ions near the specimen surface. The target specimen holder was cooled with a liquid nitrogen finger to minimize the temperature rise during implantation and control this to ~ 7°C. The projected ranges of the ions were estimated at 5 - 8 nm with a depth distribution that will depart from the Gaussian distributions predicted theoretically<sup>13</sup>, due to sputtering at the high doses employed. The para-surface concentrations are expected to be in the range 10 - 20 at. %.

### Glancing-angle Rutherford Backscattering

Rutherford backscattering (RBS) was used to determine the distribution of tantalum in the implanted surfaces both before and after electrochemical testing. (Tantalum was the only implant species that could be analyzed in this manner since for RBS the implanted atoms must generally be of greater mass than the substrate.) A glancing-angle technique was used to improve the depth resolution. A beam of 2 MeV alpha particles was directed onto the specimen to be analyzed at an angle of 80° to the normal. The signal from the detector was then amplified and analyzed by a multichannel pulse-height analyzer. The resulting energy spectrum of the analyzer could then be converted to provide an estimate of the mean projected range and concentration of implanted tantalum in the copper surface.

### Auger electron Spectroscopy

Auger electron spectroscopy (AES) combined with argon ion sputtering was used to determine the distribution of the Cr and Ti species, and of Cu and O, both before and after electrochemical testing. Auger spectra of the target surface were recorded at intervals during ion sputtering. This enabled an Auger signal/depth profile to be determined for the elements of interest. Semi-quantitative analyses were achieved by comparing the Auger signals of the implanted specimens with those from the corresponding pure elements.

### Transmission Electron Microscopy

A jet electropolishing technique was used to prepare specimens that were suitable for observation in the transmission electron microscope. Discs specimens 3.05 mm in diameter and 0.25 mm in thickness were prepared from copper metal foil. The specimens were then made the anode in an electrolytic cell and jet electropolished from both sides to approximately 0.03 mm in thickness. The electrolyte used consisted of 85 % methanol/15 % nitric acid, cooled to 238 K using liquid nitrogen. The current density was 15 A/m<sup>2</sup> at 25 - 30 V. The partially-thinned foils were then implanted using exactly the same conditions as for implantation of the bulk, disc specimens. After implantation, the implanted surface was coated with a clear lacquer and the specimen further jet electropolished, from the opposite, unimplanted face, to produce a small hole in the center of the disc. The varnish was finally removed with amyl alcohol.

## Potentiokinetic Polarization

Figures 1a and 1b illustrate the electrode holders used for the copper discs, and for the pure elements (Cr and Ta) specimens respectively. The electrochemical test cell and the external 1 l deaeration flask located above it, are illustrated schematically in Figure 2. The cell was a 1 l flat-bottomed reaction vessel with a 5-socket flanged lid. The platinum counter electrode was in a separate compartment to minimize oxygen contamination of the cell. The main cell contained the working electrode. The reference electrode was contained in a separate vessel with electrical connection maintained by means of a salt bridge and Luggin probe. The test solution was a deaerated 0.01 M  $\text{Na}_2\text{SO}_4$  solution with the pH adjusted to 12.4. Nitrogen was bubbled into the test solution in the deaeration flask for 15 hours while the specimen in the assembled cell was maintained in a dry nitrogen atmosphere. The test solution was then transferred into the cell under positive nitrogen pressure. Deaeration was continued throughout the polarization test. The investigation of the passivation behavior of copper implanted with various ions is based on the application of three sweep potentiokinetic polarization technique, starting from the immersion potential. This technique was originally devised by Ashworth et al.<sup>1</sup> for corresponding investigations with pure iron when it was observed that even with chemically inert species, the air-formed oxide film was thickened by the process of ion implantation. The present work also included identical polarization experiments on the pure metals Cr and Ta, in order to characterize their behavior under the particular experimental conditions. A three-sweep potentiokinetic polarization technique, using a sweep rate of 0.42 mV/s, was adopted that involved a positive-going sweep from the immersion potential to 875 mV (S.H.E.), followed by a negative-going sweep to -1250 mV and finally a return to 875 mV.

## Results and Discussion

### Surface Analyses

Figure 3 shows the RBS data for Ta-implanted copper while Figure 4 shows the corresponding AES sputter profile for Ti-implanted copper. These figures show that the implant distributions are both distorted Gaussian. Similar results were obtained for Cr-implanted copper. The mean projected ranges and the implant peak and surface concentrations estimated from these data together with the respective theoretical estimates<sup>13</sup> are shown in Table 1. Measured ranges are ~ 6 nm, while peak and surface concentrations are ~ 19 - 22 at. % and ~ 4 - 9 at. % respectively. The estimates of the mean projected ranges are in reasonable agreement with theory. However, the measured implant concentrations were substantially lower than the predicted values. This is attributed to extensive sputtering of the substrate during implantation which causes the release of previously implanted material and thereby produces distorted Gaussian distributions, skewed toward the surface.

### Transmission Electron Microscopy

In this study the elements Cr, Ti and Ta were implanted into pure copper to concentrations far in excess of their equilibrium solubilities in copper<sup>14</sup>. TEM was used to investigate the microstructure of the implanted layers. The analyses of the diffraction patterns obtained from the various implanted specimens indicate that in all cases the observed diffraction was characteristic of pure copper<sup>15</sup>. Figure 5 is a TEM micrograph of unimplanted copper showing a stacking fault with associated dislocations. The TEM micrograph of a Cu-implanted copper specimen (Figure 6) shows radiation damage typical of that created by the implantation of heavy ions into copper. The micrograph of a Ta-implanted specimen (Figure 7) show essentially similar radiation damage effects but no evidence of precipitation of a second phase. Similar results were obtained for both Cr-, and Ti-implanted specimens, which indicates that the implant species used in the present work, Cr, Ti and Ta all exist as single-phase metastable solid solutions in the copper substrate. These observations are consistent with those obtained by a number of other workers<sup>16, 17</sup>.

## Potentiokinetic Polarization Tests

**Unimplanted Copper.** Figure 8 shows the potentiokinetic polarization curves characteristic of unimplanted copper in deaerated 0.01 M  $\text{Na}_2\text{SO}_4$  solution of pH 12.4. The sweep cycle begins from the immersion potential (-30 mV) of the electrode (Point A), which corresponds to copper bearing a stable air-formed cuprous oxide film. On anodic polarization, the current density increases rapidly until there is an active-passive transition at 140 mV (Point B). The critical current density for passivation is  $4.2 \text{ A/m}^2$ . This transition relates to the complete coverage of the copper surface by the passivating phases of cupric oxide and/or cupric hydroxide. On further anodic polarization, the copper electrode remains passive, the minimum passive current density (Point C) is  $0.04 \text{ A/m}^2$ . However, the anodic current density increases in the later stages of this first sweep, due to the onset of the oxygen evolution reaction. The sweep direction was therefore reversed at 875 mV to minimize oxygen contamination of the test environment.

At the start of the negative-going sweep the copper surface is completely passivated, and therefore no anodic current density, apart from that attributable to oxygen evolution, is measurable on this sweep. The current becomes measurably cathodic at -130 mV (Point E) and then increases rapidly as the potential is lowered, due to the reduction of the passive film. The first reduction peak is seen at -200 mV (Point F) and on further cathodic polarization, further reduction peaks are observed, the second at -530 mV (Point G) and the third at -630 mV (Point H). Interpretation of the cathodic reduction curves obtained for unimplanted copper shows that the passive film formed on anodic polarization of copper in this environment is composed mainly of cupric oxide, together with lesser amounts of cuprous oxide and cupric hydroxide. This is consistent with the literature<sup>18, 19</sup> which indicates that the passive film that forms on copper in alkaline solutions consists of a layer of cuprous oxide in contact with the metal surface, overlaid by solid phases of the Cu(II) oxidation state. The dominant electrode process in the final section of the negative-going sweep is the evolution of hydrogen and the current density increases rapidly to  $20 \text{ A/m}^2$  at the negative limit of the sweep. The sweep direction is then reversed to begin the final positive-going sweep.

During the early stages of the final positive-going sweep, i.e., below -900 mV, the cathodic polarization curve is almost completely reversible, which indicates that the final positive-going sweep therefore characterizes the polarization behavior of an initially film-free copper electrode. The current density becomes anodic at -330 mV (Point J) and the current density increases rapidly until the metal shows an active-passive transition at -180 mV (Point K). The critical current density for passivation is  $0.40 \text{ A/m}^2$ . The active-passive transition represented by point K relates to the formation of a solution-formed cuprous oxide film<sup>20</sup>. The current density then falls to a minimum of  $0.01 \text{ A/m}^2$  and a short passive range is observed. As the potential continues to rise, the current density increases again, due to the formation of Cu(II) compounds and a second active-passive transition is seen at a potential of 130 mV (Point L). The critical current density for passivation, in this case, is  $5.3 \text{ A/m}^2$ , which is considerably greater than that associated with the preceding transition related to cuprous oxide formation. The potential of the second active-passive transition on the final sweep is close to that recorded for the corresponding active-passive transition on the first positive-going sweep. This indicates that these peaks represent similar electrode reactions. However, in this case, the critical current density for passivation is greater than that measured on the first sweep. The passive current density is also significantly higher, by a factor of two, on the final sweep. Analysis of these data suggests that this increase relates to differences between the air-formed and solution-formed cuprous oxide film; in particular, it suggests that the passive film based on an air-formed cuprous oxide film forms more readily (low critical current density) and is more protective (lower passive current density) than the corresponding film formed entirely from solution.

**Copper implanted with Inert Species.** Figure 9 shows the potentiokinetic polarization curves for Cu-implanted copper specimens. A comparison of this figure with that for the unimplanted copper specimen shows that the general features of these curves are the same. The corresponding polarization curves for both Ar-implanted copper specimens were also similar to those for unimplanted copper. These results demonstrate that the implantation of these inert species produces no significant effects on the polarization behavior of copper, and consequently, has no influence on the passivation of the metal in this environment.

**Chromium Implantation.** The potentiokinetic polarization curves characteristic of Cr-implanted copper in the test environment are shown in Figure 10. These curves are significantly different to those of unimplanted copper. The immersion potential is lower, at -200 mV compared to -30 mV for unimplanted copper. Furthermore, anodic polarization from this potential results in a new active-passive transition at a potential of -150 mV with a critical current density of  $0.06 \text{ A/m}^2$ . This potential is close to that of the active-passive transition seen on the final positive-going sweep at -180 mV for unimplanted copper and ascribed to the formation of a solution-formed cuprous oxide film. These polarization data suggest that significant differences exist between the air-formed oxide films present on unimplanted and Cr-implanted copper. Specifically, it is suggested that the presence of the implanted Cr inhibits the subsequent atmospheric oxidation of the copper substrate, thereby producing a thinner air-formed cuprous film.

A second active-passive transition is seen at a potential similar to that attributed to the formation of Cu(II) compounds on unimplanted copper. However, the critical current density for passivation,  $0.36 \text{ A/m}^2$  is considerably lower than that of unimplanted copper ( $4.2 \text{ A/m}^2$ ). On further polarization, the current density starts to increase rapidly at 250 mV and a further anodic maximum is seen at 510 mV. This behavior can be related to the transpassive dissolution of the Cr and corresponds to the increase in current density observed at the same potential on the polarization curves of pure Cr (Figure 11); this is certainly due to the oxidation of Cr(III) in the passive film to Cr(VI) in solution, which is expected<sup>20</sup> in alkaline solutions at potentials above 7 mV.

AES was used to confirm the nature of this anodic reaction, by the independent anodic polarization and analysis of two Cr-implanted specimens. The first of these was polarized to a potential chosen to coincide with the onset of the anodic peak. The second was polarized to a potential immediately above the peak. The subsequent AES analyses of these specimens (Figures 12 and 13 respectively) showed that ~ 56% of the original, retained dose of Cr was lost during polarization through this peak. Furthermore, the composition of the oxide film changed from a Cr-rich to a Cu-rich composition. These results, together with the polarization data from pure Cr, confirm that the additional anodic peak at 510 mV is due to the transpassive dissolution of the implanted Cr.

The final positive-going sweep shows a slightly reduced critical current density for passivation, the second active-passive transition occurring at  $3.7 \text{ A/m}^2$ , compared to  $5.3 \text{ A/m}^2$  for unimplanted copper. The inhibition of the anodic kinetics on this sweep is less than that on the first positive-going sweep because of the lower concentration of Cr in the surface. The final section of the sweep also shows further evidence of transpassive dissolution of the Cr.

**Titanium Implantation.** The potentiokinetic polarization curves characteristic of Ti-implanted copper in the test environment are shown in Figure 14. This figure shows several significant differences from that of unimplanted copper. The first positive-going sweep shows features very similar to those seen during the early stages of polarization of Cr-implanted copper. However, the immersion potential is lower, at -240 mV, than that of unimplanted copper. Furthermore, a new active-passive transition is seen at a potential of -140 mV, with a critical current density of  $0.04 \text{ A/m}^2$ . As in the case of Cr-implanted copper, these observations indicate that the oxide films present on Ti-implanted specimens are significantly different from those on unimplanted copper specimens.

Ti implantation significantly improves the passivation behavior of the copper. Specifically, the critical current density for the second active-passive transition (Point B in Figure 8) is reduced on the first positive-going sweep to  $0.14 \text{ A/m}^2$ , compared to  $4.2 \text{ A/m}^2$  for unimplanted copper. Furthermore, the passivation potential for this transition is lowered to 50 mV, compared to 140 mV for unimplanted copper. Similar improvements in the passivation behavior are seen on the second positive-going sweep. However, compared to unimplanted copper, Ti implantation has no significant effect on the passive current density, on either of these sweeps.

The AES sputter profile for Ti-implanted copper, following the complete polarization test in this environment is shown in Figure 15. Comparison with the as-implanted specimen profile (Figure 4) shows that the oxide film on the polarized specimen is much thicker than prior to polarization and consists mainly of Ti and O; it is probably a

TiO<sub>2</sub> film<sup>21</sup>. The AES data shows that only ~12% of the original, retained dose of Ti is lost during this test. Visual examination of the polarized specimens is consistent with the above polarization and AES data; the Ti-implanted specimens retained their polished appearance.

During the initial stages of the negative-going sweep, Ti-implanted copper exhibits a measurable anodic current density. TiO<sub>2</sub> is a n-type semiconductor with a low ionic conductivity; such a film would not be expected to sustain substantial film-thickening on the implanted surface. However, contamination or 'doping' of the TiO<sub>2</sub> by Cu<sup>2+</sup> ions may increase the ionic conductivity of the film<sup>22</sup> and thereby facilitate film-thickening on the implanted Ti. The Ti-implanted specimens show no evidence of the reduction peaks characteristic of unimplanted copper during cathodic polarization on this sweep. These observations may again be explained by the presence on these specimen surfaces of a TiO<sub>2</sub> film which is not reduced by cathodic polarization in this solution<sup>21</sup>.

**Tantalum Implantation.** The polarization curves characteristic of Ta-implanted copper in the test environment are shown in Figure 16. These curves, like those relating to Cr- and Ti-implanted specimens, also show significant differences from those of unimplanted copper. Ta, like Cr and Ti, produces a lower immersion potential and a new active-passive transition on the first positive-going sweep at a potential close to that ascribed to the formation of solution-formed cuprous oxide on unimplanted copper.

On further anodic polarization, a second active-passive transition is seen at a potential of 180 mV, with a critical current density for passivation of 0.3 A/m<sup>2</sup>. This passivation potential is higher than that for unimplanted copper (140 mV) on the corresponding sweep. However, the potentiokinetic polarization curves obtained for pure Ta in this environment (Figure 17) show that the metal exhibits an active-passive transition at 190 mV on the first positive-going sweep. The transition seen at 180 mV during the polarization of Ta-implanted copper therefore appears to be related to the formation of a Ta-based passive film. Surprisingly, the critical current density for passivation of the pure Ta is higher, at 0.4 A/m<sup>2</sup>, than that of Ta-implanted copper. Ta implantation produces no significant effect on the passive current density measured on the first sweep. The second positive-going sweep also shows significant improvements in the passivation behavior, compared to unimplanted copper. In addition, a further anodic peak, not seen on the first positive-going sweep, is observed at a potential of 110 mV and with a critical current density of 0.4 A/m<sup>2</sup>. The potential of this transition corresponds closely to that of the second active-passive transition on unimplanted copper and this peak probably also relates to the formation of Cu(II) compounds. Finally, a third active-passive transition is seen at 180 mV, with a critical current density of 0.15 A/m<sup>2</sup>. These parameters are the same as for the second active-passive transition recorded on the first positive-going sweep, which indicates that the peaks represent similar electrode reactions. The passive current density on Ta-implanted copper is 0.05 A/m<sup>2</sup>, compared to 0.09 A/m<sup>2</sup> on unimplanted copper.

The improvements in the passivation behavior of copper may be attributed, in part, to the presence of a Ta<sub>2</sub>O<sub>5</sub> film<sup>23</sup> on the implanted surface. RBS analyses indicated that only 12% of the implanted Ta was lost during the polarization tests. This result is consistent with appearance of the these polarized specimens which retained their polished finish. Comparison of the polarization data for unimplanted and Ta-implanted copper with that of pure Ta showed that of these three materials, Ta-implanted copper exhibits the best passivation behavior.

## Conclusions

1. TEM examinations of, and electron diffraction measurements on, Cr-, Ti- and Ta-implanted copper specimens show that these implant elements do not result in either phase transformation or second-phase precipitation; rather they exist as single-phase, metastable solid solutions in the copper substrate.
2. The potentiokinetic polarization data for Ar- and Cu-implanted copper show that such implantations produce no significant effects on the polarization behavior of copper. It may therefore be concluded that the ion implantation process itself has no significant influence on the passivation behavior of copper in this environment.

3. Implantation of the chemically active species Cr, Ti and Ta has significant beneficial effects on the passivation behavior of copper in this environment. These element-specific effects are attributed to the ease with which a passive film containing the implant species is formed, thereby facilitating the active-passive transitions.
4. The passivation behavior of Ta-implanted copper is superior to that of either pure copper or pure Ta in this solution. The data indicate that this superior behavior is due to the formation of a mixed Ta and Cu passivating phase which is more readily formed and more protective than the passive film on either pure copper or pure Ta.

**Acknowledgements:** The authors are indebted to the Science Research Council for financial support for this investigation and to D. J. Chivers of the A.E.R.E. Harwell for performing specimen implantations.

### References

1. V. Ashworth, W. A. Grant, R. P. M. Procter and T. C. Wellington, *Corros. Sci.*, 16, (1976), p. 661.
2. Y. Okabe, M. Iwaki, K. Hayashi, S. Namba and K. Yoshida, *Surf. Sci.*, 86, (1979), p. 257.
3. B. S. Covino, B. D. Sartwell, and P. B. Needham, *J. Electrochem. Soc.*, 125, (1978), p. 366.
4. A. H. Al-Saffar, V. Ashworth, W. A. Grant, and R. P. M. Procter, *Proc. Eurocorr. '77, Eur. Fed. Corros.*, (1977), p. 13.
5. V. Ashworth, W. A. Grant, A. R. Mohammed and R. P. M. Procter, *Proc. 7th. ICC, Brazil*, (1978).
6. C. R. Clayton, K. G. K. Doss, Y. F. Wang, and J. B. Warren, G. K. Hubler, *2nd Int. Conf. on Modification of the Surface Properties of Metals by Ion implantation*, Manchester, U. K. , (1981).
7. A. D. Street, M.Sc. Dissertation, University of Salford, U. K. , (1972).
8. J. K. Hirvonen, *J. Vac. Sci. Technol.*, 15, (1978), p. 1662.
9. B. L. Crowder and S. I. Tan, *IBM Tech. Disclos. Bull.*, 14, (1971), p. 198.
10. G. W. Kamlot, C. M. Preece, T. E. Graedel, J. P. Franey, and E. N. Staudinger, *Corros. Sci.*, 21., (1981), p. 541.
11. M. D. Tomashov, *Corros. Sci.*, Vol. 4, (1964), p. 315.
12. E. J. Wright, Ph.D., Thesis, UMIST, U. K. , October 1982.
13. G. Dearnaley, J. H. Freeman, R. S. Nelson and J. Stephen, *Ion Implantation*, North-Holland, 1973.
14. M. Hansen, *Constitution of Binary Alloys*, McGraw-Hill, New York (1958).
15. JCPDS, *Search Manual for Powder Diffraction Data*, 1st edition, JCPDS, U.S.A.
16. D. K. Sood and G. Dearnaley, *Inst. Phys. Conf. Ser. No. 28.*, (1976), p. 196.
17. J. A. Borders and J. M. Poate, *Phys. Rev. B.*, 13, (1976), p. 969.
18. J. S. Halliday, *Trans. Faraday. Soc.*, 50, (1954), p. 171
19. H. H. Strehblow and B. Titze, *Electrochim. Acta*, Vol. 25, (1980), p. 839.
20. E. Delmon, N. De Zoubov and M. Pourbaix, in, *Atlas of Electrochemical Equilibria*, Pergamon Press, Oxford, U. K. , (1966), p. 256.
21. J. Schmets, J. Van Muylder and M. Pourbaix, *ibid*, p. 213.

22. J. A. Petit, P. Lafargue, L. Porte and M. D. Tranh, *Electrochim. Acta*, 24, (1979), p. 1023.
23. J. Van Muylder and M. Pourbaix in, *Atlas of Electrochemical Equilibria*, Pergamon, U. K. , (1966), p. 251.

**TABLE 1**  
**COMPARISON OF THE THEORETICAL PREDICTIONS AND**  
**MEASURED DISTRIBUTIONS OF THE IMPLANT SPECIES.**

Implant	Mean Projected Range (nanometers)		Peak Concentration (atomic percent)		Surface Concentration (atomic percent)	
	Theoretical	Measured	Theoretical	Measured	Theoretical	Measured
Chromium	8	6	56	21	10	4
Titanium	8	6	50	19	15	9
Tantalum	5	5	70	22	8	8



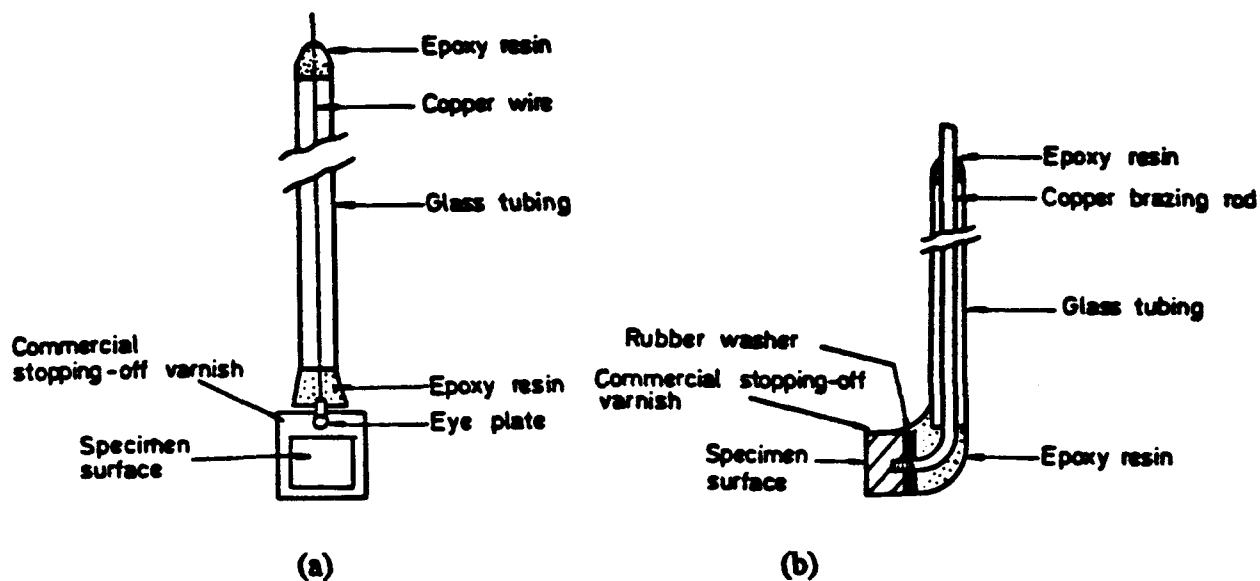


**Figure 1. Schematic diagrams of working electrode holders for, (a) copper specimens and, (b) pure metal (Cr, Ta) specimens.**

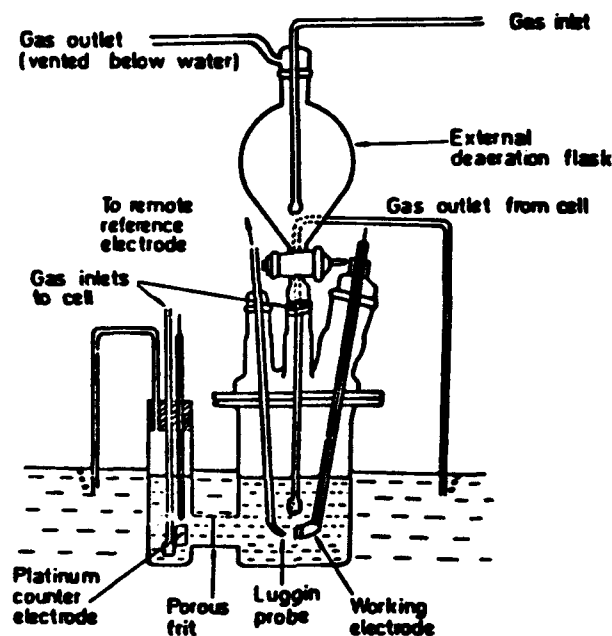


**Figure 2. Schematic diagram of electrochemical test cell and external deaeration flask.**

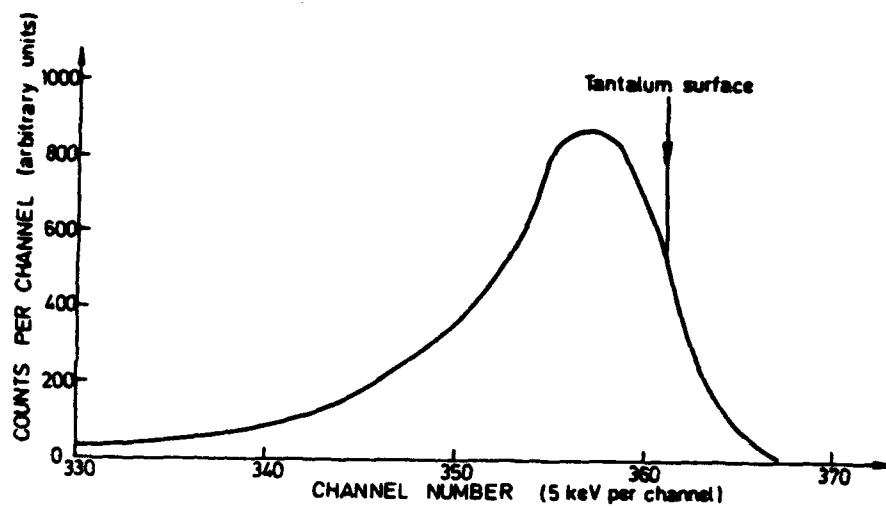


Figure 3. Rutherford Backscattering (RBS) data for Ta-implanted copper.

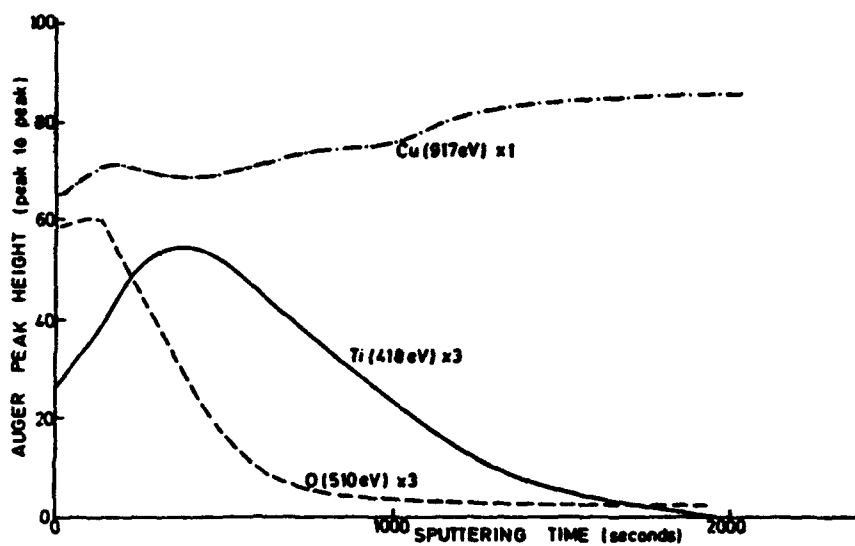
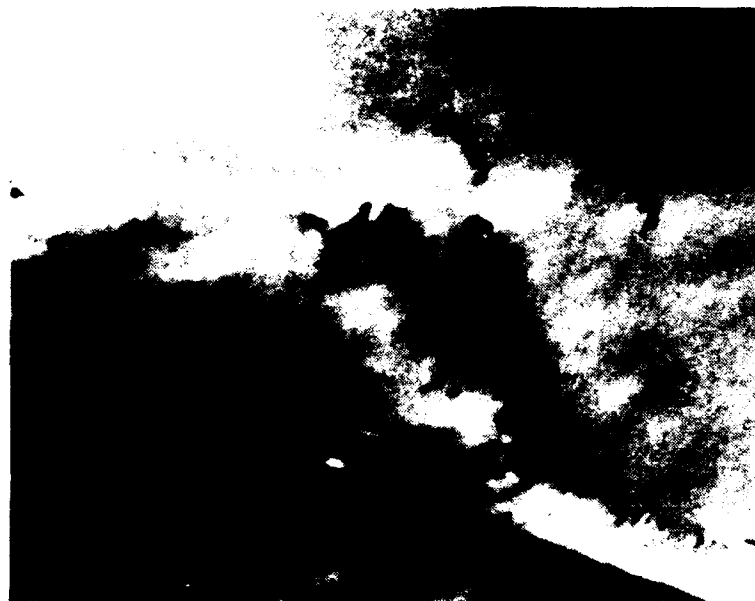
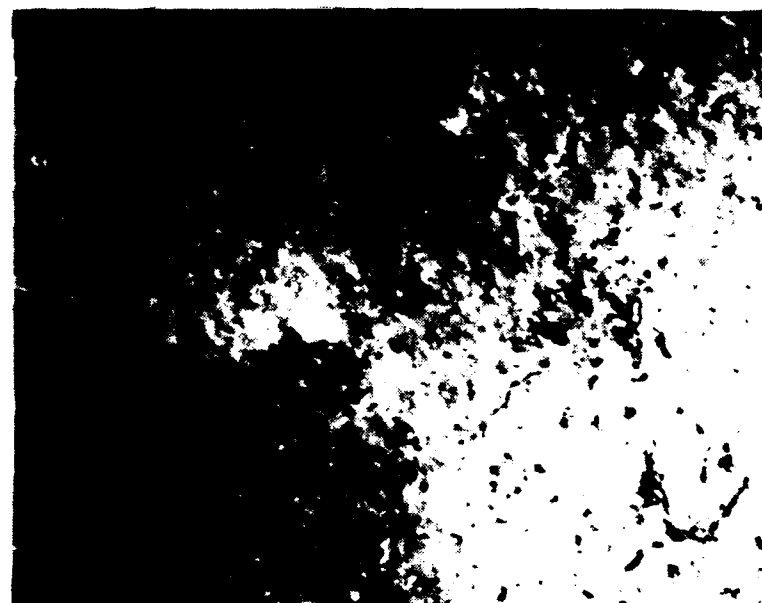


Figure 4. Auger peak heights (Cu, Ti and O) vs. sputtering time for Ti-implanted copper.



*Figure 5. Transmission electron micrograph for unimplanted copper showing a stacking fault with associated dislocations (Magnification = X 75K).*



*Figure 6. Transmission electron micrograph for Cu-implanted copper showing radiation damage typical of heavy ion implantation into a metal (Magnification = X 60K).*

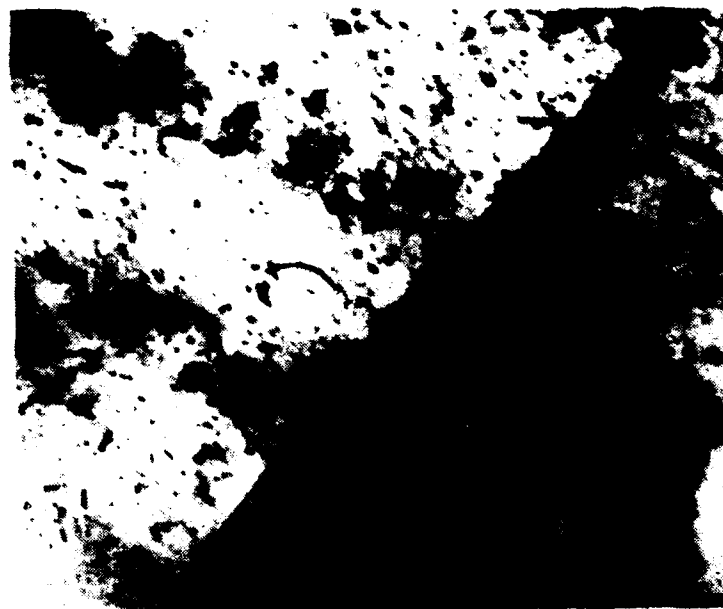


Figure 7. Transmission electron micrograph for Ta-implanted copper showing radiation damage but no evidence of precipitation of a second phase (Magnification = X 60K).

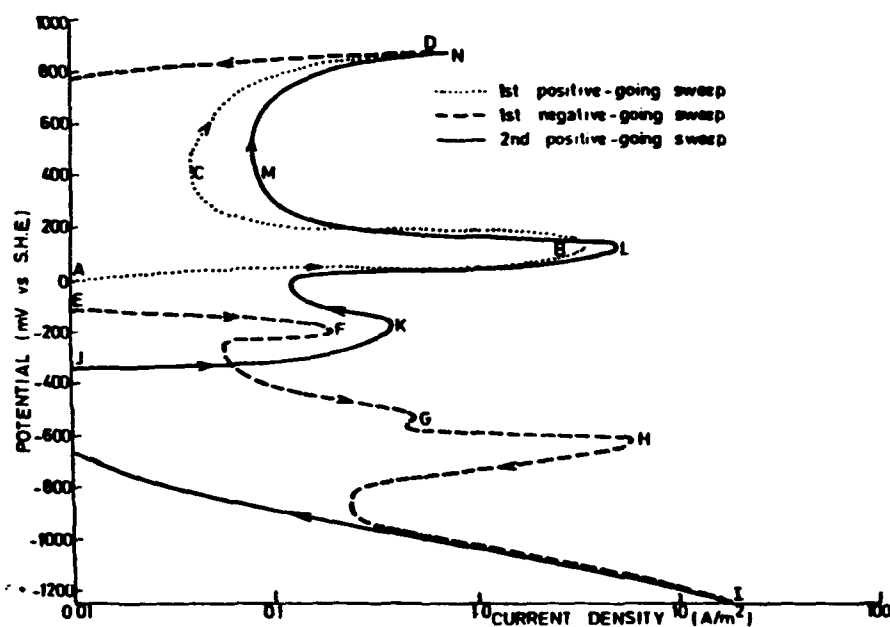
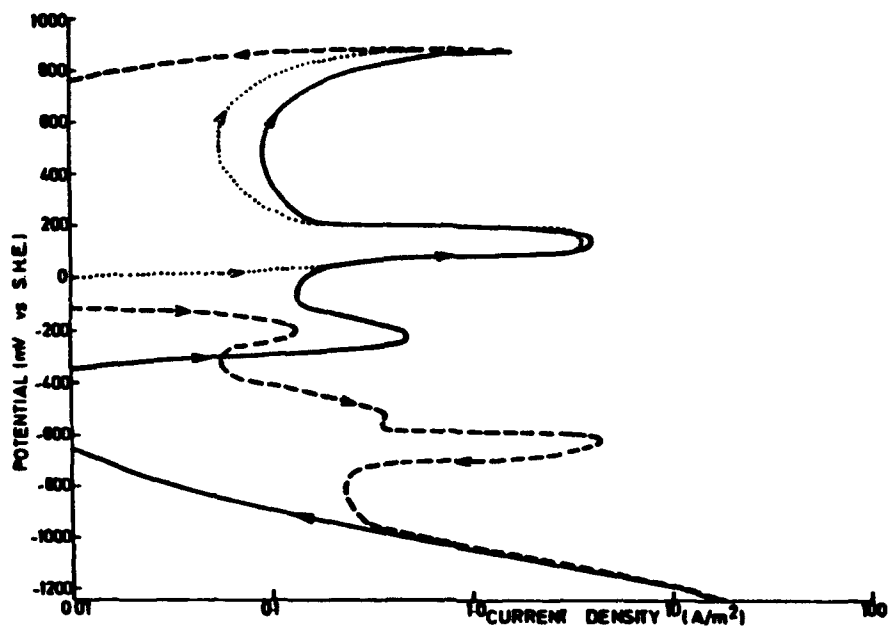
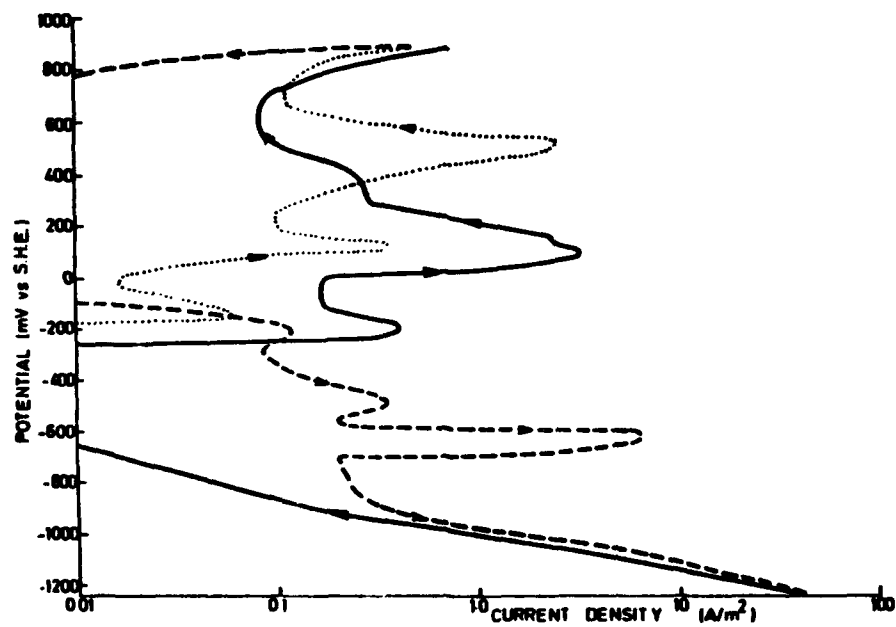


Figure 8. Potentiokinetic polarization curves of unimplanted copper in 0.01M sodium sulfate solution, pH adjusted to 12.4.



**Figure 9.** Potentiokinetic polarization curves of Cu-implanted copper in 0.01M sodium sulfate solution, pH adjusted to 12.4.



**Figure 10.** Potentiokinetic polarization curves of Cr-implanted copper in 0.01M sodium sulfate solution, pH adjusted to 12.4.

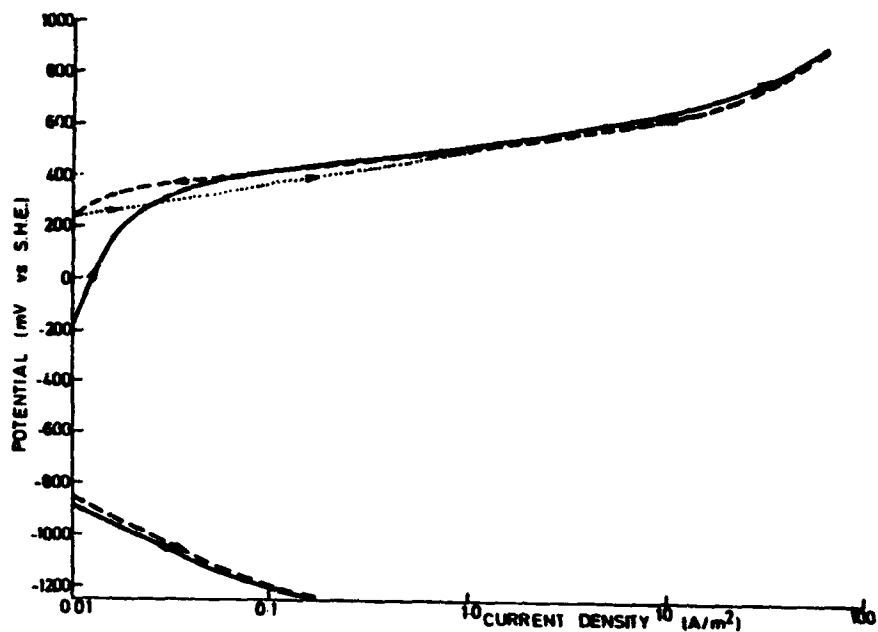


Figure 11. Potentiokinetic polarization curves of pure chromium in 0.01M sodium sulfate solution, pH adjusted to 12.4.

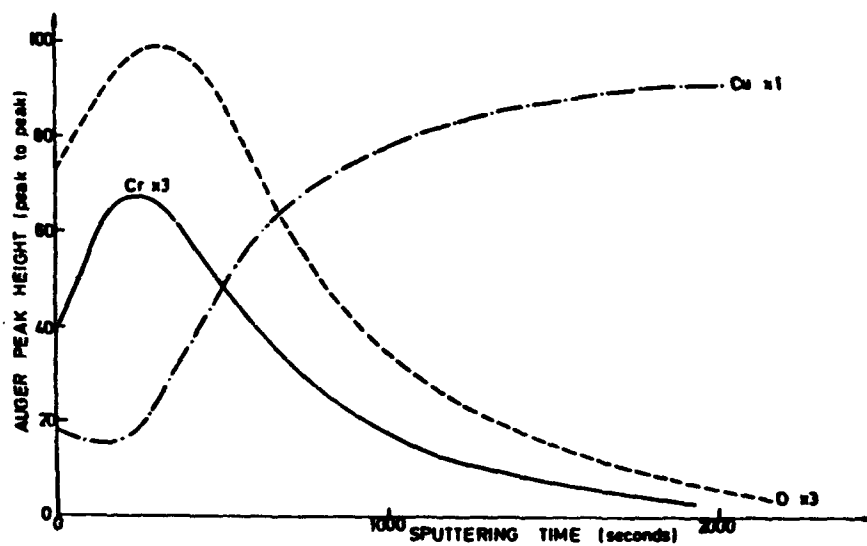
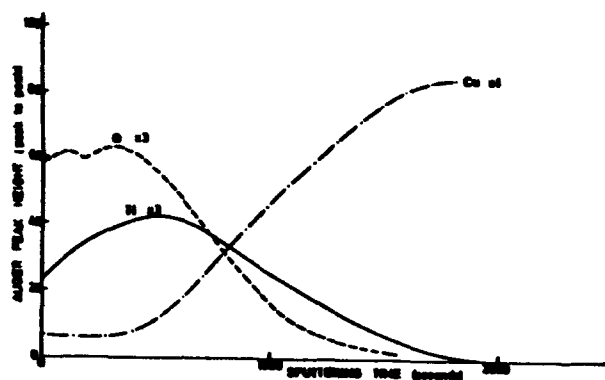
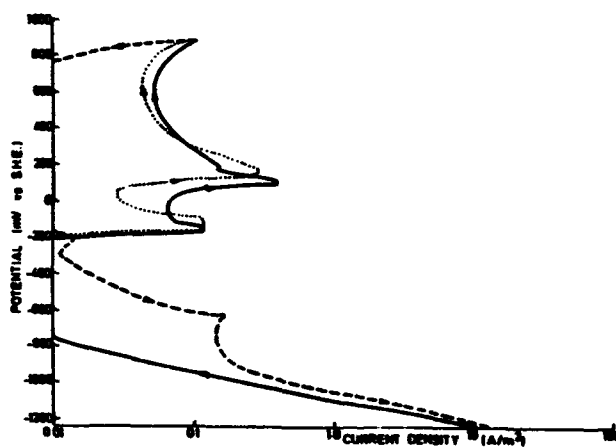


Figure 12. Auger peak heights (Cu, Cr and O) vs. sputtering time for Cr-implanted copper after polarization to 250 mV in 0.01M sodium sulfate solution, pH adjusted to 12.4.



**Figure 15.** Auger peak heights (Cu, Ti and O) vs. sputtering time for Ti-implanted copper after complete polarization test in 0.01M sodium sulfate solution, pH adjusted to 12.4.



**Figure 16.** Potentiokinetic polarization curves of Ta-implanted copper in 0.01M sodium sulfate solution, pH adjusted to 12.4.

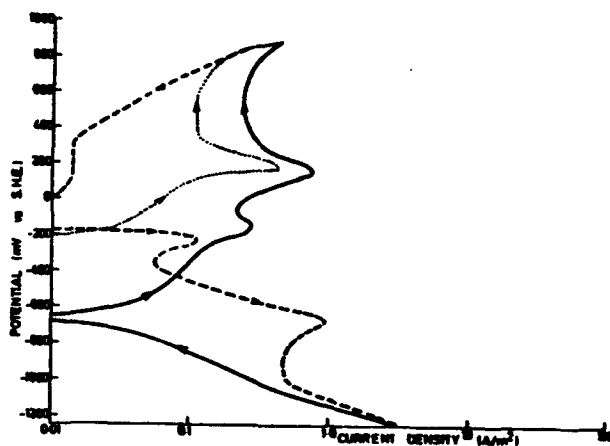


**Figure 17.** Potentiokinetic polarization curves of pure tantalum in 0.01M sodium sulfate solution, pH adjusted to 12.4.

Effect of oxygen-containing oxidizers on the Fe, Cu and Sn  
dissolution rates in acidic sulphate electrolytes

Natalya Chebotaryova  
The Institute of Physical Chemistry  
Russian Academy of Sciences  
31 Leninsky pr., Moscow  
117915 Russia

Andrey Marshakov  
The Institute of Physical Chemistry  
Russian Academy of Sciences  
31 Leninsky pr., Moscow  
117915 Russia

Vasiliy Ignatenko  
The Institute of Physical Chemistry  
Russian Academy of Sciences  
31 Leninsky pr., Moscow  
117915 Russia

Yuriy Mikhailovsky  
The Institute of Physical Chemistry  
Russian Academy of Sciences  
31 Lenin sky pr., Moscow  
117915 Russia

Abstract

The influence of hydrogen peroxide, nitrite and nitrate ions on the corrosion behavior of iron, copper and tin has been studied. Introducing these oxidizers (Ox) into solution was found to accelerate the anodic dissolution reaction on the metals. The relationship between the oxidizer concentration and the metal dissolution rate is established. In the presence of oxygen-containing Ox the anodic and cathodic reactions are shown to be interrelated: the intermediate products of oxidizer reduction are able to participate in metal dissolution process.

Key terms: dissolution rate, oxidizer, iron, copper, tin

Introduction

Oxygen and oxygen-containing oxidizers, such as hydrogen peroxide, nitrite and nitrate ions, play an essential role in the processes of metal corrosion in environment. To our knowledge the effect of oxidizers is not limited by only the depolarizing action, and they have some specific effect on the metal dissolution kinetics. There are several explanations of this specific effect of oxidizers, however, most works did not take into account the effect of intermediate reduction products on the metal dissolution process; although, it is well-known that reduction of oxidizers may result in the formation of ions which increase the metal corrosion.



The aim of our investigations is to study the corrosion behaviour of the technically important metals (Fe, Cu, Sn) in the presence of oxygen-containing oxidizers and to elucidate the role of their reduction products in the processes of metal destruction in oxidizing media.

### Experimental

The corrosion studies were carried out on static samples of metal foils in 1N Na<sub>2</sub>SO<sub>4</sub> (pH 2) and 0,01N H<sub>2</sub>SO<sub>4</sub> solutions in the presence of H<sub>2</sub>O<sub>2</sub>, NaNO<sub>2</sub> and NaNO<sub>3</sub> additions at room temperature and with free access of air. Polarization curves (1 mV.s<sup>-1</sup>) were measured on rotating disk electrodes under the deaerated conditions. The dissolution rates were determined by gravimetric and colorimetric methods.

### Results and discussion

In terms of generally accepted electrochemical concepts, active dissolution of a number of metals occurs via the stage of interaction of the metal surface with hydroxyl ions resulting from dissociative adsorption of water molecules



As the reduction of oxygen-containing oxidizers occurs with the participation of hydrogen ions the increasing oxidizer concentration should result in diffusion limitations on H<sub>3</sub>O<sup>+</sup> ions and a decrease in their concentration in the near electrode layer of solution. When some "critical" concentration is reached, at which the consumption rate of hydrogen ions becomes equal to their diffusion rate to the metal surface, the pH value of the electrode layer increases abruptly [1]. The value of the critical concentration is determined according a stoichiometric diffusion equation:

$$C_{\text{ox},c} = D_{\text{H}^+} \cdot C_{\text{H}^+}^0 \cdot (p \cdot D_{\text{ox}})^{-1} \quad (2)$$

where  $D_{\text{H}^+}$ ,  $D_{\text{ox}}$  - diffusion coefficients of hydrogen ions and oxidizer respectively;  $p$  - number of H<sub>3</sub>O<sup>+</sup> ions in the reaction of oxidizer reduction.

The relation of electrode pH with the oxidizer concentration determines the dependence of the metal dissolution rate ( $i_a^1$ ) on the content of the oxidizer in a corrosion medium:

$$i_a^1 = C_{\text{ox},c} \cdot (C_{\text{ox},c} - C_{\text{ox}})^{-1} \cdot i_a^0 \quad (3)$$

where  $i_a^0$  - dissolution rate in base solution. This dependence is in the form of a hyperbola, and a maximum increase in the dissolution rate should be observed at a critical oxidizer concentration. However, oxygen-containing oxidizers were shown to be capable of increasing the metal dissolution rate even if their concentration is lower than the critical values [2-4].

To explain the accelerating effect of oxygen-containing Ox on the iron dissolution the reduction reaction in acids was

assumed to occur in two stages:



Reaction (4) forms on the metal surface the adsorbed hydroxyl ions, which can either interact with iron according to reaction



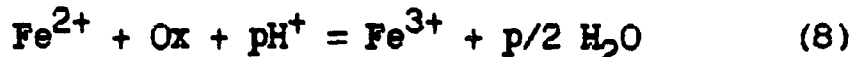
or be neutralized by reaction (5). It was established that the increase in the corrosion current on iron is equal to the diffusion flow of the oxidizer.

Thus, there are two reasons for the accelerating effect of the oxidizer on the metal dissolution rate: first, alkalification of the electrode layer of solution; second, the formation of anodic active particles during cathodic reduction. In the former case, the dependence of the dissolution rate on the oxidizer concentration at a constant potential should be hyperbolic (eq.(3)), in the second case, it is linear:

$$i_a^2 = \text{const } \gamma C_{\text{ox}} \quad (7)$$

where  $\gamma = n/m$ . If both factors act simultaneously, the total dependence may be a superposition of hyperbola and straight line.

In dependence on the nature of the oxidizer and the mechanism of metal dissolution one of these two factors is determining. As soon as the ions of intermediate valence are formed in the process of iron dissolution, they may react with oxidizer in the solution:

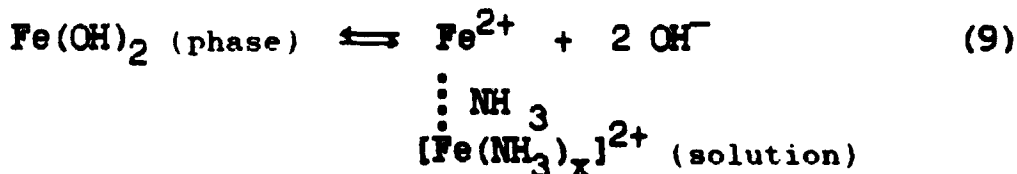


Reaction (8) results in a decrease in the concentration of the oxygen-containing oxidizer in the diffusion layer, and under specific conditions the oxidizer does not reach the metal surface at all. However, chemical reduction of oxidizer leads to alkalification of the electrode layer of solution, and the dependence of the dissolution rate on the oxidizer concentration is hyperbolic. This case takes place during iron dissolution in a instirred electrolyte, containing hydrogen peroxide (Fig.1).

In an intensively stirred solution, the diffusion rate of molecules of  $\text{H}_2\text{O}_2$  becomes higher than that of the chemical reaction; therefore, hydrogen peroxide is reduced on the electrode to form anodic active particles. The accelerating effect of the oxidizer in this case is much larger, and the change in the dissolution rate with the oxidizer concentration is described by the superposition of the hyperbola and the straight line (Fig.1, curve 1).

In the case of amphoteric metal, like tin, able to dissolve in alkaline media to form  $\text{HSnO}_2^-$  anions, the acceleration effect is observed at the oxidizer concentration above the critical value (Fig.2).

The effect of nitrite and nitrate on Fe corrosion follows general regularities typical of other oxygen-containing oxidizers. The experimental and calculated results are in satisfactory agreement too. A distinguishing feature of nitrogen oxocompounds is formation of ammonia during their reduction. Ammonia forms complexes with iron ions and, consequently, it may dissolve hydroxide iron compounds.



Therefore, the accelerating effect of nitrite and nitrate in the concentration range higher than the critical value appears to be stronger than that of hydrogen peroxide. This effect is most prominent at cathodic potentials (Fig. 3). The effect of ammonia on the iron corrosion rate may be confirmed by the following experiment. If an ammonium sulfate solution is used as a background electrolyte, then at supercritical concentrations the stimulating effect of hydrogen peroxide is the same as that of nitrite. This is due to the fact that the reduction of  $\text{H}_2\text{O}_2$  leads to alkalification of the solution diffusion layer, and the ammonium ions in this layer are converted to ammonia molecules.

The accelerating effect of oxygen-containing Ox on Fe corrosion decreases with elevating ionic strength of the sulphate solution [5]. This is connected to the substitution of more anodic active particles -  $\text{OH}^-$ -ions for less active  $\text{SO}_4^{2-}$ -ions.

If increasing the metal corrosion rate is a result of the joint action of several anodic active particles, the effect of sulphate concentration may be an alternative one. The influence of oxygen-containing oxidizers on the corrosion behaviour of copper was investigated in solutions with different sulphate concentration.

The introduction of nitrate into the concentrated sulphate solution does not increase the dissolution rate of Cu because the reduction of  $\text{NO}_3^-$ -ion is impossible at the corrosion potential (Fig.4, curve 2). The marked dissolution of copper is observed in the presence of  $\text{HNO}_2$  (Fig.5). The corrosion rate of Cu is then determined by the reduction current of the oxidizer.

As the concentration of nitrite in 1N  $\text{Na}_2\text{SO}_4$  increases, an increase in the Cu corrosion rate takes place (Fig.5, curve 1). During the course of the corrosion tests the solutions having a high content of nitrite turned from green to dark blue on neutralization of the solution. This effect is assumed to be connected to the formation of a complex compound as a result of copper corrosion. This compound is stable only in acidic media and becomes an aquocomplex when the pH is increased.

Moreover, in a concentrated sulphate solution the proportional increase in corrosion is observed only to critical nitrite concentration accounted for the reduction of  $\text{HNO}_2$  to  $\text{NO}$  ( $C_{\text{ox},c} = 8,4 \cdot 10^{-2} \text{N}$ ) (Fig.5, curve 1). This is a proof of the prevailing reduction of nitrous acid on copper to nitrogen oxide in a concentrated sulphate solutions.

In dilute sulphuric acid the copper corrosion rate decreases at much lower concentrations (Fig.5, curve 2). In the latter case, a layer of insoluble corrosion products is formed on the electrode. In the absence of sulphate ions the similar corrosion behaviour of copper is observed (Fig.5, curve 3).

$E_{\text{cor}} - \lg i_{\text{cor}}$  plots from the values of the current and corrosion potentials at different concentration of the oxidizer were constructed (Fig.6). These plots point to the activation of the anodic process in the presence of nitrous acid in a concentrated sulphate solution (Fig.6, curve 2). In dilute sulphate solution the shift of corrosion potential to more positive values is observed with increasing nitrite concentration due to surface passivation of copper by the corrosion products (Fig.6, curve 2').

The introducing hydrogen peroxide into concentrated solution leads to acceleration of copper dissolution too. However, in such a case the stimulating effect of  $\text{Ox}$  is much weaker (Fig.6, curve 3). The stronger accelerating action of nitric acid in comparison with  $\text{H}_2\text{O}_2$  may be related to the formation of  $\text{NO}$  as a main product of the oxidizer reduction.

In acidic sulphate media  $\text{NO}$  is known to give copper nitrous sulphate  $[\text{Cu}(\text{NO})\text{SO}_4]$ , in which the oxide is in the form of a neutral molecule. We have obtained a nitrous sulphate copper complex in the bulk of the solution. This had a green, changing to a blue colour on neutralization, and developed at the working electrolyte during copper corrosion in the presence of nitrite.

Taking into account the participation of the  $\text{SO}_4^{2-}$ -ion in the copper ionization and the mechanism of  $\text{Cu}$  dissolution in acidic sulphate solutions via formation of the surface complex  $(\text{CuSO}_4)_{\text{ads}}$  as suggested in [6], one may assume that in the presence of nitrous acid the copper dissolution occurs via formation of the nitrous surface complex  $[\text{Cu}(\text{NO})\text{SO}_4]_{\text{ads}}$ . This obviously has a lower instability constant than the sulphate complex and shows weak dissociation on approaching the near electrode layer of the solution.

The accelerating effect of  $\text{HNO}_2$  is assume to be connected to the participation of the anodic active particle in the dissolution process. To prove this assumption corrosion tests were conducted in a concentrated sulphate solution saturated

with gaseous nitrogen oxide. The introduction of NO into the sulphate electrolyte is shown to increase the copper corrosion rate by more than an order of magnitude (Fig.6, point 4). The result obtained indicates that it is, in fact, the nitrogen oxide molecule that is the anodic active particle in the Cu corrosion process.

Obviously, the bonding of nitrogen oxide into a nitrous sulphate complex makes its further reduction more difficult at the copper corrosion potential in the medium studied. In this case, the first wave in the cathodic polarization curve (Fig.4, curve 3) evidently corresponds to the reduction of nitrous acid to NO and NH<sub>3</sub>, and the second one to the reduction of bonded nitrogen oxide to ammonia.

The metal corrosion may occur both in the process of dissolution and the hydride compound formation on the metal surface. Sn is known to undergo the corrosion destruction under the strong cathodic polarization when its gaseous hydride may be formed [7]. The influence of oxygen-containing Ox on tin corrosion was investigated too.

Three characteristic parts are observed on the cathodic polarization curve of tin in the presence of 1.10<sup>-2</sup>N NaNO<sub>2</sub> (Fig.7, curve 2). The first part of the current growth corresponds to the Ox reduction reaction; the second - to the hydrogen cathodic evolution. On the third part the cathodic current decreases sharply, and in the range -1,2 V > E > -1,4 V the current becomes anodic (I = +0,2 A/m<sup>2</sup>) (Fig.7, curve 2). After recording the cathodic curve the electrode surface is greatly etched, and solid particles, probably, those of tin oxide or hydroxide are observed in the solution.

The similar effect is obtained in the presence of nitrate addition. In the case of hydrogen peroxide the ordinary shape of the cathodic curve is registered (Fig.7, curves 3,4). Moreover, in the nitrite- and nitrate-containing electrolytes at the potentials more negative than -1,2 V the tin corrosion rate is much higher than its dissolution rate at the currentless potential.

The tin corrosion destruction observed during a strong cathodic polarization is not related to the "cathodic sputtering" by the implantation of alkaline metal into the electrode [8], because the substitution of NH<sub>4</sub><sup>+</sup> for Na<sup>+</sup> doesn't affect the result.

From the standard potential values of the tin ionization reactions it follows that in the electrolyte with pH 2 in the potential range investigated the transition of the Sn(2+) and Sn(4+) ions to the solution is thermodynamically impossible. In accordance with the Pourbaix diagram for Sn [9] under the giving conditions the tin hydride (stannomethane) formation is possible in terms of the following reaction:



The equilibrium potential of this process is equal to:

$$E_{eq} = -1,074 - 0,059pH - 0,015 \lg P_{SnH_4}, \quad (11)$$

i.e. in the solution with pH 2 the reaction discussed becomes possible only at  $E < -1,2$  V. However, in the background electrolyte no decrease in the cathodic current (fig.9, curve 1) and in the electrode mass is observed over the potential range examined. According to [7] the formation of  $SnH_4$  only occurs in the region of water reduction, i.e. at  $E < -1,6$  V.

One may suggest that a proton donor stronger than the  $H_3O^+$ -ion or the water molecule takes part in the reaction of tin hydride formation. To our knowledge the only nitrite reduction product on Sn is the  $NH_4^+$ -ion. In the absence of an oxidizer the introducing ammonia into the electrolyte doesn't result in the corrosion losses of tin at high cathodic potentials. Therefore, in the stannomethane formation process the proton donor is assumed to be the intermediate product of the reduction of the nitrogen-containing Ox.

The  $\cdot NH$ -radical forming by the nitrate and nitrite reduction [10] may be supposed to act as a proton donor in the reaction discussed. In this case the equilibrium potential and the rate of the hydride formation become the function of near electrode donor concentration and not of the volume pH of the solution. The surface donor concentration should be determined by the oxidizer reduction rate. The increase in its concentration is expected to result in an increase in the rate of  $SnH_4$  formation and in a greater decrease in the electrode mass. This assumption is confirmed by the experiment.

#### References

1. A.I.Marshakov, O.V.Batisheva, Yu.N.Mikhailovsky, Protection of Metals, 25 6(1989): p.888.
2. Yu.N.Mikhailovsky, V.M.Popova, Protection of Metals, 17 4(1981): p.392; 19 4(1983): p.526; 20 2(1984): p.204.
3. Yu.N.Mikhailovsky, N.B.Lukina, Protection of Metals, 22 5(1986): p.629.
4. A.I.Marshakov, Yu.N.Mikhailovsky, V.M.Popova, Protection of Metals, 22 6(1986): p.922.
5. Yu.N.Mikhailovsky, N.A.Sokolov, Protection of Metals, 21 2(1985): p.214.
6. V.K.Altukhov, I.K.Marshakov, E.S.Vorontsov, T.N.Klepinina, Electrochemistry, 12 1(1976): p.88.
7. H.W.Salzberg, F.Mies, J.Electrochem.Soc., 105 2(1958): p.64.
8. B.N.Kabanov, I.I.Astakhov, I.G.Kiselyova, Uspekhi Khimii (rus.), 34 10(1965): s.1814.
9. M. Pourbaix, Atlas d'Equilibres Electrochimiques, (Paris, 1963), p.476.
10. V.P.Razygraev, R.S.Balovneva, E.Yu.Ponomaryova, M.V.Lebedeva, Protection of Metals, 21 1(1990): p.54.

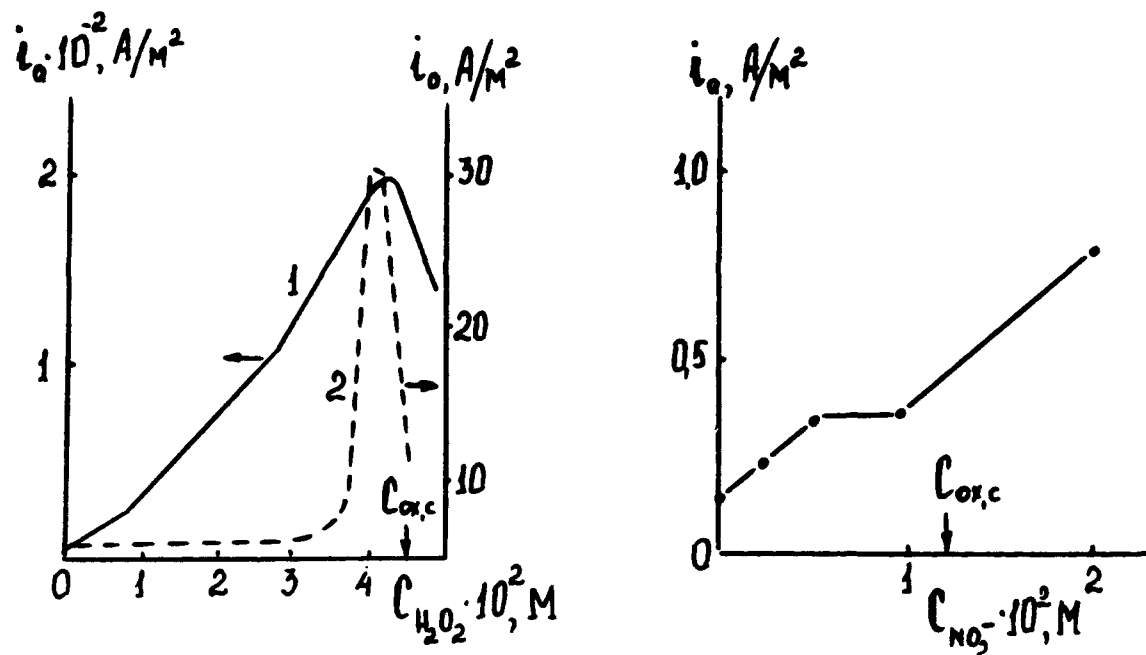


Fig.1. Dependences of dissolution rate of iron on  $H_2O_2$  concentration in stirred (1) and instirred (2) 1N  $Na_2SO_4$  (pH 2) solution at  $E = -0,35$  V.

Fig.2. Dependences of dissolution current density of Sn on nitrite concentration in 1N  $Na_2SO_4$  (pH 2) at  $E = -0,27$  V.

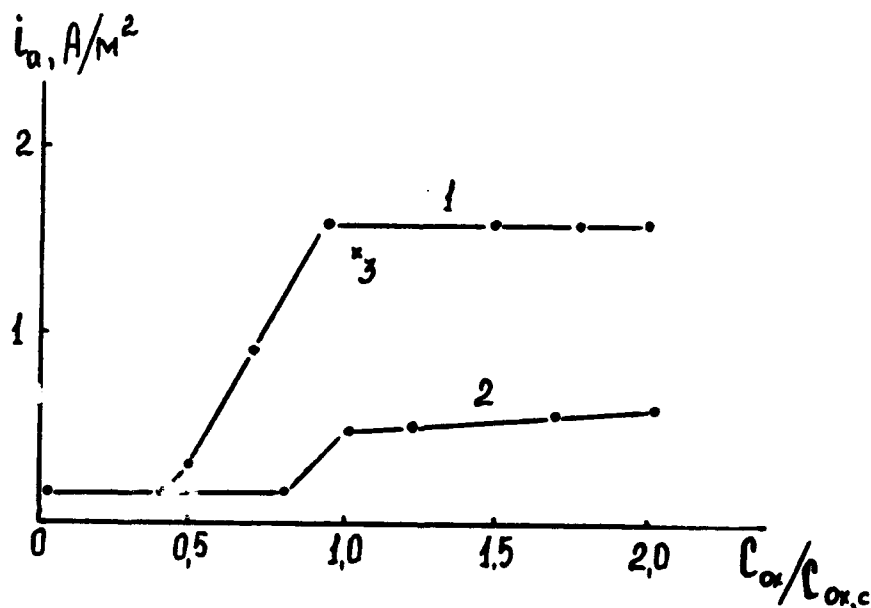


Fig.3. Dissolution rate of iron vs. the value of the ratio  $C_{ox}/C_{ox,c}$  in 1N  $Na_2SO_4$  (pH 2) at  $E = -0,5$  V in the presence of Ox: 1 -  $NaNO_3$ ; 2 -  $H_2O_2$ ; 3 -  $H_2O_2 + 0,01N (NH_4)_2SO_4$ .

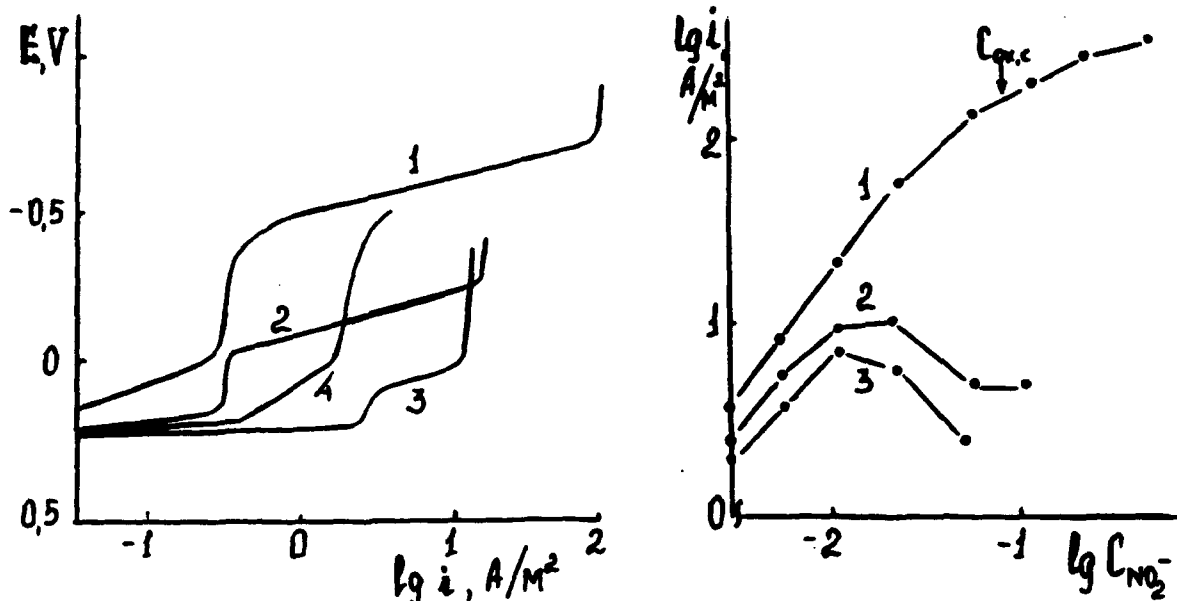


Fig.4. Cathodic polarization curves of Cu in 1N  $\text{Na}_2\text{SO}_4$  (pH 2) solution (1) and in the presence of 0,01N Ox: 2 -  $\text{NaNO}_3$ ; 3 -  $\text{NaNO}_2$ ; 4 -  $\text{H}_2\text{O}_2$ .

Fig.5. Dependences of corrosion current density of Cu on  $\text{NaNO}_2$  concentration in 1N  $\text{Na}_2\text{SO}_4$  (pH 2) (1), 0,01N  $\text{H}_2\text{SO}_4$  (2) and 0,01N  $\text{HNO}_3$  (3).

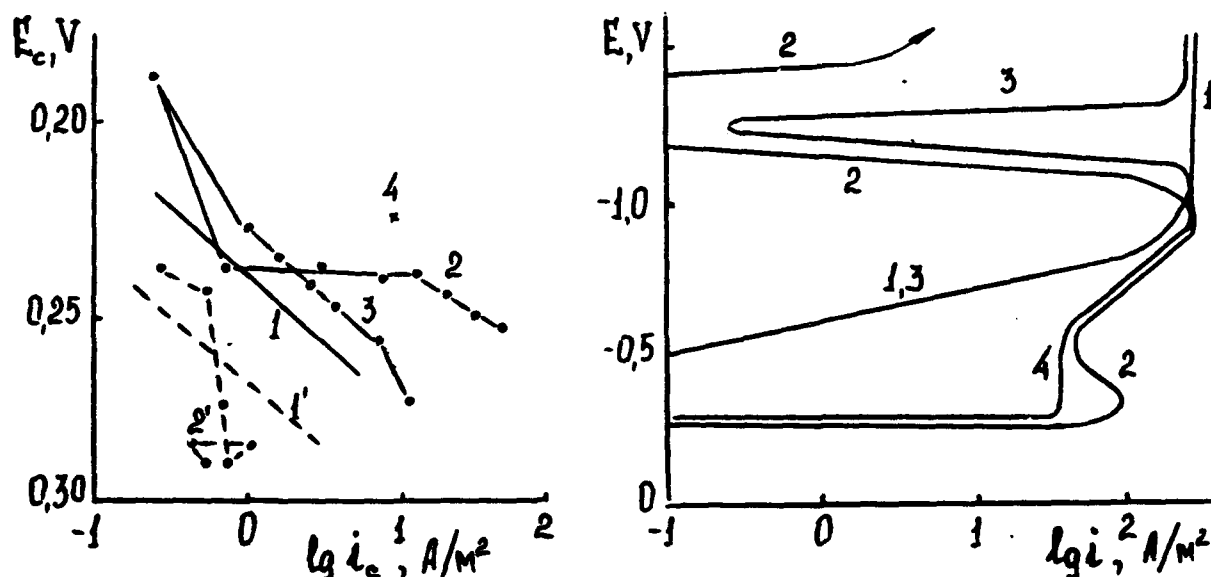


Fig.6. Dependences of corrosion current on corrosion potential of Cu in 1N  $\text{Na}_2\text{SO}_4$  (pH 2) (1-4) and 0,01N  $\text{H}_2\text{SO}_4$  (1',2') with  $\text{NaNO}_2$  (2,2'),  $\text{H}_2\text{O}_2$  (3) and gaseous NO (4) additions. 1,1' - anodic polarization curves.

Fig.7. Cathodic polarization curves of Sn in 1N  $\text{Na}_2\text{SO}_4$  (pH 2) solution (1) and in presence of 0,01N Ox: 2 -  $\text{NaNO}_2$ ; 3 -  $\text{NaNO}_3$ ; 4 -  $\text{H}_2\text{O}_2$ .



## KINETIC STUDY OF THE $\text{PbSO}_4$ REDUCTION ON LEAD USING THE HOPPING MOTION MODEL

C.V. D'Alkaine

Group of Electrochemistry and Polymers

C.P. 876 - DQ/UFSCar - 13585-905 São Carlos (SP)  
BRAZIL

L.M.M. de Souza

Group of Electrochemistry and Polymers

C.P. 876 - DQ/UFSCar - 13585-905 São Carlos (SP)  
BRAZIL

### ABSTRACT

The reduction of  $\text{PbSO}_4$  to Pb using voltammetry can be understood as a solid state reaction of a continuous film and does not present the nucleation phenomena like other techniques seems to point out.

The result are in agreemen with the Hopping-Motion model for the current density/overpotential through the film and with a Tafel description for the metal/film interface.

Key terms: Hopping Motion model, lead sulphate reduction, passivity.

### I. Introduction

The litterature of the  $\text{Pb/PbSO}_4$ ,  $\text{H}_2\text{SO}_4$  system have been fundamentally related with its oxidation process [1-10]. The reduction process has not received an equivalent attention [11-15].

In the Hampson and co-workers [11-13] papers they propose that the mechanism for the reduction of the  $\text{PbSO}_4$  film for a potentiostatic pulse condition is an instantaneous 2D nucleation and growth process. They show also that the process is independent of the stirring conditions. Their  $i/i_m$  vs  $t/t_m$  representation does not seem to follow the proposed mechanism (where  $i_m$  and  $t_m$  are the coordinates of the maximum in the transient).

Fleming and Harrison [14] point out that the reduction charge corresponds to only few monolayers but at the same time consider that a 2D mechanism is not in agreement with the data principally due to the long tail which has been atributed by Hampson et al. [13] to the hydrogen evolution taken into account that the reduction charge is higher than the oxidation one.

Varela et al. [15] propose an instantaneous 3D mechanism even when the representation of  $i/i_m$  vs  $t/t_m$  another time is higher than the theoretical one except, of course, for values near  $i/i_m$  equal one. They also point out that a parallel potential dependent reaction must take place, due to the fact that  $i$  vs  $t^{1/2}$ , at short times, does not extrapolate to zero, in a agreement with reference [13].

From all these papers the actual description of the reduction of the  $PbSO_4$  to Pb, when analysed through potentiostatic step transients seems to be controlled by a nucleation and growth mechanism even when this is an extrange description due to the fact that we are looking to the reduction of  $PbSO_4$  to Pb on Pb.

In the present paper the voltammetric reduction of Pb/ $PbSO_4$ ,  $H_2SO_4$  system will be analysed. For this, first of all the technique proposed by Fletcher [16] will be use to stablish if in this condition the nucleation and growth mechanism is working or not and then a general theoretical approach previously developed [17] will be used.

## II. Experimental

The working electrode was a 99.9998% Pb cylinder mounted inside a Pyrex® glass tube with epoxy resin, which has an exposed geometrical area of  $0.18 \text{ cm}^2$ . A Pt wire was used as auxiliary electrode and the reference electrode was Hg/ $Hg_2SO_4$ , 4.6 M  $H_2SO_4$  to which all the potentials are referred. An aqueous 4.6M  $H_2SO_4$  solution was used as electrolyte. Pure nitrogen was passed through the cell to remove oxygen from the solution. The working temperature was always  $25^\circ\text{C} \pm 0.1^\circ\text{C}$ .

The reproducibility of the measurements was possible only when the electrode was kept under vacuum to inhibit the growth of oxide layers during the periods in which it was not used. Before each measurement the electrode was mechanically polished up to 600 emery paper. Then it was rinsed in triply distilled water, dried whith a soft paper and then introduced into the cell under cathodic polarization at the initial potential  $E_i$  ( $-1.2 \text{ V}$ ). Then the electrode was swept at  $v = 10 \text{ mV/s}$  up to the growing potential ( $E_g$ ) of  $-0.89 \text{ V}$  where it was maintained up to the passage of a total charge of  $41 \text{ mC/cm}^2$ . At this moment the cathodic sweep, each time at a different sweep velocity, was initiated. Typical cathodic curves are shown in Figure 1.

## III. Results and Discussions

From Figure 2 it is possible to see that under the voltammetric conditions there is no nucleation and growth because during the cathodic sweep, when it was reversed the voltammetry at different potentials ( $E_\lambda$ ), the cathodic current was never

higher in the reverse direction. As Fletcher has pointed out [16] this is a demonstration that there is no nucleus formation and overlapping. Then it is possible to consider that a model for the reduction of a continuous  $\text{PbSO}_4$  film on Pb can be applied. To do this, it is necessary to consider one of the possible models for the current density-overpotential relation inside the film. In the present case it will be used the hopping motion model. On these bases a special equation for the peak conditions must be followed [17]

$$\ln i_p = \frac{\alpha_f f a r v}{C i_p} + \ln i_f^0 \quad (1)$$

where  $\alpha_f$ ,  $a$  and  $C$  are the transfer coefficient, jump distance and volume per unit charge of the film, respectively;  $r$  is the roughness factor of the surface;  $f = F/RT$  and  $i_p$  and  $i_f^0$  the peak and exchange current densities inside the film. One useful criteria to know when all the parameters of eq. (1) are constant (because they could be changing) it is to follow the variation of the peak charge density ( $q_p$ ) with  $v$ . Due to the fact that we are looking to a reduction peak, then the charge density which is more convenient to follow is the cathodic remanent charge up to the peak ( $q_{p,rem}^c$ ). This charge can be calculated from

$$q_{p,rem}^c = q_f^c - q_p^c \quad (2)$$

where  $q_p^c$  is the cathodic charge density up to the peak potential and  $q_f^c$  is the total cathodic peak charge density of the peak, calculated up to the potential corresponding to the minimum of current density between the peak and the hydrogen evolution (Figure 1). On Figure 3 it is possible to see this result for the present system. This charge becomes linear at  $v$  equal or higher than 150 mV/s. Then it must be expected that eq. (1) becomes valid for this region of sweep velocities.

In Figure 4 the experimental results for eq. (1) are represented and it is possible to see that the constancy of the parameters becomes observed for the high sweep velocities as was expected.

The departure of linearity in Figure 4, at slow velocities must be attributed to a change in  $i_f^0$  because the value of  $\alpha_f a r / C$  (even when we consider different films) can not account for this departure. This is in agreement with the fact that at slow sweep velocities the aging at the peak conditions must be more pronounced. Actually when in Figure 3 the charge becomes constant it must be considered as if the sweep velocity and then the growth velocity of the film have become higher than the aging phenomena and then, the  $i_f^0$  has become constant. The value of  $i_f^0$  for the present system was  $8.3 \text{ mA/cm}^2$ . If all these ideas are correct, then from the slope of the linear region of

Figure 4 it is possible to calculate a reasonable value for the "a" parameter. If we use a C value of  $2.53 \times 10^{-5} \text{ cm}^3/\text{C}$  calculated from the molecular weight and the density of the  $\text{PbSO}_4$ , and a transfer coefficient inside the film of 1 (due to the fact that the jumping ions must be  $\text{Pb}^{2+}$  and/or  $\text{SO}_4^{2-}$  and must be considered a symmetrical barrier), it is obtained an "a" value of 1.2 nm. As the lattice parameter for the crystalline  $\text{PbSO}_4$  give between 0.43 and 0.21 nm, these means an average roughness factor of 4 for the polishing of lead in the analysed conditions, which is a quite reasonable value.

If the overpotential through the  $\text{PbSO}_4$  film ( $\eta_f$ ) is substracted from the total potential, we are able to obtain the current density against the potential at the metal/film interface (like a correction for the ohmic drop inside the film). This result must give rise to a normal Tafel plot for the solid state reaction of  $\text{Pb}^{2+}$  reduction, when the inverse reaction could be disregarded. This calculation could be made at the peak potential ( $E_p$ ) conditions because it is possible to show [17] that

$$\eta_{f,p} = \frac{v}{i_p} \ln \frac{q_p}{p} \quad (3)$$

where the p index point out the peak potential conditions. For the present case (a reduction case), at the  $E_p$ , the film in fact existent is the remanescant one, then in eq. (3), from a physical point of view,  $q_p$  must be substituted by  $q_{p,rem}$ . If this is done for our case and  $\ln i_p$  is represented against ( $E - \eta_{f,p}$ ) the Figure 5 is obtained. <sup>pp</sup>

From this figure two data are possible to be obtained. The first one is <sup>m/f</sup> the transfer coefficient  $\alpha^c$  of the solid state reaction



The obtained value of  $\alpha_{m/f}^c$  0.9 which is in good agreement not only with a symmetrical barrier, but also with the anodic Tafel line which was previously determined [9].

The second date is related to the departure of the Tafel straight plot for low  $i_p$ , which as in normal solution electrochemistry will be related with the fact that the reverse reaction becomes important. This means that the extrapolation of  $\ln i_p$  to  $-\infty$  must give the Flade potential ( $E_f$ ) of the system (not the reversible potential because the film/solution interface is not reversible in relation with the  $\text{Pb}^{2+}$ ). This value gives -0.95 V. From the linear region extrapolated to the  $E_f$ , it was possible then to calculate the exchange current density at the metal/film interface ( $i^0$ ). It results to be  $4.75 \text{ mA/cm}^2$ . <sup>M/f</sup>

#### IV. Conclusions

For the case of the voltammetric reduction of a previously  $\text{PbSO}_4$  film grown on a Pb surface it is possible then to consider that: (a) There is no nucleation and overlapping phenomena; (b) The reduction of the film can be understood through the Hopping Motion model with a maximum exchange current density of  $8.3 \text{ mA/cm}^2$  and a jump distance of about  $0.4 \text{ nm}$ ; (c) The reaction at the metal/film interface follows a normal Tafel representation for the jump of a  $\text{Pb}^{2+}$  from the  $\text{PbSO}_4$  face to the Pb face, given rise to a transfer coefficient of  $0.9$  and an exchange current density of  $4.75 \text{ mA/cm}^2$ .

*Acknowledgments:* L.M.M. de Souza is grateful to CAPES for her PhD scholarship. Both authors are grateful to FAPESP for the financial support to the program to which this work belongs.

#### V. References

1. FLEISCHMANN, M. and THIRSK, H.R., Trans. Faraday Soc., 51 (1955) 71.
2. CARR, J.P.; HAMPSON, N.A. and TAYLOR, R., J. Electroanal. Chem., 33 (1971) 109.
3. VALERIOTE, E.M.L. and GALLOP, L.D., In: Power Sources 5. (D.H. Collins, ed.) Academic Press, London (1975) 55.
4. VALERIOTE, E.M.L. and GALLOP, L.D., J. Electrochem. Soc., 124 (1977) 370.
5. PAVLOV, D. and DINEV, Z., *ibid.*, 127 (1980) 855.
6. PAVLOV, D., J. Electroanal. Chem., 118 (1981) 167.
7. HAMPSON, N.A. and LAKEMAN, J.B., *ibid.*, 107 (1980) 177.
8. DANIEL, V. and PLICHON, V., Electrochim. Acta, 28 (1983) 781 and 785.
9. D'ALKAINE, C.V. and TREMILIOSI-FILHO, G., Proceedings of the VI Symp. Bras. Electrochem. and Electroanal. University of São Paulo (1988) 327 (in english).
10. TAKEHARA, Z.; KANAMURA, K. and KAWANAMI, M., J. Electrochem. Soc., 137 (1990) 800.
11. BRENNAN, M.P.J. and HAMPSON, N.A., J. Electroanal. Chem., 48 (1973) 465.

12. BRENNAN, M.P.J. and HAMPSON, N.A., *ibid.*, 52 (1974) 1.
13. HAMPSON, N.A. and LAKEMAN, J.B., *J. Electroanal. Chem.*, 108 (1980) 347.
14. FLEMING, A.N. and HARRISON, J.A., *Electrochim. Acta*, 21 (1976) 905.
15. VARELA, F.E.; GASSA, L.M. and VILCHE, J.R., *ibid.*, 37 (1992) 1119.
16. FLETCHER, S., *Electroanal. Chem.*, 118 (1981) 419.
17. D'ALKAINE, C.,V.; de SOUZA, L.M.M. and NART, F.C., *Corrosion Science*, 34 (1993) 129.

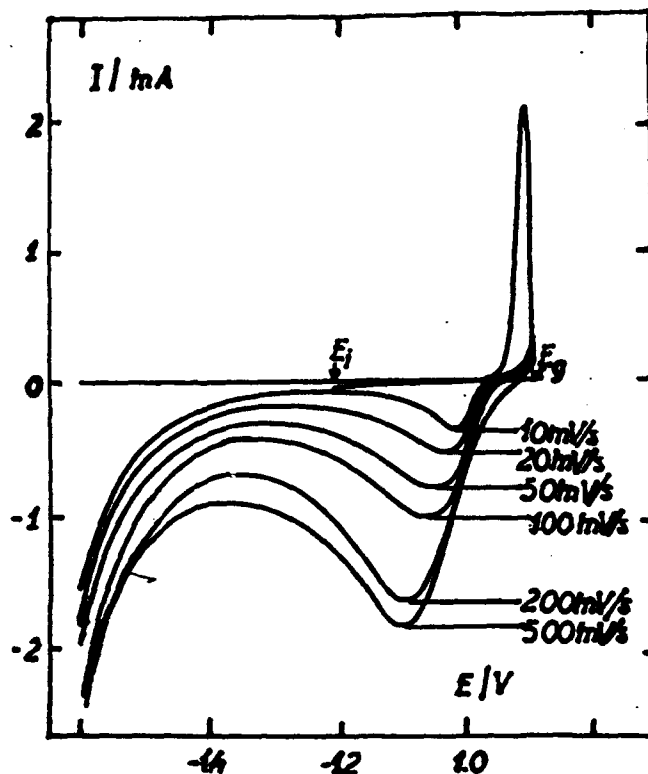


Figure 1. Typical cathodic curves at different sweep velocities after to grow  $41 \text{ mC/cm}^2$  of the  $\text{PbSO}_4$  film.

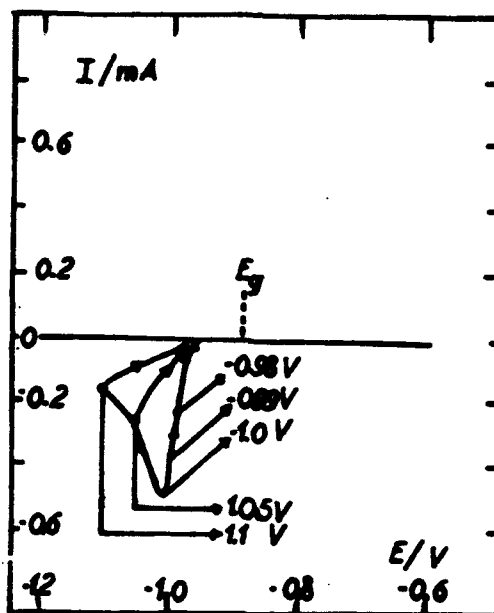


Figure 2. Inversion of the cathodic sweep at different EA to show that there is no nucleation and overlapping ( $v = 10 \text{ mV/s}$ ).

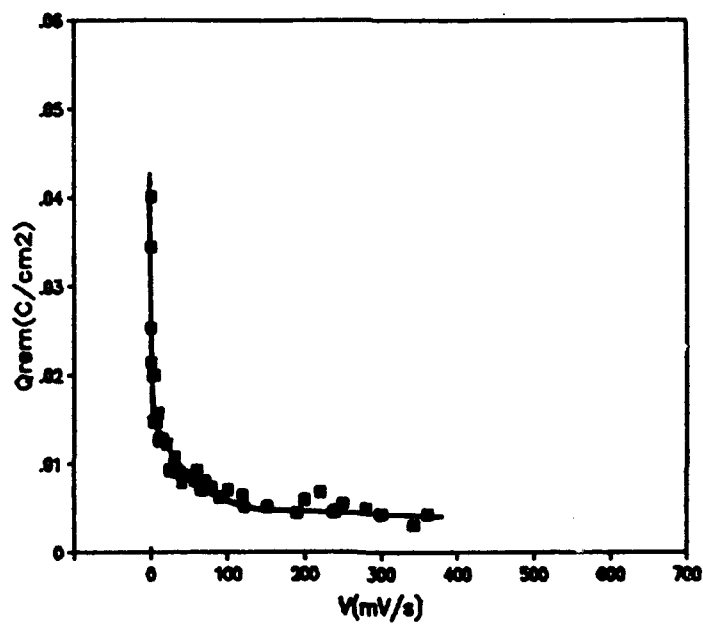


Figure 3. Remanent peak charge density of the reduction of  $\text{PbSO}_4$  film versus the cathodic sweep velocity.

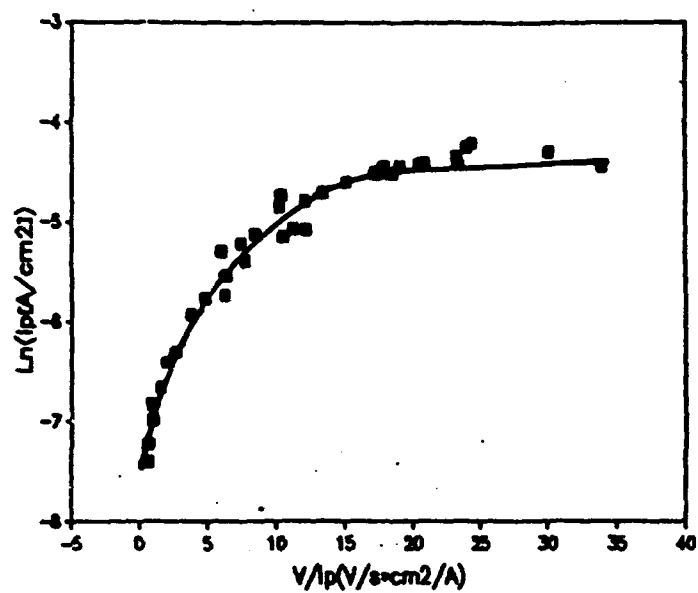


Figure 4. Representation of the equation (1) for the reduction of the Pb/PbSO<sub>4</sub> system.

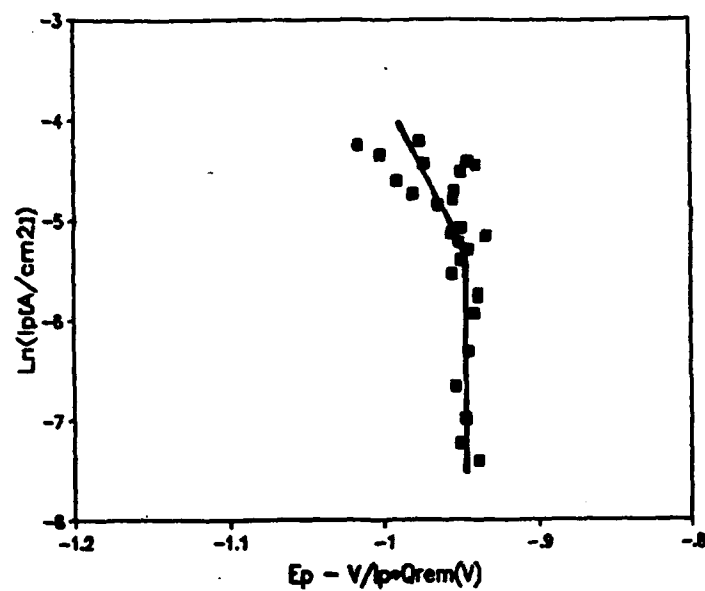


Figure 5. Tafel plot for the reduction of PbSO<sub>4</sub> to Pb at the metal/film interface.



**THE VARIATION OF THE DIELECTRIC CONSTANT AND RESISTIVITY  
DURING THE ANODIC GROWTH OF  $\text{Ni(OH)}_2$**

C. V. D'Alkaine

Group of Electrochemistry and Polymers

DQ/UFSCar - C.P. 676 - 13565-905 São Carlos (SP)

BRAZIL

R. C. Rocha-Filho

Group of Electrochemistry and Polymers

DQ/UFSCar - C.P. 676 - 13565-905 São Carlos (SP)

BRAZIL

C. L. F. de Oliveira

Group of Electrochemistry and Polymers

DQ/UFSCar - C.P. 676 - 13565-905 São Carlos (SP)

BRAZIL

**ABSTRACT**

A voltammetric impedance technique is used to follow the ionic resistivity and dielectric constant of the  $\text{Ni(OH)}_2$  during the voltammetric first growth of this passivating film on nickel. For this a non-passive equivalent circuit model is used; the results show that the dielectric constant passes through a maximum and the ionic resistivity through a minimum at the peak potential of the voltammogram.

**Key terms:** transient impedance, passivation, nickel oxidation.

**I. Introduction**

Electrochemical impedance spectroscopy (EIS) has been a powerful tool to investigate the electrical properties of several passivating films under stationary conditions, as oxides electrochemically grown on metals (e.g., zirconium [1], nickel [2], iron [3]) or oxides deposited on metals (e.g., lead [4]), in several electrolytes. These studies have been carried out in steady state conditions to enable the development of equations and to attend the requirement of the Kramers-Kronig transforms [5].

Impedance voltammetry was reported before by Sluyters-Rehbach and Sluyters [6] but has never been applied to the transient growth of continuous passivating films. For the understanding of this phenomenon we have developed a general quantitative treatment for the electrochemical growth [7] for the different possible models and for potentiostatic, galvanostatic and voltammetric transients. From this point of view it is

interesting to be able to know how the dielectric constant of the film varies during its first transient growth. This is the objective of the present work applied to study the anodic growth of  $\text{Ni(OH)}_2$  on Ni and to carry out an exploratory application of non-linear equivalent circuit concepts to analyze physical parameters like resistivity and dielectric constant of passivating films. For this purpose, the potential sweep rate ( $v$ ) cannot be high and the sinusoidal perturbation frequency ( $f$ ) cannot be too low, taking into account the  $v/f$  ratio necessary to assume that during the impedance measurement the system is invariable, although it is in transient conditions.

The system  $\text{Ni/Ni(OH)}_2/1 \text{ M NaOH}$  was chosen because of the apparent simplicity of its voltammogram, and the possibility of comparison with other works carried out in our laboratory[8,9].

## II. Experimental

The working electrode was a disk made from a nickel rod (Aldrich, 999.9 mg/g), with a geometric useful area of about  $0.315 \text{ cm}^2$ , included in epoxy resin. At the beginning of each potentiodynamic experiment, the electrode was polished with 600 grade emery paper under running water conditions and then thoroughly rinsed with purified water and dried with absorbent paper. A platinum sheet of about  $2\text{-cm}^2$  geometric area was used as counter electrode in front of the working electrode, and a  $\text{Hg/HgO}/1 \text{ M NaOH}$  electrode as reference, to which all potentials are referred. The electrolyte solution (1 M NaOH) was prepared from purified water (Milli-Q system) and Merck, P.A., NaOH. The solution was deaerated with  $\text{N}_2$  before each experiment, and during the experiment  $\text{N}_2$  was passed over the solution.

The EIS of the oxide film electroformation was carried out potentiodynamically (5 mV/s, at  $25^\circ\text{C}$ ) beginning at an initial potential ( $E_i$ ) of -1.1 V, using an a.c. perturbation of 5-mV amplitude at a fixed frequency. This procedure was carried out at several frequencies ( $5 \text{ Hz} \leq f \leq 1 \text{ kHz}$ ), obtaining the real and imaginary parts of the transfer function for discrete potential values but without stopping the sweep.

The electronic equipment used was an EG&G-PARC model 273 potentiostat/galvanostat, a Solartron model 1255 frequency response analyzer and an ECB model RB-400 X-Y recorder.

## III. Results and Discussion

A typical voltammogram is shown in Figure 1a. The impedance diagrams ( $-Z''$  vs.  $Z'$ ) for the film growth are shown in Figure 1b for different potentials in the voltammogram. Since the

lowest frequency is 5 Hz, for the reasons point out above it is not possible to obtain the complete diagrams (see Figure 1b).

Assuming a simple model in which the system is represented by two different fundamentally ionic surface charge densities, one at the metal/film ( $q_m/s$ ) and the other at the film/solution ( $q_f/s$ ) interfaces, giving rise to the field inside the film, a non-passive capacitor ( $C_f$ ) can be defined due to the facts that the dielectric constant ( $D$ ) of the film between the two charge densities can change during the film growth and the thickness of the film is also changing. The corresponding equation must be

$$C_f = D\epsilon_0 Ar/Cq \quad (1)$$

where  $\epsilon$  is the permittivity of vacuum,  $A$  the geometric area,  $r$  the roughness factor,  $C$  the film volume per unit charge and  $q$  the charge density of the film at a given stage of growth.

On the other hand, due to the current density circulating inside the film, a non-passive resistance ( $R_f$ ) can also be defined, due to the facts that the ionic resistivity of the medium can change during the film growth and the thickness of the film is also changing. This resistance must be given by

$$R_f = \rho Cq/Ar \quad (2)$$

where  $\rho$  is the oxide ionic resistivity.

As a result, the system can be imagined as equivalent to the circuit represented in Figure 2, where  $R_s$  is the electrolyte resistance, and  $C_f$  and  $R_f$  are non-passive components due to the change in thickness of the film and possible changes of  $D$  and  $\rho$ . The impedance of the circuit in Figure 2 for each potential-current operational condition is given by

$$Z_f = Z'_f + j Z''_f \quad (3)$$

$$Z_f = R_s + R_f / [1 + (\omega C_f R_f)^2] - j \omega C_f R_f^2 / [1 + (\omega C_f R_f)^2] \quad (4)$$

defining

$$Z' = Z'_f - R_s = R_f / [1 + (\omega C_f R_f)^2] \quad (5)$$

and

$$Z''_f = -\omega C_f R_f^2 / [1 + (\omega C_f R_f)^2] \quad (6)$$

then,

$$R_f = (Z'^2 + Z''^2) / Z' \quad (7)$$

and

$$C_f = -Z''/[\omega(Z'{}^2 + Z''{}^2)] \quad (8)$$

from which the resistance and the capacitance per unit area of the film can be calculated:  $r_f = R_f / A_r$  and  $c_f = C_f / A_r$ .

The values obtained for the film ionic resistance  $R_f$  and the film capacitance  $C_f$  as a function of the electrode potential are shown in Figures 3 and 4, respectively. On the other hand, the behavior of  $\rho$  and  $D$  as a function of the electrode potential is shown in Figures 5 and 6, respectively. For these calculations the values of  $C$  and  $r$  used were  $1.16 \times 10^{-4} \text{ cm}^2 \text{C}^{-1}$  and 3, respectively. These figures show that the values of  $R_f$  and  $\rho$  present minima at the peak potential in the voltammogram, while the values of  $C_f$  and  $D$  present maxima. The same type of behavior has been found before in a similar study carried out for the passivating film on Zr in an aqueous 0.5 M  $\text{NaHCO}_3$  solution [9].

In a recent paper D'Alkaine and Santanna dos Santos [8] obtained values for the resistivity of a film grown in 0.5 M  $\text{Na}_2\text{SO}_4$  and 1.0 M  $\text{NaOH}$  in voltammetric transient conditions using special equations [7], with a tendency to  $7.8 \times 10^6 \Omega \text{ cm}$  for the low field region (which corresponds to the region of the present paper) and a tendency to  $5.2 \times 10^7 \Omega \text{ cm}$  for the high field region.

The fact that  $D$  passes through a maximum can be related with the presence at the beginning, of an air-formed film formed after the polishing of the surface. Then, when the electrochemical film begins to grow, that film changes (before the peak potential) to a hydrated one, showing that it takes time and potential for the ionic hydration, hence,  $D$  increases. Finally, due to the increasing field and time, after the peak potential, the film aging produces the dehydration and, then, the reduction of  $D$  again.

The behavior of  $\rho$  can be explained also based in these ideas. Its value must be high for the air-formed film; however, it tends to decrease during the first part of the growth, before the peak, due to hydration and then it increases after the peak potential, due to the aging, as a result of field and time. Actually we are working in the understanding of the reasons why the dielectric constant and resistivity change with the frequency of the perturbation.

#### IV. Conclusions

This exploratory use of EIS to study the transient growth of an anodic film, applying a simple non-passive equivalent circuit model, yields results which seem to be reasonable when compared

to those obtained using other techniques [8]. A minimum of  $\rho$  is obtained at the peak potential in the voltammogram with a value of  $7.8 \times 10^8 \Omega \text{ cm}$  which is of the same order of that obtained before at the peak potential by other technique.

The experimental values of the dielectric constant ( $D$ ) in the passive region are reasonable when compared with those obtained for another system and seem to show that during the transient growth a double phenomenon of hydration and dehydration occur as we have proposed in several papers before.

**Acknowledgments** - The authors thank FAPESP for the financial support of the program of which this work is part of, and C.L.F. Oliveira is also grateful to CAPES for his PhD scholarship.

#### REFERENCES

1. E.M. PATRITO, R.M. TORRESI, E.P.M. LEIVA and V.A. MACAGNO, *J. Electrochem. Soc.*, 137 (1990) 524.
2. C. CLERC and D. LANDOLT, *Electrochim. Acta*, 33 (1988) 859
3. B.D. CAHAN and CHIA-TIEN CHEN, *J. Electrochem. Soc.*, 129 (1982) 474.
4. M. MAJA and N. PENAZZI, *Electrochim. Acta*, 30 (1985) 773.
5. J.R. MACDONALD, *Impedance spectroscopy*, New York, Wiley, 1987.
6. M. SLUYTERS and J.H. SLUYTERS, In: *Proceedings of the Symposium on TRANSIENT TECHNIQUES IN CORROSION SCIENCE AND ENGINEERING*, Ed. W.H. Smyrl, D.D. Macdonald and W.J. Lorens, Pennington, N.J. p. 1-12.
7. C.V. D'ALKAINE, L.M.M. de SOUZA and F.C. NART, *Corrosion Science*, 34 (1993) 129.
8. C.V. D'ALKAINE and M.A. SANTANNA dos SANTOS, In: *Proceedings of the IX CONGRESSO IBEROAMERICANO DE ELETROQUIMICA*, La Laguna, Espanha, 1990, p. 197-199. (in English)
9. C.V. D'ALKAINE, R.C. ROCHA-FILHO and C.L.F. de OLIVEIRA. In: *Proceedings of the VIII SIBEE*, Campinas (SP), Brazil, 1992, p. 392-397. (in English)

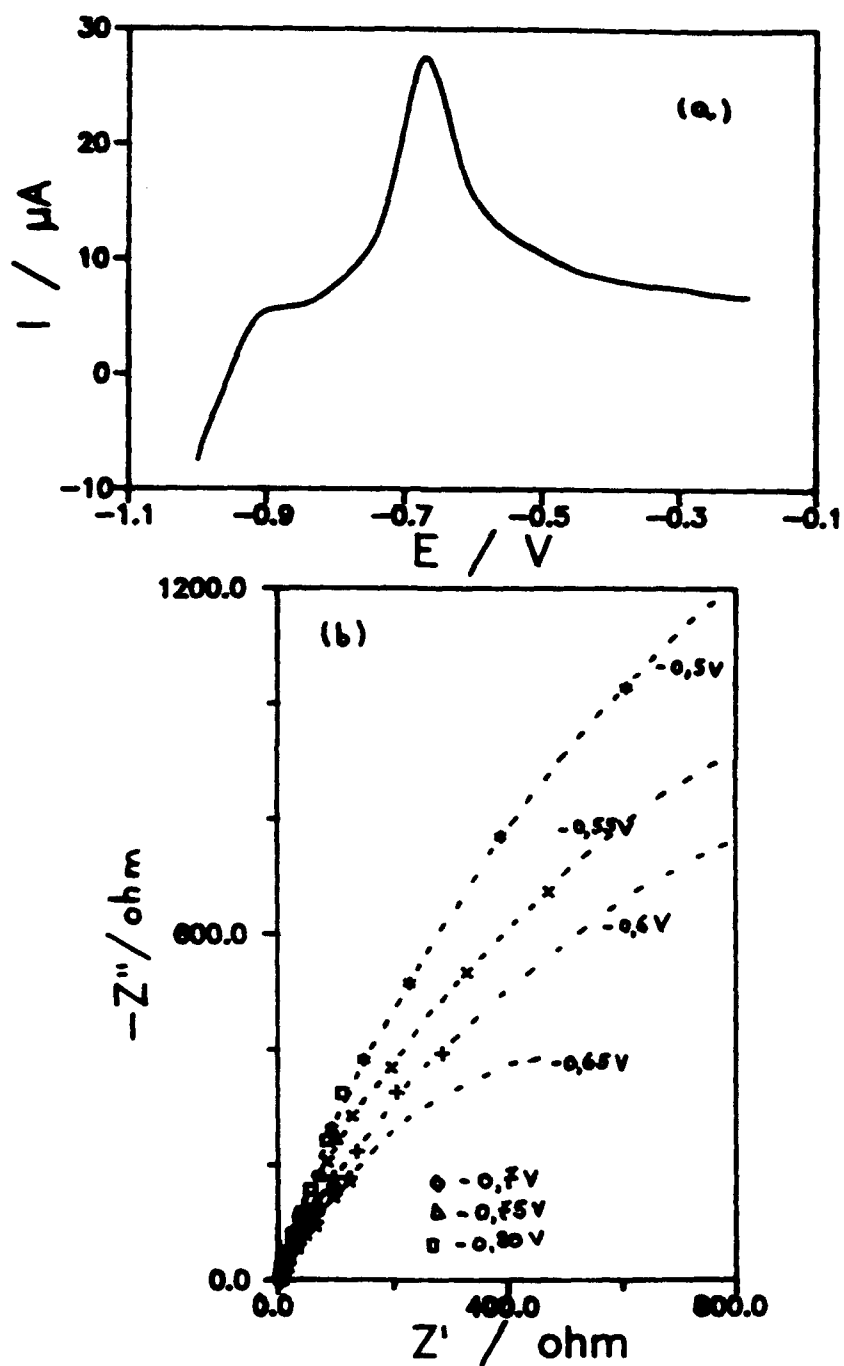


Figure 1. Typical results of voltammetric transient and electrochemical impedance measurements during the transient for Ni in 1.0 M NaOH deaerated solution. (a) Voltammogram  $\nu=5.0$  mV/s. (b) Nyquist plot for different electrode potentials during the sweep.

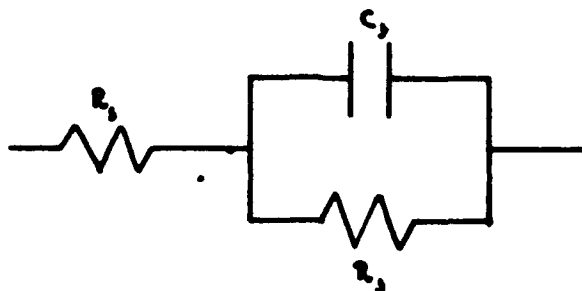


Figure 2. Simple equivalent circuit used, considering  $C_p$  and  $R_p$  as non-passive elements due to variation in  $D$ ,  $\rho$  and  $q$ .

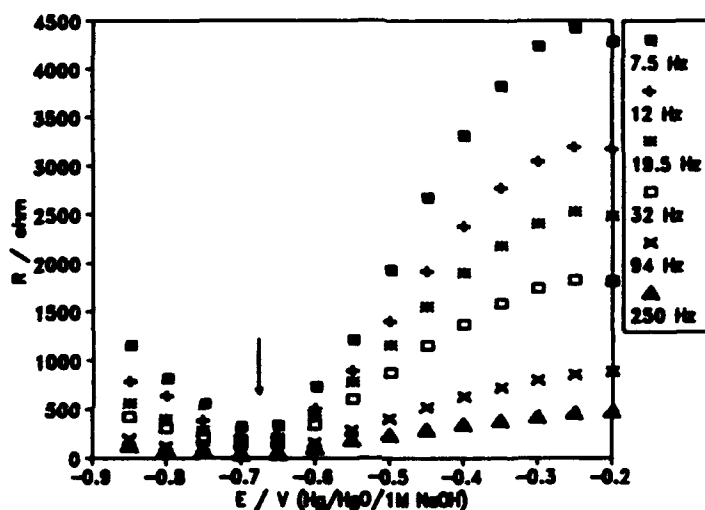


Figure 3. Film resistance variation with potential during the film growth on nickel hydroxide (different constant frequencies). The frequencies are in the figure. The arrow corresponds to the peak potential.

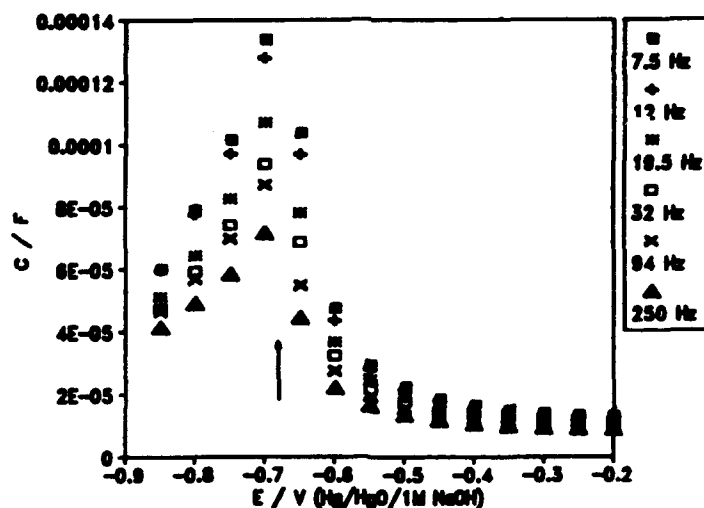


Figure 4. Capacitance variation with potential during the film growth of nickel hydroxides on nickel (different constant frequencies). The frequencies are in the figure. The arrow corresponds to the peak potential.

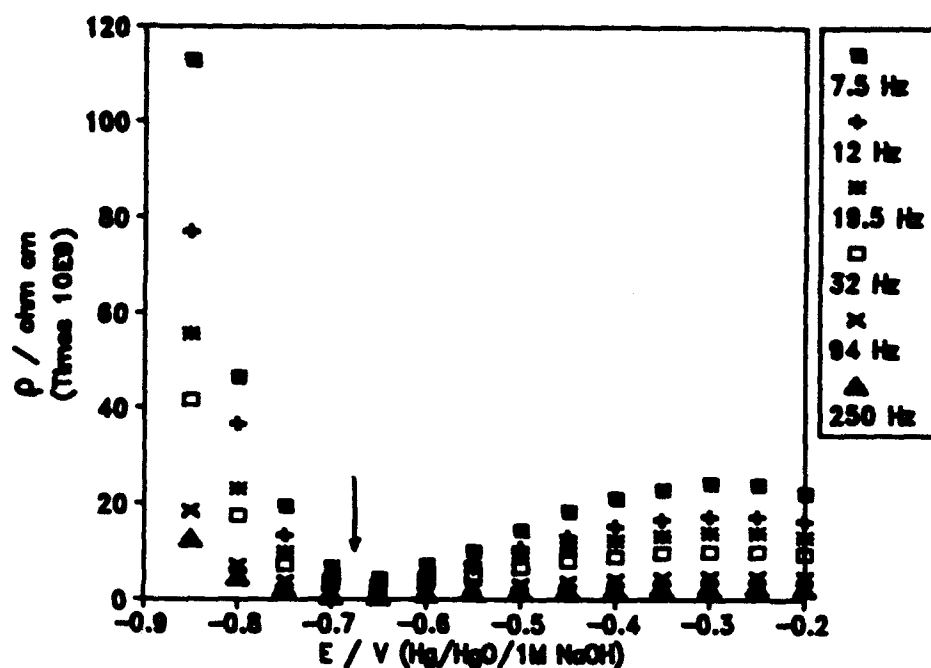


Figure 5. Film ionic resistivity variation with potential during the film growth of nickel hydroxide (different constant frequencies). The frequencies are in the figure. The arrow corresponds to the peak potential.

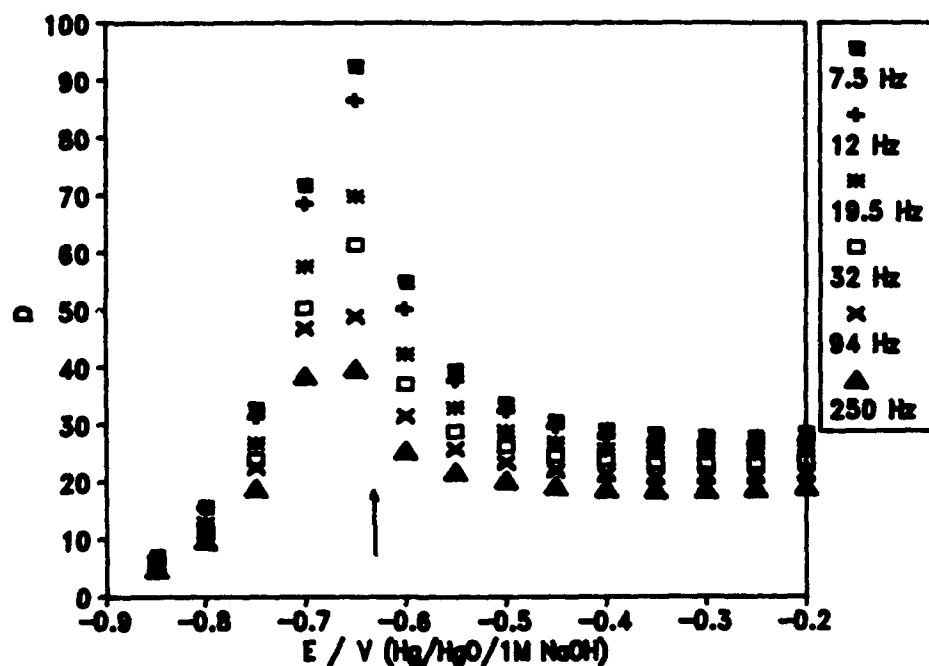


Figure 6. Film dielectric constant variation with potential during the film growth of nickel hydroxide on nickel (different constant frequencies). The frequencies are in the figure. The arrows corresponds to the peak potential.



## THE OXIDATION/REDUCTION REACTION OF ZINC AT THE Zn/ZnO INTERFACE

C. V. D'Alkaine

Group of Electrochemistry and Polymers

DQ/UFSCar - C.P. 676 - 13565-905 São Carlos (SP)

BRAZIL

L. H. Mascaro

Group of Electrochemistry and Polymers

DQ/UFSCar - C.P. 676 - 13565-905 São Carlos (SP)

BRAZIL

### ABSTRACT

On the base of the possibility of the calculation of the overpotential through the film, the oxidation and reduction reactions at the metal/film interface of the Pt/Zn/ZnO, 0.5 M NaHCO<sub>3</sub> solution system was studied. The anodic and cathodic branches of this solid state reaction give rise to typical Tafel plots from which the corresponding transfer coefficients and exchange current densities were determined.

**Key terms:** solid state reaction, zinc, oxidation/reduction.

### I. Introduction

Even when there is an extended literature on the zinc in alkaline media, the neutral pH region has not received the same attention, principally from a mechanistic point of view about the growth of passivating films. Works like does of Mishima et al. [1], Bohe et al. [2,3] and Cachet et al. [4] are interested in the characterization of the passivating films in this pH region at stationary conditions, showing that the passivating film seems to be a Zn<sub>1+x</sub>O where x depends on the history of the electrode. In the last decade we have published several paper about the mechanistic interpretation of the growth of the passivating film on zinc in neutral [5,6] slightly alkaline [7,8] and alkaline [9] solutions. Specially for the case of a NaHCO<sub>3</sub> solution (the solution of the present paper) it is necessary to point out references [5,6,10]. For the voltammetric transient conditions it has been possible to show for this pH region the existence of two peaks which has been attributed to ZnO at the surface of the passivating film and Zn<sub>1+x</sub>O near the metal/film interface [11-13].

In the present paper using a working electrode with well known roughness factor and taking into account the possibility to known the overpotential through the film through equations published before [14], it is studied the voltammetric oxidation and reduction processes of zinc at the metal/passivating film interface.

## II. Experimental

The working electrode, to be able to have a well roughness factor, was a layer of plated zinc with  $11 \text{ mC/cm}^2$  deposited on a Pt substrate, layer by layer, through out a technique previously developed [15]. Then, before each voltammetric measurement the deposit was made, washed with bidestilated water and introduced in the work solution at an initial potential ( $E_i$ ) of  $-1.4 \text{ V}$ , where it was waited up to an initial cathodic current density of  $54 \mu\text{A/cm}^2$ , moment in which the sweep was initiated. To study the cathodic reduction each time the plated zinc layer was firstly swept from  $E_i$  to the growing potential ( $E_g$ ) of  $-1.0 \text{ V}$ , where the potential was kept up to the passage of an anodic charge density of  $4.0 \text{ mC/cm}^2$ , moment in which the cathodic sweep was initiated.

For the measurement of the true electrode area, and then, of the roughness factor, this was due measuring the true area of the Pt substrate through the voltammetric peaks of the hydrogen absorption in  $\text{H}_2\text{SO}_4$  solution [16]. The kind and thickness of deposits permits to consider that the roughness will not be changed by the plating of the zinc. The obtained experimental roughness ( $r$ ) was 1.8.

The reference electrode was NCE, to which all potentials are referred. It was connected to the working solution by an ammonium nitrate salt bridge. The working solution was  $0.5 \text{ M NaHCO}_3$  prepared from an analytical grade reagent and bidestilated water.

## III. Results and Discussions

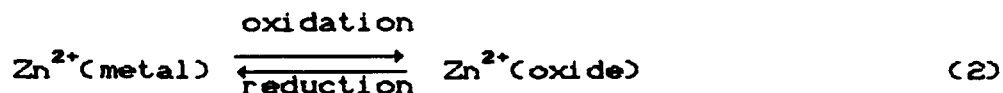
To have a general idea of the studied problems in Figure 1 it is shown typical oxidation voltammetric results at some anodic sweep rates ( $v_a$ ). In Figure 2 there is the equivalent results for some cathodic sweep rates ( $v_c$ ), after to growth the film (voltammetric + potentiostatic), as it was explain in the experimental part. In both figures two peak appears depending on the conditions. In previous works [11-13] has been shown by voltammetry for polycrystalline and deposited on Pt zinc electrodes, that  $a_1$  is related with  $c_2$  and  $a_2$  with  $c_1$ . On this base it has been attributed the  $a_1/c_2$  peaks to the  $\text{ZnO}$  formation at the external region of the film and the  $a_2/c_1$  peaks to the  $\text{Zn}_{1-x}\text{O}$  in the internal position of the film, due to the fact that this is the place where there is the  $\text{Zn}^{2+}$  injection in the film.

As has been shown in a previous paper [14] it is possible, for the peak conditions, to calculate the film overpotential ( $\eta_{f,p}$ ) which gives the same result for any of the possible models (Hopping Motion, Ohmic or Place Exchange). This value is given by

$$\eta_{f,p} = \frac{v}{i_p} q_p \quad (1)$$

where  $i_p$  and  $q_p$  are the peak current and charge densities, respectively. A comment must be made for the case of the reduction peak. Due to the fact that the charge flux at the peak is passing in this last case through the remainder film, the charge density which must be used in eq.(1) it is that corresponding to the remaining charge density ( $q_{p,rem}$ ). This could be calculated making the integration of the current from the peak potential to the potential of minimum current between the peak and the hydrogen evolution (Figure 2).

Now if it is obtained the  $\eta_{f,p}$  values and the peak potential are corrected for this "ohmic drop through the film" ( $E_p - \eta_{f,p}$ ), then the representation of  $\ln i_p$  vs ( $E_p - \eta_{f,p}$ ) must give a typical Tafel plot which will correspond to the solid state reaction



This means that through this ideas we are able to study the solid state metal oxidation and reduction processes at the metal/film interface. This was made for the anodic and cathodic voltammetric transients of the studied system (Pt/Zn/ZnO, 0.5 M NaHCO<sub>3</sub>). The results could be seen in Figure 3. Several results can be obtained from this figure and some comments must be made.

First of all, if we take the straight region of the anodic branch, given a Tafel plot, it is possible to calculate the anodic transfer coefficient  $\alpha_a$ , which if the energetic barrier is symmetric must give 1.0 because the total ionic charge transfer is 2.0. The value obtained was practically 1.04 in well agreement with the developed idea.

Secondly, when we look to the anodic sweep at the peak as it could be considered that there is no practically nothing of the  $\alpha_2$  transformation and this is the reason for which, after the  $\eta_{f,p}$  correction, we obtain a straight region in the anodic branch of the Figure 3. But when we go to the cathodic branch it is possible to see that after to come to be a straight line, there is a departure for higher  $v$  (and then higher  $i_p$ ). If we calculate the value of the cathodic transfer coefficient for the linear region, it gives an  $\alpha_c$  equal to 0.94, in very good agreement with the  $\alpha_a$ , due the fact that it must be followed

$$\alpha_a + \alpha_c = 2 \quad (3)$$

The departure from linearity for both branches for low  $i_p$  must be attributed to the inverse reaction, like in solution electrochemistry. If the potential of zero current (the Flade potential,  $E_r$ ) is taken to be -1.260 V then the extrapolation of the anodic and cathodic Tafel regions will give the anodic ( $i_{0,a}$ ) and cathodic ( $i_{0,c}$ ) exchange current densities. For the present case these values give 0.26 and 0.06 mA/cm<sup>2</sup> for the anodic and cathodic values, respectively. The fact that the cathodic value is lower than the anodic one is another time showing the correctness of the exposed ideas, due to the fact that the cathodic transient was studied on a film which during its growth was aged.

Finally it is interesting to return to the understanding of the straight line departure for the cathodic branch at high current densities. If we consider that for low  $v_c$  there is time for the transformation of  $Zn_{1-x}O$  to  $ZnO$ , but for the high  $v_c$  this is not possible, then the equation corresponding to eq.(1) must take into consideration the correction for two films. The calculation of Figure 3 has been made only for a mixture of the inner and external films, because has been considered the corresponding charge for the film before the  $Zn_{1-x}O$  becomes  $ZnO$ . This is then the reason for which the  $\eta_{f,p}$  correction was underdimensioned and then, there was this departure from linearity.

#### IV. Conclusions

Through the possibility of calculation of the overpotential drop through the film, the relations between the current density and the potential at the metal/film interface can be calculated for the oxidation and reduction of the zinc at the zinc/passivating film interface. The anodic and cathodic branches of this solid state reaction gives normal Tafel plots given anodic and cathodic transfer coefficients practically corresponding to a symmetric barrier. For the extrapolations to the Flade potential it was also possible to calculate the anodic and cathodic exchange current densities for this solid state reaction. The last one gives a lower value due to the fact that the reduction process was studied on an aged anodically growth film.

*Acknowledgments:* One of us (L.H. Mascaro) wishes to thanks to CNPq for her PhD scholarship. Both authors are grateful to FAPESP for the financial support to the program to which this work belongs.

## REFERENCES

1. H. MISHIMA et al. - *Electrochim. Acta*, 36 (1991), 1491.
2. A.E. BOHE et al. - *Electrochim. Acta*, 34 (1989), 1443.
3. A.E. BOHE et al. - *Corrosion Science*, 32 (1991), 621.
4. C. CACHET, C.P. DE PAULI and R. WIART - *Corrosion Science*, 25 (1985), 493.
5. H.A. PONTE, N. BOCCHI and C.V. D'ALKAINE - Proceedings of the VII Symp. Braz. of Electrochem. and Electroanal., São Paulo (SP), Brazil (1988), 306-315 (in english).
6. H.A. PONTE, N. BOCCHI and C.V. D'ALKAINE - In: Proceedings of the 11th International Corrosion Congress, Florence, Italy (1990), Vol. 4, p. 575-583.
7. N. BOCCHI and C.V. D'ALKAINE - In: Proceedings of the V Symp. Braz. of Electrochem. and Electroanal., São Paulo (SP), Brazil (1986), p. 458-461 (in english).
8. N. BOCCHI and C.V. D'ALKAINE - In: Proceedings of the 10th International Congress on Metallic Corrosion, Madras, India (1987), Vol. 1, p. 417-423.
9. N. BOCCHI, M.R. da CUNHA and C.V. D'ALKAINE - In: Proceedings of the 10th International Congress on Metallic Corrosion, Madras, India (1987), V. 4, p. 3941-3946.
10. H. KAESCHE - *Electrochim. Acta*, 9 (1964), 383.
11. H.A. PONTE - Master of Dissertation - DEMa/UFSCar, São Carlos (SP), Brazil (1989).
12. N. BOCCHI - PhD Thesis - IFQSC/USP, São Carlos (SP), Brazil (1986).
13. L.H. MASCARO - PhD Thesis - DQ/UFSCar, São Carlos (SP), Brazil (1992).
14. C.V. D'ALKAINE, F.C. NART and L.M.M. de SOUZA - *Corrosion Science*, 34 (1993), 129.
15. C.V. D'ALKAINE and L.H. MASCARO - In: Proceedings of the VII Symp. Braz. of Electrochem. and Electroanal., Ribeirão Preto (SP), Brazil (1990), p. 571-578 (in english).
16. T. BIEGLER, P.A.J. RAND and R.W. WOODS - *J. Electroanal. Chem.*, 29 (1971), 269.

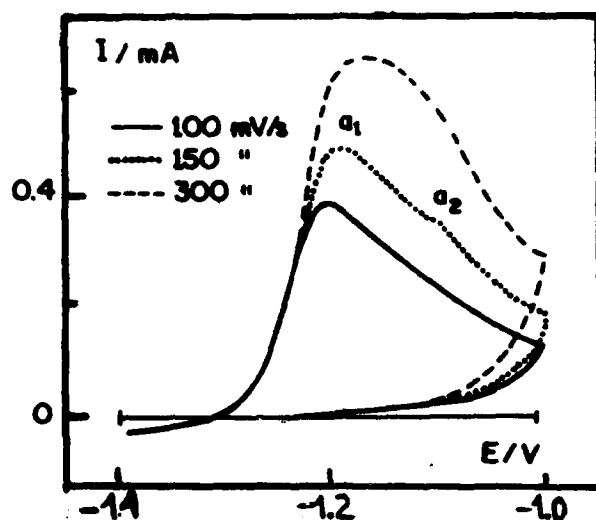


Figure 1. Typical oxidation voltammograms at three different sweep rates for plated Zn on Pt and using a 0.5 M  $\text{NaHCO}_3$  solution (RE: NCE, electrode area  $0.37 \text{ cm}^2$ ).

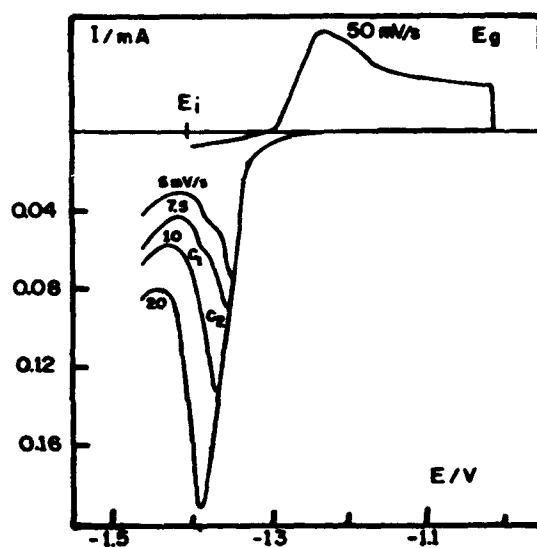


Figure 2. Typical reduction voltammograms for different sweep rates for oxidized plated Zn on Pt and using a 0.5 M  $\text{NaHCO}_3$  solution. The oxidation was made through a voltammetric + potentiostatic growth, also shown in the figure. (RE: NCE, electrode area  $0.37 \text{ cm}^2$ ).

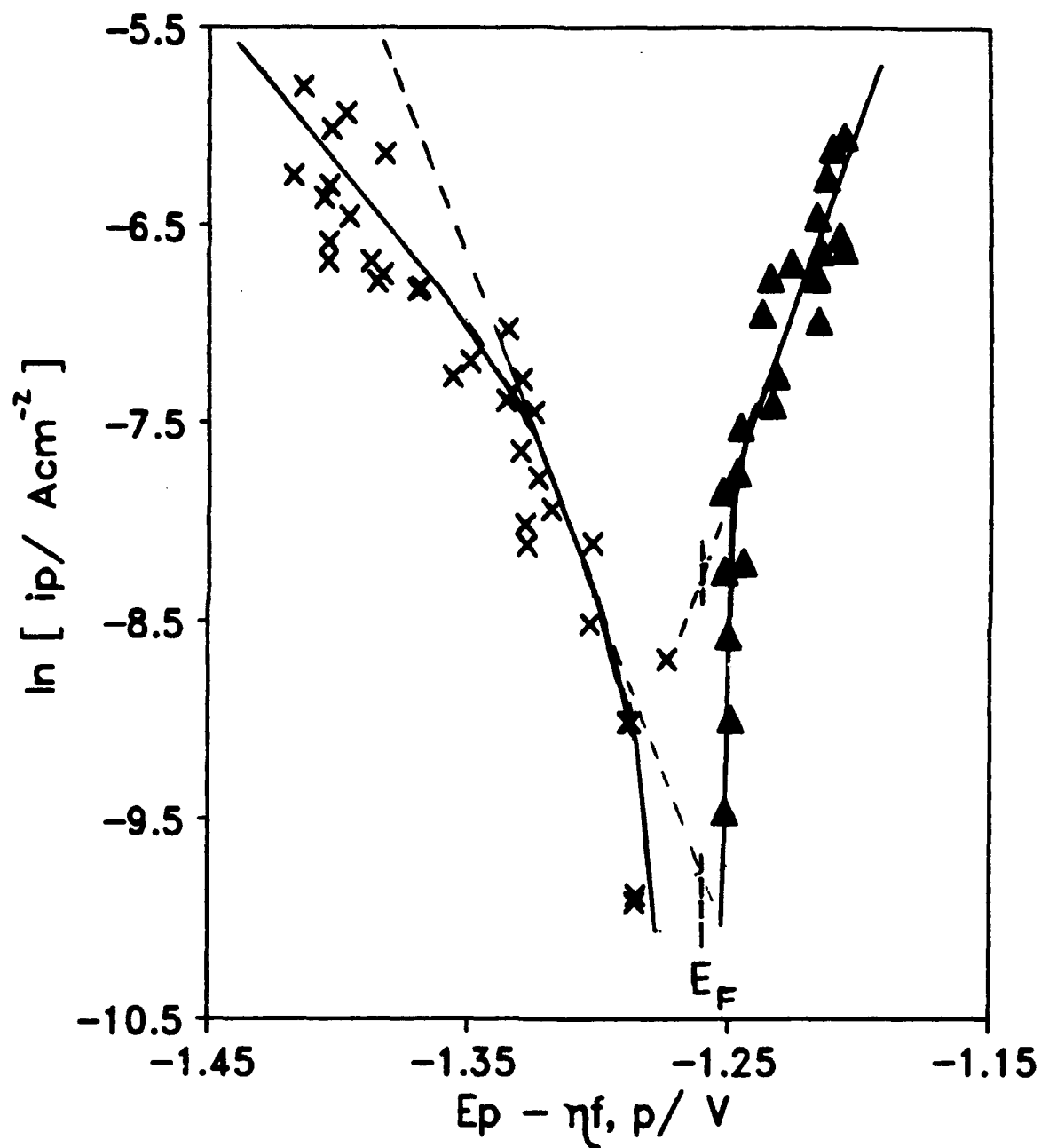


Figure 3. Anodic and cathodic Tafel plot for the oxidation and reduction reactions of zinc at the zinc/zinc oxide interface.

## **Electrochemical and corrosion behaviour of passive film on stainless steels after gamma-ray irradiation**

**G. Capobianco**

**Department of Physical-Chemistry, University of Padua,  
Via Loredan 3, 35131 Padua, Italy**

**A. Glisenti**

**Department of Inorganic, Metallorganic and Analytical Chemistry,  
University of Padua,  
Via Loredan 3, 35131 Padua, Italy**

**T. Monetta and F. Bellucci**

**Department of Materials and Production Engineering,  
University of Naples "Federico II",  
Piazzale V. Tecchio 125,  
80125 Naples Italy.**

### **Abstract**

The nature and structure of passive film on AISI 304L and AISI 446 stainless steels, after bare metal anodic oxidation and after the subsequent galvanostatic reduction or gamma-ray irradiation of the oxide film formed, were investigated by XPS and Electrochemical Impedance Spectroscopy (EIS). Atomic Absorption Spectroscopic (AAS) analysis of irradiated solution was also undertaken.

Results obtained from XPS measurement indicated that gamma-ray irradiation can have significant effects on the stability of passive film due to the release of iron and corresponding enrichment in chromium oxides. The EIS technique was used to elucidate the physical structure of passive film after irradiation and galvanostatic reduction. The passive film formed on AISI 304L and AISI 446 stainless steels have a compact structure. The galvanostatic treatment leads to a film composed of two layers, the external one showing a spongy-like structure, while the gamma-ray irradiation treatment leads to a thinner compact film exhibiting higher capacitive behaviour compared to that of unirradiated samples.

**Key terms:** stainless steels, passive film, gamma-ray, galvanostatic reduction, EIS, XPS.

### **Introduction**

Corrosion of the metallic materials is mostly prevented separating the metallic items from the external aggressive environment by an organic or inorganic coating. A particular type of inorganic coating should be an oxide layer covering the metallic surface. Aim of this work is to understand the electrochemical behaviour, and therefore the protective properties, of the passive film formed on commercial AISI 304L and AISI 446 stainless steels.



The effect of gamma-ray irradiation on such materials and in particular on the increase of the release of the corrosion products has been object of several papers<sup>1,2,3</sup>. Furthermore in the case of stainless steels it has been found that the chromium content of passive layer rises after the gamma-ray treatment<sup>4</sup>. On other hand following the 'oxide film theory' (a three dimensional layer is formed at metal-solution interface retarding the dissolution of the underlying metallic substrate), the passive layer can be described as homogeneous<sup>5</sup> or heterogeneous<sup>6-9</sup>. In the first case the passive current is provided by the ionic transport through the layer, in the second one mass transport occurs through a thick porous layer. Surface and XPS analysis have undoubtedly shown that the composition of the passive layer changes with potential and in the direction perpendicular to the metal<sup>10-11</sup>.

### Experimental method

The materials investigated in this work were a commercial AISI 304L and AISI 446 stainless steels of certified composition as reported in Table 1. The exposed surface of the ring-shaped samples were 1 cm<sup>2</sup>. The specimens were polished with fine grained emery paper (down to 1000), cleaned ultrasonically in acetone and then cathodically reduced to remove the surface oxide film formed during preparation. The specimens were passivated potentiostatically at +400mV (SCE) in a lithium sulphate solution 0.1 M deaerated with bubbling argon. Some of these samples were galvanostatically reduced ( $I=30\mu\text{A}$ ) in an equivolume mixture of 0.15 N H<sub>3</sub>BO<sub>3</sub> and Na<sub>2</sub>B<sub>4</sub>O<sub>7</sub>·10H<sub>2</sub>O in bidistilled water (pH=8.7).

Different specimens were washed in deaerated bidistilled water, after passivation, and transferred via a protecting Ar atmosphere to a glass device filled with deaerated water or methanol. These specimens were then irradiated with <sup>60</sup>Co gamma rays at a dose rate of 0.50 Gy/s at 20°C for different times. A careful deaeration of the solution, prior to irradiation, was performed since the concentration of radiolytic products and their oxidising and reducing power strongly depends on the initial concentration of dissolved oxygen. The solution recovered after gamma-ray irradiation and the standard unirradiated solution, in which samples were immersed for several days, were analysed by Atomic Absorption Spectroscopy (AAS) to determine the amount of metals released.

EIS experiments were performed in deaerated borate/boric buffer solution at 25°C, by an EGG 273 potentiostat connected with a Solartron 1255 frequency response analyser. The excitation wave form for the impedance measurements was a sine wave of 10 mV amplitude applied to the specimen in the frequency range of 100kHz-10<sup>-3</sup>Hz. The maximum number of integration cycles on the transfer function analyser was set at 10 to strike a good balance between integration speed and accuracy.

For XPS analysis the samples were transferred in the spectrometer as rapidly as possible and under a flow of argon. The measurements were obtained by a VG Scientific ESCALAB MK II photoelectron spectrometer with non monochromatized Mg K $\alpha$  X-ray radiation (1253.6 eV). The working pressure was

less than  $10^{-8}$  Pa. Binding energies (BE's) are referenced to the Fermi level. Fe 2p, Cr 2p, and O 1s peaks were monitored during the present experiments. The atomic composition were evaluated from integrated deconvoluted (after the appropriate smoothing) with a non-linear least-squares fit program using Gauss-Lorentzian peak shapes. The background was subtracted using the Shirley method. Depth profiles were carried out by Ar<sup>+</sup> sputtering at 3KV, 16 $\mu$ A/cm<sup>2</sup> with an Ar partial pressure of  $3 \times 10^{-4}$  Pa. The particular beam voltage value has been chosen in order to minimise preferential sputtering effects. We can however discard the hypothesis that preferential sputtering takes place in these samples because the experimental bulk compositions, after several minutes of Ar<sup>+</sup> sputtering, are close to the nominal stoichiometries. The etching time was estimated to be 2 nm/min.

## Results and discussion

### I XPS and AAS measurements

Results of Atomic Absorption Spectroscopic analysis show that, after immersion of anodised samples in the standard unirradiated solution, both in water and in methanol, for several days, they do not reveal the presence of metallic ions while results obtained on solutions recovered after gamma-ray irradiation showed that a large amount of iron was released from the passive film during irradiation, while only traces of chromium were present.

Results of XPS measurements are shown in Fig. 1 and 2. Fig. 1 shows the results of the AISI 446 stainless steel, namely the composition depth profiles after passivation of bare samples (a), the composition of the passivated sample after galvanostatic reduction (b), after gamma-ray irradiation in deaerated water (c), and after gamma-ray irradiation in deaerated methanol (d). The same topics are reported in Fig. 2 for the AISI 304L sample (except irradiation in methanol). The passive film formed on the bare samples consist, mainly, of chromium and iron oxides. If one computes the amount of the compounds present in the oxide, layer by layer, taking into account only Fe and Cr atoms, the presence of Fe as iron-oxide is bigger rather than the amount of Cr in chromium-oxide (see Tab. 2), passive films appear to be strongly enriched in chromium and depleted in iron primarily at the oxide/solution interface, after gamma-ray irradiation or galvanostatic reduction stopped at hydrogen evolution. Similar conclusions can apply to the AISI 304L samples (Fig. 2). In addition, for this steel it was found, also, a relative enrichment within the oxide film in metallic nickel. From Fig. 1 and 2 we can see that while in the anodised samples the steel/oxide interface is reached after a sputtering time of about 5-6 minutes, in the samples submitted to galvanostatic reduction this time is about 4 minutes and for irradiated samples is about 2 minutes.

Previous observations, together with the experimental evidence that chromium is present in the recovered solution only in traces while Fe is present in high quantity, suggest that spalling of oxide film is not an important mechanism in corrosion release. It should be assumed, however, that: (i) after treatment the oxide layer is present as a thinner film, (ii) as a spongy-like structure or (iii) in an

arrangement of those. The hypothesis of the presence of a thinner oxide film richer in chromium requires the possibility of dissolution/precipitation reactions at interface, that are most unlikely to occur in the experimental conditions, of galvanostatic reduction described in this paper.

## II EIS measurements

Since the EIS technique has been successfully applied as an in-situ technique to investigate inhomogeneities in the structure of the passive layer [6], it seems useful to apply the EIS to elucidate the physical nature of the passive film before and after galvanic and gamma-ray irradiation. Two approaches will be taken to elucidate the structure of the passive film; (i) phenomenological, and (ii) physical. These approaches are discussed below.

### II.a Phenomenological approach

The phenomenological approach is based on the assumption that the impedance data obtained reflect the response of the entire passive film. A change in the composition, and consequently in the properties of the passive film as a function of depth will therefore be 'seen' by the impedance method as a change in the 'average' value of the parameter of the passive film; this must be kept in mind when the results from the impedance measurements are analysed.

The results from the impedance measurements for the bare, passivated, galvanically and g-ray reduced are presented in Fig. 3a and b as Bode and phase angle plot, respectively. The measured impedance spectra exhibited a resistive component at high frequency. This component was attributed to the solution resistance between the Lugging capillary and the working electrode.

Frequency sweep curves for the alloys in the passive state and after reduction, exhibited a capacitive range that typically extended over several orders of magnitude. When the Bode plot is examined, is evident that it consists of a linear, pseudo capacitive response region at high and intermediate frequencies. At lower frequencies, a deviation from the linear response is observed in some cases (bare and irradiated). The corresponding phase angle plot confirms that the response at high and intermediate frequencies are pseudo capacitive, and that a resistive component which appears at low frequencies is responsible for the deviation from linear behavior of the Bode plot.

This linear region on the Bode plot could be characterized by the slope, intercept and phase angle. In order to characterize the resistive component that is present, the phase angles at the low frequency regime are useful. The difference in the magnitude of the phase angle in the pseudo capacitive regime and at the lowest excitation frequencies,  $\Delta\theta$ , is useful to illustrate the appearance of an additional resistive element in the equivalent circuit.

The intercept of the plot of  $\log Z$  versus  $\log f$ , where  $Z$  is the modulus of the impedance, provides a complement to the slope in specifying the linear portion of the Bode plot. The intercept for the alloy, corresponding to the absolute

impedance at  $f=1\text{Hz}$  is equal to 3.64, to 3.66 and to 3.31 for the passivated, galvanic and gamma-ray reduced alloys, respectively.

The only remaining parameter needed, in order to fully specify the impedance characteristics of the alloy over the linear pseudo capacitive regime, is the phase angle. For pure Fe the phase angle is fairly constant at  $82-83^\circ$  over the potential regime of  $-0.4$  to  $0.7\text{ V}$ . For pure Cr the phase angle is  $87^\circ$  in the same potential range, and fairly constant over the passive regime. The passivated alloy, exhibits a maximum value of the phase angle equal to  $77^\circ$ , while the galvanostatically reduced alloy exhibits a maximum of the phase angle equal to  $0.80$ . The irradiated specimen exhibited a maximum phase angle equal to  $0.79$ . As an indication of the appearance of a resistive component in the electrical equivalent circuit it is useful to compare the values of  $\Delta\theta=\theta_{\text{max}}-\theta_{f=10^{-2}}$ . The values of  $\Delta\theta$  are equal to 11, 1, and 1 for the anodically passivated, galvanostatically reduced and irradiated alloys. The corresponding value for the bare alloy is 60.

Results from the phenomenological analysis reported above, indicate that the passive film on the 446 alloy behaves like an imperfect capacitive element. The capacitive nature of the passive film is increased after galvanic and gamma-ray irradiation. The latter increase can be attributed to an enrichment of Cr in the passive layer. The lower value of  $\log Z$  at  $f=1\text{ Hz}$  observed in the case of the passive film after gamma-ray irradiation together with the most pronounced capacitive behaviour, can be explained assuming a decrease of the thickness of the passive layer after irradiation. Results for the galvanically reduced alloy can be explained assuming a reduction of the passive layer thickness with a contemporaneous enrichment in Cr. The first effect leads to a reduction of the impedance, while the effect of an enrichment in Cr leads to an increase in the impedance. The experimental finding of  $\log Z$  obtained at  $1\text{ Hz}$  for the galvanostatically reduced alloy, indicates that these effects seems to compensate.

Although these results are consistent with the XPS analysis, they do not provide, however, any further insight the structure of the passive layer. To detect surface inhomogeneities like macroscopic or microscopic 'pores', the impedance data must be analysed on the basis of a physical model. This approaches will be described in the next section.

## II.b Physical model

Following Juttner<sup>8</sup>, a physical description of the passive film can be attempted on the basis of a single or multilayer structure with 'passive' and 'active pit' model. Although this description is an oversimplification of the structure of the passive film as the XPS analysis showed, it can be used as first approximation to elucidate the physical nature of the oxide present on the alloy before and after reduction. A dedicated software by Boukamp<sup>12</sup> was used to analyze and to fit the experimental impedance data.

The first impedance to analyze is that of the bare alloy in the same environment. These results are represented in Figure 3a and b and were taken at

the rest potential (-0.805 V vs SCE). The impedance spectrum or electrode impedance, can be described by the solution resistance,  $R_s$ , in series with a parallel combination of a pure charge transfer resistance,  $R_p$ , in parallel with a double layer capacitance,  $C_{dl}$ . The overall transfer function of this model correspond to an ideal capacitive semicircle in a Nyquist plot. In a real situation, metals and alloys at their rest potential exhibit a deviation from a pure semicircle. Different theories have been used to account for these deviations. Such deviations were attributed to inhomogeneities of the solid surface and were described using the Cole-Cole frequency dispersion formula<sup>13</sup> or introducing a constant phase element (Q) whose empirical impedance is of the type  $Z = A(j\omega)^n$  where A and n are constant. This empirical impedance has proved of considerable value in data fitting, even if its physical meaning is not yet clear<sup>14</sup>. When the value of n is close to 1, the constant phase element behaves like a pure capacitor; for  $n=0.5$ , it is equivalent to a Warburg impedance, for  $n=0$ , the Q is equivalent to a pure resistor.

To evaluate the most probable equivalent circuit capable to fit the experimental data for the investigated samples, two models were analyzed: (i) a single layer of thickness L, (ii) a two layers of thickness L1 and L2, the  $\alpha$  values show if the layer is homogeneous or heterogeneous. Since it is always possible to find an equivalent electrical circuit whose transfer function can fit the experimental impedance data, the analysis carried out in this paper was based on the basis of both mathematical fitting parameters ( $\chi^2$ , and residuals) and on the basis of the physical meaning of the fitting parameters. Notwithstanding, it is not a simple task to discriminate among the different electrical circuits. This fact is due to the lack of data at very low frequencies even if experiments were carried up to  $10^{-3}$  Hz. Fit parameters evaluated with these models for the bare (B), anodically passivated (AP), galvanostatically reduced (GR), and gamma-ray irradiated ( $\gamma$ I) 446 alloys, are reported in Table 3. A lower value of the parameter  $\chi^2$ , indicates that the experimental data are well fitted by the transfer function of the equivalent circuit represented in the same Table.

Experimental data relative to bare 446 alloy reported in Figure 3a and b are well described by a simple parallel RQ circuit with a value of  $n=0.95$ , suggesting that its electrochemical and corrosion behaviour in the test solution can be properly described by a simple parallel RQ equivalent circuit (see Table 3).

The AP 446 alloy is described by model (i) with  $R_1=71 \Omega$ ,  $R_2=1.3 \times 10^6 \Omega$ ,  $Q_2=7.3 \times 10^5$   $n_2=0.88$  even if this is not a very good fit. The physical structure of the passive layer of anodized 446 alloy is, probably, composed of a single layer showing a resistive behaviour at low frequencies and a quasi-capacitive behaviour.

The GR alloy show the best fit for model (ii). As can be seen both models can fit reasonable well the experimental findings. According to model (i) the passive layer after galvanostatic reduction behaves like a porous monolayer film ( $n=0.85$ ); according to model (ii) the passive layer has a heterogeneous structure composed of an external (low resistive porous,  $n=0.85$ ) and an inner (high resistive and quasi-capacitive,  $n=1$ ) layer.

Optimum fits, for the gamma-ray irradiated specimen, were obtained with model (i). Fit parameters are:  $R_1=71 \Omega$ ,  $R_2=9 \times 10^6 \Omega$ ,  $Q_2=8.6 \times 10^{-5}$   $n_2=0.95$ .

Time dependence of impedance,  $Z$ , and phase,  $\theta$ , are reported in Fig. 4a and 4b, for AISI 446 stainless steel sample after gamma-ray treatment (same behaviour has been found for other specimens), no difference exist at various exposure time at test solution, for all samples, showing that the oxide layer, before and after every treatments, is hard and compact. Because the value of impedance for high frequencies, that is related to resistance of solution, do not change and more, an visual inspection do reveal presence of any kind of compound, not even in this situation one has loose of ions or oxides.

Fig. 5 shows the capacitance,  $C^{(1)}$  vs frequency,  $f$ , for the bare, anodised and irradiated samples, it points out that the capacitive nature of the passive film is increased after gamma-ray irradiation. This could be attributed to an enrichment of Cr in the passive layer.

### Conclusions

Data presented in this paper further support earlier results on the nature and composition of passive film on AISI 446 and AISI 304L stainless steels. Main conclusions are: (i) the oxide layer on AISI 446 and AISI 304L after galvanostatic reduction is composed of two layers, the external one showing a spongy-like structure. (ii) the oxide film after gamma-ray irradiation is thinner and richest in the Cr content.

---

<sup>(1)</sup> Calculated as  $C=1/(2\pi fZ'')$ , in which  $f$  is the frequency and  $Z''$  is the imaginary part of impedance.

## References

- 1 K. Ishigure, N. Fujita, T. Tamura and K. Oshima, Nucl. Technol. 50,169,(1980).
- 2 M. Kawaguchi, K. Ishigure, N. Fujita and K. Oshima, Radiat. Phys. Chem. 18, 733, (1981).
- 3 D. H. Lister, R. D. Davidson and E. MacAlpine, Corr. Sci. 27, 113, (1987).
- 4 C.Y.Chao,L.F. Lin, D.D. Macdonald, J. electroch. Society, 129, 1974, (1982).
- 5 Impedance Spectroscopy, ed. J.R. Macdonald, J.Wiley and Son Inc. New York 1987).
- 6 J.R. Park,D.D. Macdonald, Corr. Sci. 23, 295 (1983).
- 7 K. Juttner, W.J. Lorenz, M.W. Kending, F. Mansfel, J. electroch. Soci. 135, 332 (1988).
- 8 K. Juttner, Electroch. Acta, 35, 1501, (1990).
- 9 D. H. Lister, E. MacAlpine and W. H. Hocking, Proc. Int. Eng. Soc. West PA43,242,(1982).
- 10 N. Sato Proc. Fourth Int. Simp. on Passivity, ed. R.P. Frankenthal, J. Kruger, The Electrchem. Soc., Princerton, New Jersey, 29, (1978).
- 11 G. Capobianco, G. Palma, G. Granozzi, A. Glisenti Corr. Sci., 33, 729, (1988).
- 12 B.A. Boukamp, Proc. 9th Eur. Con. Corr., Utrecht, The Netherlands, (1989), FU-252.
- 13 K.S. Cole, R.H. cole, J. Chem.Physi.,9,341, (1941).
- 14 J.R. Macdonald, J. electroan. Chem., 223, 25, (1987).

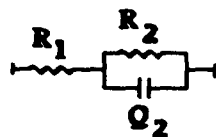
Tab. 1. Chemical composition of test materials, wt% (balance Fe).

	Cr	Si	Ni	P	Mo	Mn	C	N	S
AISI 446	26.5	.51		.19		.81	.18	.14	.03
AISI 304L	18.1		9.15	.03	.36	1.75	1.02		.016

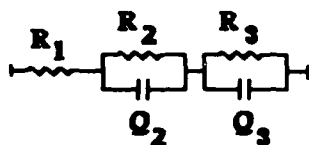
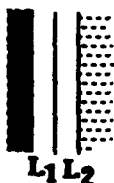
Tab. 2. Atomic percentage of passive layer on AISI446 computed taking into account only Fe and Cr atoms, at various etching times (in minutes) from XPS measurement. (AP=anodic oxidation, GR=galvanostatic reduction,  $\gamma$ I=gamma-ray irradiation)

	AP		GR		$\gamma$ I	
Etching time	0	6	0	6	0	6
Fe	$\approx 0$	70	7	70	13	72
Cr	$\approx 0$	20	2	20	3	27
Cr oxide	55	10	53	10	70	$\approx 0$
Fe oxide	42	$\approx 0$	38	$\approx 0$	14	$\approx 0$

Tab. 3. Physical model, discrete model and  $\chi^2$  values, for the AISI 446 stainless steel bare (B), anodised (AP), galvanically reduced (GR) and gamma-ray irradiated ( $\gamma$ I).



(i)



(ii)

B	AP	GR	$\gamma$ -I
$2.2 \times 10^{-2}$	0.12	$4 \times 10^{-3}$	$3 \times 10^{-3}$
1.63	0.2	$1.6 \times 10^{-4}$	$3 \times 10^{-2}$



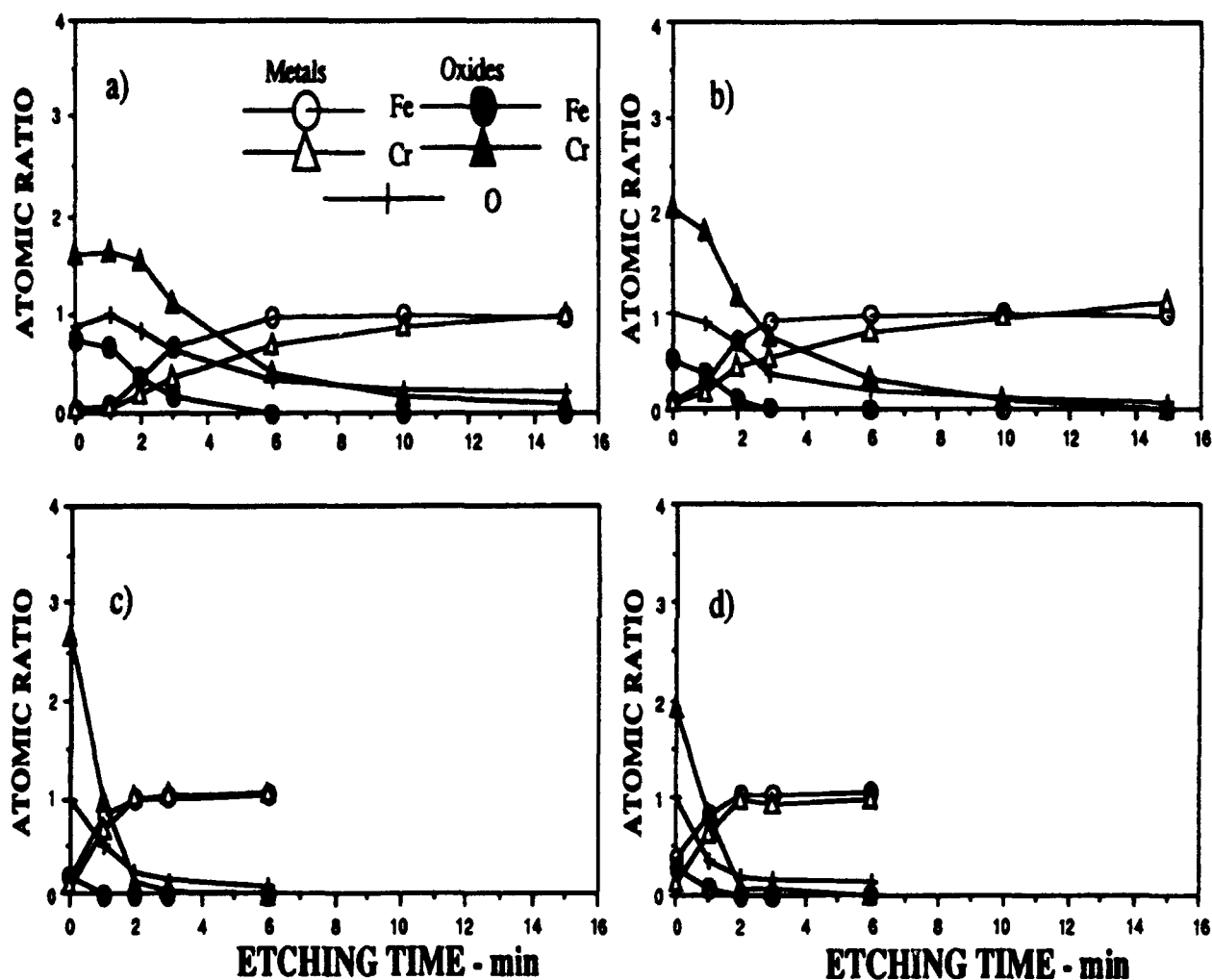


Fig. 1. XPS depth profiles of AISI 446 stainless steel samples ( $16 \text{ mCcm}^{-2}$ ) after : a) passivation, b) galvanostatic reduction ( $30 \text{ mAcm}^{-2}$ ), c) gamma-ray irradiation in deaerated water with 276 KGy, d) gamma-ray irradiation in deaerated methanol with 130 KGy.

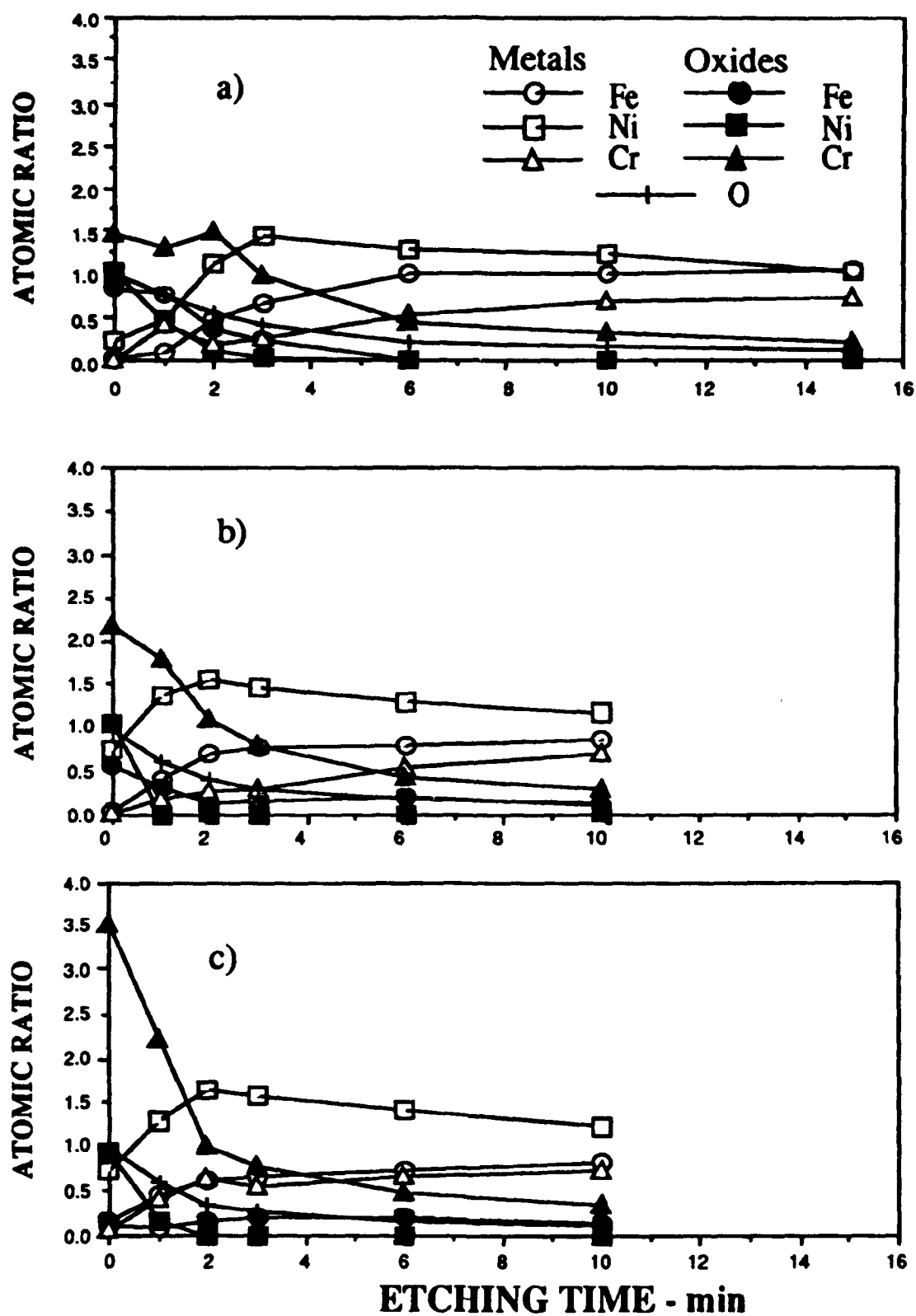


Fig. 2. XPS depth profiles of AISI 304L stainless steel samples ( $16 \text{ mCcm}^{-2}$ ) after : a) passivation, b) galvanostatic reduction ( $30 \text{ mAcm}^{-2}$ ) , c) gamma-ray irradiation in deaerated water with 276 KGy.

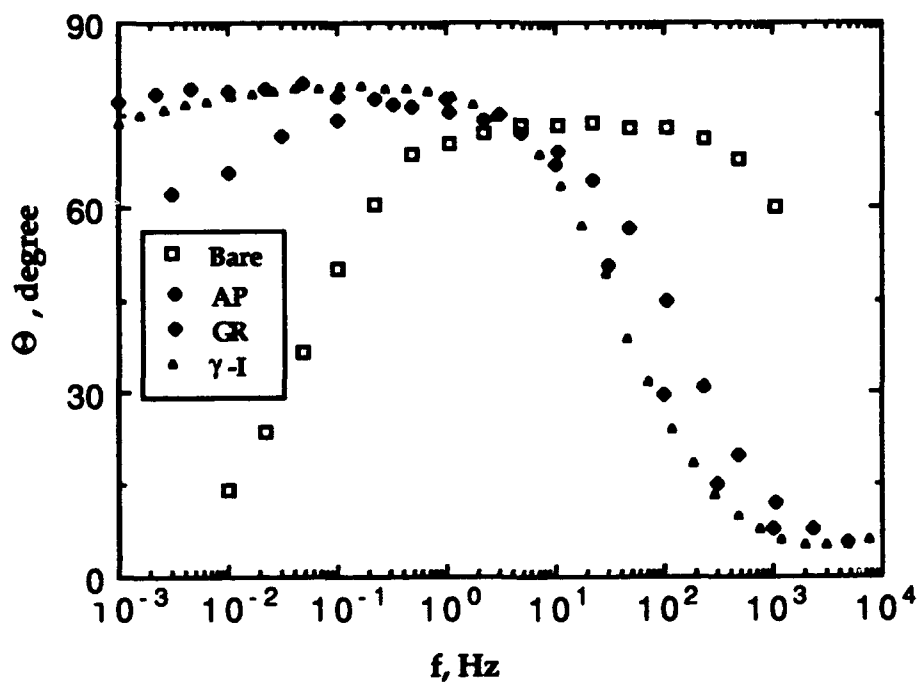
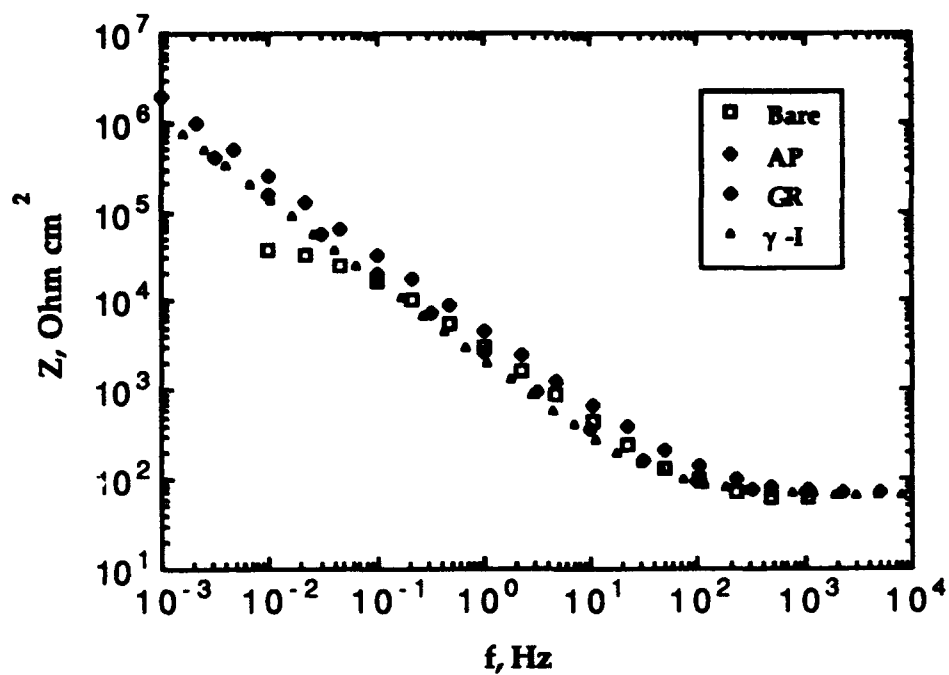


Fig.3. Bode (a) and phase angle (b) plot of bare , anodized (AP), galvanostatically (GR) and gamma-ray (gI) reduced 446 stainless steel in deaerated borate/boric buffer solution.

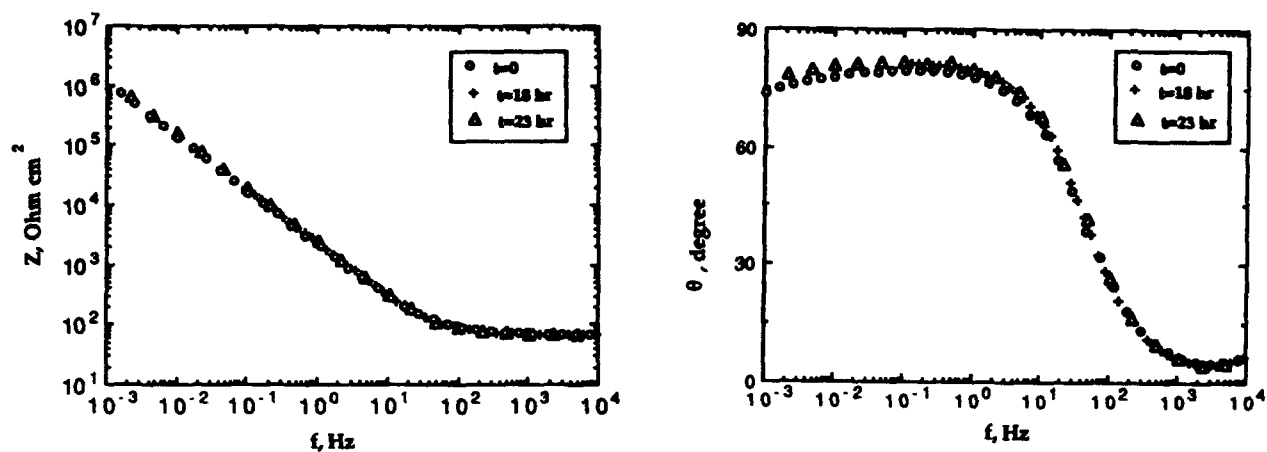


Fig. 4. Bode (a) and phase angle (b) plot of AISI 446 stainless steel sample gamma-ray treatment in deaerated borate/boric solution as a function of time.

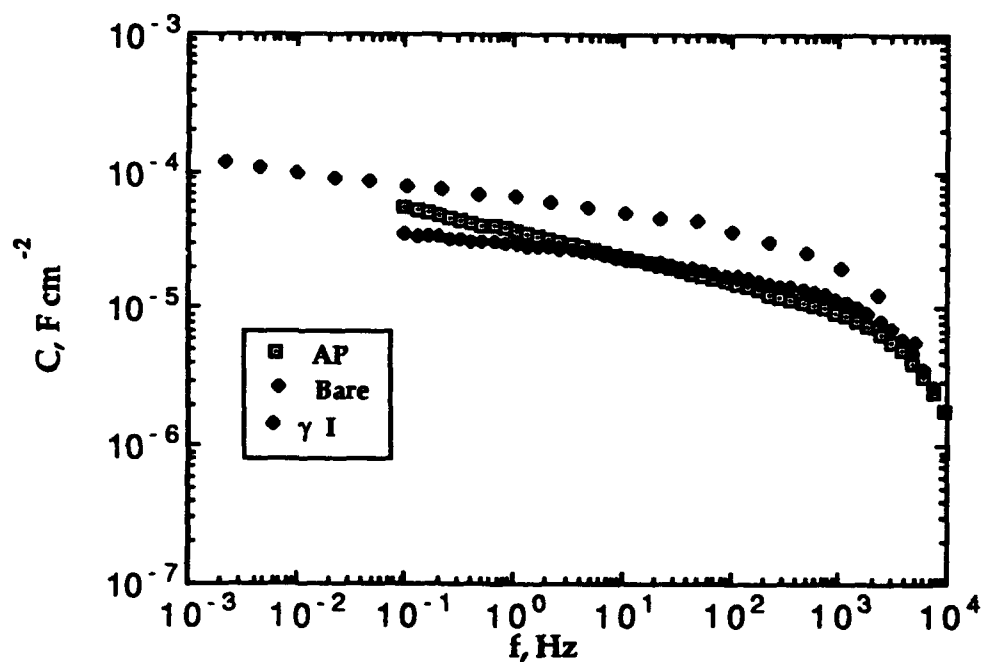


Fig. 5. Capacitance vs time for the bare, anodized (AP), and gamma-ray (gI) reduced AISI 446 stainless steel sample in deaerated borate/boric buffer solution.